NASA CR-72701
Aerotherm Report 71-36

FINAL REPORT

ABLATIVE RESPONSE OF A SILICA PHENOLIC TO SIMULATED LIQUID PROPELLANT ROCKET ENGINE OPERATING CONDITIONS

by

Mitchell R. Wool
Carl B. Moyer
Charles A. Powars
Roald A. Rindal

AEROTHERM CORPORATION
485 Clyde Avenue
Mountain View, California 94040

prepared for

NATIONAL AERONAUTICS AND SPACE ADMINISTRATION

June 1971

CONTRACT NAS3-10291

NASA Lewis Research Center
Cleveland, Ohio
Erwin A. Edelman, Project Manager
Liquid Rocket Technology Branch

ABSTRACT

The effect of off-optimum rocket engine operating conditions on ablative material performance is investigated theoretically and experimentally. Experiments are conducted utilizing an arc plasma generator as the energy source to simulate the products of combustion of N_2O_4 - N_2H_4/UDMH for mixture ratio varying from pure oxidizer to nearly pure fuel and for simulated characteristic velocity ratio from 0.85 to 1.10. Calorimetric measurements reveal a 70 percent heat-transfer-coefficient increase associated with surface roughness similar to the ablating surface. Silica phenolic nozzle test results reveal the strong dependence of ablation magnitude and character upon mixture ratio. For constant stream temperature minimum surface recession occurs for oxidizer-to-fuel mass ratio of 1.0 and departures from this (lean or rich) result in significant surface recession increases. Surface recession decreases with temperature for all mixture ratios. Ablation predictions sucessfully predict the trend and magnitude of ablation for high mixture ratio ($O/F \gtrsim 2.0$) and high simulated characteristic velocity ratio but fail to correctly predict the observed decrease in surface recession with decrease in characteristic velocity. Predictions of graphite phenolic ablation in a FLOX-propane rocket nozzle lead to the conclusion that consideration of only chemical erosion and the assumption of chemical equilibrium is adequate for representing important energy and mass transfer events for this material-propellant combination.

SUMMARY

Simulation of five oxidizer to fuel ratios of a liquid propellant rocket engine operating on N_2O_4 - 50 percent N_2H_4/50 percent UDMH over a wide range of off optimum propellant energy content were achieved, and the material response of MXS-89 silica phenolic to these environments was recorded. An arc plasma generator powered by a 1.1 megawatt DC power supply was utilized to heat the simulation gases. The following operating parameters which were identified as being important to the simulation were duplicated in the arc plasma generator tests:

1. Chemical composition of the free stream gas.
2. Total enthalpy of the free stream gas.
3. Boundary layer heat and mass transfer coefficients.
4. Chamber pressure.
5. The variation of nozzle area ratio in the streamwise direction in the throat region.

A total of 57 calorimetric tests and 35 MXS-89 silica phenolic ablative nozzle tests were performed. Nozzle throat calorimetric measurements revealed increasing heat transfer coefficient with decreasing stream energy content (C* ratio) and comparative measurements made with smooth and rough surface calorimeters revealed that surface roughness simulating the ablating surface results in a 70 percent increase in heat rate above smooth wall values. The matrix of test conditions obtained corresponded to all boundary conditions which would reasonably be expected to occur in a silica phenolic lined liquid propellant rocket engine. Trends in the silica phenolic ablation response mechanisms with respect to test stream composition and energy content are defined and possible explanations are offered. The data acquisition and presentation are sufficiently detailed that empirical ablation response laws could be defined. Although being strictly applicable to only the simulator operating conditions, these laws could be utilized to quantitatively assist in estimating the response of silica phenolic in an actual rocket nozzle (providing that suitable assumptions were applicable). In addition, sufficient basic data were accumulated to provide an experimental basis for the improvement and verification of current ablation analysis techniques.

Computational experiments using a specially modified ablation computer code to predict the response of the test models for O/F ratios of 2, 4, and ∞, were partially successful. Excellent agreement between observed and predicted recession was obtained for the high C* ratio case for a uniform set of values for the adjustable parameters of the code. This agreement spanned the O/F ratio range considered; the code reproduced the O/F dependence of recession exactly. The observed trend of recession rates with C* ratio was, however, not predicted by the program. The code predicted little change of recession rate with C* ratio, failing to match the observed decline of recession rates. Part of the trend discrepancy may stem from systematic trends in input quantities, particularly for convective transfer coefficient. Another contributing fact may be a departure from liquid layer control of the recession rate at low C* ratios. It is possible that the code was pushed beyond the range of its applicability in this respect.

Computations of ablative material response are presented for a graphite phenolic nozzle throat in a FLOX-propane environment. It is concluded that consideration of only chemical erosion and the assumption of chemical equilibrium is quite adequate for representing important energy and mass transfer events for this material propellant combination.

TABLE OF CONTENTS

Section		Page
1	INTRODUCTION	1
2	EXPERIMENTAL SIMULATION OF ROCKET-ENGINE ABLATIVE MATERIAL RESPONSE PHENOMENA	3
	2.1 EXPERIMENTAL APPROACH	3
	2.1.1 Simulation Requirements	3
	2.1.2 Simulation Technique	4
	2.1.3 Experimental Apparatus	9
	2.1.4 Test Procedures	11
	2.2 EXPERIMENTAL RESULTS	13
	2.2.1 Arc Plasma Generator Operating Conditions	13
	2.2.1.1 Simulation Gas Compositions	14
	2.2.1.2 Chamber Pressure and Test Durations	14
	2.2.1.3 Test Stream Enthalpy	15
	2.2.2 Heat Transfer Coefficient Boundary Conditions	16
	2.2.2.1 Calorimeter Heat Transfer Measurements	16
	2.2.2.1.1 Steady State Calorimeter Data	16
	2.2.2.1.2 Transient Calorimeter Data	17
	2.2.2.2 Heat Transfer Coefficient Data Correlation	21
	2.2.2.2.1 Comparisons to Theoretical Predictions	22
	2.2.2.2.2 Application of Results to Ablative Nozzle Tests	24
	2.2.3 Ablative Nozzle Response Measurements	26
	2.2.3.1 Nozzle Throat Recession Data	26
	2.2.3.1.1 Pre- and Post-Test Ablative Nozzle Dimension Measurements	26
	2.2.3.1.2 Inferred Recession and Recession Rate Histories	28
	2.2.3.2 Nozzle Thermal Responses	29
	2.3 SUMMARY OF OBSERVED SILICA PHENOLIC ABLATION RESPONSE TRENDS	30
	2.3.1 Trends in Post-Test Nozzle Appearances	30
	2.3.2 Trends in Recession Rate Data	32
	2.3.3 Ablation Response Mechanisms	33
3	ABLATIVE DATA CORRELATION USING ABLATIVE COMPUTER CODES	35
	3.1 DESCRIPTION OF COMPUTER CODES	35
	3.2 ASSIGNED SURFACE TEMPERATURE AND RECESSION RATE CALCUALTION TO BACK-OUT MATERIAL PROPERTIES	36
	3.3 ITERATIVE ABLATION CALCULATIONS ON SELECTED MODEL TEST CASES TO DEFINE CERTAIN COMPUTER CODE PARAMETERS	37
	3.4 ABLATION CALCULATIONS ON ALL MODEL TEST CASES WITH UNIFORM SET OF PARAMETER VALUES	42
	3.5 SUMMARY OF COMPUTATIONAL EXPERIMENTS	44

4 FLOX-PROPANE ROCKET ABLATION PREDICTIONS
4.1 COMPUTER PROGRAM INPUT 45
4.2 SUMMARY OF RESULTS 46
5 CONCLUSIONS AND RECOMMENDATIONS 48
5.1 CONCLUSIONS 48
5.2 RECOMMENDATIONS 49
APPENDIXES
A - AEROTHERM CHARRING MATERIAL ABLATIVE PROGRAM (CMA)
B - AEROTHERM CHARRING MATERIAL ABLATION PROGRAM AS MODIFIED FOR SILICA-CARBON REACTIONS INCLUDING MELTING PHENOMENA (SCRIMP)
C - AEROTHERM THERMOCHEMICAL STATE CODE (ACE)
D - SYMBOLS
REFERENCES

LIST OF TABLES

Table		Page
1	Simulation Gas Compositions	51
2	Arc Plasma Generator Test Conditions	52
3	Operating Conditions During Transient Calorimeter Tests	53
4	Summary of Ablative Nozzle Test Data	54
5	Summary of Calorimeter Nozzle Heat Transfer Coefficient Measurements and Predictions	55
6	General Appearances of Throat Surfaces	56
7	Overview of All Model Tests Showing Those Cases Studied by Assigned Surface Temperature & Recession Rate Computer Runs	57
8	Summary of Computed Results for Iterative Test Calculations SCRIMP Program	58
9	Summary of SCRIMP Program Prediction Results for all Test Models at O/F = 2, 4, and ∞, for Uniform Set of Parameter Values	58
10	Summary of Flox-Propane Rocket Test Conditions	59
11	Elemental Compositions of Constituents	60
12	Summary of Measured and Predicted Throat Responses of FM 5064, Graphite Phenyl-Aldehyde to Flox-Propane Propellant	60

LIST OF FIGURES

Figure		Page
1	Characteristic Velocity Ratio (C^*/C^*_{opt}) as a Function of Temperature for O/F = 2.0	61
2	Temperature-Enthalpy Characteristics for Various Oxidizer to Fuel Ratios of N_2O_4- N_2H_4/UDMH (50/50)	61
3	Enthalpy of Off-Optimum Mixture Ratio Required to Produce Temperature Corresponding to Indicated Characteristic Velocity Ratio for O/F of 2.0	62
4	Range of Rocket Engine Operating Conditions for Which Heat Transfer Coefficient is Simulated in Arc Plasma Device for N_2O_4-N_2H_4/UDMH Propellant	63
5	Rocket Nozzle & Arc-Plasma Test Nozzle Designed to Duplicate $A/A^* = f(x)$ for a Distance of 0.25 Inches (.0635 Meters) Up & Down Stream of the Throat	63
6	Simulation Apparatus Schematic	64
7	Arc Plasma Generator, Mixing Plenum, and Trap Door Assembly Schematic	64
8	Experimental Setup	64
9	Schematic Representation of Gas Metering and Control System	68
10	Chamber Pressure Histories for Ablative Nozzle Tests	69
11	Enthalpy Histories of Ablative Nozzle Tests	87
12	Enthalpy Histories of Transient Calorimeter Tests	105
13	Schematic Drawing of Typical Heat-Transfer Calibration Nozzle	115
14	Section Representation of the Copper Transient Calorimeter Nozzle	115
15	Section Representation of the Molybdenum Transient Calorimeter Nozzle	116

Figure		Page
16	Measured and Predicted Thermal Responses of the Transient Calorimeter	117
17	Heat Flux Histories for Copper Transient Calorimeter Tests	127
18	Heat Transfer Coefficient Histories for Copper Transient Calorimeter Tests	136
19	Molybdenum Transient Calorimeter Heat Flux Histories Predicted from Measured Thermocouple Data by Inverse Heat Conduction Code	145
20	Convective Transfer Coefficient Histories Derived From Transient Molybdenum Calorimeter Heat Flux Data	145
21	Ratio of Nozzle Throat Heat Transfer Coefficient Measured with Calorimeter to that Calculated from Bartz Equation for Same Conditions - As a Function of Characteristic Velocity	146
22	Predicted Profiles of Velocity, Total Enthalpy, and Temperature for a Fully Turbulent Boundary Layer at λ = 0.2067 for a Typical Steady State Calorimeter (Test 1109A O/F = 2.0)	148
23	Predicted Species Concentration Profiles for a Fully Turbulent Boundary Layer at λ = 0.2067 ft for a Typical Steady State Calorimeter (Test 1109A O/F = 2.0)	148
24	BLIMP Predictions of Heat Transfer Coefficient Distributions Showing Nozzle Geometry and Momentum Thickness Reynolds Number	149
25	Heat Transfer Coefficient Histories for Ablative Nozzles	150
26	Pre- and Post-Test Ablative Nozzle Throat Contours Including Measured Char Depth and Thermocouple Locations	160
27	Sectioning of Tested Ablative Nozzles	178
28	Photographs of Ablative Nozzle Wafers	179
29	Ablative Nozzle Setup for X-Ray Photography	188
30	Typical X-Ray Photograph of an Ablation Nozzle Showing In-Depth Thermocouple	188
31	Ablative Nozzle Recession Histories	189
32	Measured and Predicted Ablative Nozzle Thermal Response Histories	199
33	Thermocouple Installation in Ablative Nozzle Section	217
34	Photographs of Ablative Nozzle Throat Surfaces	218
35	Photographs of Ablative Nozzle Exit Characteristics	221
36	Average Surface Recession Rate as a Function of Characteristic Velocity Ratio	223
37	Photograph of Ablative Nozzle Response - Three-Dimensional Model	226
38	Effect of Test Gas Chemical Composition on MXS-89 Silica Phenolic Recession Rate at $C^*/C^*_{opt})_{O/F=2}$ of 1.0	227
39	MSX-89 Silica-Phenolic Thermal Conductivity Models	228
40	Parametric Calculations, Surface Temperature Results, Surface Recession, and Liquid Layer Thickness Results	229
41	Surface Thermochemical Response of FM 5064, Graphite Phenyl-Aldehyde to Flox-Propane Propellant	237
42	Specific Heat of FM 5064, Graphite Phenolic	238
43	Thermal Conductivity of 60° Layup FM 5064, Graphite Phenolic	238
44	Enthalpy of FM 5064, Graphite Phenyl-Aldehyde Pyrolysis Gases	239
45	Comparison of Measured and Predicted FM 5064 Graphite Phenyl-Aldehyde Response (Flox-Propane Propellant)	240
46	Predicted Temperature Responses for FM 5064 Graphite Phenyl-Aldehyde (Flox-Propane Propellant)	241

ABLATIVE RESPONSE OF A SILICA PHENOLIC TO SIMULATED LIQUID PROPELLANT ROCKET ENGINE OPERATING CONDITIONS

SECTION 1

INTRODUCTION

Silica phenolic ablative materials provide a low cost, reliable means of insulating rocket engine components from high temperature, corrosive combustion product environments. Specification of ablative material composition and thickness for adequate thermal protection with minimum weight requires that consideration be given to a number of high temperature thermal, chemical, and mechanical interactions between the ablative material and the environment to which it is exposed. The phenomena requiring quantitative specification include 1) boundary layer transfer rates of energy and chemical species to and from the ablating surface, 2) the rates of reactions between the combustion products, the char surface, and organic polymer degradation products, 3) the rate at which inorganic reinforcement fibers melt and are removed from the surface, 4) fragmentation and departure of portions of the char layer from the surface, and 5) energy, mass transfer, and chemical degradation events below the ablating surface. The complicated interactions of the phenomena do not readily lend themselves to quantification via simplifying analytical developments. Of necessity the rocket nozzle designer must utilize experimentation to provide insight into the effects of varying engine operating conditions, nonuniform propellant mixing, and film cooling techniques on the nozzle insulation material integrity. The experimental input which the designer requires may take the form of empirical material response laws. Alternatively, experimental data may be utilized to improve and verify analytical capabilities to the extent that analysis could be a more fruitful part of the ablative rocket nozzle design process. The primary purpose of the investigation described in this final report was to generate, for a particular material/propellant combination of interest, experimental information suitable for either of the above applications. A secondary objective was to continue the development of current ablative response prediction capabilities.

The effort was therefore performed to acquire and correlate experimental information on the response of MXS-89 silica-phenolic to a simulated nitrogen tetroxide-Aerozine rocket engine operating over a range of mixture ratios and combustion efficiencies. The experimental approach employed an arc-plasma generator to produce a high temperature, chemically reacting gas stream. The technique for simulating rocket exhaust streams in an arc-plasma generator was developed and reported in Reference 1 where successful operation was achieved on gases required for simulating two rocket exhaust environments: H_2-O_2, and nitrogen tetroxide-Aerozine. In the study reported in Reference 2, the

technique was further improved and ablation data for six materials were acquired for a simulated nitrogen tetroxide-Aerozine rocket engine operating at optimum conditions. The present investigation is directed toward acquiring ablation data for simulated "off-optimum" rocket engine conditions. The investigation is unique in that ablation data were obtained over a wide range of simulated mixture ratio and combustion efficiency, each being varied independently. The basic experimental approach (Refs. 1 & 2) consists of heating appropriate gas mixtures with an arc-plasma generator such that a wide range of test stream energy content may be achieved for a given mixture ratio. Conversely, the energy content may be held constant while varying test gas composition to simulate a wide mixture ratio range. The experiments were accompanied by measurement of many parameters necessary for correlation of ablative material phenomena. The basic experimental approach and results are presented first, in Section 2, and are followed, in Section 3, by a description of data correlation efforts employing ablation computer codes. An additional task of this program was the prediction of graphite-phenolic ablation in the throat of a FLOX-Propane rocket engine. These calculations are compared to measured data in Section 4. Conclusions and recommendations for further efforts are presented in Section 5.

SECTION 2

EXPERIMENTAL SIMULATION OF ROCKET-ENGINE ABLATIVE MATERIAL RESPONSE PHENOMENA

An experimental program has been conducted to characterize the ablation of silica-phenolic in a nitrogen tetroxide-Aerozine rocket engine environment. A wide range of off-optimum conditions were simulated including oxidizer-to-fuel mass ratio (O/F) ranging from 0.38 to ∞ and gas stream energy content corresponding to characteristic velocity ratios (C^*/C^*_{OPT}) ranging from 0.85 to 1.05. The experimental approach is presented first and is followed by a presentation of all test results.

2.1 EXPERIMENTAL APPROACH

The experimental approach is described in four parts:

1. Simulation requirements.
2. Simulation technique.
3. Test apparatus.
4. Test procedure.

2.1.1 Simulation Requirements

In Reference 2 consideration is given to necessary simulation parameters for duplicating degradation mechanisms for a variety of material types. Duplication of parameters in the following list is rationalized as adequate for investigating degradation of silica-phenolic type materials:

1. Chemical compostion of the free-stream gas.
2. Total enthalpy of the free-stream gas.
3. Boundary layer heat and mass transfer coefficients.
4. Chamber pressure.
5. A/A* = same function of S in subscale and full scale experiments.

The first three parameters above are of primary importance for chemical erosion since they govern the reactivity of the chemical species approaching the surface, the rate at which chemically reactive species are transported to the surface, and the surface heat transfer rate which, for a given ablation material, establishes the surface temperature. The importance of the pressure depends on the degree of chemical equilibrium

achieved at the ablating surface. If chemical equilibrium is achieved, the chemical ablation rate will not change substantially for a chamber pressure change of a factor of 2 or 3, provided the first three items are held fixed. The last parameter (area ratio as a function of distance) is included in the above list because of a desire to model liquid layer removal phenomena. Duplication of liquid layer flow would require duplicating nozzle geometry and size upstream of the point of interest; however it is argued in Reference 2 that local modeling of liquid layer flow will result if the streamwise derivatives of shear and pressure gradient are duplicated ($d\tau_w/ds$, and d^2P/ds^2). If the levels of shear and pressure are duplicated, then duplication of area ratio as a function of distance will result in duplicating the derivatives of shear and pressure as well.

The above list of simulation parameters is based upon reasonable assumptions and is believed to represent most of the significant phenomena which affect degradation of ablative materials. The experimental ablative material test program includes the following two considerations in its primary objectives: (1) to duplicate, as nearly as possible, each of the five parameters in the above list, and (2) to monitor accurately each of the five parameters so the observed results may be employed to infer what the material response would be in the actual application being considered.

The above discussion has been perfectly general with respect to material, environment, and experimental simulation device. In the following sections consideration is given to simulating the environmental characteristics of the throat region of a rocket nozzle. The propellant considered is N_2O_4 - N_2H_4/UDMH and the experimental device is an arc-plasma generator.

2.1.2 Simulation Technique

The parameters to be duplicated for a meaningful ablative material test have been identified. In this section, a specific technique is described for achieving duplication of the requisite simulation parameters for a rocket engine operating on N_2O_4 - 50% N_2H_4/50% UDMH propellant. A wide range of arc plasma generator operating conditions are utilized to simulate "off optimum" rocket engine operation. The correspondence between the plasma generator test conditions (chemical composition and enthalpy) and the liquid propellant rocket conditions (local mixture ratio and overall C*) is not obvious. In a rocket engine off optimum conditions result from a number of non-ideal events which include incomplete mixing and non-adiabatic combustion. For the arc-plasma generator, however, all chemical species are completely mixed and are effectively in overall thermodynamic equilibrium, but their compositions and energy content may be varied over wide ranges independently.

For the present investigation, the "off optimum" rocket operating conditions simulated by the arc-plasma generator were defined consistent with the following assumptions about flow in the rocket nozzle:

1. The relation between characteristic velocity and total temperature is defined by one-dimensional isentropic flow of the optimum rocket mixture ratio (O/F of 2.0).
2. "Off optimum" characteristic velocities are simulated by adjusting the total temperature of the arc heated gases.
3. Local mixture ratios at the boundary layer edge in the rocket nozzle are in thermodynamic equilibrium and are at the total temperature defined by the above assumptions.

The first assumption acts as the basis to relate simulation gas energy content directly to rocket engine performance. Moreover, since simulation test ablation data must be taken in terms of stream energy, it is the only basis for directly relating the measurements to an anticipated rocket engine performance. The most fruitful and meaningful use of the arc-plasma generator data is, of course, to utilize it in combination with the accurately known surface boundary conditions to adequately characterize the important ablative phenomena and then, to utilize this basic understanding to predict the rocket engine performance.

In a rocket engine, the characteristic velocity is an easy-to-measure indicator of overall combustion efficiency. This combustion efficiency has been employed in the manner described above as a guide for selecting simulation gas energy content for "off-optimum" conditions. The characteristic velocity is defined as follows:

$$C^* = \frac{P_c A^*}{\dot{m}} \qquad (1)$$

where P_c = chamber pressure
A^* = throat area
$\dot{m}$ = propellant mass flow rate

The ratio of measured-to-ideal C* for equilibium isentropic flow is typically designated the characteristic velocity ratio (C^*/C^*_{OPT}). For the arc-plasma generator tests, the results are reported in terms of the effective (C^*/C^*_{OPT}) for an O/F of 2.0 mixture of N_2O_4 - N_2H_4/UDMH operating at the equilibrium total temperature determined from the measured enthalpy. This quantity is notated as $C^*/C^*_{OPT})_{O/F\,=\,2}$. This characteristic velocity ratio is shown in Figure 1 as a function of temperature. For purposes of establishing the chamber-temperature range-of-interest a nominal O/F ratio of 2.0 is assumed and characteristic velocity ratios ranging from 0.85 to 1.0 are considered. It is noted from Figure 1 that

this characteristic velocity range corresponds to chamber temperatures ranging from 4500°R to 5700°R (2500°K to 3165°K).

The experiments were conducted over a wide range of mixture ratio ($0.38 \leq O/F < \infty$) and chamber temperature (4500°R to 5700°R). The resulting data may be correlated with such fundamental parameters as chemical composition and enthalpy or with more gross parameters such as characteristic velocity ratio.

The desired levels of the various simulation parameters are achieved by introducing a specially tailored gas mixture to an arc-plasma generator, by dissipating the appropriate amount of electrical energy to increase the gas total enthalpy to correspond to that in the rocket engine, and then by expanding this high temperature gas mixture through an ablative material test nozzle. Each of the parameters is listed and the means of achieving duplication are given here:

Simulation Gas Elemental Composition (K_{ke}) - The simulation gases selected for a particular propellant environment are established by considering the chemical composition of the propellant. The quantity of each chemical element in the simulation gas mixture is required to equal that in the propellant. The following chemical balances may be written between the propellant (on the left) and the simulation gases (on the right) for the mixture ratios considered in this program assuming 33.3 grams of fuel in each case:

$O/F = 0$

$$\overbrace{0.52\ N_2H_4 + 0.277\ C_2N_2H_8}^{\text{Propellant}} \rightarrow \underbrace{0.797\ N_2 + 1.594\ H_2 + 0.277\ C_2H_4}_{\text{Simulation Gas}} \qquad (2)$$

$O/F = 0.38$

$$0.1385\ N_2O_4 + 0.52\ N_2H_4 + 0.277\ C_2N_2H_8 \rightarrow 0.936\ N_2 + 0.554\ CO + 2.148\ H_2 \qquad (3)$$

$O/F = 1.0$

$$0.363\ N_2O_4 + 0.52\ N_2H_4 + 0.277\ C_2N_2H_8 \rightarrow 1.160\ N_2 + 1.804\ H_2 + 0.554\ CO_2 + 0.344\ H_2O \qquad (4)$$

$O/F = 2.0$

$$0.725\ N_2O_4 + 0.52\ N_2H_4 + 0.277\ C_2N_2H_8 \rightarrow 1.522\ N_2 + 0.356\ H_2 + 0.554\ CO_2 + 1.792\ H_2O \qquad (5)$$

O/F = 4.0

$$1.45\ N_2O_4 + 0.52\ N_2H_4 + 0.277\ C_2N_2H_8 \rightarrow 2.247N_2 + 0.554\ CO_2 + 1.272\ O_2 + 2.148\ H_2O \quad (6)$$

O/F = ∞

$$N_2O_4 \rightarrow N_2 + 2O_2 \quad (7)$$

The above chemical balances serve to illustrate the simulation gas composition employed for duplicating the elemental make-up for each mixture ratio. Duplication of the molecular composition will also result if the total enthalpy and pressure match those of the rocket engine to be simulated.

It was initially intended to operate with a simulated O/F ratio of 0 as shown by reaction (2) above. Subsequent efforts to accomplish this experimentally however were accompanied by the production of much soot as a result of ethylene decomposition. This was an unrealistic modeling of rocket phenomena. The substitute O/F ratio (0.38) shown in Reaction (3) was selected on the basis of being as low as possible without resulting in soot production. That is, all carbon is injected in the form of stable carbon monoxide.

The mass fractions of each of the gases required for precise duplication of the particular propellant mixture ratios is shown in Table 1.

Total Enthalpy (H_o) - The desired total enthalpy of the simulation gas mixture is obtained by arc-heating the gas with the appropriate amount of electric energy. The amount of arc-heating required is determined by considering the enthalpy of the propellant and the enthalpy of the simulation gas mixture. The enthalpy of the injected simulation gas is evaluated from

$$H_{inj} = \sum K_i \left[\int_{T_d}^{T_i} C_{pi}\,dt + \Delta H_{f_i}^{T_d} \right] \quad (8)$$

The temperature, T_i, is the injection temperature for each simulation gas species, i, and T_d is the enthalpy datum temperature. The amount of energy which must be added to the simulation gas by the arc-heater is equal to the difference between the desired total enthalpy and the enthalpy of the injected simulation gases.

$$\Delta H_{arc} = H_o - H_{inj} \quad (9)$$

The range of desired total enthalpy (H_o) is shown for each mixture ratio in Figure 2 as a function of total temperature. Figure 2 in conjunction

with Figure 1 enables relating total enthalpy for each mixture ratio to the characteristic velocity ratio for O/F = 2.0. Figure 3 shows the enthalpy for various mixture ratios required to produce the chamber temperature corresponding to a range of characteristic velocity for O/F = 2.0.

Heat Transfer Coefficient ($\rho_e U_e C_H$)- The relationship between the heat-transfer coefficient in a simulation test and a rocket engine may be evaluated approximately by referring to the simplified Bartz equation (Ref. 4). This equation is approximate, but it does give a relatively accurate indication of the change in heat-transfer coefficient with chamber pressure and throat diameter. Utilizing the simplified Bartz equation and forming the ratio of heat-transfer coefficients in the arc (sub A) and rocket (sub R) yields:

$$\frac{(\rho_e U_e C_H)_A}{(\rho_e U_e C_H)_R} = \left(\frac{P_A}{P_R}\right)^{0.8} \left(\frac{D_R^*}{D_A^*}\right)^{0.2} \qquad (10)$$

where C_H is the Stanton number defined by:

$$q_w = \rho_e U_e C_H (H_r - H_w)$$

In order to duplicate the heat-transfer coefficient ($\rho_e U_e C_H$), the ratio in Equation 10 must equal unity. It is apparent that if the pressure is to be duplicated ($P_A = P_R$), then the throat diameter in the simulation test must equal that in the rocket as well ($D_A^* = D_R^*$). In an arc plasma generator, for a given pressure and enthalpy (ΔH_{arc}), the throat diameter is limited by the available electrical power. Giving consideration to chamber pressures in the vicinity of 100 psia with typical propellants, the present Aerotherm constrictor arc unit is limited to throat diameters in the range of 0.3 to 0.5 inch. With this restriction on throat diameter, or for any subscale test, the simulation test pressure must be less than the actual case in order to duplicate the heat-transfer coefficient.

As discussed in Reference 2, duplication of the heat-and-mass-transfer coefficients is of prime importance, while pressure duplication is of secondary importance. Based on this premise, it is reasonable to sacrifice pressure duplication in order to achieve heat-transfer-coefficient duplication. Duplication of the mass-transfer coefficient will result directly if the heat-transfer coefficient is duplicated since the boundary-layer Lewis number will be the same in the simulation test and rocket engine.

Employing equation 10, rocket-nozzle heat transfer coefficient simulation capabilities for the N_2O_4 - N_2H_4/UDMH environment are shown in Figure 4. Shown in the figure are established operating conditions and lines of

constant heat-transfer coefficient. The shaded region between the lines represents the range of rocket engine operating conditions for which duplication of throat heat transfer coefficient may be achieved in the simulation device. It is noted that as ablation of the throat occurs the throat diameter will increase which will result in a drop in chamber pressure and heat transfer coefficient. Simulation tests are normally continued until the chamber pressure has dropped from 100 psia to 50 psia. This corresponds to a change in throat diameter from 0.30 to 0.43 inches. The two operating conditions shown in Figure 4 correspond to initial and final test conditions.

Area Ratio Variation, $A/A^* = f(s)$ - The test nozzle area ratio variation for the present test series was selected to be the same as reported in Reference 2. In Reference 2 the test nozzle area ratio variation was selected to match the area ratio variation in a particular rocket nozzle. Both the rocket nozzle and arc-plasma simulation nozzle contours are shown in Figure 5. Although the present test series was not directed at simulating conditions in a particular engine, utilization of the same nozzle geometry as previously employed better enabled comparisons to be made with previous results.

2.1.3 Experimental Apparatus

The experimental apparatus for simulating rocket nozzle ablative material performance is a modification of the apparatus described in Reference 2. The basic apparatus consists of an arc-plasma generator to add energy to a gas stream; a mixing plenum chamber in which the arc-heated and other simulation gases are introduced for mixing to achieve mechanical, thermal, and chemical equilibrium; a nozzle test section designed to provide well defined and repeatable boundary layer heat-and mass-transfer coefficients; and a gas metering and control system.

An overall simulation apparatus schematic is shown in Figure 6 which represents the major apparatus components and their relation to each other. The present experimental program was performed in two facilities. The first half (Series A) of the experiments were conducted in Aerotherm's previous experimental facility located in Palo Alto, California. The DC power supply for these tests consisted of two railroad diesel electric units operated in parallel to provide up to 1.2 megawatts. The second half of the experiments (Series B) were performed in Aerotherm's new facility located in Mountain View, California. The new facility has a 1.1 megawatt rectifier power supply which provides substantially more versatility in available voltage - current combinations.

Modifications to the basic experimental apparatus described in Reference 2 consisted of the following:

1. A new arc-plasma generator unit which enables increased power levels and better control was installed.
2. A new mixing plenum chamber was fabricated with provision for exhausting the simulation gas mixture through a bypass port and then switching the flow from the bypass to the test nozzle during a firing. This bypass flow and switching system enables keeping the high temperature flow away from a test nozzle during the start-up transient while operating conditions are being established. After the desired values of gas flow rates and electrical energy input have been obtained, the flow is switched from the bypass line to the nozzle test section, thus producing an instantaneous exposure of the test nozzle to the desired boundary conditions.
3. Gas handling and control systems for accomodating the several different gas mixtures required for simulating five different oxidizer-to-fuel ratios were added. The gas flow control system for the different simulation mixtures is described in the following section.
4. A new hot water heater was added prior to these tests. The old hot water heater, (which provided cooling water to the mixing plenum chamber) tended to produce a surging flow which made it difficult to perform a steady state energy balance on the apparatus.

The modified simulator system is shown in Figures 7 and 8. Figure 7 is a section view of the mixing plenum with a bypass port and test nozzle in place. The figure illustrates the relative location of primary (arc-heated) and secondary flow injection ports, the location of the gas bypass port, the position of the test nozzle, and the trap door assembly for flow transfer. The purpose of the bypass port and trap-door assembly is to provide the means for establishing desired test conditions prior to exposing the test nozzle to the high-temperature environment. The bypass flow port leads to a heat exchanger for cooling the simulation gases, and then to a flow control valve, and a solenoid valve. When the primary and secondary flow rates have been established, and the desired arc-energy input level is obtained, the flow control valve is adjusted until the plenum pressure reaches the value it will have when all flow is going through the test nozzle. During this period, cold nitrogen gas enters through the trap door and passes over the test nozzle to keep it cool. After the desired plenum conditions have been achieved (10-15 seconds), the trap door is opened and the bypass solenoid is closed. The transfer process is completed in less than a second.

An overall view of the experimental apparatus is presented in Figures 8(a) through 8(f). Figures 8(a) and (b) are end views (looking into the nozzle) with the trap door in the open and closed positions respectively. Figures 8(c) and (d) are side views of the plenum section with the door open and closed respectively. These figures also show the tubular heat

exchanger on the bypass control system which runs from the plenum chamber to the bottom of the picture. Figure 8(e) is an overall side view of the entire apparatus showing the arc-plasma generator on the right and the old (Series A) hot water heater on the extreme left. The hot water heater supplies high temperature water for cooling the plenum chamber. Figure 8(f) shows an end view of the apparatus with the water-cooled calorimeter in place.

The test apparatus instrumentation for measuring heat transfer coefficient and ablative material response is described subsequently along with a presentation of the test data.

2.1.4 Test Procedures

The test procedures for the arc-plasma generator tests performed in this program are described in this section. The procedure for each gas mixture used was slightly different because of the various flow systems required. In addition, the use of hydrogen required special handling systems and pre- and post test purging procedures. A general test procedure applicable to all gas mixtures is described first and is then followed by specific requirements for each gas mixture.

The basic test procedure utilized for all tests is as follows:

1. The test nozzle is mounted, the trap door is closed and sealed, and the by-pass port is opened.
2. All auxiliary supply systems such as the hot water generator, the boilers, and the power supply are prepared.
3. Pre-test instrumentation calibration is performed.
4. Cooling water systems, including plenum hot water preheat (if needed) are started.
5. Gas sources are opened to operator's console; supply lines are pressurized to the arc test stand; and trap door purge flow is started and checked.
6. Primary and plenum start gas flows are set.
7. Voltage is applied to the arc, and the arc is started with a radio frequency spark.
8. Shortly after arc start, solenoid valves transfer flow from purge to test gases as required.
9. Flow rates are checked and adjusted if necessary.
10. Arc current is adjusted to achieve the desired arc-plasma generator test condition.
11. Trap-door is opened and by-pass port is closed.

12. Interruption of electrical current terminates the test and returns all gas systems to their off or purge conditions via solenoid valves.
13. Flammable gas system is completely purged.

A schematic representation of the gas metering and control system required for the gas mixtures tested in this program is shown in Figure 9. This schematic is a composite for the following five systems:

System 1:
O/F = ∞, Source 2: N_2
Source 3: O_2

System 2:
O/F = 4.0, Source 1: CO_2
Source 2: N_2
Source 3: O_2
steam

System 3:
O/F = 2.0 Source 1: H_2
Source 2: N_2
Source 3: CO_2
steam

System 4:
O/F = 1.0 Source 1: H_2
Source 2: N_2
Source 3: CO_2
steam

System 5
O/F = 0.38 Source 1: Mix S (CO and H_2)
Source 2: N_2

By comparing the above list to Figure 9, the specific plumbing and control systems used for any particular gas mixture are defined. Gas systems 3, 4, and 5 were the only ones requiring special purge flow procedures because of flammable gases. For these tests the flow rates of the flammable gases were pre-set during calibration runs by the hand operated throttle valve (see Figure 9). Two solenoid valves were therefore placed in the Source 1 system to provide a dual on-off capability only. The first was automatically controlled by the power supply and could only be open while the arc was running. The other was manually actuated when the flammable gases were desired.

For systems 1 and 2 (the non-flammable gas mixtures), both primary and secondary gas flows were controlled by standard hand throttling valves.

Arc ignition was accomplished on the nitrogen primary flow and then plenum injections flows were adjusted by hand while the arc was running.

2.2 EXPERIMENTAL RESULTS

A detailed definition of the simulation environments and the corresponding nozzle responses requires the acquisition of a large quantity of data. All of the pertinent raw data needed for interpretation and analysis of the material/propellant interactions are included in this section. In addition, basic results derived directly from the raw data are also included here. All results from both the Series A and the Series B test programs are given.

The test data may be conveniently divided into three categories;

- Arc plasma generator (APG) operating test conditions
- Heat Transfer coefficient boundary conditions
- Ablative nozzle response data

The APG test conditions are the specified independent variables which control the boundary conditions during ablative nozzle tests. In order to firmly establish these test conditions, numerous arc plasma generator calibration tests were run utilizing a water cooled, steady state calorimeter nozzle which had the same basic dimensions as the ablative nozzles. All important arc plasma generator test condition data for calibration tests, calorimeter tests, and ablative nozzle tests are presented in Section 2.2.1. The heat transfer coefficient boundary conditions for each ablative test must be inferred secondarily from calibration test data. All measured calorimeter response data, a discussion of the techniques utilized to correlate the heat transfer data and the resulting ablative nozzle transfer coefficient boundary conditions are presented in Section 2.2.2. Finally, the measured surface and in-depth response of each ablative nozzle tested is given in Section 2.2.3.

2.2.1 Arc Plasma Generator Operating Conditions

As was explained in Section 2.1, the Aerotherm arc plasma generator is a versatile tool for the production of precise and accurately defined thermal and chemical environments. In a typical APG test, all of the following system properties may be independently defined:

- Test stream chemical composition.
- Total enthalpy (or temperature).
- Total (or local) pressure.

In this section, all useful measurements of these independent variables as well as other pertinent quantities are presented.

Table 2 gives detailed arc plasma generator operating data for nearly all test conditions at which ablative nozzles were tested. Condition numbers are in most cases useful in relating calibration test data to the corresponding transient calorimeter and ablative nozzle test results. In some cases, only extremes in enthalpy for a given oxidizer to fuel ratio were calibrated and subsequent conditions were defined between the extremes without the need for calibration or calorimeter tests. Tables 3 and 4 summarize measured arc plasma generator operating conditions obtained during the transient calorimeter and ablative nozzle tests. The independent operating variables presented in Tables 2,3, and 4 are discussed in the following four subsections. Other information given in these tables are discussed subsequently in Sections 2.2.2 and 2.2.3.

2.2.1.1 Simulation Gas Compositions

As explained in Section 2.1, the actual fuel and oxidizer compositions have been replaced by various amounts of nitrogen, oxygen, hydrogen, carbon monoxide, carbon dioxide, or steam. The chemical composition of the test stream is therefore defined by the relative amounts of these injected species. The mass fractions of each of the injected species required to simulate each O/F ratio were presented in Table 1. Tables 2,3, and 4 present those relative amounts which were determined from mass flow rate measurements during each test in this program. Other gas composition related data which are included in the tables are the nominal O/F ratio, the equivalent N_2O_4 mass fraction and the total mass flow rates.

It should be noted that the maximum error of any one injected test gas was below 2 percent. This is felt to be well within the accuracy required for the simulation tests.

2.2.1.2 Chamber Pressure and Test Durations

A nominal maximum chamber pressure of 100 psia (6.8 atm) was achieved in all tests. For typical ablative nozzle tests, where recession was important, the chamber pressure decayed from the nominal value as the nozzle throat area increased. For these cases the tests were terminated when chamber pressure had decayed to one-half its initial value; i.e., 50 psia (3.4 atm). For those tests where no recession occurred, tests durations were a minumum of 130 seconds, but in some cases, as much as 225 seconds.

In Tables 2 and 3, the measured chamber pressures obtained in the calibration and transient calorimeter tests are given. The variation of chamber pressure with time during each ablative nozzle test is shown graphically in Figure 10a through 10ii and the maximum and minimum values for each test are listed in Table 4. Also tabulated are the total exposure times for each nozzle.

2.2.1.3 Test Stream Enthalpy

Evaluation of the energy added to the simulation gas by the arc plasma generator is accomplished by a system energy balance technique. The net power input to the gas is obtained by subtracting losses to the arc cooling water from the total electrical power dissipated into the gas. The net enthalpy increase of the gas is then obtained by dividing the net power to the gas by the total mass flow rate of gas; i.e.,

$$\Delta H_{arc} = \frac{\text{Electrical Power Input - Rate of Coolant Energy Increase}}{\text{Simulation Gas Flow Rate}} \qquad (11)$$

An alternate form of equation 11 is written in terms of arc efficiency

$$\Delta H_{arc} = \frac{\text{Efficiency x Voltage x Current}}{\text{Simulation gas flow rate}}$$

where

$$\text{Efficiency} = \frac{\text{Electrical Power Input - Rate of Coolant Energy Increase}}{\text{Electrical Power Input}}$$

For each calibration test, Table 2 gives the arc current, arc voltage, overall efficiency and enthalpy increase of simulation gas. The test stream total enthalpy is then represented by the sum of the enthalpy of the injected gases (H_{inj}) and the energy added by the arc (ΔH_{arc})

$$H_o = H_{inj} + \Delta H_{arc} \qquad (12)$$

The values of total enthalpy and injected gas enthalpy are also presented in Table 2 for each calibration test.

Evaluation of the enthalpy history is subject to more error than the other measurements because the rate of energy loss to the cooling water is between 70 and 80 percent of the electrical power input and errors in the measurement of either quantity tend to be amplified. A further difficulty in the measurement of stream total enthalpy for transient colorimeter and ablative nozzle tests is associated with the somewhat transient behavior of the electrical power input and energy loss rates to cooling water. The calculated enthalpy histories shown in Figure 11 for the ablative nozzle tests and Figure 12 for transient calorimeter tests, have resulted from rather careful consideration of these transient effects to the

extent that time lags between a measured power input fluctuation and the corresponding cooling water energy increase fluctuation have been accounted for. It will be noted from the results that in some instances, significant total enthalpy fluctuations still remain. Study of the primary data indicate that these trends are real. For convenience, time integrated average enthalpy values are also given for applicable tests in Tables 3 and 4. In addition, for each value of total enthalpy given in Tables 2, 3 and 4, the corresponding values of total stream temperature and equivalent $C^*/C^*_{OPT})$ O/F=2 are given. These correspondence were defined via Figures 2 and 3 (see Section 2.1).

2.2.2 Heat Transfer Coefficient Boundary Conditions

Because the boundary layer heat transfer phenomena which occur in an ablative nozzle test can never be precisely duplicated in either steady state or transient calorimeter experiments, a certain amount of theoretical and empirical adjustment to the calorimeter data is required to obtain the ablative nozzle heat transfer coefficient boundary conditions. All important calorimeter data are discussed in Section 2.2.2.1 and the basic calorimetric information are then presented. The correlation and subsequent application of this data to ablative nozzle tests are described in Section 2.2.2.2.

2.2.2.1 Calorimeter Heat Transfer Measurements

Data taken during steady state calorimeter tests are described in Section 2.2.2.1.1 and transient calorimeter data are presented in Section 2.2.2.1.2.

2.2.2.1.1 Steady State Calorimeter Data

The 0.3 inch diameter steady state calorimeter nozzle which is described in Reference 2 was reused in this program for each arc plasma generator calibration test. Figure 13 shows a schematic drawing of this nozzle. The figure shows two throat segments although for some calibration tests only one was utilized. Because the exposed surfaces of this nozzle were all water cooled, heat transfer data were only taken when the arc operating conditions had reached steady constant values.

The measurement of the energy increase of the cooling water flowing in the throat segments of this nozzle, combined with a knowledge of the heat transfer area gave the throat heat transfer rate per unit area. Those data have already been presented in Table 2. Also given there are the calculated values of calibration test heat transfer coefficient

based on enthalpy potential. This quantity is defined as follows:

$$\rho_e U_e C_{H_o} = \frac{q_{cw}}{H_o - H_w} \tag{13}$$

where H_o is the test stream total enthalpy and H_w is the enthalpy of the test stream gas in equilibrium at the calorimeter surface temperature, here taken as 720°R (400°K).

2.2.2.1.2 Transient Calorimeter Data

There were three types of transient calorimeter data utilized in this experimental test program. These were (1) a smooth wall copper calorimeter nozzle, (2) a smooth wall, molybdenum nozzle, and (3) a molybdenum calorimeter nozzle with a mechanically roughened internal surface contour. The copper calorimeter was utilized in the Series A test program to obtain additional data on the convection of energy in the various simulation gas environments. A schematic diagram of the copper transient calorimeter is shown in Figure 14. The design is identical to the transient calorimeter described in References 1 and 2. Tests of this nozzle were important because the surface temperatures achieved during the transient response of the calorimeters were higher than the condensation temperatures of the H_2O in the test gas stream (about 720°R). Data taken by this instrument are, therefore, expected to represent ablative nozzle test events more accurately than did the steady state, cold wall calorimeter used in the calibration tests.

The molybdenum nozzles which were tested in the Series B program were a further attempt to accurately simulate with a calorimeter nozzle the convective heat transfer phenomena which occur in ablative nozzle tests. Molybdenum was selected because its melt temperature is much higher than that of copper, (2883°K compared to 1356°K). This allowed data to be taken for surface temperature approaching those observed during the Series A ablative nozzle tests. The basic features of the molybdenum nozzles are shown schematically in Figure 15. The design is conceptually the same as the previously described copper calorimeter but small changes were incorporated to accomodate the higher temperatures which were anticipated. These changes include: 1) use of tungsten-rhenium thermocouples, 2) use of beryllia thermocouple insulation tubing, 3) and use of a revised technique for bringing thermocouple leads into the tubular heat sink element.

Two different molybdenum calorimeter nozzles were fabricated and tested in the Series B program. One had a smooth internal surface with the basic dimensions of the copper transient calorimeter. Direct

comparisons to define the effect of surface temperature were therefore possible. The second molybdenum nozzle was initially fabricated identical to the first but was then mechanically roughened on its inner surfaces. Nominal roughness was comparable to that observed in post-test examinations of the Series A ablative nozzles. By testing both molybdenum nozzles at the same test condition, the effects of surface roughness on heat transfer coefficients were defined. A detailed discussion of the comparisons afforded by the molybdenum calorimeter data are included in Section 2.2.2.1.2.2 and later in Section 2.2.2.2.

The primary data from which heat flux and subsequently heat transfer coefficient values were obtained consisted of the transient millivolt response of thermocouple imbedded in the short tubular throat sections of each calorimeter. The resultant temperature history measurements for all transient calorimeter tests are shown as symbols in Figures 16a through 16t. In addition, each figure shows the distance of each thermocouple below the exposed surface. Also shown are thermocouple response predictions for the copper calorimeter tests. These predictions and the techniques utilized to evaluate heat flux from these data for the copper calorimeters are described in Section 2.2.2.1.2.1, while the techniques utilized in the molybdenum calorimeter data reduction are presented in Section 2.2.2.1.2.2.

2.2.2.1.2.1 Copper Calorimeter

For tests of the copper transient calorimeter, the surface heat flux was obtained from the measured subsurface temperature histories utilizing a transient, axisymmetric conduction solution computer program. The computer code utilized for these calculations required as input the thermal properties of the calorimeter material (OFHC Copper) and the surface temperature history of the calorimeter throat section. The code then computed the surface heat flux and predicted the in-depth temperature response of the thermocouples. Since the surface temperature histories are not measured directly during these calorimeter tests, an iterative procedure is required to obtain the correct heat flux. That is, a surface temperature history is estimated and the corresponding in-depth response is computed and compared to the measured (thermocouple) response. Depending on the discrepancies between predicted and measured, a new surface temperature history estimate is generated and the computations are repeated. Approximately five such iterations were required to adequately match the predicted to the measured. The final predicted thermocouple temperature histories for the copper transient calorimeters are shown as lines on the same figure that presented the measured data (Figures 16a through 16r).

The surface heat flux histories corresponding to these temperature histories are shown in Figures 17a through 17r. Also, time integrated averages of heat flux are given for each test condition in Table 3.

The measurement of surface heat flux by this technique is remarkably accurate. A good feeling for its accuracy was gained during the iterative evaluation. It was found that predicted internal temperature histories which bracketed the measured data corresponded to surface heat flux variations of only two to five percent in the range of useful data. It is thus concluded that the surface heat flux measurement by this technique is accurate to within five percent.

The evaluation of transient calorimeter heat transfer coefficient values was performed utilizing equation 13 (See Section 2.2.2.1.1). For the transient calorimeters, the enthalpy of the surface gases and the test stream total enthalpy, as well as the surface heat flux were changing with time. The resulting heat transfer coefficient histories are given in Figure 18a through 18r for the copper transient calorimeter tests. In addition, time integrated averages of heat transfer coefficient for the transient calorimeter tests are given in Table 3.

2.2.2.1.2.2 Molybdenum Calorimeter

Two tests featured molybdenum calorimeters. These runs had a dual purpose: 1) to provide "hot wall" heat transfer coefficient data for use in improving the heat transfer coefficient prediction scheme and in the ablative model analysis studies, and 2) to provide an idea of the effect of ablative model surface roughness on the heat transfer coefficient. For this second purpose, one of the two calorimeters had an artificially roughened surface.

Figure 15 shows the molybdenum calorimeter assembly, which was the same for the smooth and rough nozzles, and which was conceptually the same as the calorimeter assembly described in Reference 2. The molybdenum parts were machined from bar billets of climelt (R) CMX-WB-LC-1 arc-cast molybdenum supplied by The Climax Molybdenum Company. The rough nozzle was roughened by a number of intersecting V-shaped cuts or grooves made in the 0.300 ID throat surface. The width of the individual grooves approximately equalled the nominal depth of 0.015 inches. Cuts were made as to remove approximately 70% of the original surface area.

The two calorimeters were each instrumented with six in-depth thermocouples at various depths. The thermocouple installation is

illustrated in Figure 15; the six 3-mil tungsten-rhenium thermocouples were peened into holes drilled into the molybdenum throat segment. Two additional thermocouples are peened into the back-wall of each calorimeter.

The molybdenum calorimeter exposures received the test numbers 1353 (smooth) and 1354 (rough). Section 2.2.1 above presents the arc operating test data for these two runs. Table 3 summarizes the physical parameters of the tests.

Figures 16s and 16t show the thermocouple responses obtained from the two arc test exposures. The temperature rises were less than expected due to heat leaks in the axial direction from the calorimeter throat segment. Nevertheless, the response was adequate for the hot-wall effects analysis purposes of Section 2.2.2.2. and also adequate for studying the relative effects of roughness, as will be seen from the reduced data presented below.

Data reduction for these molybdenum calorimeters differed from that used for the copper calorimeter. Surface heat flux was inferred not from iterative calculations with a direct transient heat conduction computer code (trying to match or predict the measured thermocouple responses), but rather from solutions obtained from an inverse finite difference heat conduction program (Reference 5). The inverse code performed essentially the same kind of iteration done by the user of a direct code for thermocouple matching, but does it automatically at each finite difference time step in the solution (rather than examining retrospectively a thermocouple prediction for the entire test time history).

The inverse procedure requires as input the same kind of property and finite difference nodal data as required by a direct solution, plus the measured thermocouple responses. These latter were smoothed to a very slight degree to improve the smoothness of the predicted surface heat fluxes. Molybdenum properties were taken as the recommended values from Reference 6, with a density of 639.3 lb/ft^3 (1.024×10^4 kg/m^3).

Ideally, the inverse conduction code would predict the same surface heat flux history using each of the measured thermocouple response inputs to the code. A variety of experimental errors combine to cause a spread in the predicted heat flux histories. Figure 19 shows the mean predictions for the smooth and rough molybdenum calorimeters; the actual predictions with the various thermocouple responses scattered about ±15 percent around the mean value lines. For times less than four seconds, the scatter was about ±15 percent.

These heat flux results served to yield convective heat transfer coefficients $\rho_e U_e C_H$ when divided by the appropriate enthalpy difference

driving force ($H_o - H_w$). The total enthalpy H_o is presented in Figures 12s and 12t, the wall enthalpy H_w is shown as the 3 atm pressure curve for O/F=.38 in Figure 2. Note that the gas is assumed to be frozen at temperatures below 1800°R (1000°K). Figure 20 shows the transfer coefficients thus derived, as well as the ratio of the rough calorimeter transfer coefficient to the smooth wall transfer coefficient. Both $\rho_e U_e C_H$ curves drop steadily throughout the test (disregarding the first few seconds of data, which are presumably not reliable). This drop is a result of the axial heat leaks in the calorimeters, which cause the inferred one-dimensional heat flux into the calroimeter to be less than the actual throat heat flux. Since the data reduction process has ignored the possibility of heat leaks, the computed $\rho_e U_e C_H$ values are artifically depressed. Despite these flaws in the data, $\rho_e U_e C_H$ values extrapolated to zero time should be acceptably accurate, and the ratios of rough to smooth $\rho_e U_e C_H$ values should be reliable. This latter assertion is supported by the uniform ratio of $\rho_e U_e C_H$ rough/$\rho_e U_e C_H$ smooth at a value of 1.7. This value is used in Section 2.2.2.2 below. An absolute value for $\rho_e U_e C_H$ smooth is taken as 0.180 lb/ft^2 sec (.880 kg/m^2 sec). An absolute value for $\rho_e U_e C_H$ rough is less certain and is taken as 1.7 times the smooth value of 0.180 lb/ft^2 sec or 0.306 lb/ft^2 sec (1.50 kg/m^2 sec). These values are cited in Section 2.2.2.2 below as part of the analysis of hot wall effects on the convective transfer coefficient.

2.2.2.2 Heat Transfer Coefficient Data Correlation

In the previous section (2.2.2.1) all data measured and determined from calorimeter tests were presented. In this section, the calculations performed to interpret the data and estimate the heat transfer coefficient boundary conditions imposed during the ablative nozzle tests are described. These correlation efforts are required because the heat transfer coefficient values which apply during ablative nozzle tests are not measurable. In addition since the boundary layer heat and mass transfer phenomena have such a strong dependence on flow geometry, surface temperature, surface roughness, and gas mixture thermal and transport properties, the slight differences in arc plasma generator operating conditions between calorimeter tests and ablative nozzle tests mean that measured calorimeter coefficient values could not be applied directly to the ablative nozzle tests. The steps taken to obtain the heat transfer coefficient boundary conditions during each ablative material test were as follows:

1. The empricially defined simplified Bartz equation was utilized to obtain a baseline coefficient value for both calorimeter and ablative nozzle test conditions.
2. The steady state and the transient calorimeter results along with the Bartz calorimeter result was utilized to generate a Bartz "test condition" correction factor for each test condition.
3. The transient calorimeter rough and smooth wall heat transfer data was utilized to generate a "hot rough wall" correction factor (=1.7, see Section 2.2.2.1.2.2).
4. The more sophisticated Aerotherm Boundary Layer Integral Matrix Procedure (BLIMP) was utilized to verify the evaluation techniques described here.
5. The results of the correlation studies (Items 2, 3, and 4) were combined with the baseline Bartz equation predictions of the heat transfer coefficient histories.

Successful correlation of the available calorimeter data by the techniques outlined above insured that the heat transfer coefficient boundary conditions to the ablative nozzles were adequately determined. Detailed descriptions of the correlation activities are presented in Sections 2.2.2.2.1 and 2.2.2.2.2. below.

2.2.2.2.1 Comparisons to Theoretical Predictions

The calorimeter nozzle heat transfer coefficients were predicted first by employing a modified form of the simplified Bartz equation. This relation, which was based on the work of Reference 4, is described in detail in Appendix A of Reference 1. Equation 14 shows the currently used form of the relation:

$$\rho_e U_e C_H = \frac{0.026}{D^{.2}} \left(\frac{\mu'^{.2}}{Pr'^{.6}} \right) \left(\frac{\rho'}{\rho_e} \right)^{.8} (\rho_e U_e)^{.8} \qquad (14)$$

where the primed quantities are evaluated at the boundary layer reference enthalpy.

Calorimeter nozzle throat heat transfer coefficients calculated using the Bartz equation are listed in Table 5. Time average values of pressure and enthalpy, also shown in Table 5, were used for these calculations, and the Aerotherm Chemical Equilibrium (ACE) program (Reference 7) was utilized to calculate the transport properties and to predict $\rho_e U_e$ at the calorimeter throats assuming one dimensional isentropic flow. Previous experience (References 1, 2, and 8) indicates that the Bartz equation usually overpredicts experimentally measured heat transfer coefficients for arc-tested calorimeter nozzles. This was also the case for the present program as

may be observed from Table 5, the average ratio of experimentally measured to Bartz calculated heat transfer coefficient (excluding the molybdenum nozzles) being 0.437.

In order to define the effects of test stream chemical composition (O/F ratio) and energy content, $C^*/C^*_{OPT)O/F=2}$, the measured to Bartz calculated ratio was plotted as a function of $C^*/C^*_{OPT)O/F=2}$ for each O/F ratio tested. These plots are shown in Figures 21a through 21e. While there is scatter, Figure 21 shows definite variations of the experimental to Bartz heat transfer coefficient ratio with both O/F and $C^*/C^*_{OPT)O/F=2}$. This variation will be discussed subsequently in Section 2.2.2.2.2.

The disparity between the experimental heat transfer measurements and the predictions based on the Bartz correlation was somewhat greater than expected. While there are a variety of potential reasons for this disparity, the existence of laminar or transitional (rather than turbulent) flow in the calorimeter nozzles is the most likely.

In order to provide an additional check on the heat transfer coefficients calculated by the Bartz relation and measured using calorimeters, a sophisticated boundary layer solution procedure was employed to calculate the heat transfer coefficient, momentum thickness Reynolds number, etc., as a function of boundary layer running length for several selected calorimeter tests. These solutions were obtained employing the Boundary Layer Integral Matrix Procedure (BLIMP) computer program. The BLIMP program employs an integral strip technique to solve the boundary layer equations for nonsimilar multicomponent chemically reacting laminar or turbulent flows subject to very general boundary conditions (References 9 and 10).

Boundary layer solutions, assuming real gas one-dimensional isentropic core flow with fully turbulent boundary layer flow, were performed for conditions corresponding to two transient calorimeter tests at each O/F ratio (total of ten cases). The predicted heat transfer coefficients for a streamwise location just into the throat are given in Table 5. The heat transfer coefficients predicted using the BLIMP program are in approximate agreement with those calculated using the Bartz relation, the BLIMP predictions being about 10 to 20 percent less than the Bartz calculations for most cases.

Typical predicted boundary layer profiles of velocity, total enthalpy, and temperature are illustrated in Figure 22. Typical chemical species concentration profiles are illustrated in Figure 23. These predictions are for steady state calorimeter test 1109A (O/F=2.0) and the profiles illustrated are for a streamwise location just inside the nozzle throat section. Note that the enthalpy thickness is about double the momentum thickness and. since the wall is cold relative to the edge gas, compressibility results in a negative displacement thickness.

turbulent boundary layers. These calculations over-predict the experimentally measured heating rates and the suspicion naturally arises as to the possibility of laminar flow in the calorimeter nozzles and perhaps the ablative nozzles. Indeed, this suspicion was partially responsible for the implementation of the rough-wall molybdenum calorimeter nozzles as discussed previously in Section 2.2.1. The state (laminar vs. turbulent) of the boundary layer is traditionally estimated by applying some transition criteria, commonly a critical momentum thickness Reynolds number. For simple flat plate flows, transition is usually assumed to occur at a critical momentum thickness Reynolds number of about 360 (Reference 11). However, since this flow is significantly different from simple flat plate flow, the critical Reynolds number may be quite different as well. The effects responsible for this difference include the accelerating nozzle flow, the large T_e/T_w ratio, the relatively high Mach number, the axisymmetric geometry, and the potential effects of arc generated free stream turbulence. In addition, the ablative nozzles differ from the calorimeter nozzles in that they have hot, ablating, rough surfaces. Because of these effects, a precise transition criteria cannot be applied with confidence to either the calorimeter nozzles or the ablative nozzles.

In order to estimate the laminar heating rates and momentum thickness, Reynolds number distribution, the BLIMP program was utilized to perform additional calculations assuming laminar flow. Figure 24 illustrates some of the results of these calculations for the conditions of transient calorimeter nozzle test 1357B (O/F=∞). Presented here is the predicted $R_{e\theta}$ and heat transfer coefficient distributions assuming fully turbulent flow, fully laminar flow, and flow with transition at $R_{e\theta}$ = 200. Also plotted are the corresponding experimentally measured and Bartz-predicted heat transfer coefficients.

Figure 24 illustrates the typical result that the experimentally measured heat transfer coefficients are roughly midway between the expected laminar and turbulent values. Also, the laminar momentum thickness Reynolds number ranges up to about 400, which is within the range of uncertainty relative to transition. Thus, no firm conclusions can be drawn as to whether the boundary layer flow in the calorimeter nozzles was laminar or turbulent. The only speculation supported by the calculations presented here is that the calorimeter nozzle boundary layer flow is transitional.

2.2.2.2.2 Application Of Results To Ablative Nozzle Tests

The heat transfer coefficient histories for the ablative nozzles were estimated by employing a combination of experimental measurements

and empirical correlations. The formula utilized to calculate the no-blowing heat transfer coefficients subsequently input to ablation prediction calculations (Section 3) may be written as:;

$$\rho_e U_e C_H \Big]_A = \rho_e U_e C_H \Big]_{BA} \times \left(\frac{\rho_e U_e C_H \quad XC}{\rho_e U_e C_H \quad BC} \right) \times \left(\frac{\rho_e U_e C_H \quad XR}{\rho_e U_e C_H \quad XS} \right) \qquad (15)$$

where subscripts are:

A - Ablative nozzle heat transfer coefficient boundary condition (function of time).

BA - Bartz equation prediction of ablative nozzle coefficient (function of time).

BC - Bartz equation prediction of corresponding copper calorimeter coefficient.

XC - Experimentally determined transfer coefficient for copper calorimeter operating at the ablative nozzle O/F and C* ratios.

XR - Experimental rough wall molybdenum coefficient.

XS - Experimental smooth wall molybdenum coefficient.

This formula is predicated on the assumption that, except for rough wall and mass addition effects, the prediction error of the Bartz relation is the same for both the ablative nozzles and calorimeter nozzles. Also, it is assumed that rough wall effects on heat transfer are the same for the ablative nozzles relative to the calorimeter nozzles as for the rough wall molybdenum calorimeter nozzle relative to the smooth wall molybdenum calorimeter nozzle. Given these assumptions, the ablative nozzle heat transfer coefficient histories were calculated by correcting the value calculated from the Bartz relation (first term in equation) by the ratio of experimentally measured to Bartz-calculated calorimeter heat transfer coefficient (second term in equation) and by the ratio of rough to smooth wall molybdenum calorimeter nozzle heat transfer coefficients (third term in equation).

The time dependence of the ablative nozzle heat transfer coefficients (due to the nozzle throat enlargement and resultant chamber pressure decrease) is of course accounted for by the first term in equation 15. The ratios of experimentally measured to Bartz-predicted heat transfer coefficient for each calorimeter nozzle are plotted in Figure 21a through 21e and were discussed in Sections 2.2.2.2.1. Since this ratio may be expected to be a function of the chemistry associated with a particular test condition (i.e., O/F and $C^*/C^*_{OPT})_{O/F=2)}$, the value of the second bracketed term in equation 15 was taken to be a simple linear function of $C^*/C^*_{OPT})_{O/F=2}$ for each O/F as indicated by the line in Figures 21a through 21e. The value of the third bracketed term in equation 15 is

1.70 as discussed previously in Section 2.2.1. The ablative nozzle heat transfer coefficient histories estimated in the fashion described in this section are presented in Figures 25a through 25ii.

2.2.3 Ablative Nozzle Response Measurements

Those measurements which established the environmental boundary condition to which the ablative nozzles were exposed have been presented in the previous sections. The ablative response of the nozzles is described here. Measurements of the nozzle responses may be conveniently divided into two categories:

- Ablative material recession response
- Ablative material temperature response

Recession response includes all data related to the amount that a given nozzole is thermally degraded or chemically and mechanically eroded. Included in this category are surface recession, surface recession rate, char depth, and all quantities required to obtain recession data as a function of time. These data are presented in Section 2.2.3.1. The temperature responses, which includes in-depth and surface measurements, are presented in Section 2.2.3.2.

2.2.3.1 Nozzle Throat Recession Data

If the throat of each ablative nozzle had eroded at a constant rate in all radial directions, the definition of total recession, recession histories, and recession rate would be simple. Pre- and post-test diameter measurements would define all needed recession response quantities. Post-test examinations of several of the nozzles showed considerable non-symmetrical ablation at the throat. In addition, measured chamber pressure histories (Figures 10a through 10ii) indicated that in several cases recession did not begin until well into the tests. Since the chamber pressure is essentially proportional to the nozzle throat area by sonic flow relations, the recession and recession rate histories can be inferred from measured pressure data using pre- and post-test dimension measurement as scaling factors. The techniques utilized to define the pre- and post-test nozzle throat dimensions including the circumferential variation of throat erosion are described in Section 2.2.3.1.1, and the techniques employed to obtain recession and recession rate histories are presented in Section 2.2.3.1.2.

2.2.3.1.1 Pre- and Post-Test Ablative Nozzle Dimension Measurements

Pre-test throat diameters were accurately measured with a bore micrometer. Nominal internal diameter for all ablative nozzles was 0.30 inches (0.0076 meters). The measured nozzle diameters were within 1 percent of

nominal, although two nozzles, NL-11 and NL-35, were over machined 1.7 and 3.3 percent respectively. The exact pre-test diameters for each nozzle are included in Figures 26a through 26ii. An additional pre-test machining parameter of potential interest is related to the concentricity of the inner and outer surfaces of each ablative nozzle. Machining tolerances were such that at the throat the center of the nozzle internal circumference was within 0.002 inches ($5x10^{-5}$ meters) of the center of the outer circumference. This fact was utilized in the subsequent data reduction as described below.

The evaluations of the post-test ablative nozzle throat contours were performed by two unique techniques. The first technique was utilized in the Series A arc plasma generator tests and the second was employed during the Series B tests. Comparisons to obtain the relative accuracy of each method were also performed. Each technique required the sectioning of the tested nozzles to obtain a wafer of the nozzle at the throat location. This sectioning is shown schematically in Figure 27. Cuts were made perpendicular to the nozzle centerline roughly 1/8 of an inch upstream and downstream of the thermocouple plane. Photographs of these nozzle throat wafers are shown in Figures 28a through 28ii.

In the Series A ablative nozzle tests, the internal nozzle contours were obtained from enlarged shadowgraphs of the throat wafers. These shadowgraphs were made by passing a beam of roughly collimated light through the nozzle wafers and through a focusing lens in such a manner as to achieve a 10 to 1 amplification of the throat contour. The amplification factor was calibrated utilizing a steel wafer with a known internal diameter. Reduced versions of the shadowgraphs for the Series A ablative nozzles are shown in Figures 26.

Also shown on these figures are the pre-test circular contours. The pre-test centers required to define these contours were obtained by referencing a cross-hair grid to the outer circumference of the throat wafer. As was described above, the pre-test inner and outer circumferences were essentially concentric and as such the grid center represented the nozzle centerline. This determination was very useful in defining the degree of non-symmetrical ablation which occurred in each test.

In the Series B ablation tests, the internal nozzle contours were defined from photographs of the nozzle wafers (Figure 28). To obtain a consistent amplification of the contour, the distances from wafer to lens to film were maintained at constant values for all nozzles. Slide prints of the exposures were then projected a distance sufficient to again achieve a 10 to 1 amplification of the throat contours and the contours were hand aketched. As a check on the amplification, the contour of one of the ablative nozzle throat wafers from the Series A tests was defined by this method. The results for the two methods were effectively identical.

The pre-test nozzle centers for these wafers were defined during the machining process. Reference lines were drawn at 90° intervals on the faces of the wafers, so that, during the sketching of the nozzle contours, intersecting diameters could also be defined. The resulting pre- and post test nozzle contours are shown along with Series A contours in Figure 26.

The following additional data is given for each ablative nozzle in Figure 26:

- Post-test integrated average diameter.
- Average net surface recession.
- Surface recession in thermocouple plane.
- Char depth in thermocouple plane.
- Depth of thermocouples.
- Circumferential location of thermocouple plane.

The surface recession and post-test diameter measurements were taken directly from the contour sketches (or shadowgraphs), and char depths were determined by measuring the char thickness with a machinists rule and adding to it the surface recession in the thermocouple plane. Recession measurements in the thermocouple plane are important because of their subsequent use in the analytical evaluation of the ablative material responses (see Section 3), particularly if circumferential variations in erosion result in local recessions adjacent to the thermocouples which are significantly different from the average.

The measurements of the thermocouple depths were performed by the X-ray technique described in References 1 and 12. This technique consists of measuring the depths of the thermocouples from X-rays taken of the ablative nozzle after they have been instrumented but before they are tested. A study of the accuracy of the measurements taken in this manner was performed in Reference 13. For thermocouples at any depth below the surface, the measurement was found to be within ±0.002 inches (5×10^{-5} meters) of exact. An example of an instrumented nozzle ready for X-ray is shown in Figure 29, and a typical X-ray photograph showing three imbedded thermocouples is given in Figure 30. Accurate determinations of these thermocouple depths are essential to relating predicted material response to the thermal measurements described in the Section 2.2.3.2.

2.2.3.1.2 Inferred Recession and Recession Rate Histories

Because of the transient nature of the ablation phenomena which occurred in the nozzles tested in this program, the variation of recession with time could not be assumed linear between initiation and completion of exposure. For constant values of mass flow rate, total enthalpy, and

isentropic exponent, one-dimensional sonic flow theory states that throat flow area is proportional to chamber pressure. The desired variation of recession with time was obtained utilizing the following procedure for each ablation test.

- A baseline pressure (usually either the calibration condition pressure or the measured peak pressure) was selected to correspond to zero recession, i.e. pre-test throat area.
- A prediction of the variation of recession with time was then made based on the measured chamber pressure history and the linear relation described above.
- The predicted trend based on chamber pressure was then adjusted so that final predicted recession matched the measured final recession.

The third step was required since non-ideal effects usually resulted in the final predicted recession being different from the measured average recession and/or the measured thermocouple plane recession. Curves of these recession histories are shown in Figures 31a through 31ii for all ablative nozzle tests. The values of recession rate as a function of time were then easily defined by graphically differentiating the curves of Figure 31.

2.2.3.2 Nozzle Thermal Responses

Two types of thermal measurements were taken for each ablative nozzle tested in this program. Surface temperatures were measured by an optical pyrometer. In depth thermal response measurements were taken by three thermocouples imbedded at the throat axial plane. The optical pyrometer utilized to measure the material surface temperature histories during the ablative nozzle tests senses 0.8 micron thermal radiation. In Reference 2, a study of the effects of ablation products and simulation gas on the surface temperature indicated by the pyrometer was reported. Also given was the effect of surface emissivity uncertainties on temperature measurement. It was concluded that for the same materials and gases tested in this program the surface temperature measurements were accurate to within 8 percent. Surface temperature histories measured during the Series A and Series B test programs are shown in Figure 32a through 32ii. Also shown in Figure 32 are the in-depth temperature measurements and some predictions which are described subsequently in Section 3.

The subsurface temperature histories were measured with fine wire thermocouple probes. A number of different thermocouple instrumentation techniques have been considered for obtaining internal temperature histories. The prime requirement for an accurate temperature measurement is that the sensor does not disturb the heat flow at the point of interest. To satisfy

this, the sensor should be as small as is practical, and the thermocouple leads in the vicinity of the junction should be placed in an isothermal plane. This last consideration is particularly important in low-conductivity materials and is impressively illustrated in Reference 14. Also, the thermocouple junction must be in intimate contact with the material in order to minimize errors due to contact resistance.

Considering these requirements and the practical aspects of fabrication the thermocouple installation scheme shown in Figure 33 was selected. Three thermocouple ports 0.040-inch-diameter were drilled into the ablation nozzles at nominal depths of 0.125, 0.20, and 0.275 inch. The thermocouple probes employed are similar to those described in Reference 2. Small changes in the design were required to accommodate the different nominal thermocouple depths utilized in this program. Each nozzle was instrumented with two Chromel-Alumel probes and one tungsten-5 percent rhenium/tungsten-26 percent rhenium probe. The probes are inserted into the test nozzle so that they are tangent to an isotherm at their junction. The thermocouples are spring-loaded against the bottom of the thermocouple-probe hole to insure good contact of the thermocouple junction with the ablation material. Thermocouple location and continuity are verified prior to testing by X-ray photographs and electrical resistance measurements.

2.3 SUMMARY OF OBSERVED SILICA PHENOLIC ABLATION RESPONSE TRENDS

Simulation of five oxidizer to fuel ratios of a liquid propellant rocket engine operating on N_2O_4 - 50 percent N_2H_4/50 percent UDMH over a wide range of off-optimum propellant energy content were achieved. The material responses of MXS-89 silica phenolic to these environments were observed and measured. In this section the identifiable trends in the material response with respect to changing O/F ratio and stream energy content are described. These observations are then used to support conclusions about the mechanisms of silica phenolic ablation. Trends in post-test nozzle appearance are presented in Section 2.3.1. Trends in recession rate data are described in Section 2.3.2. The apparent ablation response mechanisms are discussed in Section 2.3.3.

2.3.1 Trends in Post-Test Nozzle Appearances

Identification of significant trends in the variation of the post-test nozzle appearances provided valuable qualitative insight into the phenomonological aspects of the silica phenolic response. To facilitate the definition of these trends, the matrix of environmental conditions tested during the two experimental series have been divided into fifteen groups (three stream energy content levels for each of five O/F ratios). Specific descriptions of the throat surfaces are given for each of these groups in Table 6.

Photographs of the nozzle wafers corresponding to the descriptions in Table 6 are given as Figure 34. The effect of decreasing stream energy content on surface appearance for each O/F ratio is presented below and is followed by comments on the trends with respect to changing O/F ratio.

For O/F = 0.38, the surface appearance does not depend on the stream energy content, i.e., $C^*/C^*_{OPT})_{O/F=2.0}$. The surface appears carbonaceous with no change in composition between the surface and the in-depth char. This surface appearance was peculiar to the O/F = 0.38 nozzles. For all other O/F ratios some amount of white solidified melt flow was present on or near the surface. For the O/F = 1.0 nozzles, decreasing C* resulted in greater percentages of the carbonaceous char being covered by the solidified melt. Presumably the lower stream energy content resulted in more melt formation and/or high melt layer viscosity values, such that the flow could not as readily be swept away. This same trend was apparent in the O/F = 2.0 nozzles. For the lowest C* tests of O/F = 2.0 series, the melt formation was sufficiently large as to result in a net surface buildup.

Tests conducted at both O/F = 4.0 and ∞ resulted in nearly identical response trends with decreasing stream energy content. For the higher energy content tests where significant recession occurred, the nozzle throat surface char was covered with near continuous layers of white (silica) material. At lower effective C* values for these O/F ratios, the white material was also prominent but other species also appeared to be present on the post-test throat surfaces. The low C* O/F = 4.0 tests produced nozzle throat surfaces containing black shiny metallic appearing particles. A thin, pink layer of particles covering the white melt layer was evident in the low C*, O/F = ∞ test nozzles.

The variation of general post-test nozzle appearance with O/F ratio indicated the significant effect that boundary layer chemical composition has on the silica phenolic response mechanisms. The oxygen available to react with surface material appears to be the key parameter defining the response mechanism. A non-obvious conclusion obtainable from the experiments performed is that a certain amount of oxygen at the surface can have a positive value in protecting silica phenolic from chemical and mechanical erosion. This conclusion is discussed further in the following sections. The trend of post-test surface appearance with increasing O/F ratio is that of increasing amounts of white (silica) melt on or downstream of the nozzle throat.

The melt flow phenomena created some interesting effects at the nozzle exit plane. Photographs of the exact flow pattern for eight different conditions are shown in Figure 35. The exit patterns shown for O/F ratios of ∞, 4.0, and 2.0 are presumably silica which has flowed downstream from the nozzle and solidified. Figures 35a and 35c show that higher total temperature

associated with higher C* condition had the effect of making the exit pattern whiter and fluffier for the two most oxygen-rich O/F ratios. Figures 35b and 35d show the opposite end of the total temperature scale for these O/F ratios. Figure 35e is a similar flow pattern for an O/F of 2.0 nozzle tested at $C^*/C^*_{OPT})_{O/F=2} = 1.024$.

The post-test exit configuration given in Figure 35f shows that a small amount of melt flow occurred during O/F of 1.0 tests. The O/F of 1.0 test at a lower total temperature which is pictured in Figure 35g also shows small traces of white material although no recession and hence no melt flow occurred. This should be compared with Figure 35h where the typical O/F of 0.38 is shown.

2.3.2 Trends in Recession Rate Data

The trends in recession data are best compared in terms of recession rate, since the effects of varying test time are somewhat lessened. For the purposes of this discussion the average test recession rate as defined in Table 4 are used even though the transient nature of the silica phenolic response means that the instantaneous recession rates, once recession begins, can be considerably larger than average. The effect of changing the test stream energy content on recession rate is shown in Figure 36a through 36e for each O/F ratio tested in this program. Although anomalies do exist, it is obvious that as the stream total temperature was increased average recession rate also increased. These trends are, of course, reasonable since higher stream temperatures typically result in a more chemically reactive, thermally hostile environment, independent of the particular O/F ratio being tested.

The effects of the test stream chemical composition (O/F ratio) are not so easily defined. To visualize the variation of recession rate with O/F while still indicating the above mentioned C* trends, a three-dimensional model of surface recession rate, $C^*/C^*_{OPT})_{O/F=2}$, and effective N_2O_4 mass fraction was constructed. A photograph of this model is shown in Figure 37. The model roughly shows that the recession rate data creates a surface contour which describes the effects of both O/F ratio and C* on recession rate. The shape of this 3-D model could be used to quantitatively estimate the effects of changing boundary layer composition and temperature on total nozzle ablation response.

A more quantitative description of these trends in the simulator tests is shown in Figure 38. This curve represents the intersection of the surface contour with the plane at $C^*/C^*_{OPT})_{O/F=2}$ of 1.0 (ideal O/F of 2 combustion). Points were obtained by cross plotting the intersections of the data fit curves of Figure 37 and the $C^*/C^*_{OPT})_{O/F=2}$ value against the respective K_{ox} for each O/F. The figure shows that a minimum point exists near O/F of 1.0

and that the addition of oxidizer increases recession rate only to a point. Above O/F ratio of 4.0 increased oxidizer had only a small effect on recession rate.

Figures 36 and 38 (or alternately Figure 37) may be used as an empirical material ablation response law for the interaction of silica phenolic with the N_2O_4-N_2H_4/UDMH liquid propellant. Quite obviously the qualitative effects of varying rocket nozzle boundary layer composition and boundary layer edge temperature can be seen. Utilizing the assumptions and definitions about the meaning of the simulation gas C* ratio (as given in Section 2.1.2), a crude quantitative characterization of the effects of varying conditions on material response may also be obtained from Figures 36 through 38.

2.3.3 Ablation Response Mechanisms

Possible explanations for the trends described above are offered here but more detailed analysis of the material response are deferred to Section 3. The comments given below about the chemical events are based upon the elemental compositions of the various test gases and the silica phenolic, and from calculations of the molecular compositions of the test gases at nozzle throat conditions. Chemical equilibrium studies of gas systems containing various amounts of hydrogen, carbon, nitrogen, oxygen and silicon have shown that the following qualitative "basic principles" are applicable for the materials, temperatures, and pressures characteristic of silica phenolic ablation in the N_2O_4-N_2H_4/UDMH propellant environments.

- nitrogen is isolated (effectively inert)
- carbon most actively bonds with any of the other elements
- as oxygen becomes increasingly available, the important molecular species oxidize in the following order:

(1) $C + \frac{1}{2} O_2 \rightarrow CO$ (16-A)

(2) $Si + \frac{1}{2} O_2 \rightarrow SiO$ (16-B)

(3) $SiO + \frac{1}{2} O_2 \rightarrow SiO_2^*$ (condensed phase) (16-C)

(4) $H_2 + \frac{1}{2} O_2 \rightarrow H_2O$ (16-D)

(5) $CO + \frac{1}{2} O_2 \rightarrow CO_2$ (16-E)

- in MXS-89 silica phenolic, sufficient SiO_2 is available for oxidation of all carbon in the char (i.e. once temperatures are sufficient to reduce SiO_2).

These "principles" can provide some qualitative insight into the erosion mechanisms of silica phenolic, even though a full explanation of the detailed ablation events is not possible from the studies performed to date.

Assuming that the in-depth material response of the MXS-89 silica phenolic is characterized by the pyrolysis of the phenolic resin followed by the reaction of the residual carbon with the silica reinforcement, the gases arriving at the surface from the ablative material consist of CO, SiO, and small amounts of hydrocarbons.* The surface recession rate of the silica (SiO_2*) char is then governed by the chemical reactions and the amount of mechanical (melt) removal occuring at the surface.

In the range of O/F ratio from 2.0 to ∞, recession is evidently controlled by melt removal. Both the apparent chemical events and the internal surface appearances of the nozzles, as described in the following section, confirm this conclusion. Furthermore, for the $C^*/C^*_{OPT})_{O/F=2}$ near unity tests, surface temperatures for this O/F ratio range were all roughly 4200°R (2330°K), the apparent silica ($Si\theta_2$*) flow temperature. The recession trends over this range are heuristically explicable from the oxidation reactions given above as equations 16C through 16E. For O/F ratios of 4.0 and ∞, oxygen is sufficiently availably at the surface to oxidize all of the silica phenolic decomposition products via these reactions. Hence the plateau region shown in Figure 36 results because all possible exothermic reactions occur, independent of further oxygen availability.

The significant reduction of recession rate as the available oxygen is decreased below O/F of 4.0 seems, therefore, to be due to the decrease of exothermic chemical events (reaction 16-C through 16-E) at the surface. At O/F of 2.0 the available oxygen is split between the reactions 16-C and 16-D leaving some free H_2, while for O/F of 1.0 only a small amount of silica is apparently being formed via 16-C. As discussed in Section 3, the surface response may not even be controlled by the silica melt layer for O/F of 1.0.

For the tests at O/F ratio of 0.38, the oxygen reactions described above cannot occur at the nozzle surface since no free stream oxygen is available to oxidize any decomposition products. The propellant composition at these conditions is basically CO, N_2, and H_2, all of which are relatively inert to the CO, SiO and hydrocarbons from the silica phenolic. The observed increase in surface recession rate at this O/F ratio must, therefore, be due to reactions between the carbon rich hydrocarbons and the silica char. In this respect the minimum point near O/F of 1.0 is a logical result since, as small amounts of oxygen become available to oxidize the pyrolysis gases, silica remains on the surface to inhibit the surface removal. Moreover, these conclusions are again substantiated by the post-test appearances of the ablative nozzle. For O/F of 1.0 slight traces of silica could be seen (though very little melt flow occurred), while for O/F of 0.38 only a black carbonaceous char surface was apparent.

*Note that this model is consistent with SCRIMP program formulation (Section 3).

SECTION 3

ABLATIVE DATA CORRELATION USING ABLATIVE COMPUTER CODES

This section describes the results of a number of "computational experiments" made with ablation computer codes to predict the ablation actually observed in the arc test cases. These calculations served to

(1) illuminate many of the physical ablation mechanisms occuring in silica-phenolic.
(2) establish some confidence in the ability of a complex ablation computer code to predict ablation and temperature response.
(3) "tune up" the computer codes for the prediction of rocket nozzle ablation.

This section contains five sub-sections. The first of these, Section 3.1, decribes the computer codes employed in the study (Appendices A, B, and C supply more detail). Sections 3.2 through 3.4 describe details of the calculations, and Section 3.5 presents some conclusions about the predictive correlation effort.

3.1 DESCRIPTION OF COMPUTER CODES

The computer codes used for the predictive calculations are of two kinds. The first kind treats the in-depth transient thermal and pyrolysis events in the ablating material. Two codes were used for this purpose. The first is the Aerotherm Charring Material Ablation (CMA) code. This program treats transient heat conduction in a charring material and accounts for the organic pyrolysis (gas generation) decomposition events. Appendix A describes this program in some detail. References 15, 16, 17, and 18 describe the CMA code more completely. The second in-depth response code used in these calculations is a modification of the CMA code denoted SCRIMP. This code considers additional in-depth events which were felt to be important in the thermal response of silica reinforced materials: in depth chemical reactions between the silica reinforcement and the carbonaceous char residue at high temperatures, and the formation and flow of a thick layer of liquid silica at the heated surface. Appendix B describes the SCRIMP code in more detail. References 2 and 19 provide other background information about SCRIMP. For present purposes, it may be observed that the SCRIMP code is an exploratory code which contains a number of adjustable parameters. It was believed that a systematic exploration of various values of these parameters would reveal

interesting aspects of some of the complicated physics of silica-phenolic ablation response and thus point the way to possible future refinements in analytical models used in the SCRIMP program.

In addition to these two in-depth response programs, a second kind of code is required for the ablation calculations. This program supplies certain thermochemical erosion information necessary for computing the heated surface energy balance and the associated surface recession rates. The code used for this chemical information is the Aerotherm Chemical Equilibrium Program (ACE).* A brief overview of ACE is given in Appendix C and it is described in detail in References 7 and 21.

3.2 ASSIGNED SURFACE TEMPERATURE AND RECESSION RATE CALCULATION TO BACK-OUT MATERIAL PROPERTIES

Use of the ablation computer codes naturally requires the user to assemble material property data for thermal conductivity, specific heat, density, pyrolysis kinetics, and certain thermochemical information. Reference 2 describes the generation of the required specific heat, density, pyrolysis kinetics, and thermochemical data required for the MXS-89 silica phenolic used in the present series of experiments. During the conduct of the present effort, the thermal conductivity and the silica-carbon reaction kinetic parameters remained to be better defined. An initial essay at this definition was made by running the CMA and SCRIMP codes on certain of the arc-test model cases with the surface temperature and recession rate assigned to be the measured experimental values. The in-depth thermal response prediction generated by the computer codes includes predicted thermocouple temperature response histories; these responses may be compared with the measured thermocouple responses and certain conclusions drawn about the adequacy of the thermal property data employed in the in-depth prediction. The thermal conductivity of charring materials is often defined in this manner (References 2 and 22).

Table 7 gives an overview of the total test program. The table identifies cases examined by the assigned - temperature - and - recession rate computations. Figures 32a-i, 32l-y, 32dd, and 32ff show the thermocouple response predictions produced by the two in depth computer codes

*Naturally the computations required for this purpose could, if desired, be included as part of the in-depth codes. For various practical reasons, however, as discussed for example in Reference 20, it usually proves more convenient to keep the thermochemical calculations entirely separate from the in-depth calculations, supplying the needed thermochemical information to the in-depth calculation as pre-computed tables.

(CMA and SCRIMP) compared with the experimental data. Comparisons between the predicted in-depth temperature histories with these two codes reveals the importance of in-depth silica-carbon reactions upon predicted subsurface temperature histories. The CMA code was used mainly for tests at O/F = .38, 1.0 and 2.0, although isolated CMA runs were made at some O/F=4.0 and ∞ conditions. SCRIMP runs were made principally at O/F=4.0 and ∞, with an isolated O/F=2 case. It was subsequently decided to confine all ablation correlation attempts to the SCRIMP program; therefore, it is these runs which are of the most interest.

It will be noted from those figures displaying SCRIMP results for the assigned - surface - temperature and - recession rate calculations (Figures 32b-g, 32i, 32 l-m, and 32q) that although the predictions match the data fairly well the thermocouple response predictions are in most instances somewhat below the data. Likely explanations for the differences between predictions and data include (a) a faulty reported surface temperature, (b) an inaccurate thermal conductivity model, (c) bad silica-carbon reaction kinetics rates, and (d) inappropriate enthalpy-temperature relationship for pyrolysis gas and reaction gas. Since some of these parameters were to be subject to revision in the actual ablation correlation calculations (which do not specify the surface temperature and recession rate but compute them from thermochemical data) there was little purpose in attempting to adjust these parameters during the initial, exploratory phase of the work reported here. These exploratory runs serve to establish whether major deficiencies exist in either the data or the analytical model employed.

3.3 ITERATIVE ABLATION CALCULATIONS ON SELECTED MODEL TEST CASES TO DEFINE CERTAIN COMPUTER CODE PARAMETERS

The main part of the computational correlation efforts involved repeated runs of the SCRIMP ablative code on certain selected test model cases, using surface thermochemistry data pre-prepared by the ACE code for defining the surface temperature and ablation rate. The SCRIMP code was selected for this effort because most test models developed, during test, a thick "liquid" silica layer at the heated surface. The CMA code does not account for this phenomenon; the SCRIMP code was developed from the predecessor CMA code specifically to account for this liquid layer. As noted in Appendix B, however, the SCRIMP code is not a finished code in the sense of having a well defined physical model for each physical phenomenon of importance. Rather, SCRIMP is a developmental code with some rather crude physical models featuring adjustable parameters. It was expected that repeated runs of SCRIMP over a variety of these parameter values would (a) "tune up" a useful data correlation computer code and thus allow some predictions of rocket nozzle erosion, and (b) point

the way toward improved physical modes for later incorporation in future computer codes.

The parameters of interest in this regard derive from a rudimentary treatment of the liquid layer flow. As discussed in some detail in Appendix B, the liquid silica layer in SCRIMP is treated with two overall aspect parameters: a local carbon density (in pounds of carbon char residue per cubic foot) which defines the lower edge (and thus the depth or thickness) of the liquid layer, and a maximum allowed thickness of the liquid layer. In-depth reactions between silica and carbon residue lower the local carbon content, eventually leading to some liquid layer thickness defined through the first parameter. The second parameter requires surface recession (ablation) to occur so as to prevent growth of this liquid layer thickness beyond the maximum allowed.

This feature of the SCRIMP code introduces two parameters requiring numerical definition: the carbon density marking the liquid layer edge, and the allowed liquid layer thickness. Additional required parameters do not derive from simplified physical models, as it happens, but from basic uncertainties within the more completely modeled aspects of the ablation problems. These uncertainties concern: (a) the thermal conductivity associated with the silica-carbon reaction zone, (b) the kinetic rate data for the in-depth silica-carbon reactions, and (c) the basic thermochemical model to be employed at the heated surface. The nature of the uncertainties associated with the reaction zone thermal conductivity and the silica-carbon reaction kinetics are rather evident: no well established numbers are available for these quantities. The heated surface thermochemical model involves more complex issues. It is not known, for example, whether full chemical equilibrium at the surface is a good assumption or whether various kinetically controlled reactions must be considered. Thus, the ablative-prediction correlation effort with the SCRIMP code necessarily involves an examination of the effects on the prediction of the five ill-defined parameters discussed above. The paragraphs following discuss the ranges considered (in the calculations) for each of these five unknown input quantities.

Liquid Layer Edge Carbon Density. The density of carbon in the char after complete pyrolysis but before any silica carbon reactions have taken place is 12.8 lb carbon/ft^3 material (205 kg/m^3). During the numerical experimentations, the liquid layer edge carbon density was assigned values of 7 lb/ft^3 (106 kg/m^3), 5 lb/ft^3 (80 kg/m^3),and 3 lb/ft^3 (48 kg/m^3).

Allowed Liquid Layer Thickness. Runs were made for liquid layer thicknesses of 2 mils (50.8 μm), 5 mils (127 μm), 10 mils (254 μm) and

20 mils (508 μm), which approximately cover the range of observed values on the post test specimens from the runs at O/F=2, 4, and ∞.

Silica-Carbon Reaction Kinetics Data. Reference 2 cites a reference value for the pre-exponential factor A (see Appendix B) of 9×10^7 sec^{-1} and a value for the activation energy E of 80000 cal/gr mole (334,700 joules/gr mole). In this report, these values are referred to as the "nominal" values of the kinetic parameters. They were used for some of the computations. Most computations employed values described ".1 x nominal"; which used A= 9×10^6 sec^{-1}.

Thermal Conductivity Associated With The Silica-Carbon Reaction Zone. Since temperature is by far the most important variable determining the state of the in-depth material, it is possible to obtain thermal conductivity values for the silica-carbon reaction zone as an extension of the temperature dependent char thermal conductivity values into that temperature range where silica-carbon reactions are occuring. Actual conductivity values for this range are purely conjectural, however, and represent extrapolations of data obtained experimentally for the silica phenolic char. The iterative computer runs used two conductivity-temperature functions, denoted as "low" and "high" and illustrated in Figure 39. The "low" conductivity represents char data from Reference 23 covering the range 530^oR (294^oK) to 3000^oR (1670^oK) for the Fiberite silica-phenolics MX2600 and MX2600-96, which are quite similar to the Fiberite MXS-89 used in this program. These harmonize well with the values of char conductivity reported in Reference 2 specifically for MXS-89 in the range 530^oR (294^oK) to 2000^oR (1110^oK) but are somewhat lower than the values reported at 3000^oR (1670^oK). The lower values seemed to be somewhat preferable based on numerical comparisons (not reported here) of predictions and model thermocouple responses for temperatures less than 3000^oR (1670^oK). The extrapolations to temperatures above 3000^oR (1670^oK) are based partly on the high temperature data of Reference 2, which are based on CMA correlations but are adjusted upward to compensate for the endothermic in-depth silica-carbon reaction accounted for by SCRIMP but not by CMA. The "high" and "low" adjustments were tried in the present iterative calculations merely to assess the importance of the conductivity assumptions.

Thermochemical Model Of Surface Thermochemistry. At the high surface temperatures observed in the ablation experiments (~ 4000^oR, or 2220^oK) it seems that full equilibrium should be achieved between the boundary layer edge gases diffusing to the surface, the pyrolysis gas and silica-carbon reaction gas being injected at the surface from in-depth, and the char structure being eroded. About half of the iterative calculations were made with the full-equilibrium assumption. An important consequence

of this assumption is that the SiO produced in-depth by the silica-carbon reaction reacts with oxygen at the surface to form SiO_2^* in an extremely exothermic reaction (References 2 and 24). This reaction helps support high predicted surface temperatures, which in most cases are well above the reported experimental values. An alternative thermochemical model, which holds any silica-carbon reaction gas out of chemical equilibrium with the other surface species (but in equilibrium with itself), eliminate this precipitation reaction and yields much lower predicted surface temperatures. For the calculations cited below, the full equilibrium surface thermochemistry model is identified as the "active" model; the isolated reaction gas model is identified as the "inert" model.

Other property values required in the ablation calculations were not varied during the iterative runs. These quantities included virgin and char material chemical compositions, densities, specific heats, and heats of formation; pyrolysis rate kinetics; virgin material conductivity; and pyrolysis and reaction gas enthalpy-temperature relationships. Reference 2 gives values for these parameters.

Table 8 provides an overview of the iterative calculations. The primary test cases selected were one each from the three experimental O/F ratios of 2, 4, and ∞, all on the "hot" end of the C^* ratio sequence: 1125/NL22, 1092/NL14, and 1084/NL12 respectively. For some predictions, 1083/NL11 was substituted for 1084/NL12 because it had a smoother and possibly more accurate enthalpy history (See Section 2.2.1.3 above). In addition, two runs were made at the "cold" end of the C^* ratio scale at O/F=2, for 1121/NL20.

Table 8 reveals that the surface temperatures predicted by the active model are much higher than the measured temperatures, although the predicted recessions are generally in the correct neighborhood of the measured results. The inert model predictions show surface temperatures near the measured temperatures, with a mixed pattern of recession predictions. A hoped for result of the parametric study was a single combination of the iterated parameters which produced satisfactory predictions for all cases. No such single combination of parameters predicts both measured temperatures and recessions for the inert case. One might imagine that, even though a single combination of parameters will not predict the measured data, an orderly sequence of parameter values might suffice. For the inert cases, however, even this objective cannot be realized, particulary due to difficulties with the O/F=∞ case. The active model predictions, by contrast, do show a single combination of parameter settings which yields good predictions

of recessions for 1125/NL22, 1092/NL14, 1084/NL12, and 1083/NL11. These are:

- 3 lb/ft^3 (48 kg/m^3) liquid layer edge criterion
- 20 mils (508 μm) maximum liquid layer thickness
- low conductivity model

The surface temperature predictions for the above settings are much higher than the measured data, but it is at least possible that the measured data, taken by pyrometer, represent the lower temperatures of the carbon in the structure below the translucent silica layer on the surface.* More weight can therefore be attached to a correct prediction of recession than of temperature. The case 1121/NL20, a low C* ratio firing, is very poorly predicted, however.

Figures 40a through 40p give a more detailed view of the iterative calculation results, showing predicted histories for the surface temperature, the liquid layer thickness, and the net surface recession, as well as the experimental data for surface temperature and post test average surface recession, with an experimental surface recession history interpreted as described in Section 2.2.3.1 above. These graphs confirm the overview provided by Table 8, but indicate that the single surface temperatures cited in Table 8 are rough averages of somewhat oscillatory data and prediction results. Note also that the recession rate data are formed from simple ratios of net ΔS to total exposure time, with no attempt made to account for the "induction time" for recession to start shown in Figure 40 for both experimental data and computer predictions. It is interesting that the computed induction times are in general, quite comparable to those inferred from the experimental data.

The overall conclusion drawn from the comparisons offered by Table 8 and Figure 40 is that the active model with the low conductivity data and liquid layer parameter of 3 lb/ft^3 and a 20 mil liquid thickness has a fair chance of predicting surface recession in the test models.

To test this conclusion further, a complete set of predictions was run, with this provisional best estimate of parameter values, for all the model test cases. The results of this battery of runs are reported in the next section.

---

*In this regard it is interesting that the detailed computer outputs show that surface temperatures correlate rather well with the temperatures predicted to occur at a location where the local density is 30 lb/ft^3, for all cases. This density corresponds to a local carbon density of 3 lb/ft^3, the lowest carbon density considered in the calculations as a liquid layer edge density. This lends some additional support to the belief that the pyrometer temperatures might represent carbon structure temperature.

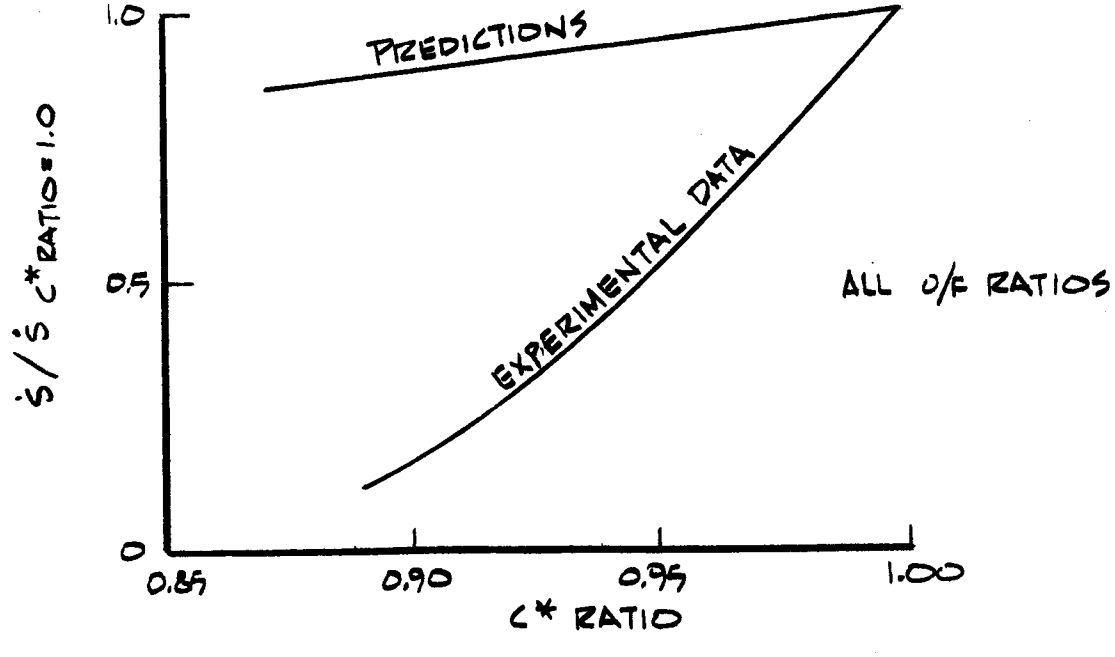
3.4 ABLATION CALCULATIONS ON ALL MODEL TEST CASES WITH UNIFORM SET OF PARAMETER VALUES

A single SCRIMP program prediction was made for each ablation test case (for O/F=2, 4, and ∞ cases) with the parameter values identified in Section 3.3 as most promising for accurate recession predictions: The active surface thermochemistry model, the low thermal conductivity function, a 3 lb/ft^3 (48 kg/m^3) liquid layer edge carbon density, and a 20 mil (508 μm) allowed liquid layer thickness. Table 9 gives an overview of the results of the calculations and compares them to the experimental data.

Table 9 shows that recession predictions for the high C^* ratio cases for all three O/F ratios are quite good, as was expected based on the good results of the iterative calculations for the best cases in this area of the test case map. However, at lower C^* ratios, the high recession trend presaged by the 1121 NL20 test case shown in Table 8 is also confirmed. Recession predictions become gradually worse as C^* ratio decreases, eventually becoming worse by an order of magnitude.

Predicted surface temperatures are quite high, as expected, but, as noted previously, it is not clear that the experimental data truly represent the liquid layer surface temperatures. Therefore, less weight may be attached to this discrepancy.

The general recession prediction situation may be illustrated by the following qualitative graph:



The same general situation is true for all O/F ratios, even though the $\dot{S}$ values near C^* ratio $\cong$ 1 are quite a strong function of O/F. The predictions have the correct O/F ratio dependence, but not the observed dependence on the C^* ratio. The discrepancy between observed and expected trends is so great that some careful thought is clearly required to assess the general predictive situation and to estimate what changes are indicated for the predictive efforts. These suggested reasons for the discrepancy between predicted and observed trend with C^* ratio may be divided into two groups. The first includes possible changes in numbers input into the basic predictive scheme; the second includes fundamental changes in the predictive scheme itself.

In the first group may be listed the following input quantities for which the basic trend with C^* ratio may be suspect:

Convective Transfer Coefficient. Figure 25 shows the input transfer coefficient histories used for the ablative nozzle predictions. There is a distinct upward trend of $\rho_e U_e C_H$ with decreasing C^* ratio which is in the proper direction to yield over-predictions of recession at low C^* ratios. This $\rho_e U_e C_H$ trend derives from the considerations of Section 2.2.2.2 above and seems well-founded, but in view of the ablative prediction results it may bear review. One hesitates, however, to disqualify the calorimeter results, based on heat transfer studies of simple copper and molybdenum bodies, in favor of computed results from a complex ablation model; the SCRIMP program should not be used to discover $\rho_e U_e C_H$ values.

Surface Roughness. The transfer coefficients used in the ablation predictions were all computed with a 1.7 factor to account for roughness effects. Examinations of the actual ablative models indicate that the roughest surfaces are found at the high C^* ratios, and that at low C^* ratios the roughness elements (which are silica globs and rivulets) have somewhat smaller sizes and are noticeably more spaced out, with roughness element spacing being several times the roughness height. This trend, if quantified in terms of its effect on a roughness factor to apply to the transfer coefficient predictions, may assist in bringing the predicted and observed recession trends (with C^* ratio) closer together.

Surface Equilibrium Model. It is possible that a shift toward the inert surface thermochemistry model should be made at the lower surface temperatures characteristic of the low C^* ratio tests. This would reduce predicted surface recession at the lower C^* ratio values by a substantial amount, judging by direct comparisons of active and inert runs made during the iterative calculations reported in Section 3.3.

In addition to the above first group of possible defects, it is possible to list a second group of suspected defects which are related to the

basic computational models of the SCRIMP code. In particular, the following might be suspect:

Assumption of Chemically Homogeneous Surface. The thermochemical erosion calculations performed by ACE presume that the heated surface is chemically uniform. Inspection of the post test models reveals that this is not the case for the lower O/F and C^* ratios, where the surface consists of both exposed carbon and silica. Hence more general thermochemical erosion calculations might be required.

Liquid Layer Recession Model. The SCRIMP code computes recession rates with a liquid layer thickness model. Post-test examinations of the models confirms that there is indeed a relatively thick liquid layer covering the surface at high C^* ratio values for all O/F ratios greater than 1.0 but that at lower C^* ratio values the surface becomes more heterogeneous in character, as discussed above. The idea that the liquid layer controls the recession rate may therefore not be a uniformly sound one, and may need supplementing in certain response regimes.

3.5 SUMMARY OF COMPUTATIONAL EXPERIMENTS

The computational experiments using a specially modified ablation computer code to predict the response of the test models for O/F ratios of 2, 4, and ∞, was partially successful. Agreement between predicted and measured subsurface temperature histories was good when the measured surface temperature and recession histories were employed as boundary conditions. It appears that treatment of subsurface energy transfer and absorption events is adequate. Excellent agreement between observed and predicted recession was obtained for the high C^* ratio cases for a uniform set of values for the adjustable parameters of the code. This agreement spanned the O/F ratio range considered; the code reproduced the O/F dependence of recession exactly. The observed trend of recession rates with C^* ratio was, however, not predicted by the program. The code predicted little change of recession rate with C^* ratio, failing to match the observed decline of recession rates. Part of the trend discrepancy may stem from systematic trends in input quantities, particularly for convective transfer coefficient. Another contributing factor may be a departure from liquid layer control of the recession rate at low C^* ratios. It is possible that the code was pushed beyond the range of its applicability in this respect.

SECTION 4

FLOX-PROPANE ROCKET ABLATION PREDICTIONS

Ablation predictions were performed for conditions corresponding to two tests of an FM-5064, Graphite Phenyl-aldehyde rocket nozzle. These tests were performed at NASA Lewis Research Center and are designated Runs 115 and 150. The propellant utilized in these tests was FLOX (0.76 flourine, 0.24 oxygen by mass) - propane (C_3H_8). A summary of the test operating conditions is given in Table 10.

Predictions were performed by the Aerotherm Charring Material Ablation (CMA) computer program with surface thermochemical boundary conditions generated by the Aerotherm Chemical Equilibrium (ACE) computer code. These two programs are described briefly in Appendices A and C and in more detail in References 15, 16, 21 and 7. All necessary input is described in Section 4.1 and a summary of the results and a comparison to measurements are given in Section 4.2.

4.1 COMPUTER PROGRAM INPUT

The ACE computer program which generated the surface thermochemical boundary conditions for the CMA predictions required as input the edge gas elemental composition, the pyrolysis gas elemental composition, the char material elemental composition, the edge gas thermodynamic state, and parametrically assigned values of normalized pyrolysis gas and char ablation rates.

The elemental compositions of the three components are given in Table 11. The edge gas thermodynamic state was obtained from an isentropic expansion calculation performed by the ACE program. Equilibrium flow was assumed, and real gas effects were accounted for. The important throat edge gas properties were as follows:

	Run 115	Run 150
Static Pressure, psia (MN/m^2)	54.7(.377)	56.5(.390)
Edge Enthalpy, Btu/Lbm (kJ/kg)	-626.(-1455.)	-611.(-1420.)
Recovery Enthalpy, Btu/Lbm (kJ/kg)	-286.(-665.)	-263.(-611.)

Recovery enthalpy is, of course, required as input to the CMA code.

The results of the surface equilibrium thermochemistry calculations are shown in Figures 41a and 41b. Curves of normalized char ablation

rate versus discovered surface temperature for several values of normalized pyrolysis gas rate are shown for each run.

The thermophysical properties of the FM5064, Graphite Phenyl-aldehyde material required as input to the CMA program were estimated from the properties of a similar material for which properties were known (MX4500, Reference 8). The values of specific heat and thermal conductivity for both virgin plastic and charred material are shown in Figures 42 and 43 as a function of material temperature. The other variation which must be input to the CMA code is the pyrolysis gas enthalpy as a function of temperature. This variation is shown in Figure 44.

The heat transfer coefficient boundary conditions existing in the two rocket test runs were estimated by utilizing the simplified Bartz equation given as Equation 13 in Section 2. Since this equation typically overpredicts, the values employed were taken to be 70 percent of the computed values. For Run 115 the initial "cold wall" value was 0.200 lb/ft^2 sec (0.977 Kg/m^2sec) and the "hot wall" value was 0.162(.791); corresponding values for Run 150 were 0.197(.962) and 0.165(.805). Finally, the nozzle surfaces were assumed to be in radiation equilibrium (no net radiation heat transfer) and the ratio of mass-to-heat transfer coefficient was taken as the two-thirds power of the ACE computed Lewis number (C_M/C_H = 0.866 for Run 115 and 0.895 for Run 150).

4.2 SUMMARY OF RESULTS

The predicted responses of the FM-5064, graphite phenyl-aldehyde material are shown in Table 12 for Runs 115 and 150. Also given are the measured average recessions for each run. Two predictions were performed for each run. The first, no char swell, calculation was performed before measured results were available. The second prediction, including the effects of char swell, was performed after the measured pressure history was analyzed (Reference 26). These data showed that considerable swelling of the graphite phenyl-aldehyde had occurred during the firing. An attempt was therefore made to include the effect of swell on the prediction. This phenomena was observed in the work of Reference 8 and a crude model was devised to account for it in Reference 23 . Briefly, the amount that the char swells is assumed proportional to the thickness (relative to the instantaneous surface) of the char. This relation was built in to the CMA computer code and used to correct the transfer coefficient via the radius ratio correction on heat transfer coefficient (see Reference 16). Figures 45a and 45b show the two predicted recession histories and the recession history inferred from the measured pressure data and from the final measured recession for each run.

Surface and backwall temperature histories for the two predictions are also shown in Figure 46a and 46b.

Figure 45 shows that the char swell model does predict the recession trends accurately. It is encouraging that the difference between predicted and measured recession is less than 0.1 inch (2.54 mm) for the two cases. The predicted surface recession trends with temperature (Figures 41a and 41b) reveal that no chemical erosion will occur for surface temperatures less than about 3500^{o}K. Once this temperature level is reached, however, surface recession increases rapidly with temperature due to attack of the carbon char by hydrogen in the propellant stream. It is apparent that differences between predicted and measured recession are well within differences in predicted recession associated with heat transfer coefficient uncertainties. It is concluded that the prediction technique, which considers only chemical erosion and the assumption of chemical equilibrium, is quite adequate for representing the physics of important energy and mass transfer events for the material-propellant environment considered.

SECTION 5

Major conclusions reached during the study are summarized first and are followed by a list of recommendations for logical future effort in the light of these conclusions and anticipated future system requirements.

5.1 CONCLUSIONS

1. A technique has been demonstrated for simultaneously duplicating many of the parameters appropriate to simulating rocket nozzle thermal protection system response. The technique has been demonstrated for nitrogen tetroxide-Aerozine propellant over a wide range of mixture ratio and simulated characteristic velocity.
2. For sufficiently high temperature levels in a nitrogen tetroxide-Aerozine combustion product environment, the ablation rate of silica-phenolic is a strong function of mixture ratio. Minimum surface recession occurs for O/F=1.0 and departures from this mixture ratio in either direction result in substantially increased surface recession.
3. The fundamental mechanism of surface recession for silica phenolic depends strongly upon free stream oxygen content. For high free stream oxygen content, surface recession is governed by production and flow of a liquid silica layer whereas for low free stream oxygen content surface recession is governed by gas phase producing reactions between silica fibers and carbon char matrix. No liquid layer is present in this case.
4. Silica phenolic surface recession is a relatively monotonic function of gas stream energy content for all oxidizer to fuel ratios.
5. The SCRIMP computer program enables accurate predictions of silica phenolic ablation rate for high O/F ratios ($2.0 \leq O/F \leq \infty$) and high gas stream total temperature, but it fails to predict the proper trend of decreasing recession rate with decreasing temperature.
6. The surface roughness on an ablating silica-phenolic nozzle may result in as much as a 70 percent increase in surface heat flux over the smooth wall value.
7. For ($2.0 \leq O/F \leq \infty$) the calorimetric measured heat transfer coefficient experienced a 30 to 35 percent increase with decreasing C* ratio (from 1.0 to 0.85) whereas the corresponding predicted increase is only about 10 percent.

8. The experimental data presented in this report are accompanied by accurate measurements of the fundamental parameters controlling silica phenolic ablation (heat transfer coefficient, enthalpy, free stream chemical composition, and pressure). These data could provide an excellent basis for confirming mathematical models of silica phenolic response over a wide range of free stream chemistry conditions.

9. Based upon comparisons between predicted and measured ablative performance of graphite phenolic in a FLOX-propane rocket nozzle, it may be concluded that consideration of only chemical erosion and the assumption of chemical equilibrium is quite adequate for representing important energy and mass transfer events for this material-propellant combination.

5.2 RECOMMENDATIONS

1. It is recommended that the rocket engine simulation apparatus be modified to accomodate other propellant systems. Giving consideration to the space shuttle and future deep space missions, it would seem appropriate that hydrogen-oxygen, fluorine-hydrogen, and FLOX-hydrocarbon propellant systems be considered.

2. The modified simulation apparatus should be employed to experimentally investigate the thermal and chemical compatibility of candidate thermal protection materials to the above environments. Because the same fundamental simulation parameters are appropriate to ablative and nonablative systems, these experiments should include consideration of both types of thermal protection systems.

3. The observed calorimetric trend of increasing heat transfer coefficient with decreasing stream energy content (C* ratio) should be investigated further in order to learn the reason for the observed trend.

4. Surface roughness effects on heat transfer have been shown to be substantial (as much as a 70 percent increase for measured roughness heights) and these effects should be considered in design and correlation efforts.

5. With respect to better understanding silica phenolic ablation, future work should concentrate on identifying more certainly the reasons for prediction success in one area of the O/F ratio - C* ratio space, and failure in other areas. A review of the input quantities should be made, and further computations done at O/F of 1.0 and 0.38 to add a broader view. It seems likely that failure to predict recession accurately can be correlated with the disappearance of a uniform liquid layer at the surface in favor of globs and rivulets; ablative recession models can then be considered for this regime. Very valuable insight can be gained from a set of calculations using the "fail temperature" approach to silica phenolic ablation described in References 7, 21, and 26.

Analysis of the char layers from the present studies should be performed to yield density and chemical composition profiles. This information will be valuable for formulating or verifying correlative mathematical models of the silica phenolic ablation process.

6. The present effort resulted in a complete description of silica phenolic ablation in terms of local O/F ratio and temperature. Techniques such as those reported in Reference 27 should be employed and generalized in order to enable relating these quantities to measurable injector and rocket engine performance parameters.

7. It is recommended that additional ablation calculations be performed for FLOX-hydrocarbon rocket engine firings in order to verify the computational models for different materials and chamber conditions.

TABLE 1

SIMULATION GAS COMPOSITIONS

O/F RATIO	OXIDIZER FRACTION (Ko_x)	MASS FRACTIONS OF INJECTED SPECIES					
		N_2	O_2	H_2	CO_2	H_2O	MixS[a]
∞	1.000	0.304	0.696	--	--	--	--
4.0	0.800	0.378	0.244	--	0.146	0.232	--
2.0	0.677	0.426	--	0.007	0.244	0.323	--
1.0	0.500	0.488	--	0.054	0.365	0.093	--
0.38	0.277	0.569	--	--	--	--	0.431

[a]Mix Composition 78.2% CO, 21.8% H_2 by mass.

TABLE 2

ARC PLASMA GENERATOR TEST CONDITIONS[a]

Cond	Test No	O/F Ratio	Effective N_2O_4 Frac.	C^*/C^*_{OPT} O/F=2	Total Temp. (°R)	Total Temp. (°K)	Total Enthalpy[b] (Btu/lbm)	Total Enthalpy[b] (MJ/kg)	Enthalpy Inj. Gases (Btu/lbm)	Enthalpy Inj. Gases (MJ/kg)	Enthalpy Addition (Btu/lbm)	Enthalpy Addition (MJ/kg)	η %	Current (Amps)	Volt. (Volts)	Cold Wall Heat Flux (Btu/ft²-sec)	Cold Wall Heat Flux (MW/m²)	Cold Wall Heat Trans. Coeff. (lbm/ft²sec)	Cold Wall Heat Trans. Coeff. (kg/m²sec)	Chamber Pressure (psia)	Chamber Pressure (MN/m²)	Total Mass Flow Rate (lbm/sec)	Total Mass Flow Rate (kg/sec)	Mass Fractions of Injected Gases H_2	O_2	H_2	CO_2	H_2O	Mix S[c]
Series A																													
1-A	1079	∞	1.0	1.004	5650	3139	1882	4.374	0	0	1882	4.374	29	544	647	340	3.859	.186	.908	103.	.710	.0511	.0232	.306	.694	-	-	-	-
	1080			1.023	5820	3233	1969	4.576			1969	4.576	30	544	641	307	3.484	.163	.796	103.	.710	.0511	.0232	.305	.695	-	-	-	-
2 A	1086	4.0	0.8	1.004	5700	3167	911	2.117	-1877	-4.362	2788	6.479	27	740	660	525	5.959	.202	.986	94.9	.654	.0456	.0207	.382	.251	-	.133	.234	-
	1087			1.055	6025	3347	1178	2.738			3055	7.100	30	746	663	525	5.959	.177	.864	95.7	.660	.0457	.0207	.384	.246	-	.134	.236	-
4 A	1109A	2.0	0.667	1.042	5940	3300	601	1.397	-2802	-6.512	3403	7.909	26	863	685	566	6.424	.168	.820	100.	.690	.0427	.0194	.433	-	.007	.232	.328	-
	1110A			.992	5620	3122	335	.778			3137	7.290	25	853	671	470	5.334	.152	.742	95.8	.660	.0432	.0196	.433	-	.007	.232	.328	-
5 A	1109B			1.026	5840	3244	370	.859			3172	7.372	25	833	686	596	6.765	.191	.933	102.	.703	.0432	.0196	.433	-	.007	.231	.329	-
	1110B			.962	5410	3006	69	.160			2871	6.672	25	793	667	505	5.732	.178	.869	96.2	.663	.0433	.0196	.433	-	.007	.232	.328	-
6 A	1109C			.957	5370	2983	-285	-.662			2517	5.850	26	664	679	539	6.118	.219	1.070	100.	.690	.0444	.0201	.432	-	.007	.232	.329	-
	1110C			.916	5075	2819	-372	-.864			2430	5.647	25	674	666	465	5.278	.195	.952	95.5	.658	.0444	.0201	.433	-	.007	.232	.328	-
7 A	1109D			.933	5195	2886	-520	-1.208			2282	5.303	29	561	690	460	5.221	.206	1.010	101.	.696	.0468	.0212	.432	-	.007	.232	.329	-
	1110D			.870	4700	2611	-747	-1.736			2055	4.776	27	564	665	430	4.880	.214	1.040	95.3	.657	.0468	.0212	.433	-	.007	.232	.328	-
8 A	1109E			.860	4620	2567	-1048	-2.436			1754	4.076	26	505	681	443	5.028	.259	1.260	104.	.717	.0492	.0223	.432	-	.007	.232	.329	-
	1110E			.824	4285	2380	-1067	-2.480			1735	4.032	29	455	681	386	4.381	.228	1.110	95.8	.660	.0493	.0224	.432	-	.007	.232	.329	-
3 A	1094	1.0	0.5	1.004	5700	3167	1868	4.341	-1902	-4.420	3770	8.761	27	796	670	674	7.650	.156	.762	96.5	.665	.0368	.0167	.511	-	.052	.341	.096	-
	1095			1.035	5900	3278	1608	3.737			3510	8.157	26	793	672	642	7.287	.158	.772	97.2	.670	.0369	.0167	.500	-	.053	.347	.100	-
9 A	1142	0.38	0.277	.934	5200	2889	2593	6.026	-572	-1.329	3165	7.355	19	850	697	700	7.945	.159	.776	96.8	.667	.0331	.0150	.571	-	-	-	-	.429
Series B																													
13 B	1357A	∞	1.0	1.080	6165	3425	2139	4.971	0	0	2139	4.971	30	580	652	478	5.425	.228	1.110	105.	.724	.0506	.0230	.305	.695	-	-	-	-
14 B	1357B			1.014	5765	3203	1789	4.158			1789	4.158	28	516	649	462	5.244	.265	1.290	104.	.717	.0506	.0230	.305	.695	-	-	-	-
15 B	1356			.881	4800	2667	1293	3.004			1293	3.005	31	375	667	390	4.426	.313	1.530	108.	.745	.0563	.0255	.306	.694	-	-	-	-
	1357D			.930	5170	2872	1428	3.319			1428	3.319	33	384	669	391	4.438	.283	1.380	108.	.745	.0562	.0255	.306	.694	-	-	-	-
16 B	1357C			.965	5425	3014	1551	3.604			1551	3.604	29	457	652	434	4.926	.288	1.410	106.	.731	.0531	.0241	.307	.693	-	-	-	-
1 B	1327A	4.0	0.8	.961	5400	3000	296	.687	-1877	-4.362	2173	5.050	24	636	716	569	6.458	.227	1.110	97.8	.674	.0467	.0212	.581	.244	-	.141	.233	-
	1328A			.980	5530	3072	474	1.102			2351	5.464	25	647	713	560	6.356	.207	1.010	98.6	.680	.0466	.0211	.382	.245	-	.139	.234	-
2 B	1327B			.866	4670	2594	-295	-.685			1582	3.676	24	499	708	558	6.333	.312	1.520	104.	.717	.0518	.0235	.380	.243	-	.141	.234	-
	1328C			.885	4825	2680	-184	-.427			1693	3.934	26	499	713	533	6.050	.277	1.350	105.	.724	.0518	.0235	.380	.245	-	.141	.234	-
3 B	1328D			.852	4550	2528	-374	-.869			1503	3.493	28	418	701	500	5.675	.295	1.440	101.	.696	.0518	.0235	.380	.245	-	.141	.234	-
4 B	1328B			.931	5180	2878	97	-.225			1974	4.588	24	579	701	550	6.242	.243	1.190	97.2	.670	.0466	.0211	.382	.245	-	.139	.234	-
5 B	1334C	1.0	0.5	.920	5100	2833	652	1.515	-1902	-4.420	2554	5.935	22	667	716	700	7.945	.192	.938	99.5	.686	.0398	.0180	.492	-	.050	.357	.100	-
	1335C			.897	4925	2736	501	1.164			2403	5.585	21	665	716	753	8.546	.217	1.060	99.1	.683	.0395	.0179	.496	-	.053	.359	.094	-
6 B	1334A			.862	4640	2578	289	.671			2191	5.092	31	461	698	560	6.356	.173	.845	97.0	.669	.0426	.0193	.492	-	.052	.359	.094	-
	1335B			.834	4380	2433	106	.246			2008	4.667	28	461	699	619	7.026	.207	1.010	97.8	.674	.0425	.0193	.494	-	.052	.360	.094	-
8 B	1334B			.906	5000	2778	551	1.280			2453	5.701	28	563	708	671	7.616	.183	.893	101.	.696	.0426	.0193	.492	-	.052	.359	.094	-
	1335A			.891	4875	2708	459	1.067			2361	5.487	26	572	708	648	7.355	.189	.923	102.	.703	.0425	.0193	.494	-	.052	.360	.094	-
9 B	1346B	0.38	0.277	.937	5225	2903	2611	6.068	-572	-1.329	3183	7.387	25	736	647	650	7.378	.163	.796	96.0	.662	.0351	.0159	.573	-	-	-	-	.427
11 B	1346A			.923	5120	2844	2513	5.840			3085	7.170	29	658	659	634	7.196	.163	.796	100.	.690	.0385	.0175	.564	-	-	-	-	.436
12 B	1346C			.982	5545	3080	3021	7.021			3593	8.350	23	836	652	703	7.979	.160	.781	93.6	.645	.0330	.0150	.576	-	-	-	-	.424

[a] 0.3 inch diameter steady-state calorimeter nozzle

[b] JANAF Thermochemical base state (298°K)

[c] Mix S composition .782 CO, .218 H_2 by mass.

[d] Efficiency defined by Equation , Section

TABLE 3

OPERATING CONDITIONS DURING TRANSIENT CALORIMETER TESTS[a]

Cond	Test No.	Calorimeter type[b]	O/F Ratio	Effective N_2O_4 Frac	C^*/C^*_{OPT} O/F=2	Total Temp. (^oR)	Total Temp. (^oK)	Total Enthalpy[c] (Btu/lbm)	Total Enthalpy[c] (MJ/kg)	Exposure Time (sec)	Heat Flux (Btu/ft²sec)	Heat Flux (MW/m²)	Heat Transfer Coeff. (lbm/ft²sec)	Heat Transfer Coeff. (kg/m²sec)	Chamber Pressure (psia)	Chamber Pressure (MN/m²)	Total Mass Flow Rate (Lb/sec)	Total Mass Flow Rate (kg/sec)	Mass Fractions of Injected Gases N_2	O_2	H_2	CO_2	H_2O	Mix S[d]
Series A																								
1-A	1081	C	∞	1.0	1.058	6040	3356	2020	4.694	14.9	427	4.846	.220	1.070	101.	.696	.0511	.0232	.305	.695	-	-	-	-
1-A	1082		|	|	1.034	5890	3272	1890	4.392	14.7	395	4.483	.228	1.110	101.	.696	.0511	.0232	.305	.695	-	-	-	-
2-A	1089		4.0	0.8	1.045	5960	3311	1050	2.440	13.0	505	5.732	.179	.874	92.0	.634	.0453	.0206	.387	.243	-	.132	.238	-
2-A	1090		|	|	1.028	5860	3256	910	2.115	10.1	537	6.095	.207	1.010	93.0	.641	.0454	.0206	.384	.244	-	.134	.238	-
4-A	1132		2.0	0.667	1.048	5980	3322	700	1.627	8.0	565	6.413	.169	.825	95.6	.659	.0427	.0194	.433	-	.007	.232	.328	-
5-A	1123		|	|	1.021	5810	3228	360	.838	10.5	485	5.505	.158	.772	97.4	.672	.0438	.0199	.435	-	.007	.234	.324	-
5-A	1122		|	|	1.015	5770	3206	260	.605	13.4	400	4.540	.137	.669	94.8	.654	.0430	.0195	.433	-	.007	.230	.330	-
6-A	1127		|	|	1.006	5710	3172	120	.279	10.2	510	5.788	.184	.899	95.6	.659	.0445	.0202	.433	-	.007	.230	.330	-
7-A	1113		|	|	.986	5575	3097	-70	-.163	12.9	409	4.642	.157	.767	95.5	.658	.0469	.0213	.432	-	.007	.233	.328	-
6-A	1126		|	|	.987	5580	3100	-80	-.186	11.9	470	5.334	.179	.874	95.5	.658	.0445	.0202	.432	-	.007	.233	.328	-
7-A	1115		|	|	.936	5220	2900	-490	-1.139	12.3	415	4.710	.190	.928	97.7	.674	.0468	.0212	.433	-	.007	.233	.327	-
7-A	1114		|	|	.934	5200	2889	-500	-1.162	15.3	360	4.086	.167	.816	94.5	.652	.0468	.0212	.433	-	.007	.231	.329	-
8-A	1119		|	|	.893	4890	2717	-800	-1.859	12.0	460	5.221	.246	1.200	95.9	.661	.0491	.0223	.433	-	.007	.230	.330	-
8-A	1118		|	|	.866	4670	2594	-940	-2.185	8.6	423	4.801	.239	1.170	94.3	.650	.0491	.0223	.433	-	.007	.230	.330	-
3-A	1096		1.0	0.5	1.048	5975	3319	1720	3.997	8.4	630	7.150	.163	.796	93.0	.641	.0366	.0166	.502	-	.057	.355	.096	-
3-A	1097		|	|	1.056	6025	3347	1850	4.299	9.5	635	7.207	.158	.772	94.0	.648	.0366	.0166	.503	-	.057	.344	.096	-
9-A	1143		0.38	0.277	.963	5415	3008	2850	6.623	5.2	815	9.250	.183	.894	94.8	.653	.0331	.0150	.571	-	-	-	-	.429
9-A	1144		|	|	1.029	5870	3261	3510	8.157	8.0	840	9.534	.169	.825	93.5	.645	.0334	.0152	.566	-	-	-	-	.434
Series B																								
9-B	1353	MS	0.38	0.277	1.046	5970	3317	3713	8.629	83.2	878[d]	9.965[d]	.180[d]	.879[d]	104.	.717	.0355	.0161	.566	-	-	-	-	.434
9-B	1354	MR	|	|	1.057	6020	3344	3859	8.968	29.8	1580[d]	17.93[d]	.306[d]	1.490[d]	106.	.731	.0352	.0160	.571	-	-	-	-	.429

[a]Operating variables are time integrated averages.

[b]C = copper, MS = smooth molybdenum, MR = rough molybdenum.

[c]JANAF Thermochemical base state (298°K).

[d]Mix S composition .782 CO, 2 .218 H_2 by mass.

[e]Extrapolated values at time = 0.

TABLE 4

SUMMARY OF ABLATIVE NOZZLE TEST DATA

Cond	Test No.	O/F Ratio	Eff. N_2O_4 Frac.	$C^*/C^*_{O/F=2}$	Nozzle No.	Total Enthalpy[a]		Total Temperature		Maximum Chamber Pressure		Minimum Chamber Pressure		Nozzle Exp. Time	Recession Initiation Time	Average Throat Recession		Average Throat Recession Rate		Average Surface Temperature		Total Mass Flow Rate		Mass Fractions of Injected Gases					
						(Btu/lb)	(MJ/kg)	(°R)	(°K)	(psia)	(MN/m²)	(psia)	(MN/m²)	(sec)	(sec)	(mils)	(mm)	(mils/sec)	(mm/sec)	(°R)	(°K)	(lb/sec)	(kg/sec)	N_2	O_2	H_2	CO_2	H_2O	Mix S[b]
1-A	1083	-	1.0	1.083	NL-11	2340	5.348	6185	3436	111	.765	48	.331	19	5.0	100	2.54	5.26	.134	3400	1889	.0511	.0232	.305	.695	-	-	-	-
13-B	1358			1.055	NL-42	2000	4.648	6020	3344	127	.876	47	.324	17	2.5	88	2.24	5.12	.130	4300	2389	.0507	.0230	.306	.694	-	-	-	-
14-B	1359			1.027	NL-43	1850	4.299	5820	3233	126	.869	51	.352	20	2.5	80	2.03	3.93	.100	4250	2361	.0507	.0241	.306	.694	-	-	-	-
1-A	1084			1.021	NL-12	1830	4.253	5915	3286	107	.738	47	.324	18	2.0	97	2.46	5.39	.137	4200	2333	.0511	.0241	.305	.695	-	-	-	-
16-B	1361			.988	NL-40	1650	3.835	5590	3106	125	.862	53	.365	40	6.0	85	2.16	2.14	.0543	4040	2244	.0532	.0255	.306	.694	-	-	-	-
17-B	1362			.914	NL-41	1350	3.137	5050	2806	127	.876	52	.358	92	10.0	82	2.08	0.89	.0226	3860	2144	.0531	.0207	.307	.693	-	-	-	-
15-B	1360			.833	NL-44	1250	2.905	4810	2672	134	.924	53	.365	225	25.0	78	1.98	0.35	.0089	3820	2122	.0563	.0255	.306	.694	-	-	-	-
2-A	1091	4.0	0.8	1.056	NL-13	1200	2.789	6020	3344	133	.917	64	.441	16	4.0	74	1.88	4.75	.120	4000	2222	.0457	.0207	.382	.246	-	.135	.237	-
2-A	1092			1.046	NL-14	1070	2.487	5980	3322	111	.765	50	.345	19	3.0	78	1.98	4.11	.104	4500	2500	.0451	.0204	.386	.240	-	.137	.237	-
1-B	1329			.945	NL-28	200	.464	5300	2944	110	.758	65	.448	20	5.0	88	1.27	2.50	.0635	4150	2306	.0466	.0211	.382	.245	-	.139	.234	-
4-B	1332			.938	NL-31	175	.406	5265	2925	97	.669	45	.310	16	4.0	77	1.96	2.14	.0543	4200	2333	.0467	.0212	.382	.245	-	.139	.234	-
2-B	1330			.899	NL-29	-100	-.232	4950	2750	125	.862	58	.400	89	10.5	67	1.70	0.75	.0190	4000	2222	.0517	.0234	.381	.246	-	.139	.234	-
3-B	1331			.838	NL-30	-440	-1.022	4440	2467	122	.841	64	.441	215	28.0	52	1.32	0.24	.0061	3850	2139	.0521	.0236	.378	.251	-	.139	.232	-
4-A	1135	2.0	0.667	1.055	NL-26	850	1.975	6030	3350	110	.758	51	.352	28	4.5	83	2.11	2.96	.0752	4100	2278	.0426	.0193	.432	-	.007	.232	.329	-
4-A	1134			1.049	NL-25	750	1.743	6000	3333	112	.772	52	.358	37	9.0	76	1.93	2.05	.0521	4200	2333	.0426	.0193	.432	-	.007	.232	.329	-
5-A	1124			1.034	NL-21	740	1.720	5980	3322	116	.800	51	.352	37	9.0	76	1.93	2.05	.0521	4300	2389	.0433	.0196	.434	-	.007	.231	.328	-
5-A	1125			1.027	NL-22	430	.999	5860	3256	115	.793	55	.379	38	7.0	71	1.80	1.87	.0475	4000	2222	.0433	.0196	.434	-	.007	.233	.328	-
6-A	1128			1.024	NL-23	400	.929	5850	3250	114	.786	54	.372	44	9.0	73	1.85	1.66	.0422	4200	2333	.0442	.0200	.434	-	.007	.229	.330	-
6-A	1129			.992	NL-24	20	.046	5620	3122	115	.793	56	.386	56	13.0	71	1.80	1.27	.0322	4200	2333	.0443	.0201	.434	-	.007	.230	.329	-
7-A	1120			.904	NL-19	-720	-1.673	4980	2767	120	.827	54	.372	155	47.0	75	1.90	0.48	.0122	3700	2056	.0466	.0211	.433	-	.007	.230	.330	-
7-A	1117			.892	NL-18	-800	-1.895	4890	2717	126	.869	110	.758	135	98.0	15	.38	0.11	.0028	3000	1667	.0468	.0212	.432	-	.007	.233	.328	-
8-A	1121			.891	NL-20	-810	-1.882	4880	2711	125	.862	118	.814	135	50.0	2	.05	0.01	.0025	3700	2056	.0491	.0223	.432	-	.007	.232	.329	-
8-A	1116			.871	NL-17	-940	-2.814	4720	2622	120	.827	105	.724	133	-	-	-	-	-	3000	1667	.0467	.0212	.432	-	.007	.231	.330	-
3-A	1098	1.0	0.5	1.017	NL-16	1410	3.277	5790	3217	118	.814	59	.407	133	35.0	76	1.93	0.57	.0145	4100	2278	.0368	.0167	.503	-	.057	.345	.095	-
3-A	1099			1.006	NL-15	1310	3.044	5710	3172	104	.717	60	.414	105	24.0	65	1.65	0.62	.0157	3900	2167	.0368	.0167	.505	-	.055	.345	.095	-
7-B	1338			.939	NL-34	780	1.813	5250	2917	113	.779	54	.372	98	10.0	67	1.70	0.68	.0173	4250	2361	.0395	.0179	.494	-	.053	.359	.094	-
5-B	1336			.900	NL-32	520	1.208	4950	2750	104	.717	54	.372	133	10.0	54	1.37	0.41	.0104	4020	2233	.0396	.0180	.494	-	.053	.359	.094	-
8-B	1339			.865	NL-35	300	.697	4670	2594	113	.779	82	.565	172	43.0	19	.48	0.11	.0028	4025	2236	.0425	.0193	.494	-	.053	.359	.094	-
6-B	1337			.827	NL-33	70	.162	4310	2394	146	1.007	104	.717	145	-	-28	-.71	-	-	3550	1972	.0426	.0193	.494	-	.053	.359	.094	-
9-A	1145	0.38	0.277	1.005	NL-10	3250	7.533	5700	3167	105	.724	55	.379	35	7.0	82	2.08	2.34	.0594	4000	2222	.0332	.0151	.569	-	-	-	-	.431
10-B	1348			1.000	NL-37	3200	7.437	5660	3144	105	.724	49	.338	48	6.0	80	2.03	1.67	.0424	4000	2222	.0331	.0150	.574	-	-	-	-	.426
9-A	1146			.998	NL-27	3180	7.390	5640	3133	108	.745	55	.379	33	13.5	84	2.13	2.55	.0648	4000	2222	.0331	.0150	.572	-	-	-	-	.428
12-B	1350			.980	NL-39	3000	6.972	5530	3072	104	.717	54	.372	57	23.5	76	1.93	1.34	.0340	4000	2222	.0332	.0151	.572	-	-	-	-	.428
9-B	1347			.938	NL-36	2630	6.112	5250	2917	111	.765	55	.379	92	23.0	76	1.93	0.83	.0211	3830	2128	.0353	.0160	.569	-	-	-	-	.431
11-B	1349			.840	NL-38	1900	4.416	4450	2472	120	.827	119	.820	167	-	-6	-.15	-	-	3350	1861	.0382	.0173	.568	-	-	-	-	.432

[a] JANAF thermochemical base state (298°K)

[b] Mix S Composition, 78.2% CO, 21.8% H_2 by mass

TABLE 5

SUMMARY OF CALORIMETER NOZZLE HEAT TRANSFER COEFFICIENT MEASUREMENTS AND PREDICTIONS

Cond	O/F	CAL. TYPE AND TEST SERIES[a]	TEST NO.	C^*/C^*_{OPT} O/F=2	AVERAGE H_c (Btu/Lbm)	AVERAGE H_c (MJ/kg)	AVERAGE T_c (°R)	AVERAGE T_c (°K)	AVERAGE P_c (Atm)	AVERAGE P_c (MN/m^2)	HEAT TRANSFER COEFFICIENTS: EXPERIMENTAL (Lbm/ft²-sec)	EXPERIMENTAL (kg/m^2-sec)	BARTZ PRED (Lbm/ft²-sec)	BARTZ PRED (kg/m^2-sec)	BLIMP PRED[b] (Lbm/ft²-sec)	BLIMP PRED[b] (kg/m^2-sec)	$Ch_{exp.}/Ch_{Bartz}$
9-A	0.38	CW-1	1142	1.042	3683.	8.559	5940	3300	6.61	.670	.159	.777	.467	2.28	.379	1.85	.340
11-B		CW-2	1346A	.923	2513.	5.840	5140	2856	6.81	.690	.163	.796	.540	2.64	.391	1.91	.302
9-B		CW-2	1346B	.883	2611.	6.068	5230	2906	6.53	.662	.163	.796	.516	2.52	–	–	.316
12-B		CW-2	1346C	.982	3021.	7.021	5550	3084	6.37	.646	.160	.781	.475	2.32	–	–	.336
9-A		HW-1	1143	.964	2850.	6.623	5420	3011	6.45	.654	.183	.894	.474	2.32	–	–	.386
9-A		HW-1	1144	1.028	3510.	8.157	5860	3256	6.36	.645	.169	.825	.446	2.18	–	–	.379
9-B		HW-2	1353	1.015	3350.	7.780	5760	3200	7.07	.717	.180	.879	.457	2.23	–	–	.394
9-B		HWR-2	1354	1.039	3650.	8.483	5920	3289	7.28	.738	.306	1.490	.453	2.21	–	–	.676
3-A	1.0	CW-1	1094	1.058	1868.	4.341	6050	3361	6.56	.665	.156	.762	.458	2.24	.372	1.82	.341
3-A		CW-1	1095	1.036	1608.	3.737	5910	3284	6.61	.670	.158	.772	.477	2.33	–	–	.332
6-B		CW-2	1334A	.856	248.	.576	4590	2550	6.59	.668	.173	.845	.579	2.83	–	–	.300
8-B		CW-2	1334B	.899	510.	1.185	4610	2561	6.87	.697	.183	.894	.582	2.84	–	–	.314
5-B		CW-2	1334C	.914	611.	1.420	5070	2816	6.77	.686	.192	.938	.566	2.76	–	–	.338
8-B		CW-2	1335A	.884	418.	.971	4820	2678	6.94	.704	.189	.923	.595	2.90	–	–	.317
6-B		CW-2	1335B	.826	66.	.153	4310	2395	6.65	.674	.207	1.01	.591	2.89	.411	2.01	.349
5-B		CW-2	1335C	.891	463.	1.076	4870	2706	6.74	.683	.217	1.06	.577	2.82	–	–	.375
3-A		HW-1	1096	1.046	1720.	3.997	5960	3311	6.33	.642	.163	.796	.438	2.14	–	–	.372
3-A		HW-1	1097	1.057	1850.	4.299	6040	3356	6.38	.647	.158	.772	.434	2.12	–	–	.364
4-A	2.0	CW-1	1109A	1.040	601.	1.396	5940	3300	6.84	.694	.168	.820	.406	1.98	.375	1.83	.414
5-A		CW-1	1109B	1.022	370.	.859	5830	3239	6.92	.702	.191	.933	.413	2.02	–	–	.462
4-A		CW-1	1110A	1.019	335.	.778	5810	3228	6.52	.661	.152	.742	.399	1.95	–	–	.381
5-A		CW-1	1110B	.996	69.	.160	5650	3139	6.54	.663	.178	.869	.403	1.97	–	–	.442
6-A		CW-1	1109C	.959	-285.	-.662	5400	3000	6.80	.690	.219	1.070	.431	2.10	–	–	.508
6-A		CW-1	1110C	.949	-372.	-.864	5320	2956	6.50	.659	.195	.952	.425	2.08	–	–	.459
7-A		CW-1	1109D	.930	-520.	-1.208	5180	2878	6.90	.700	.206	1.010	.449	2.19	–	–	.458
7-A		CW-1	1110D	.900	-747.	-1.736	4960	2756	6.48	.657	.214	1.040	.444	2.17	–	–	.482
8-A		CW-1	1109E	.852	-1048.	-2.436	4560	2534	7.05	.715	.259	1.260	.488	2.38	–	–	.532
8-A		CW-1	1110E	.849	-1067.	-2.480	4530	2517	6.52	.661	.228	1.110	.460	2.25	.395	1.93	.496
4-A		HW-1	1132	1.046	700.	1.627	5980	3322	6.50	.659	.169	.825	.389	1.90	–	–	.435
5-A		HW-1	1123	1.021	360.	.836	5820	3234	6.62	.671	.158	.772	.401	1.96	–	–	.394
5-A		HW-1	1122	1.013	260.	.604	5780	3211	6.45	.654	.137	.669	.395	1.93	–	–	.347
6-A		HW-1	1127	1.003	120.	.278	5700	3167	6.50	.659	.184	.899	.399	1.95	–	–	.461
7-A		HW-1	1113	.983	-70.	-.162	5560	3089	6.50	.659	.157	.767	.400	1.95	–	–	.392
6-A		HW-1	1126	.982	-80.	-.185	5550	3084	6.50	.659	.179	.874	.400	1.95	–	–	.447
7-A		HW-1	1115	.979	-100.	-.232	5540	3078	6.65	.674	.162	.791	.406	1.98	–	–	.399
7-A		HW-1	1114	.933	-500.	-1.162	5200	2889	6.43	.652	.167	.816	.425	2.08	–	–	.393
8-A		HW-1	1119	.892	-800.	-1.859	5880	2711	6.52	.661	.246	1.200	.441	2.15	–	–	.557
8-A		HW-1	1118	.871	-940.	-2.185	4720	2622	6.41	.650	.239	1.170	.441	2.15	–	–	.542
2-A	4.0	CW-1	1086	1.031	911.	2.117	5880	3267	6.46	.655	.202	.986	.413	2.02	–	–	.488
2-A		CW-1	1087	1.055	1178.	2.738	6030	3350	6.51	.660	.177	.864	.411	2.01	.365	1.78	.432
1-B		CW-2	1327A	.956	274.	.636	5370	2984	6.65	.674	.227	1.110	.444	2.17	–	–	.512
2-B		CW-2	1327B	.860	-316.	-.734	4630	2572	7.06	.716	.312	1.520	.497	2.43	–	–	.627
1-B		CW-2	1328A	.980	452.	1.050	5540	3078	6.71	.680	.207	1.010	.433	2.12	–	–	.476
4-B		CW-2	1328B	.927	75.	.174	5160	2867	6.60	.669	.243	1.190	.454	2.22	–	–	.536
2-B		CW-2	1328C	.880	-206.	.478	4800	2667	7.14	.724	.277	1.350	.497	2.43	–	–	.556
3-B		CW-2	1328D	.846	-396.	-.980	4540	2522	6.87	.697	.295	1.440	.494	2.41	.416	2.03	.599
2-A		HW-1	1089	1.044	1050.	2.440	5960	3311	6.26	.635	.179	.874	.398	1.94	–	–	.449
2-A		HW-1	1090	1.031	910.	2.115	5880	3267	6.33	.642	.207	1.010	.404	1.97	–	–	.513
1-A	∞	CW-1	1079	1.032	1882.	4.374	5880	3267	6.99	.709	.186	.908	.470	2.30	–	–	.395
1-A		CW-1	1080	1.047	1969.	4.576	6000	3334	6.99	.709	.163	.796	.467	2.28	–	–	.328
15-B		CW-2	1356	.900	1293.	3.005	4900	2722	7.38	.748	.313	1.530	.542	2.65	.474	2.32	.578
13-B		CW-2	1357A	1.056	2139.	4.971	6180	3434	7.16	.726	.228	1.110	.468	2.28	.430	2.10	.488
14-B		CW-2	1357B	1.012	1789.	4.157	5780	3211	7.09	.719	.265	1.290	.486	2.37	.438	2.14	.545
16-B		CW-2	1357C	.962	1551.	3.604	5430	3017	7.22	.732	.288	1.410	.516	2.52	–	–	.558
15-B		CW-2	1357D	.933	1428.	3.319	5800	3222	7.31	.741	.283	1.380	.528	2.58	–	–	.536
1-A		HW-1	1081	1.057	2020.	4.694	6060	3367	6.88	.698	.220	1.070	.457	2.23	–	–	.481
1-A		HW-1	1082	1.033	1890.	4.392	5900	3278	6.87	.697	.228	1.110	.463	2.26	–	–	.492

[a] CW - Denotes Cold Wall (Steady State) Calorimeter Nozzle
HW - Denotes Hot Wall (Transient) Calorimeter Nozzle
HWR- Denotes Hot Wall Calorimeter with Roughened Surface
-1 Denotes Test Series A
-2 Denotes Test Series B

[b] Blimp predicted $\rho_e U_e C_H$ is for a location at the entrance of the tubular section of the throat (λ = .20667 Ft, See Fig. 24) assumes fully turbulent flow.

TABLE 6

GENERAL APPEARANCES OF THROAT SURFACES

C* Range	Oxidizer To Fuel Ratio				
	∞	4.0	2.0	1.0	0.38
HIGH	Significant melt layer coverage of surface with minimal exposed char material; melt consists of many small beads closely packed together; evidence of surface bubbles; and metallic flecks; rough contour but nearly symmetrical ablation.	Melt layer - nearly covering charred suface; contour is rough but ablation was approximately symmetrical.	Melt beads covering most surface char. Occasionally areas of char are exposed. Rough but mostly symmetrical surface recession.	Exposed char material with no apparent melt; surface of char is harder than in-depth char showing possible melt impregnation of surface; contour is smooth but ablation was non-symmetrical.	Exposed char material with no melt appearance; surface char has same hardness or in-depth char; somewhat non-symmetrical recession but contour smooth.
MEDIUM	Melt beads cover a portion of the char surface. Exposed char contains melt and metallic flecks and is much harder than subsurface char. Recession very non-symmetrical.	Small melt beads covering less than 50 percent of surface; hard surface char appears impregnated with melt; rough non-symmetrical ablation.	Melt beads covering roughly 50 percent of surface. Exposed char appears to contain impregnated melt but in-depth char does not.	Exposed char which has been impregnated with melt making the surface char harder than in-depth char. Very non-uniform ablation.	Exposed char with no evidence of anything other than carbonaceous material at the surface.
LOW	Occasional beads of melt which have been colored by a pink material at the char surface. The mixture of pink melt shows many minute bubbles. Ablation was extremely non-symmetrical.	Black hard surface material with occasional beads of melt appearing. Impregnation of surface char with melt and occasional flecks of a metallic material. Smooth contour but extremely non-symmetrical recession.	Relatively thick sheets of melt completely covering the char surface; melt thickness uniform about circumference; no recession.	A few small melt droplets apparent and the surface char was deeply impregnated with melt material; surface was therefore much stronger and chemically resistant than that for any other condition. Rough surface with no recession.	Exposed char with no melt as above but no recession.

TABLE 7

OVERVIEW OF ALL MODEL TESTS SHOWING THOSE CASES STUDIED BY ASSIGNED SURFACE TEMPERATURE & RECESSION RATE COMPUTER RUNS

C* RATIO	O/F RATIO									
	.38		1.0		2.0		4.0		∞	
	Test No.	Nozzle No.	Test No.	Nozzle No.	Test No.	Nozzle No.	Test No.	Nozzle No.	Test No.	Nozzle No.
1.083									1083	NL-11*
1.056							1091	NL-13*		
1.055					1135	NL-26*			1358	NL-42+
1.049					1134	NL-25*				
1.046							1092	NL-14*+		
1.034					1124	NL-21*				
1.027					1125	NL-22*+			1359	NL-43+
1.024					1128	NL-23*				
1.021									1084	NL-12*+
1.017			1098	NL-16*						
1.006			1099	NL-15*						
1.005	1145	NL-10*								
1.000	1348	NL-37								
.998	1146	NL-27*								
.992					1129	NL-24*				
.988									1361	NL-40+
.980	1350	NL-39								
.945							1329	NL-28		
.939			1338	NL-34						
.938	1347	NL-36					1332	NL-31		
.914									1362	NL-41+
.904					1120	NL-19*				
.900			1336	NL-32						
.899							1330	NL-29+		
.892					1117	NL-18*				
.891					1121	NL-20*				
.883									1360	NL-44+
.871					1116	NL-17*				
.865			1339	NL-35						
.840	1349	NL-38								
.838							1331	NL-30+		
.827			1337	NL-33						

*CMA Option 2 predictions

+SCRIMP Option 2 predictions

Table 8

SUMMARY OF COMPUTED RESULTS FOR ITERATIVE TEST CALCULATIONS
SCRIMP PROGRAM

		COMPUTER CODE PARAMETERS					1125 NL-22 O/F=2						1121 NL-20 O/F=2						1092 NL-14 O/F=4						1084 NL-12 O/F=∞						1083 NL-11 O/F=∞					
		Kinetics	ρ_{min}		δ_{max}		Conductivity	T_w (°R)	T_w (°K)	ΔS (mils)	ΔS (mm)	$\dot{S}$ (mils/sec)	$\dot{S}$ (μm/sec)	T_w (°R)	T_w (°K)	ΔS (mils)	ΔS (mm)	$\dot{S}$ (mils/sec)	$\dot{S}$ (μm/sec)	T_w (°R)	T_w (°K)	ΔS (mils)	ΔS (mm)	$\dot{S}$ (mils/sec)	$\dot{S}$ (μm/sec)	T_w (°R)	T_w (°K)	ΔS (mils)	ΔS (mm)	$\dot{S}$ (mils/sec)	$\dot{S}$ (μm/sec)	T_w (°R)	T_w (°K)	ΔS (mils)	ΔS (mm)	$\dot{S}$ (mils/sec)	$\dot{S}$ (μm/sec)
	Measured Values →							4650	2220	82	2.08	2.2	56.	3700	2500	3	.0762	0	0	4500	2500	78	1.98	4.1	104.	4600	2556	97	2.46	5.4	137.0	—	—	100	2.54	5.3	135.
ACTIVE RUNS		(x-Nominal)[a]	(Lbm/ft³)	(kg/m³)	(mils)	(μm)																															
		.1	7	112.	2	51	L	4100	2300	198	5.03	5.3	140.							4400	2450	257	6.53	13.5	340.	4800	2650	297	7.54	17.1	430.						
		.1	3	48.	10	254	L	4590	2500	109	2.77	2.9	74.	4300	2400	257	6.53	1.9	4.8	5100	2850	137	3.48	7.2	180.	5200	2900	188	4.78	10.0	250.						
		.01	3	48.	10	254	L	4750	2600	23	.58	.6	15.							5100	2900	44	1.12	2.3	58.	5300	2950	52	1.32	2.9	70.						
		.01	3	48.	10	254	H	4859	2600	15	.38	.4	10.							5100	2850	45	1.14	2.4	61.	5200	2900	70	1.78	3.9	100.						
		.1	3	48.	20	508	H	4590	2500	77	1.96	2.1	53.							5000	2800	102	2.59	5.4	140.							5400	3000	188	4.78	10.0	250.
		.1	3	48.	20	508	L	4850	2650	71	1.80	1.9	48.	4200	2350	163	4.14	1.2	3.1	5200	2900	87	2.21	4.6	120.	5300	2950	116	2.95	6.5	160.	5400	3000	136	3.45	7.6	190.
INERT RUNS																																					
		.1	3	48.	10	254	L	4400	2450	80	2.03	2.1	53.							4600	2550	29	.74	1.5	38.	4500	2500	5	.127	.3	7.						
		.1	3	48.	10	254	H	4400	2450	78	1.98	2.0	51.							4400	2450	26	.66	1.4	36.	4300	2400	2	.051	.1	2.						
		.1	3	48.	5	127	H	4400	2450	93	2.36	2.4	61.							4400	2450	34	.86	1.8	46.	4300	2400	7	.178	.4	10.						
		.1	7	112.	10	254	H	4350	2400	120	3.05	3.2	81.							4300	2400	48	1.22	2.5	64.	4300	2400	14	.356	.8	20.						
		.1	5	80.	10	254	H	4400	2450	99	2.51	2.6	66.							4300	2400	36	.91	1.9	48.	4300	2400	8	.203	.4	10.						
		.1	5	80.	2	51	H	4200	2350	103	2.61	2.8	71.							4300	2400	40	1.02	0.1	21.	4300	2400	11	.279	.6	15.						
		.1	7	112.	2	51	H	4300	2400	146	3.71	3.9	99.							4200	2350	66	1.68	3.5	89.	4300	2400	24	.610	1.3	33.	4000	2200	32	.81	1.7	40.
		1.0	7	112.	2	51	H	3900	2200	229	5.82	6.1	160.							4000	2200	117	2.97	6.2	160.							3800	2100	77	1.96	4.0	100.
		1.0	3	48.	10	254	H	4190	2300	149	3.78	4.0	100.							4100	2300	68	1.73	3.6	91.							3900	2150	36	.91	1.9	48.
		1.0	3	48.	2	51	H	4000	2200	183	4.65	4.9	120.							4000	2200	92	2.34	4.8	120.							3900	2150	53	1.35	2.7	69.
		1.0	7	112.	10	254	H	4000	2200	193	4.90	5.1	130.							4000	2200	90	2.29	4.7	120.							3900	2150	56	1.42	2.9	74.

[a] Nominal Kinetics: $A=9\times10^7$ sec^{-1}, E=80000 cal/gr-mole (.335 MJ/gr-mole)

TABLE 9

SUMMARY OF SCRIMP PROGRAM PREDICTION RESULTS FOR ALL TEST MODELS
AT O/F=2, 4 AND ∞, FOR UNIFORM SET OF PARAMETER VALUES[a]

			O/F = 2.0										O/F = 4.0										O/F = ∞									
			ΔS Measured (mils)	ΔS Measured (mm)	ΔS Predicted (mils)	ΔS Predicted (mm)	$\dot{S}$ Measured (mils/sec)	$\dot{S}$ Measured (μm/sec)	$\dot{S}$ Predicted (mils/sec)	$\dot{S}$ Predicted (μm/sec)	T_w Measured ($^\circ$R)	T_w Measured ($^\circ$K)	T_w Predicted ($^\circ$R)	T_w Predicted ($^\circ$K)	ΔS Measured (mils)	ΔS Measured (mm)	ΔS Predicted (mils)	ΔS Predicted (mm)	$\dot{S}$ Measured (mils/sec)	$\dot{S}$ Measured (μm/sec)	$\dot{S}$ Predicted (mils/sec)	$\dot{S}$ Predicted (μm/sec)	T_w Measured ($^\circ$R)	T_w Measured ($^\circ$K)	T_w Predicted ($^\circ$R)	T_w Predicted ($^\circ$K)	ΔS Measured (mils)	ΔS Measured (mm)	ΔS Predicted (mils)	ΔS Predicted (mm)	$\dot{S}$ Measured (mils/sec)	$\dot{S}$ Measured (μm/sec)	$\dot{S}$ Predicted (mils/sec)	$\dot{S}$ Predicted (μm/sec)	T_w Measured ($^\circ$R)	T_w Measured ($^\circ$K)	T_w Predicted ($^\circ$R)	T_w Predicted ($^\circ$K)
C Ratio	Test	Model																																		
1.083	1083	NL11																																		
1.056	1091	NL13													74	1.88	76	1.93	4.8	120.	4.9	120.	4000	2200	5200	2900	100	2.54	136	3.45	5.3	130.	7.0	180.			5400	3000
1.055	1135	NL26	83	2.11	52	1.32	3.0	76.	1.8	46.	4100	2300	4700	2600																						
1.055	1358	NL42																									84	2.13	103	2.61	4.9	120.	6.0	150.	4400	2450	5300	2950
1.049	1134	NL25	76	1.93	100	2.54	2.0	51.	2.7	69.	4200	2350	4800	2650	78	1.98	87	2.21	4.1	100.	4.6	120.	4500	2500	5200	2900										
1.046	1092	NL14																																		
1.034	1124	NL21	76	1.93	105	2.67	2.0	51.	2.8	71.	4200	2350	4800	2650																						
1.027	1125	NL22	82	2.08	71	1.80	1.9	48.	1.9	48.	4000	2200	4800	2650																						
1.027	1359	NL43																									81	2.06	130	3.30	4.0	100.	6.4	160.	4300	2400	5300	2950
1.024	1128	NL23	73	1.85	107	2.72	1.7	43.	2.4	61.	4100	2300	4600	2550													97	2.46	116	2.95	5.4	140.	6.5	160.	4600	2550	5300	2950
1.021	1084	NL12																																		
.992	1129	NL24	71	1.80	107	2.72	1.3	33.	1.9	48.	4100	2300	4600	2550													75	1.90	324	8.23	1.9	48.	8.1	210.	4100	2300	5400	3000
.988	1361	NL40																																		
.954	1332	NL31													70	1.78	159	4.04	2.0	51.	4.4	110.	4250	2350	5100	2850										
.945	1329	NL28													42	1.07	72	1.83	2.1	53.	3.6	91.	4200	2350	5000	2800										
.914	1362	NL41																									75	1.90	755	19.2	.8	20.	8.2	210.	4000	2200	5300	2950
.904	1120	NL19	75	1.90	187	4.75	.5	13.	1.2	30.	3600	2000	4200	2350																						
.899	1330	NL29													62	1.57	764	19.4	.7	18.	8.6	220.	4000	2200	5000	2800										
.892	1117	NL18	15	.38	183	4.65	.1	2.	1.4	36.	3100	1700	4300	2400																						
.891	1121	NL20	2	.05	163	4.14	0	0	1.2	30.	3700	2050	4200	2350																						
.883	1360	NL44																									71	1.80	1256	31.9	.3	8.	7.9	200.	3900	2150	5200	2900
.871	1116	NL17			105	2.67	0	0	.8	20.	3000	1650	4200	2350																						
.838	1331	NL30													40	1.02	1065	27.0	.2	5.	5.0	130.	3900	2150	4700	2600										

[a] ρ_c = 3 lb/ft³ (48.1 kg/m³) δ_f = 20 mils (508 μm)
Kinetics = 0.1 x Nominal
Low Conductivity Model
Active Surface Thermochemistry Model

TABLE 10

SUMMARY OF FLOX-PROPANE ROCKET TEST CONDITIONS[a]

	RUN 115	RUN 150
Chamber Pressure, psia (MN/m^2)	95.4(.658)	98.2(.677)
Oxidizer Flow Rate, lbm/sec (kg/sec)	.4366(.1980)	.4306(.1953)
Fuel Flow Rate, lbm/sec (kg/sec)	.1171(.0531)	.1049(.0476)
Total Flow Rate, lbm/sec (kg/sec)	.5537(.2511)	.5355(.2429)
Oxidizer-To-Fuel Ratio	3.73	4.11
Total Enthalpy, Btu/lbm (kJ/kg)[b]	-224.5(-522.)	-203.4(-473.)
Total Temperature,[c] ^{o}R (^{o}K)	7272.(4040.)	7472.(4151.)
Vacuum Thrust, lbf (N)	157.3(699.7)	155.2(690.4)
C* Efficiency, percent (based on thrust)	95.0	97.6
Total Run Time, sec	165.0	111.0
Flourine in Flox, Mass Fraction	0.76	0.76
Initial Diameter, Inch (m)	1.20(.0305)	1.20(.0305)

[a]Average values where applicable.

[b]JANAF Thermochemical Base State (Reference 3); ideal combustion.

[c]Equilibrium composition at given total enthalpy and pressure.

TABLE 11

ELEMENTAL COMPOSITIONS[a] OF CONSTITUENTS

ELEMENT	EDGE GAS RUN 115	EDGE GAS RUN 150	PYROLYSIS GAS[b]	CHAR
HYDROGEN	.03838	.03553	.00894	--
CARBON	.01442	.01334	.05089	.08326
OXYGEN	.01182	.01206	.02373	--
FLOURINE	.03152	.03216	--	--

[a]Units are ATOMIC WEIGHT PER UNIT MASS(e.g. gram-atoms/gm).

[b]Pyrolysis gas composition is defined from assuming 44 percent resin residual of a phenyl-aldehyde resin (C_7H_6O). The pyrolysis gas functional formula is therefore $C_{3.186}H_6O$.

TABLE 12

SUMMARY OF MEASURED AND PREDICTED THROAT RESPONSES OF FM 5064, GRAPHITE PHENYL-ALDEHYDE TO FLOX-PROPANE PROPELLANT

RUN NUMBER	RUN DURATION	MEASURED RECESSION		PREDICTED RESPONSES							
				NO CHAR SWELL				CHAR SWELL			
				RECESSION		SURFACE TEMP		RECESSION		SURFACE	TEMP.
	(Sec)	(inch)	(mm)	(inch)	(mm)	(^oR)	(^oK)	(inch)	(mm)	(^oR)	(^oK)
115	165.	0.040	1.01	0.	0.	5880.	3270.	-0.051	-1.30	6000.	3330.
150	111.	-0.004	-0.10	0.007	0.18	5990.	3325.	-0.036	-0.91	6040.	3345.

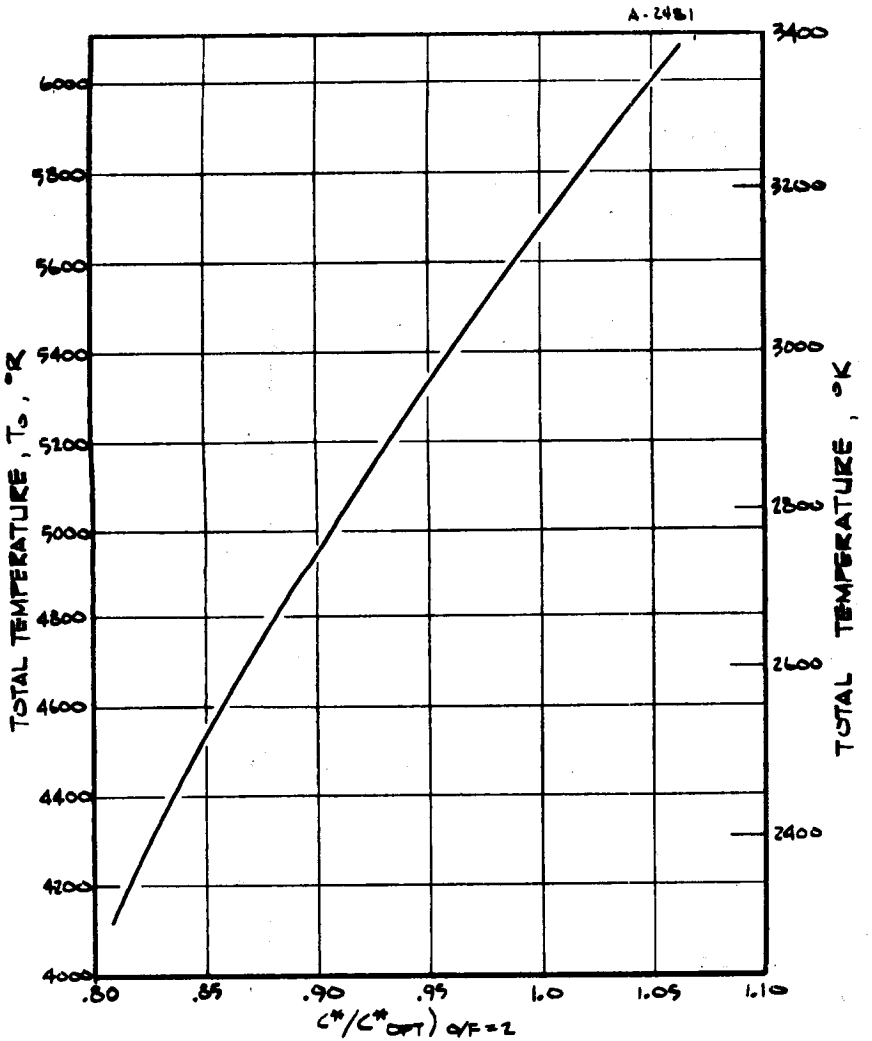


FIGURE 1 CHARACTERISTIC VELOCITY RATIO (C^*/C^*_{OPT}) AS A FUNCTION OF TEMPERATURE FOR O/F = 2.0 (K_{ox} = .667) P_c = 103 PSIA (7.0×10^5 N/M²)

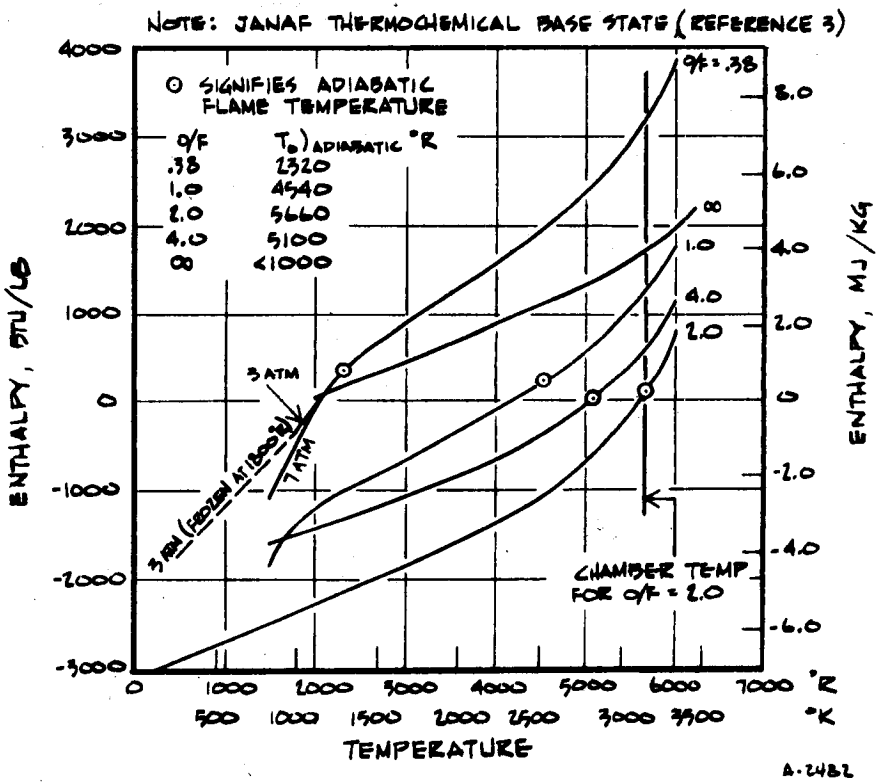


FIGURE 2 TEMPERATURE - ENTHALPY CHARACTERISTICS FOR VARIOUS OXIDIZER TO FUEL RATIOS OF N_2O_4 - N_2H_4/UDMH (50/50) P = 7ATM (103 psia)

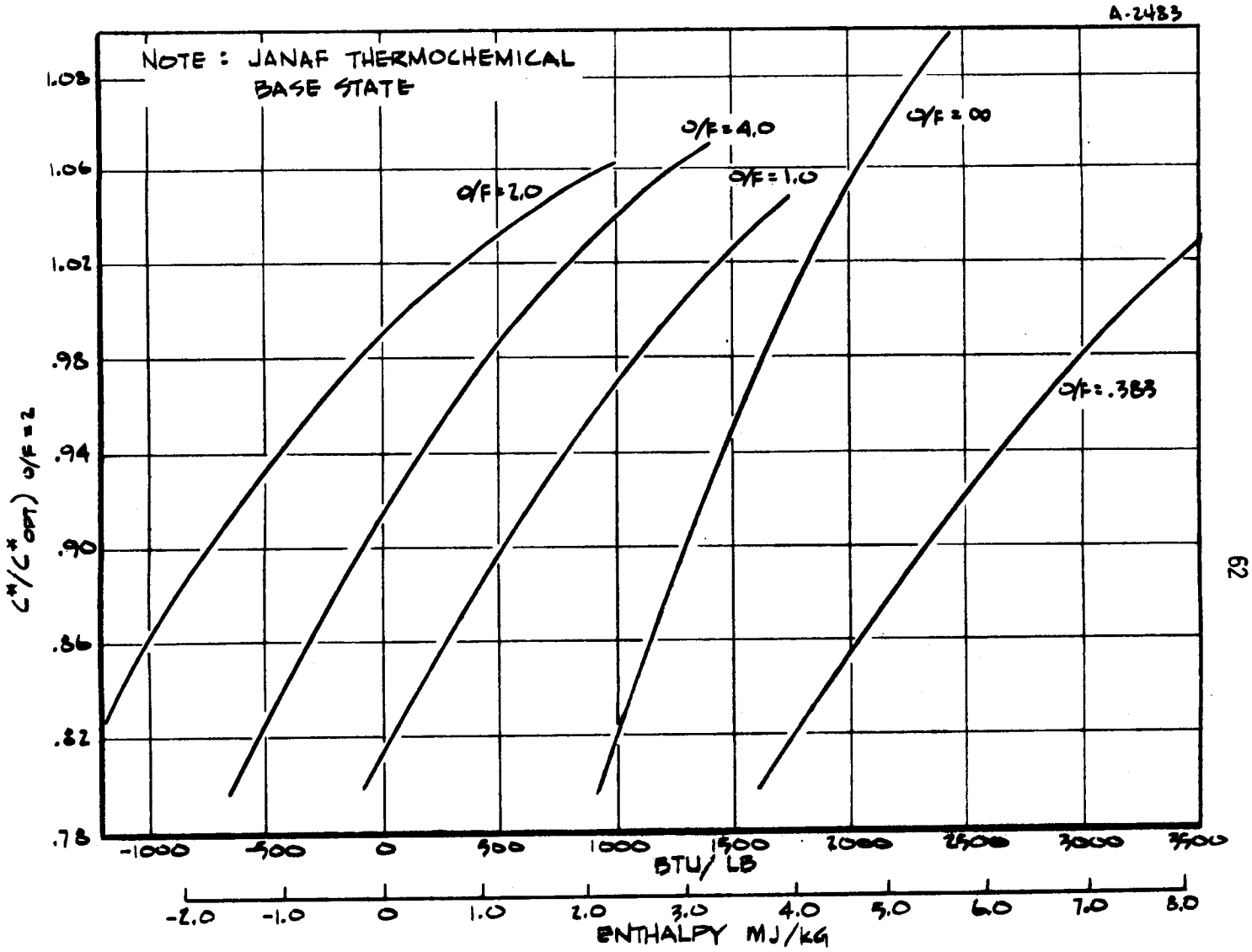


FIGURE 3 ENTHALPY OF OFF-OPTIMUM MIXTURE RATIO REQUIRED TO PRODUCE TEMPERATURE CORRESPONDING TO INDICATED CHARACTERISTIC VELOCITY RATIO FOR O/F OF 2.0

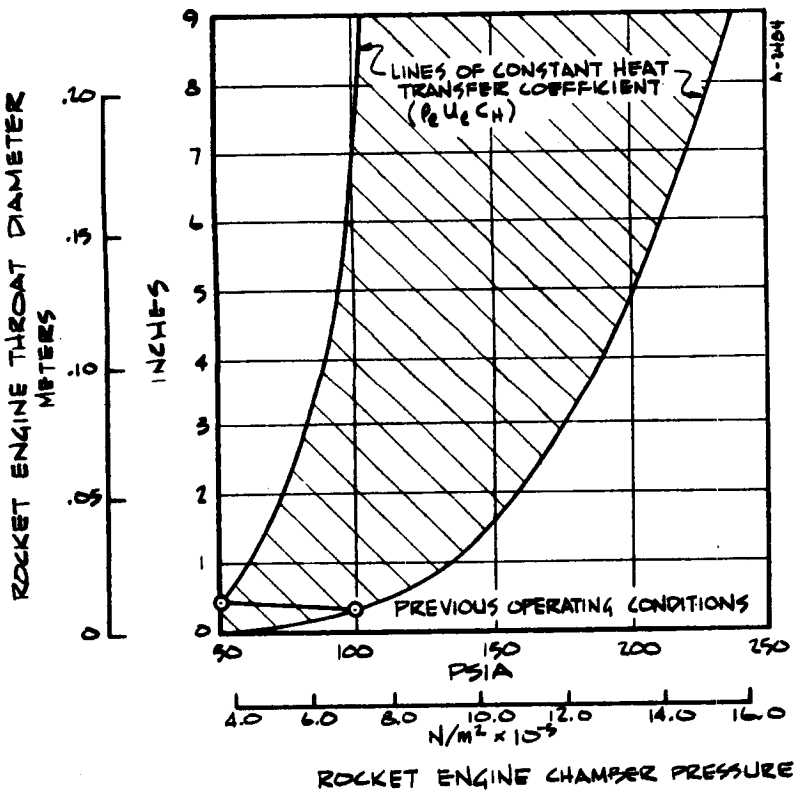
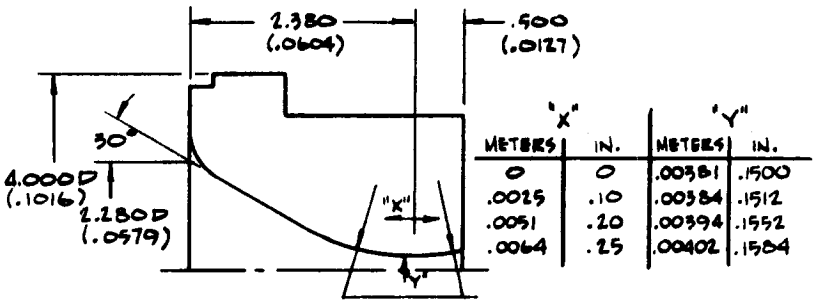
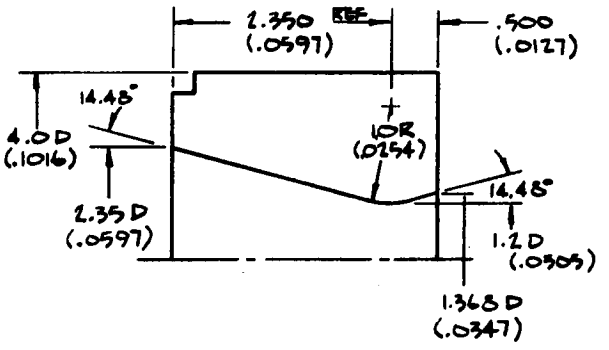


FIGURE 4 RANGE OF ROCKET ENGINE OPERATING CONDITIONS FOR WHICH HEAT TRANSFER COEFFICIENT IS SIMULATED IN ARC PLASMA DEVICE FOR N_2O_4-N_2H_4/UDMH PROPELLANT



"X" METERS	"X" IN.	"Y" METERS	"Y" IN.
0	0	.00381	.1500
.0025	.10	.00384	.1512
.0051	.20	.00394	.1552
.0064	.25	.00402	.1584

a) ARC-PLASMA TEST NOZZLE



b) ROCKET NOZZLE

ALL DIMENSIONS IN INCHES & (METERS)

FIGURE 5 ROCKET NOZZLE & ARC-PLASMA TEST NOZZLE DESIGNED TO DUPLICATE $A/A^* = f(x)$ FOR A DISTANCE OF 0.25 INCHES, (.0635 METERS) UP & DOWN STREAM OF THE THROAT

A-1485

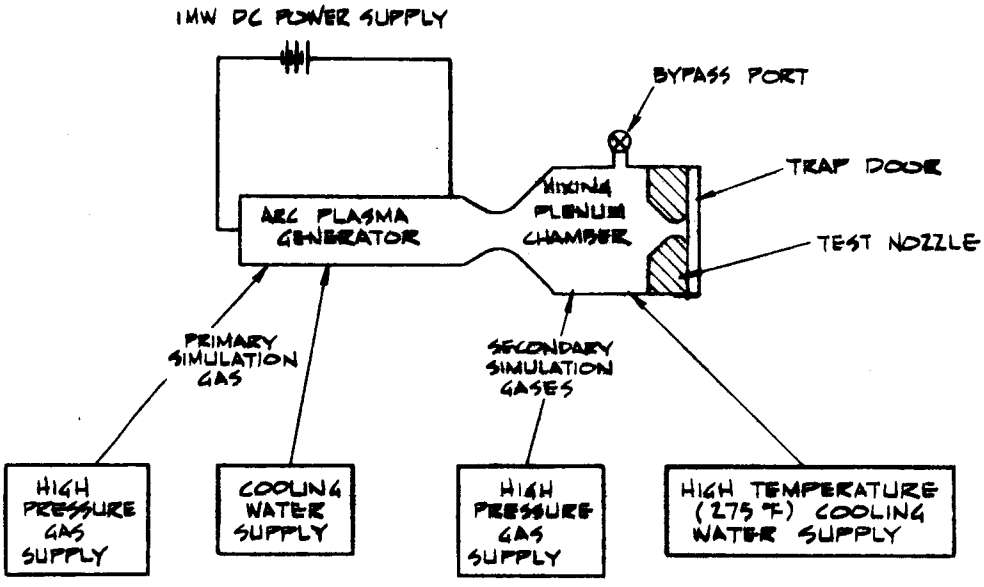


FIGURE 6 SIMULATION APPARATUS SCHEMATIC

A-1486

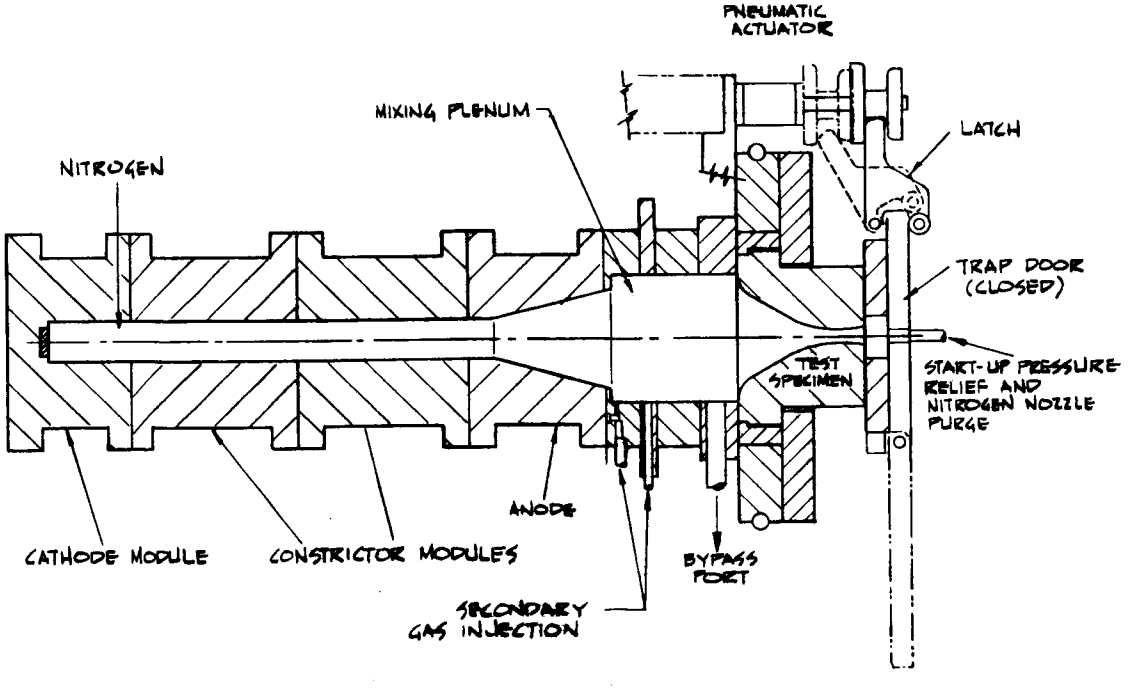
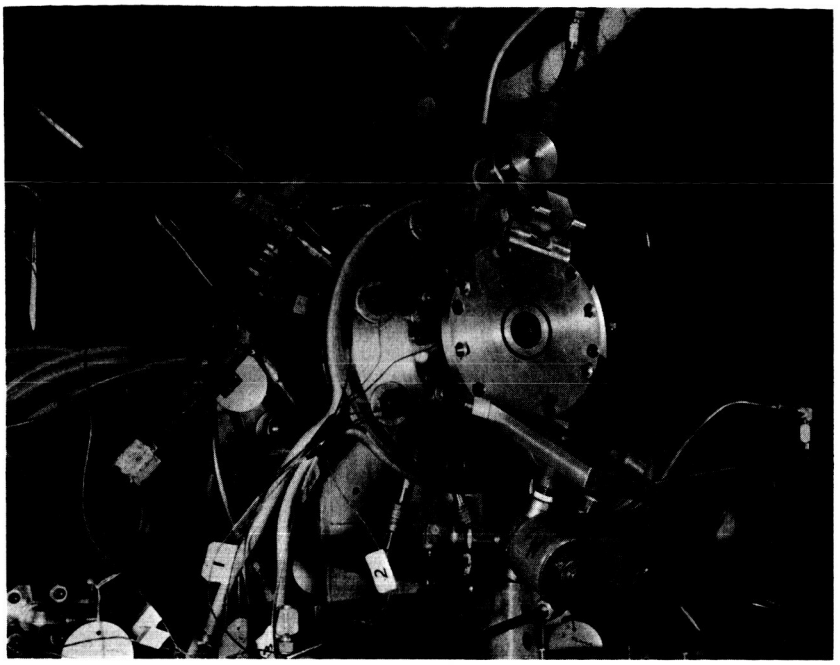
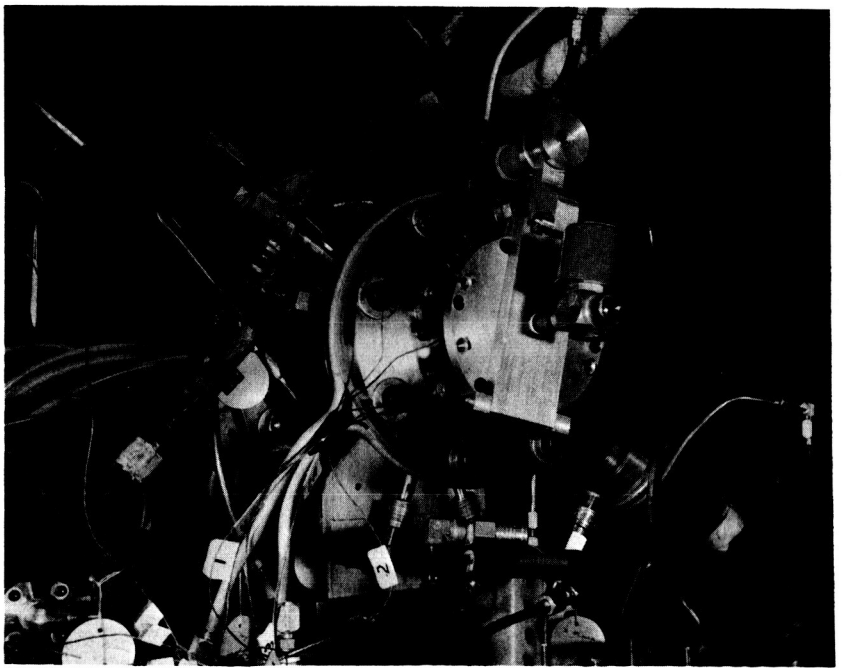


FIGURE 7 ARC PLASMA GENERATOR, MIXING PLENUM, AND TRAP DOOR ASSEMBLY SCHEMATIC.

A-1487

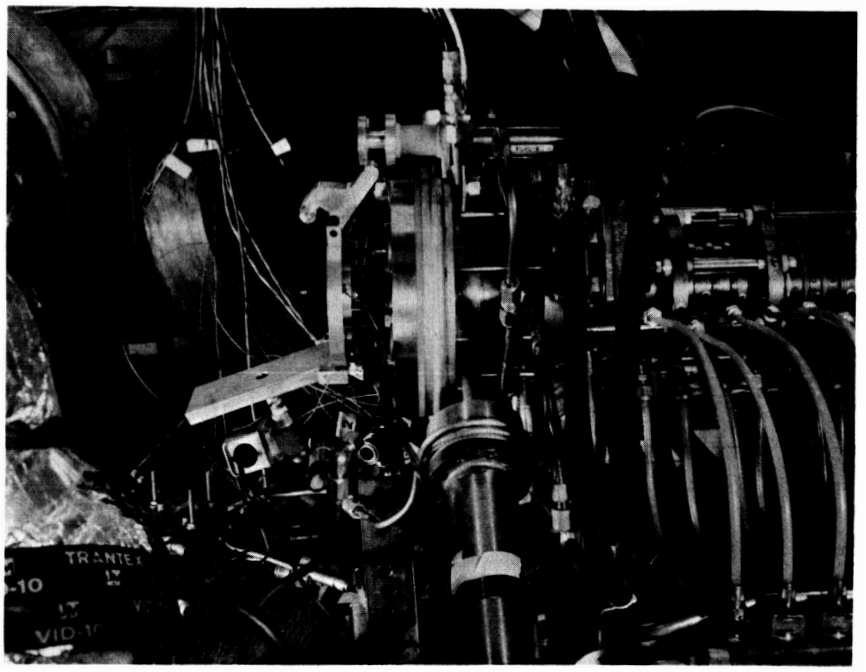


A) END VIEW OPEN

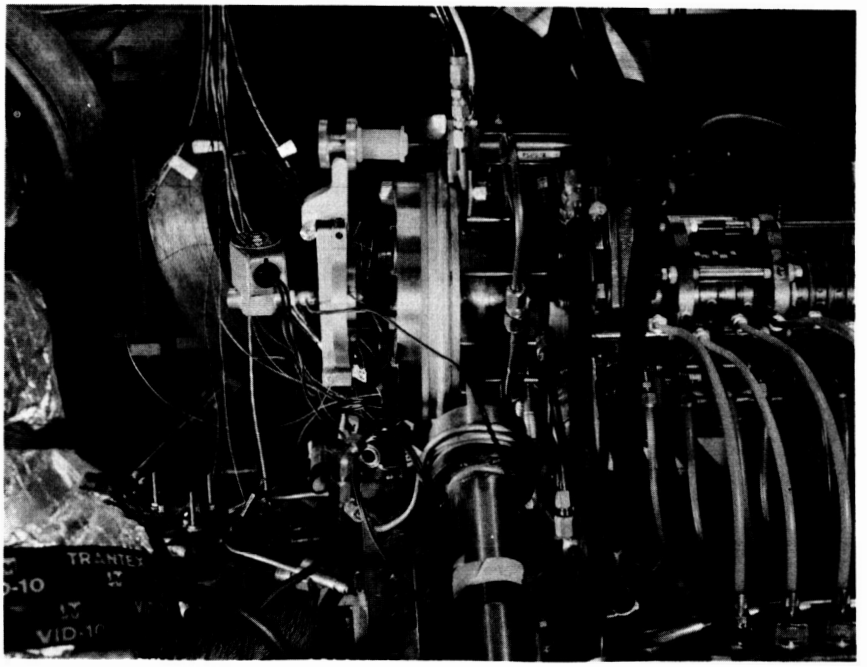


B) END VIEW CLOSED

FIGURE 8 EXPERIMENTAL SETUP

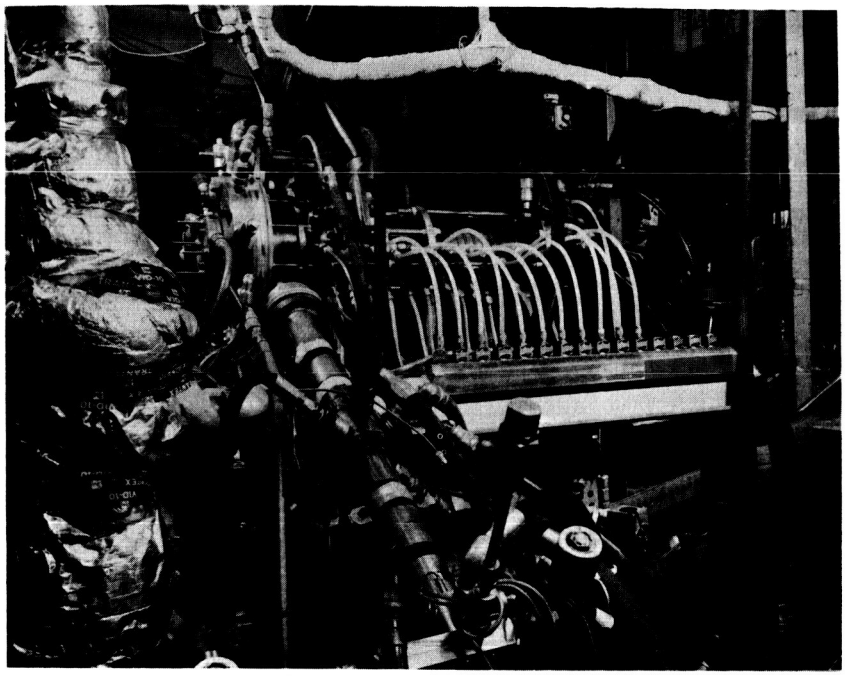


C) SIDE VIEW OPEN

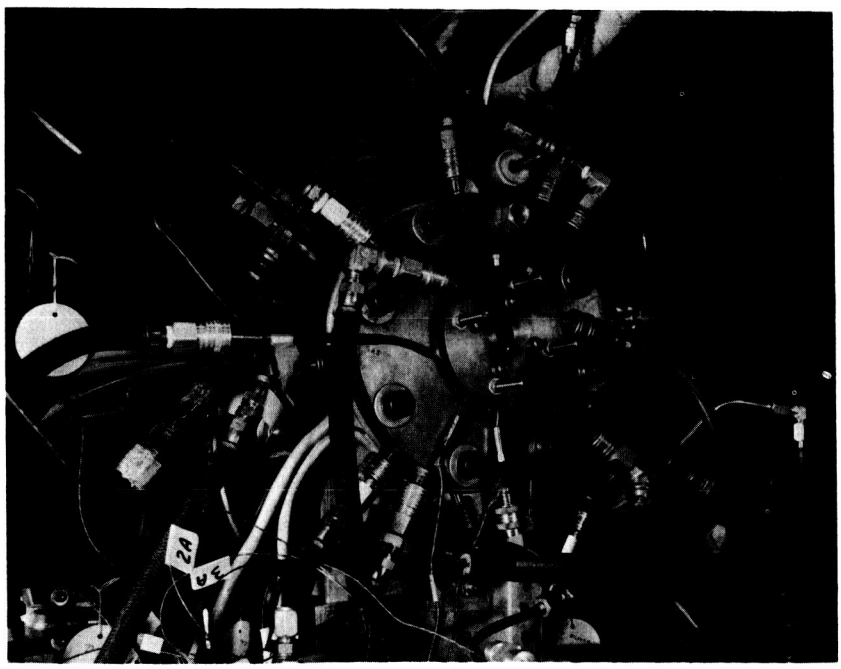


D) SIDE VIEW CLOSED

FIGURE 8 CONTINUED



E) OVERALL VIEW



F) COLD WALL CALORIMETER

FIGURE 8 CONCLUDED

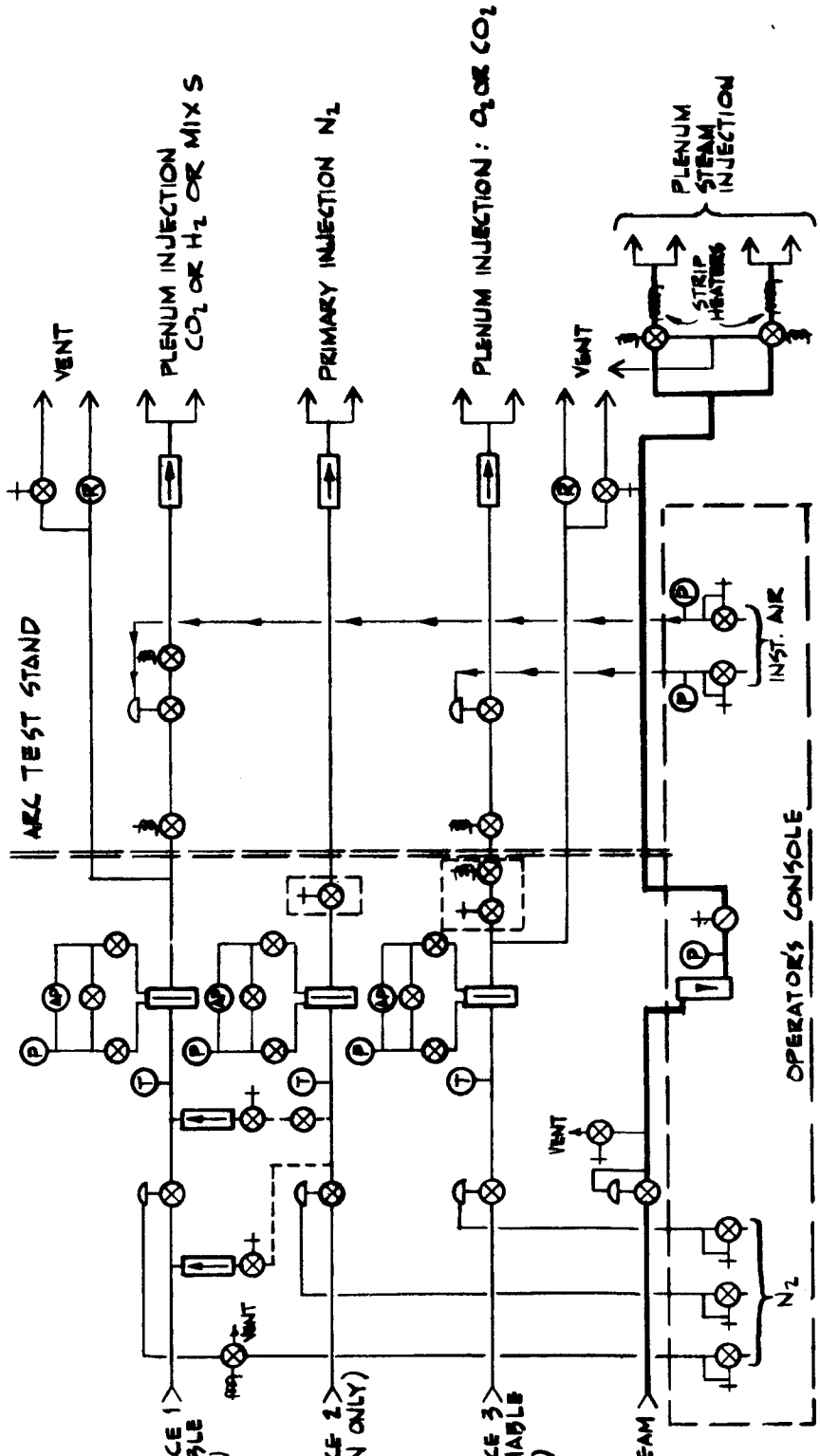
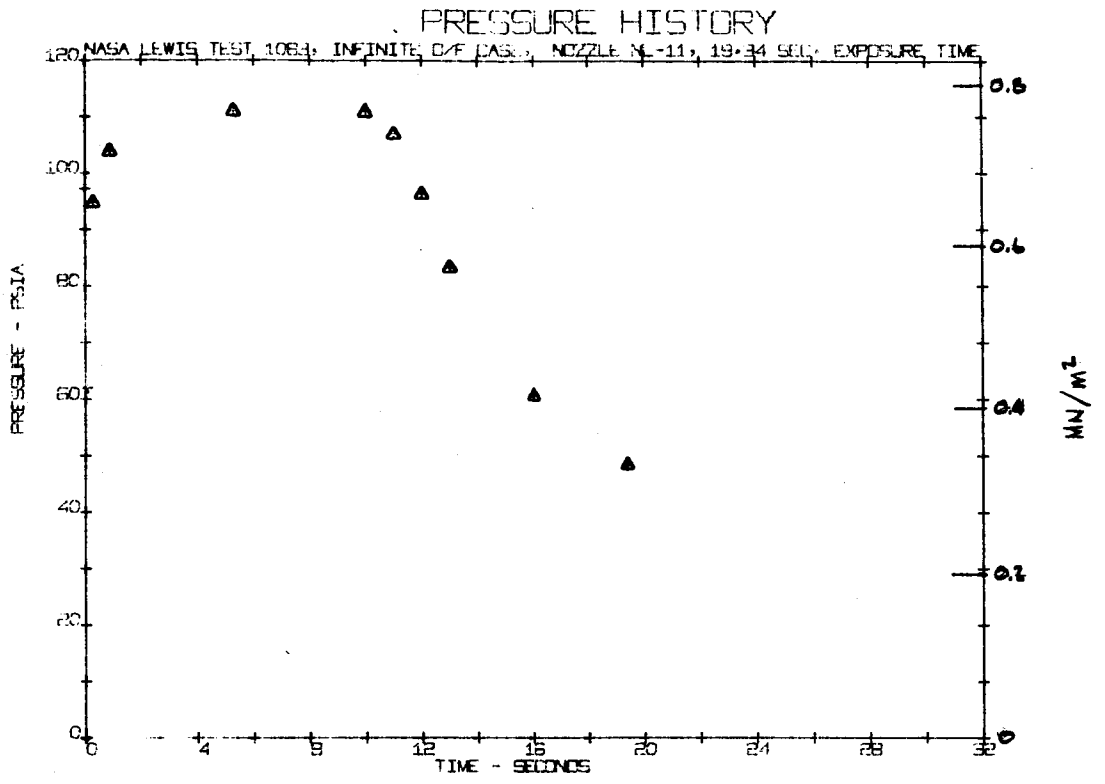


FIGURE 9 SCHEMATIC REPRESENTATION OF GAS METERING AND CONTROL SYSTEM

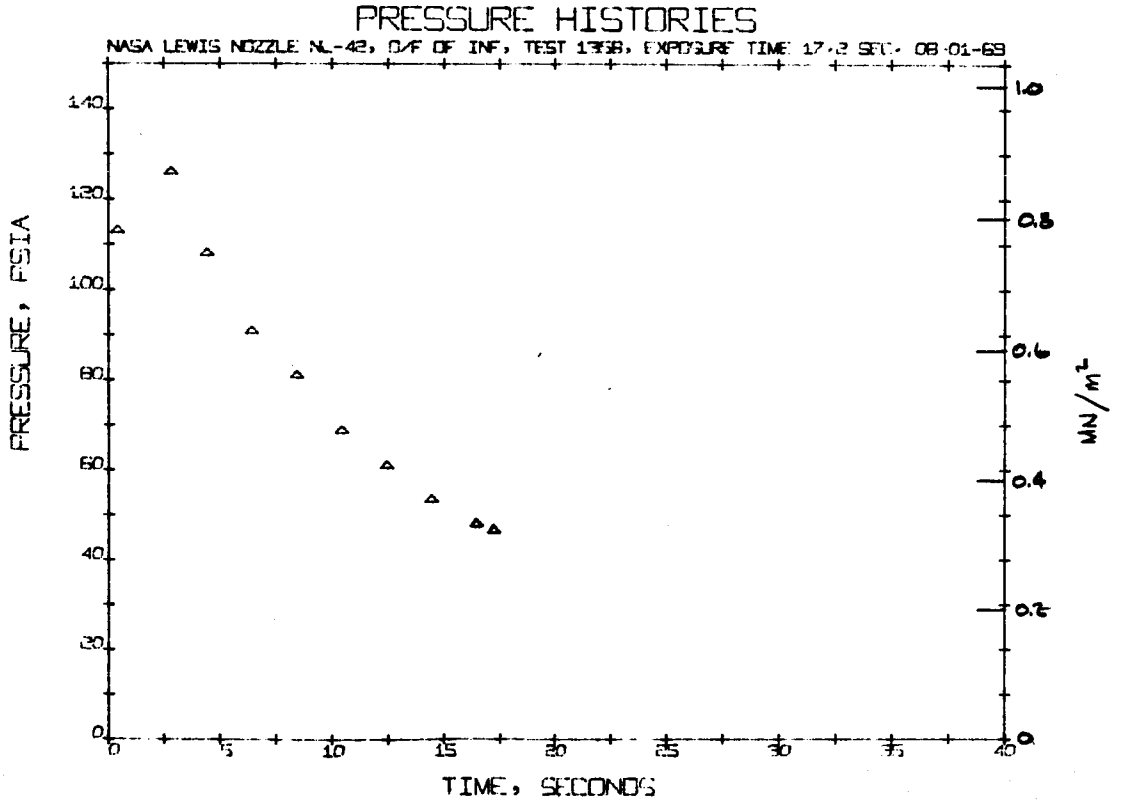
A-2486



A) TEST 1084, O/F = ∞, NL-11

FIGURE 10 CHAMBER PRESSURE HISTORIES FOR ABLATIVE NOZZLE TESTS

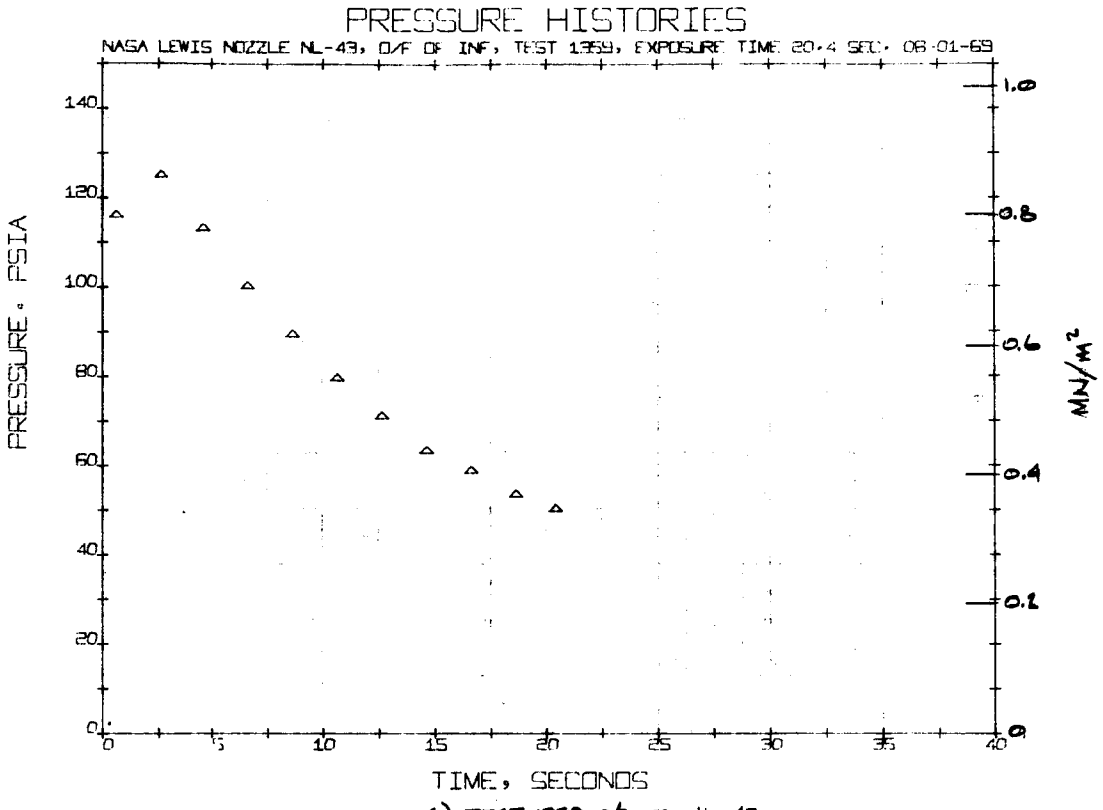
A-1489



B) TEST 1358, O/F = ∞, NL-42

FIGURE 10, CONTINUED

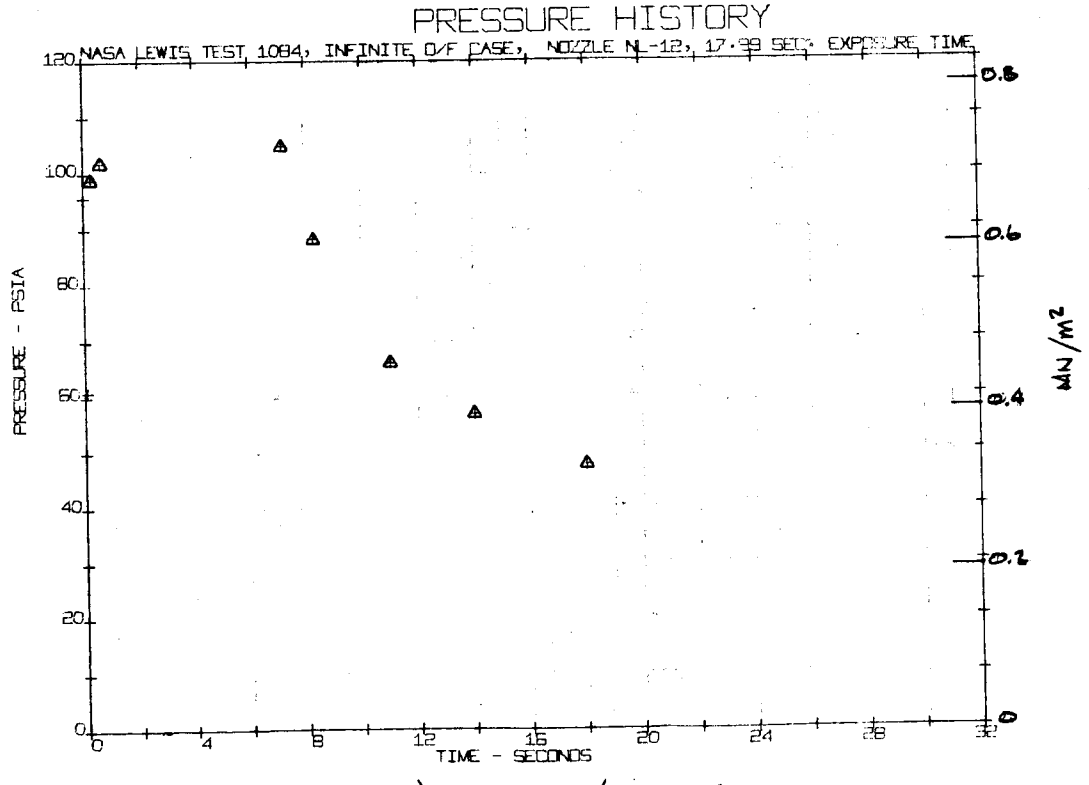
A-1490



C) TEST 1359, O/F = ∞, NL-43

FIGURE 10, CONTINUED

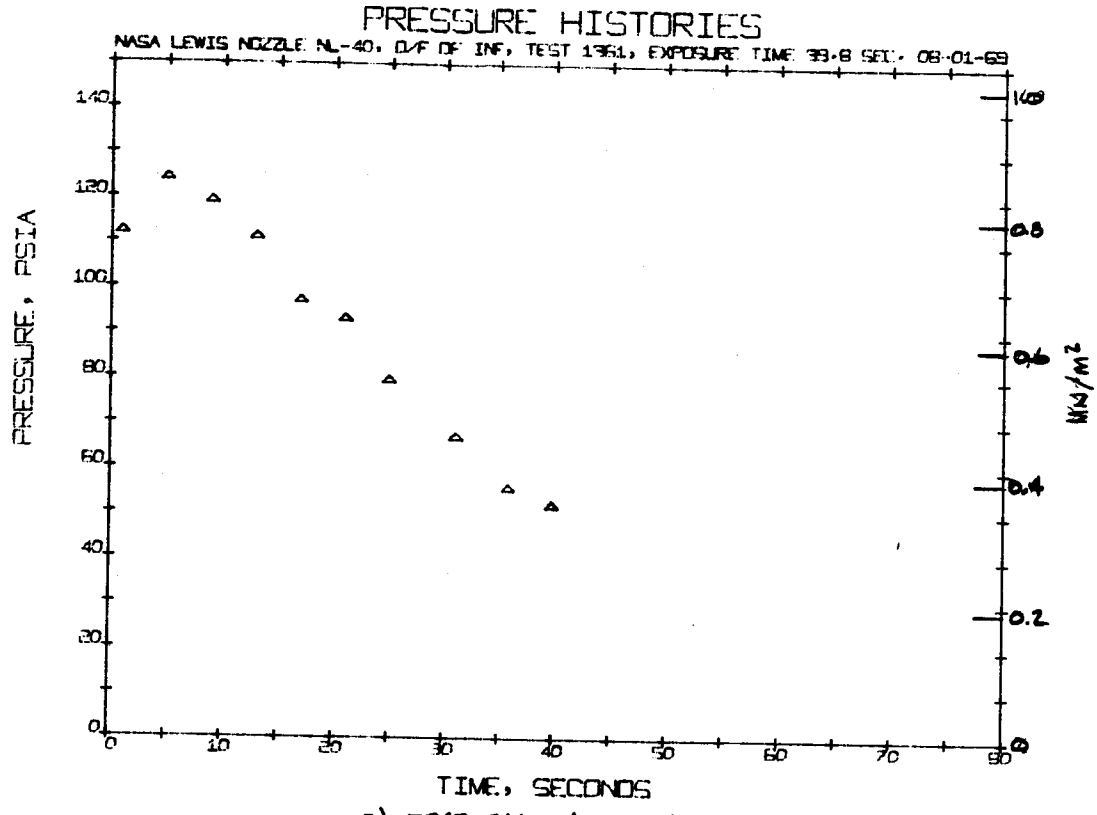
A-2491



D) TEST 1084, O/F = ∞, NL-12

FIGURE 10, CONTINUED

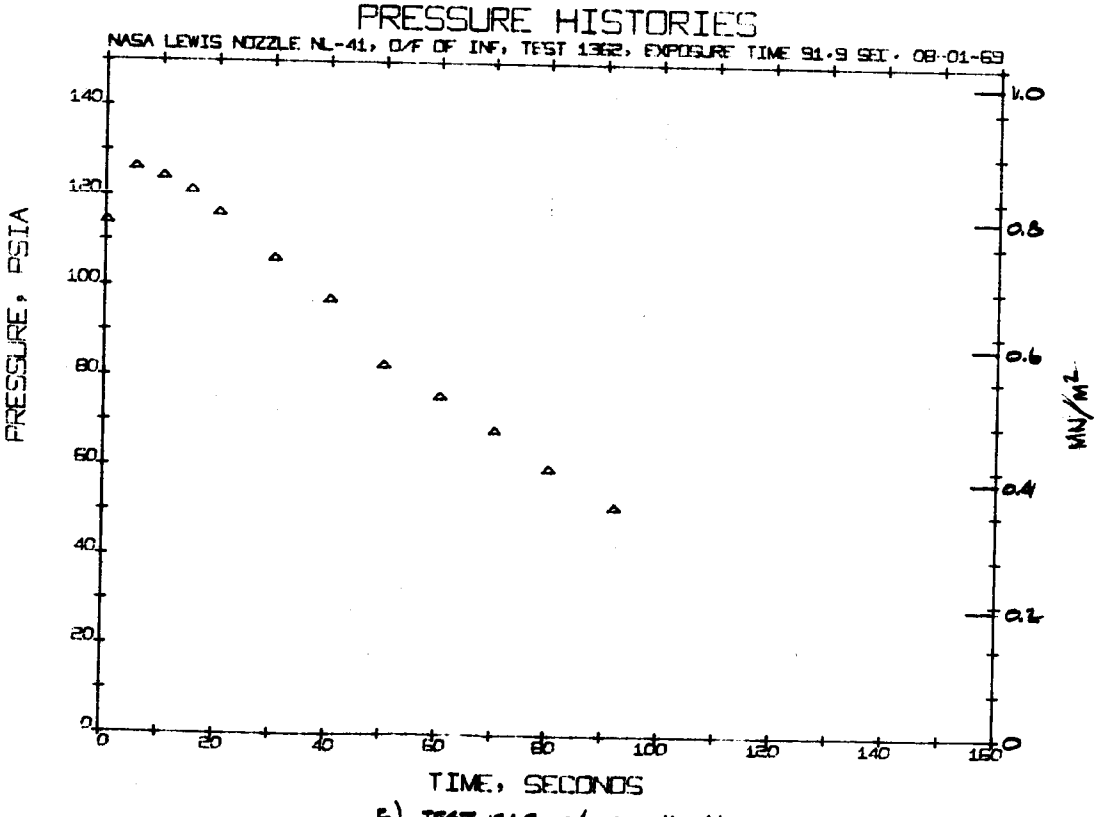
A-2492



E) TEST 1361, O/F = ∞, NL-40

FIGURE 10, CONTINUED

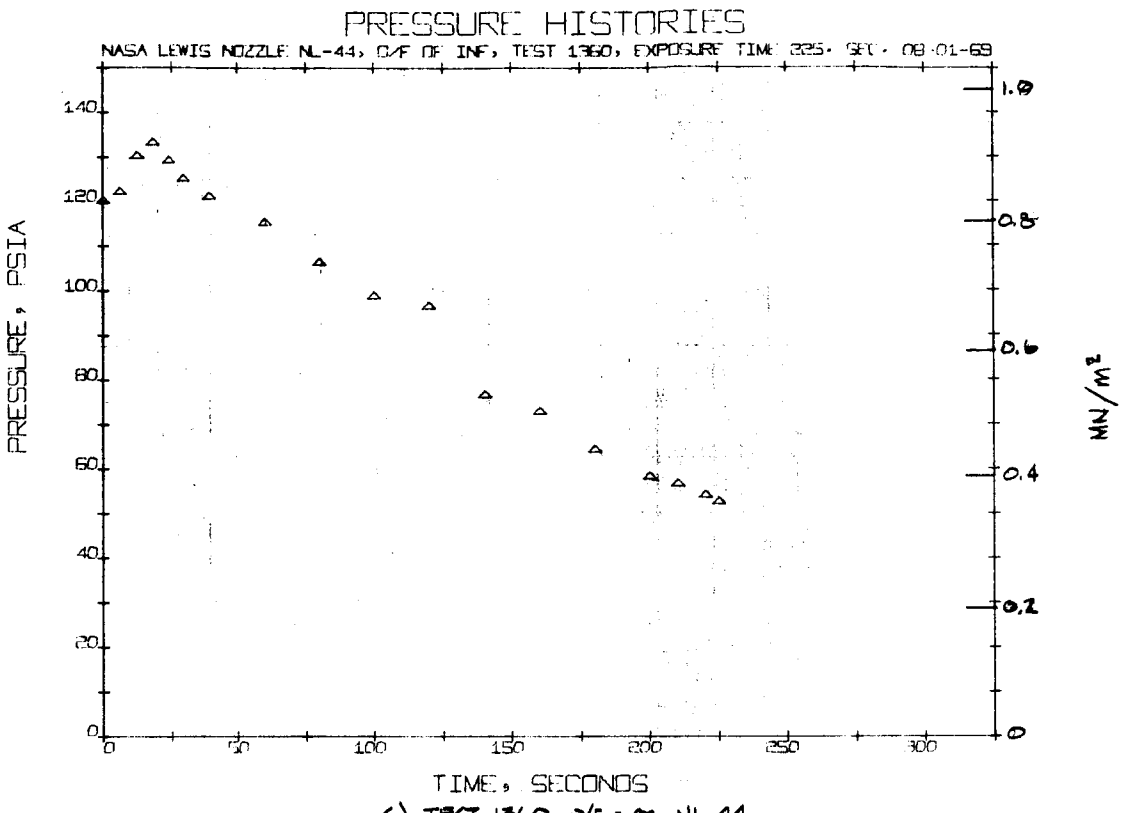
A-1493



F) TEST 1362, O/F = ∞, NL-41

FIGURE 10, CONTINUED

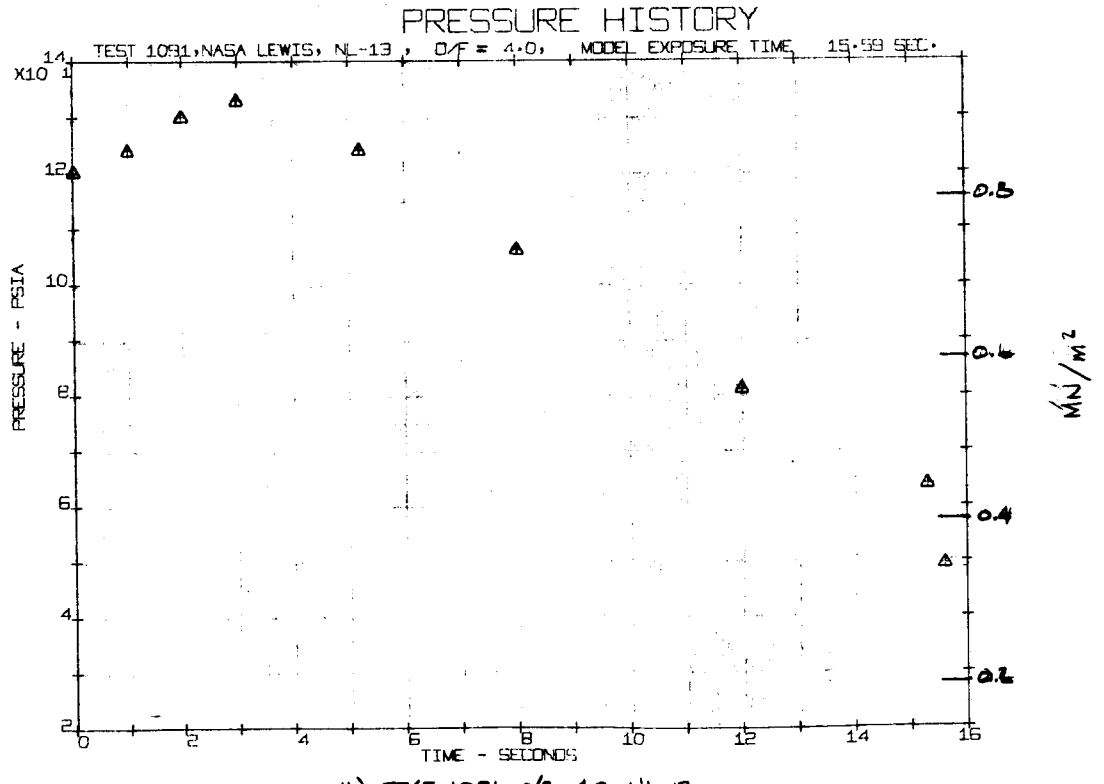
A-1494



G) TEST 1360, O/F = ∞, NL-44

FIGURE 10, CONTINUED

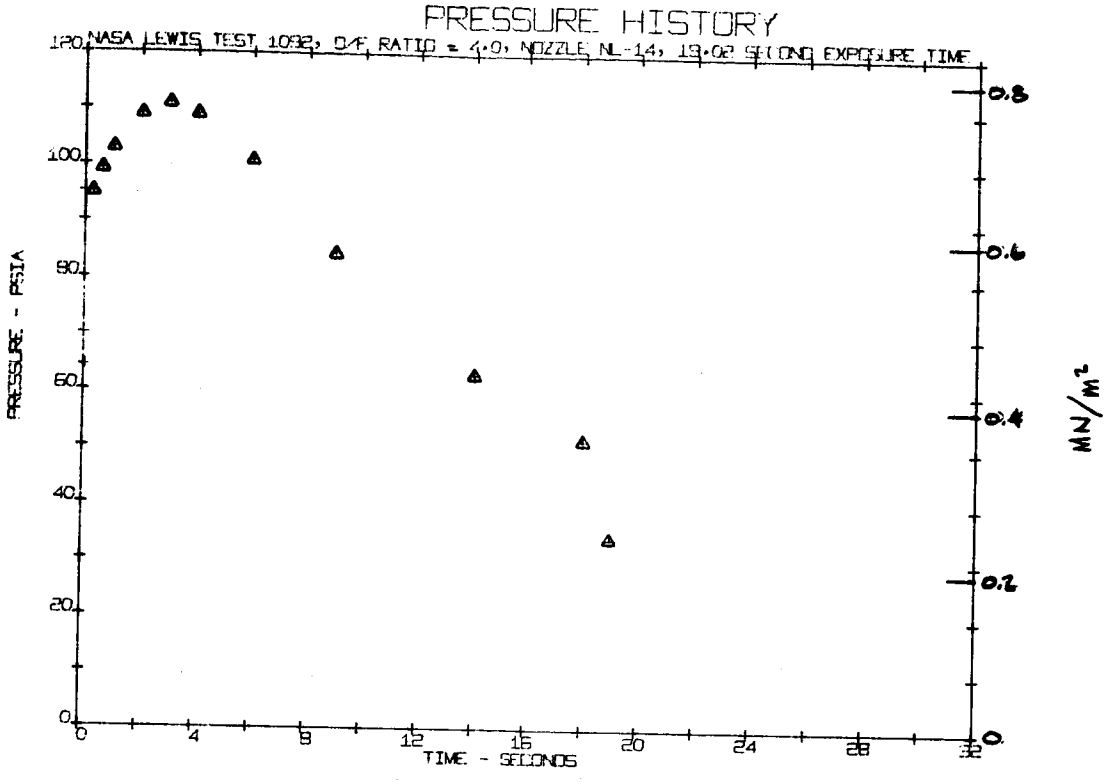
A-2495



H) TEST 1091, O/F = 4.0, NL-13

FIGURE 10, CONTINUED

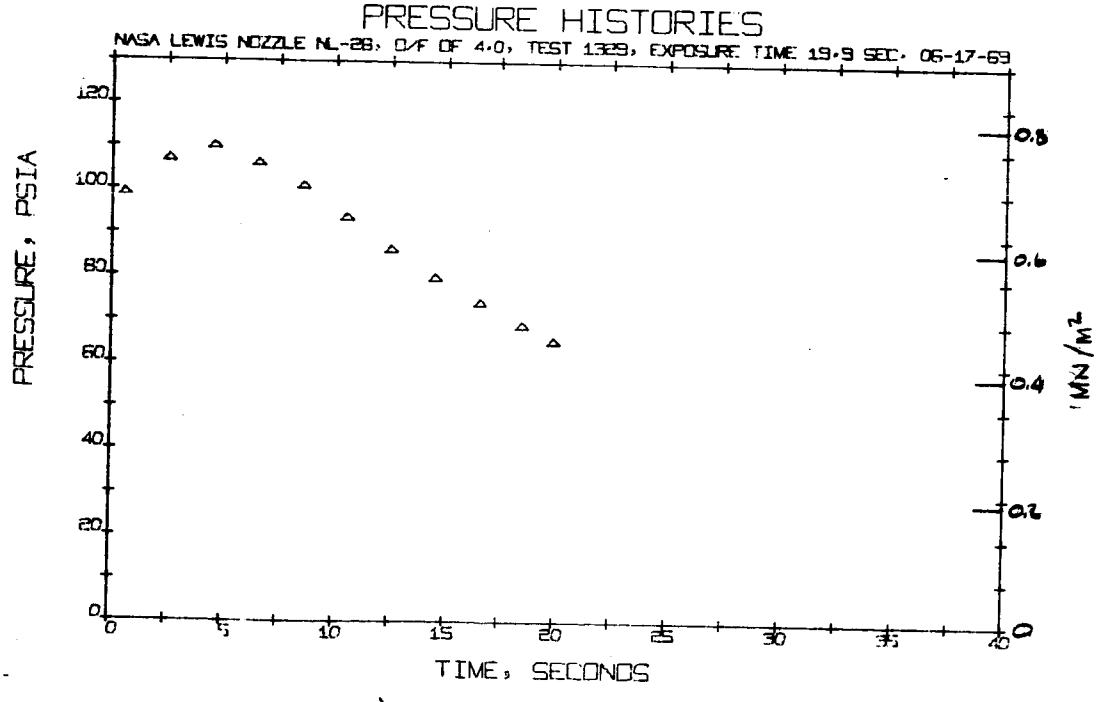
A-2496



I) TEST 1092, O/F = 4.0, NL-14

FIGURE 10, CONTINUED

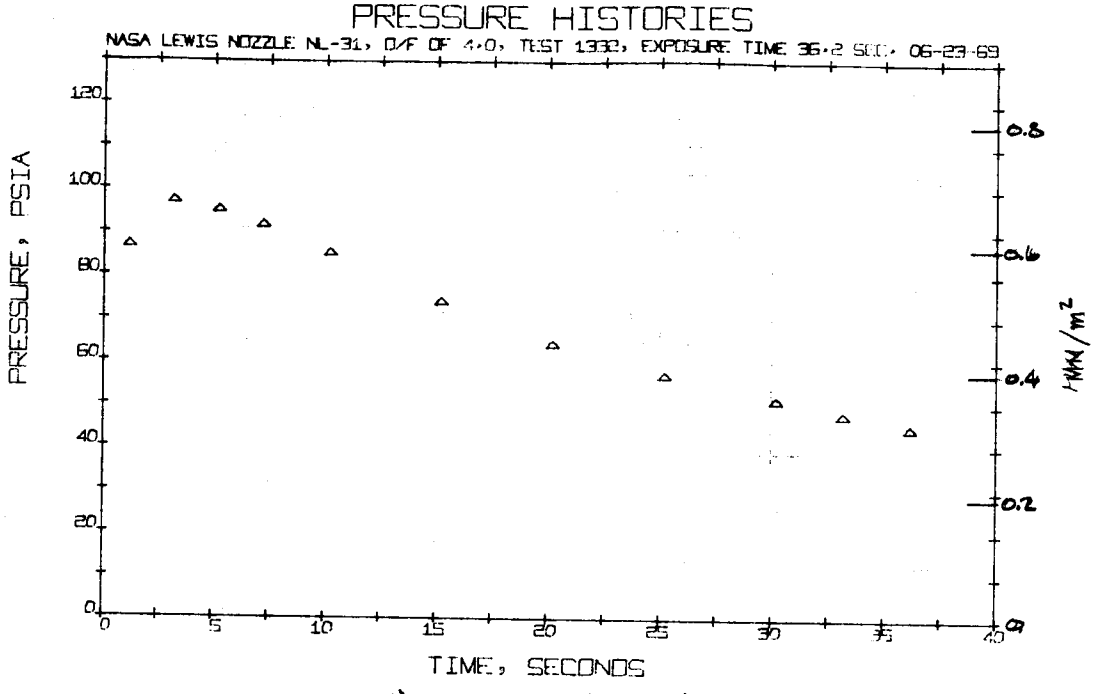
A-2497



J) TEST 1329, O/F = 4.0, NL-28

FIGURE 10, CONTINUED

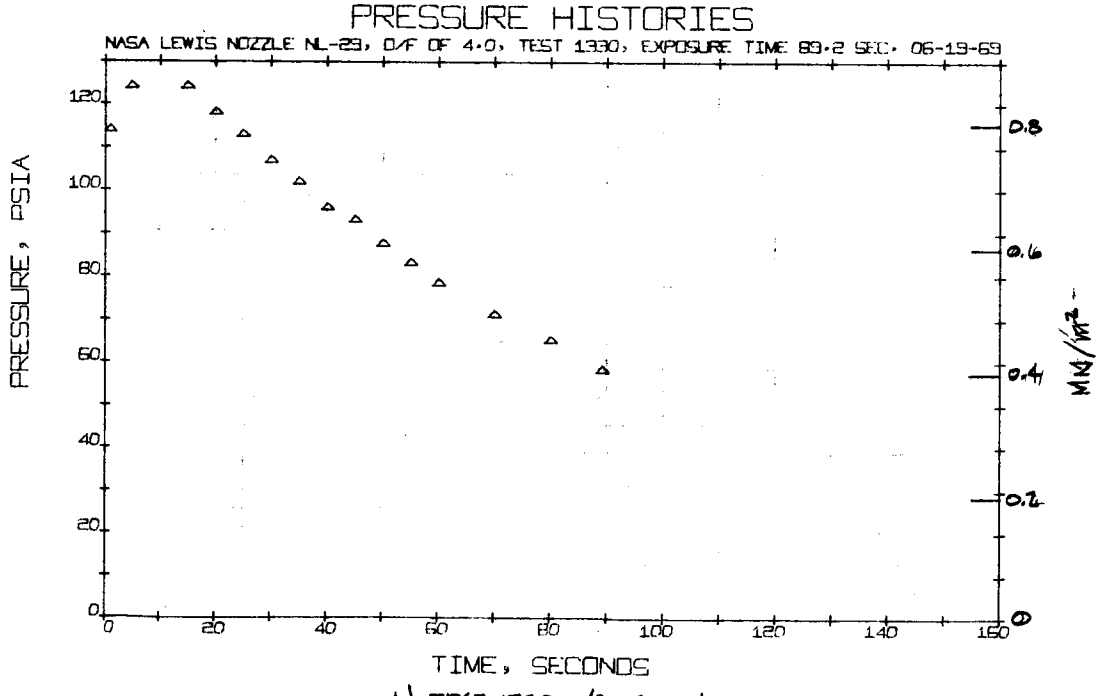
A-2498



K) TEST 1332, O/F = 4.0, NL-31

FIGURE 10, CONTINUED

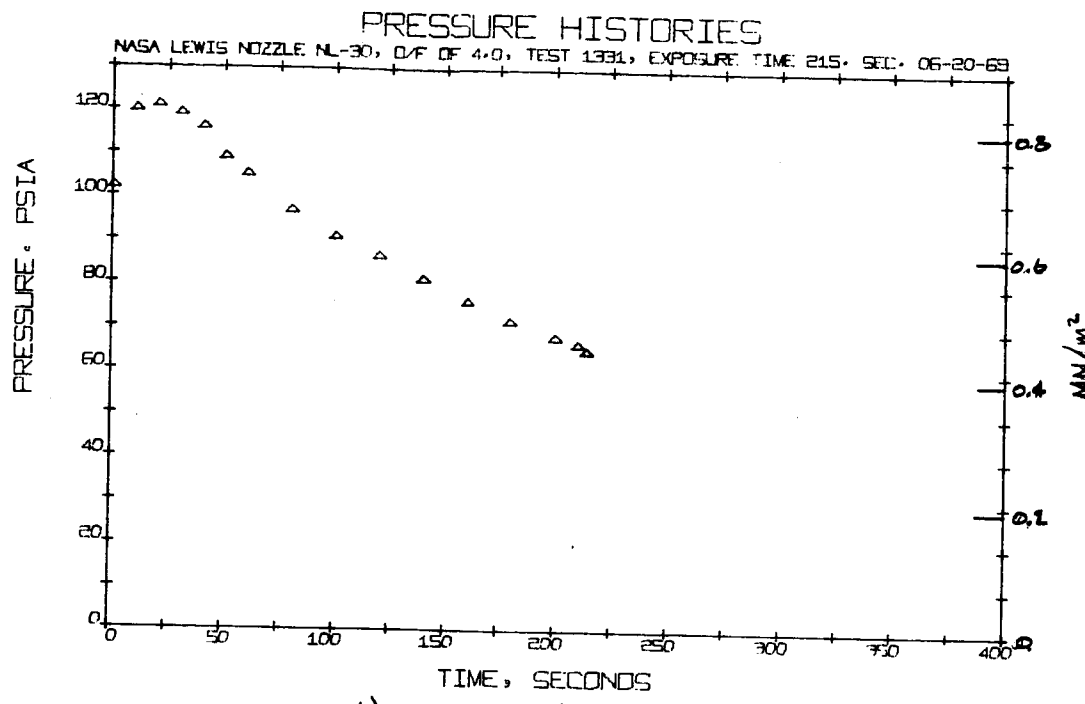
A-2499



L) TEST 1330, O/F = 4.0, NL-29

FIGURE 10, CONTINUED

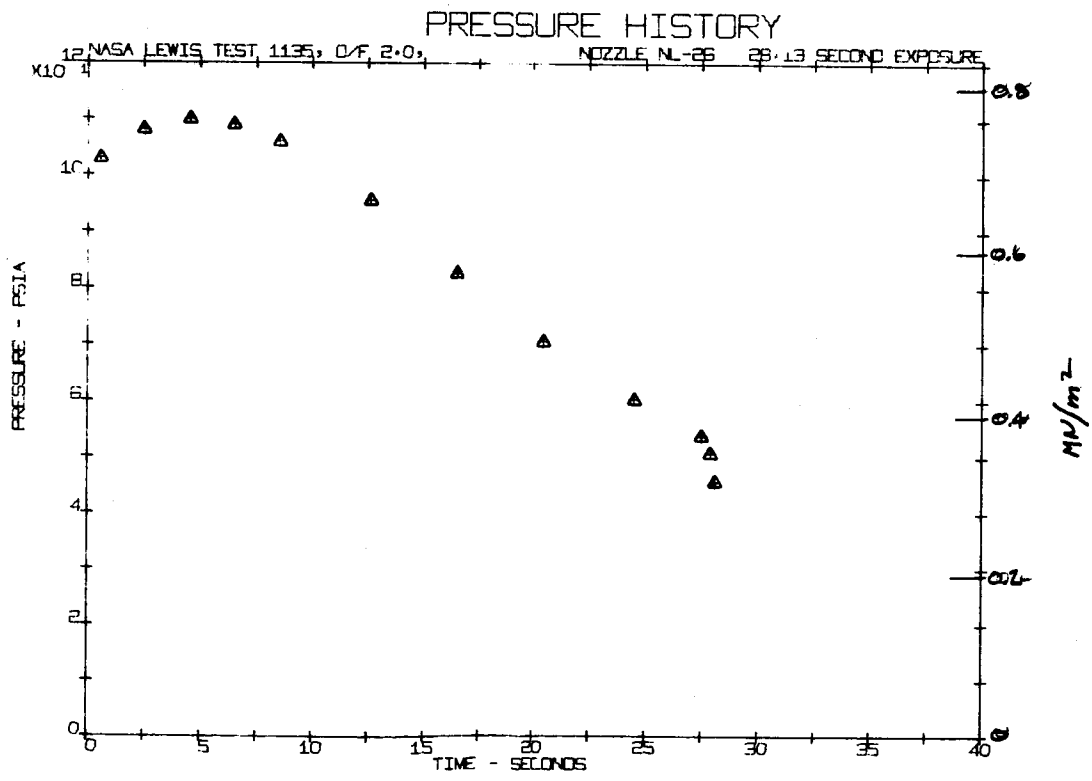
A-2500



N) TEST 1331, O/F=4.0, NL-30

FIGURE 10, CONTINUED

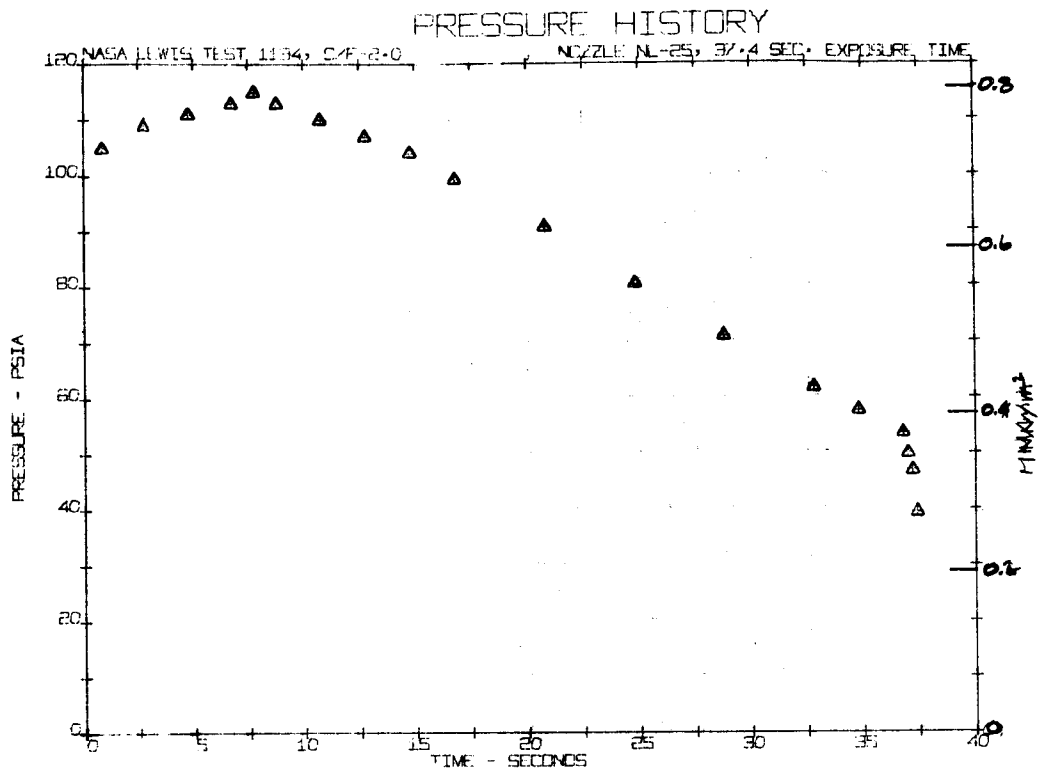
A-1501



N) TEST 1135 O/F= 2.0, NL-26

FIGURE 10, CONTINUED

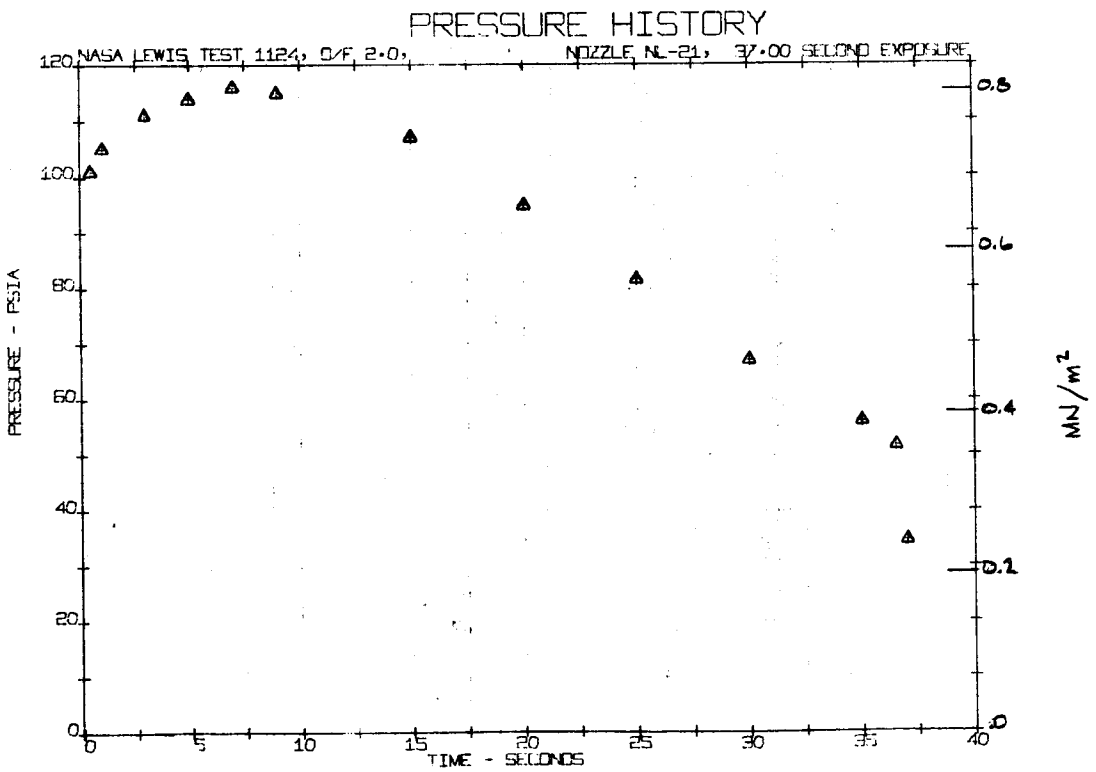
A-1502



O) TEST 1134, O/F=2.0, NL-25

FIGURE 10, CONTINUED

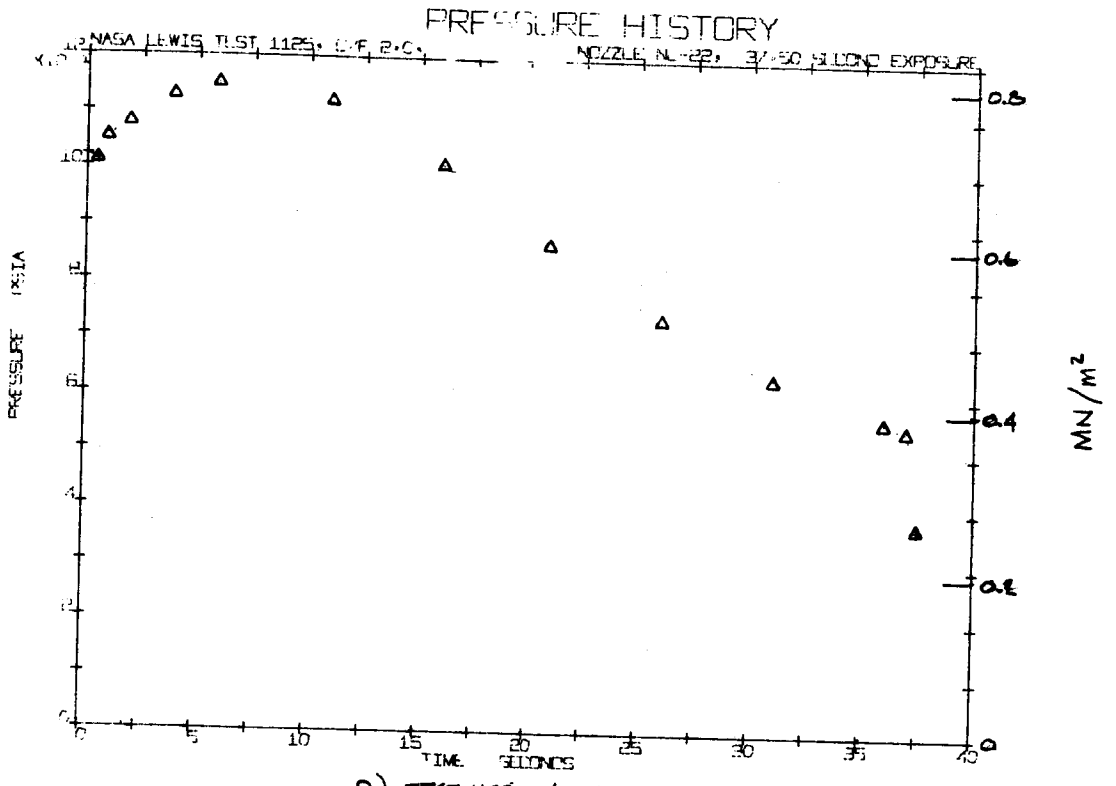
A-1503



P) TEST 1124, O/F = 2.0, NL-21

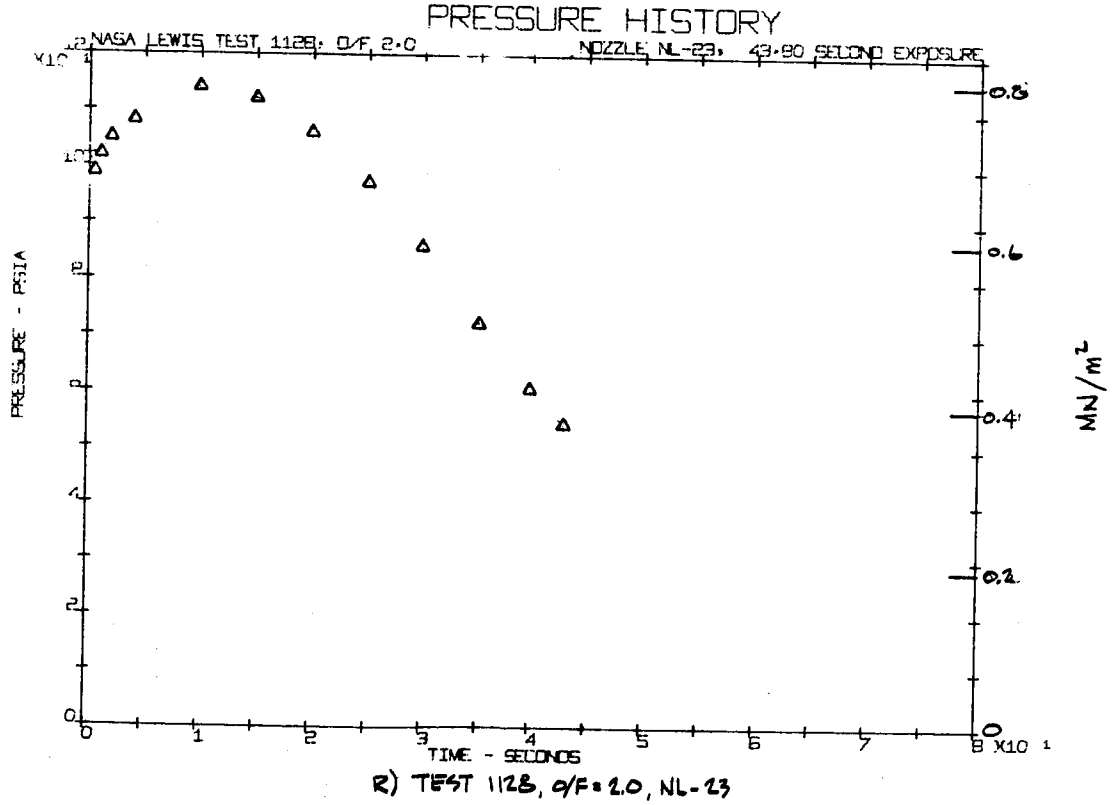
FIGURE 10, CONTINUED

A-1504



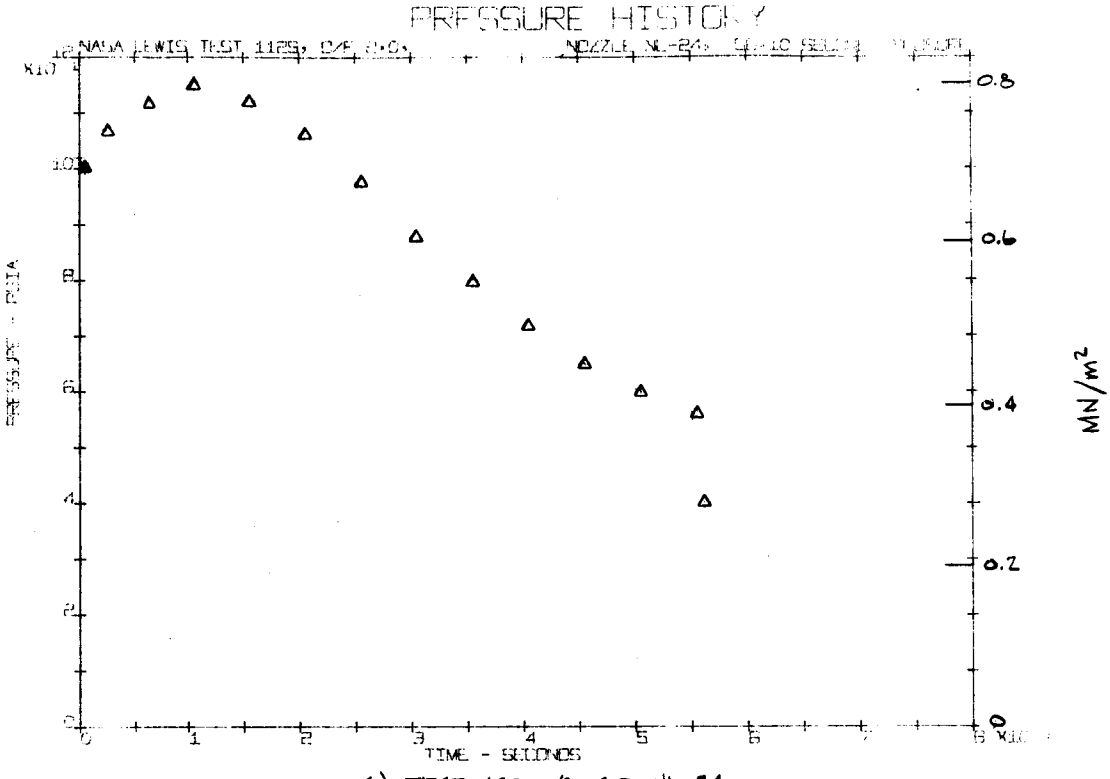
Q) TEST 1125, O/F = 2.0, NL-22

FIGURE 10, CONTINUED



R) TEST 1128, O/F = 2.0, NL-23

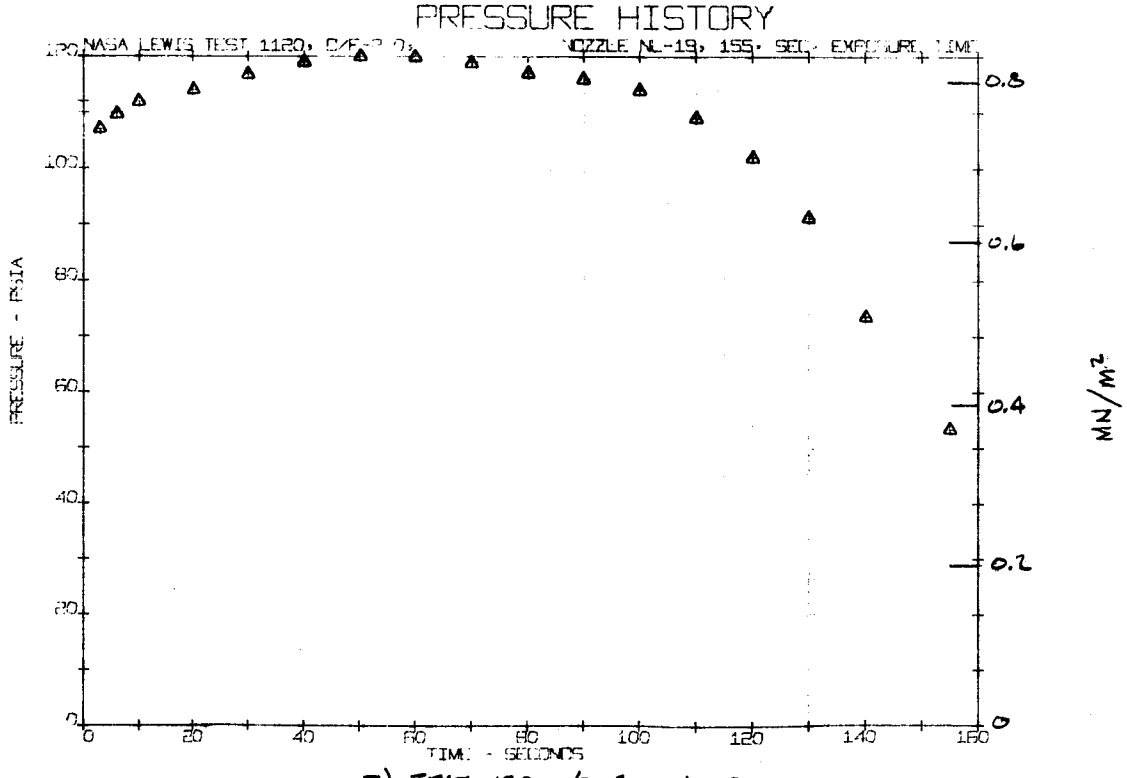
FIGURE 10, CONTINUED



S) TEST 1129, O/F = 2.0, NL-24

FIGURE 10, CONTINUED

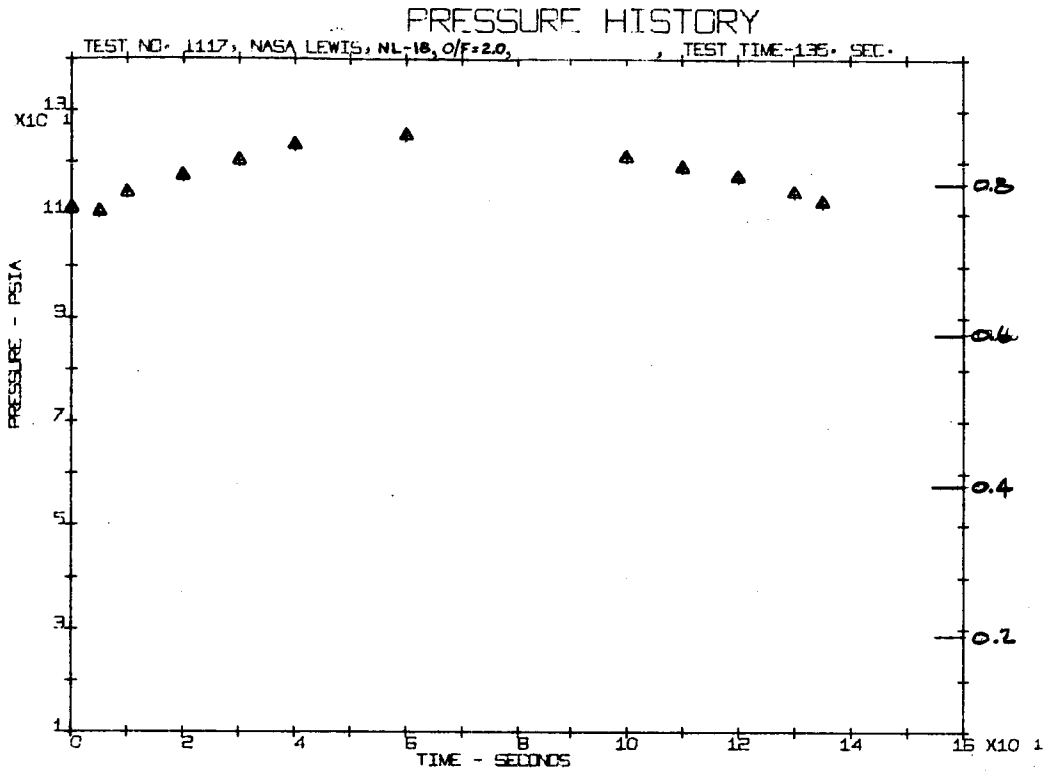
A-1401



T) TEST 1120, O/F = 2.0, NL-19

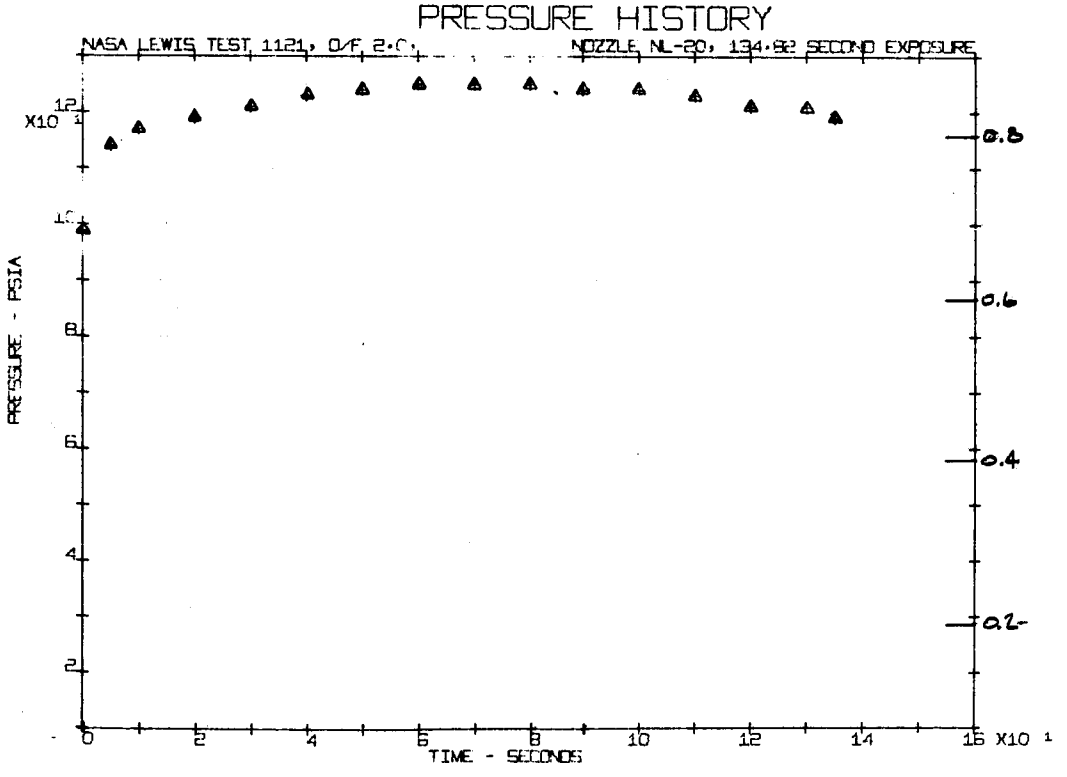
FIGURE 10, CONTINUED

A-1408



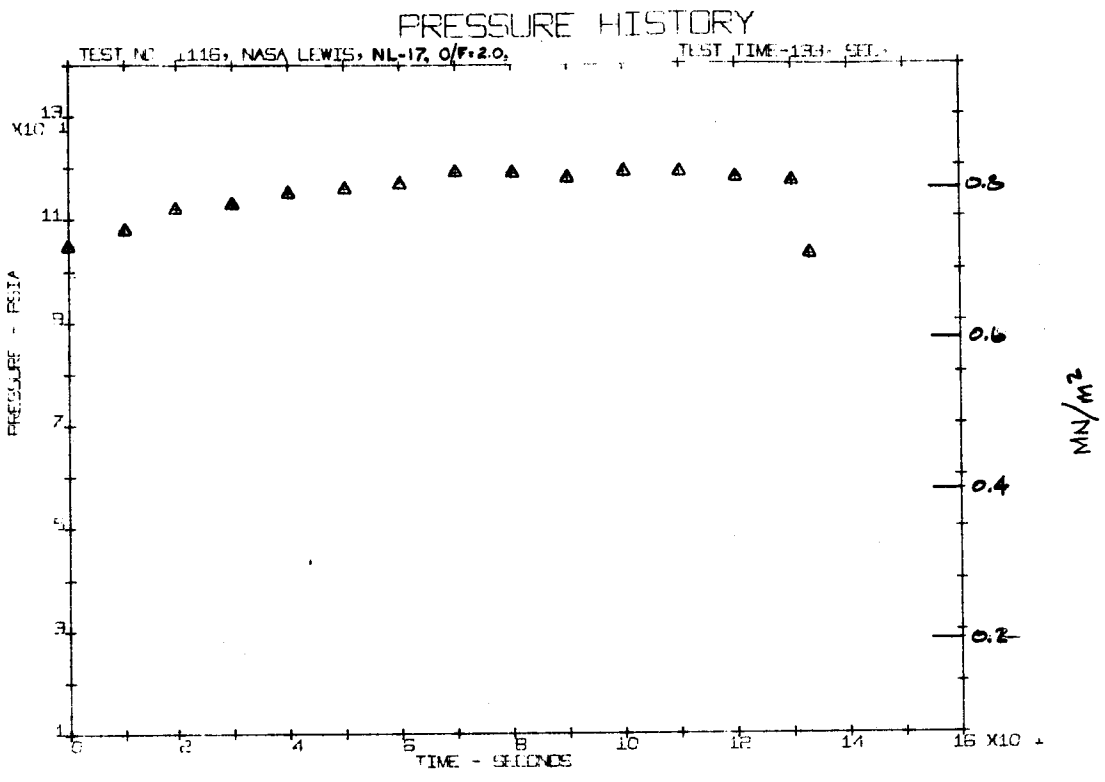
U) TEST 1117, O/F = 2.0, NL-18

FIGURE 10, CONTINUED



V) TEST 1121, O/F = 2.0, NL-20

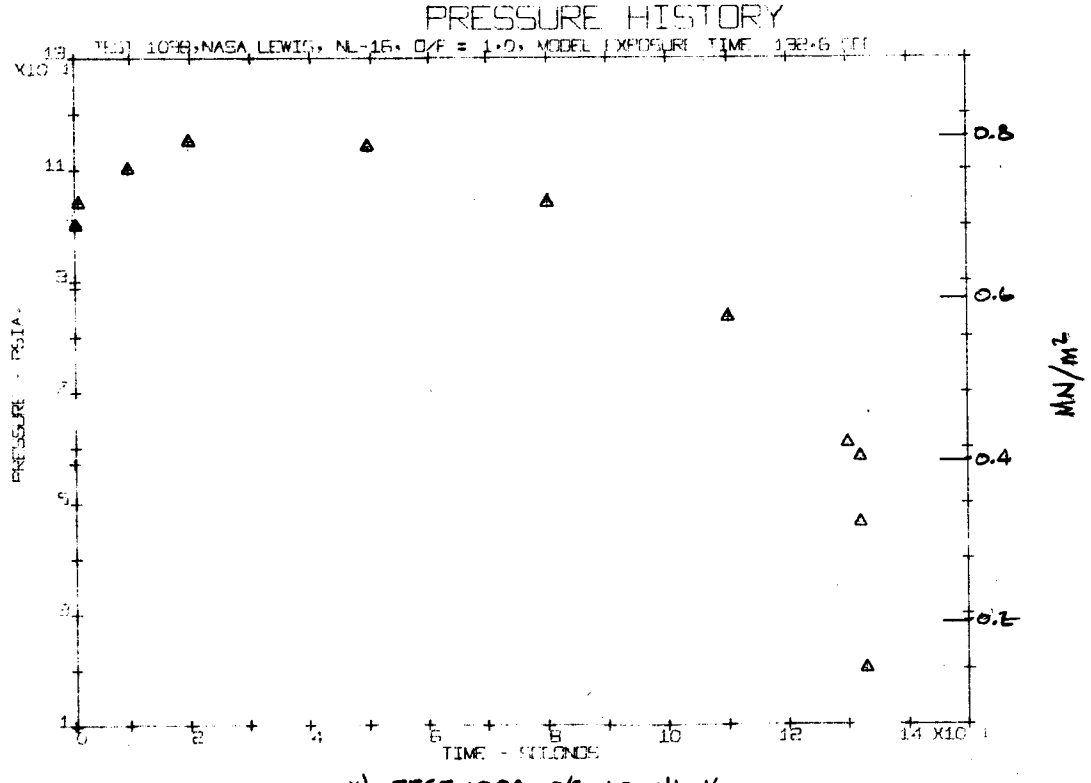
FIGURE 10, CONTINUED



W) TEST 1116, O/F=2.0, NL-17

FIGURE 10, CONTINUED

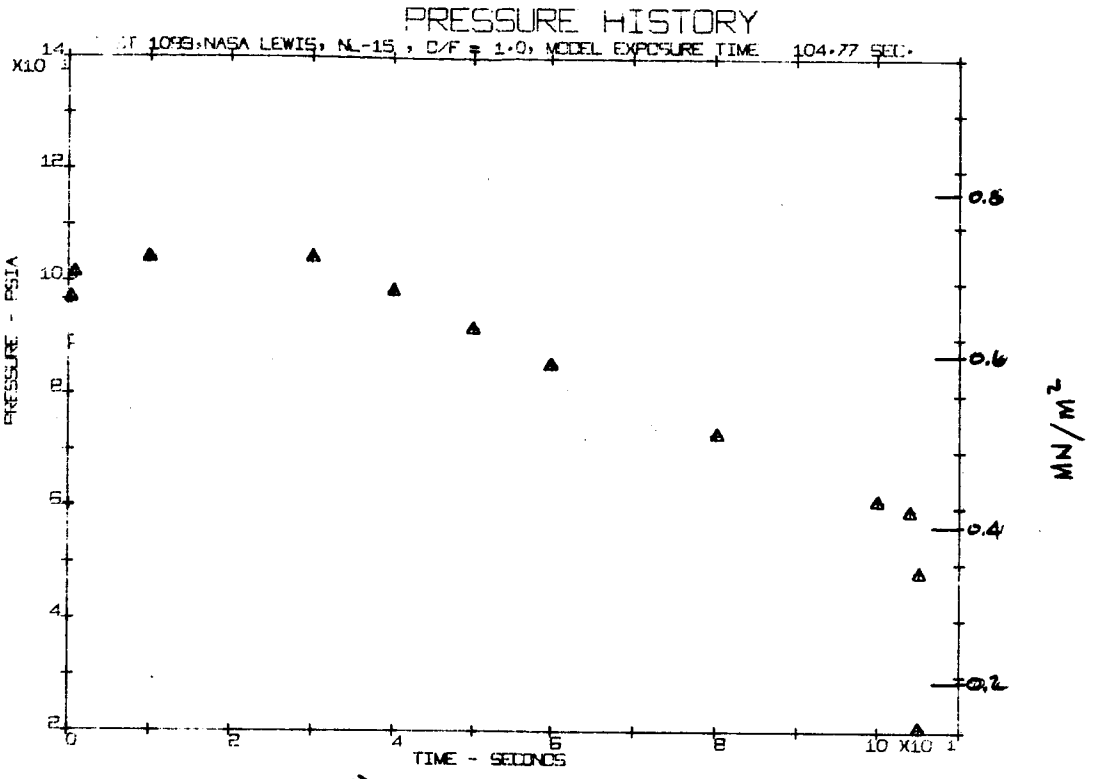
A-1911



X) TEST 1098, O/F=1.0, NL-16

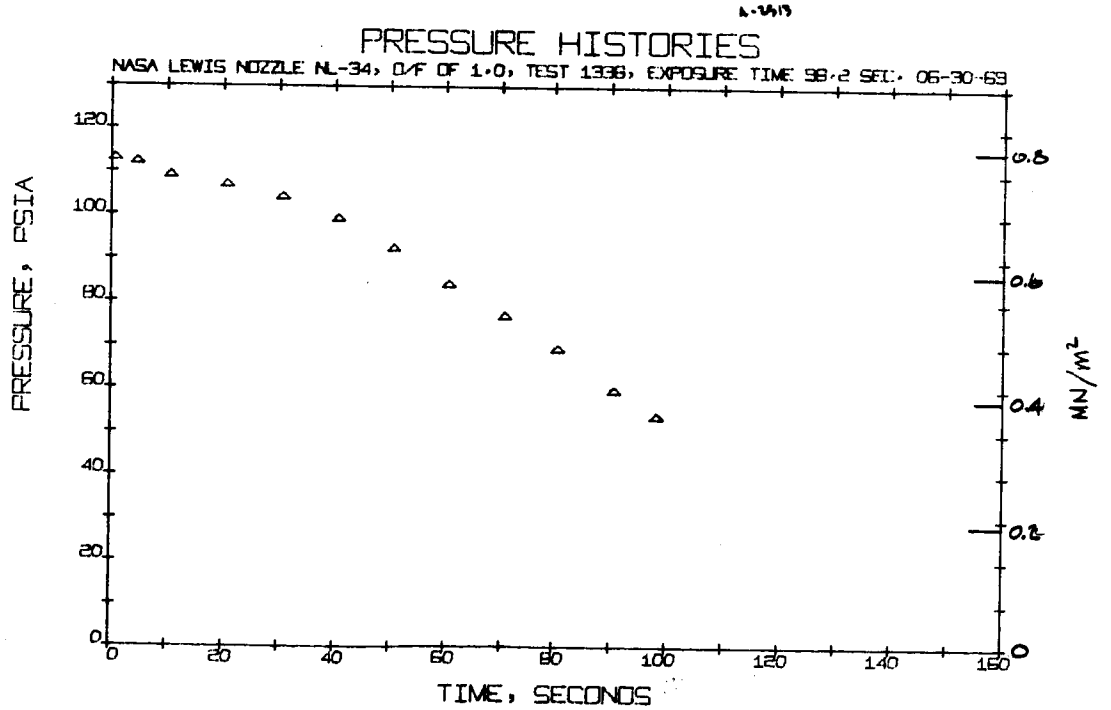
FIGURE 10, CONTINUED

A-1512



Y) TEST 1099, O/F=1.0, NL-15

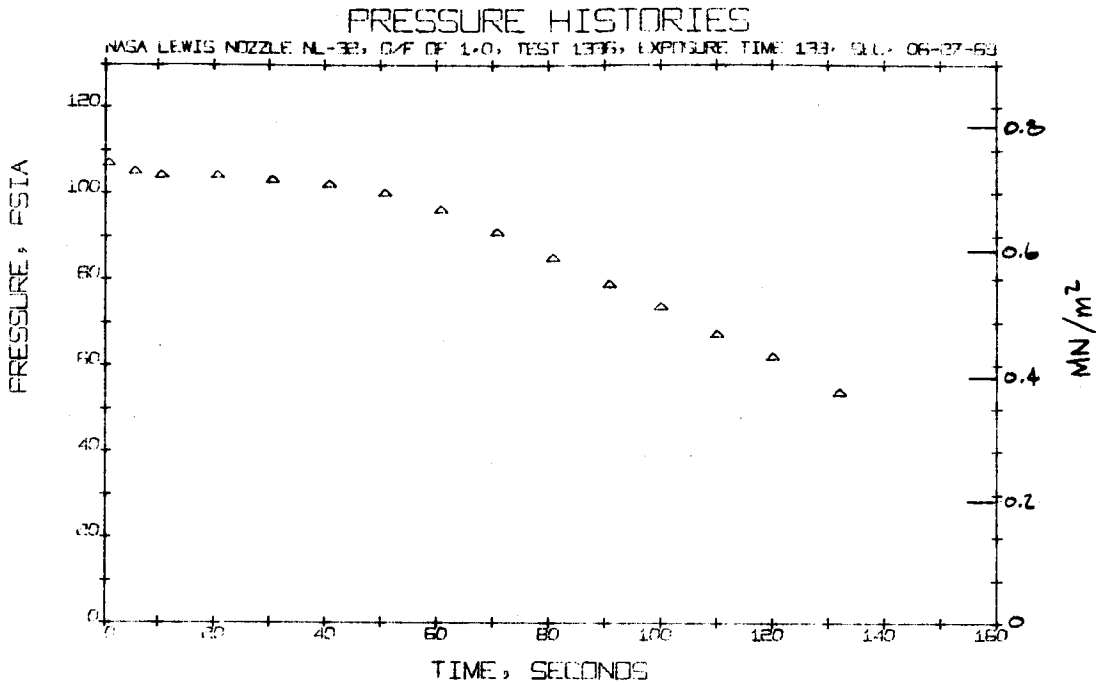
FIGURE 10, CONTINUED



Z) TEST 1338, O/F=1.0, NL-34

FIGURE 10, CONTINUED

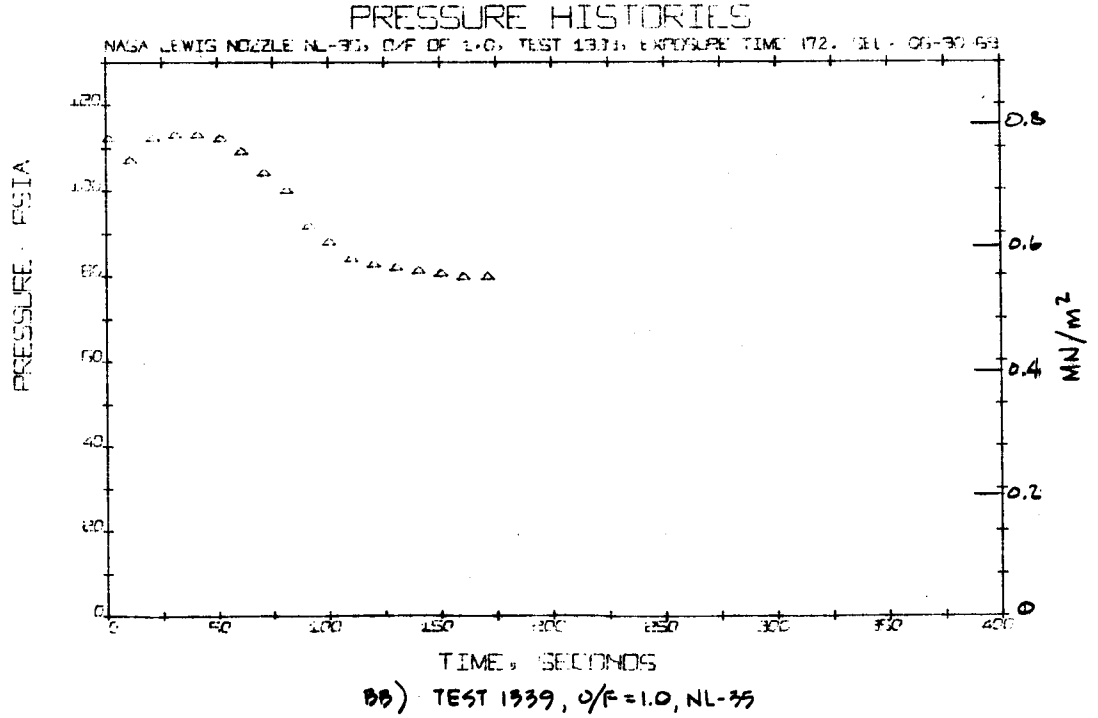
A-3514



AA) TEST 1336, O/F = 1.0, NL-32

FIGURE 10, CONTINUED

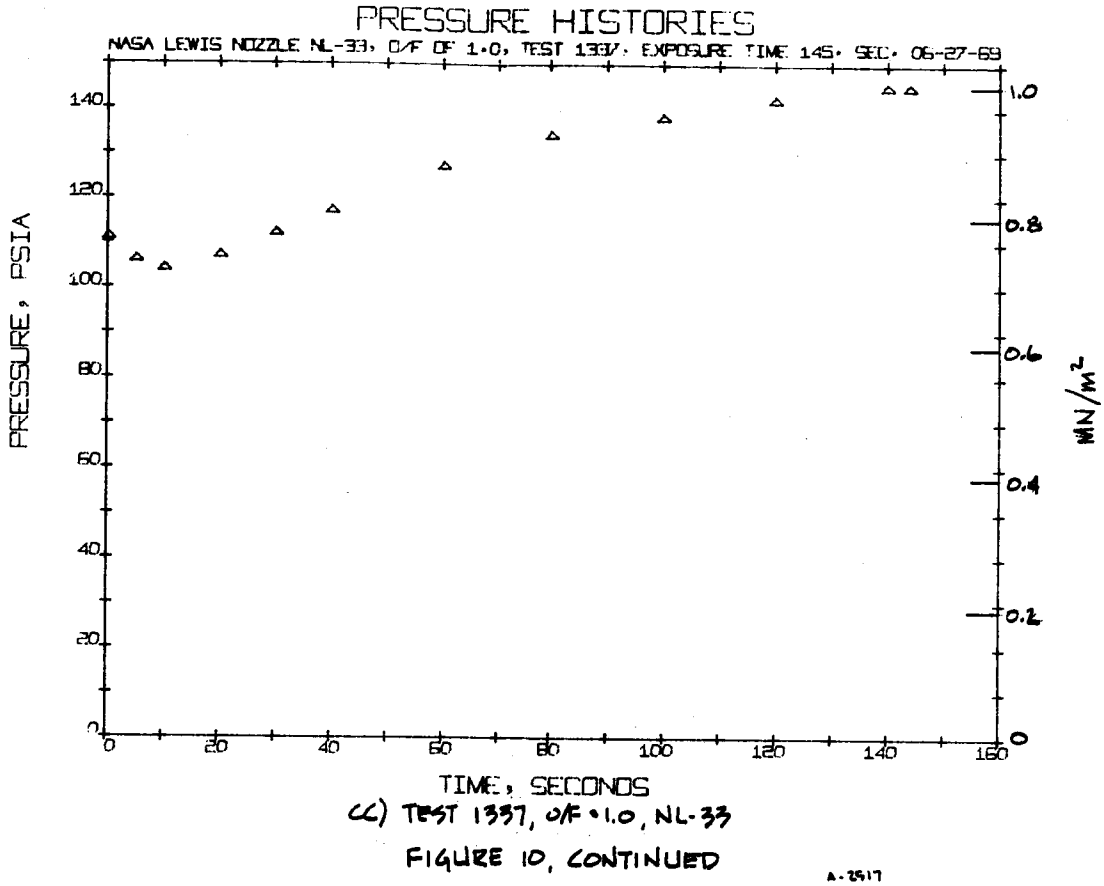
A-2515



BB) TEST 1339, O/F = 1.0, NL-35

FIGURE 10, CONTINUED

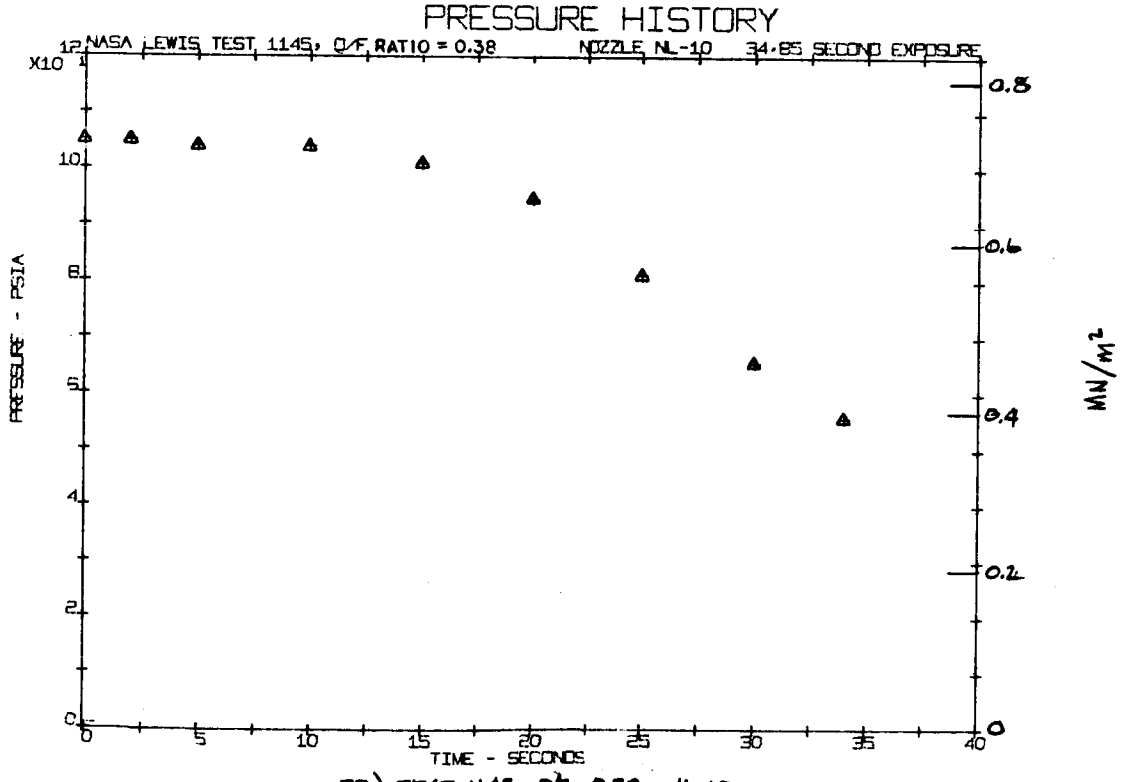
A-2516



CC) TEST 1337, O/F = 1.0, NL-33

FIGURE 10, CONTINUED

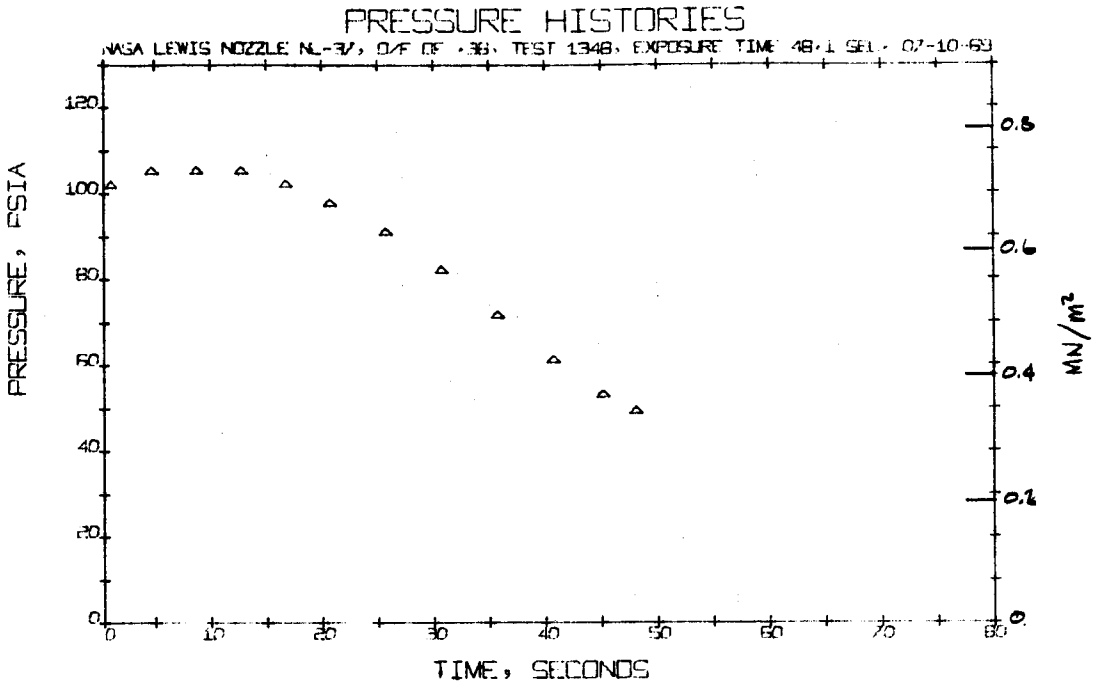
A-2517



DD) TEST 1145, O/F = 0.38, NL-10

FIGURE 10, CONTINUED

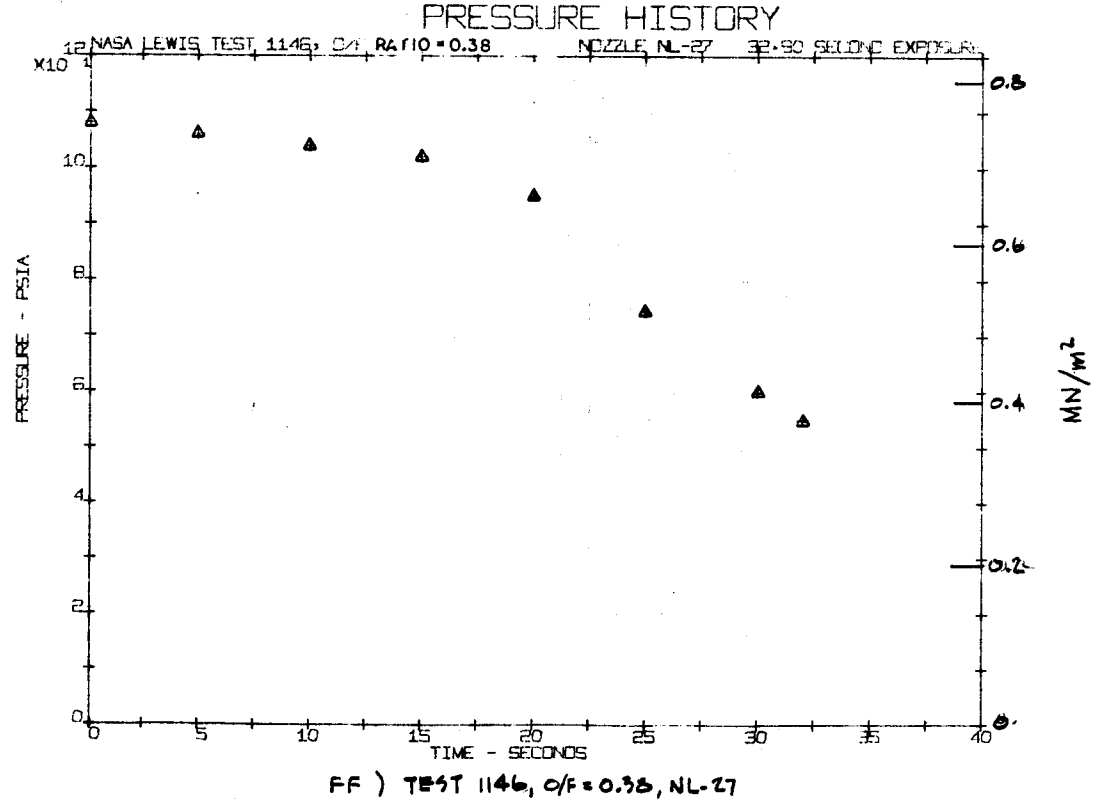
A-2518



EE) TEST 1348, O/F = 0.38, NL-37

FIGURE 10, CONTINUED

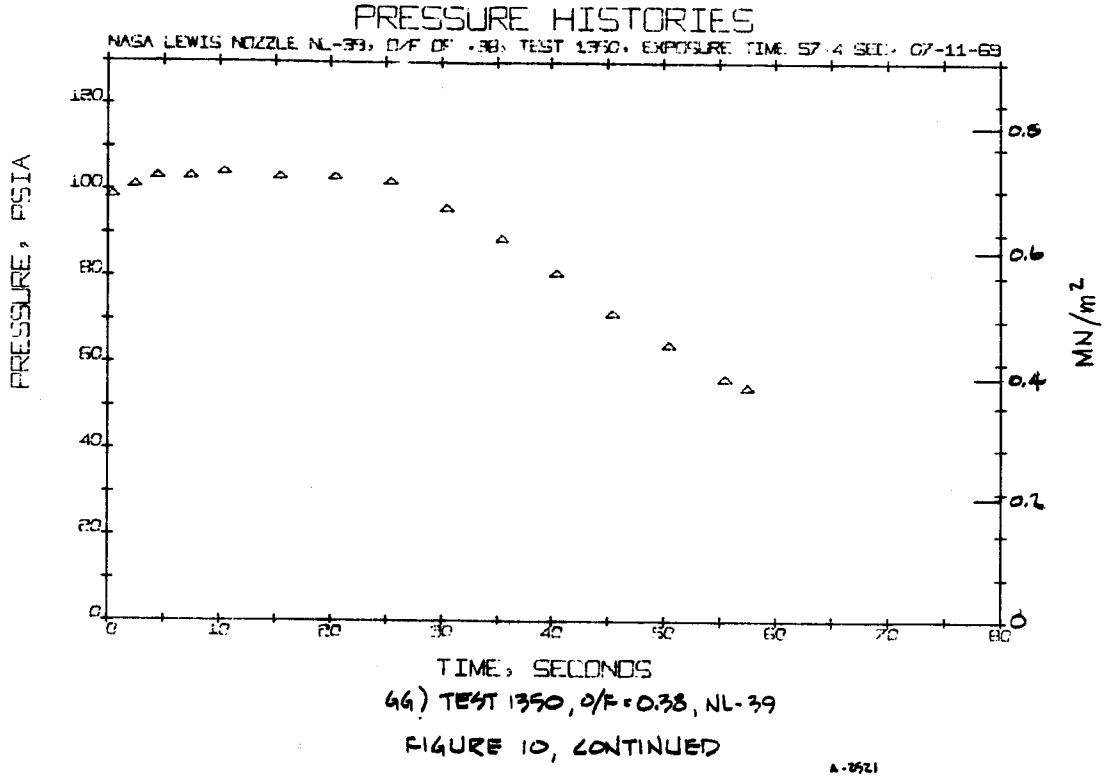
A-2519



FF) TEST 1146, O/F = 0.38, NL-27

FIGURE 10, CONTINUED

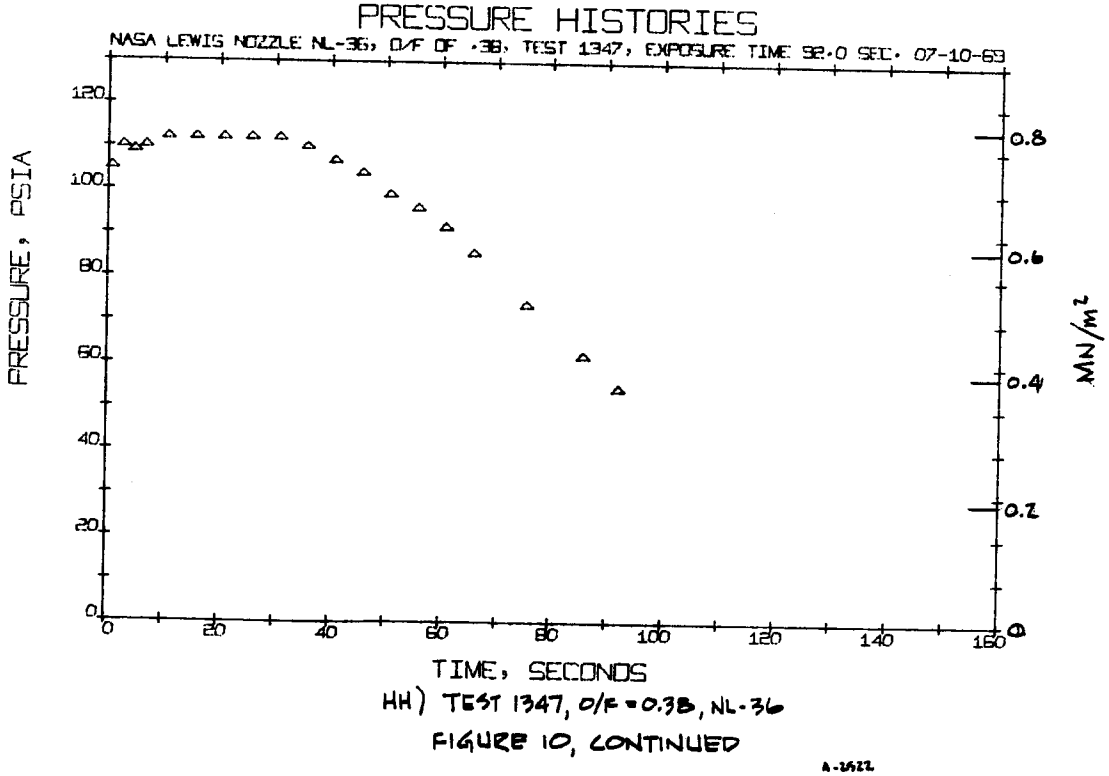
A-2520



GG) TEST 1350, O/F = 0.38, NL-39

FIGURE 10, CONTINUED

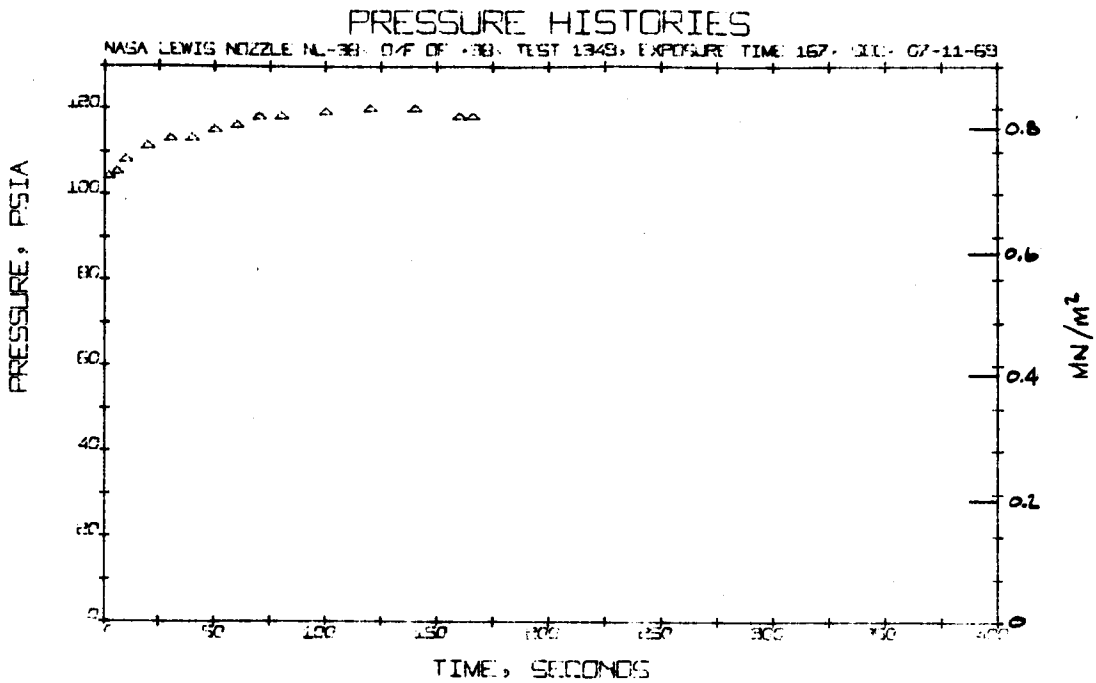
A-3521



HH) TEST 1347, O/F = 0.38, NL-36

FIGURE 10, CONTINUED

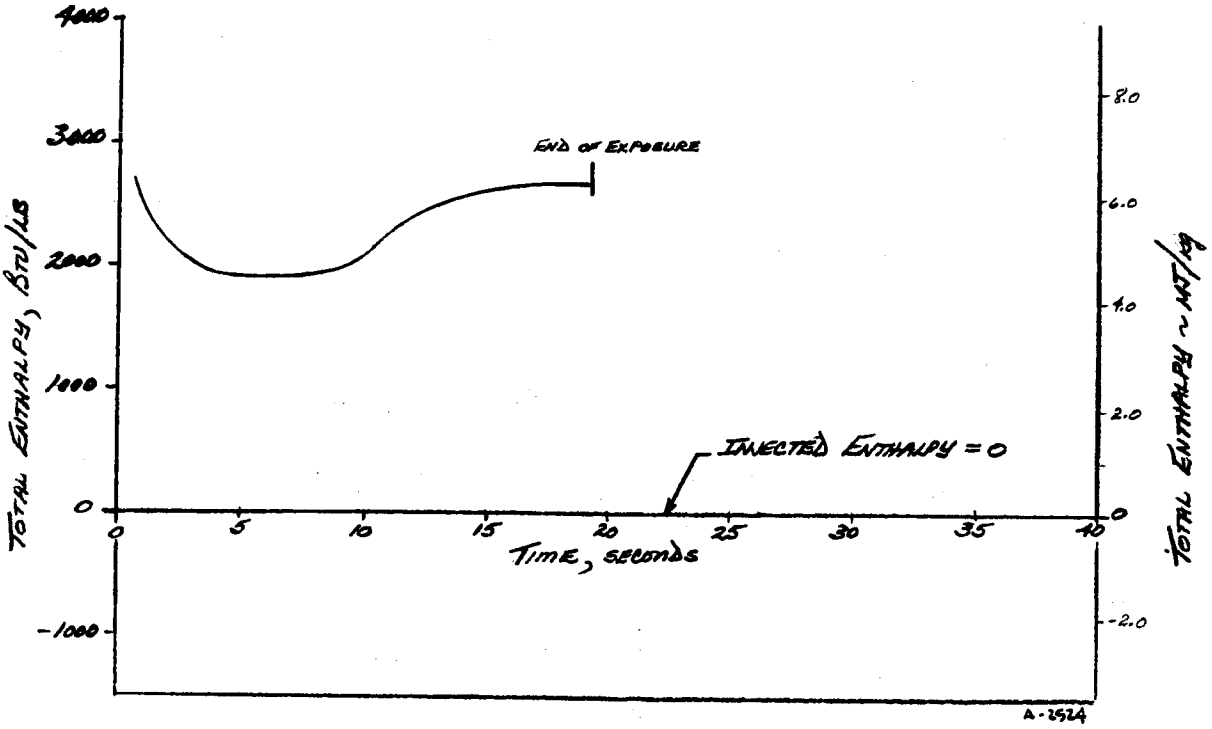
A-3522



II) TEST 1349, O/F: 0.38, NL-38

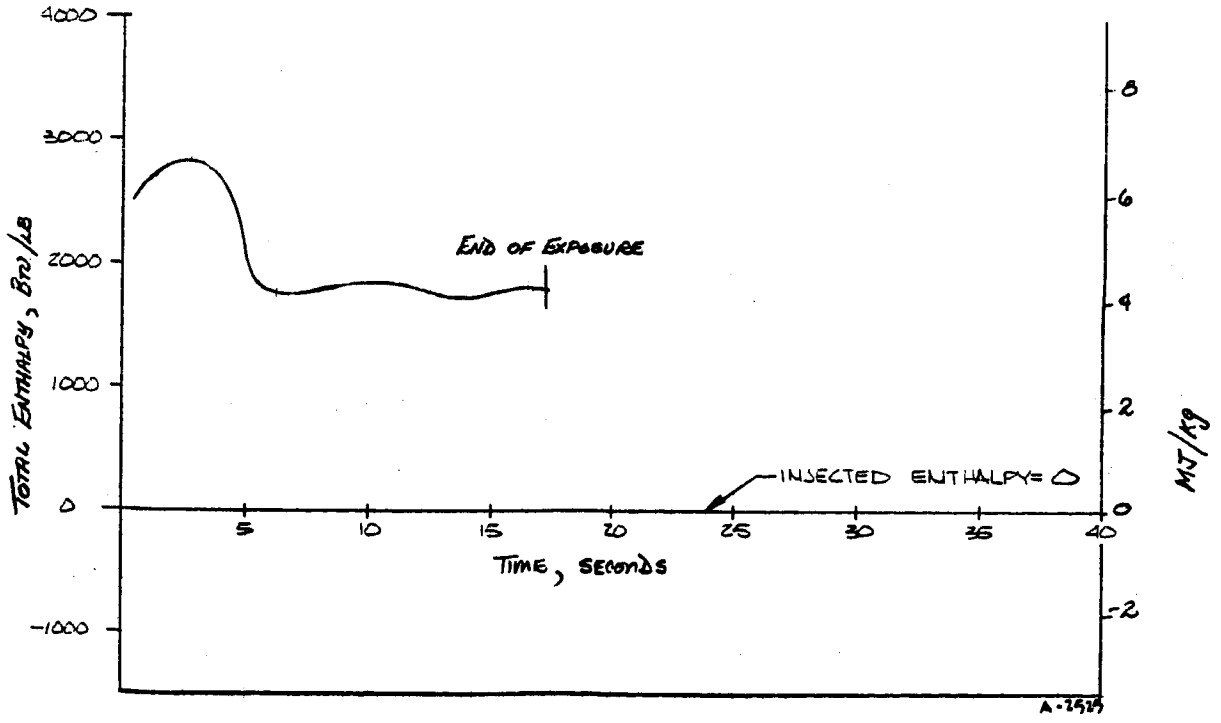
FIGURE 10, CONCLUDED

A-2523



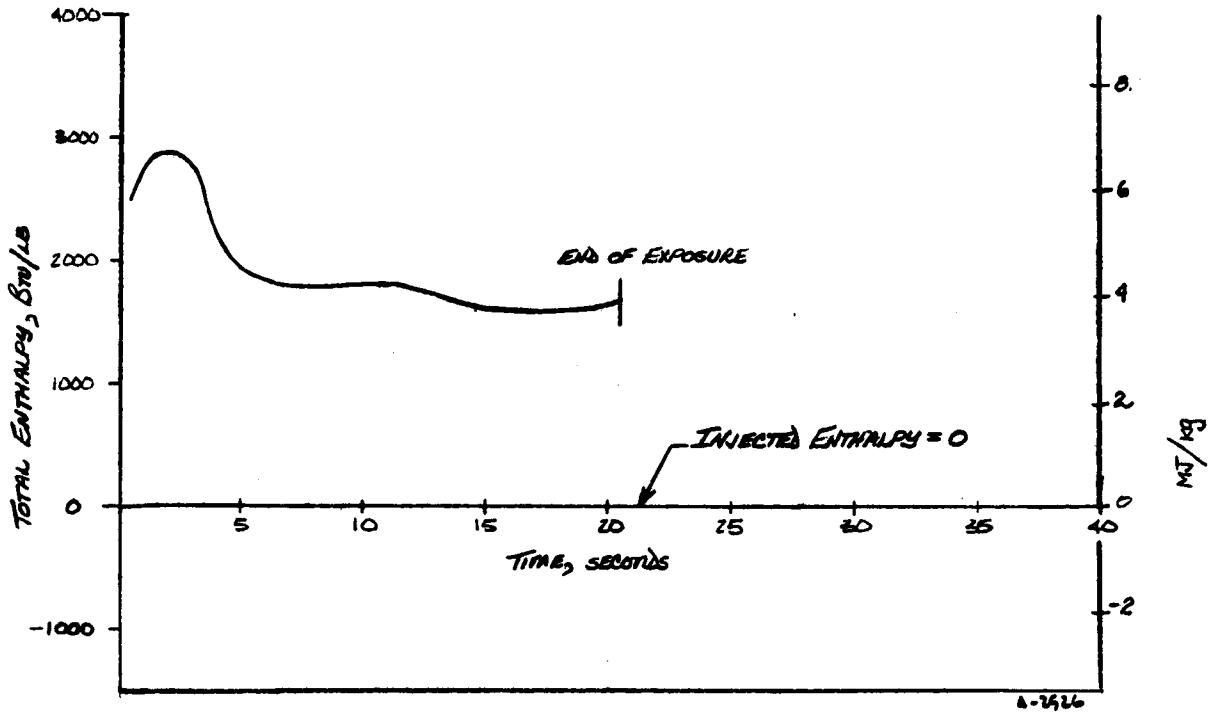
A) TEST 1083, O/F ∞, NL-11

FIGURE 11 - ENTHALPY HISTORIES OF ABLATIVE NOZZLE TESTS.



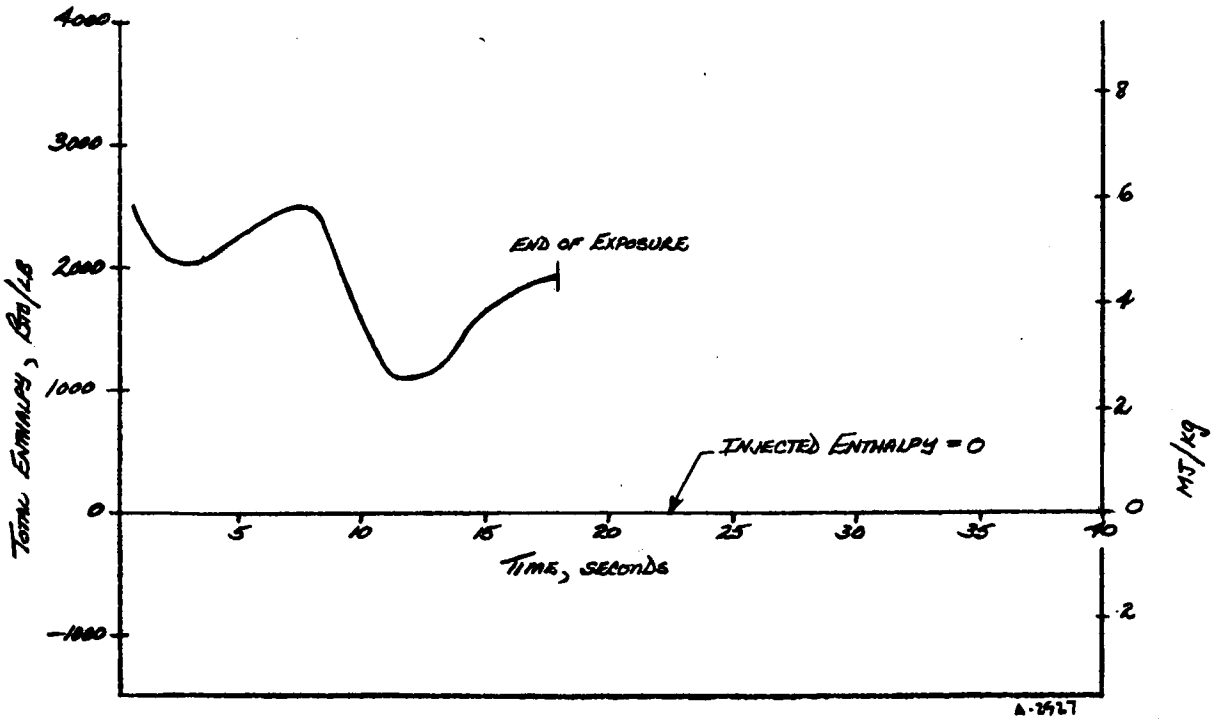
B) TEST 1358, O/F ∞, NL-42

FIGURE 11, CONTINUED.



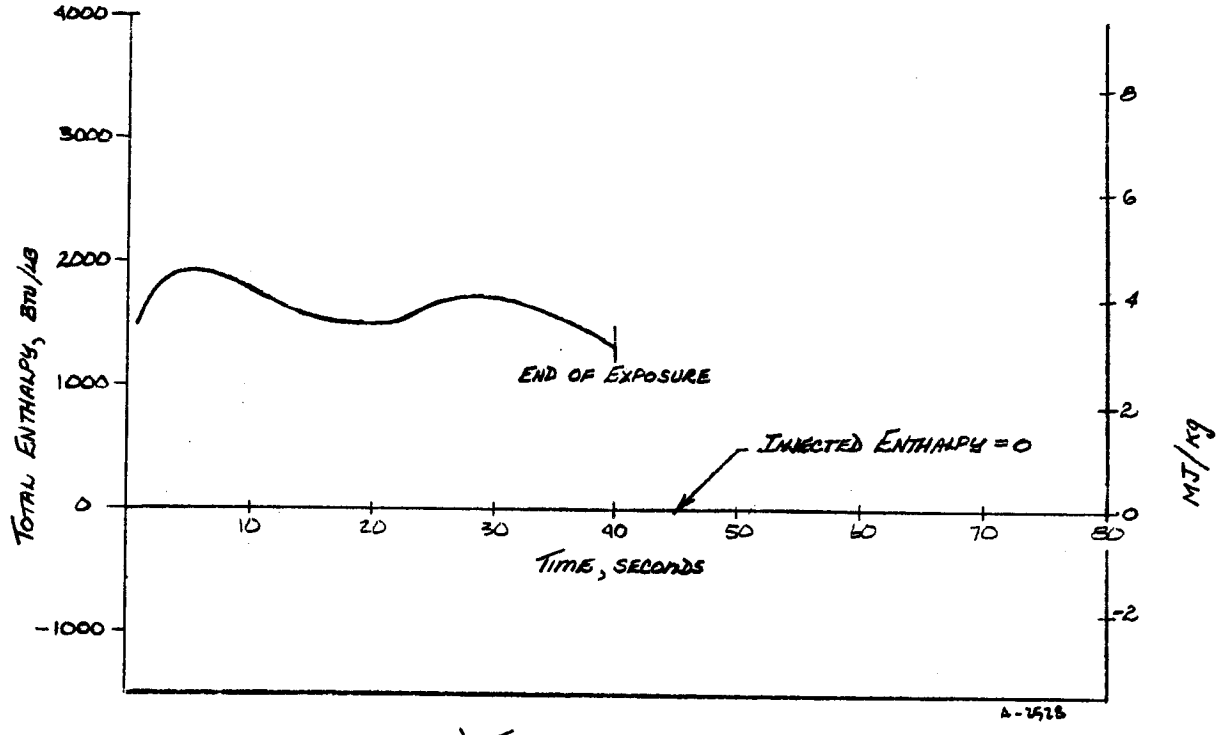
c) TEST 1359, O/F ∞, NL-13

FIGURE 11, CONTINUED.



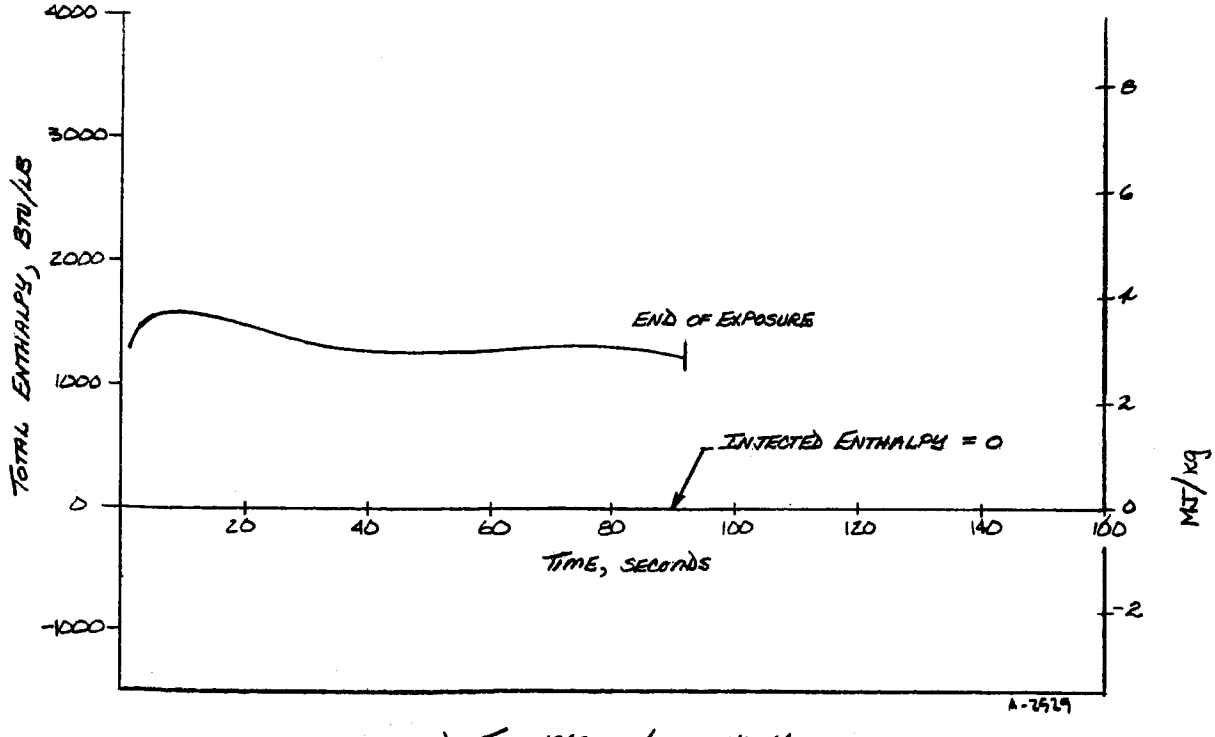
D) TEST 1084, O/F ∞, NL-12

FIGURE 11, CONTINUED.



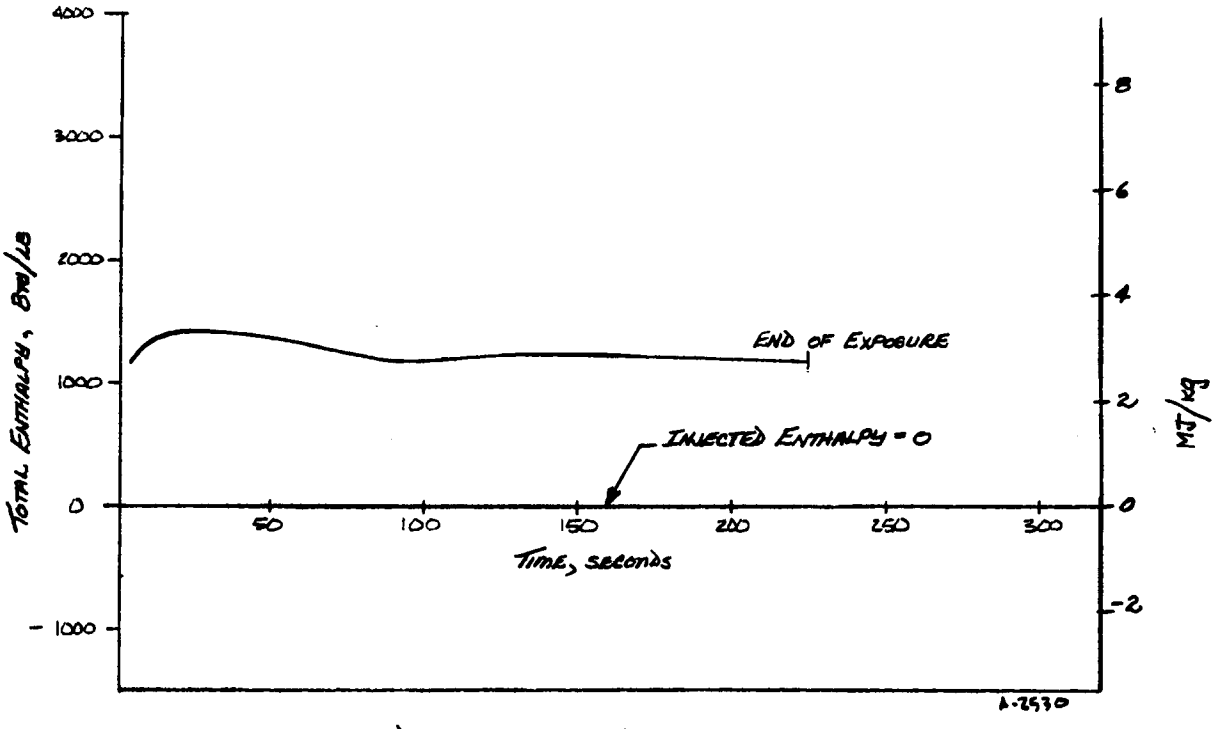
E) TEST 1361, O/F ∞, NL-10

FIGURE 11, CONTINUED.



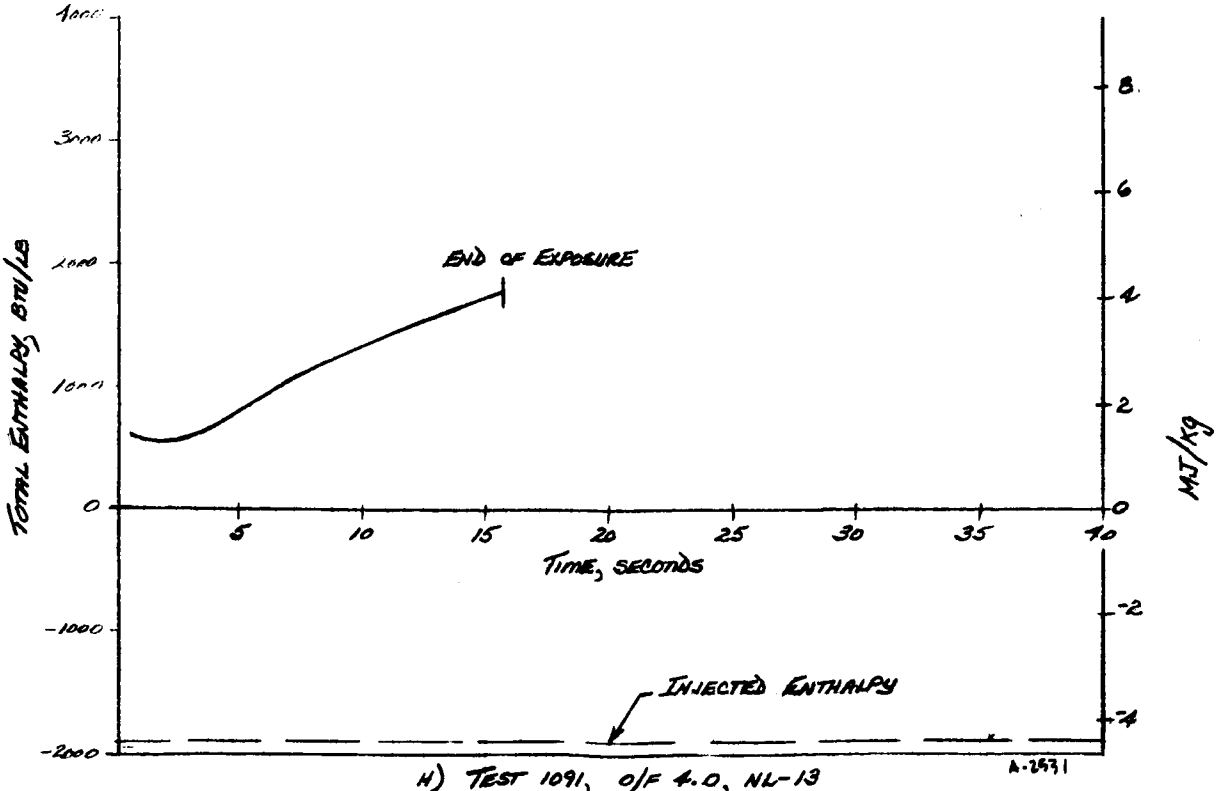
F) TEST 1362, O/F ∞, NL-11

FIGURE 11, CONTINUED.



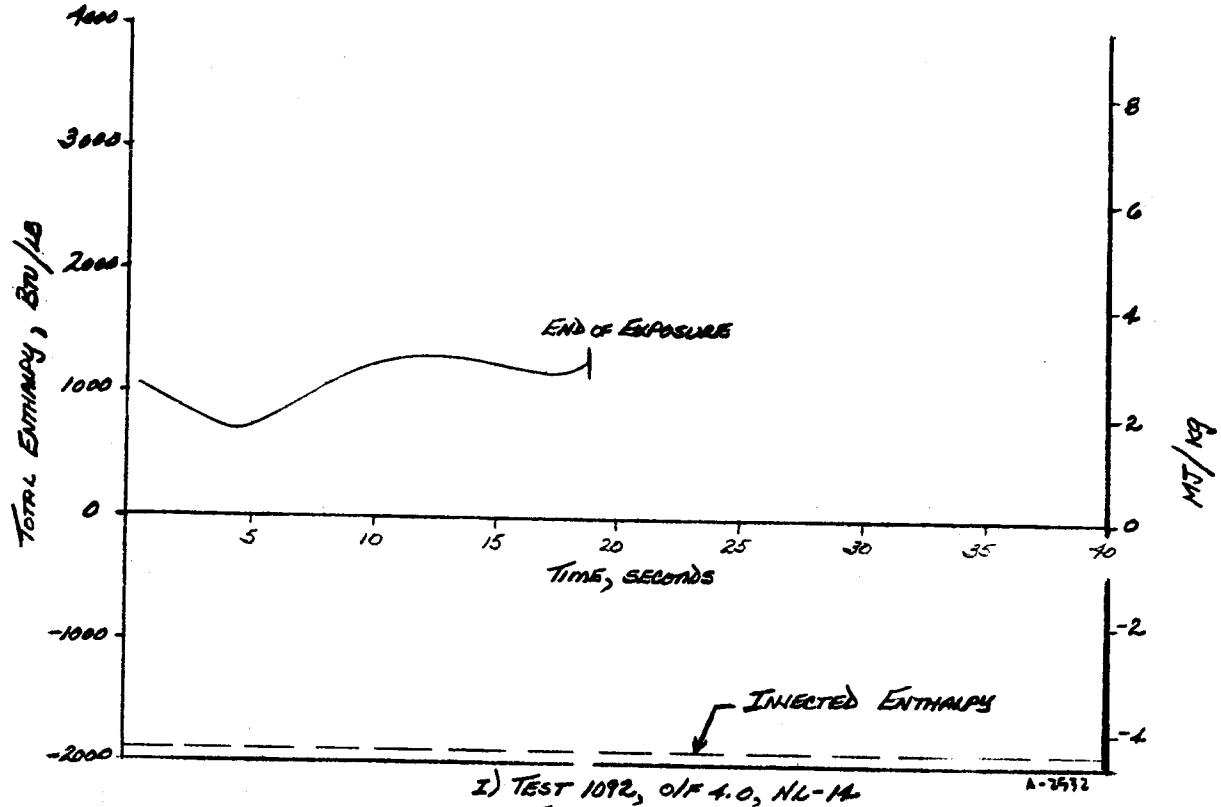
G) TEST 1360, O/F ∞, NL-44

FIGURE 11, CONTINUED.

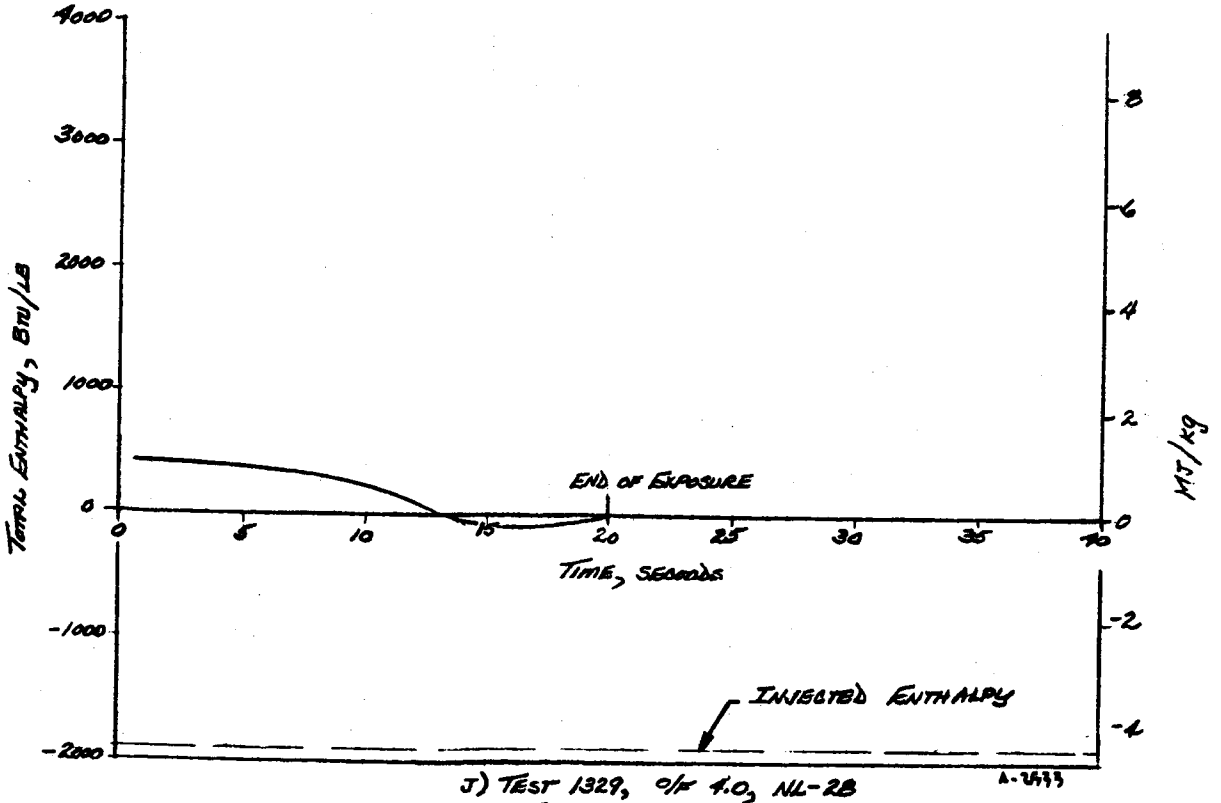


H) TEST 1091, O/F 4.0, NL-13

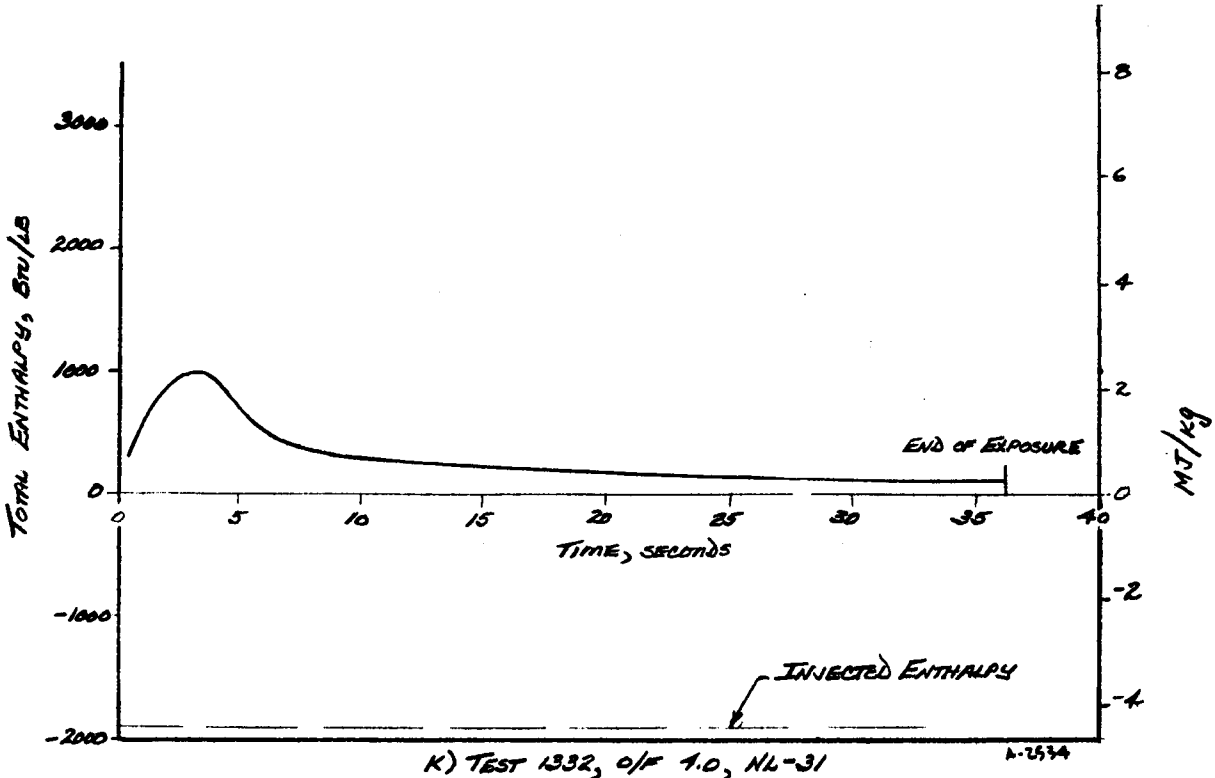
FIGURE 11, CONTINUED.



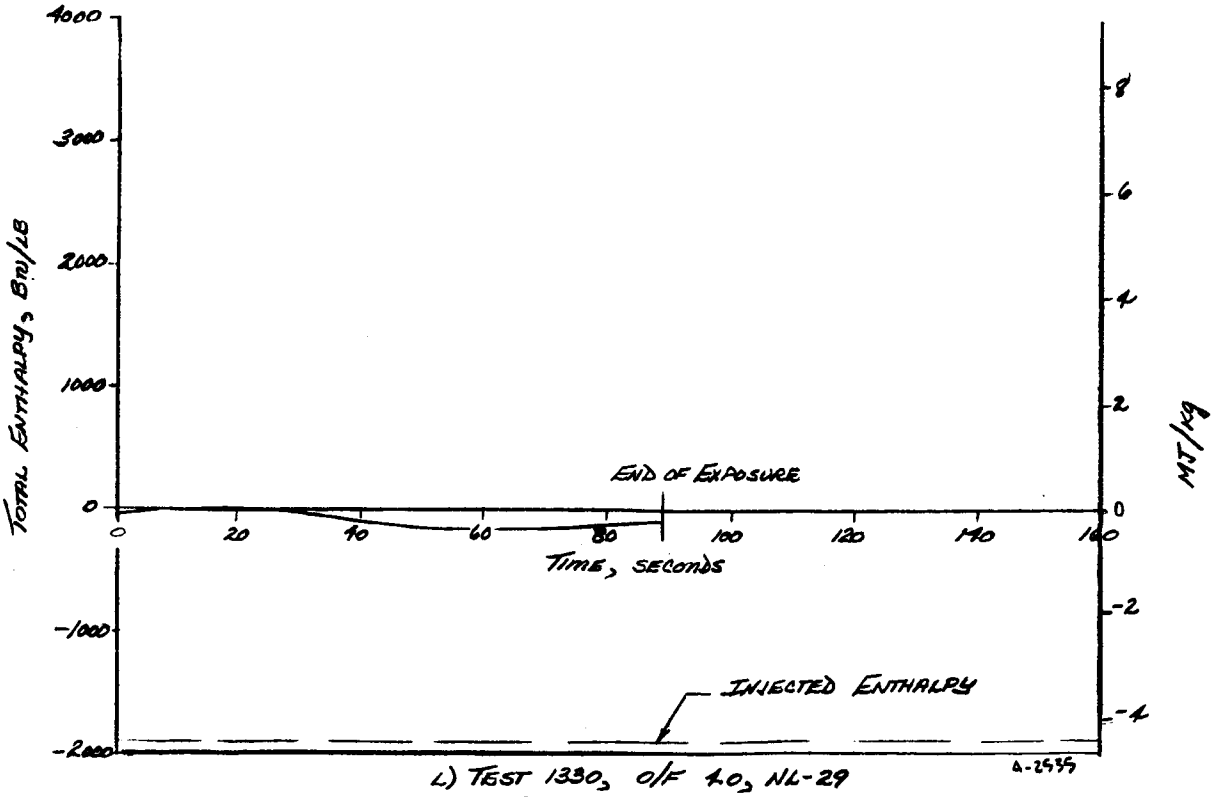
I) TEST 1092, O/F 4.0, NL-14
FIGURE 11, CONTINUED.



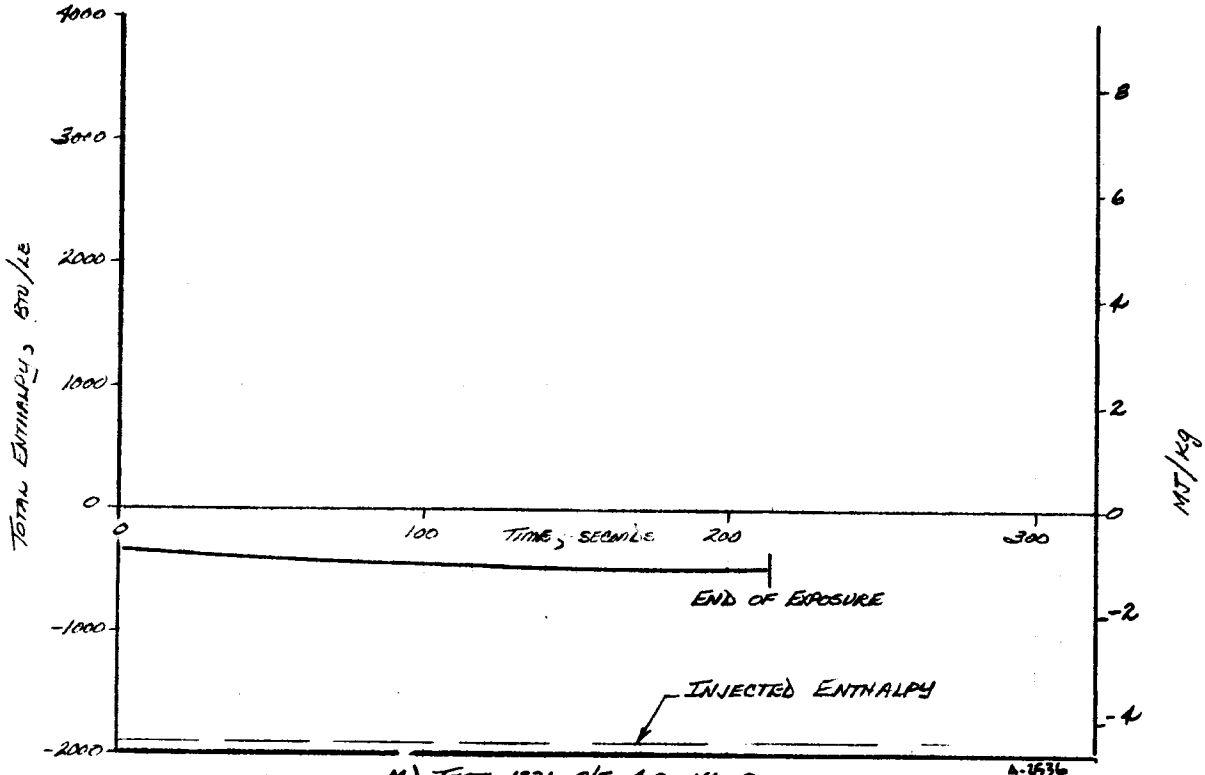
J) TEST 1329, O/F 4.0, NL-28
FIGURE 11, CONTINUED.



K) TEST 1332, O/F 1.0, NL-31
FIGURE 11, CONTINUED.

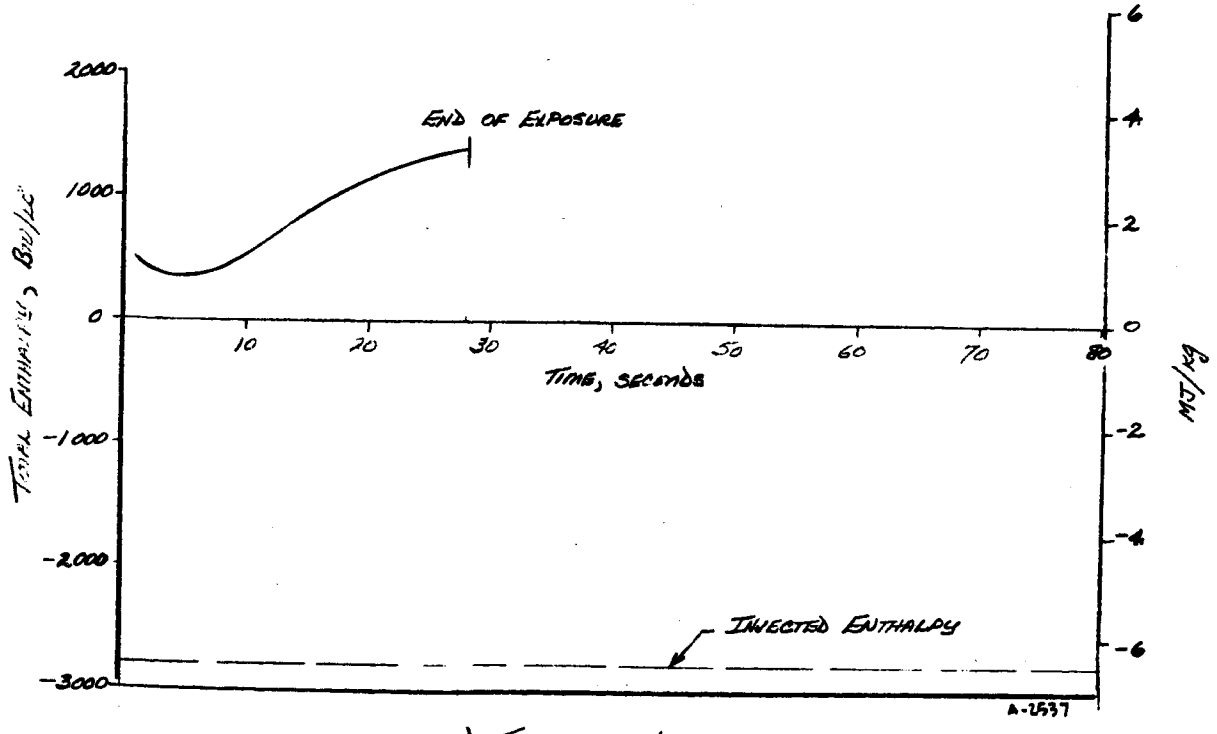


L) TEST 1330, O/F 1.0, NL-29
FIGURE 11, CONTINUED.



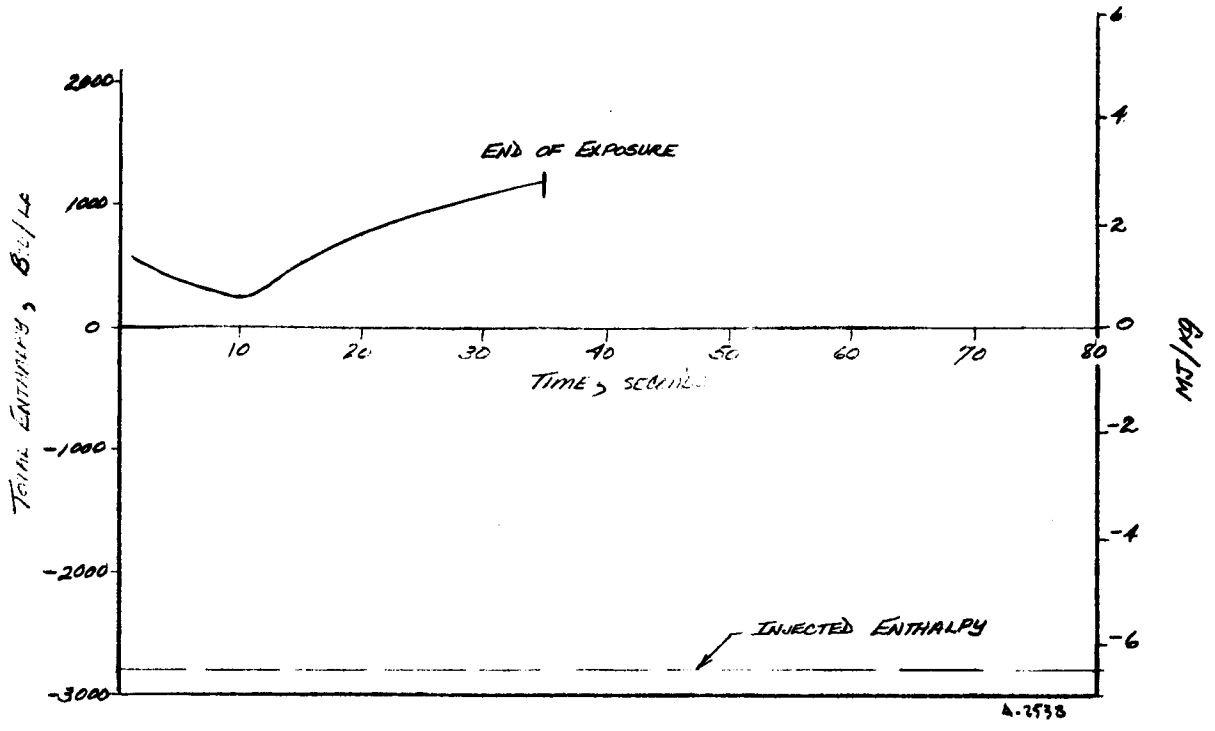
M) TEST 1331, O/F 1.0, NL-30

FIGURE 11, CONTINUED.



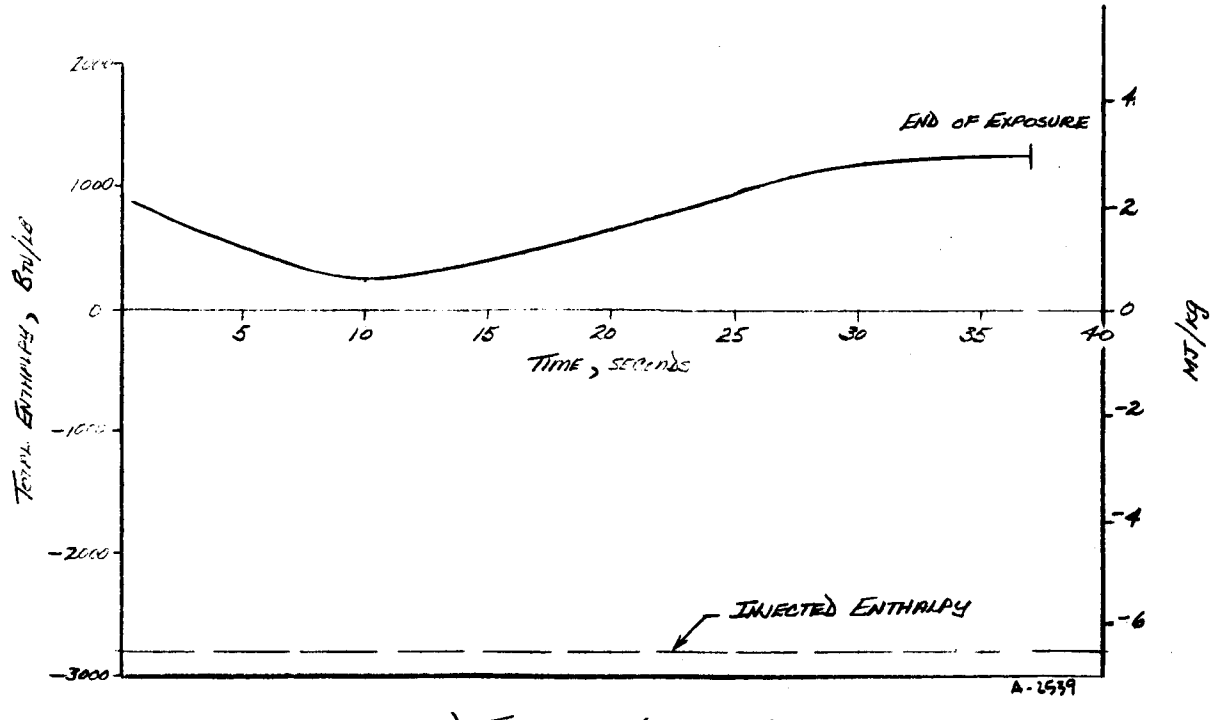
N) TEST 1135, O/F 2.0, NL-26

FIGURE 11, CONTINUED.



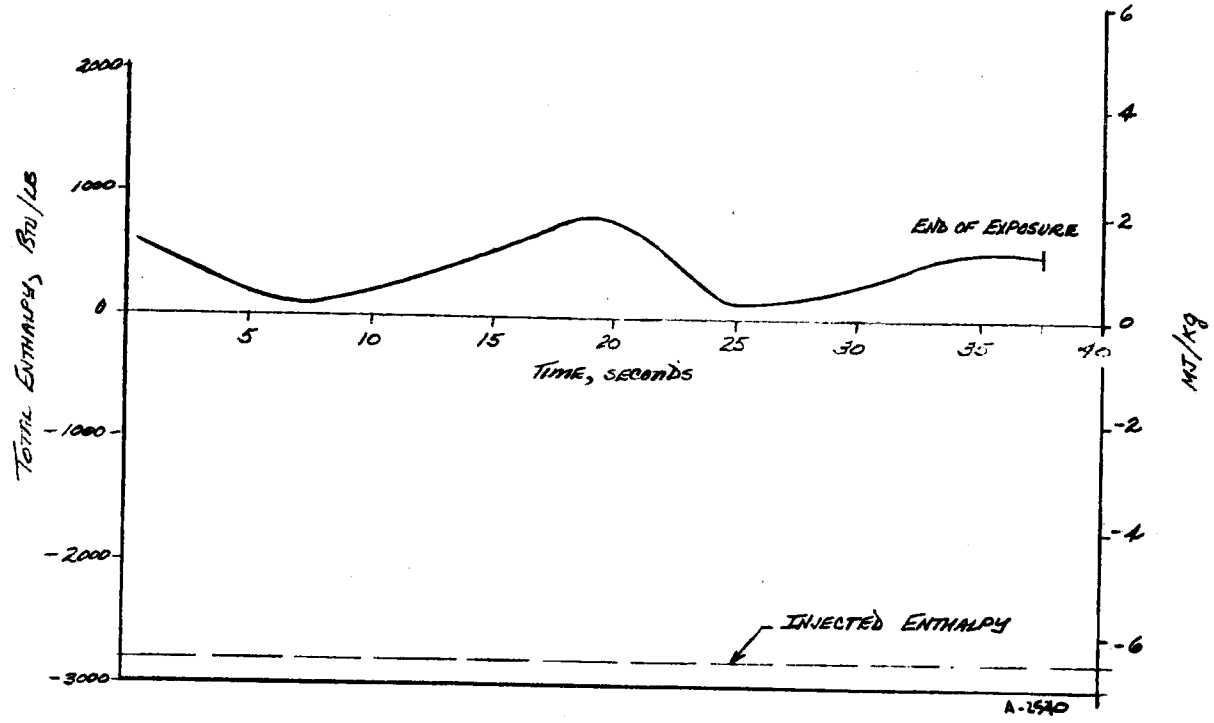
o) TEST 1134, O/F 2, NL-25

FIGURE 11, CONTINUED.



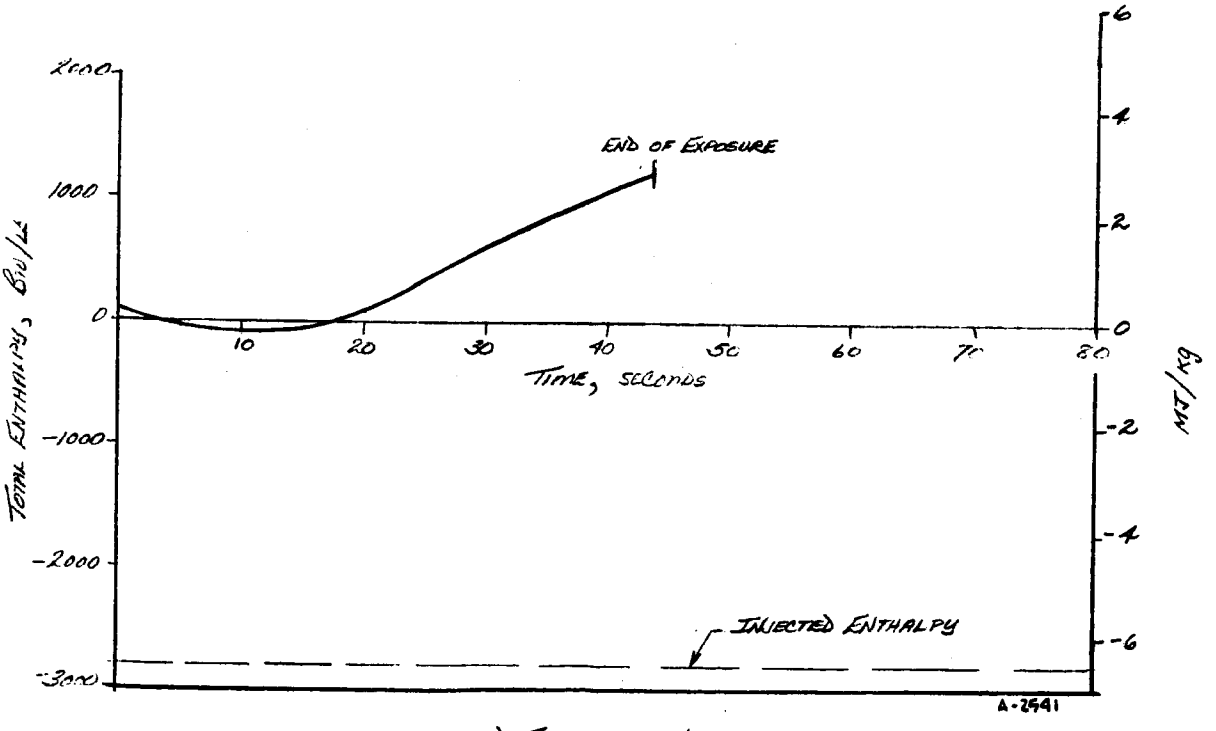
P) TEST 1124, O/F 2.0, NL-21

FIGURE 11, CONTINUED.



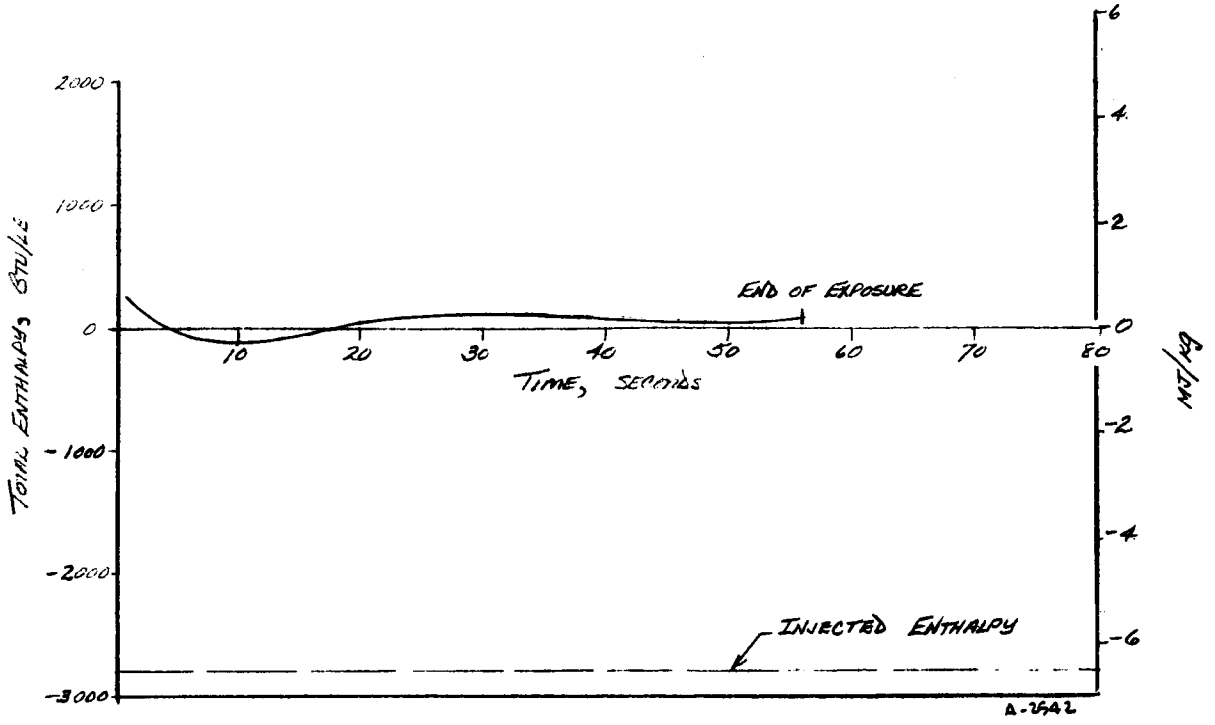
Q) TEST 1125, O/F 2.0, NL-22

FIGURE 11, CONTINUED.



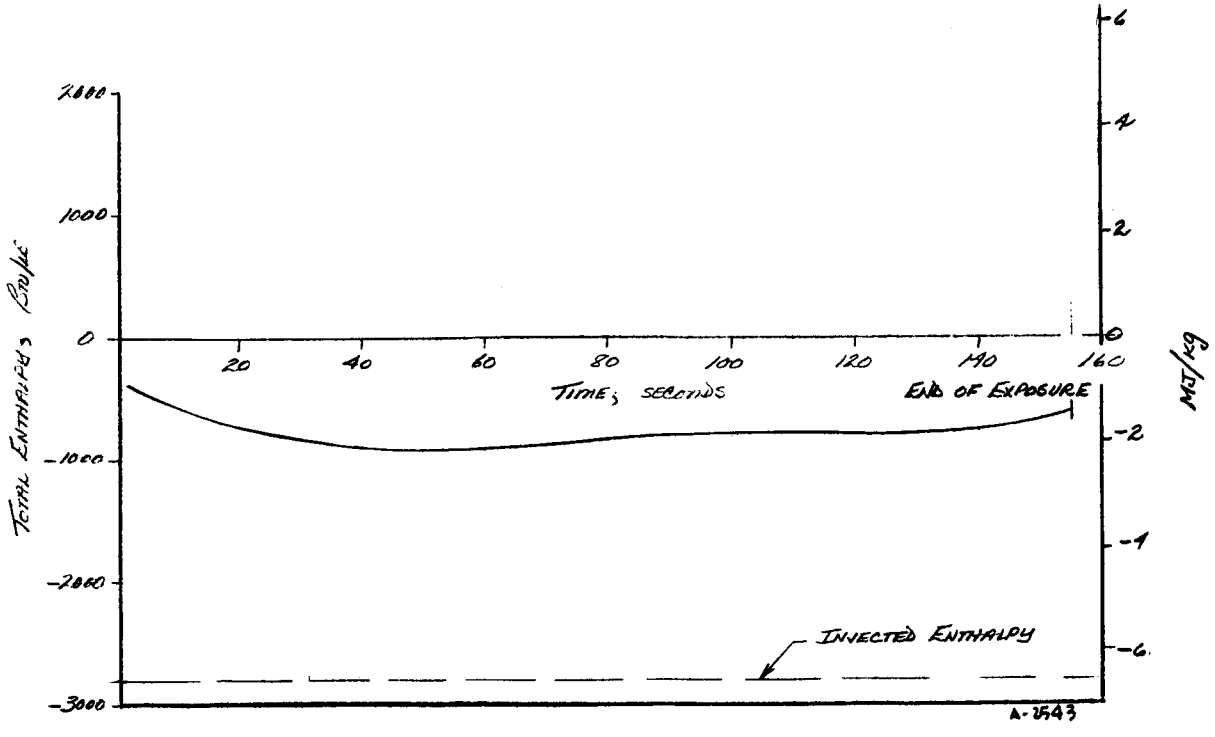
R) TEST 1128, O/F 2.0, NL-23

FIGURE 11, CONTINUED.



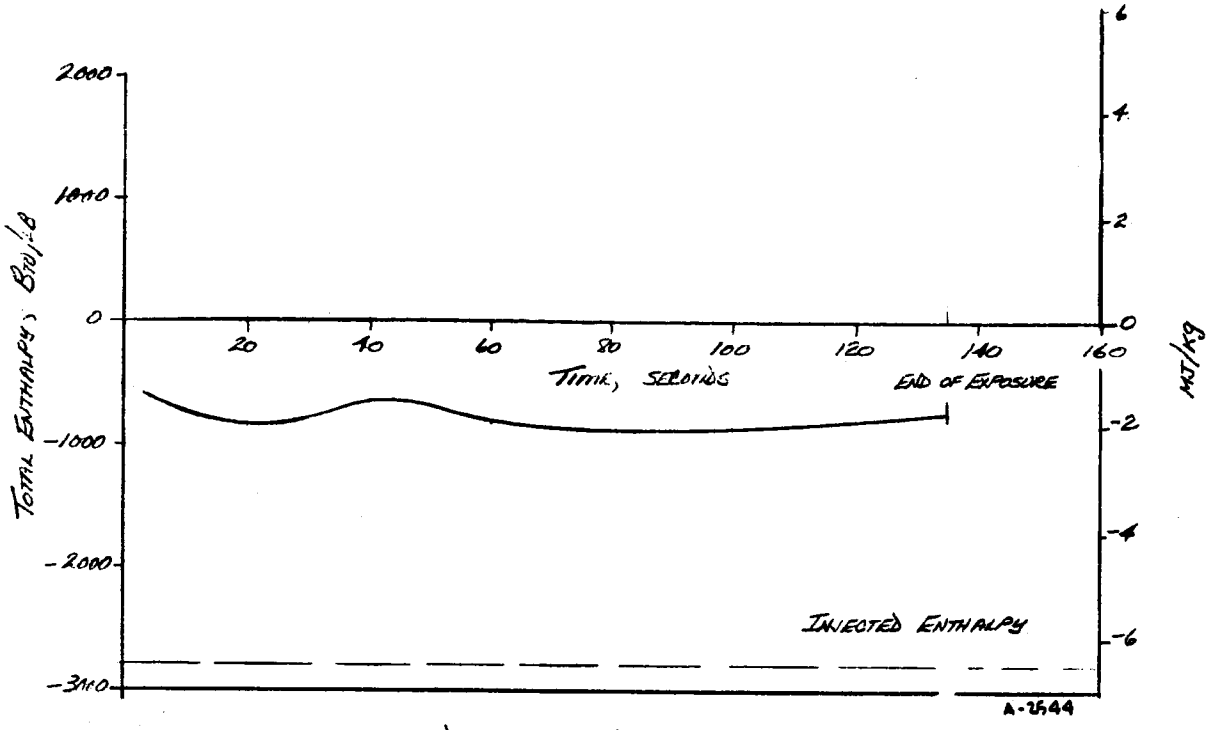
S) TEST 1129, O/F 2.0, NL-24

FIGURE 11, CONTINUED.



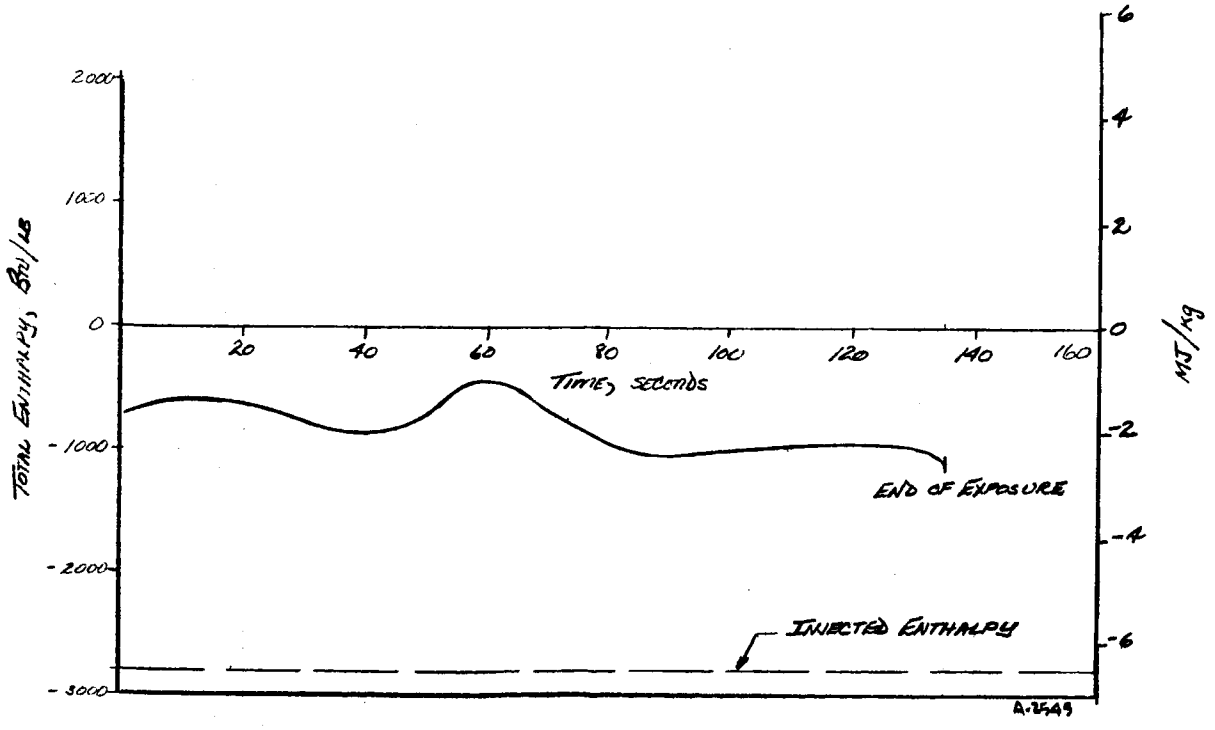
T) TEST 1120, O/F 2.0, NL-19

FIGURE 11, CONTINUED.



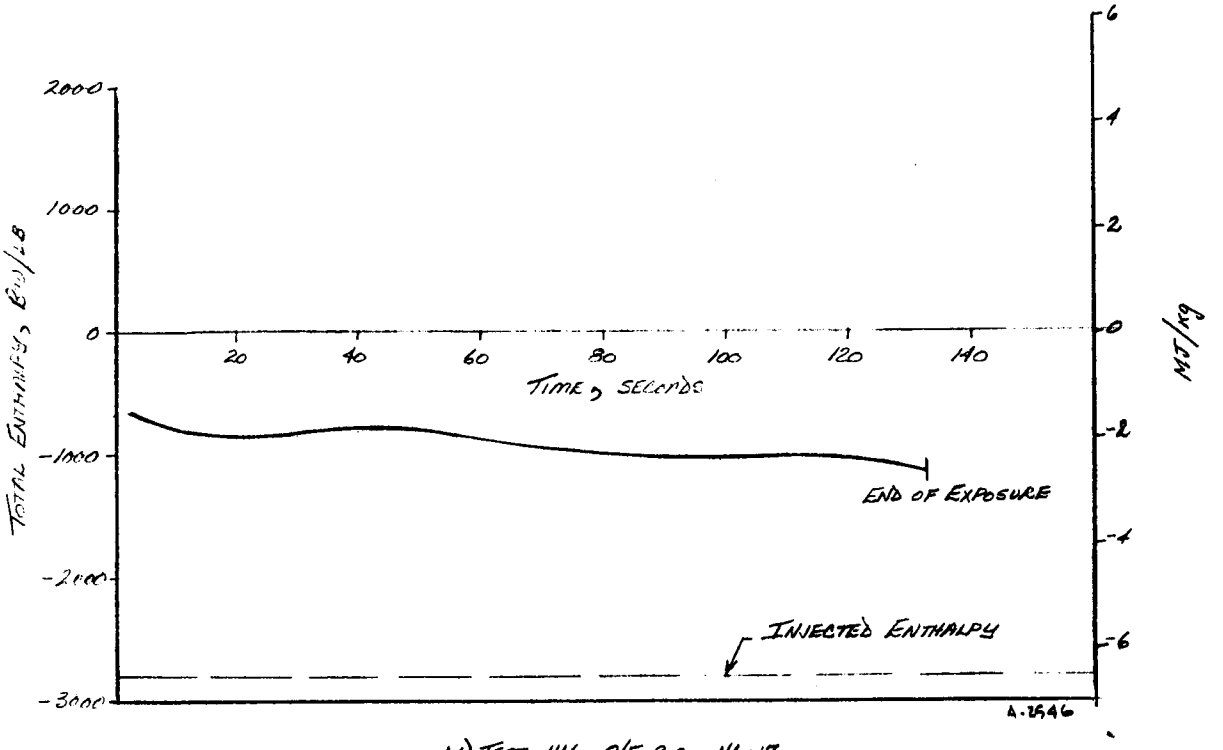
U) TEST 1117, O/F 2.0, NL-18

FIGURE 11, CONTINUED.



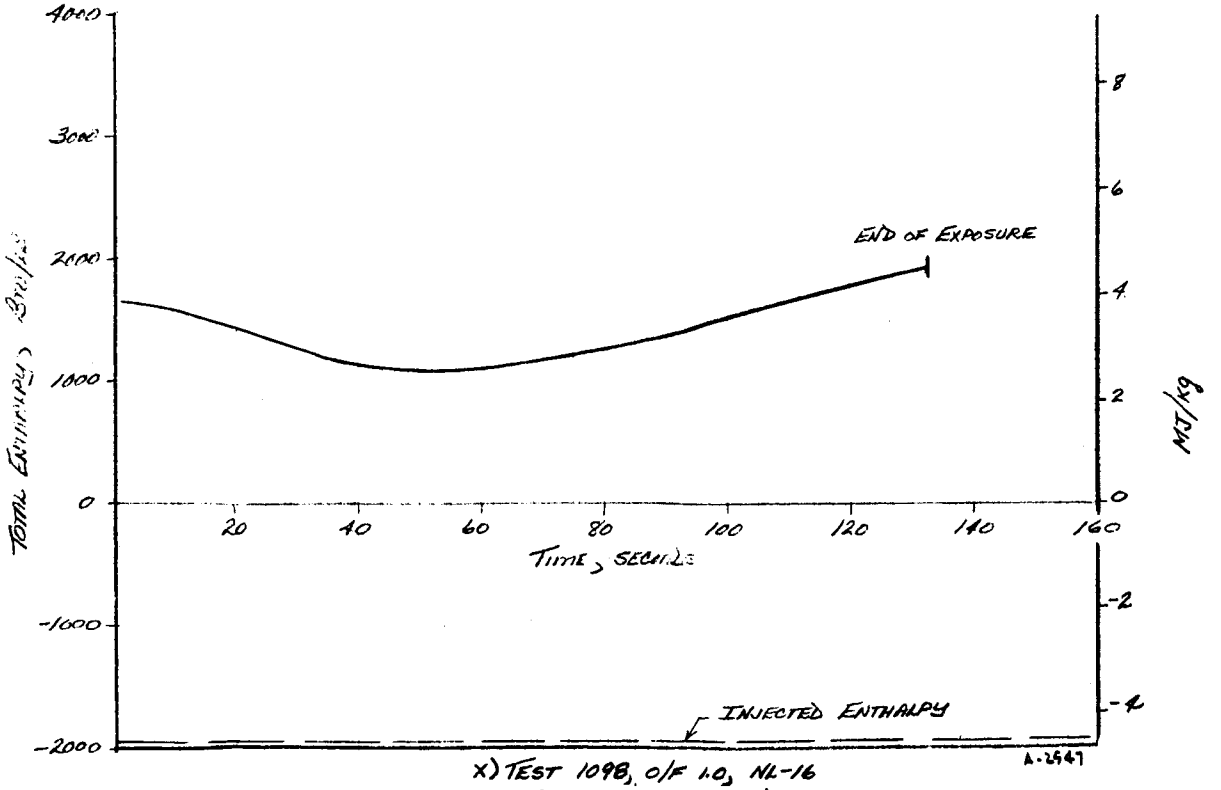
V) TEST 1121, O/F 2.0, NL-20

FIGURE 11, CONTINUED.



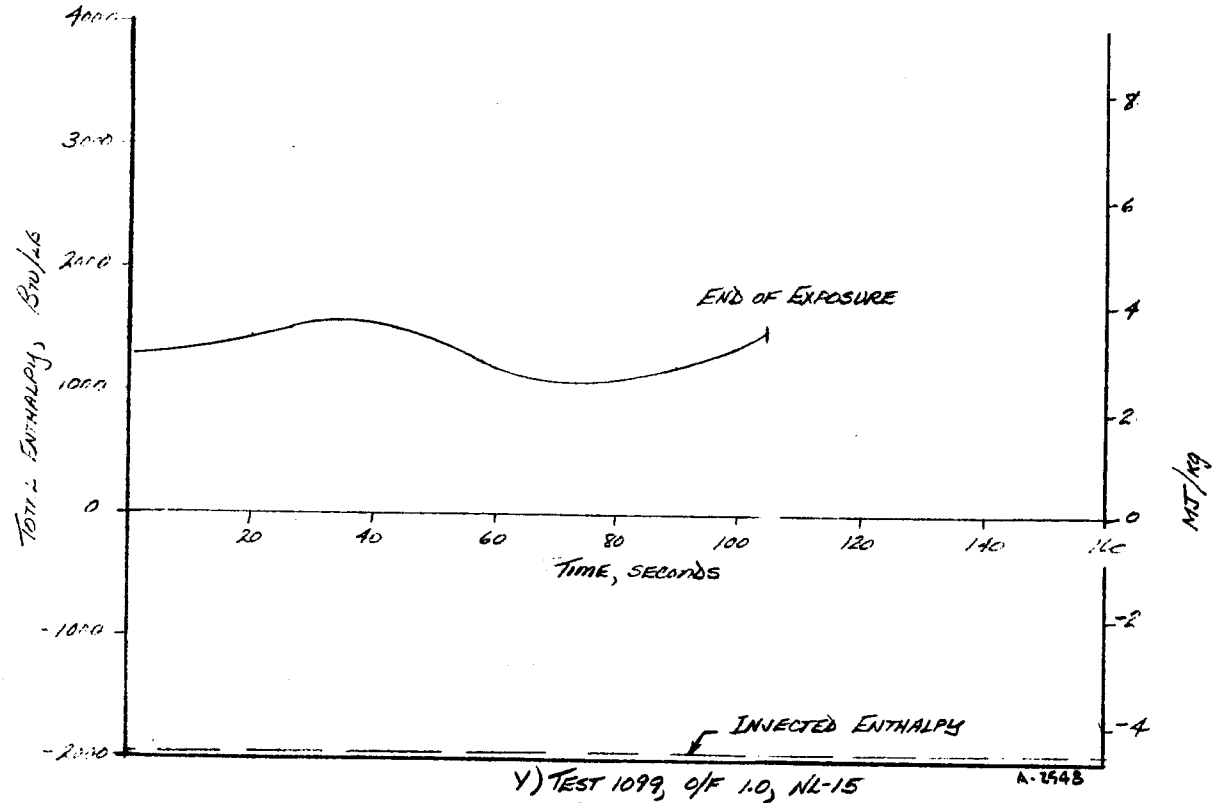
W) TEST 1116, O/F 2.0, NL-17

FIGURE 11, CONTINUED.

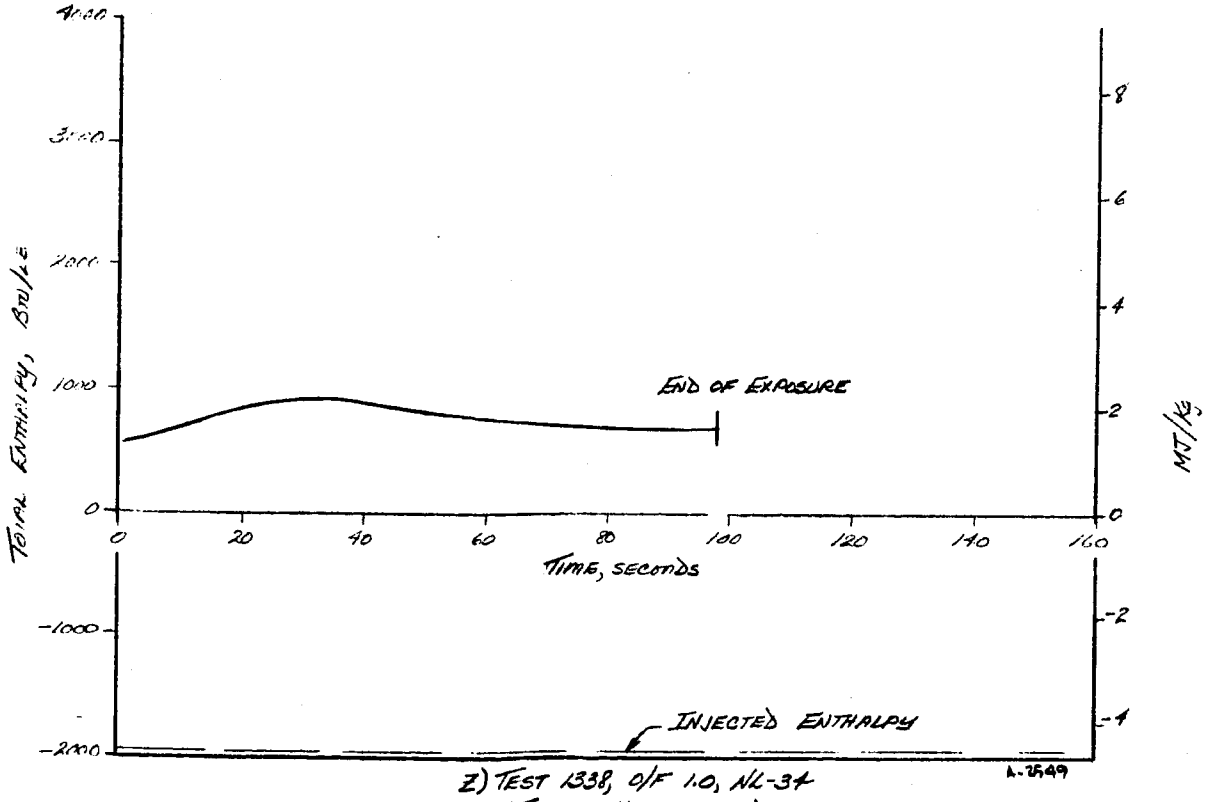


X) TEST 1098, O/F 1.0, NL-16

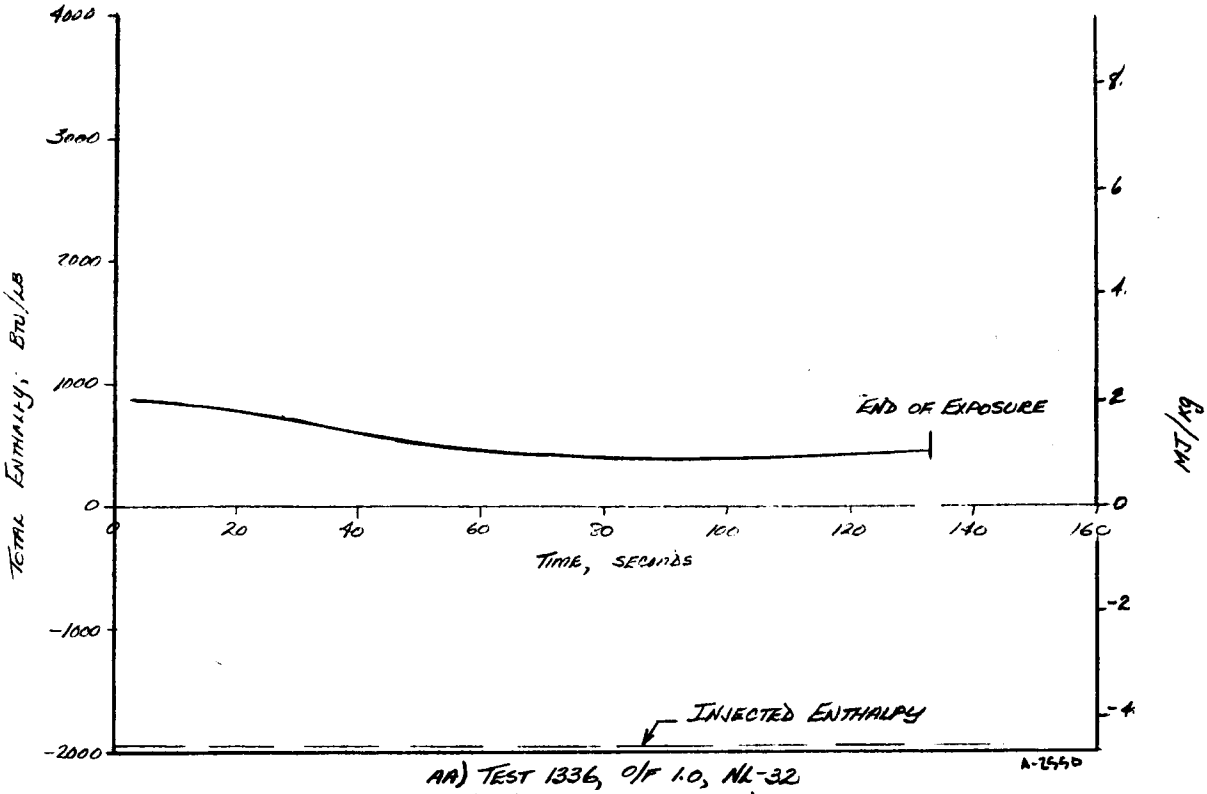
FIGURE 11, CONTINUED.



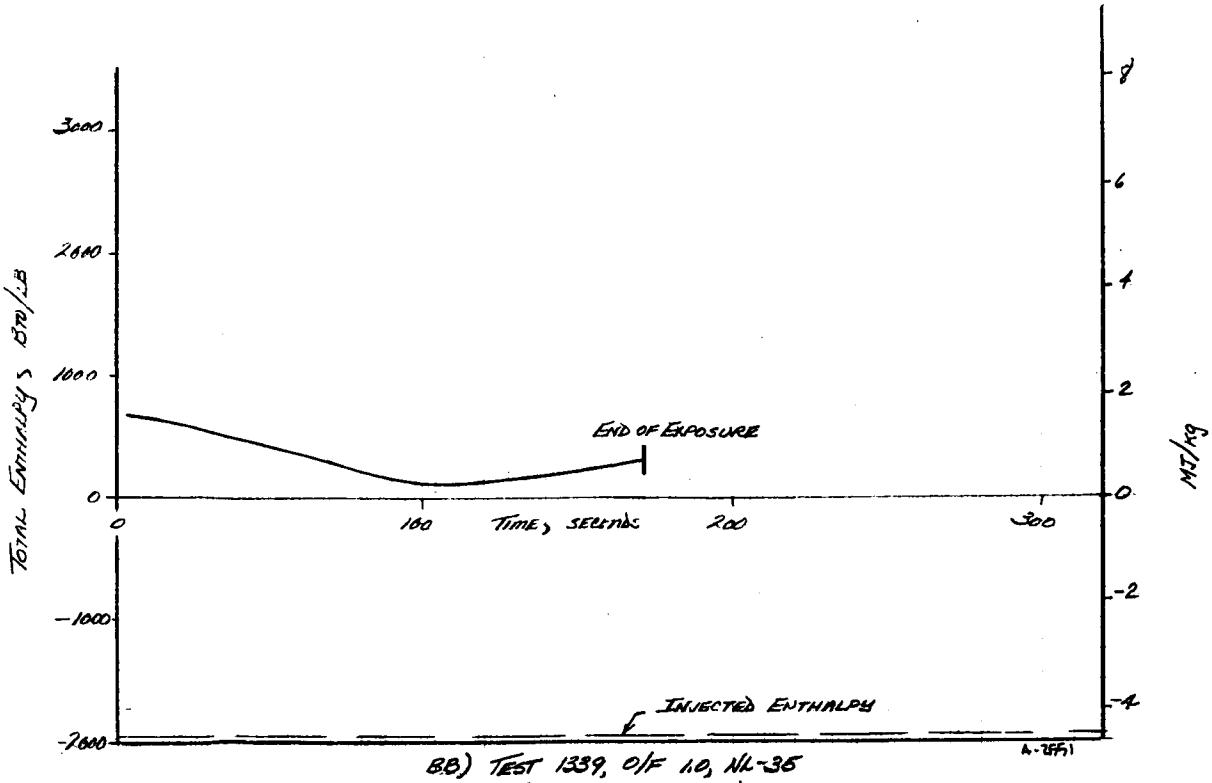
Y) TEST 1099, O/F 1.0, NL-15
FIGURE 11, CONTINUED.



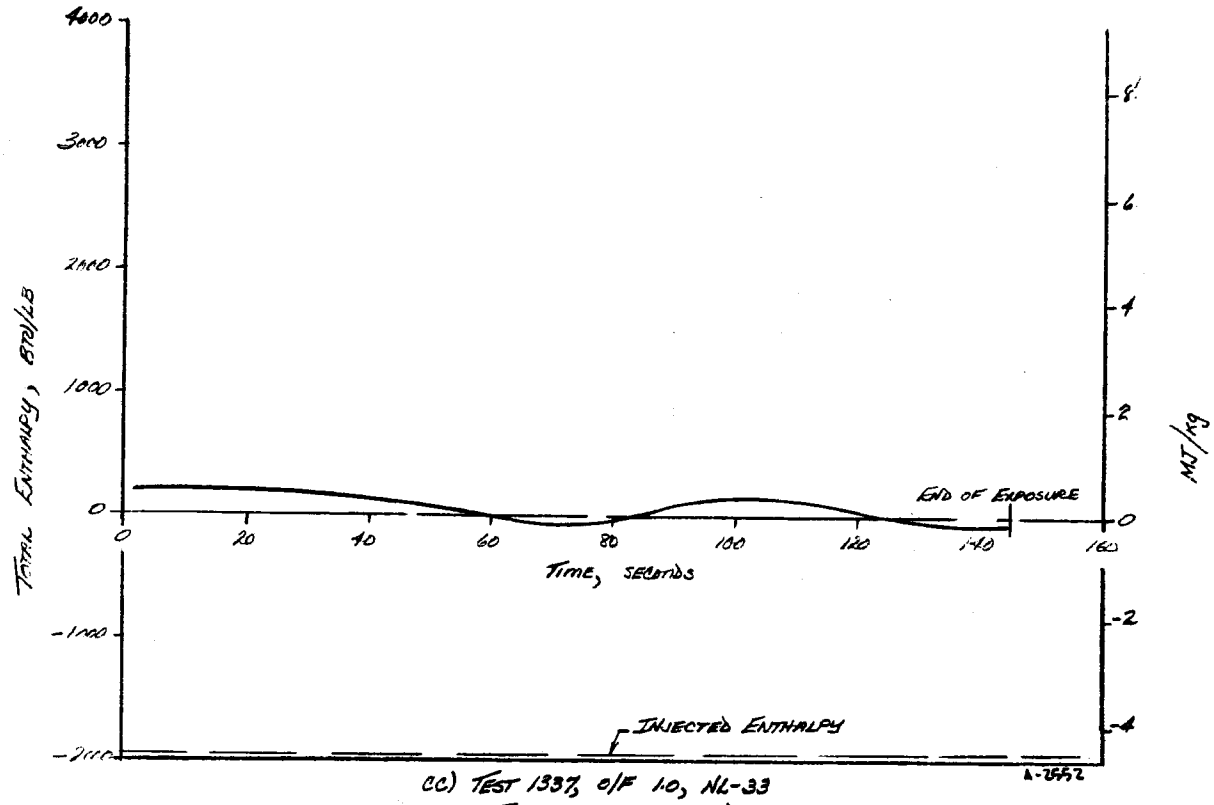
Z) TEST 1338, O/F 1.0, NL-34
FIGURE 11, CONTINUED.



AA) TEST 1336, O/F 1.0, NL-32
FIGURE 11, CONTINUED.

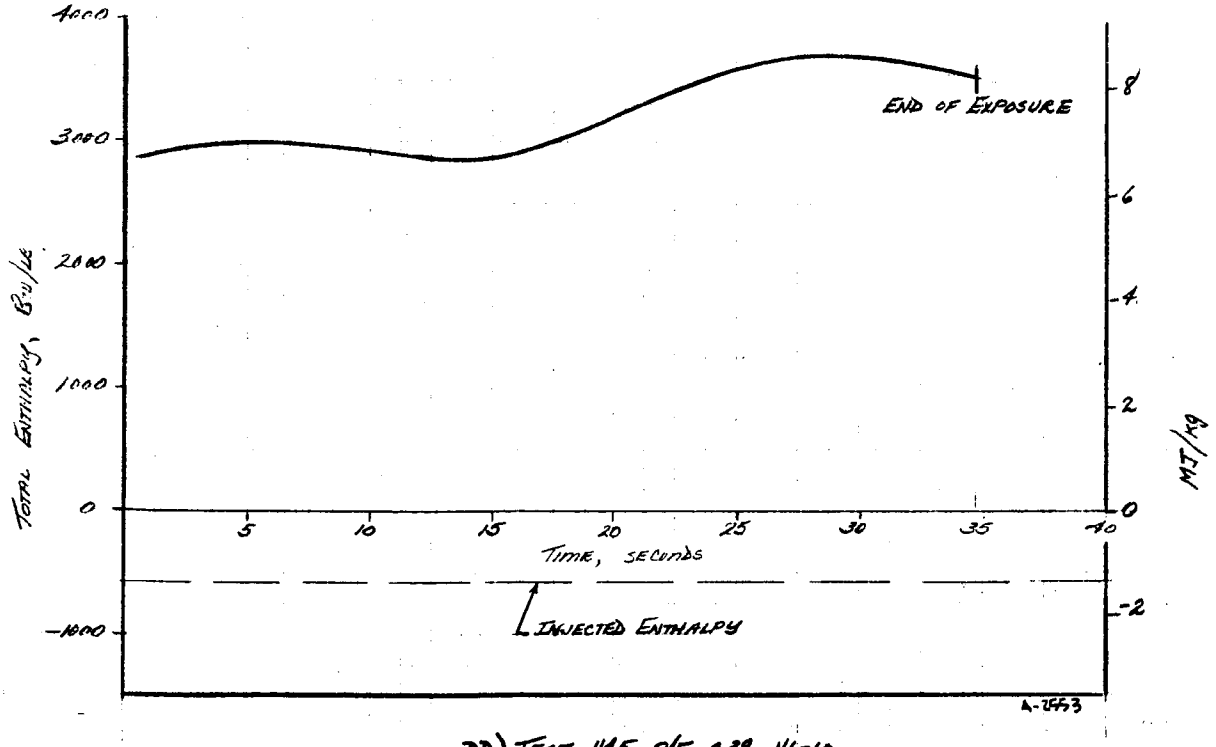


BB) TEST 1339, O/F 1.0, NL-36
FIGURE 11, CONTINUED.



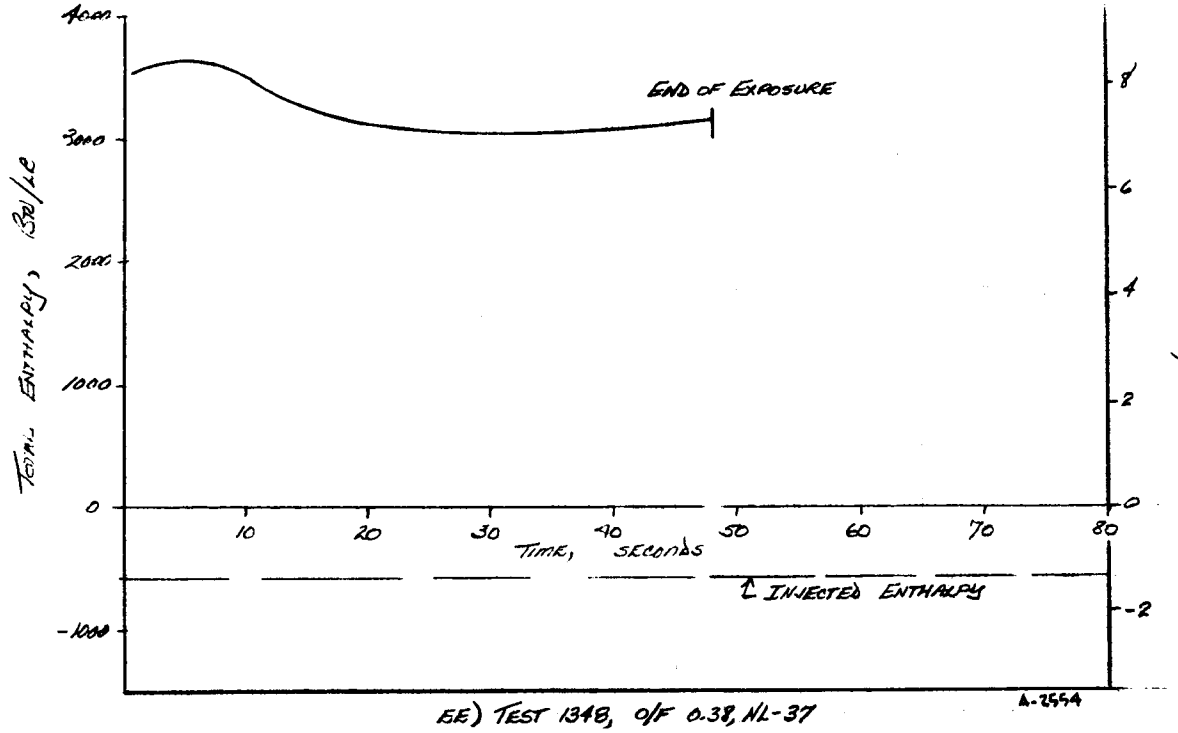
CC) TEST 1337, O/F 1.0, NL-33

FIGURE 11, CONTINUED.

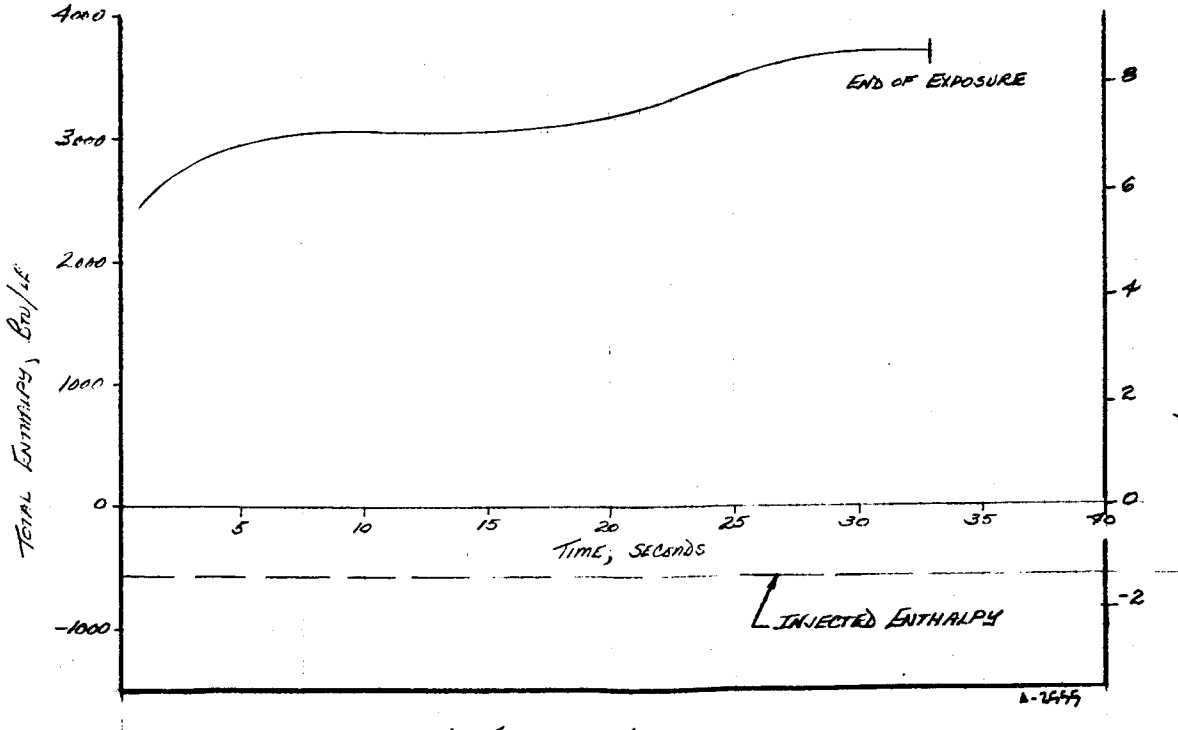


DD) TEST 1145, O/F 0.38, NL-10

FIGURE 11, CONTINUED.

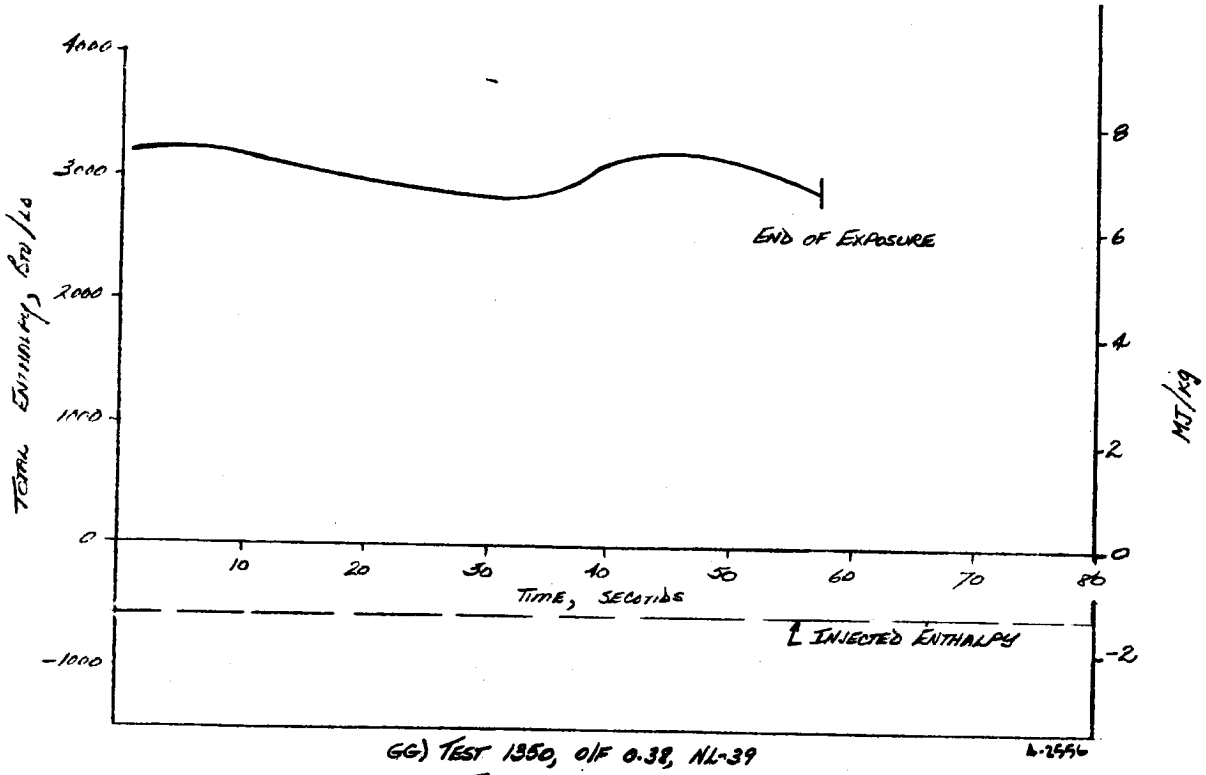


EE) TEST 1348, O/F 0.38, NL-37
FIGURE 11, CONTINUED.

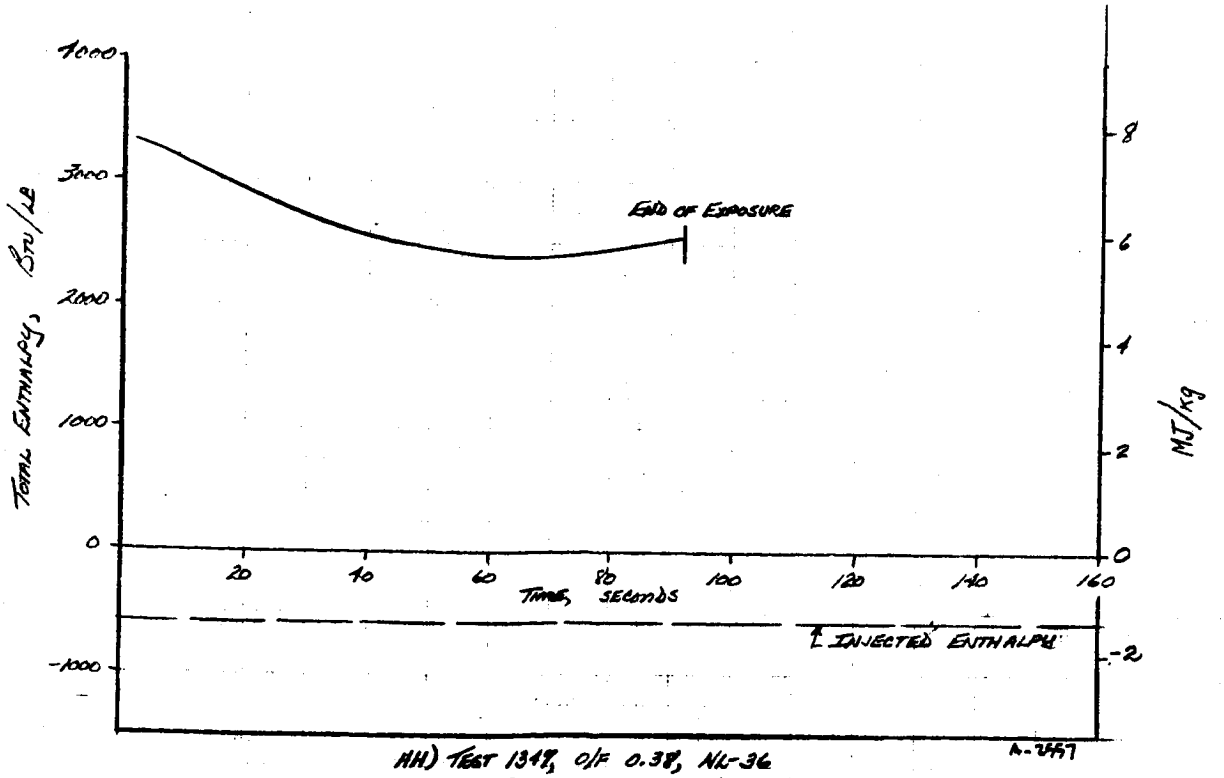


FF) TEST 1146, O/F 0.38, NL-27

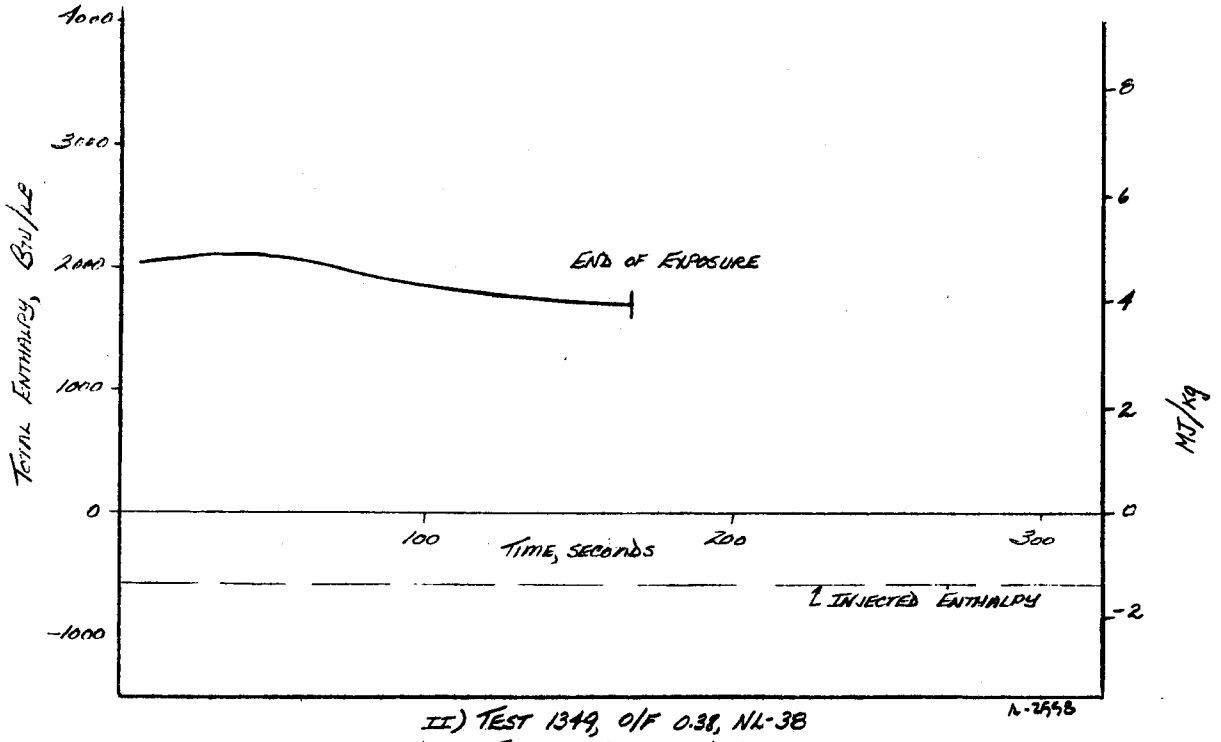
FIGURE 11, CONTINUED.



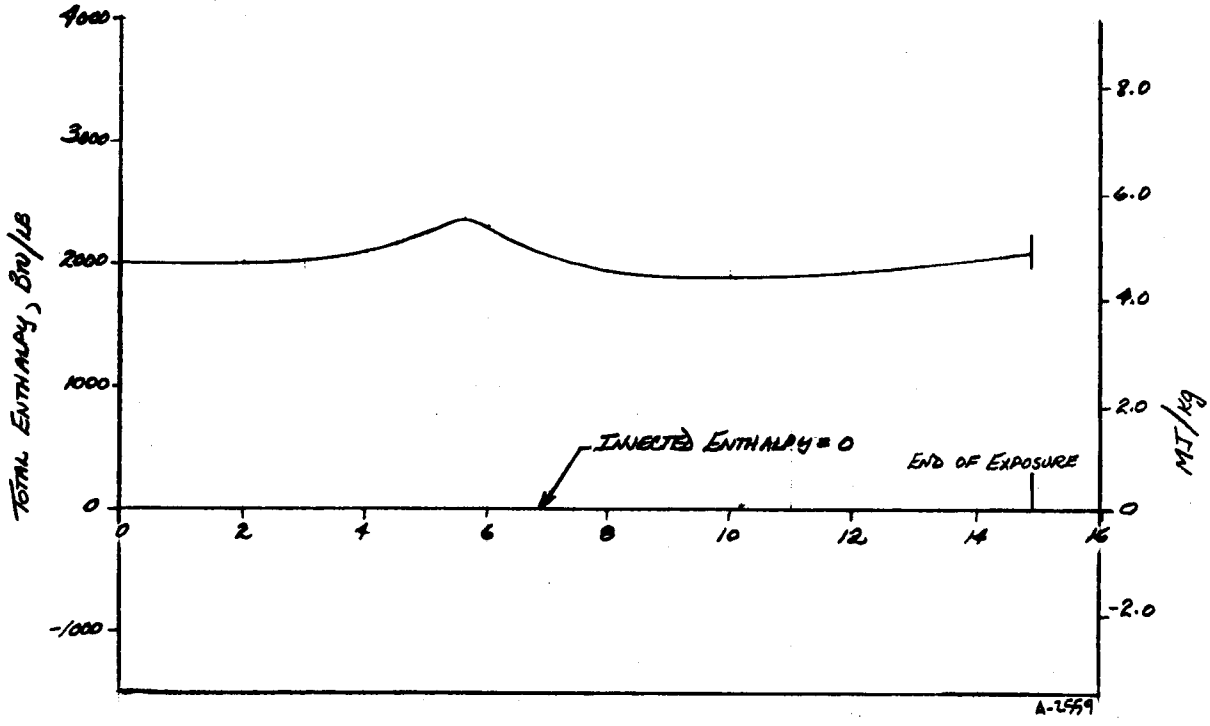
GG) TEST 1350, O/F 0.38, NL-39
FIGURE 11, CONTINUED.



HH) TEST 1348, O/F 0.38, NL-36
FIGURE 11, CONTINUED.

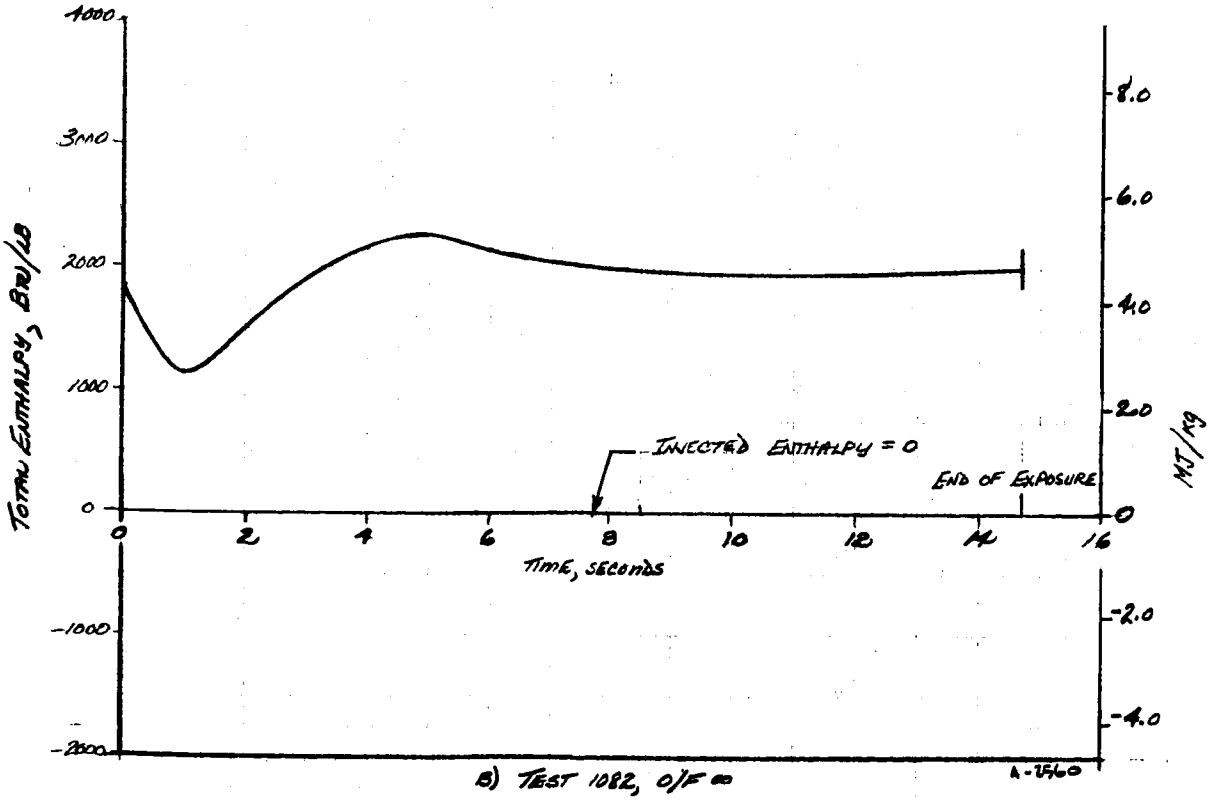


II) TEST 1349, O/F 0.38, NL-38
FIGURE 11, CONCLUDED.



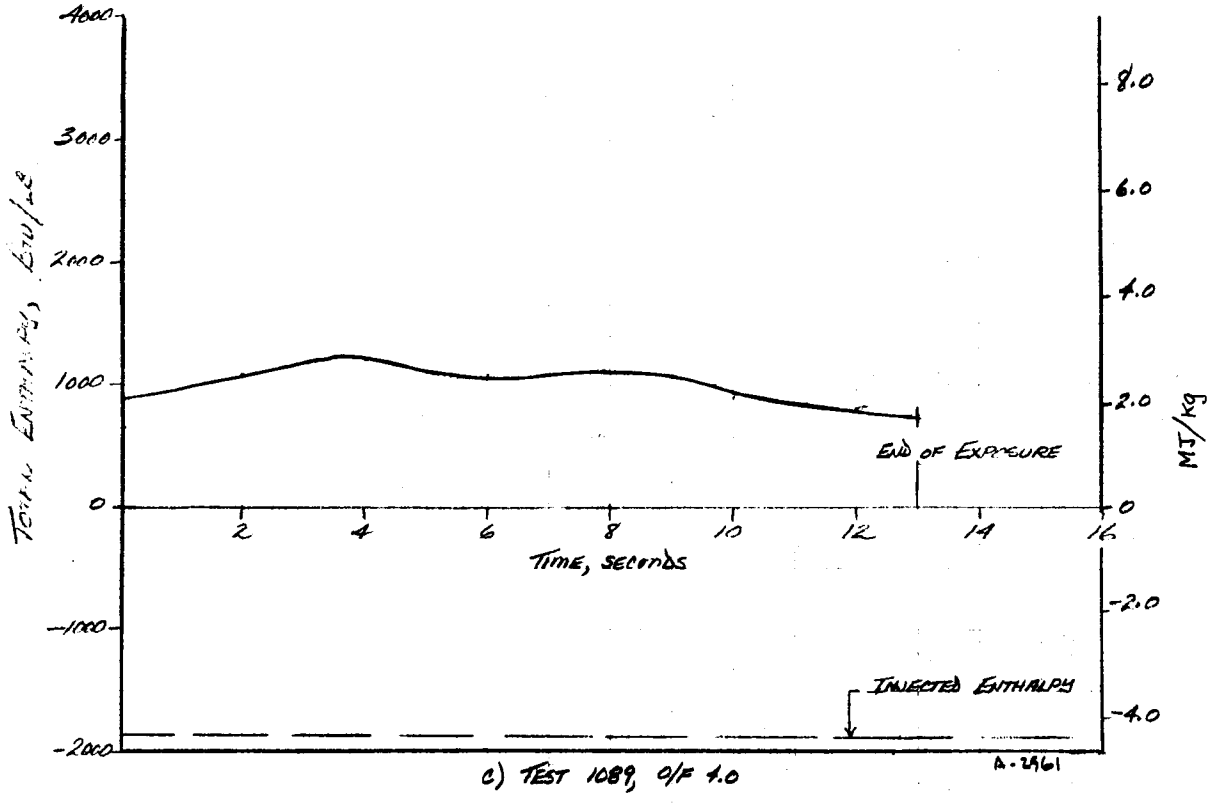
A) TEST 1081, O/F ∞

FIGURE 12 - ENTHALPY HISTORIES OF TRANSIENT CALORIMETER TESTS



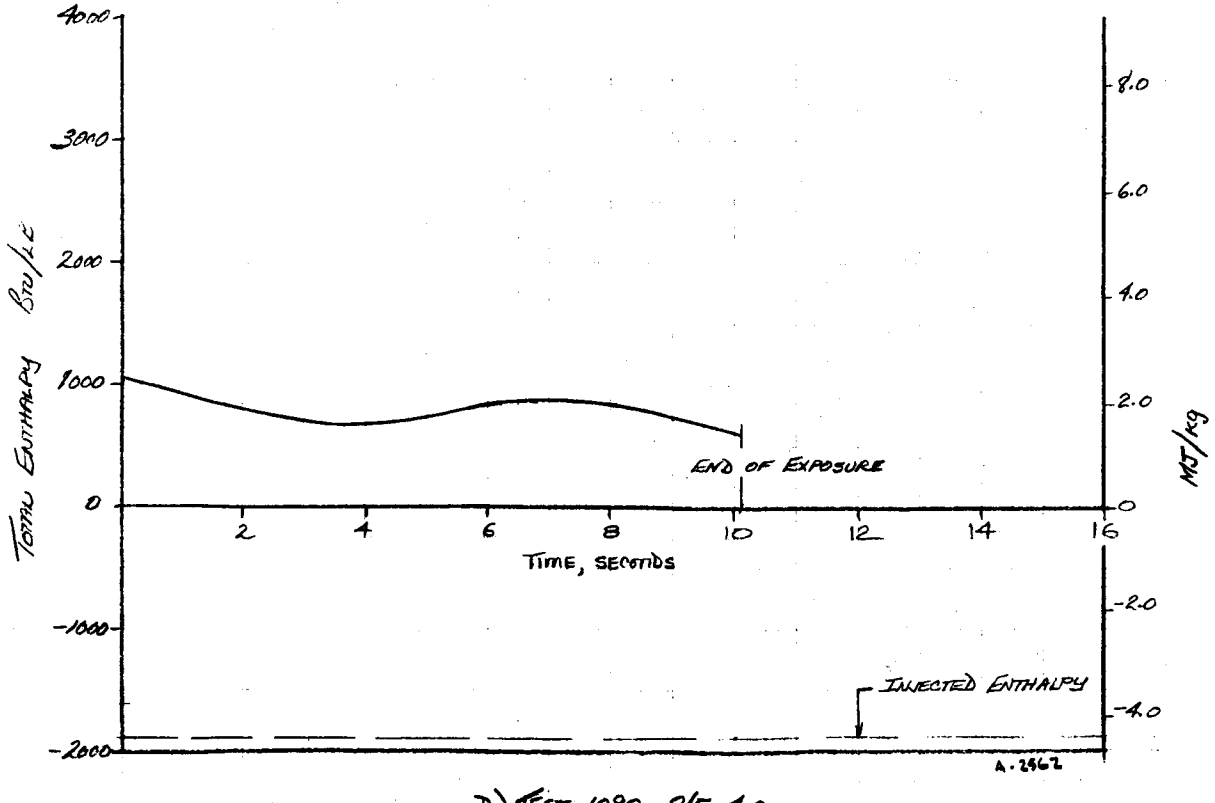
B) TEST 1082, O/F ∞

FIGURE 12, CONTINUED.



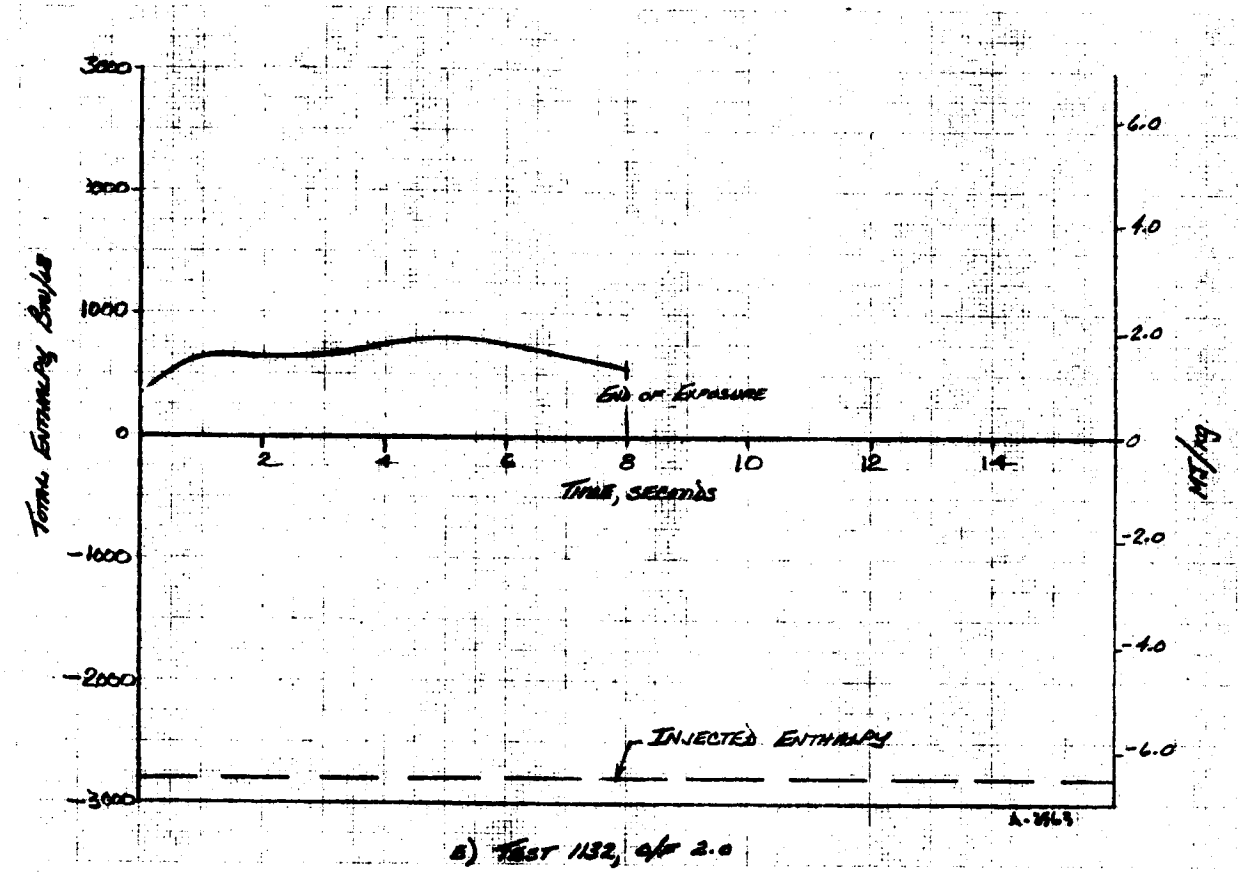
c) TEST 1089, O/F 4.0

FIGURE 12. CONTINUED.



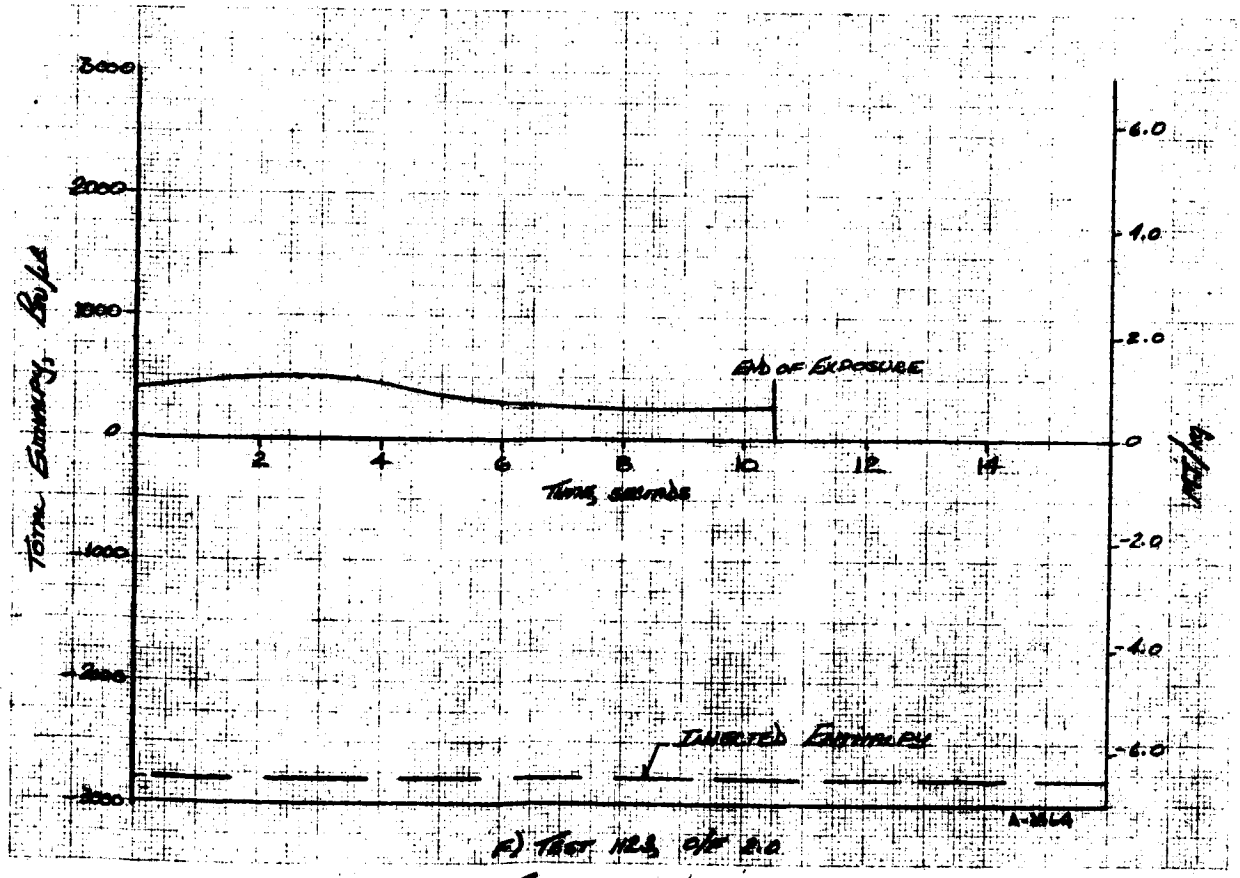
D) TEST 1090, O/F 4.0

FIGURE 12, CONTINUED.



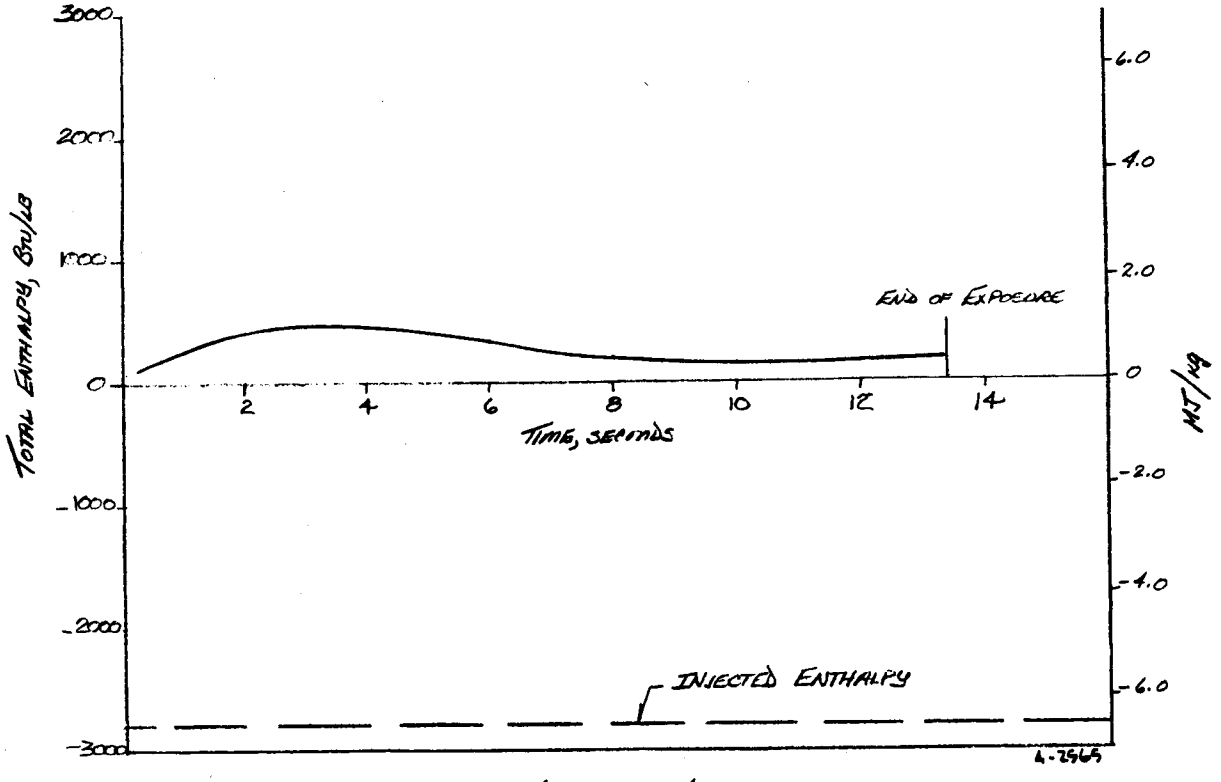
b) Test 1132, ϕ/ϕ' 2.0

FIGURE 12, CONTINUED.



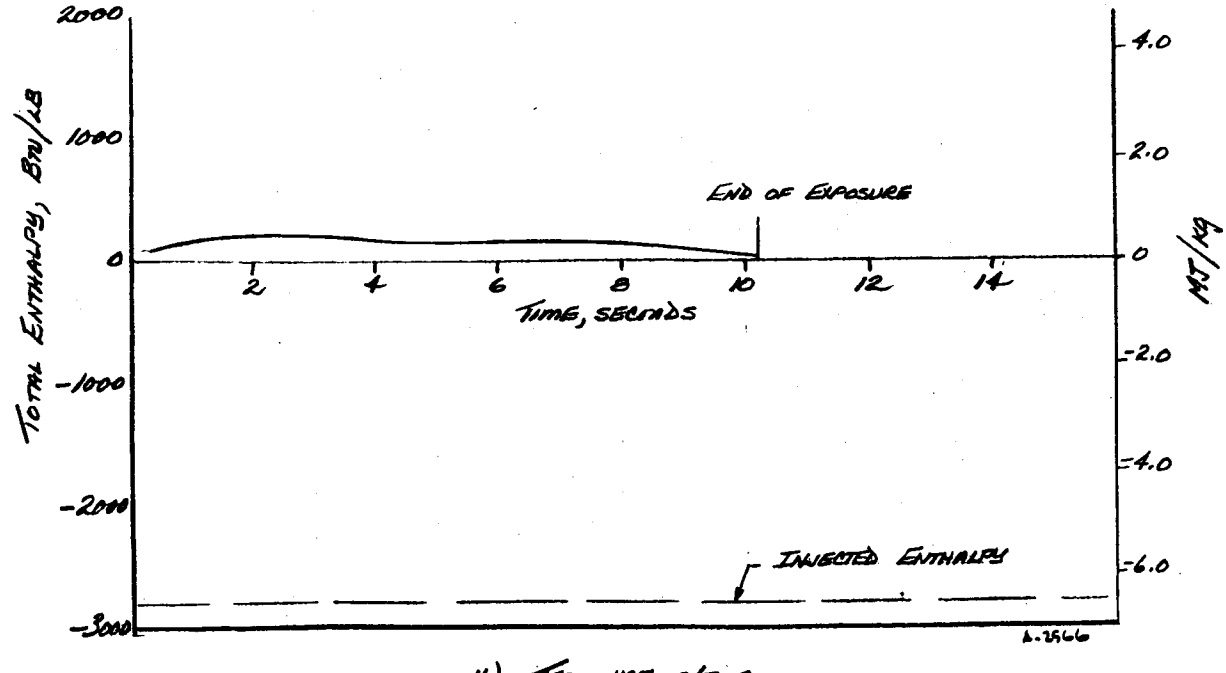
c) Test 1128, ϕ/ϕ' 2.0

FIGURE 12, CONTINUED.



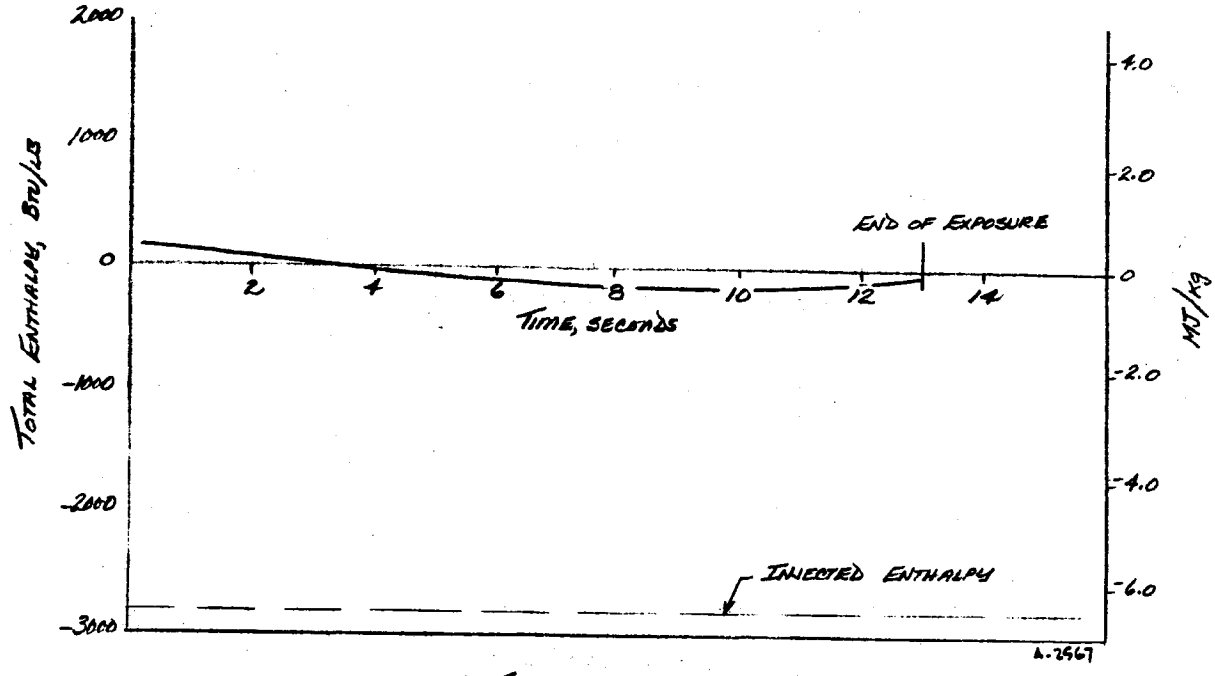
G) TEST 1122, O/F 2.0

FIGURE 12, CONTINUED.



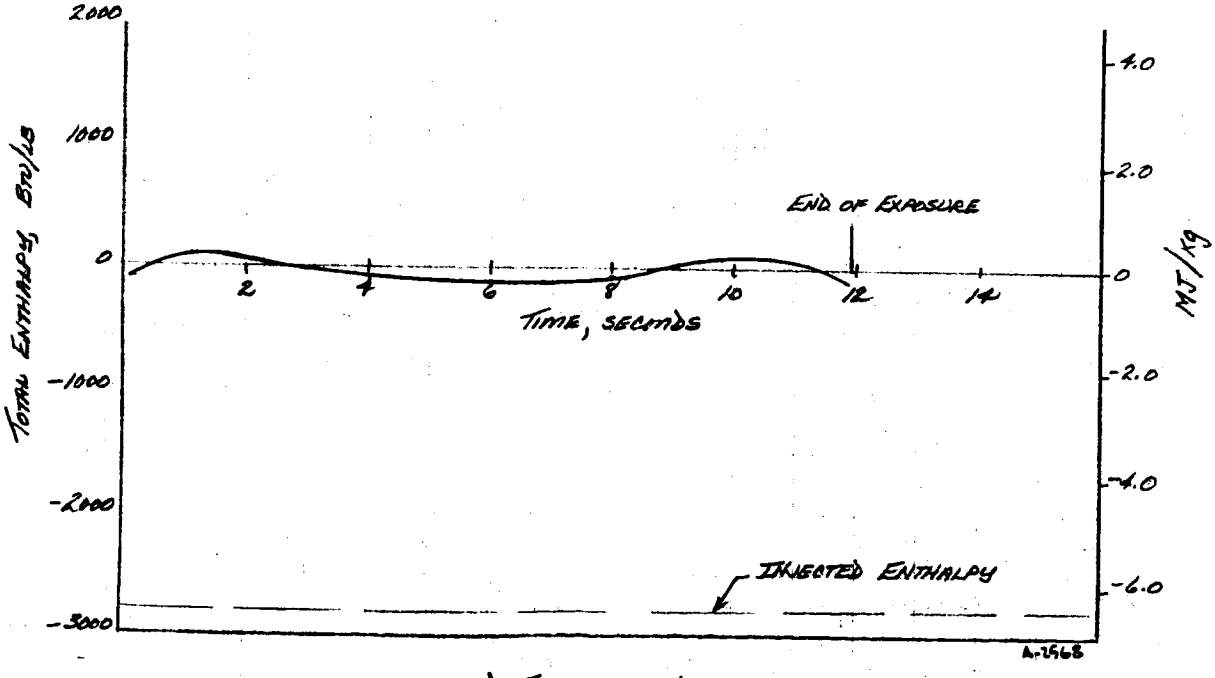
H) TEST 1127, O/F 2.0

FIGURE 12, CONTINUED.



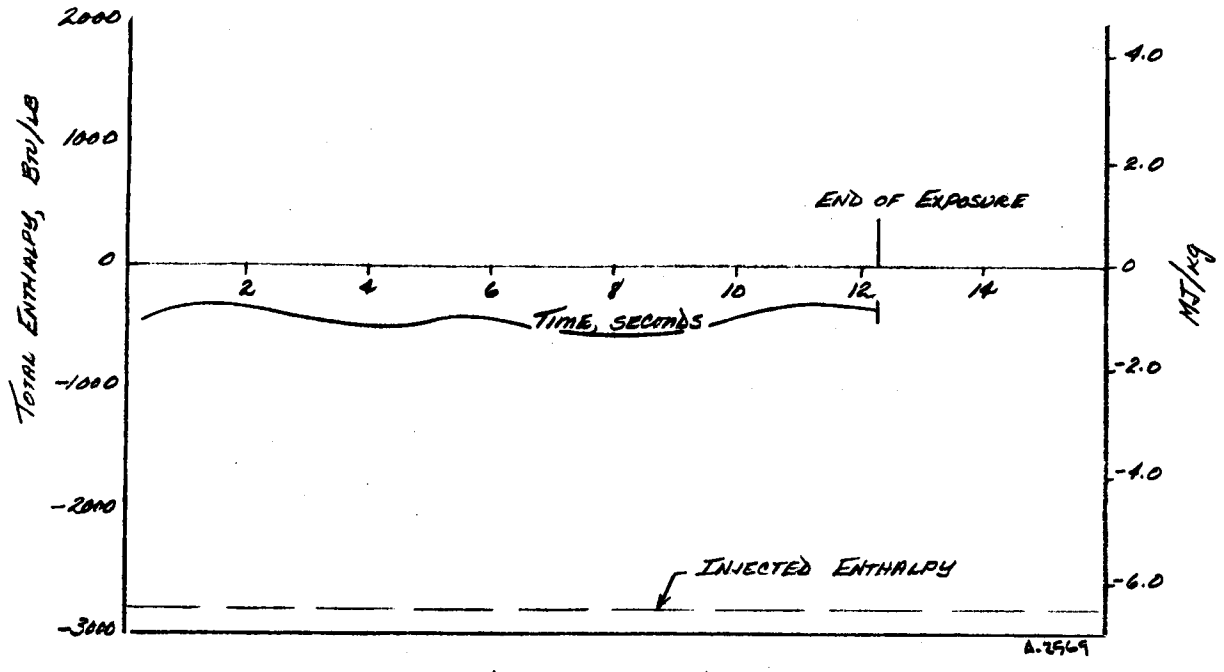
I) TEST 1113, O/F 2.0

FIGURE 12, CONTINUED.



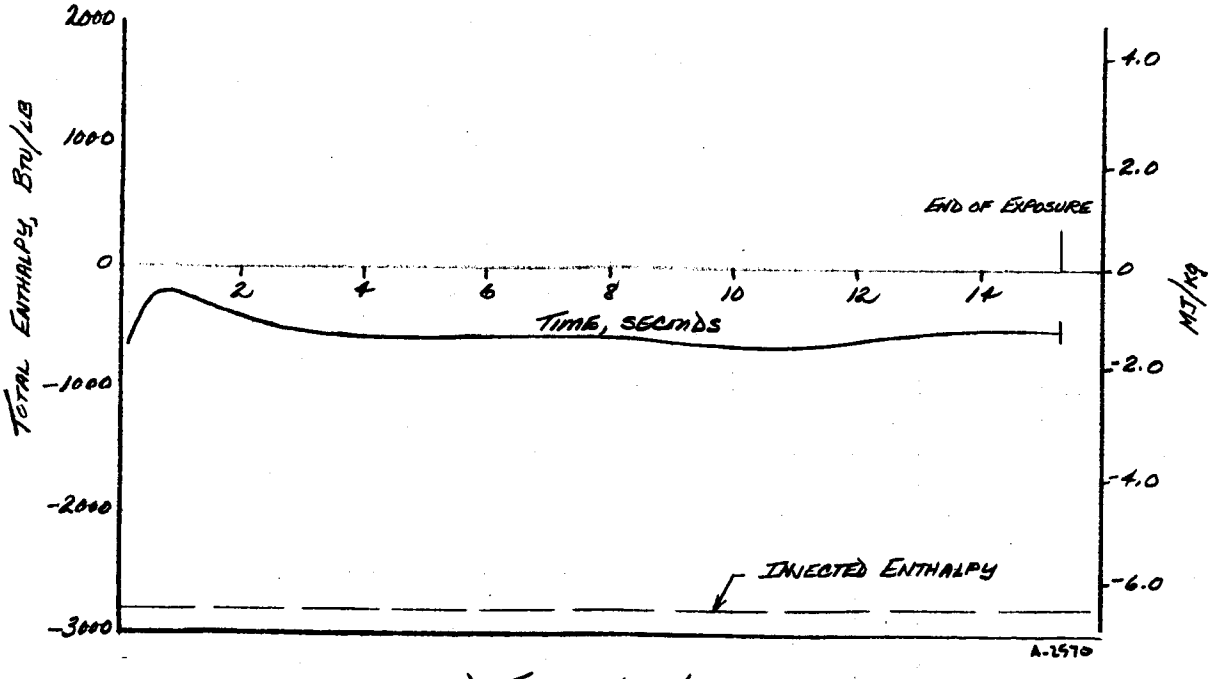
J) TEST 1126, O/F 2.0

FIGURE 12, CONTINUED.



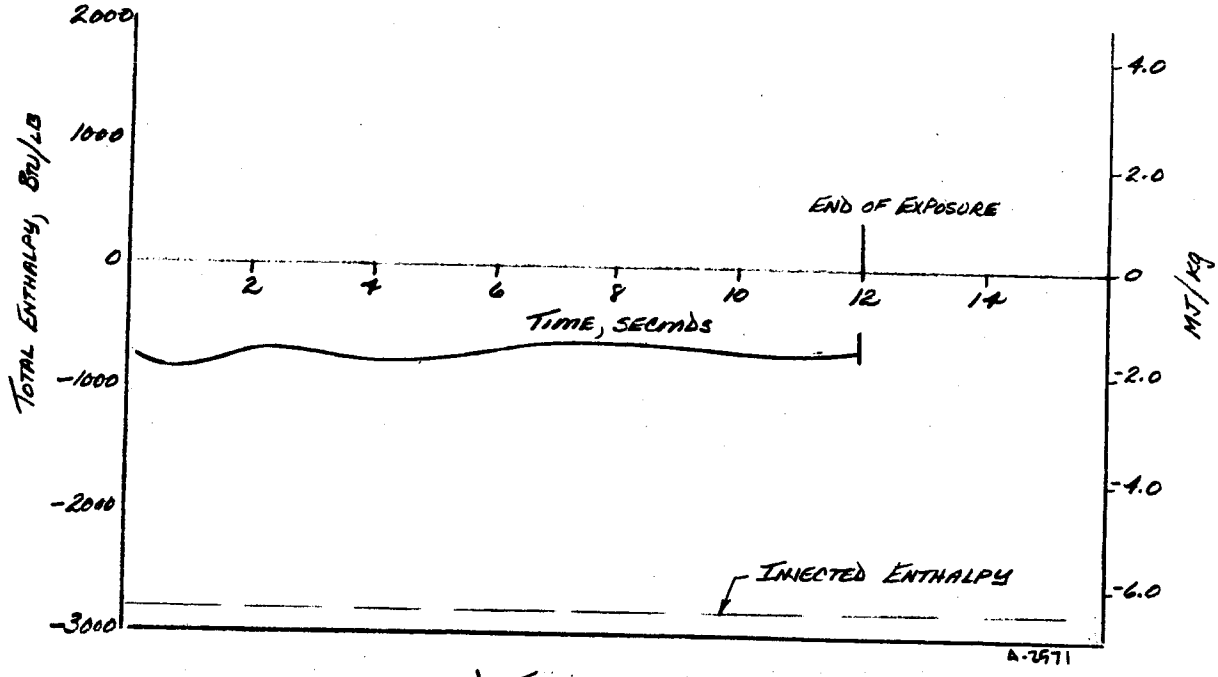
K) TEST 1115, O/F 2.0

FIGURE 12, CONTINUED.



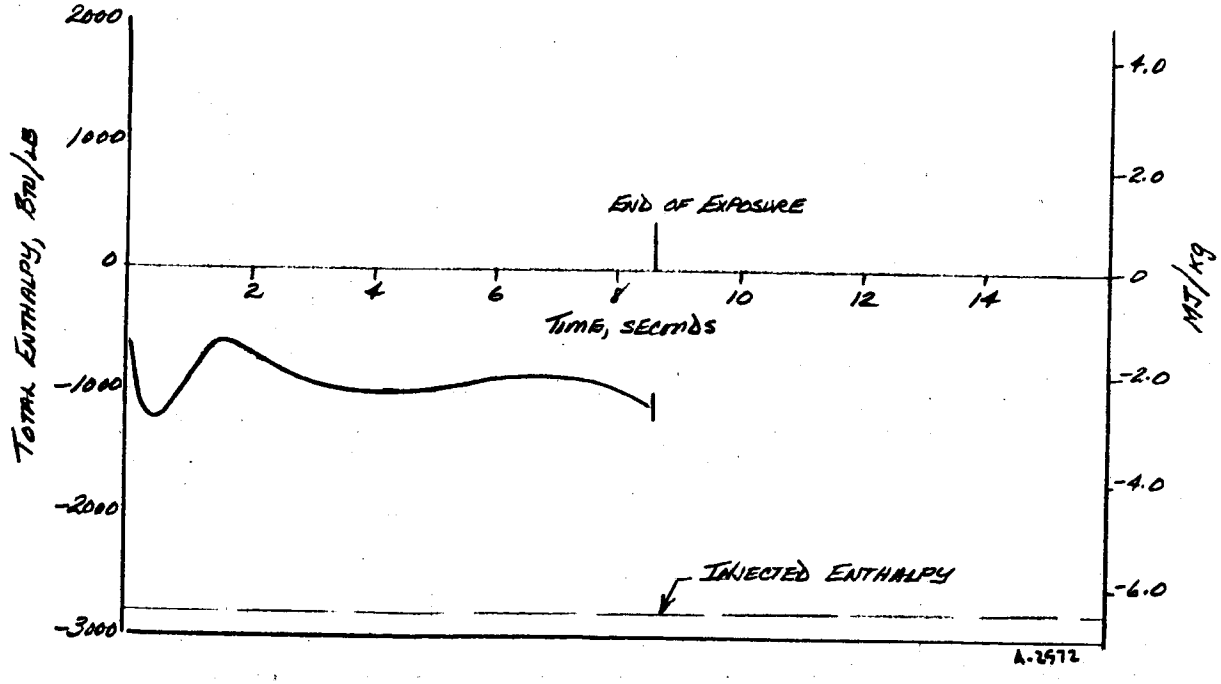
L) TEST 1114, O/F 2.0

FIGURE 12, CONTINUED



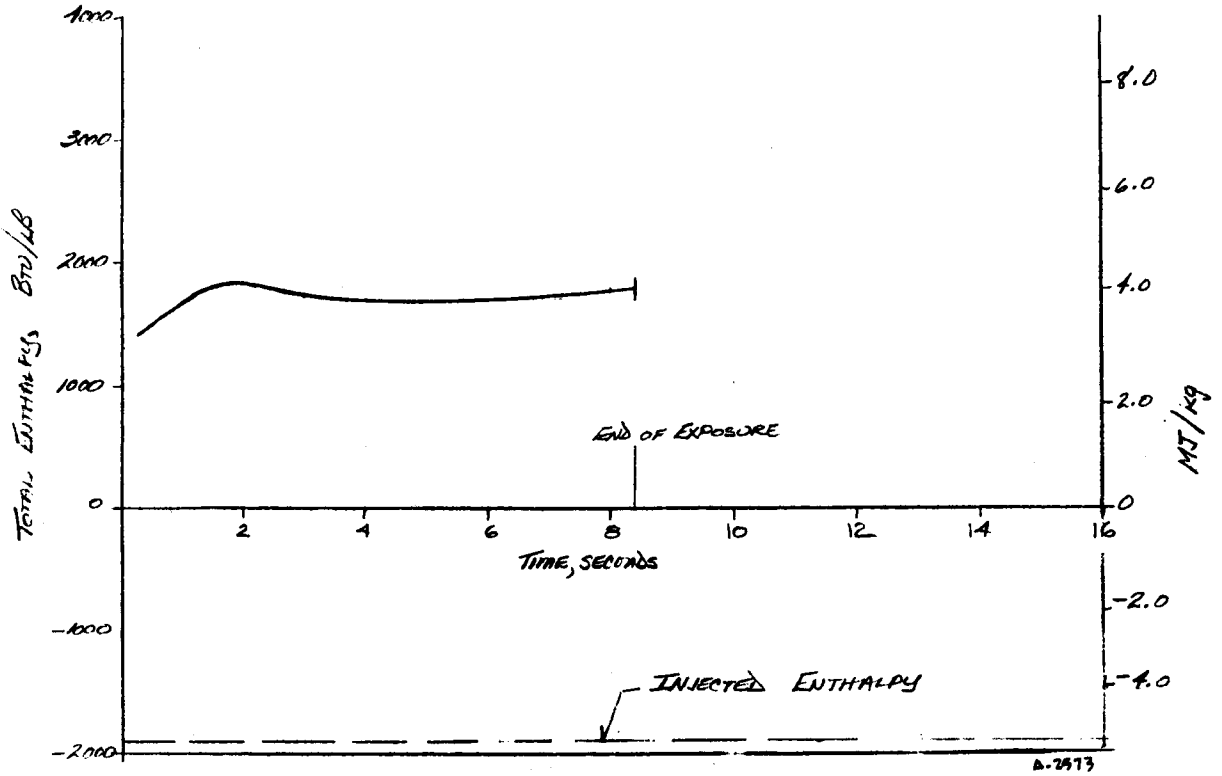
M) TEST 1119, O/F 2.0

FIGURE 12, CONTINUED



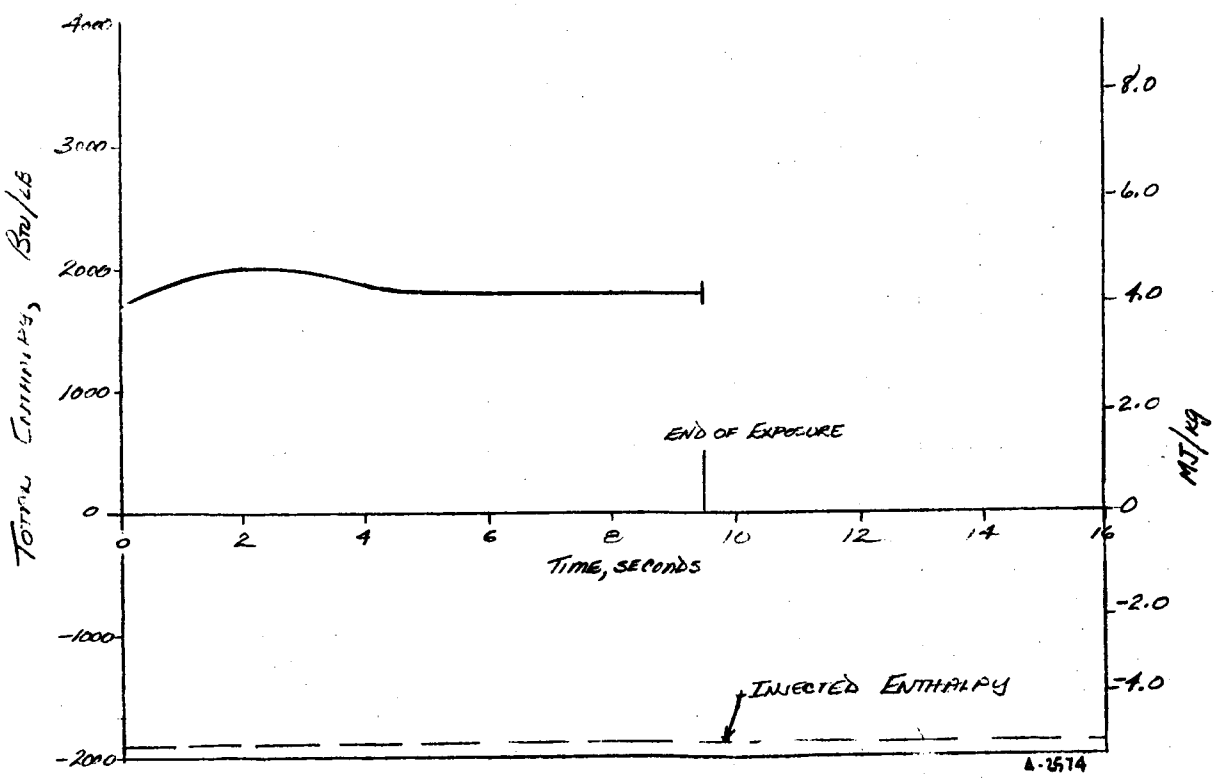
N) TEST 1118, O/F 2.0

FIGURE 12, CONTINUED



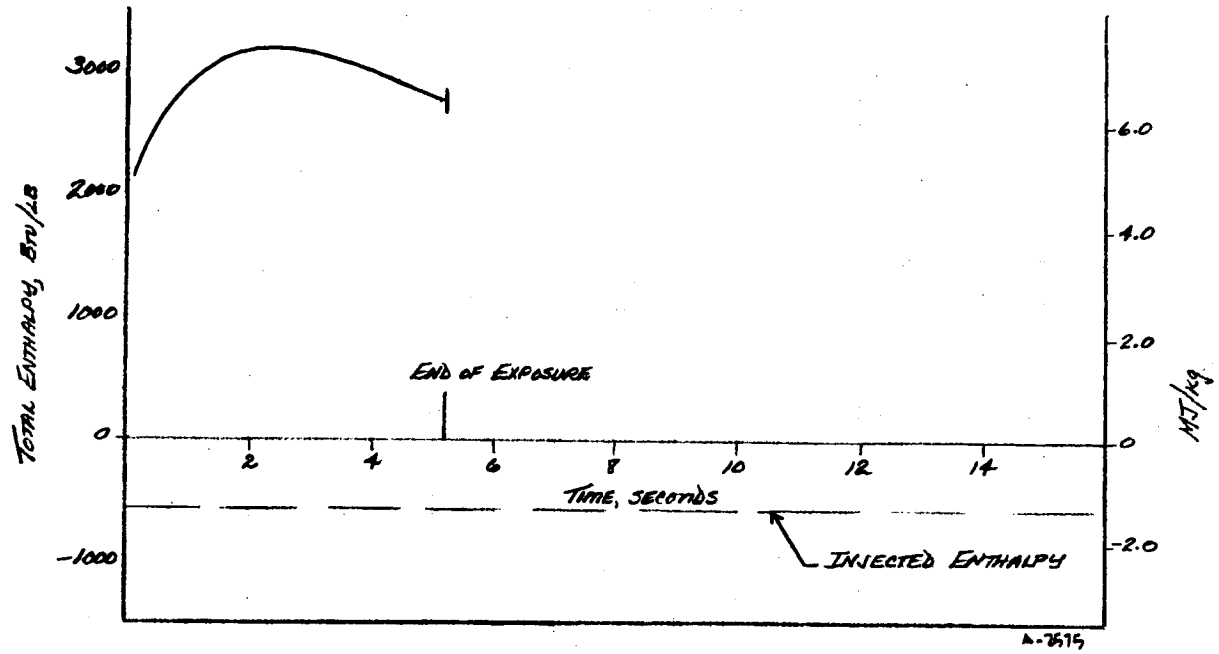
o) TEST 1096, O/F 1.0

FIGURE 12, CONTINUED



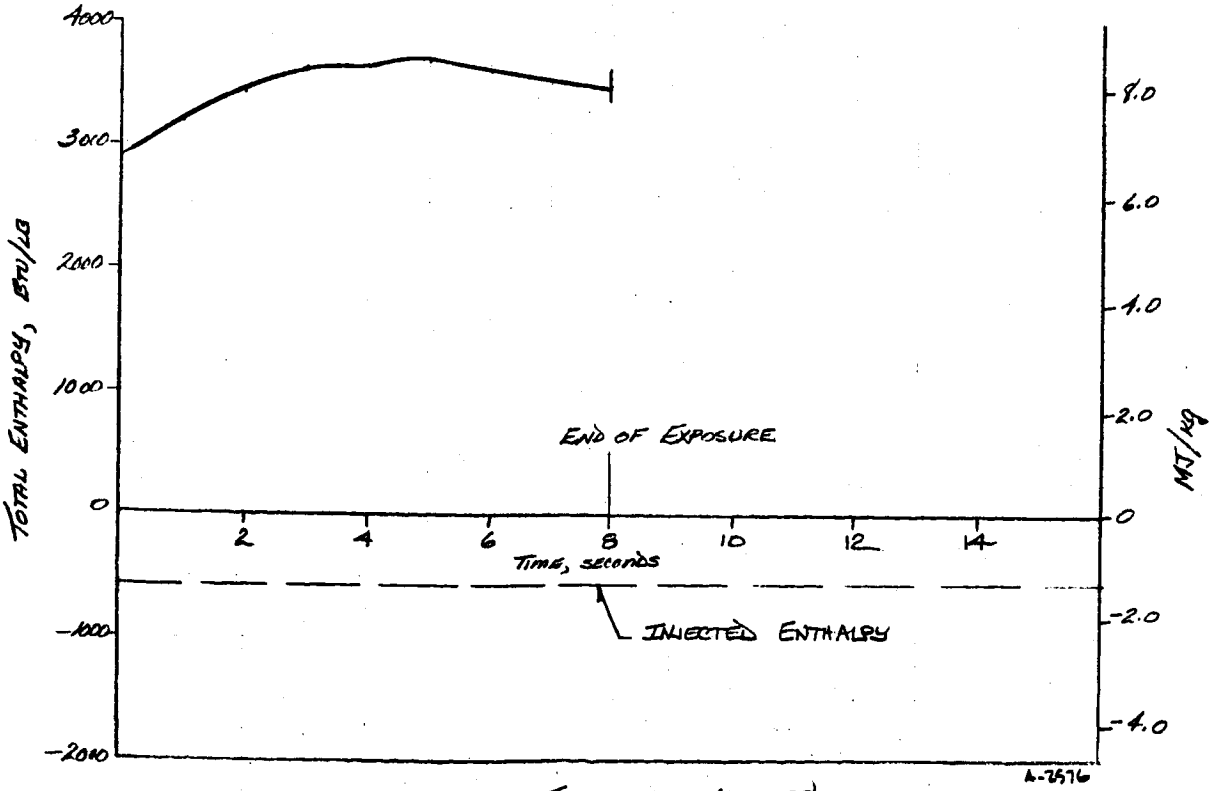
p) TEST 1097, O/F 1.0

FIGURE 12, CONTINUED.



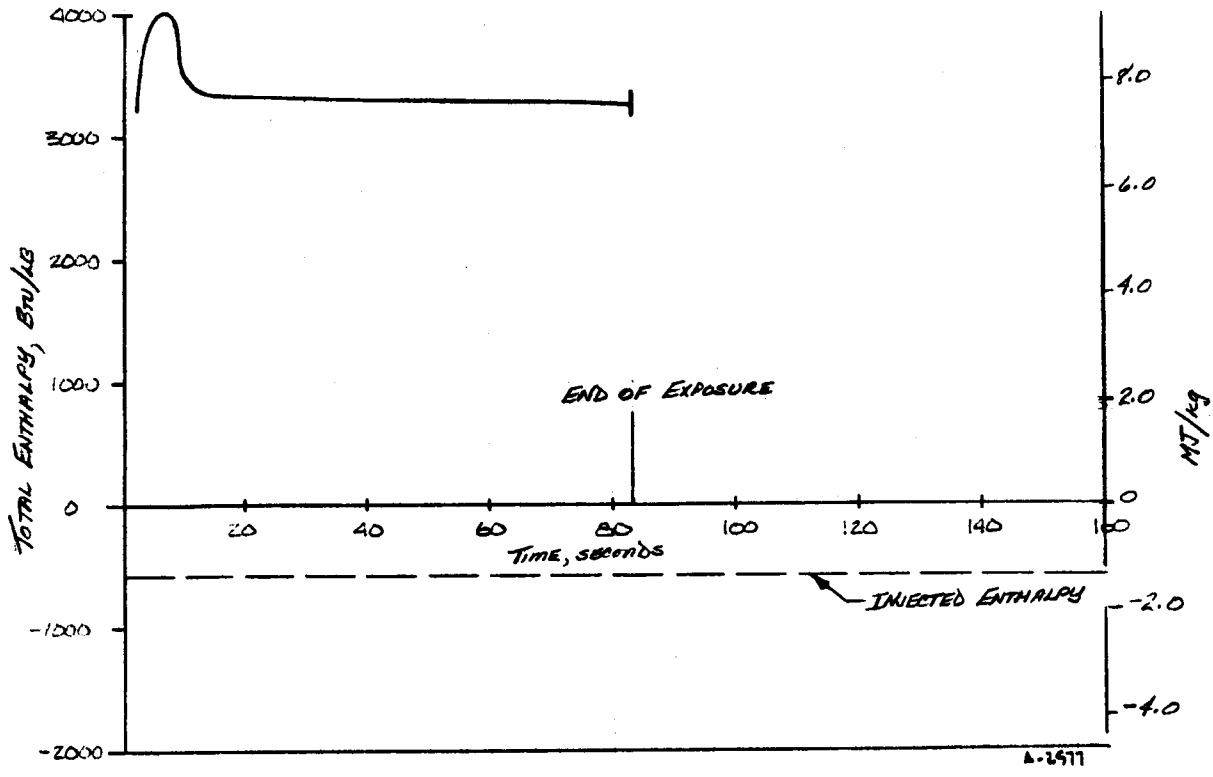
Q) TEST 1143, O/F 0.38

FIGURE 12, CONTINUED



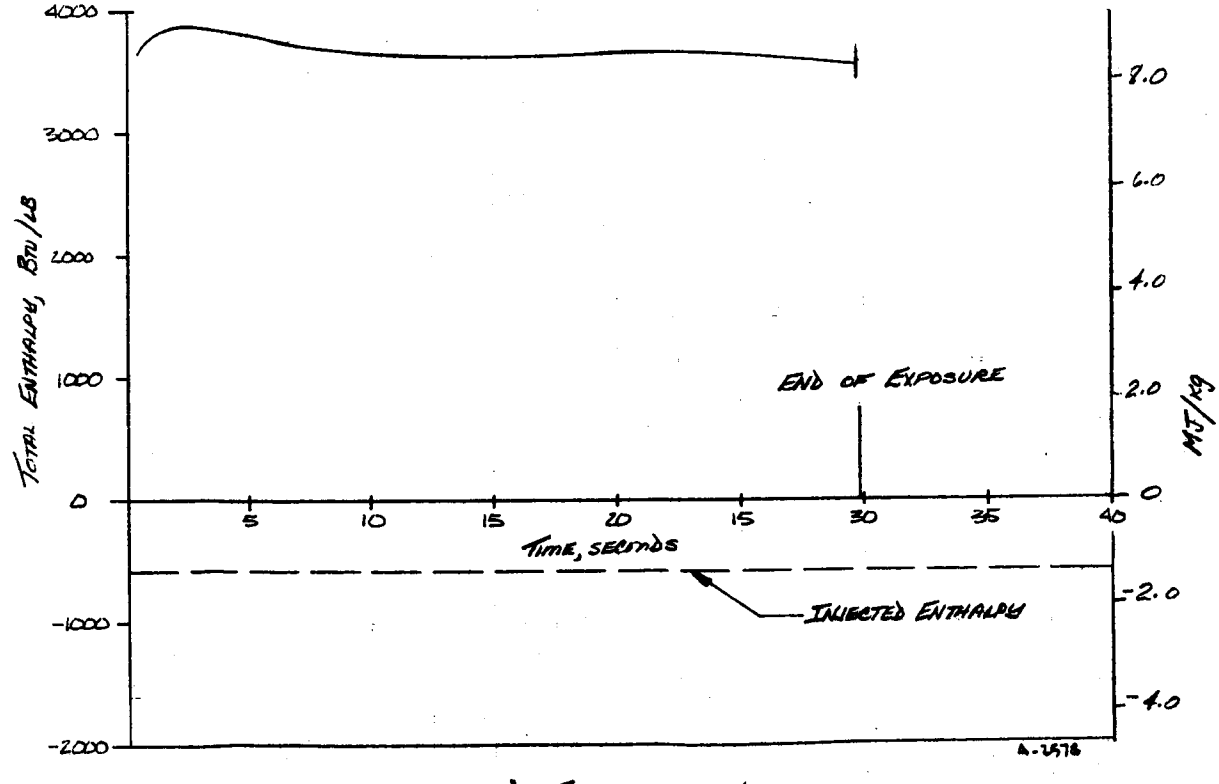
R) TEST 1144, O/F 0.38

FIGURE 12, CONTINUED.



s) TEST 1353, O/F 0.38

FIGURE 12, CONTINUED



t) TEST 1354, O/F 0.38

FIGURE 12, CONCLUDED

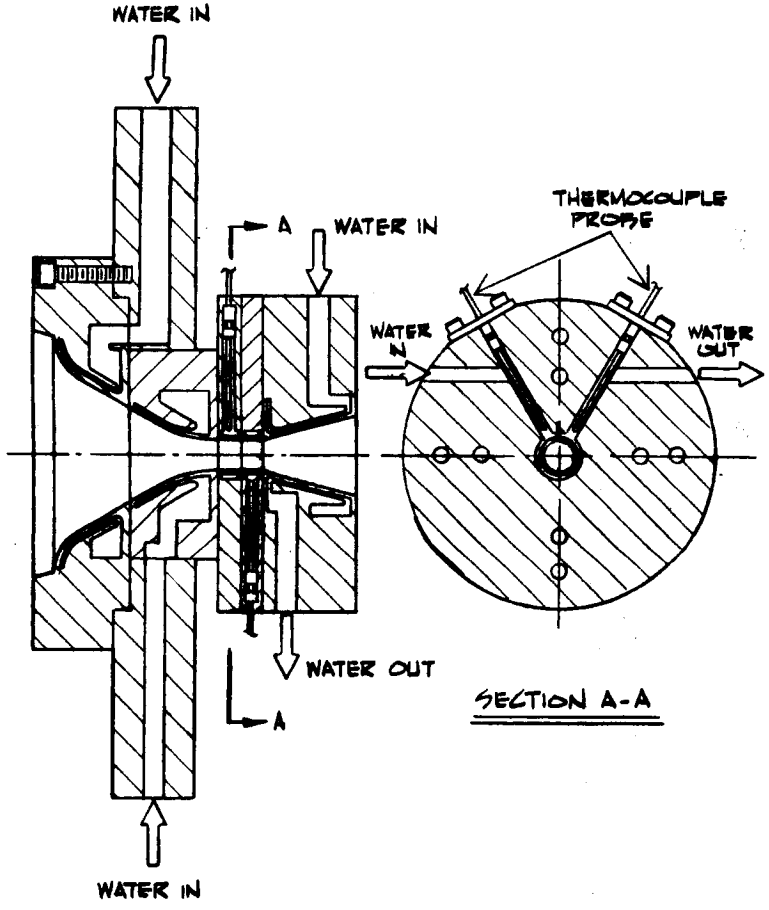


FIGURE 13 SCHEMATIC DRAWING OF TYPICAL HEAT-TRANSFER CALIBRATION NOZZLE

A-2579

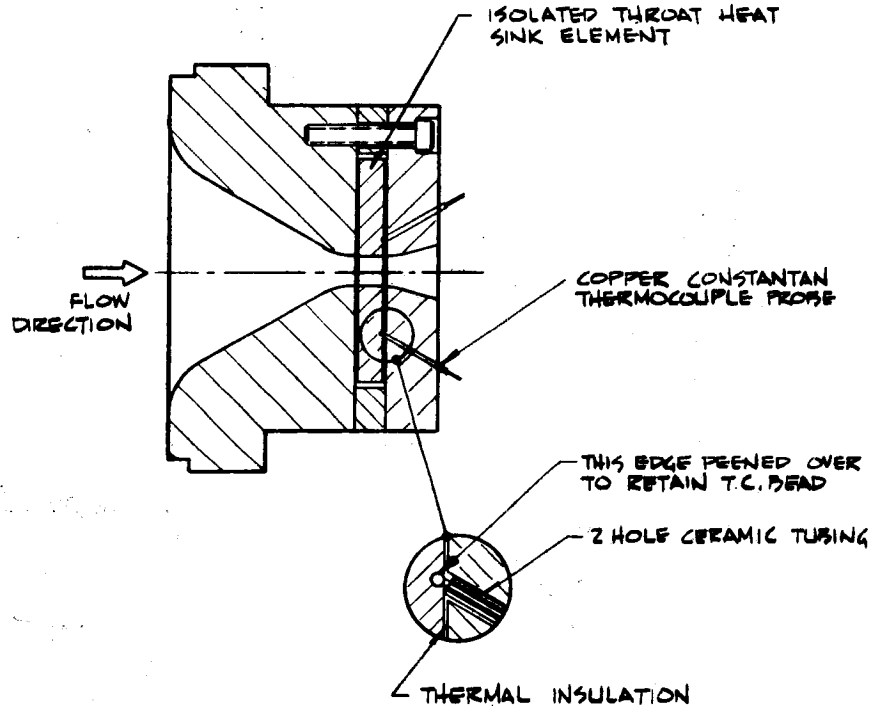


FIGURE 14 SECTION REPRESENTATION OF THE COPPER TRANSIENT CALORIMETER NOZZLE

A-2580

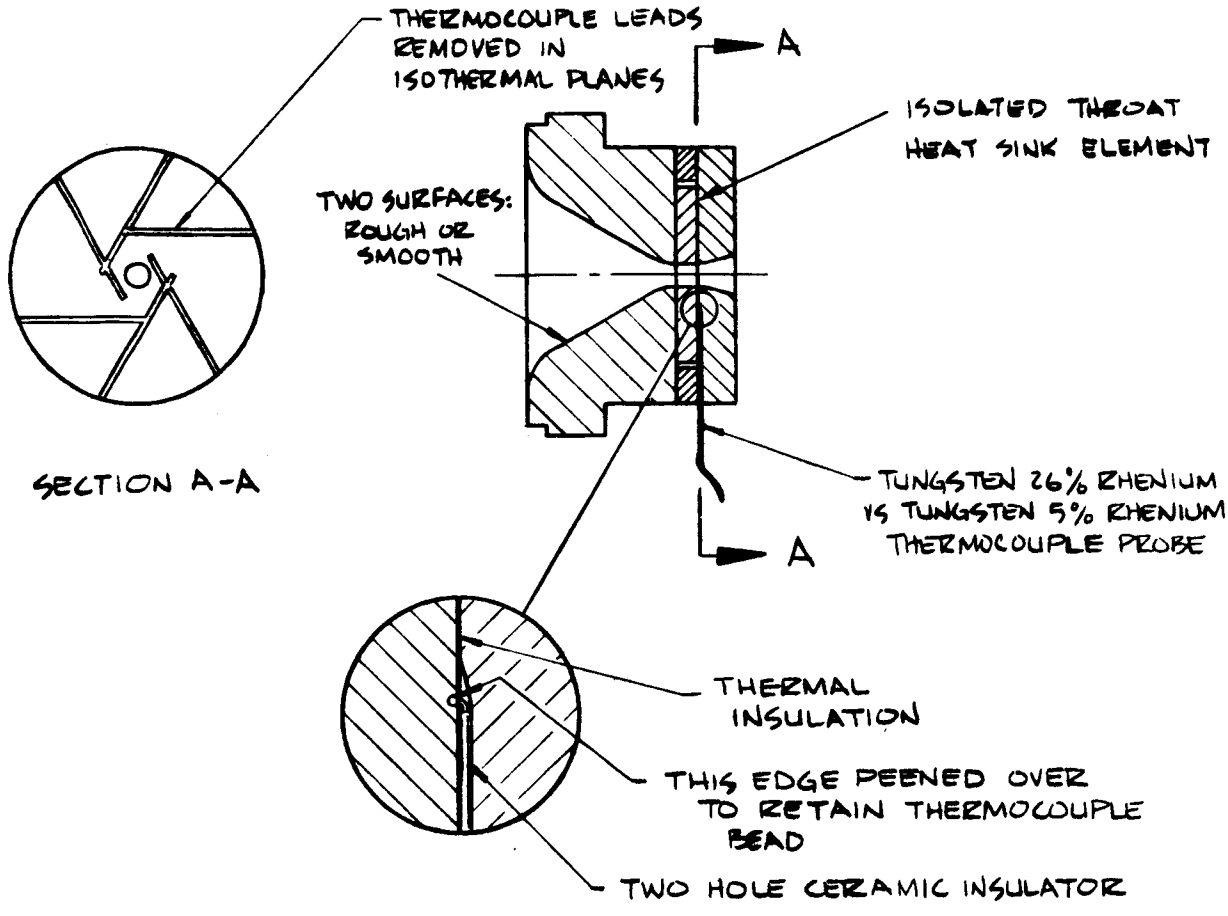
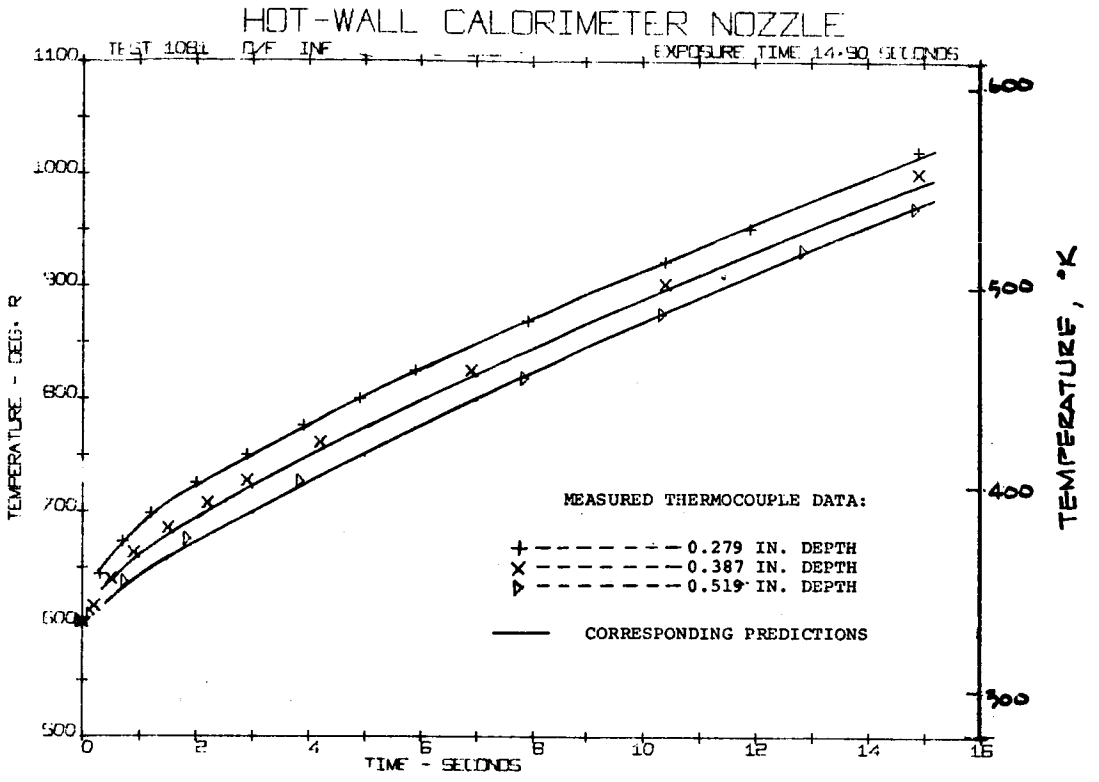


FIGURE 15 SECTION REPRESENTATION OF THE MOLYBDENUM TRANSIENT CALORIMETER NOZZLE

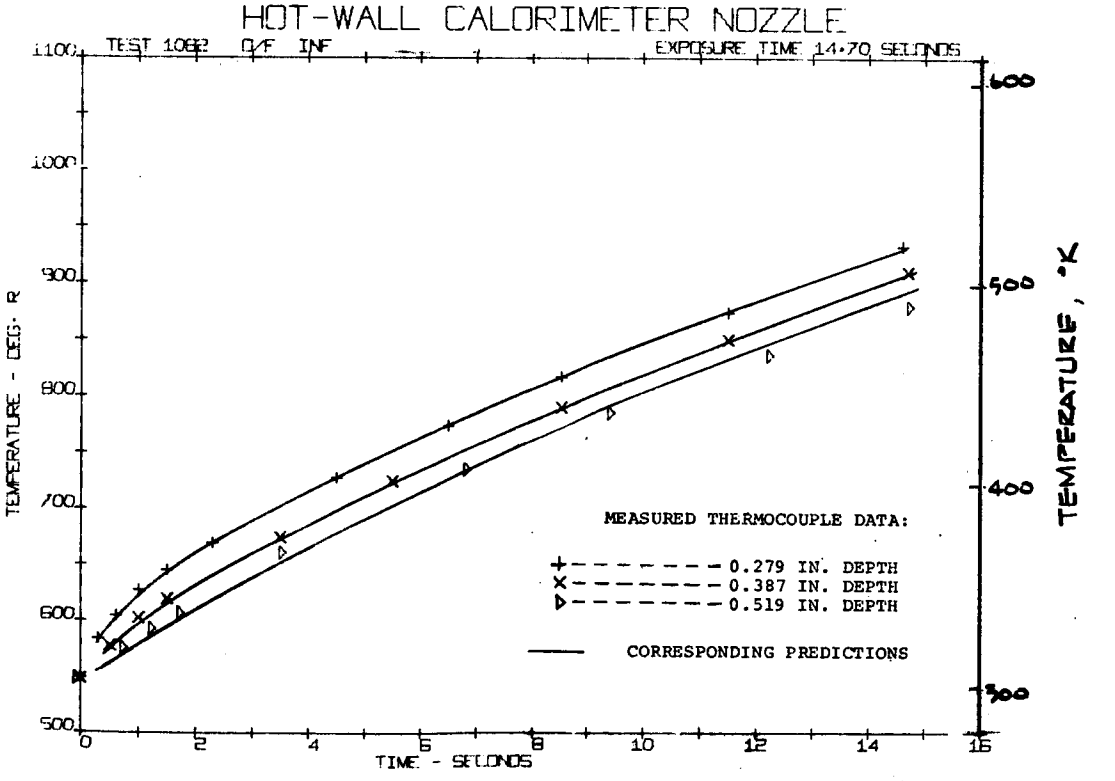
A-2581



A) TEST 1081, O/F = ∞

FIGURE 16, MEASURED AND PREDICTED THERMAL RESPONSES OF THE TRANSIENT CALORIMETER

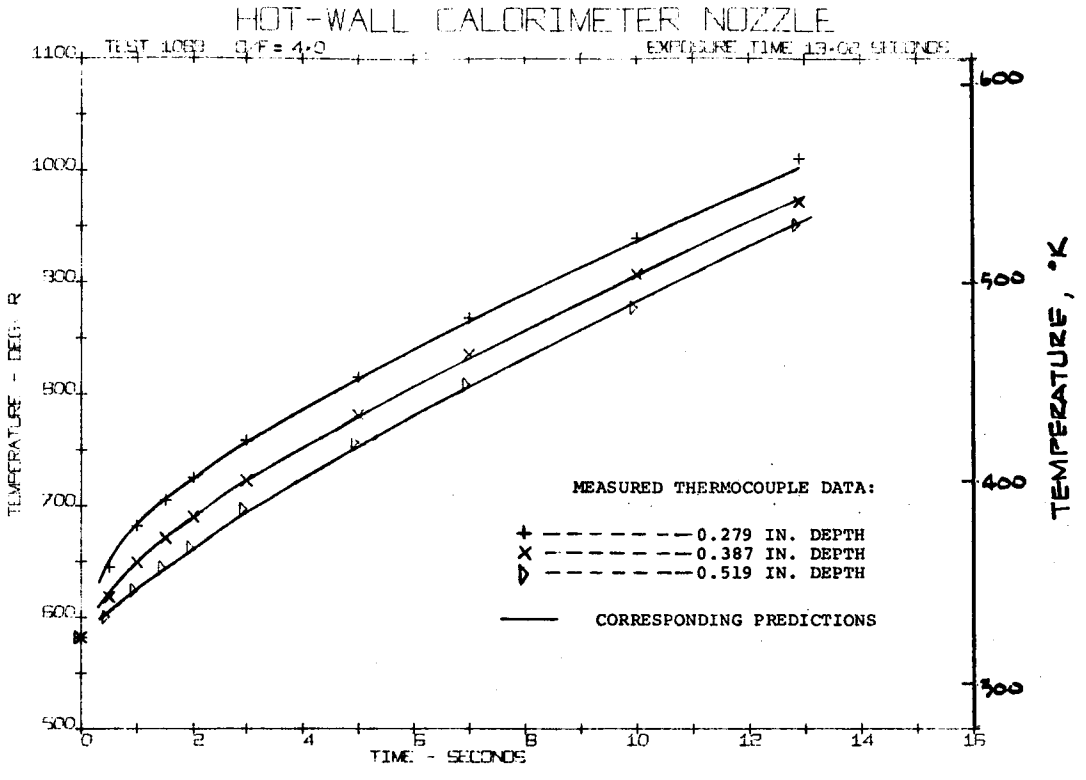
A-2582



B) TEST 1082, O/F = ∞

FIGURE 16, CONTINUED

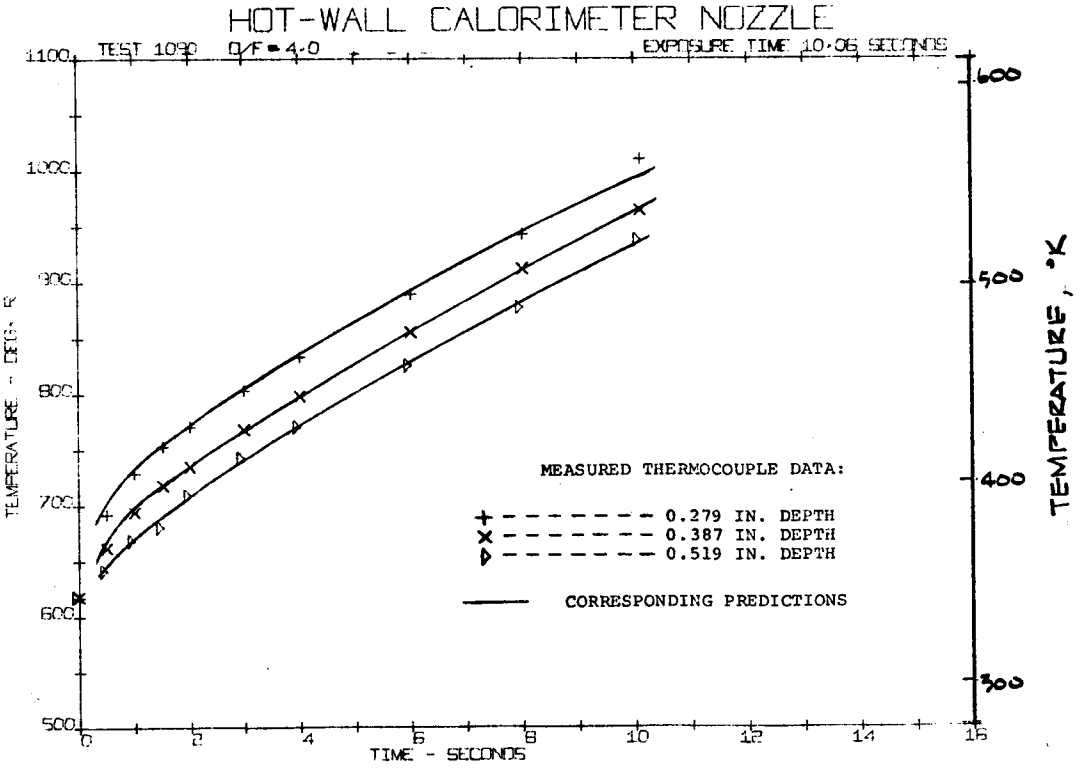
A-2584



C) TEST 1089, O/F = 4.0

FIGURE 16, CONTINUED

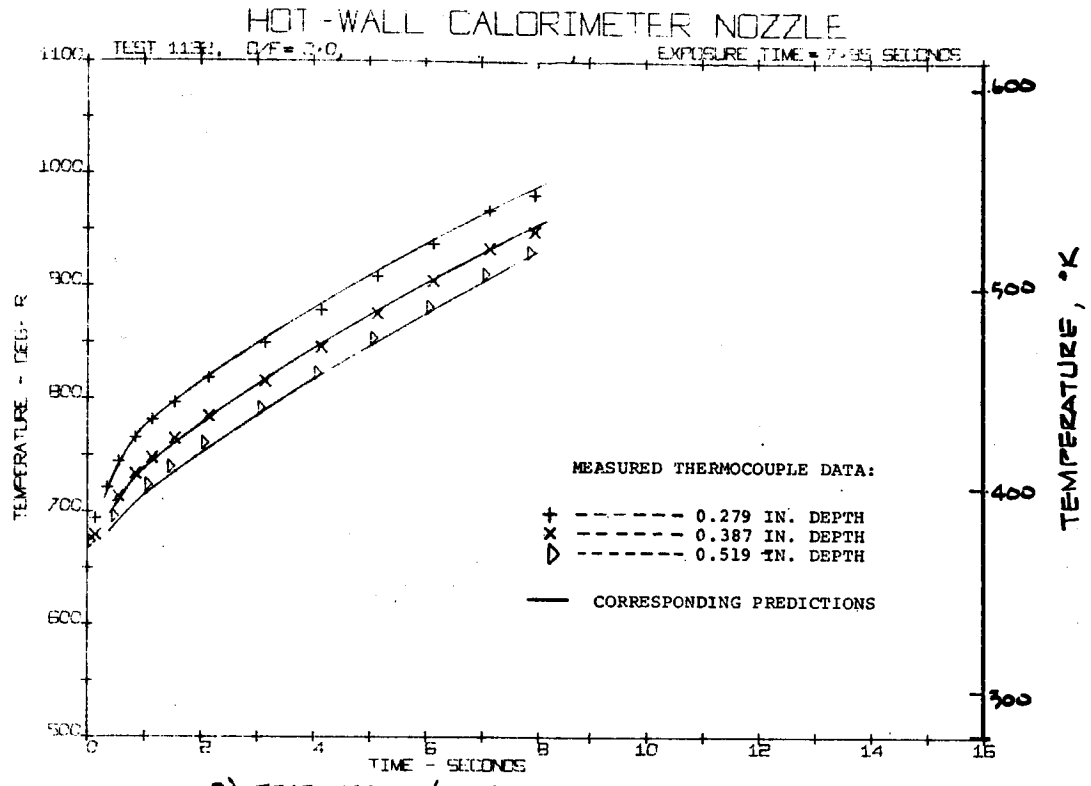
A-1584



D) TEST 1090, O/F = 4.0

FIGURE 16, CONTINUED

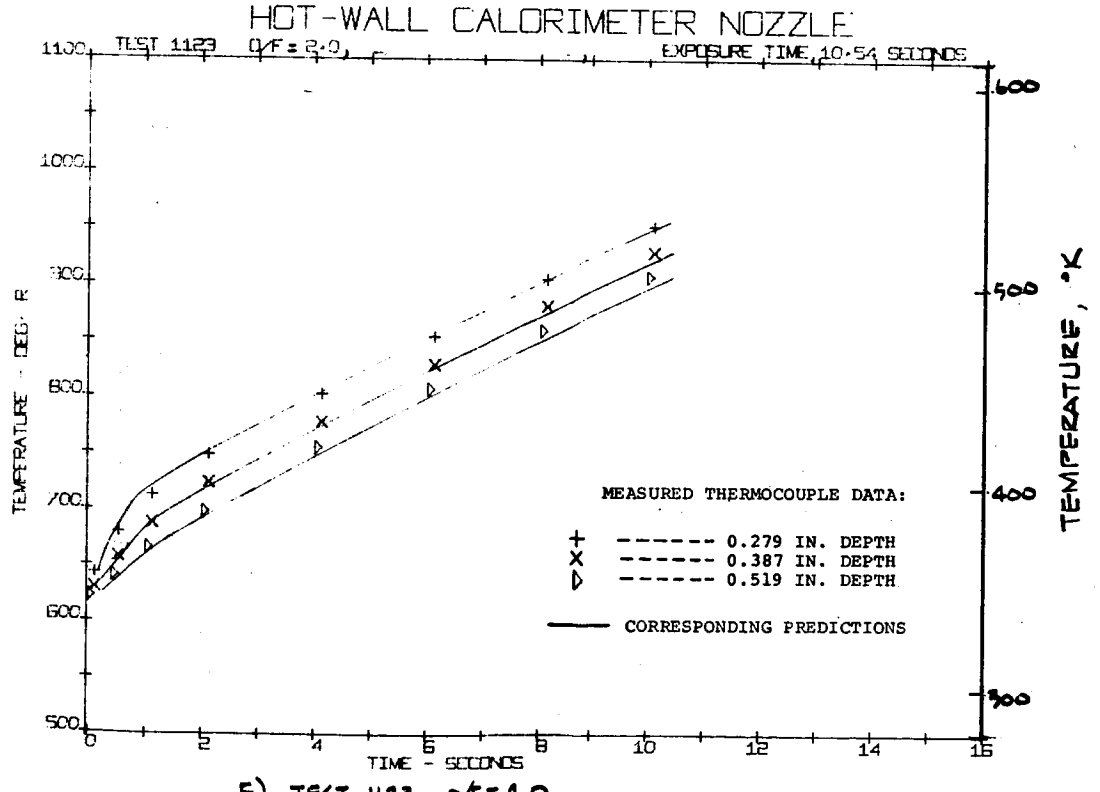
A-1585



E) TEST 1132, O/F = 2.0

FIGURE 16, CONTINUED

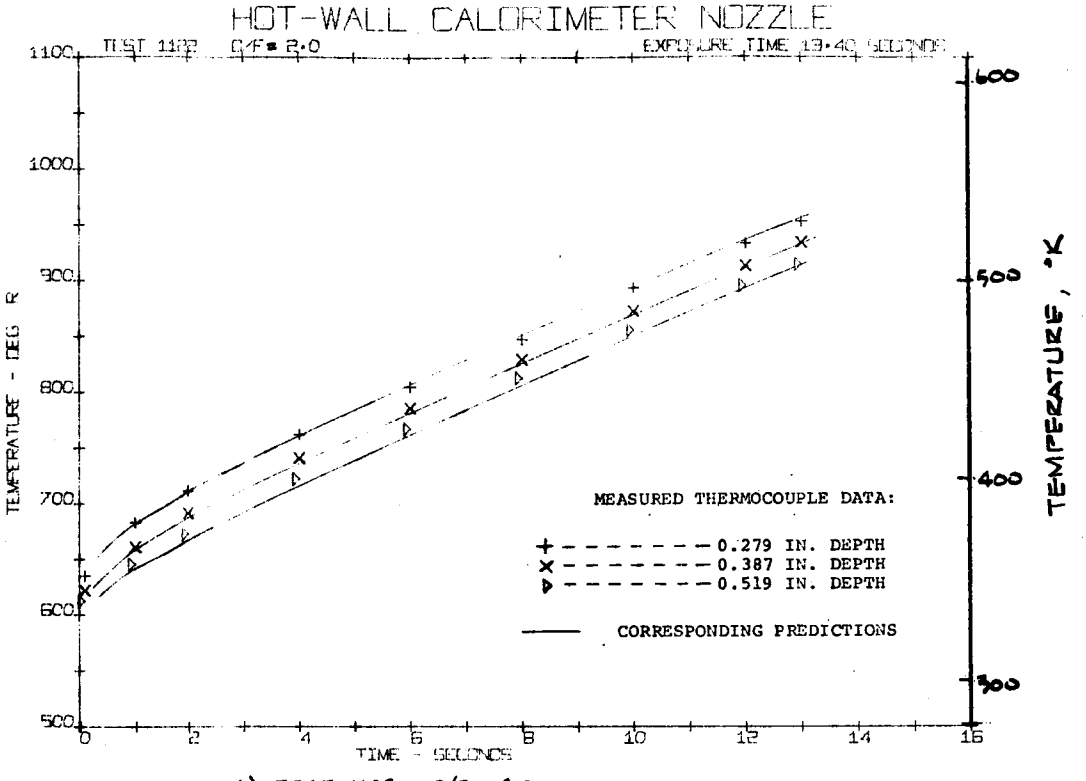
A-1586



F) TEST 1123, O/F = 2.0,

FIGURE 16, CONTINUED

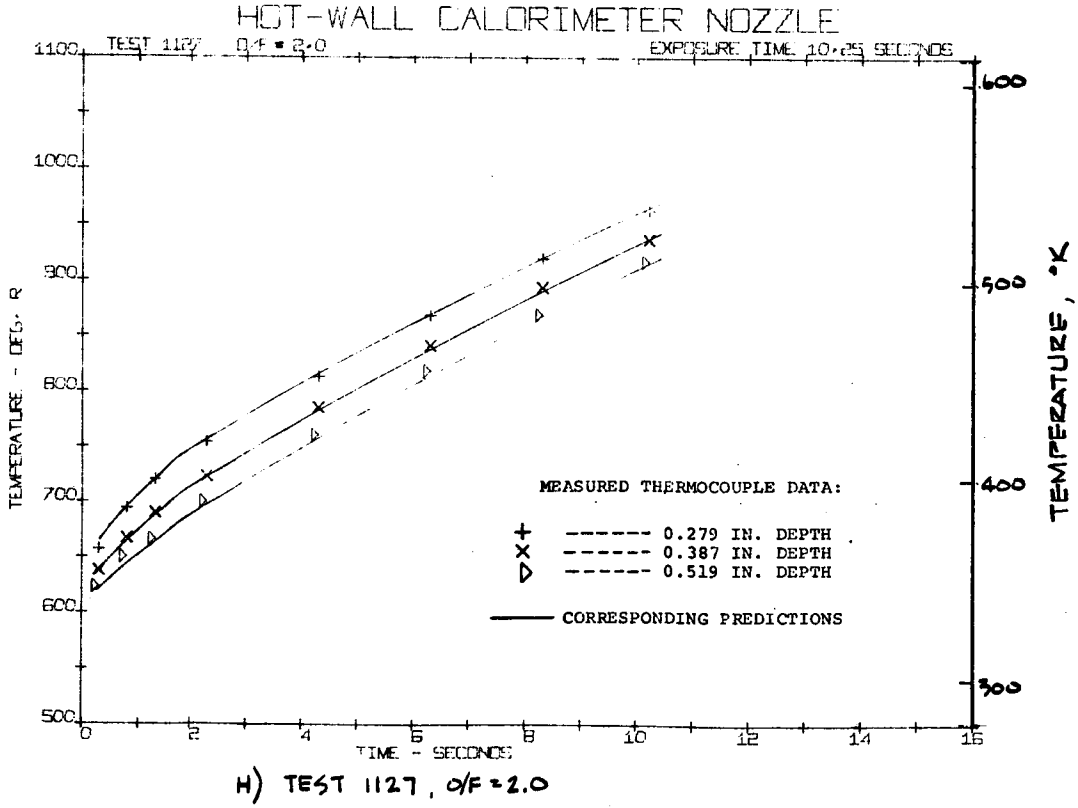
A-1587



G) TEST 1122, O/F = 2.0

FIGURE 16, CONTINUED

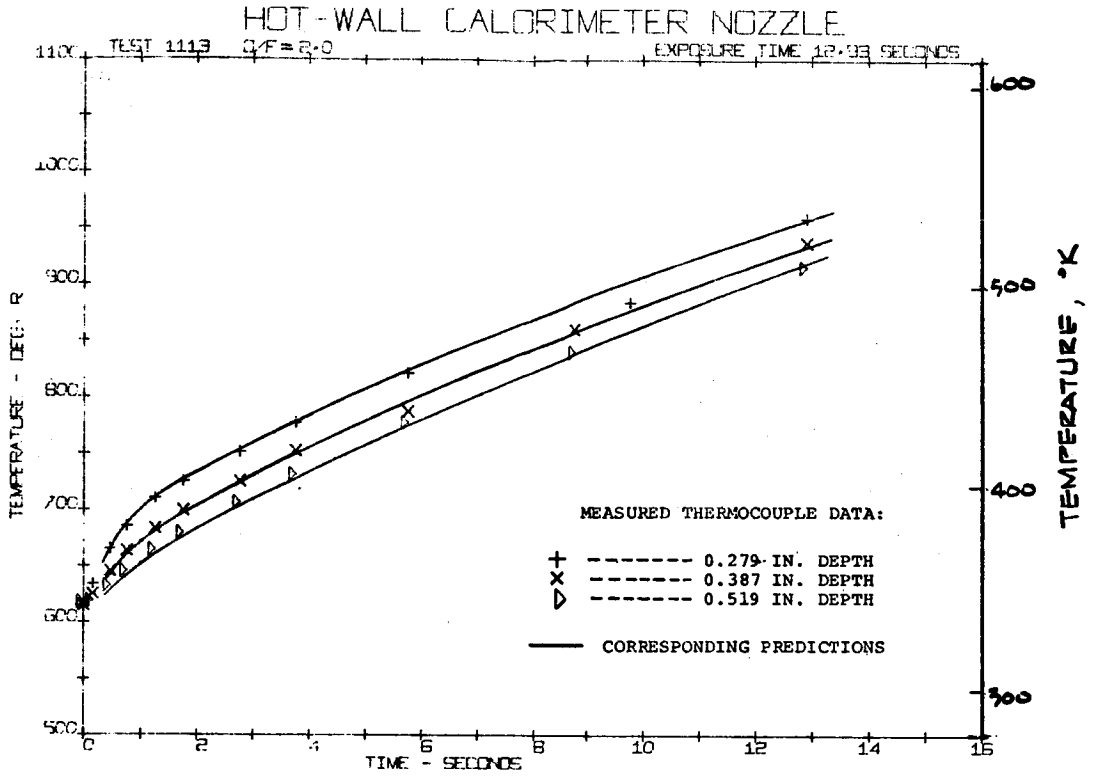
A-2588



H) TEST 1127, O/F = 2.0

FIGURE 16, CONTINUED

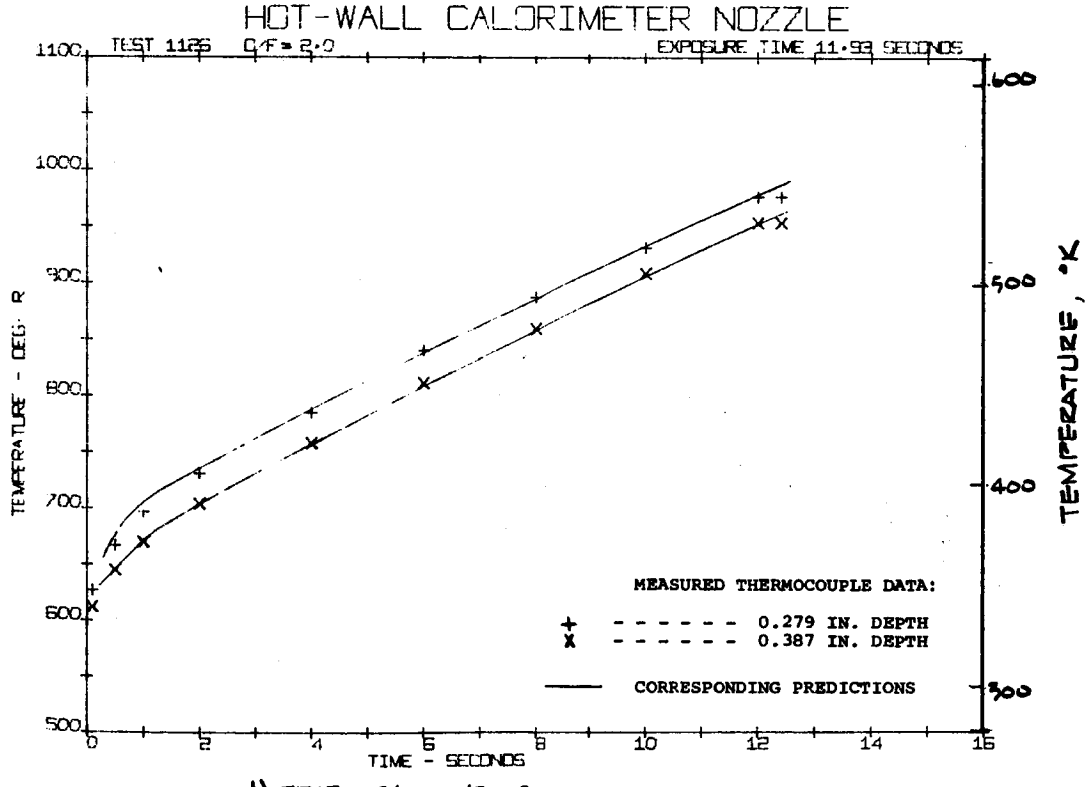
A-2589



I) TEST 1113, O/F = 2.0

FIGURE 16, CONTINUED

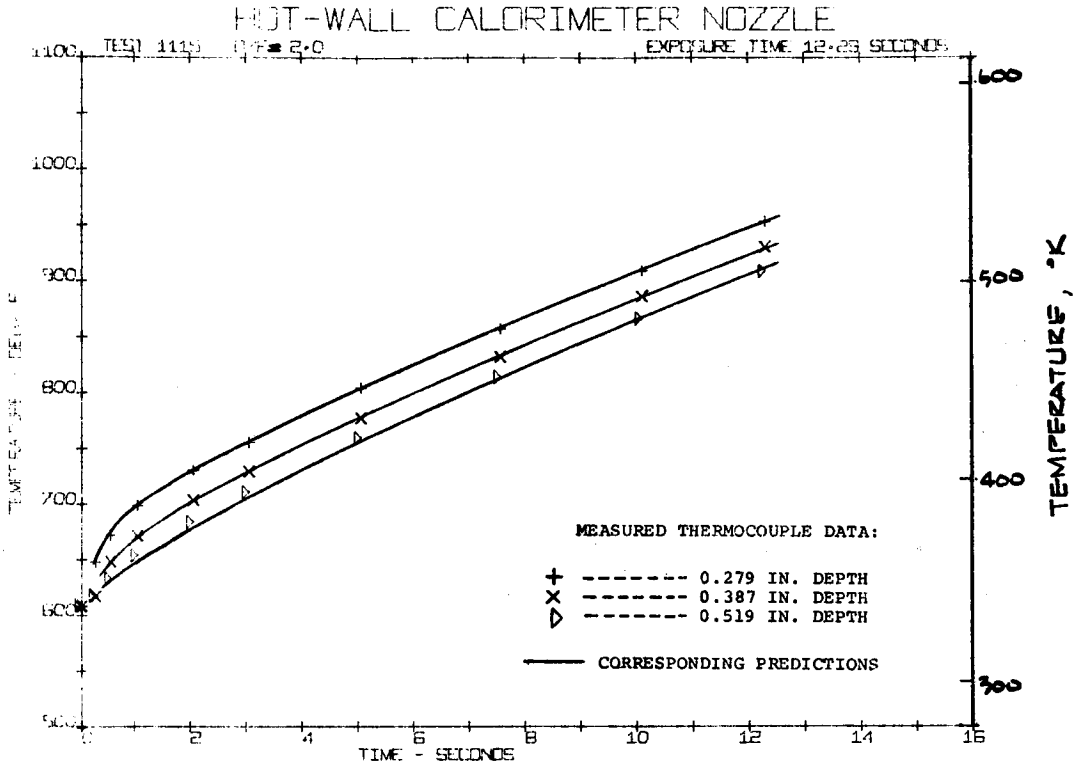
A-2590



J) TEST 1126, O/F = 2.0

FIGURE 16, CONTINUED

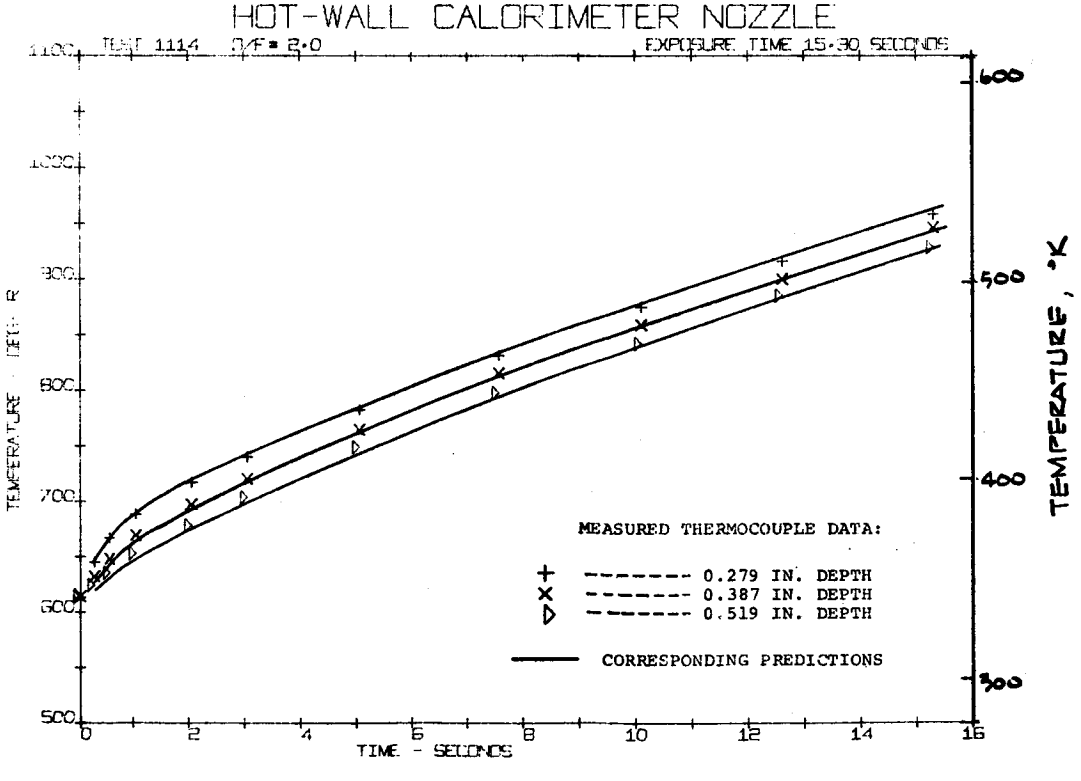
A-2591



K) TEST 1115, O/F = 2.0

FIGURE 16, CONTINUED

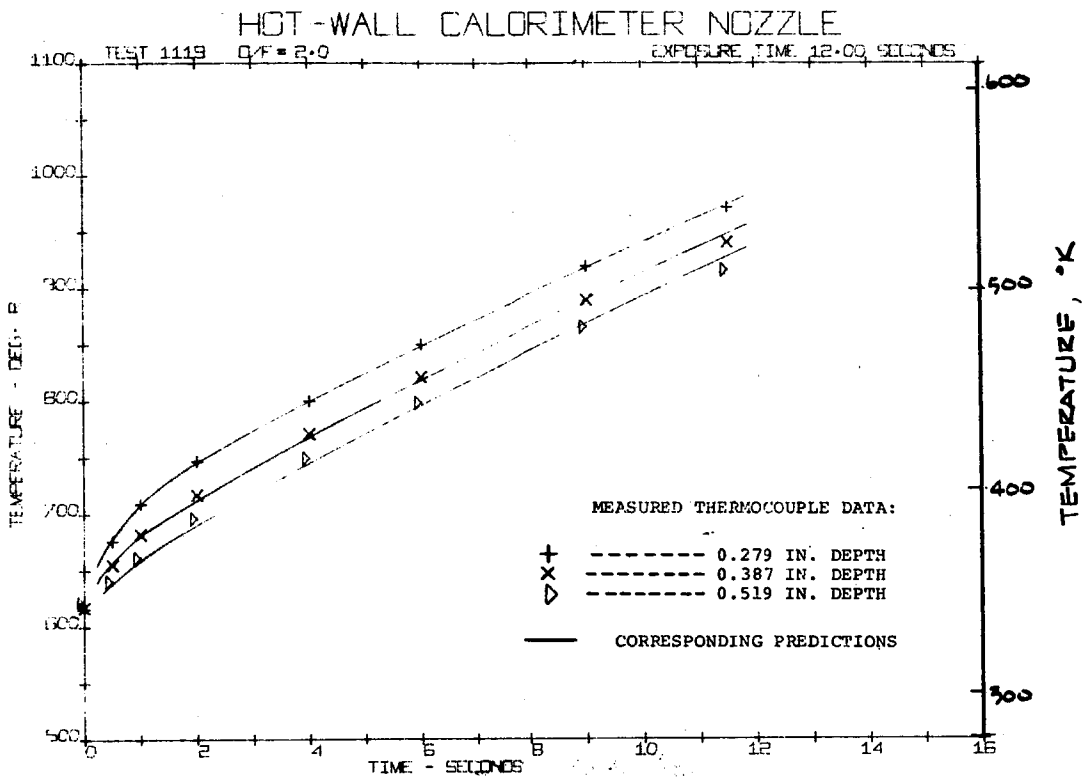
A-1592



L) TEST 1114, O/F = 2.0

FIGURE 16, CONTINUED

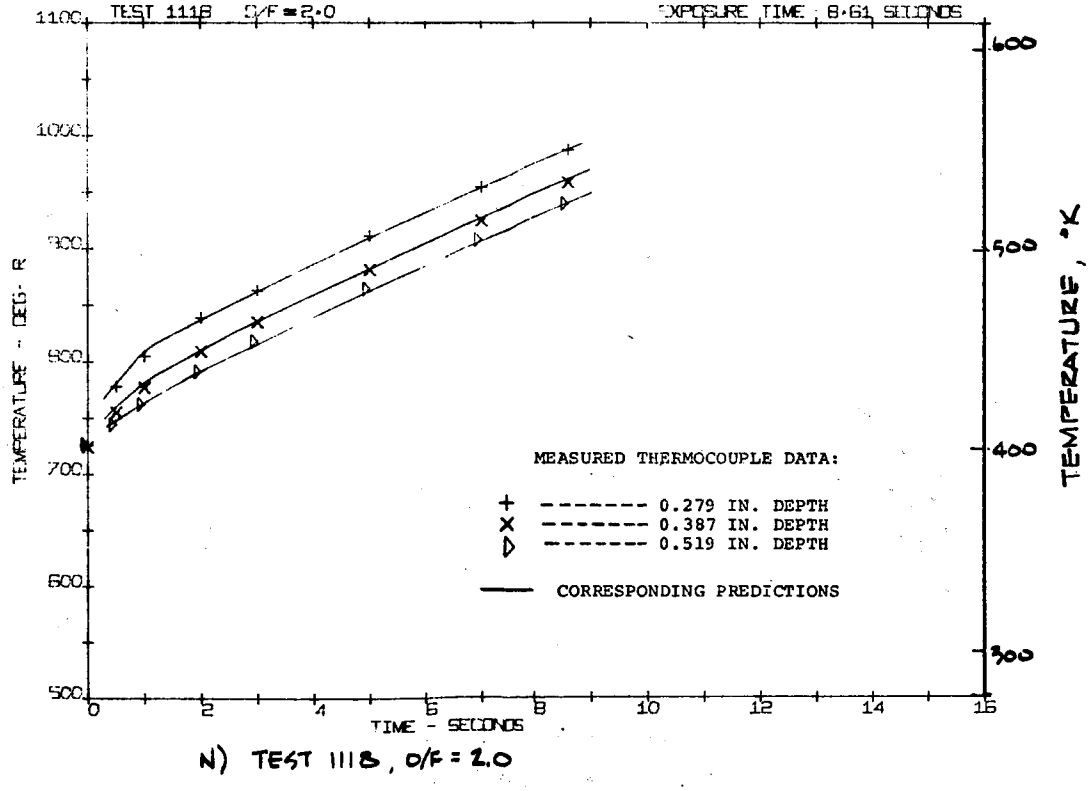
A-2593



M) TEST 1119, O/F = 2.0

FIGURE 16, CONTINUED

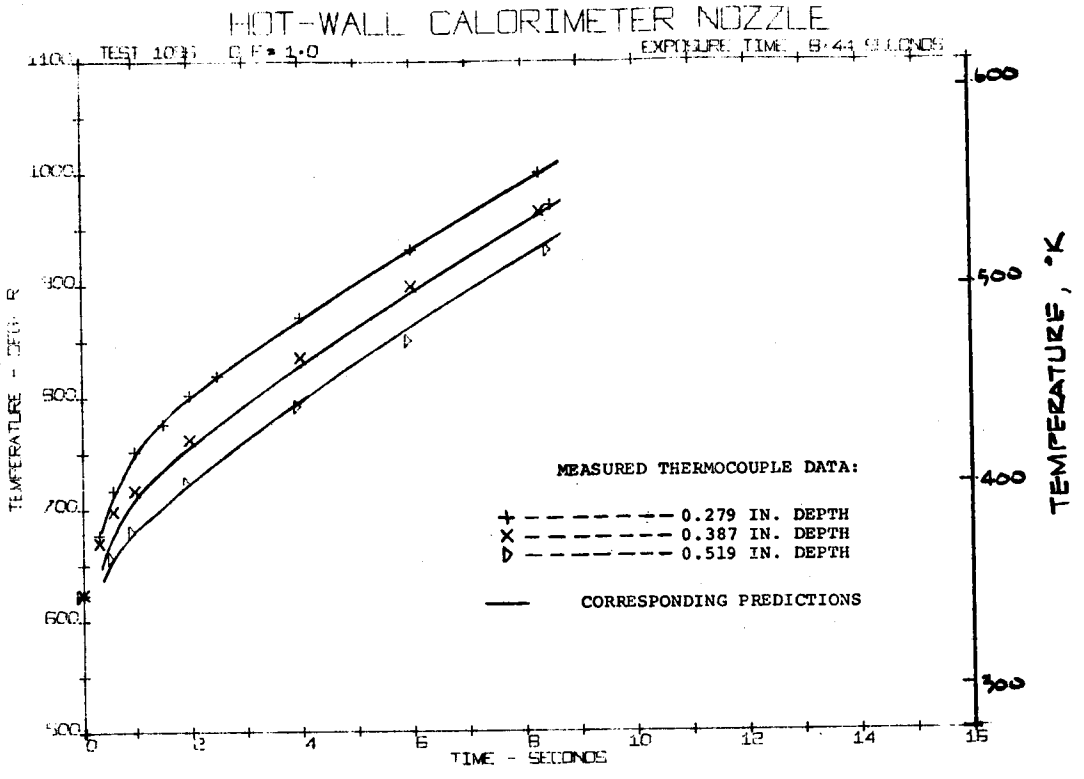
A-2994



N) TEST 1118, O/F = 2.0

FIGURE 16, CONTINUED

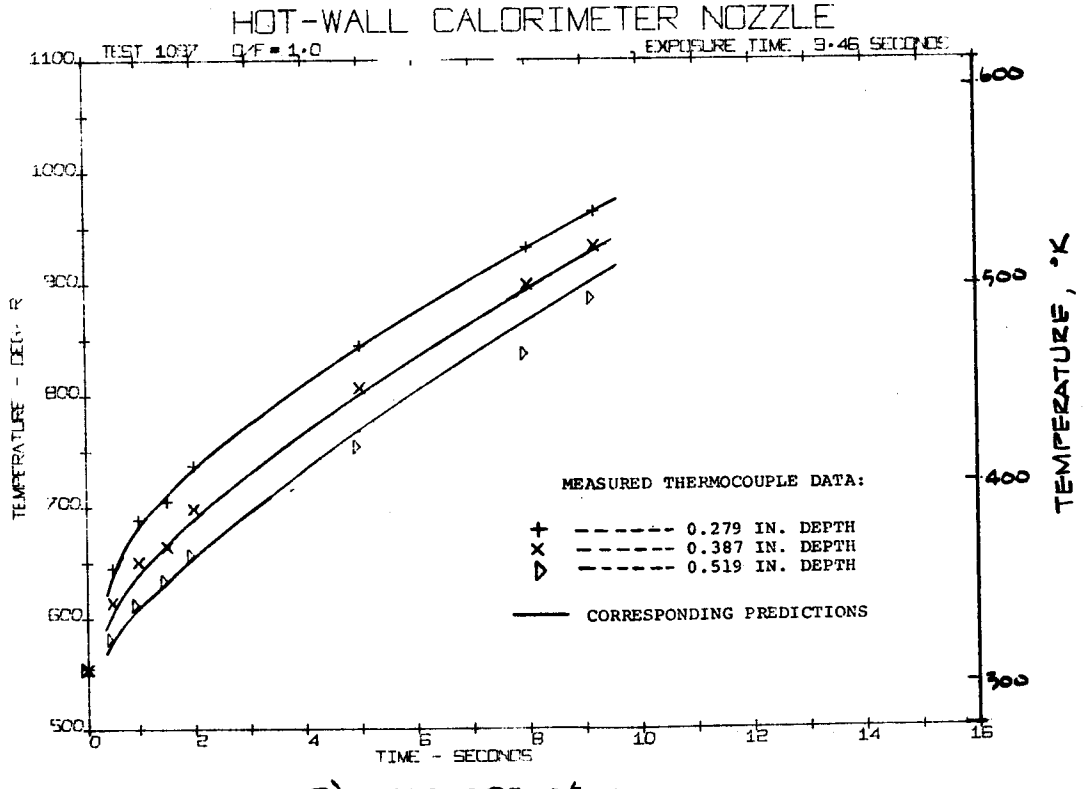
A-2995



a) TEST 1096, O/F = 1.0

FIGURE 16, CONTINUED

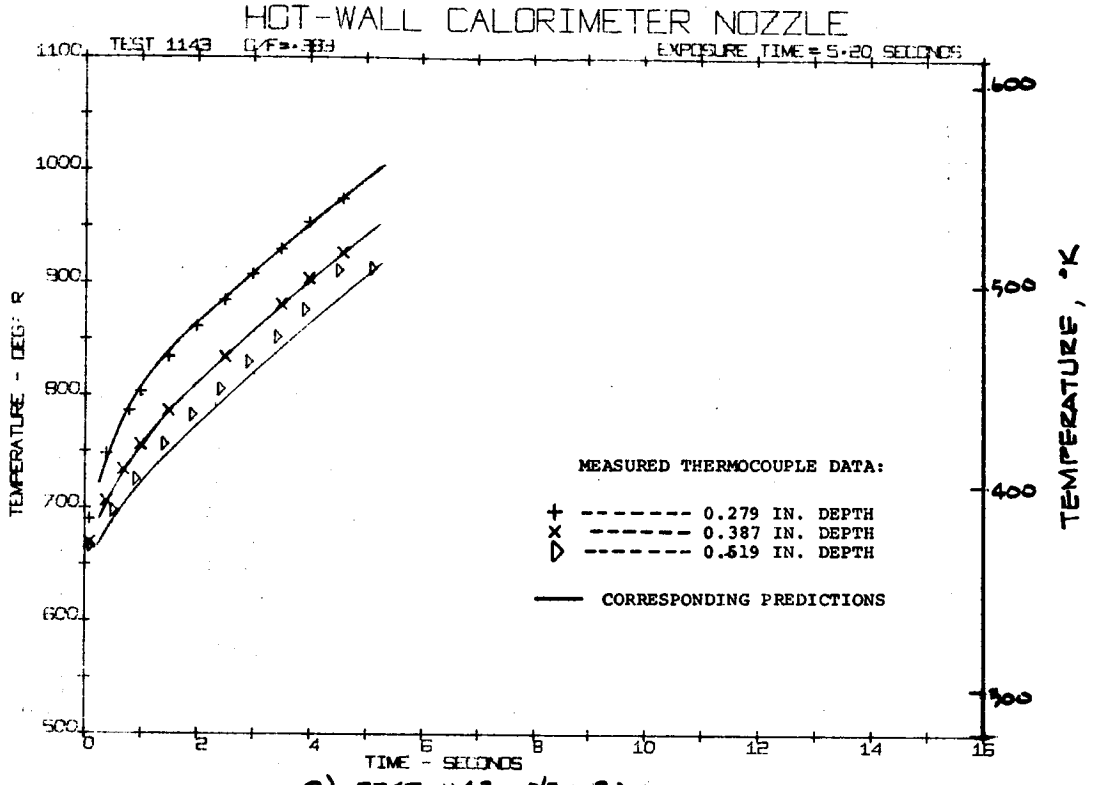
A-2516



b) TEST 1097, O/F = 1.0

FIGURE 16, CONTINUED

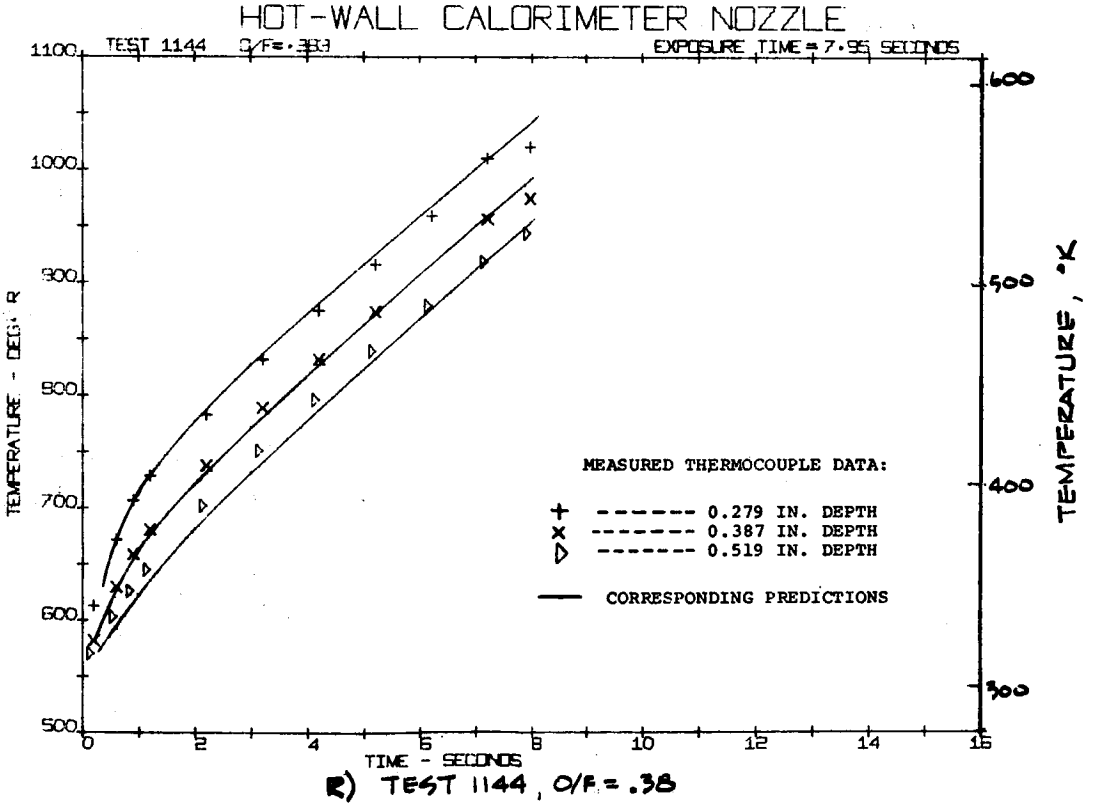
A-2517



Q) TEST 1143, O/F = .38

FIGURE 16, CONTINUED

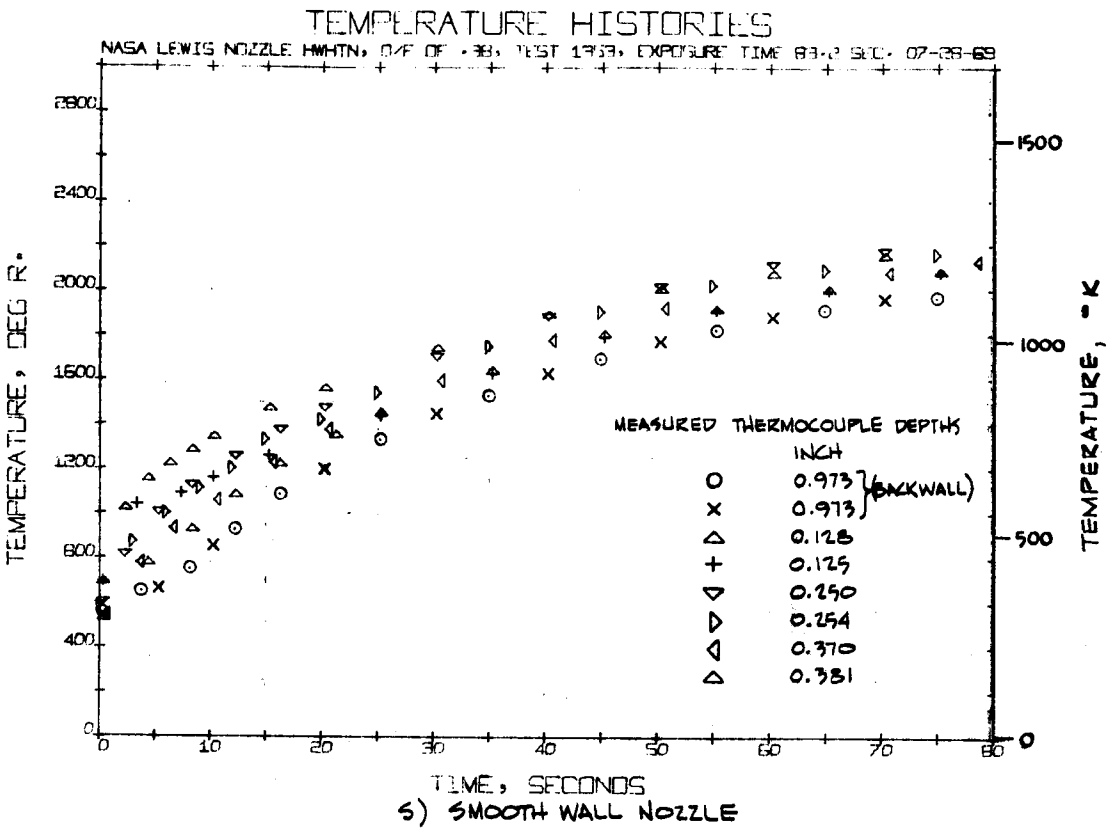
A-2498



R) TEST 1144, O/F = .38

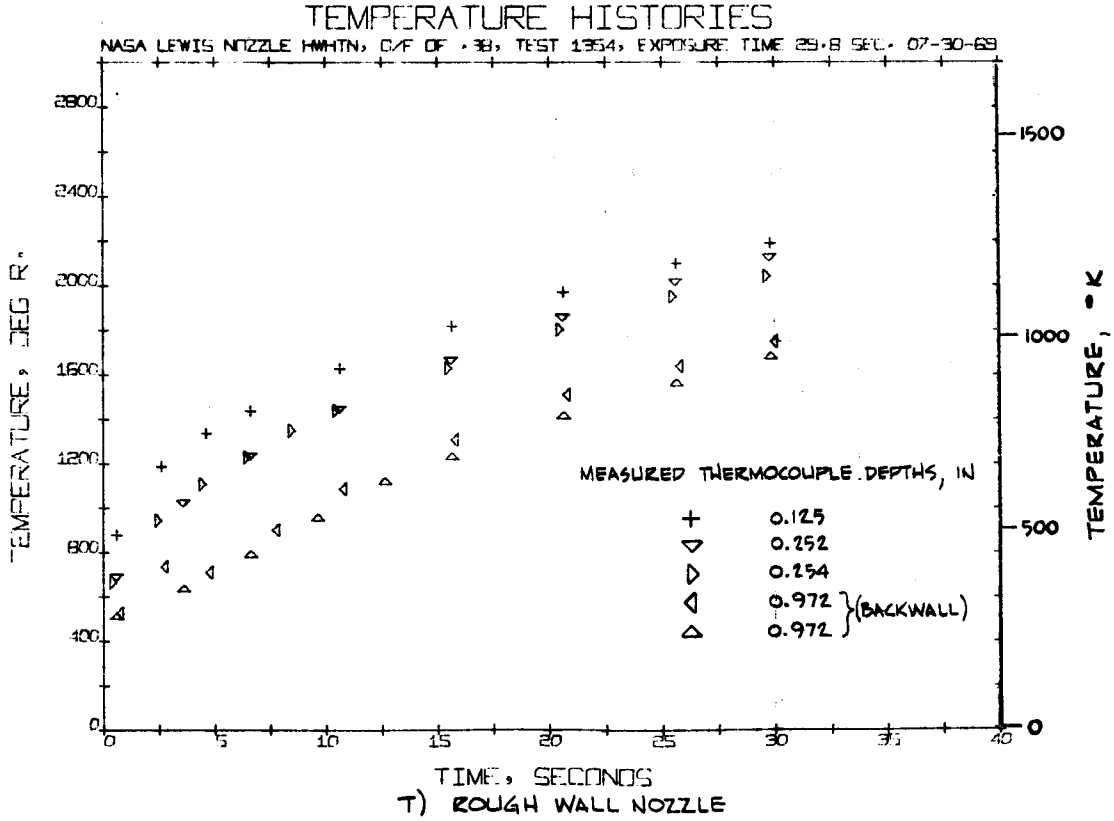
FIGURE 16, CONTINUED

A-2499



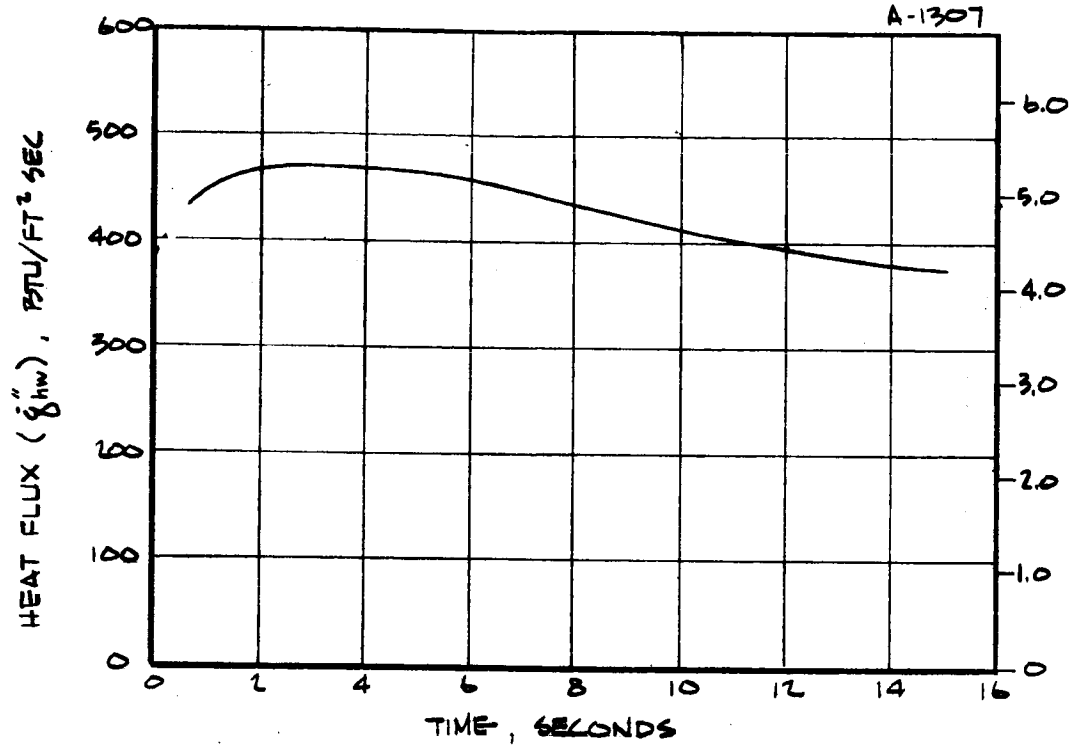
S) SMOOTH WALL NOZZLE

FIGURE 16, CONTINUED A-2600

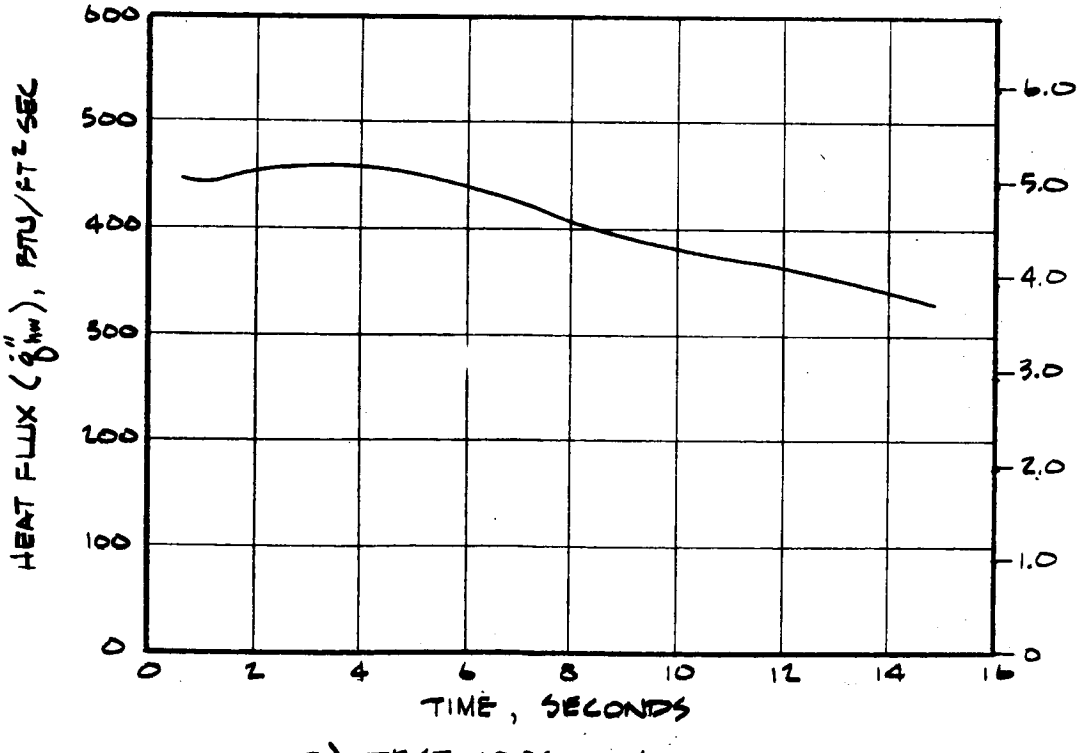


T) ROUGH WALL NOZZLE

FIGURE 16, CONCLUDED A-2601

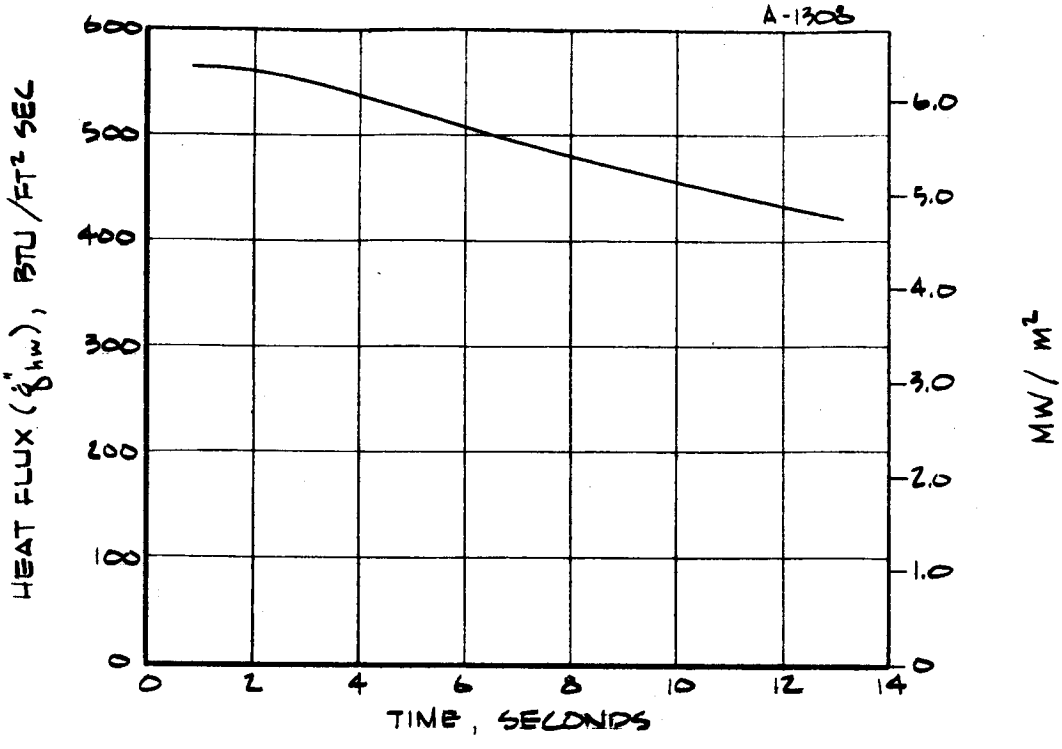


A) TEST 1081, O/F = ∞

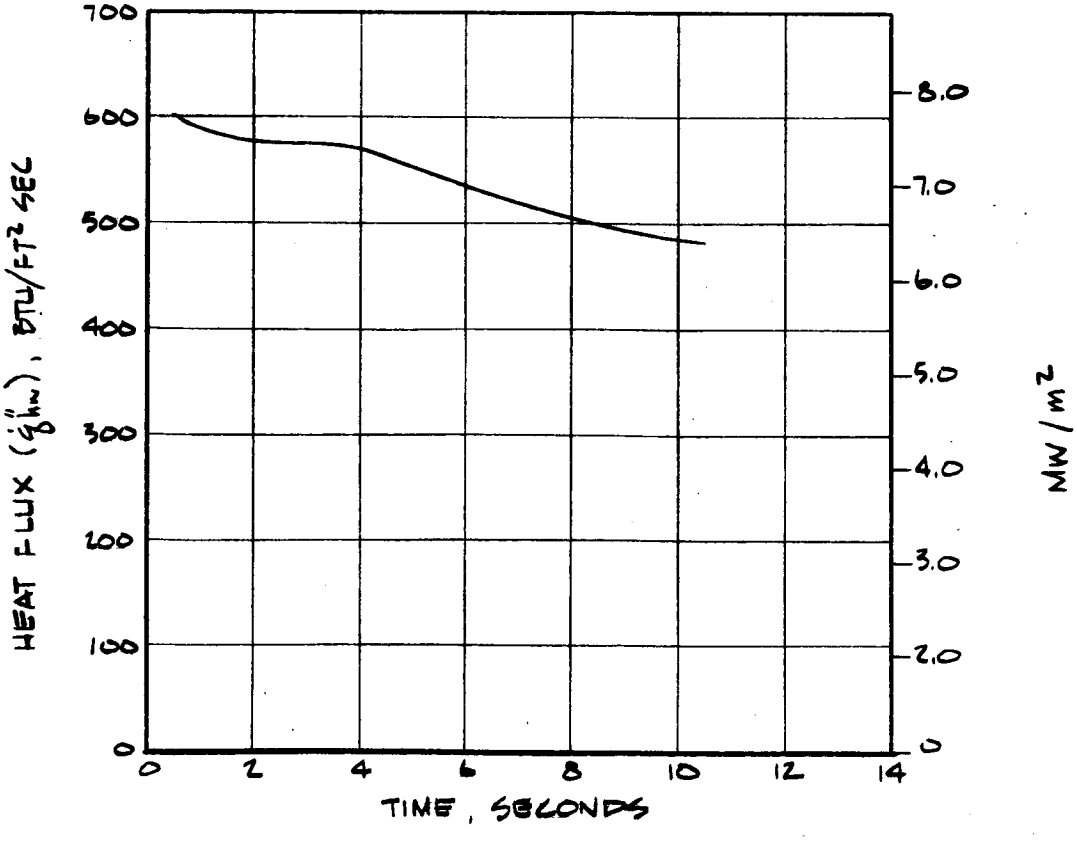


B) TEST 108L, O/F = ∞

FIGURE 17 HEAT FLUX HISTORIES FOR COPPER TRANSIENT CALORIMETER TESTS.

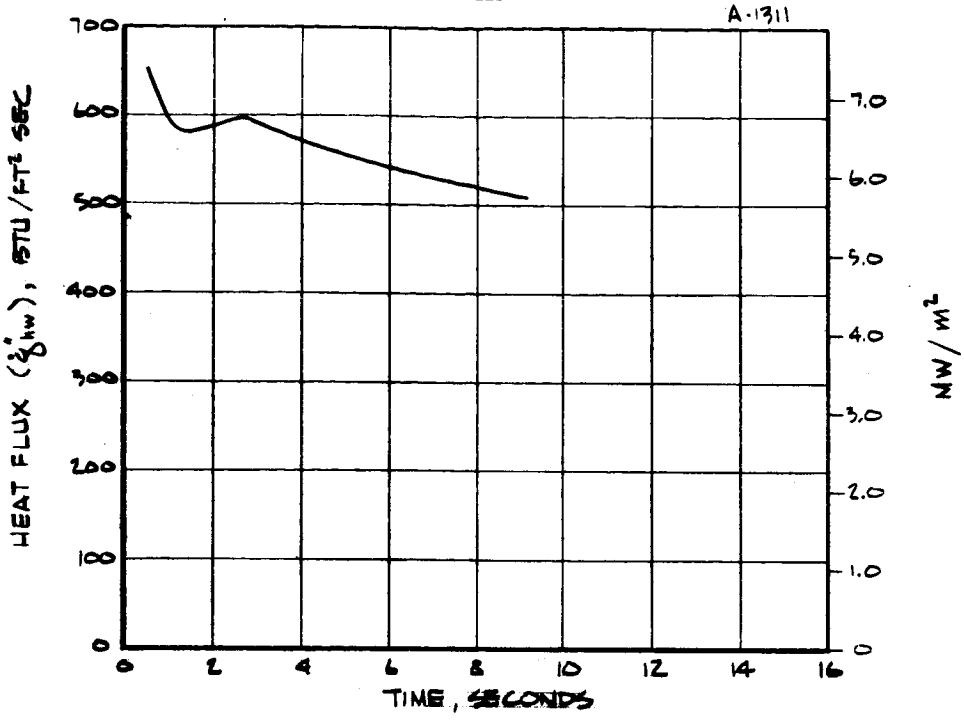


c) TEST 1089, O/F = 4.0

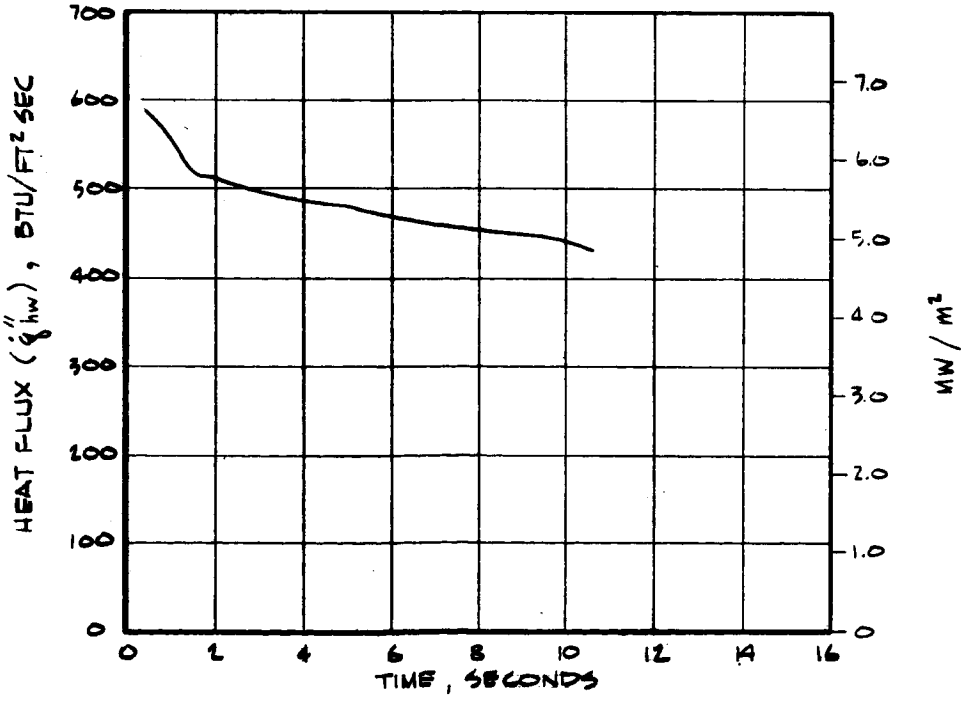


D) TEST 1090, O/F = 4.0

FIGURE 17 (CONTINUED)

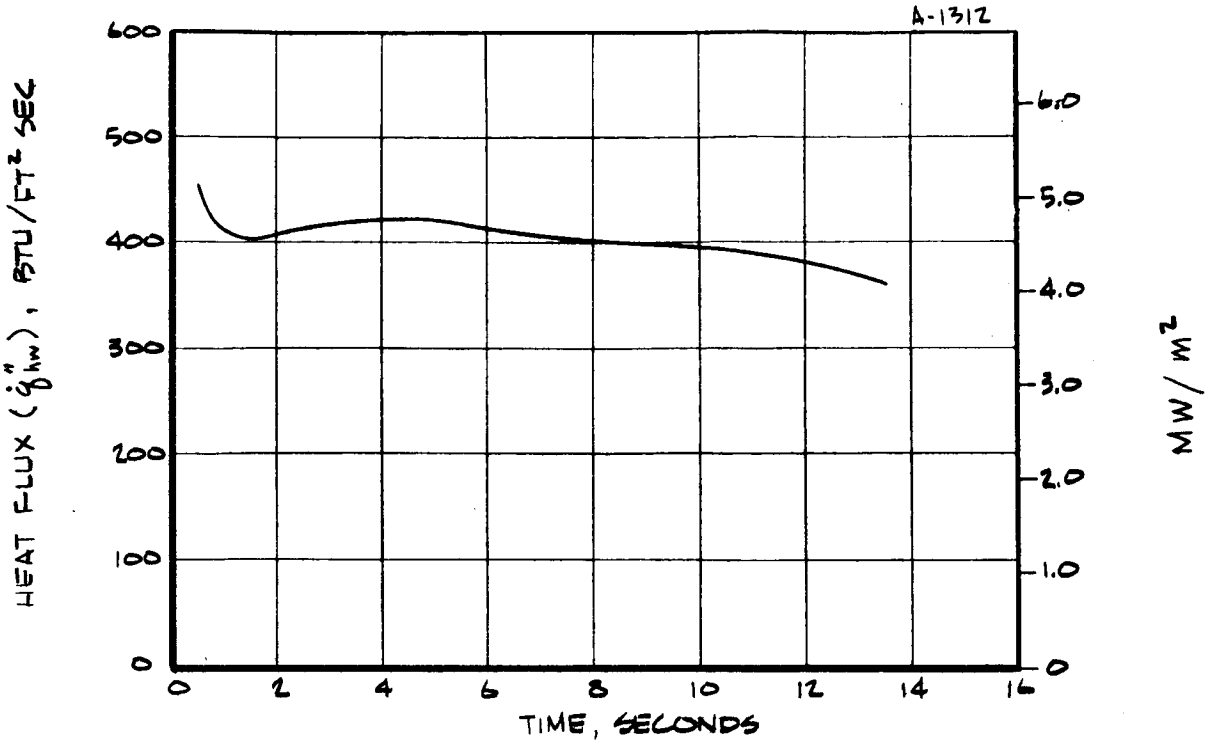


E) TEST 1132, O/F ~ 2.0

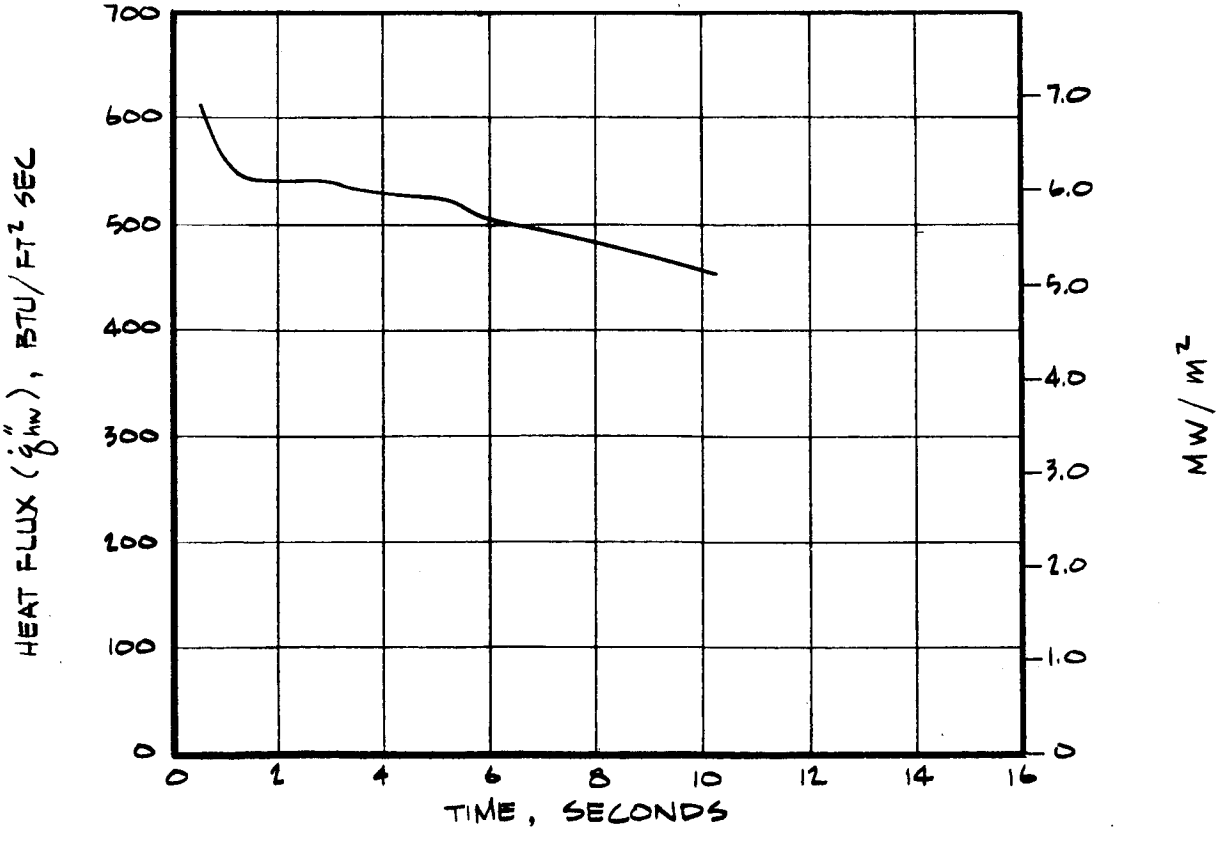


F) TEST 1123, O/F = 2.0

FIGURE 17 (CONTINUED)

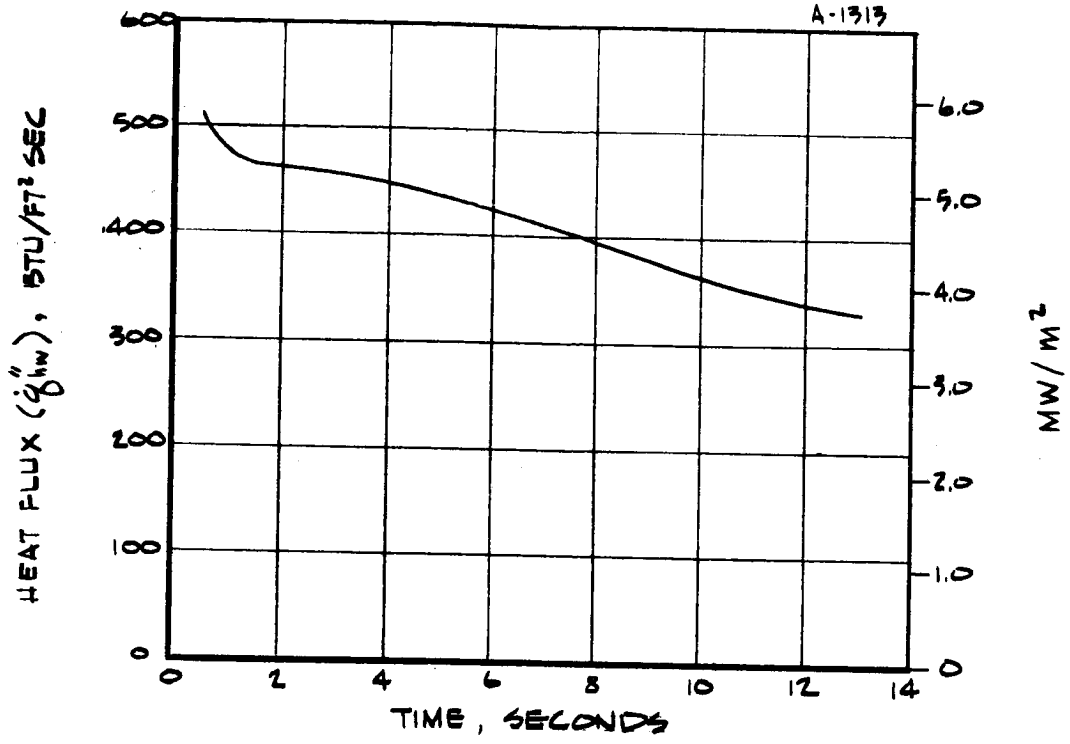


G) TEST 1122, O/F = 2.0

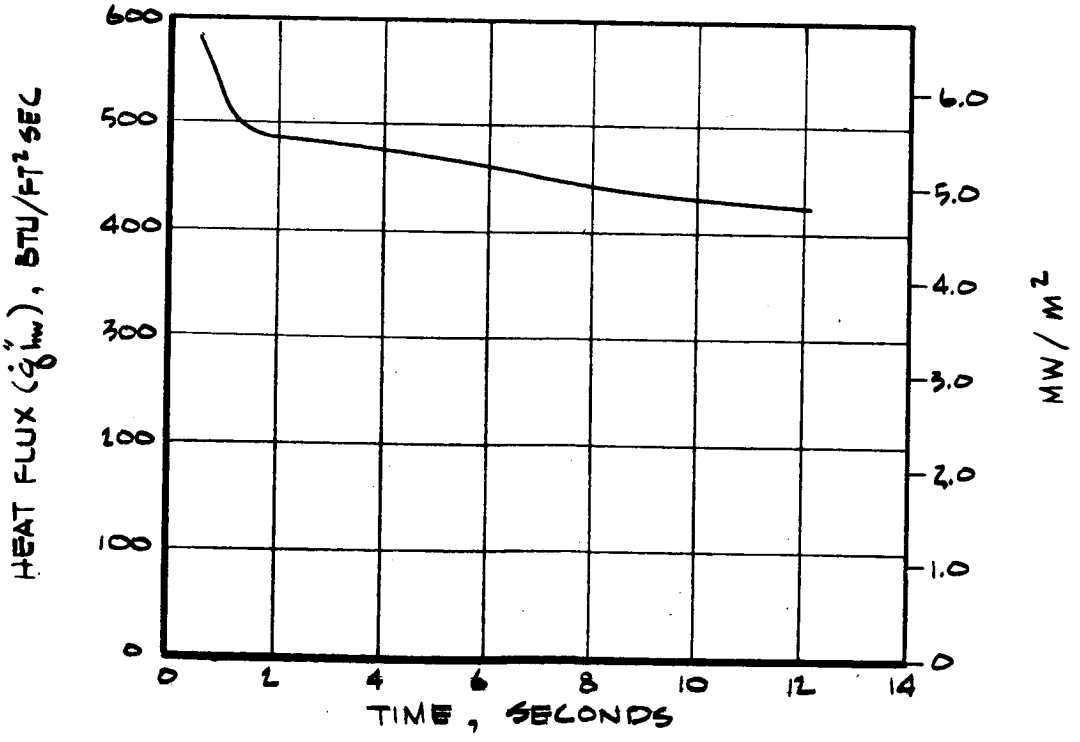


H) TEST 1127, O/F = 2.0

FIGURE 17 (CONTINUED)

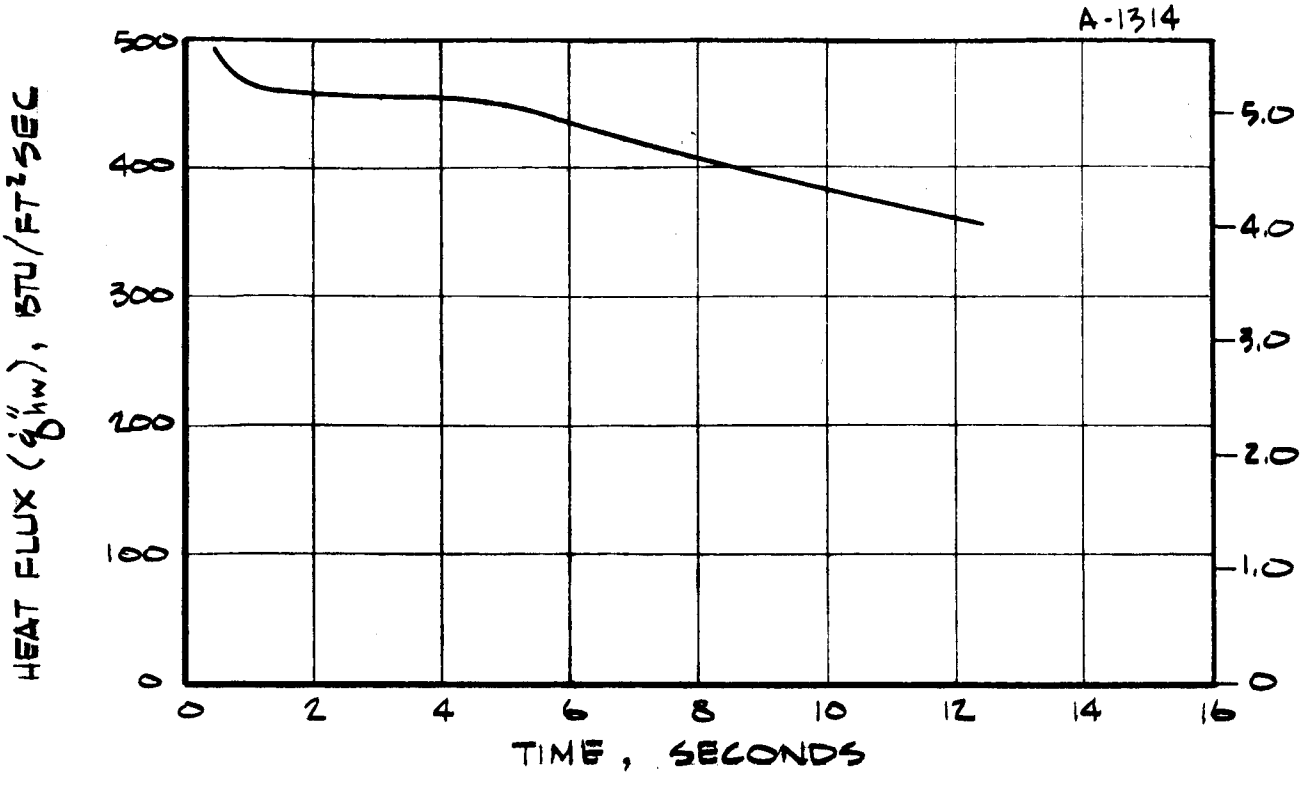


I) TEST 1113, O/F = 2.0

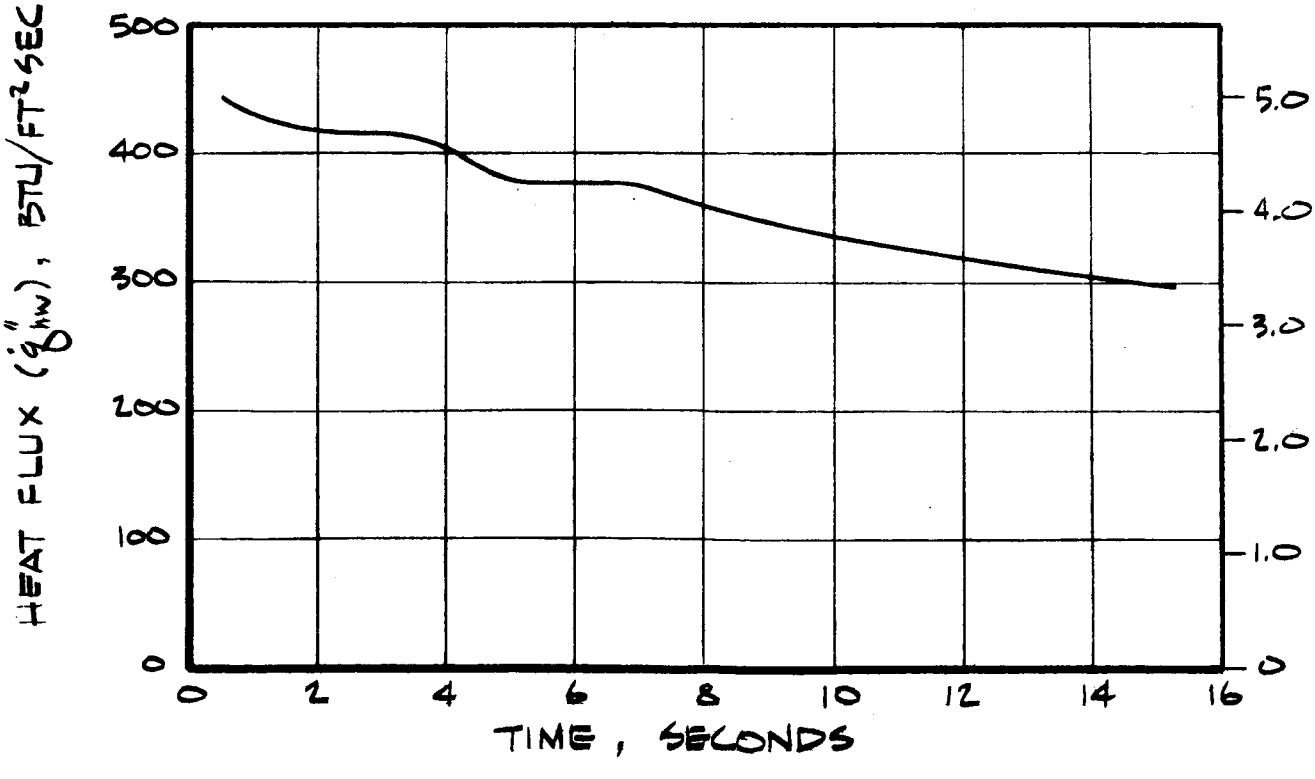


J) TEST 1126, O/F = 2.0

FIGURE 17 (CONTINUED)

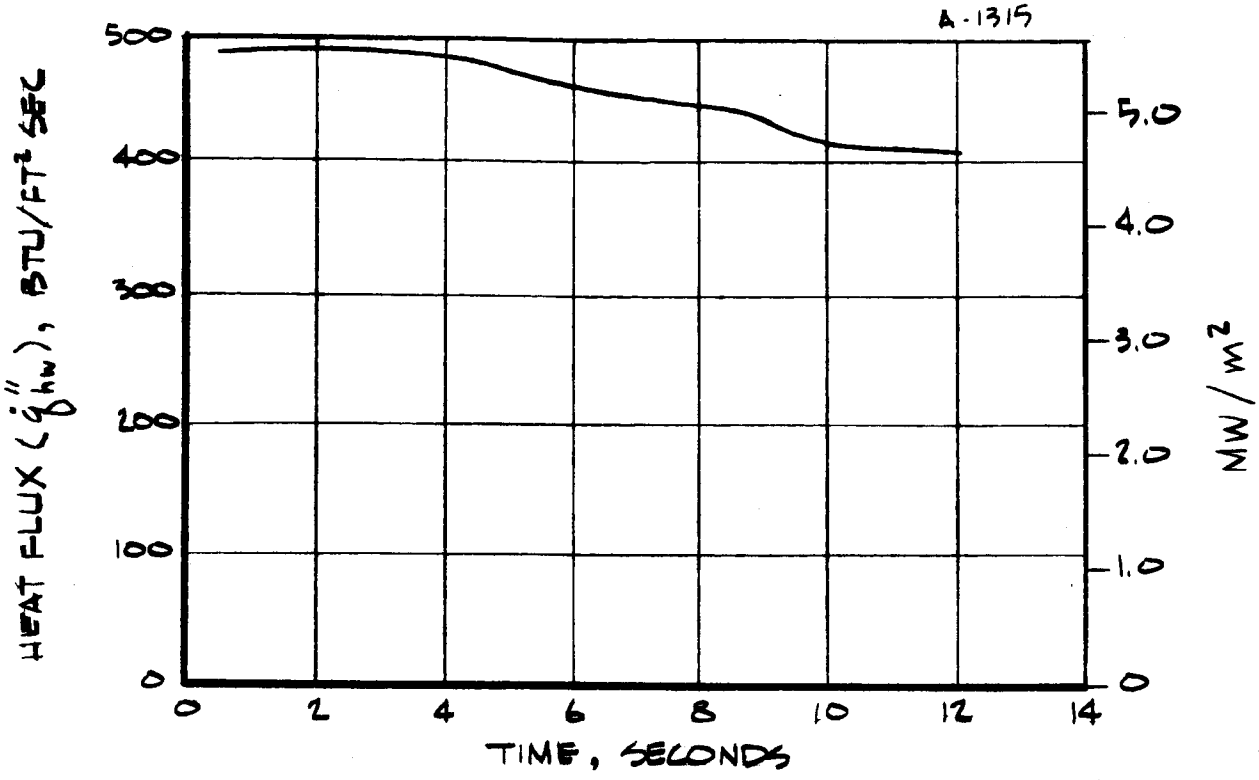


K) TEST 1115, O/F = 2.0

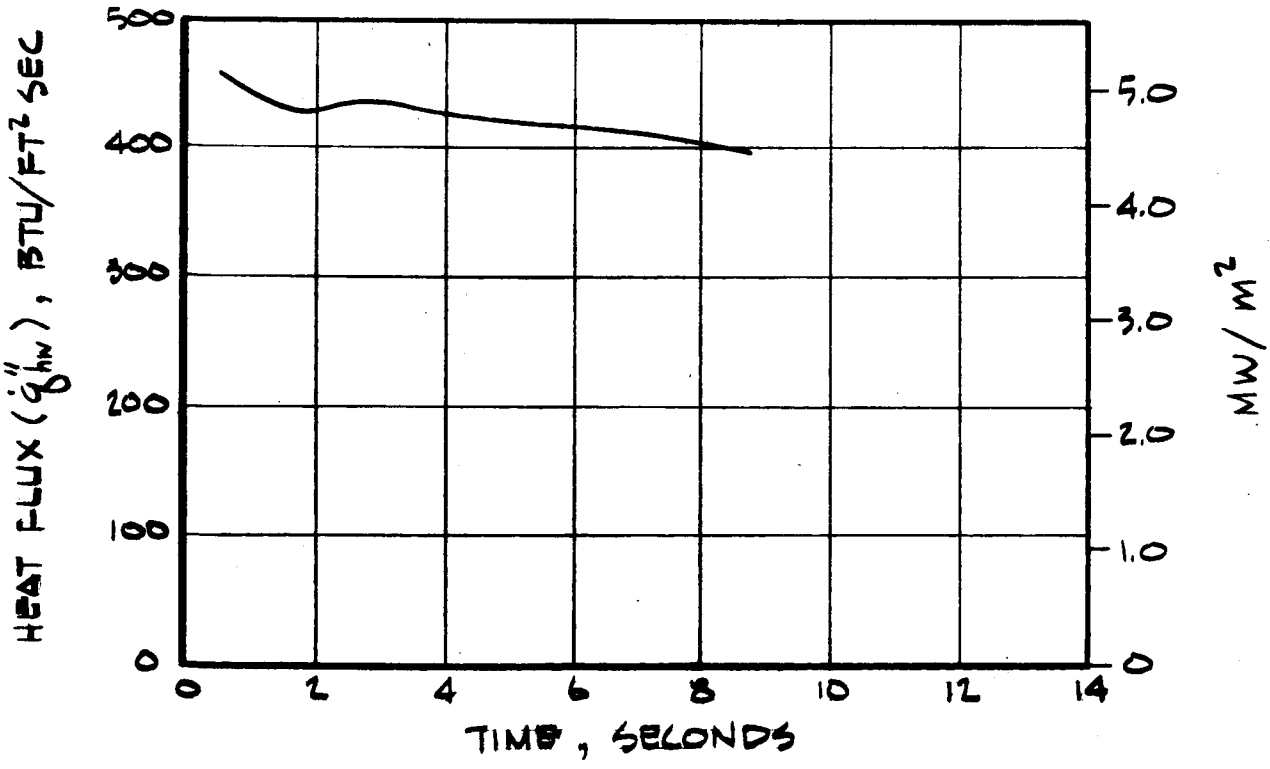


L) TEST 1114, O/F = 2.0

FIGURE 17 (CONTINUED)

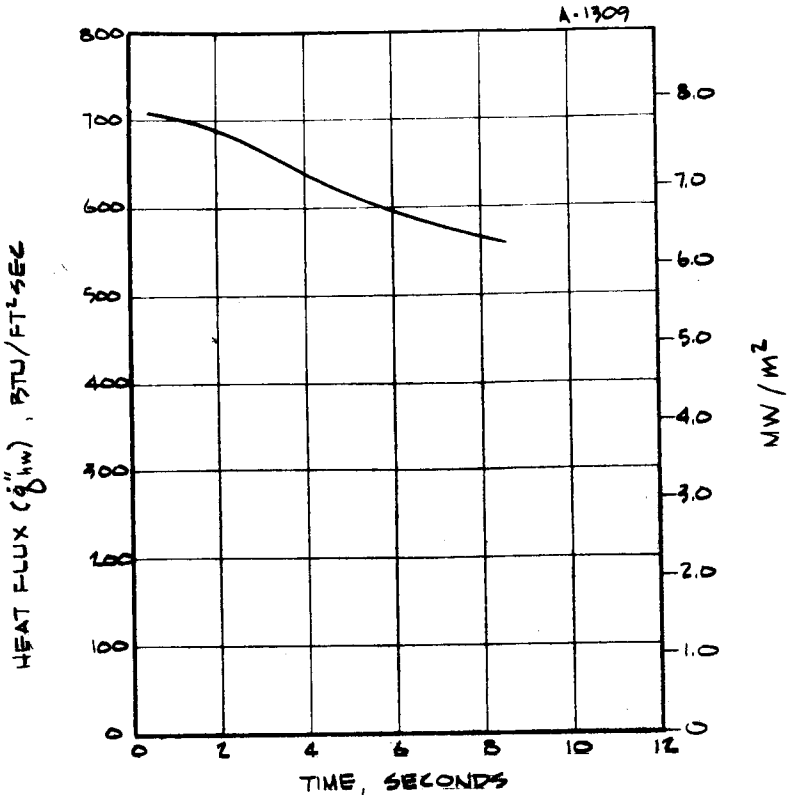


M) TEST 1119, O/F = 2.0

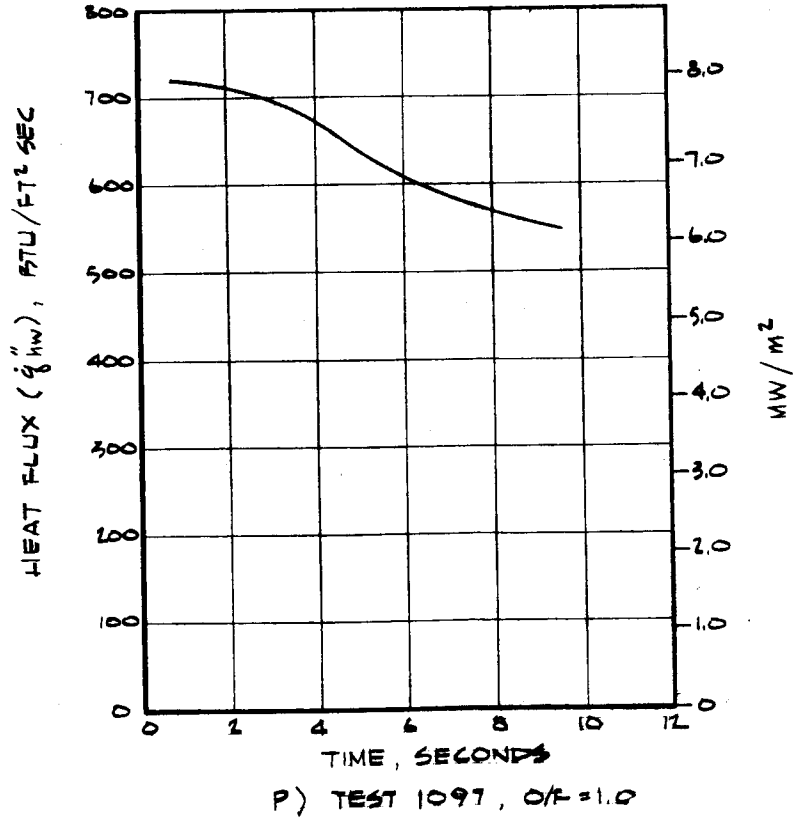


N) TEST 1118, O/F = 2.0

FIGURE 17, (CONTINUED)

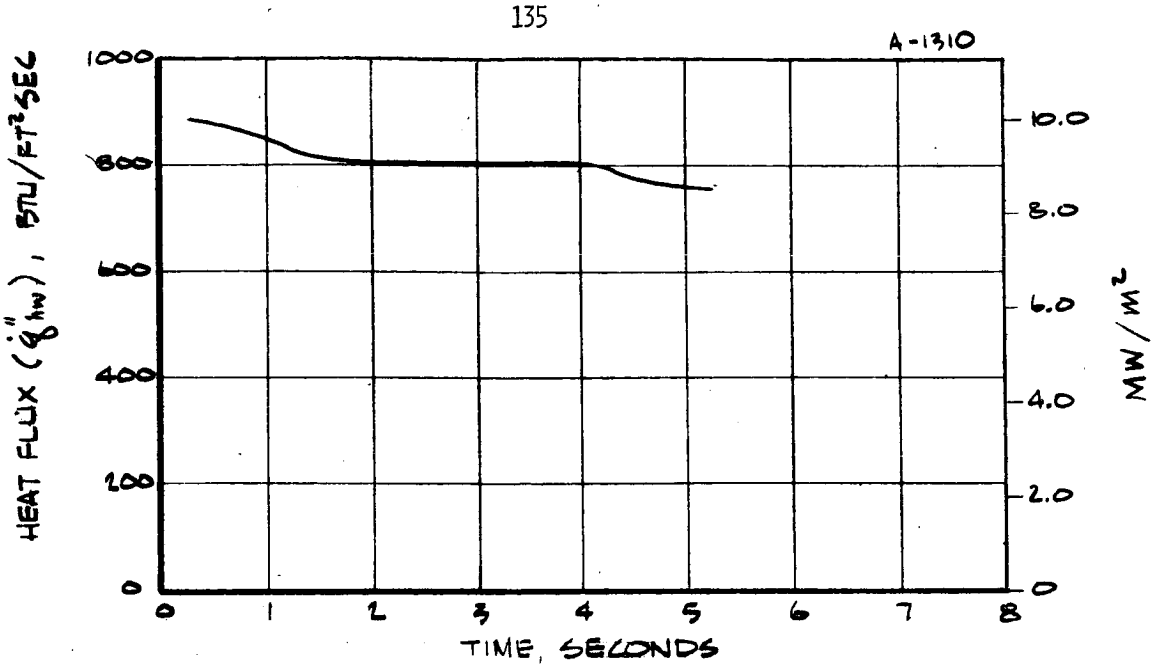


O) TEST 1096 O/F = 1.0

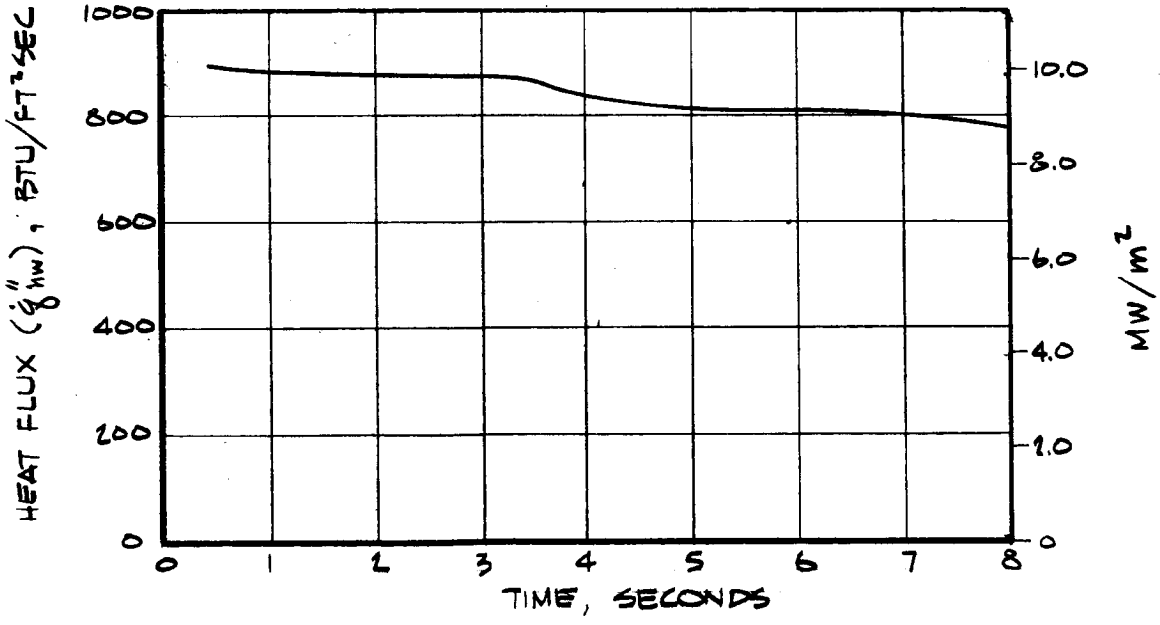


P) TEST 1097, O/F = 1.0

FIGURE 17 (CONTINUED)

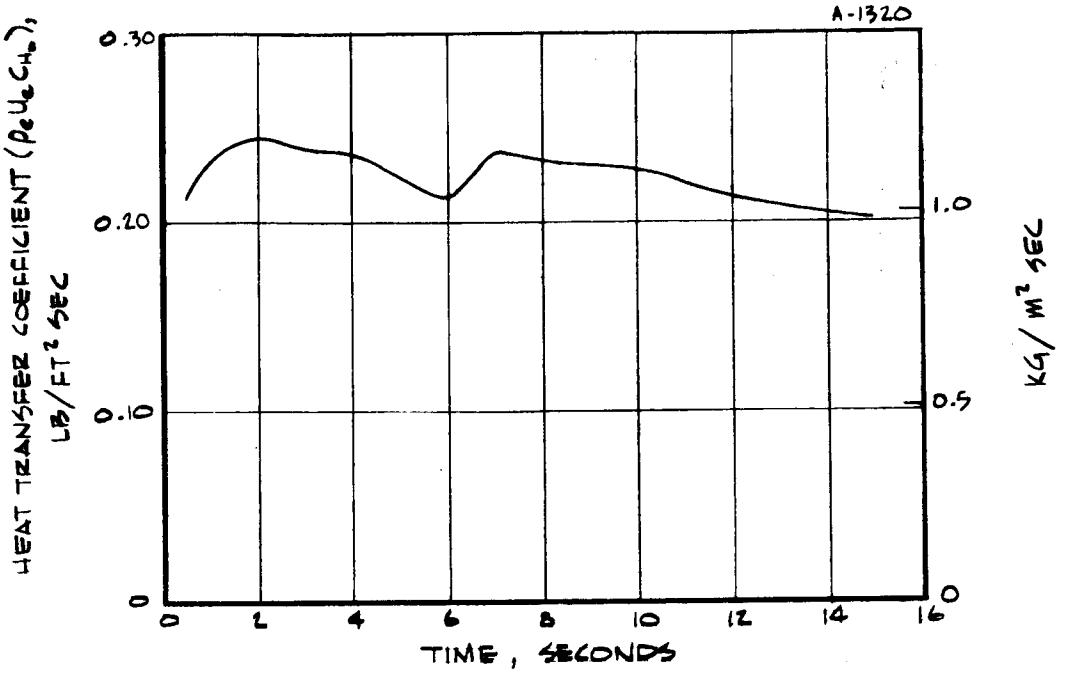


Q) TEST 1143, O/F = 0.38

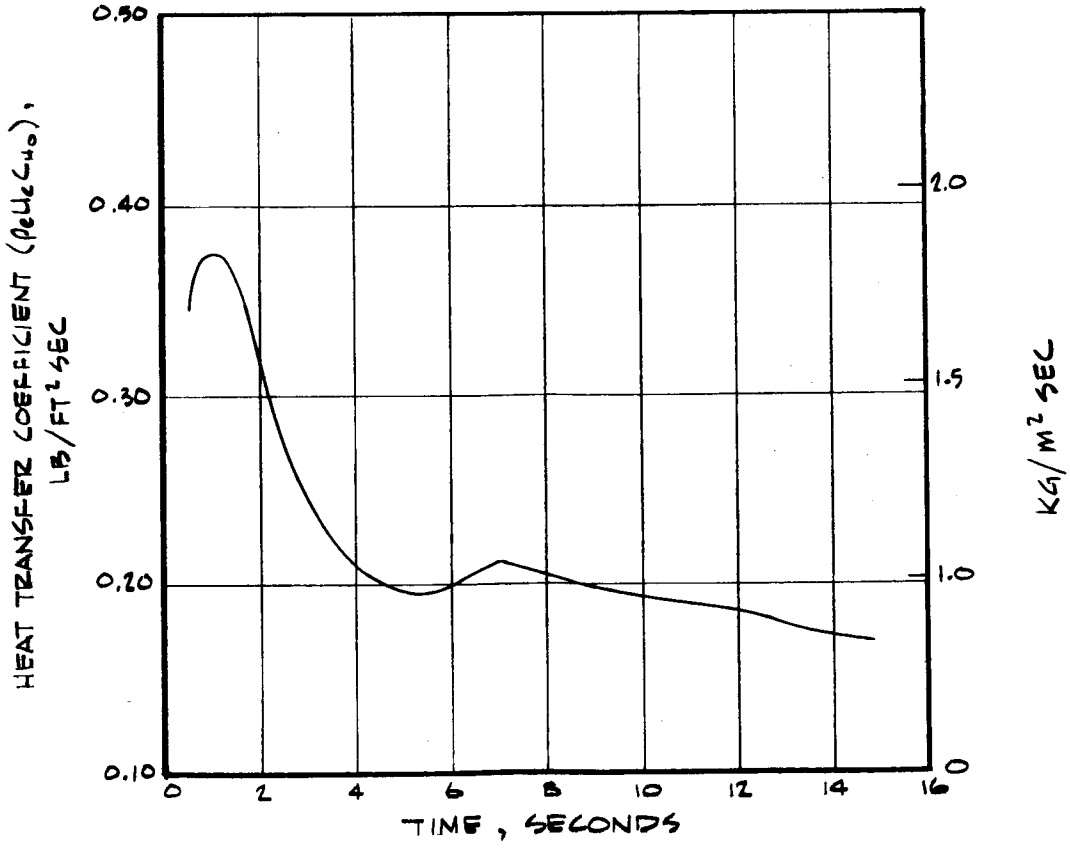


R) TEST 1144, O/F = 0.38

FIGURE 17 (CONCLUDED)

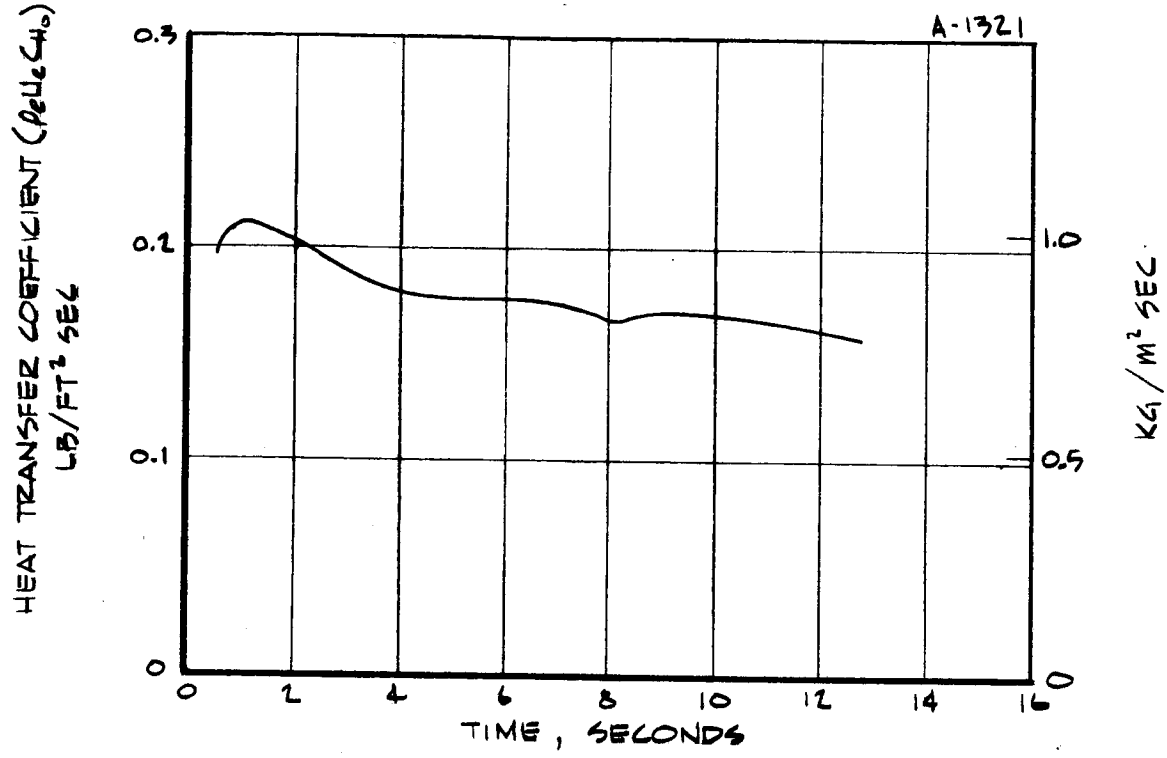


A) TEST 1081, O/F = ∞

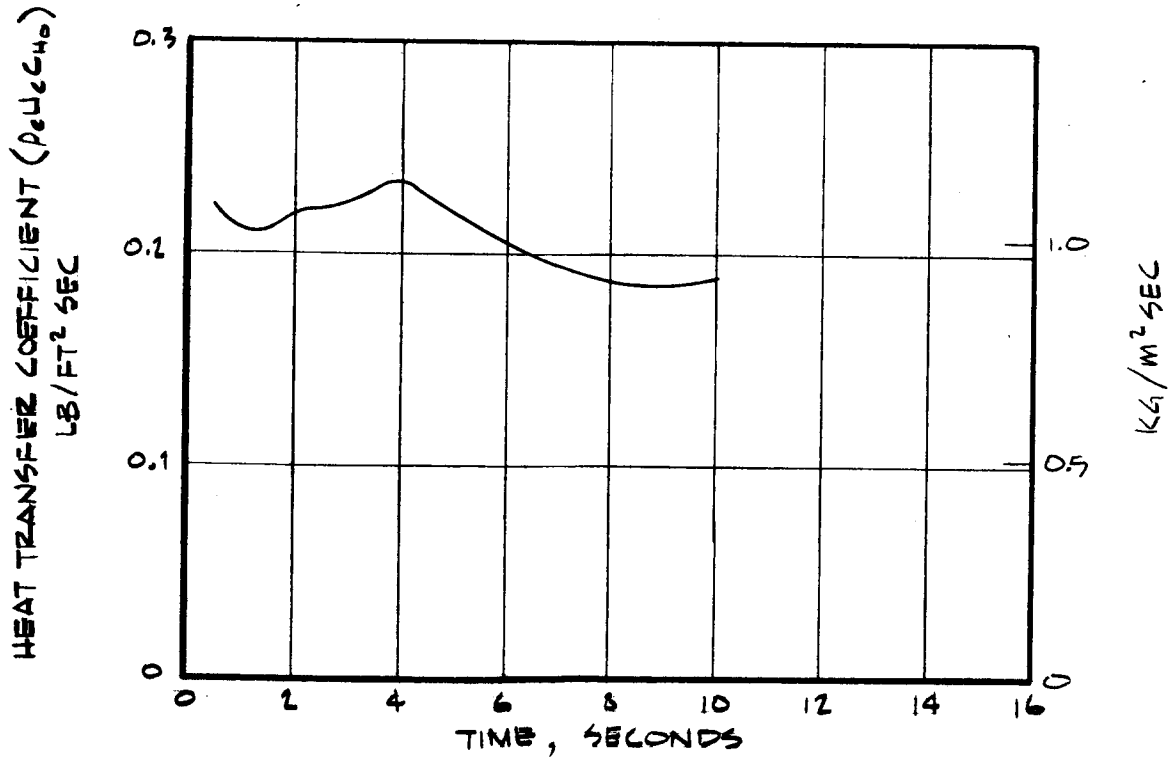


B) TEST 1082, O/F = ∞

FIGURE 18 HEAT TRANSFER COEFFICIENT HISTORIES FOR COPPER TRANSIENT CALORIMETER TESTS.

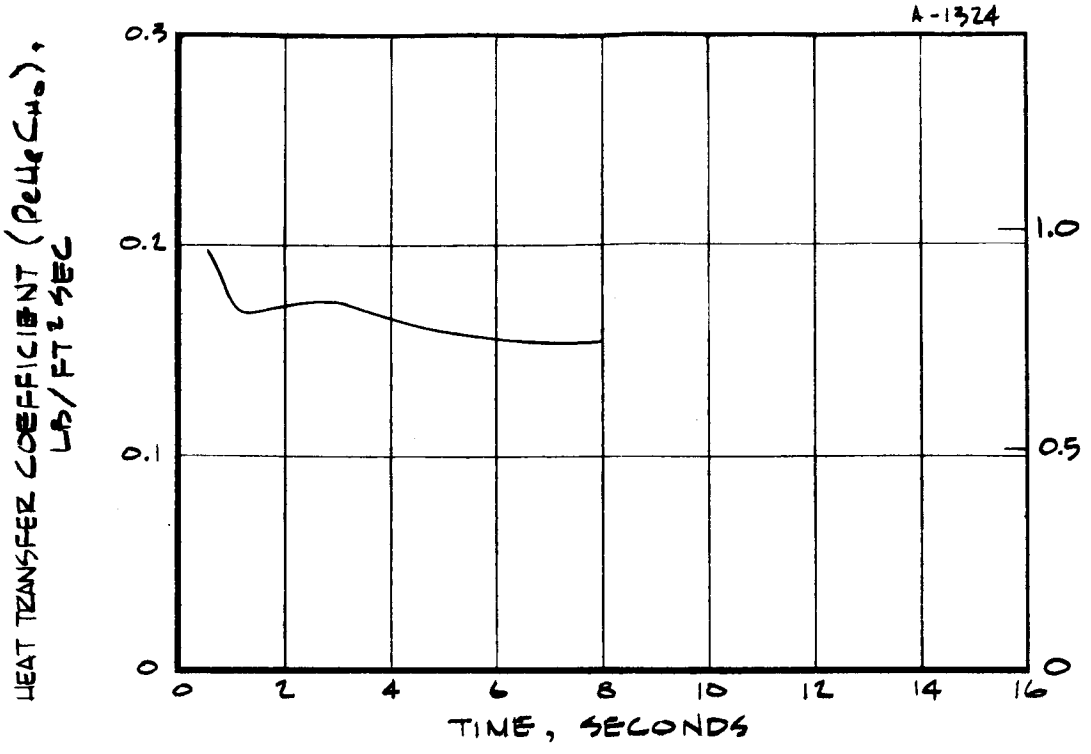


C) TEST 1089, O/F = 4.0

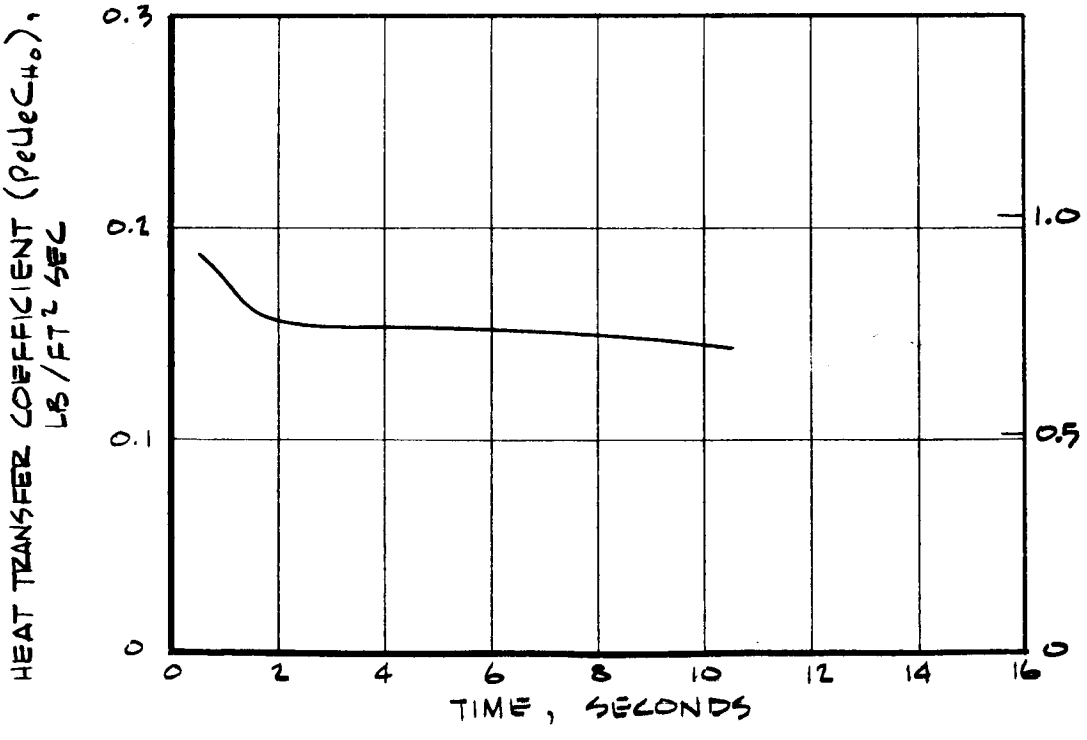


D) TEST 1090, O/F = 4.0

FIGURE 18 (CONTINUED)

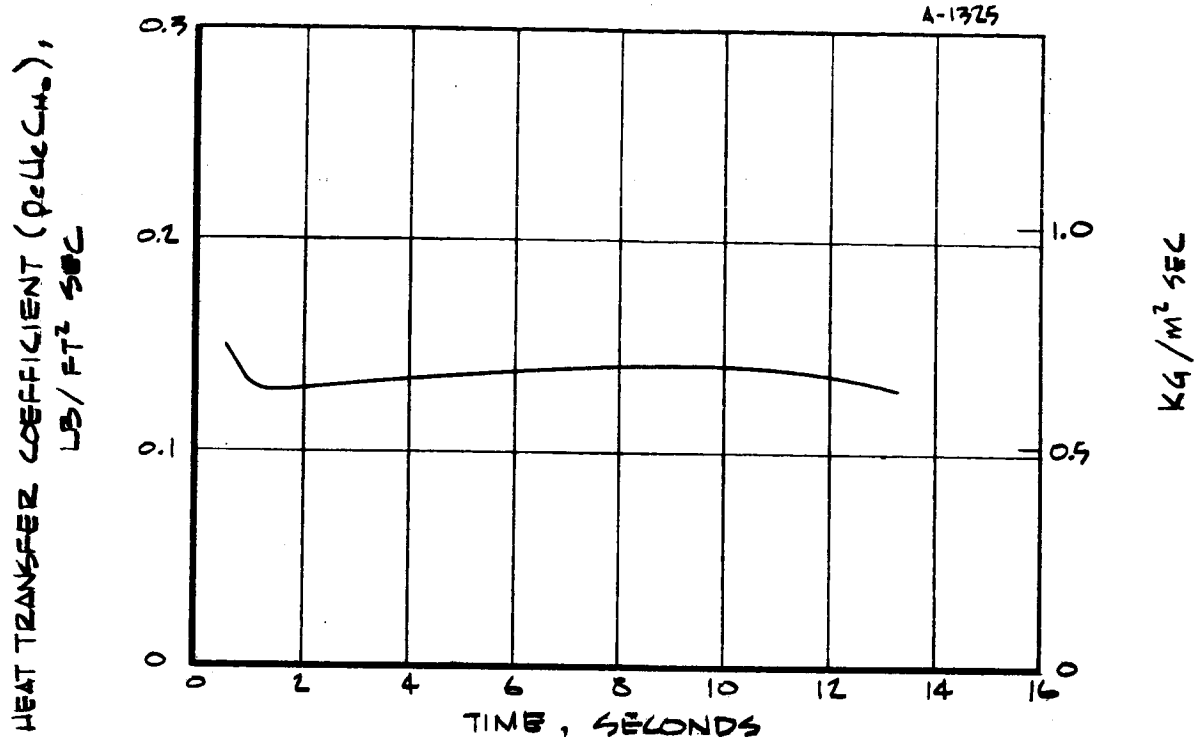


E) TEST 1132, O/F = 2.0

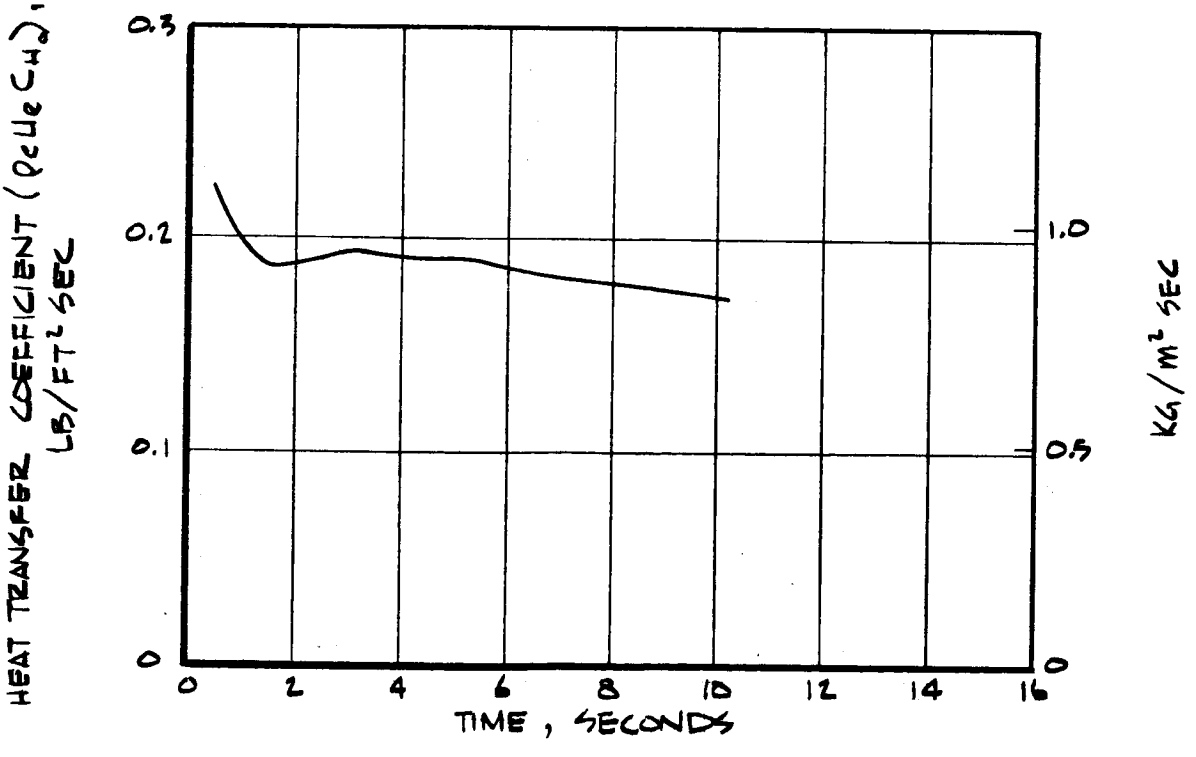


F) TEST 1123, O/F = 2.0

FIGURE 18 (CONTINUED)

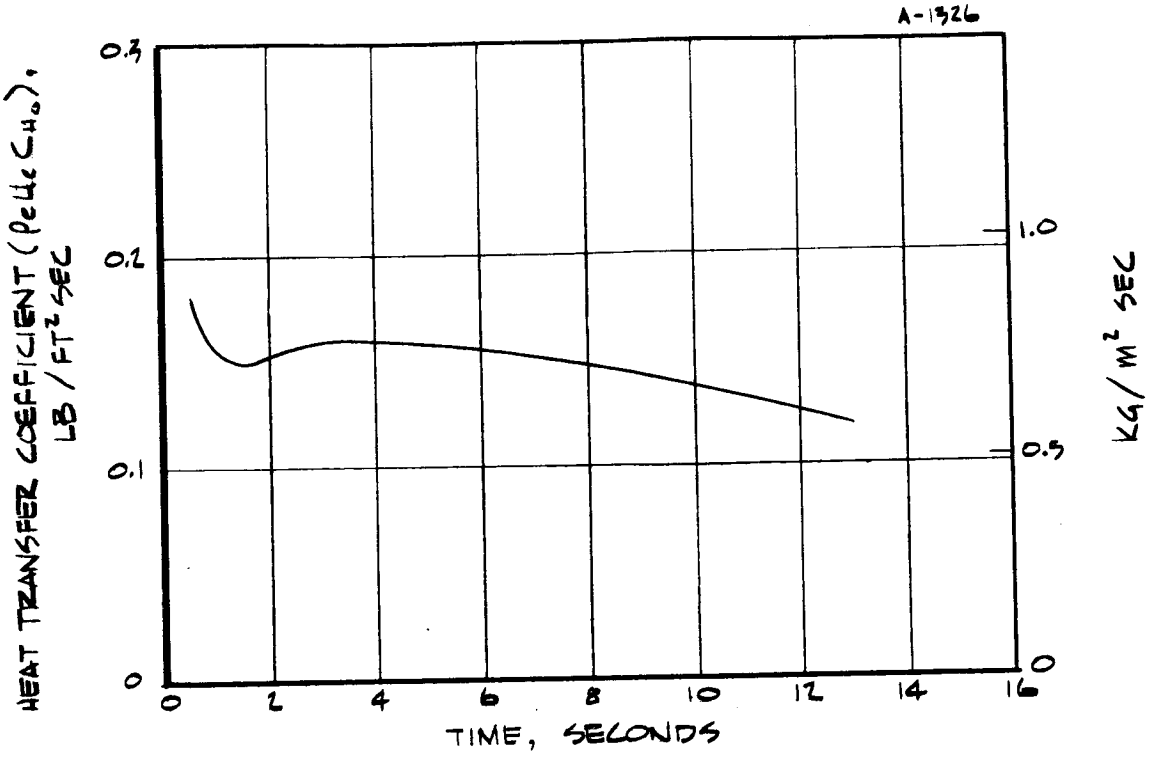


G) TEST 1122, O/F = 2.0

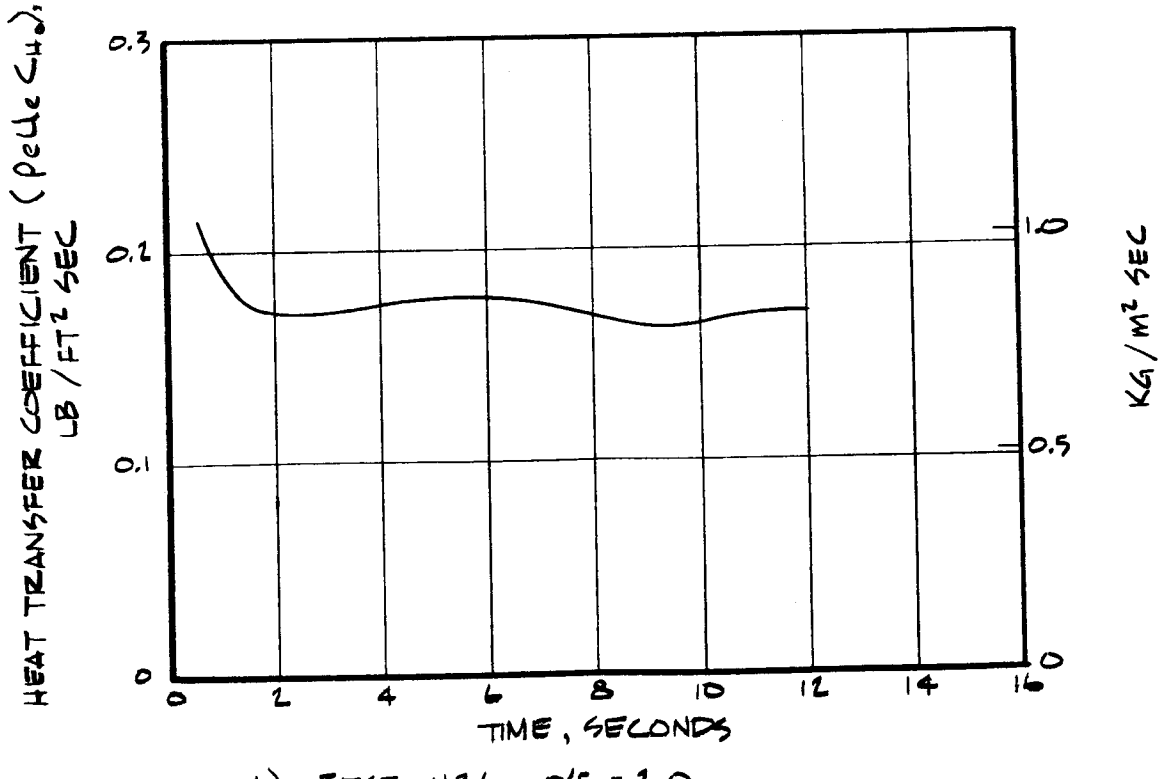


H) TEST 1127, O/F = 2.0

FIGURE 18 (CONTINUED)

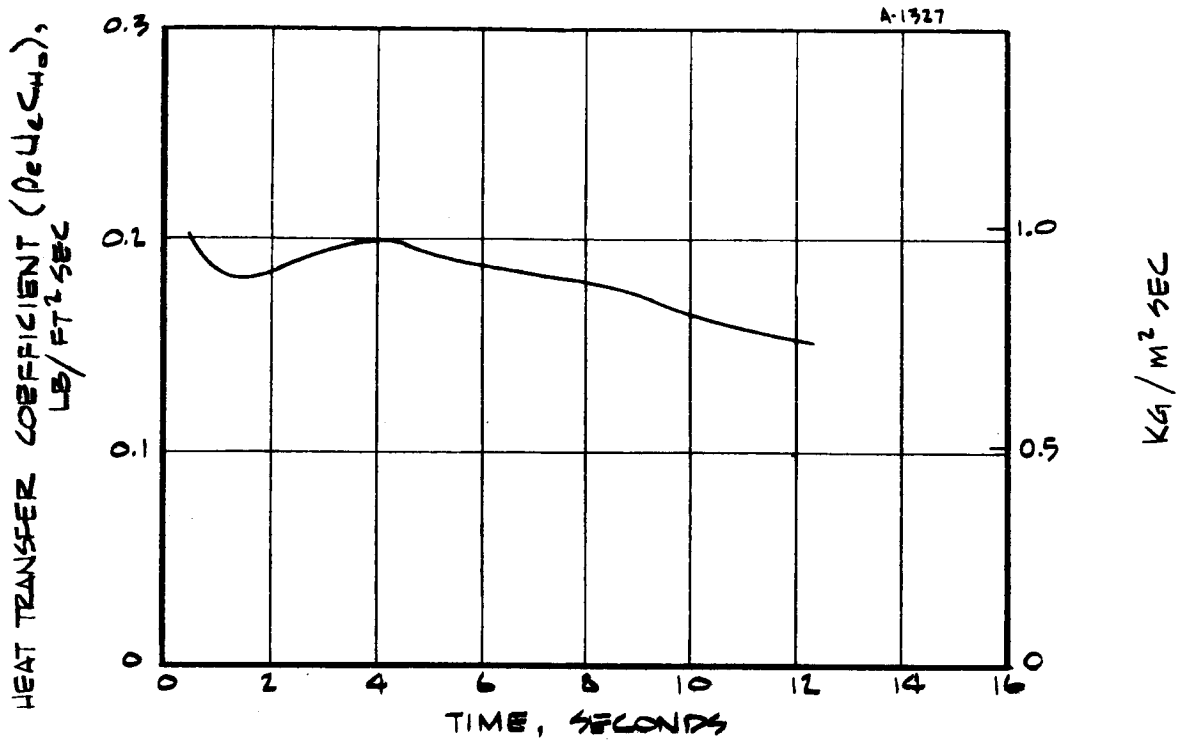


I) TEST 1113, O/F = 2.0

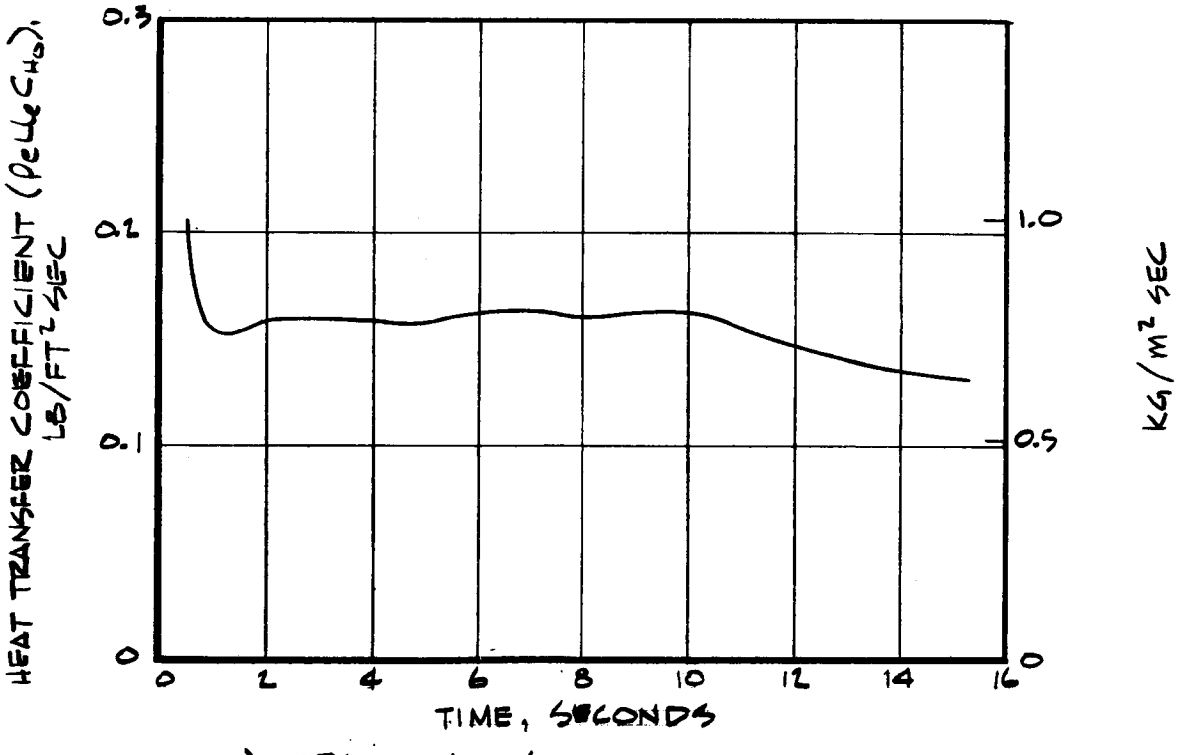


J) TEST 1126, O/F = 2.0

FIGURE 18 (CONTINUED)

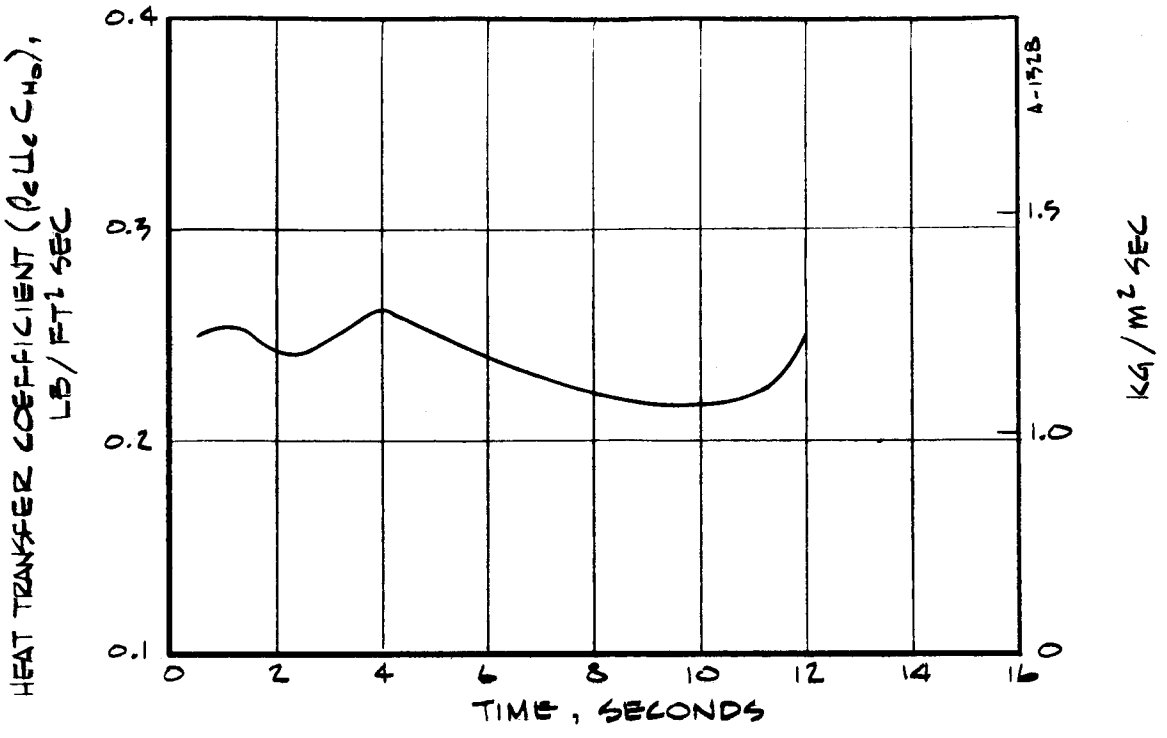


K) TEST 1115, O/F = 2.0

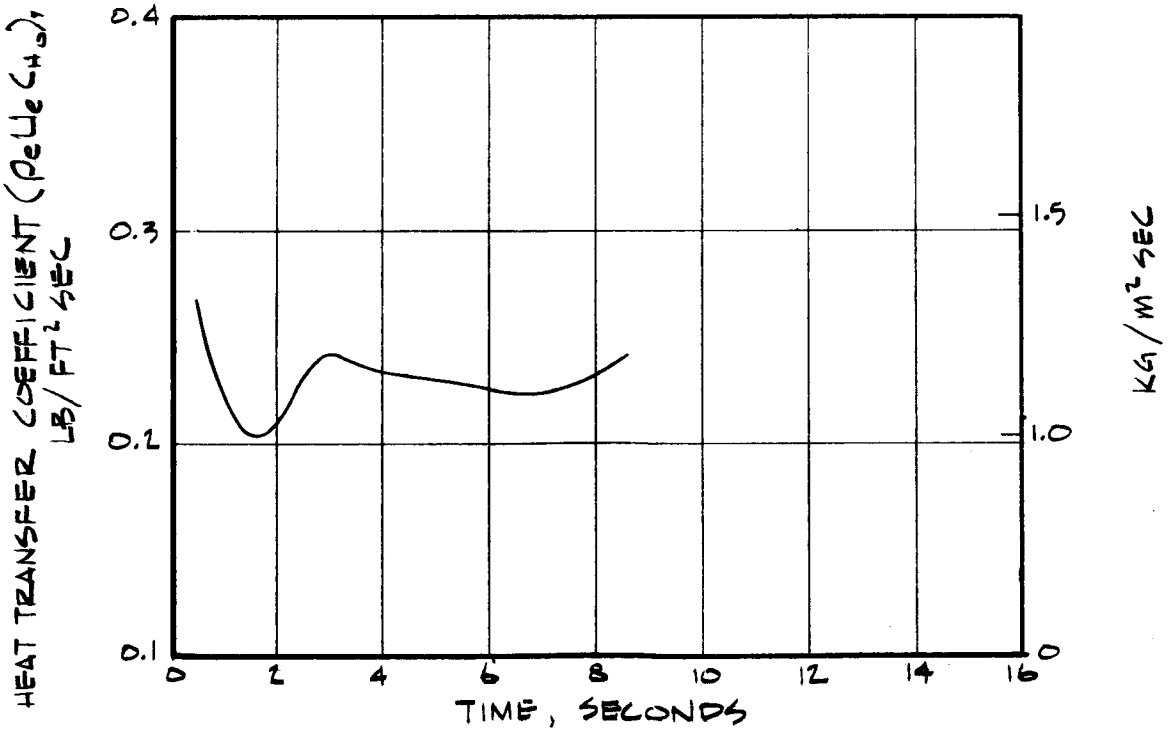


L) TEST 1114, O/F = 2.0,

FIGURE 18 (CONTINUED)

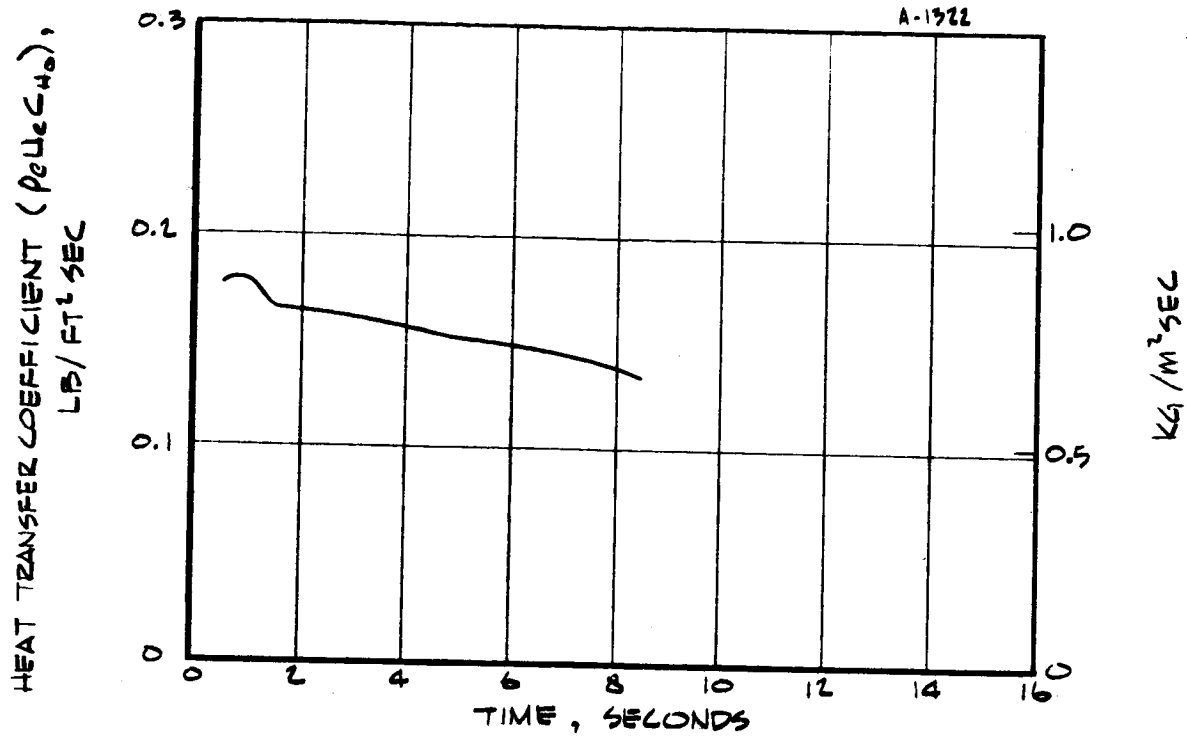


M) TEST 1119, O/F = 2.0

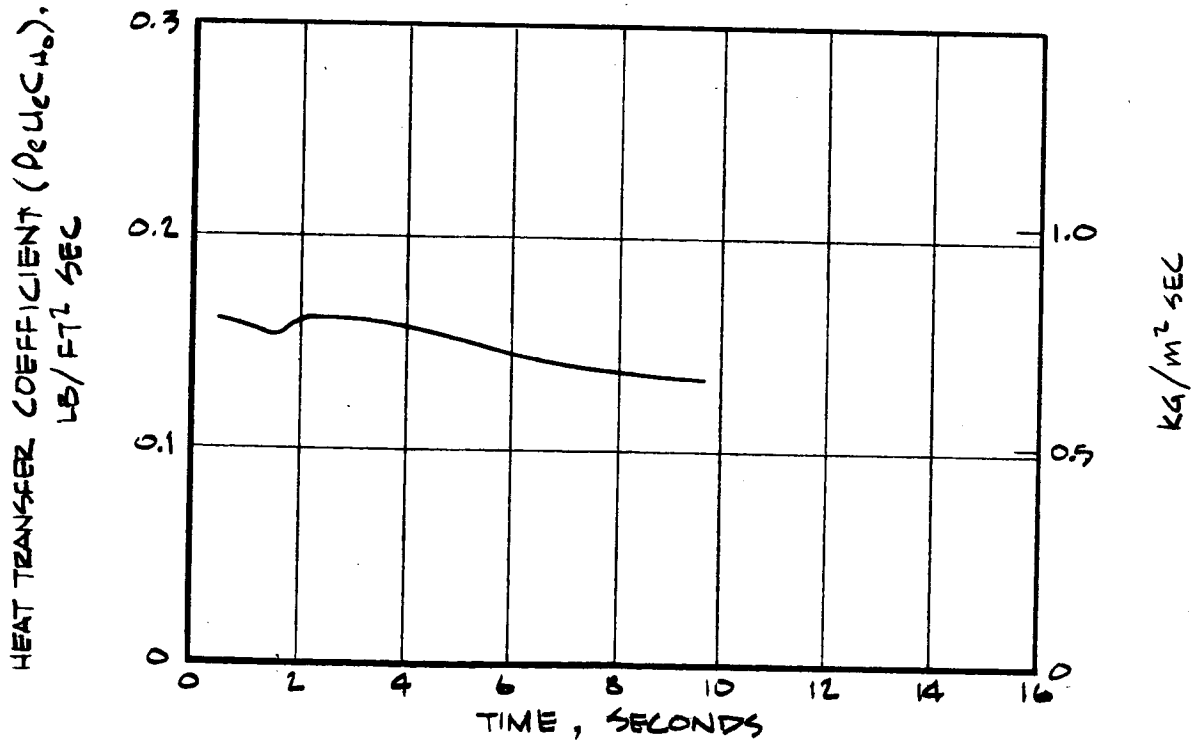


N) TEST 1118, O/F = 2.0

FIGURE 18, (CONTINUED)

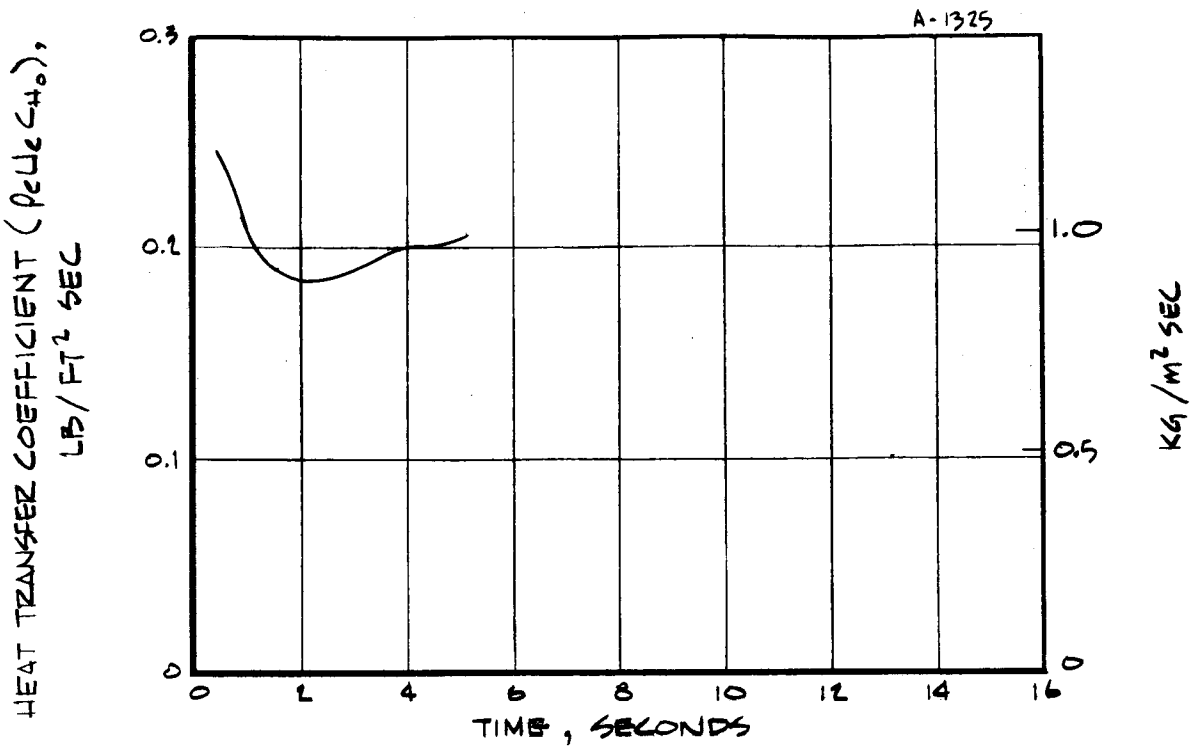


O) TEST 1096, O/F = 1.0

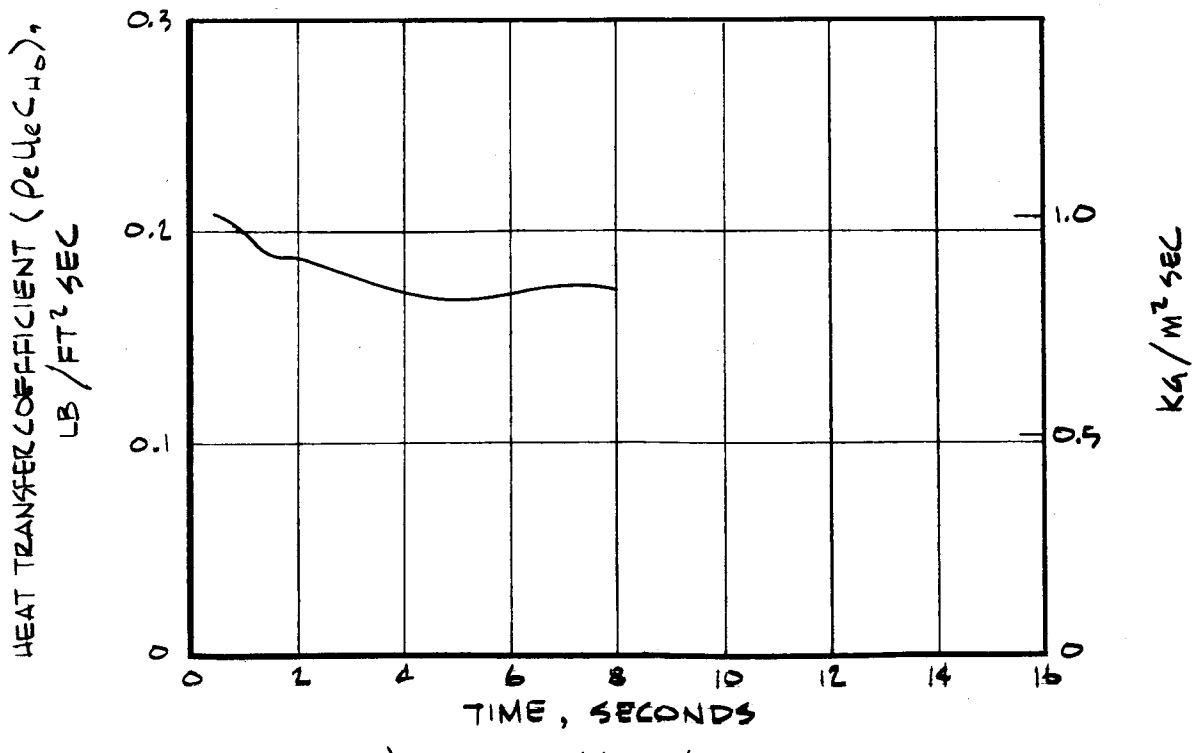


P) TEST 1097, O/F = 1.0

FIGURE 18 (CONTINUED)



Q) TEST 1143, O/F = 0.38



R) TEST 1144, O/F = 0.38

FIGURE 18 (CONCLUDED)

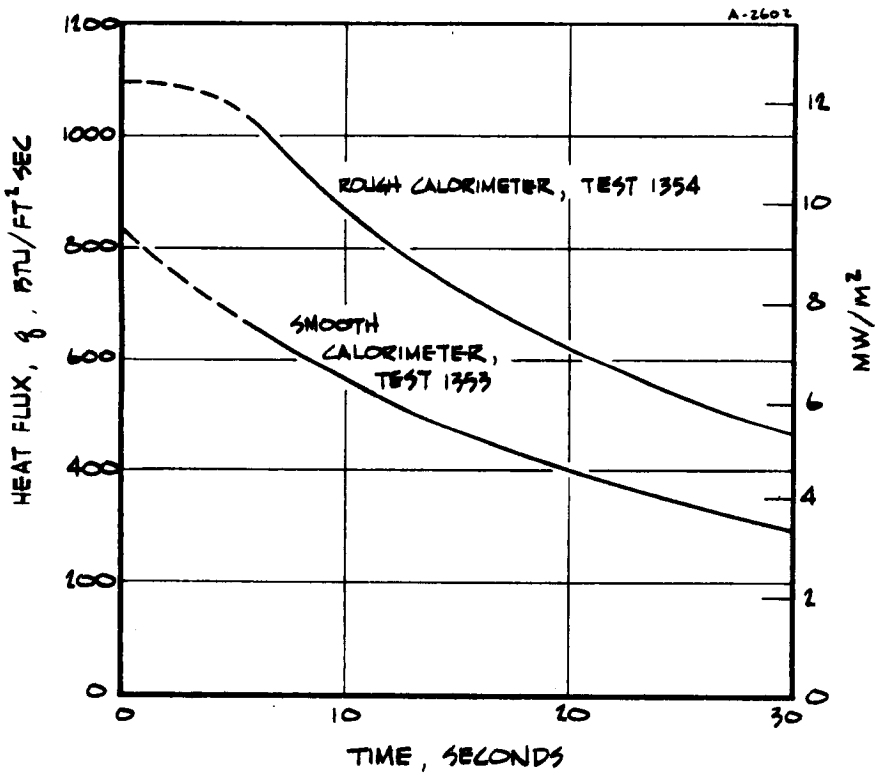


FIGURE 19, MOLYBDENUM TRANSIENT CALORIMETER HEAT FLUX HISTORIES PREDICTED FROM MEASURED THERMOCOUPLE DATA BY INVERSE HEAT CONDUCTION CODE

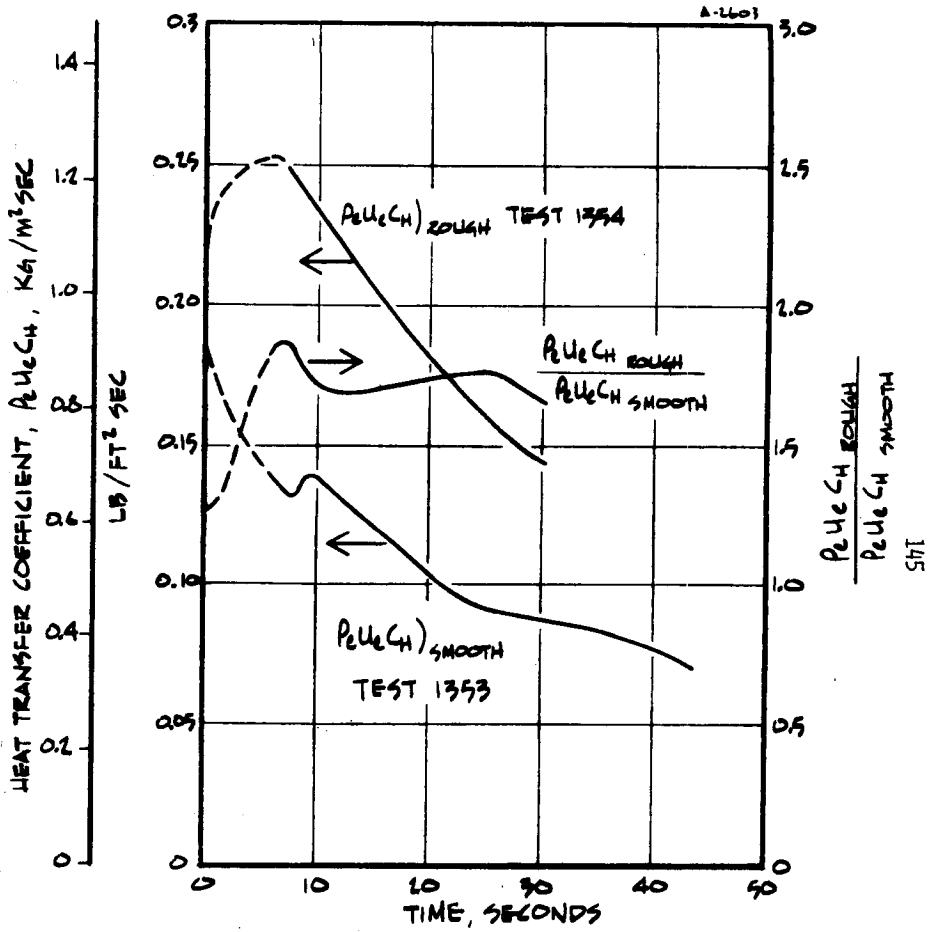


FIGURE 20 CONVECTIVE TRANSFER COEFFICIENT HISTORIES DERIVED FROM TRANSIENT MOLYBDENUM CALORIMETER HEAT FLUX DATA

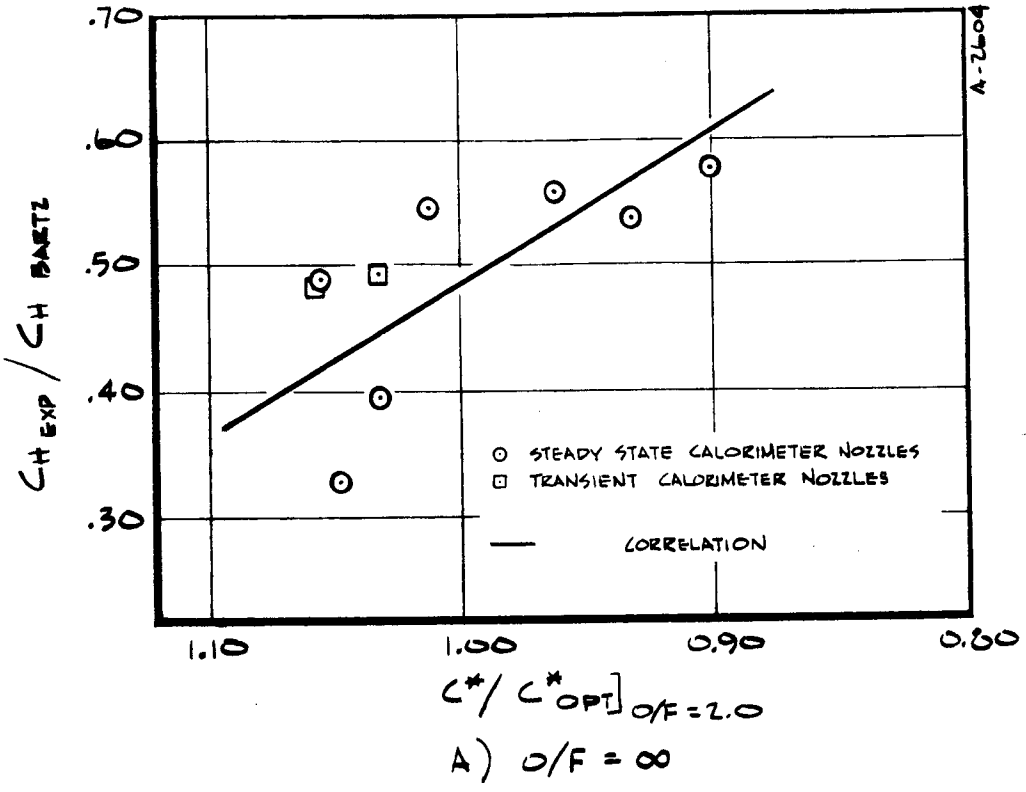
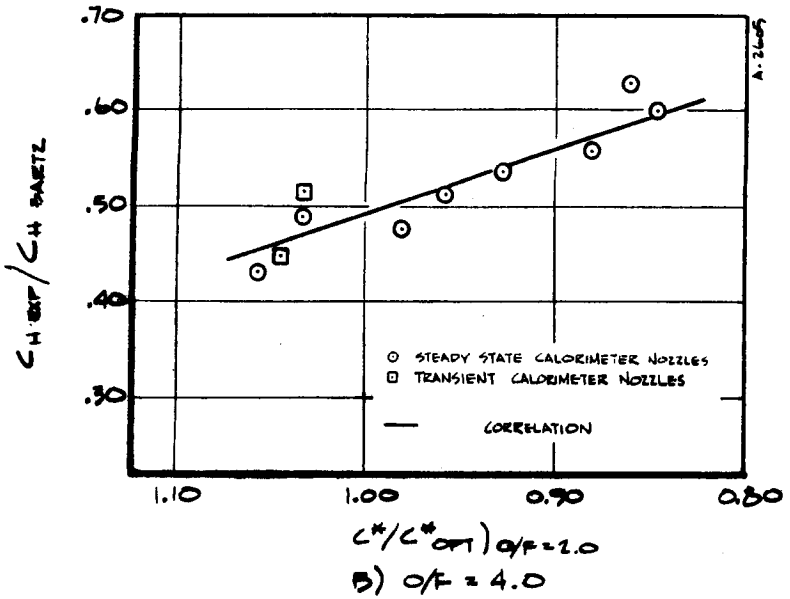
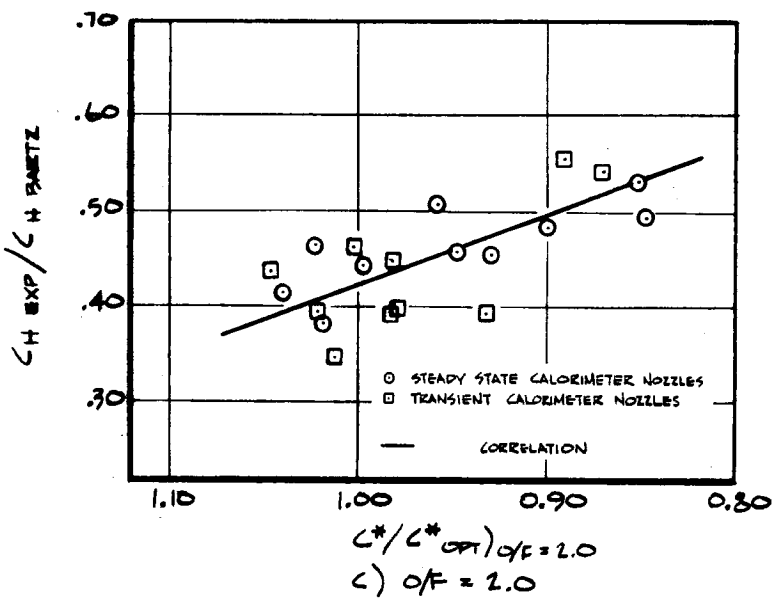


FIGURE 21 RATIO OF NOZZLE THROAT HEAT TRANSFER COEFFICIENT MEASURED WITH CALORIMETER TO THAT CALCULATED FROM BARTZ EQUATION FOR SAME CONDITIONS — AS A FUNCTION OF CHARACTERISTIC VELOCITY RATIO

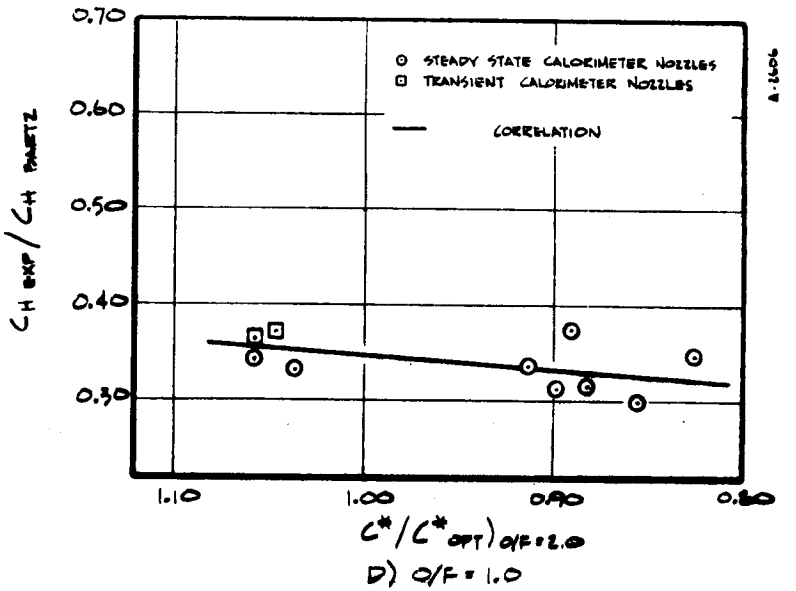


B) O/F = 4.0

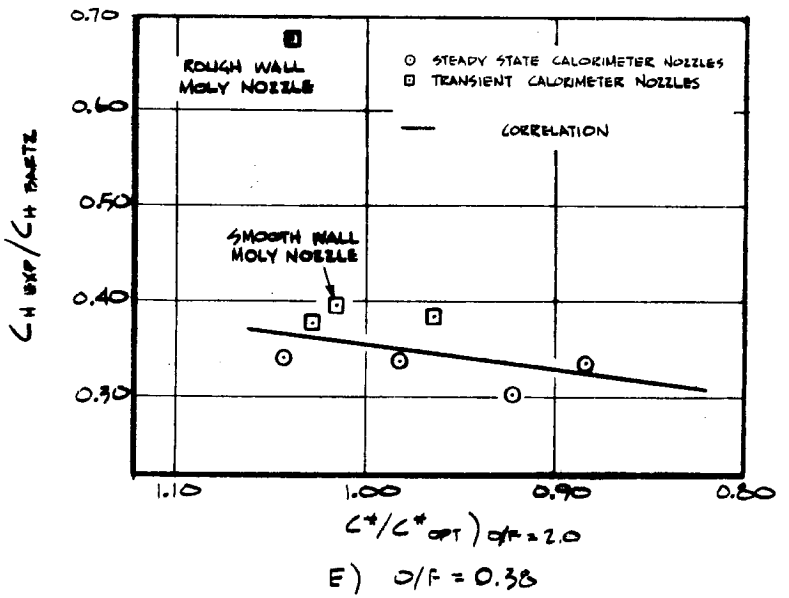


C) O/F = 2.0

FIGURE 21, CONTINUED



D) O/F = 1.0



E) O/F = 0.38

FIGURE 21, CONCLUDED

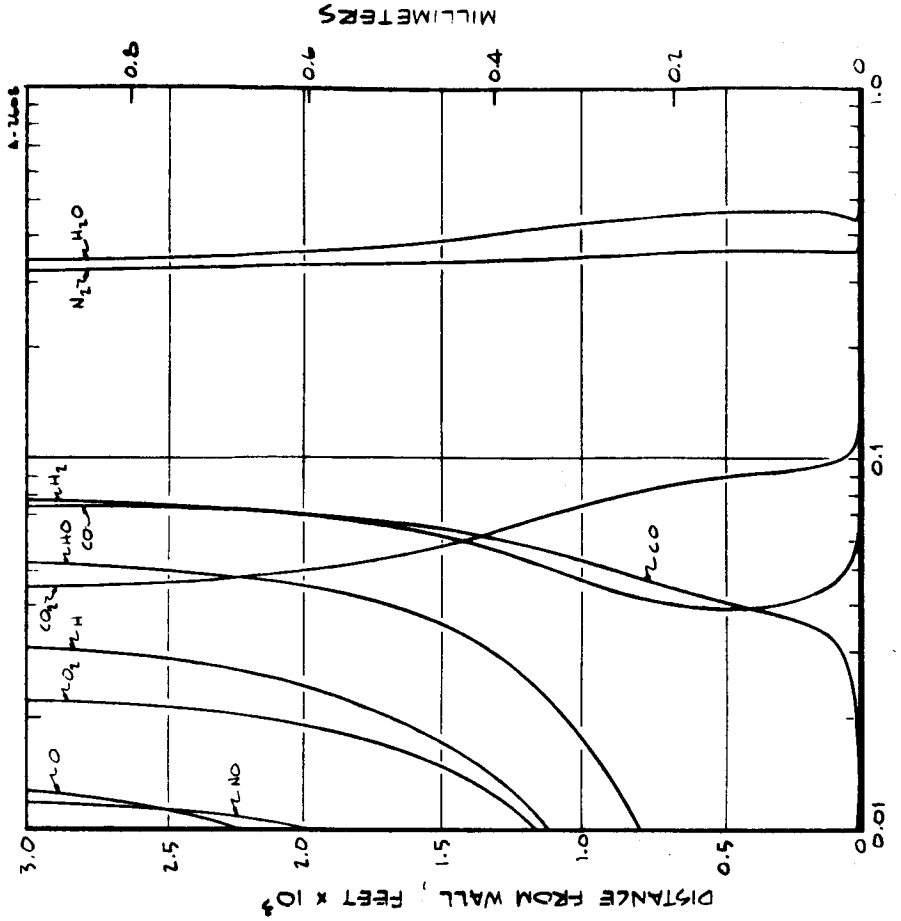


FIGURE 13 PREDICTED SPECIES CONCENTRATION PROFILES FOR A FULLY TURBULENT BOUNDARY LAYER AT $\lambda = 0.2067$ FT FOR A TYPICAL STEADY STATE CALORIMETER (TEST 1109 A O/F = 1.0)

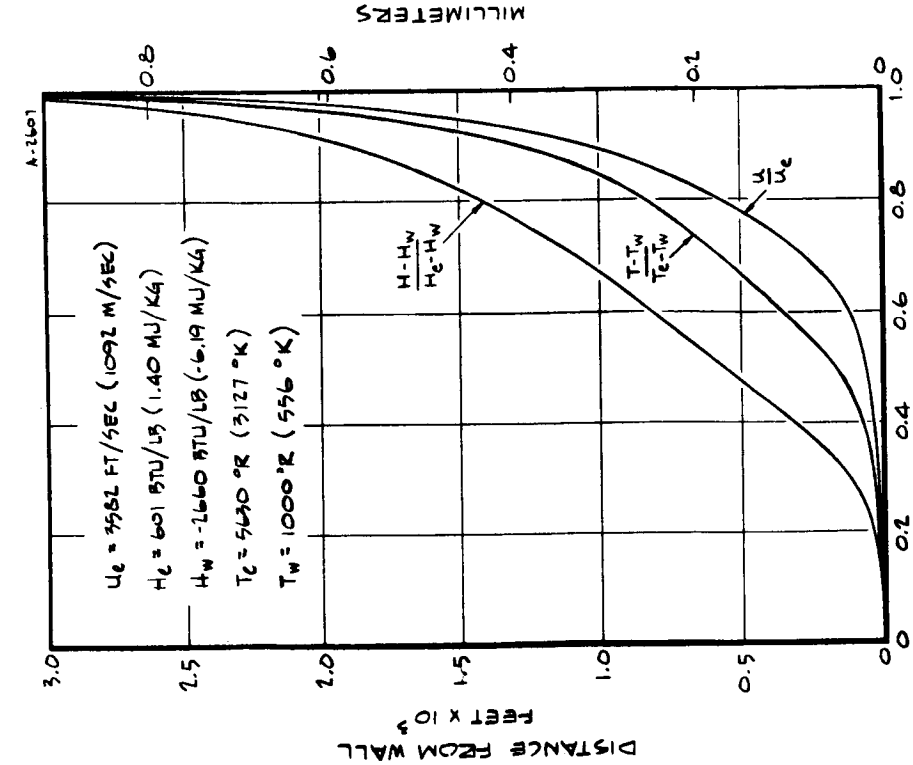


FIGURE 12 PREDICTED PROFILES OF VELOCITY, TOTAL ENTHALPY, AND TEMPERATURE FOR A FULLY TURBULENT BOUNDARY LAYER AT $\lambda = 0.2067$ FT FOR A TYPICAL STEADY STATE CALORIMETER (TEST 1109 A O/F = 1.0)

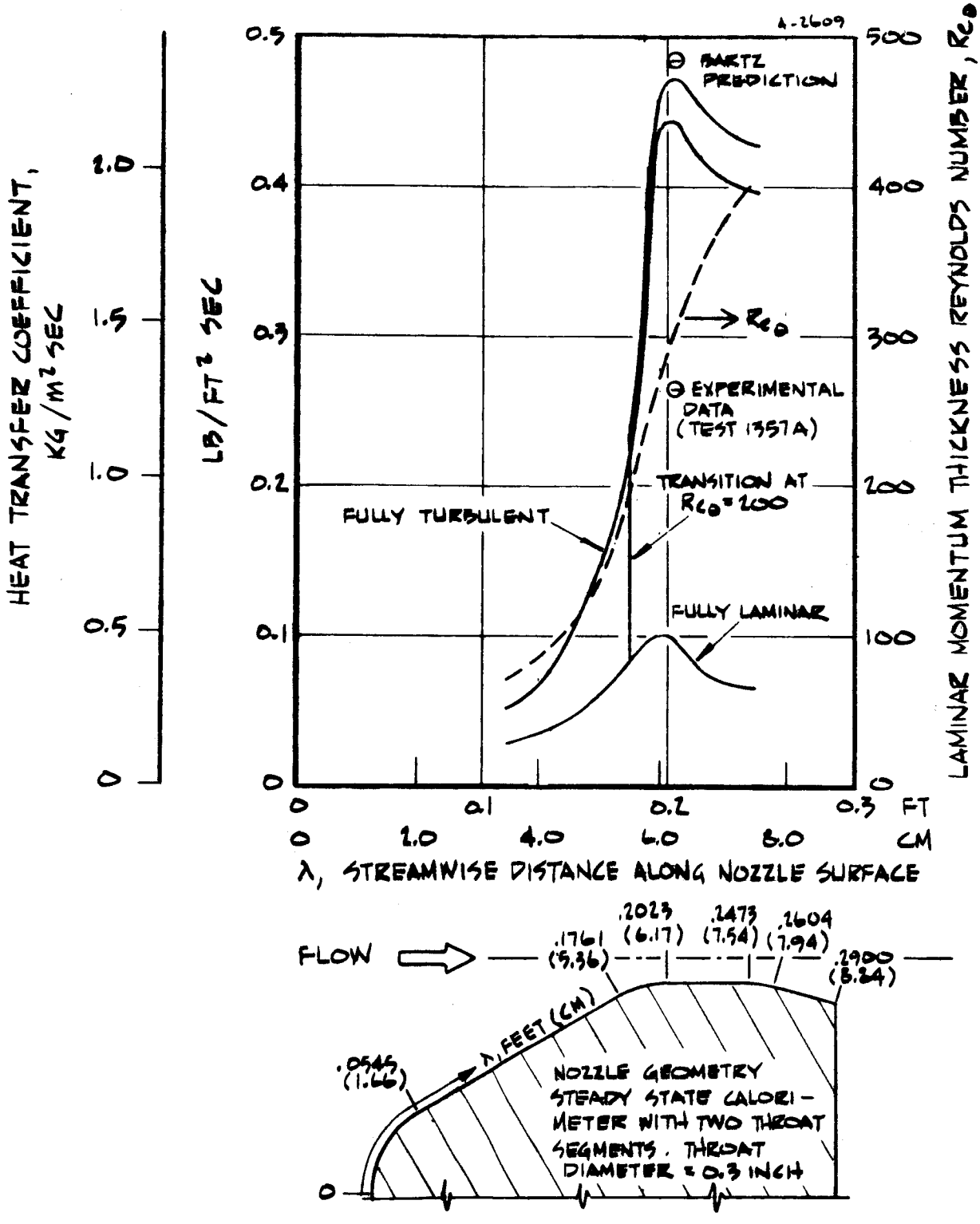
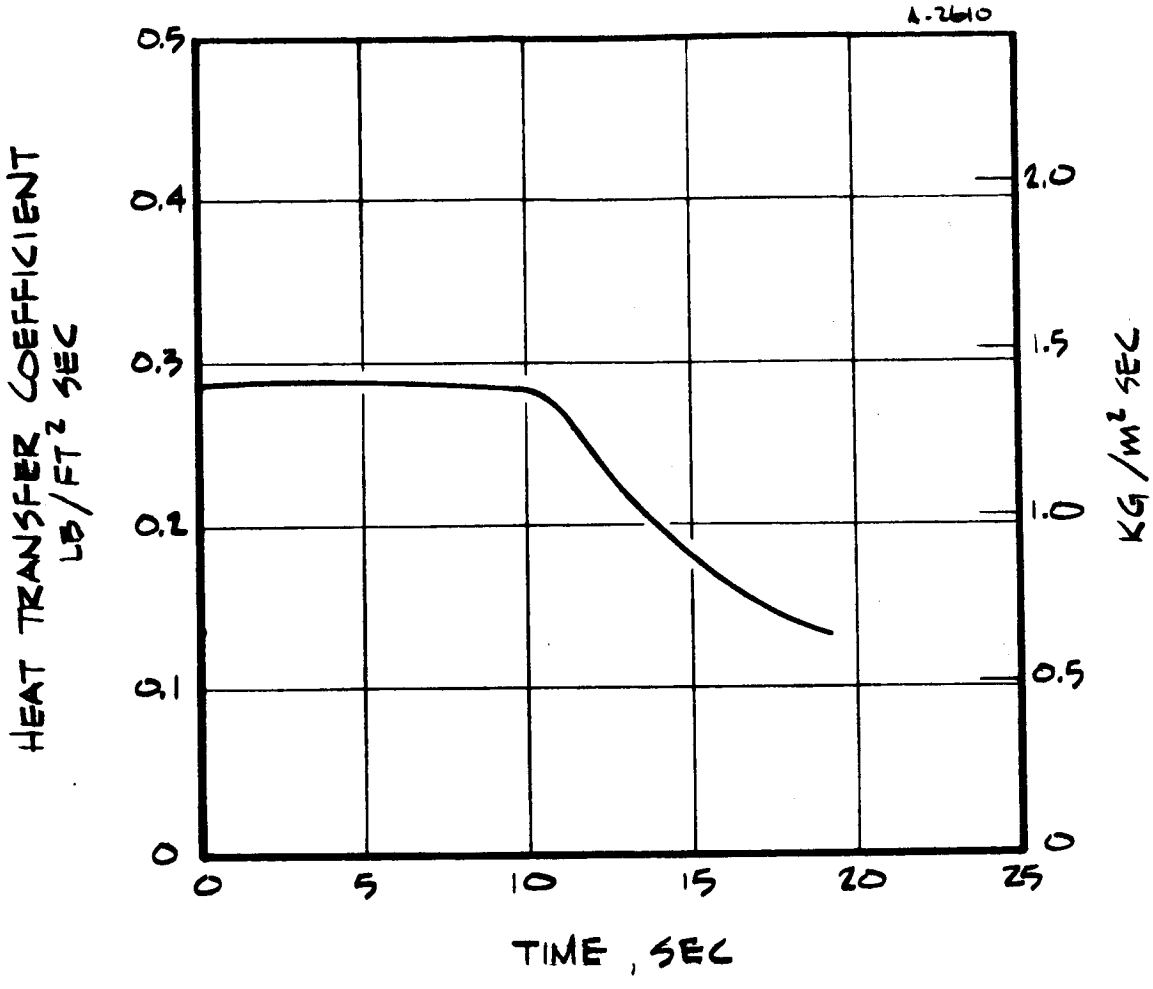
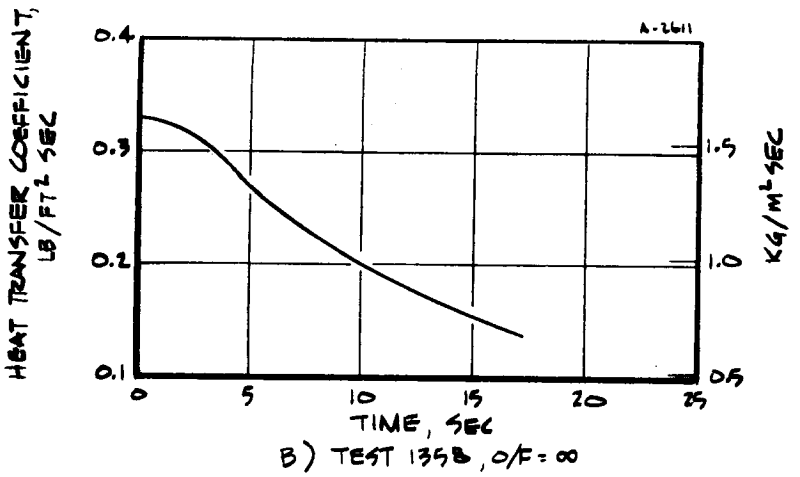


FIGURE 14 BLIMP PREDICTIONS OF HEAT TRANSFER COEFFICIENT DISTRIBUTIONS SHOWING NOZZLE GEOMETRY AND MOMENTUM THICKNESS REYNOLDS NUMBER

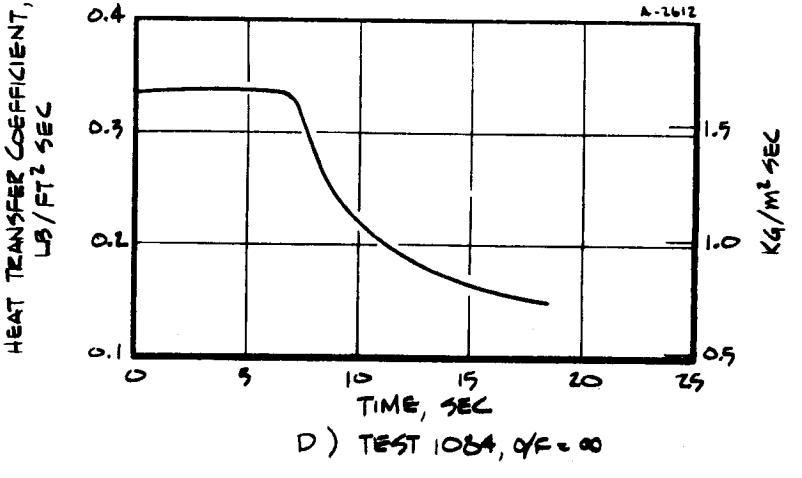


A) TEST 1083, O/F = ∞

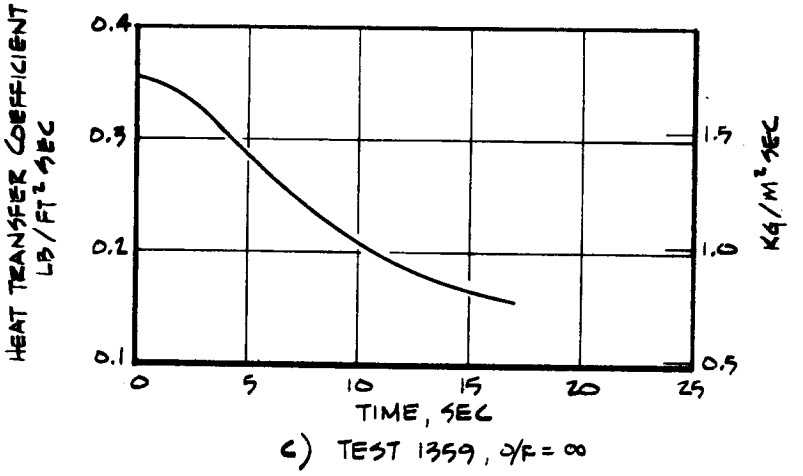
FIGURE 25 HEAT TRANSFER COEFFICIENT HISTORIES FOR ABLATIVE NOZZLES



B) TEST 1358, O/F = ∞

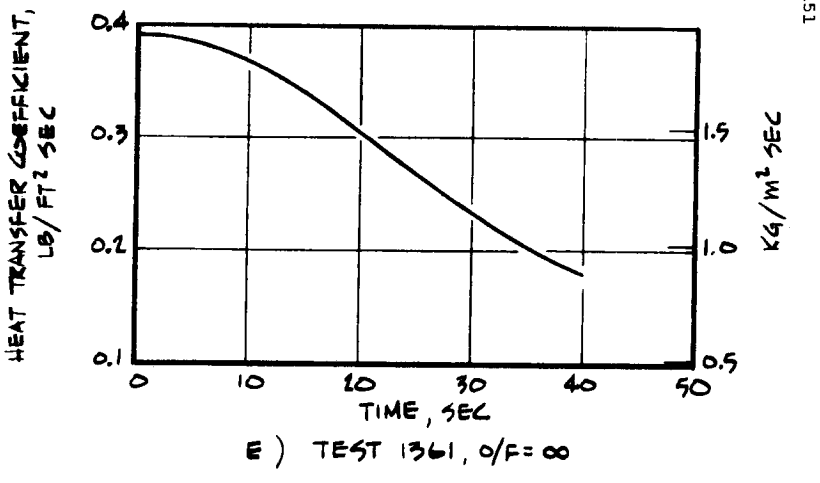


D) TEST 1084, O/F = ∞



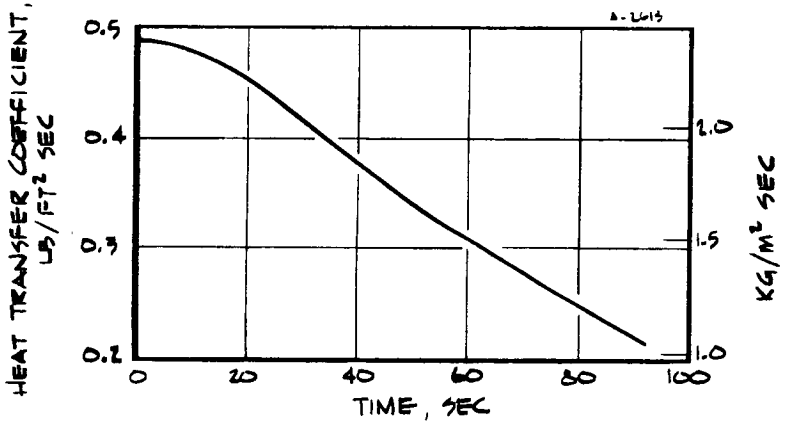
C) TEST 1359, O/F = ∞

FIGURE 25, CONTINUED

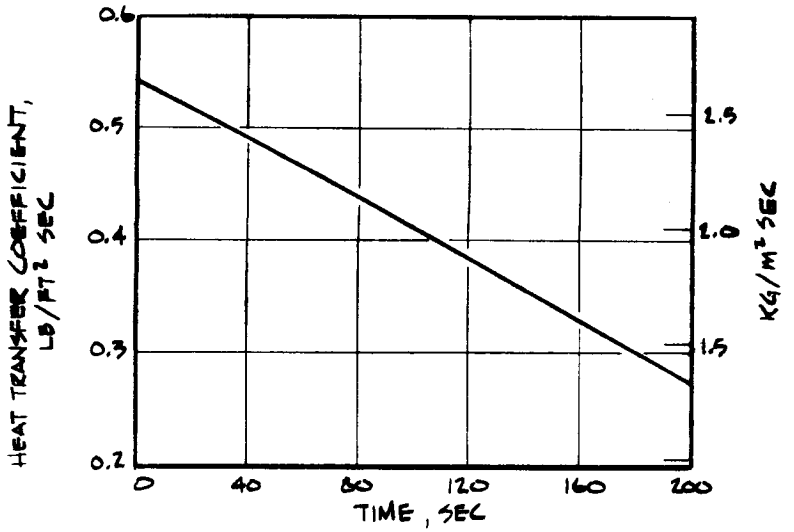


E) TEST 1361, O/F = ∞

FIGURE 25, CONTINUED

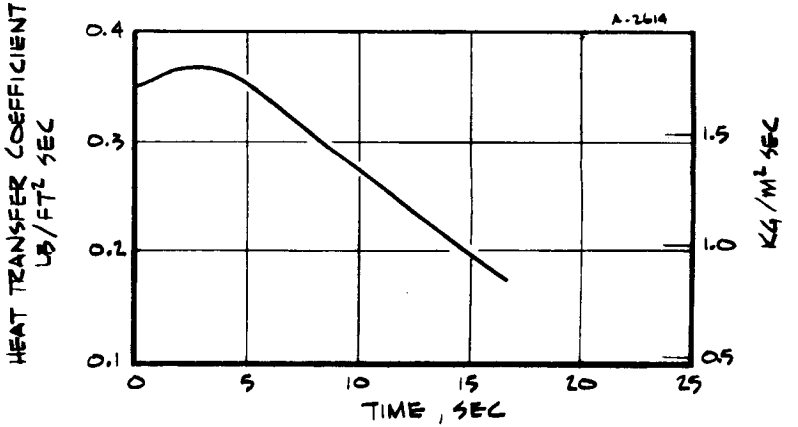


F) TEST 1362, O/F = ∞

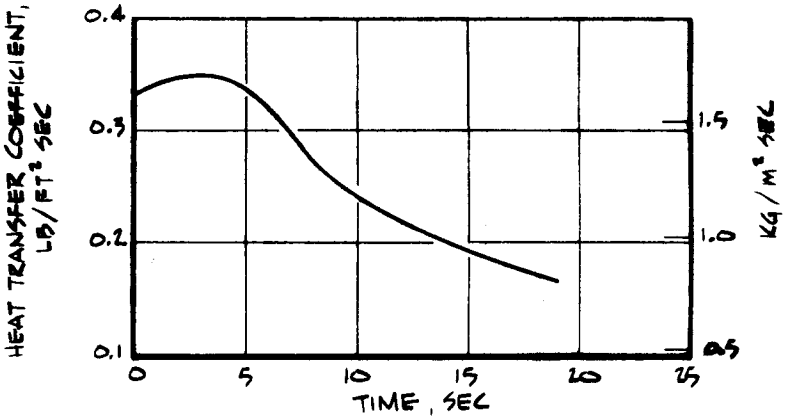


G) TEST 1360, O/F = ∞

FIGURE 25, CONTINUED



H) TEST 1091, O/F = 4.0



I) TEST 1092, O/F = 4.0

FIGURE 25, CONTINUED

J) TEST 1329, O/F=4.0

K) TEST 1332, O/F=4.0

FIGURE 15, CONTINUED

L) TEST 1330, O/F=4.0

M) TEST 1331, O/F=4.0

FIGURE 15, CONTINUED

O) TEST 1134, O/F = 1.0

N) TEST 1135, O/F = 2.0

FIGURE 15, CONTINUED

Q) TEST 1125, O/F 2.0

P) TEST 1124, O/F = 2.0

FIGURE 15, CONTINUED

R) TEST 1128, O/F = 2.0

S) TEST 1129, O/F = 2.0

FIGURE 15, CONTINUED

T) TEST 1120, O/F = 2.0

U) TEST 1117, O/F = 2.0

FIGURE 15, CONTINUED

X) TEST 1098, O/F = 1.0

Y) TEST 1099, O/F = 1.0

FIGURE 15, CONTINUED

V) TEST 1121, O/F = 2.0

W) TEST 1116, O/F = 2.0

FIGURE 15, CONTINUED

AA) TEST 1336, O/F = 1.0

Z) TEST 1338, O/F = 1.0

FIGURE 25, CONTINUED

CC) TEST 1337, O/F = 1.0

BB) TEST 1339, O/F = 1.0

FIGURE 25, CONTINUED

FF) TEST 1146, O/F = 0.38

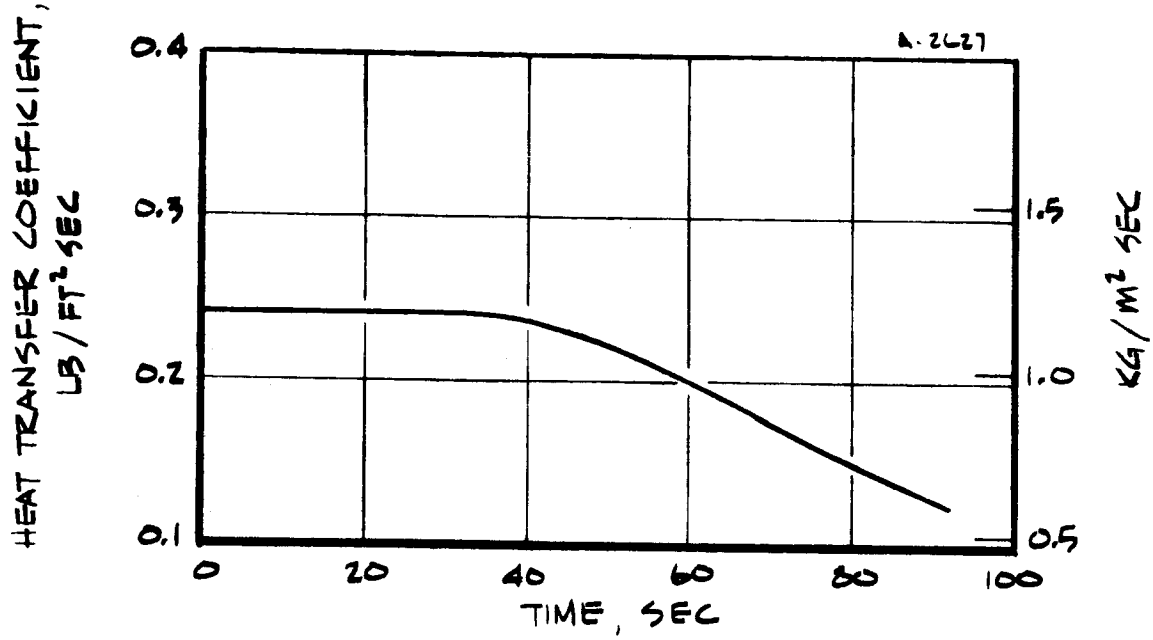
GG) TEST 1350, O/F = 0.38

FIGURE 25, CONTINUED

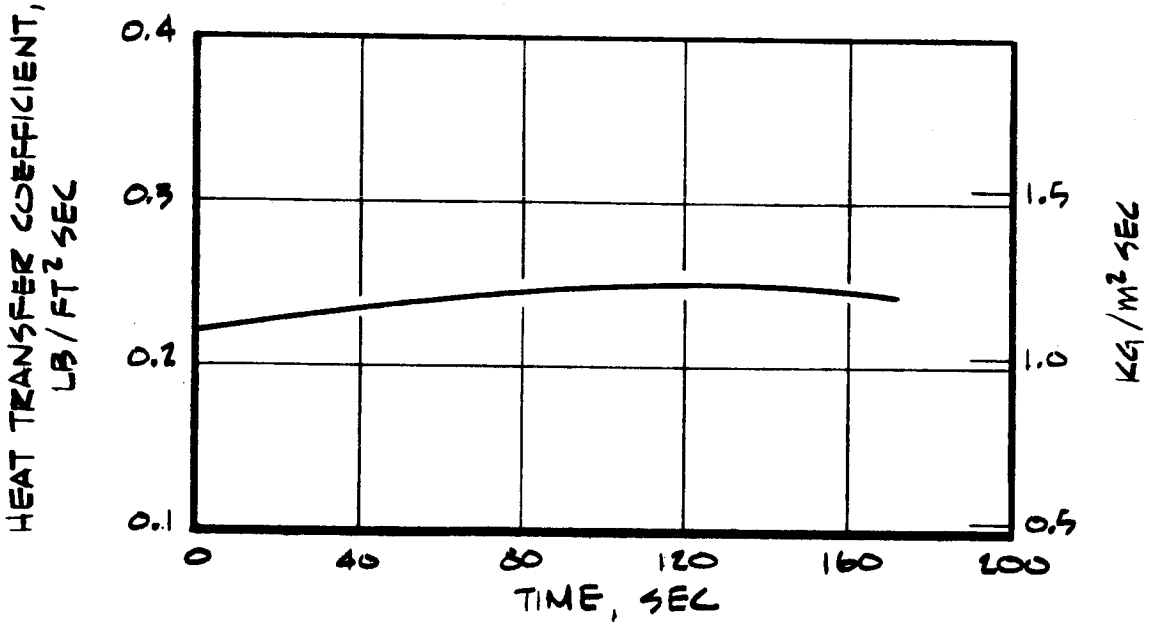
DD) TEST 1145, O/F = 0.38

EE) TEST 1348, O/F = 0.38

FIGURE 25, CONTINUED

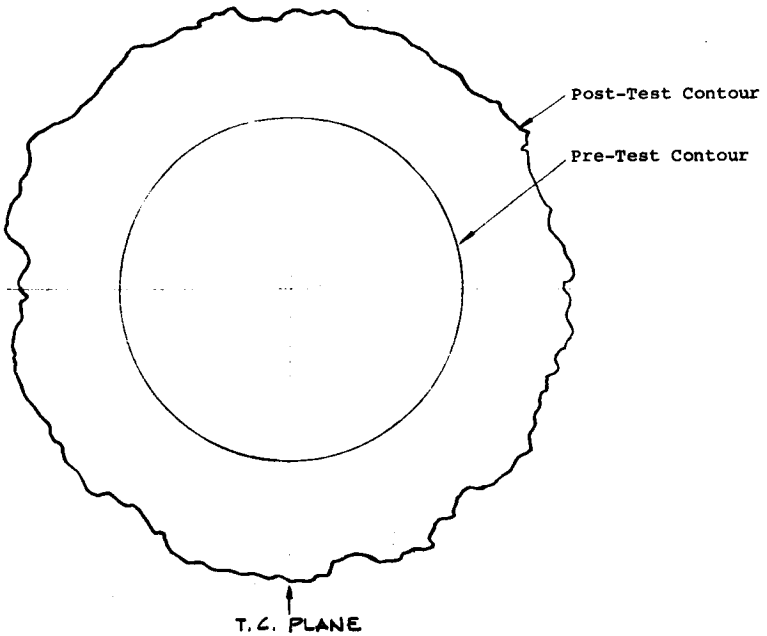


HH) TEST 1347, O/F = 0.38



II) TEST 1349, O/F = 0.38

FIGURE 25, CONCLUDED



Pre-Test Diameter 0.305
Post-Test Average Diameter 0.506
Average Surface Recession 0.1005
Surface Recession at Thermocouple Plane 0.1035
Char Depth at Thermocouple Plane 0.217

THERMOCOUPLE DEPTHS

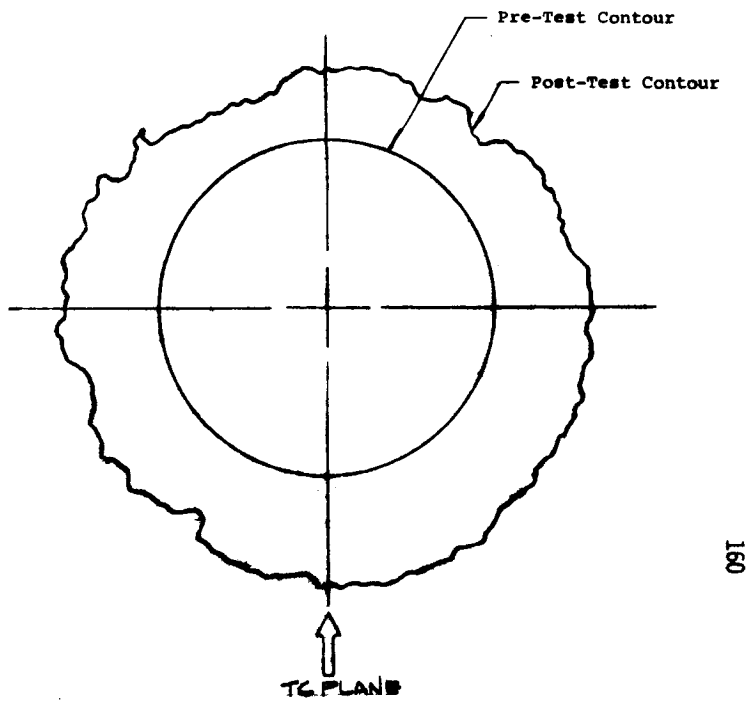
#1 0.130
#2 0.192
#3 0.261

Char and T.C. depths relative to initial surface.
All dimensions in inches.

A) Test 1083, Nozzle NL-11, O/F = ∞

Figure 26, Pre- and Post-Test Ablative Nozzle Throat Contours Including Measured Char Depth and Thermocouple Locations

A-2678



Pre-Test Diameter 0.302
Post-Test Average Diameter 0.477
Average Surface Recession 0.088
Surface Recession at Thermocouple Plane 0.106
Average Char Depth 0.229

THERMOCOUPLE DEPTHS

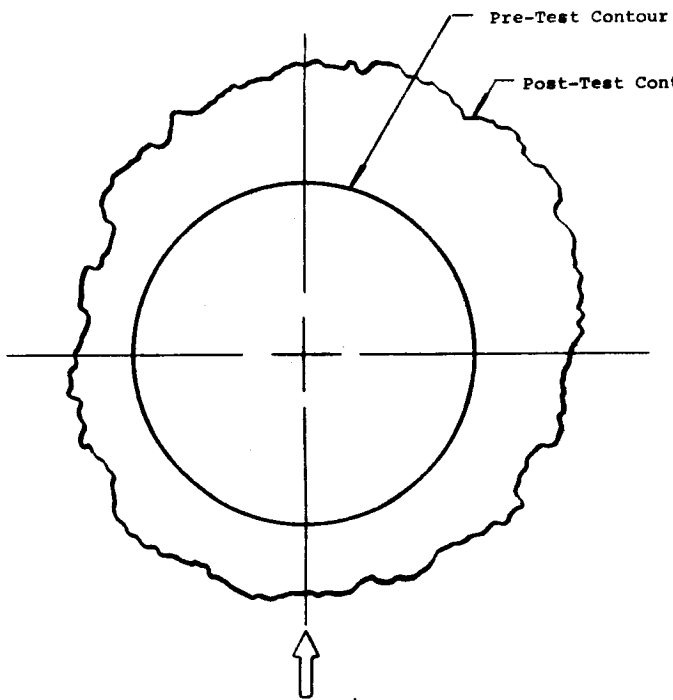
#1 0.124
#2 0.211
#3 0.276

Char and T.C. depths relative to initial surface.
All dimensions in inches.

B) Test 1358, Nozzle NL-42, O/F = ∞

Figure 26, continued.

A-2678



Pre-Test Diameter 0.299
Post-Test Average Diameter 0.459
Average Surface Recession 0.080
Surface Recession at Thermocouple Plane 0.057
Average Char Depth 0.236

THERMOCOUPLE DEPTHS

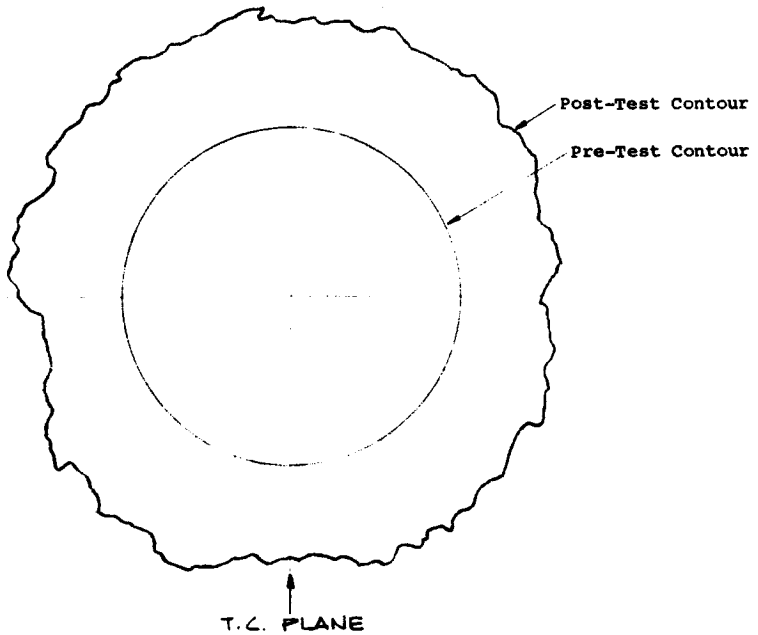
#1	0.125
#2	0.219
#3	0.270

Char and T.C. depths relative to initial surface.
All dimensions in inches.

C) Test 1359, Nozzle NL-43, O/F = ∞

Figure 26, continued.

A-2630



Pre-Test Diameter 0.298
Post-Test Average Diameter 0.492
Average Surface Recession 0.097
Surface Recession at Thermocouple Plane 0.097
Char Depth at Thermocouple Plane 0.225

THERMOCOUPLE DEPTHS

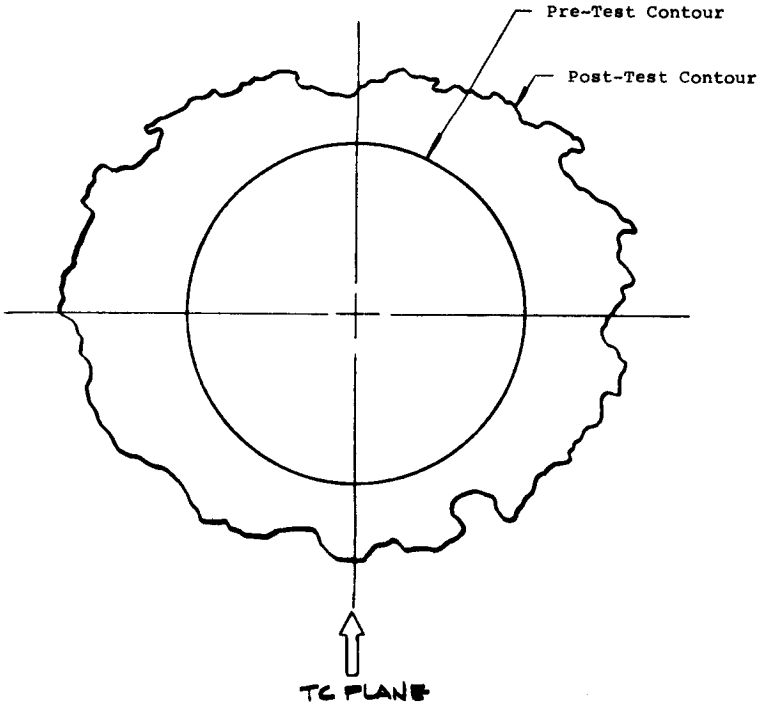
#1	0.125
#2	0.194
#3	0.298

Char and T.C. depths relative to initial surface.
All dimensions in inches.

D) Test 1084, Nozzle NL-12, O/F = ∞

Figure 26, continued.

A-2631



Pre-Test Diameter 0.300
Post-Test Average Diameter 0.470
Average Surface Recession 0.085
Surface Recession at Thermocouple Plane 0.074
Average Char Depth 0.300

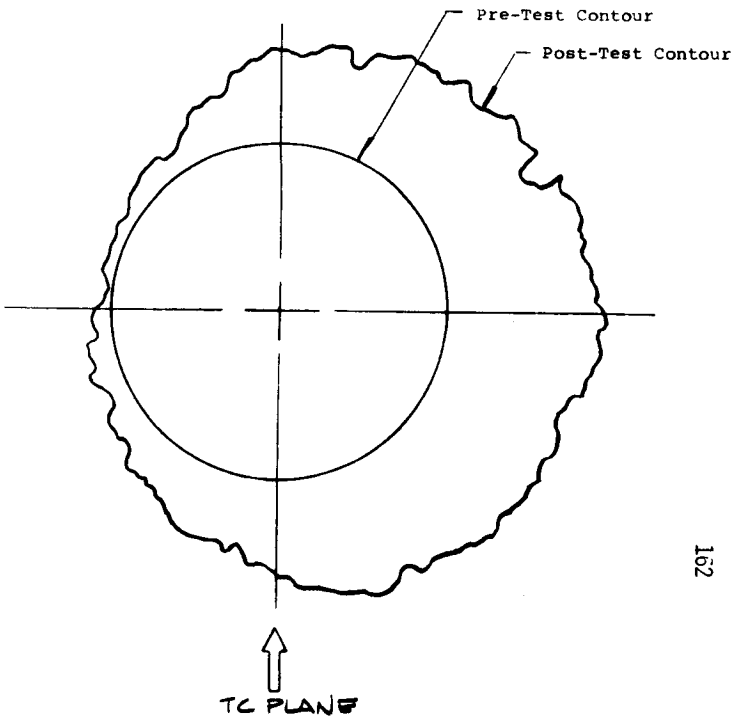
THERMOCOUPLE DEPTHS

#1	0.121
#2	0.203
#3	0.262

Char and T.C. depths relative to initial surface.
All dimensions in inches.

E) Test 1361, Nozzle NL-40, O/F = ∞
Figure 26, continued

A-2632



Pre-Test Diameter 0.300
Post-Test Average Diameter 0.464
Average Surface Recession 0.082
Surface Recession at Thermocouple Plane 0.089
Average Char Depth 0.420

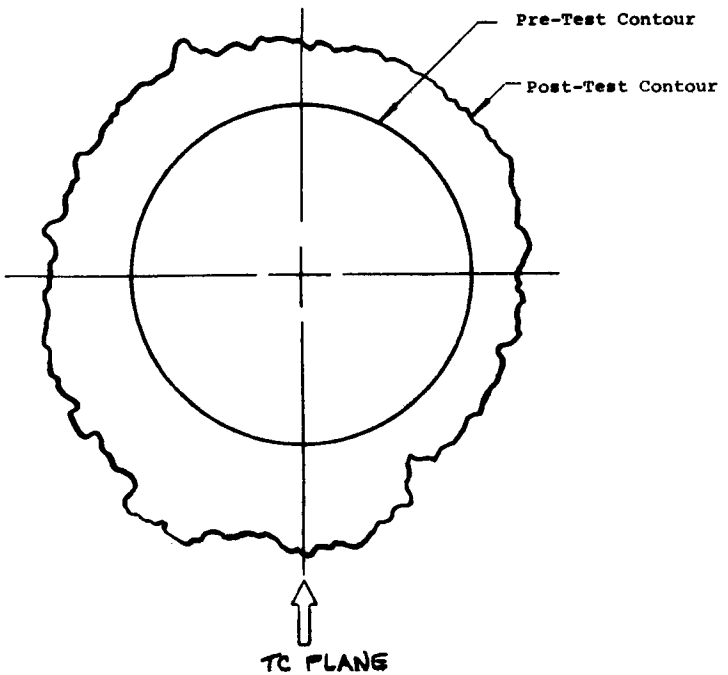
THERMOCOUPLE DEPTHS

#1	0.136
#2	0.188
#3	0.273

Char and T.C. depths relative to initial surface.
All dimensions in inches.

F) Test 1362, Nozzle NL-41, O/F = ∞
Figure 26, continued.

A-2633



Pre-Test Diameter 0.299
Post-Test Average Diameter 0.454
Average Surface Recession 0.078
Surface Recession at Thermocouple Plane 0.113
Average Char Depth 0.621

THERMOCOUPLE DEPTHS

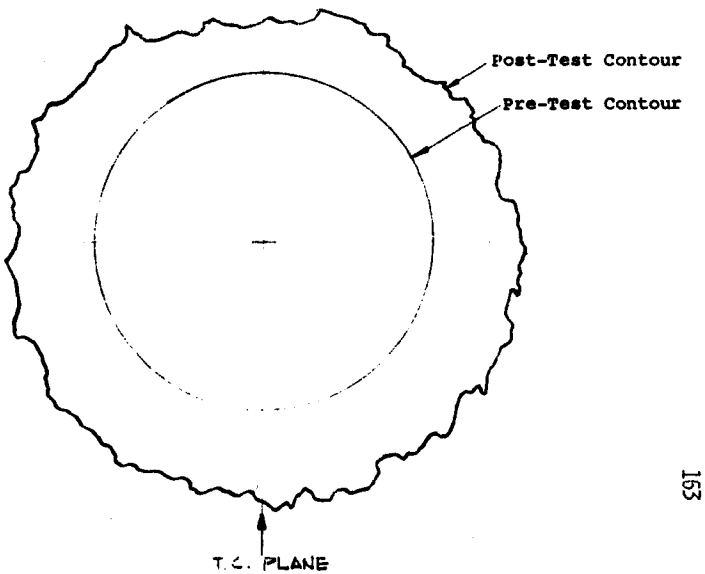
#1	0.128
#2	0.187
#3	0.272

Char and T.C. depths relative to initial surface.
All dimensions in inches.

G) Test 1360, Nozzle NL-44, O/F = ∞

Figure 26, continued.

A-2654



Pre-Test Diameter 0.300
Post-Test Average Diameter 0.447
Average Surface Recession 0.0735
Surface Recession at Thermocouple Plane 0.072
Char Depth at Thermocouple Plane 0.208

THERMOCOUPLE DEPTHS

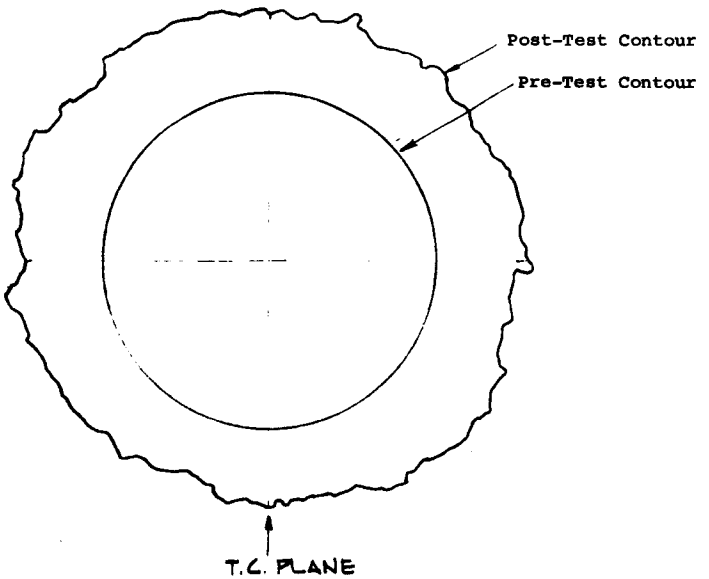
#1	0.107
#2	0.199
#3	0.262

Char and T.C. depths relative to initial surface.
All dimensions in inches.

H) Test 1091, Nozzle NL-13, O/F = 4.0

Figure 26, continued.

A-2655



Pre-Test Diameter 0.300
Post-Test Average Diameter 0.455
Average Surface Recession 0.0775
Surface Recession at Thermocouple Plane 0.072
Char Depth at Thermocouple Plane 0.218

THERMOCOUPLE DEPTHS

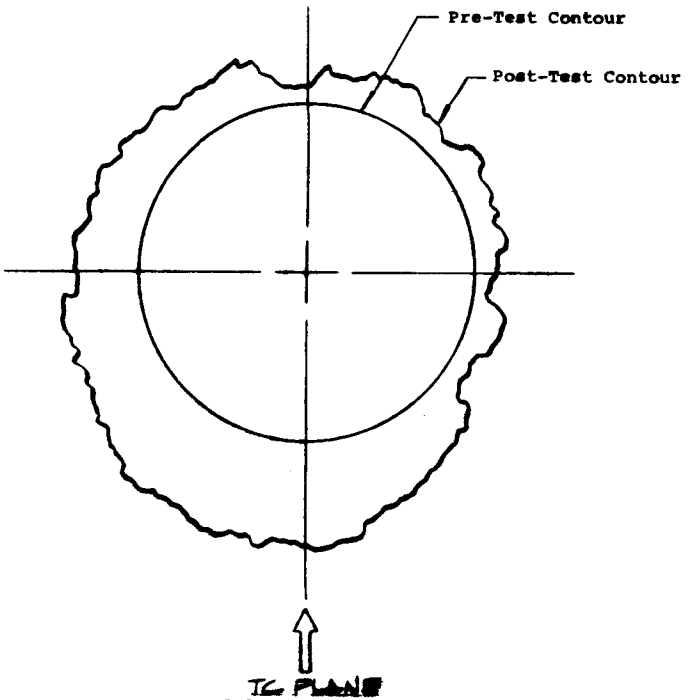
#1 0.123
#2 0.184
#3 0.263

Char and T.C. depths relative to initial surface
All dimension in inches

I) Test 1092, Nozzle NL-14, O/F = 4.0

Figure 26, continued.

A-2636



Pre-Test Diameter 0.301
Post-Test Average Diameter 0.406
Average Surface Recession 0.050
Surface Recession at Thermocouple Plane 0.046
Average Char Depth 0.227

THERMOCOUPLE DEPTHS

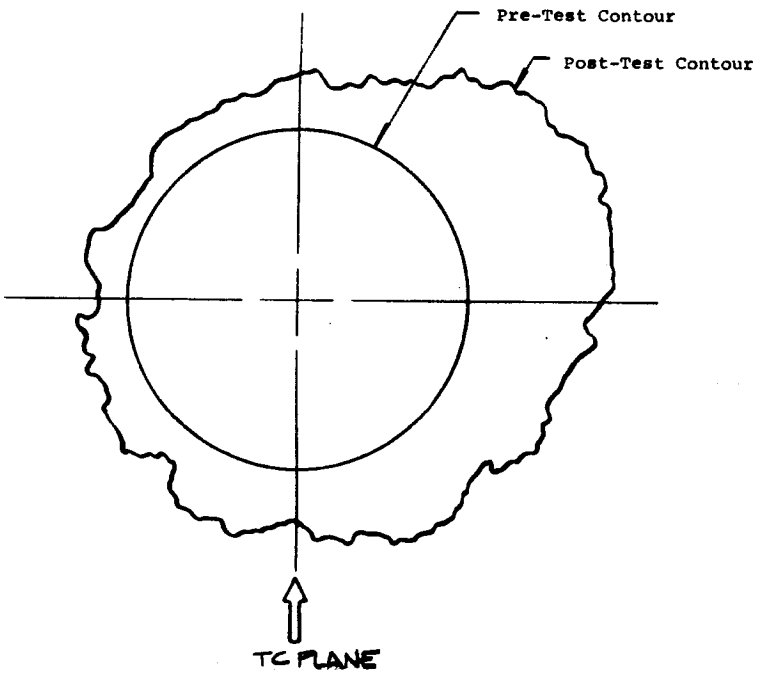
#1 0.131
#2 0.216
#3 0.274

Char and T.C. depths relative to initial surface.
All dimensions in inches.

J) Test 1329, Nozzle NL-28, O/F = 4.0

Figure 26, continued.

A-2647



Pre-Test Diameter 0.300
Post-Test Average Diameter 0.453
Average Surface Recession 0.077
Surface Recession at Thermocouple Plane 0.053
Average Char Depth 0.310

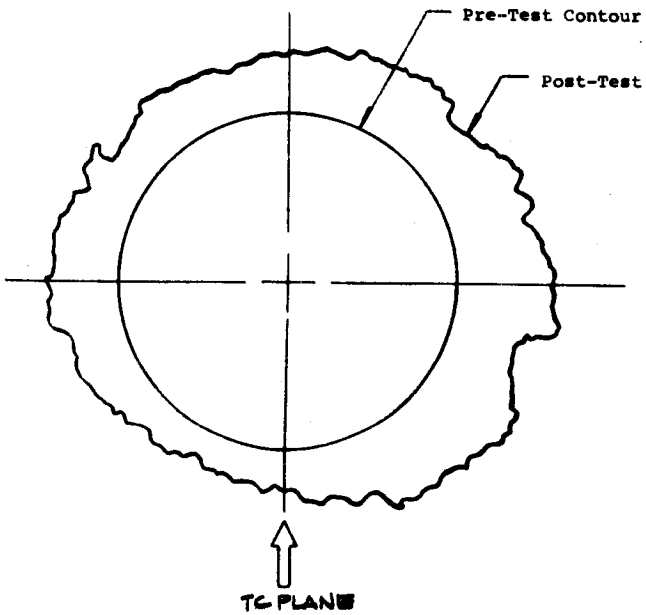
THERMOCOUPLE DEPTHS

#1	0.133
#2	0.199
#3	0.282

Char and T.C. depths relative to initial surface.
All dimensions in inches.

K) Test 1332, Nozzle NL-31, O/F = 4.0
Figure 26, continued.

A-2438



Pre-Test Diameter 0.299
Post-Test Average Diameter 0.433
Average Surface Recession 0.067
Surface Recession at Thermocouple Plane 0.045
Average Char Depth 0.430

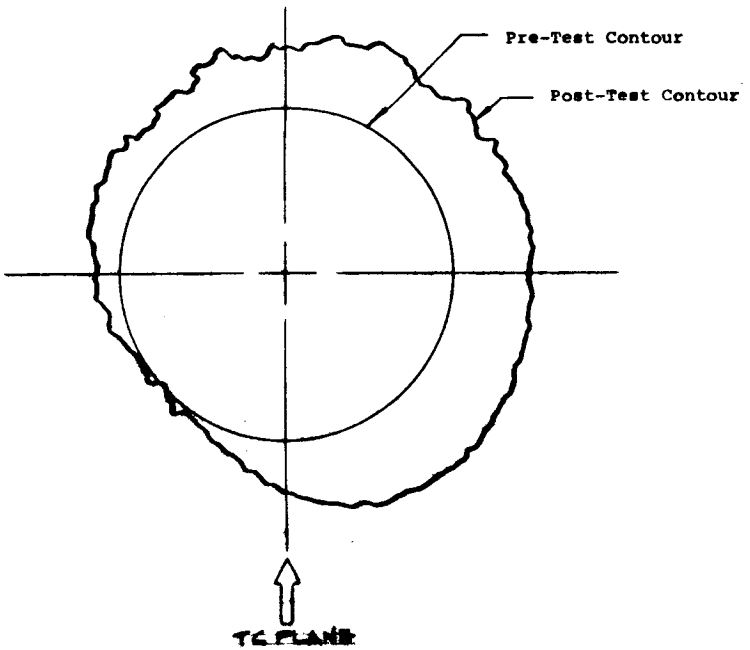
THERMOCOUPLE DEPTHS

#1	0.142
#2	0.196
#3	0.271

Char and T.C. depths relative to initial surface.
All dimensions in inches.

L) Test 1330, Nozzle NL-29, O/F = 4.0
Figure 26, continued.

A-2437



Pre-Test Diameter 0.300
Post-Test Average Diameter 0.404
Average Surface Recession 0.063
Surface Recession at Thermocouple Plane 0.063
Average Char Depth 0.591

THERMOCOUPLE DEPTHS

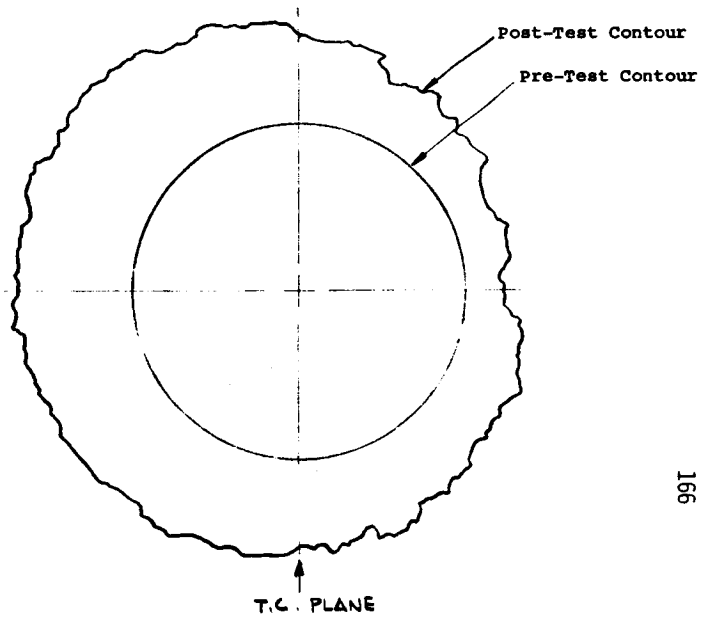
#1	0.261
#2	0.207
#3	0.273

Char and T.C. depths relative to initial surface.
All dimensions in inches.

M) Test 1331, Nozzle NL-30, O/F = 4.0

Figure 26, continued.

A-2640



Pre-Test Diameter 0.300
Post-Test Average Diameter 0.465
Average Surface Recession 0.083
Surface Recession at Thermocouple Plane 0.089
Char Depth at Thermocouple Plane 0.235

THERMOCOUPLE DEPTHS

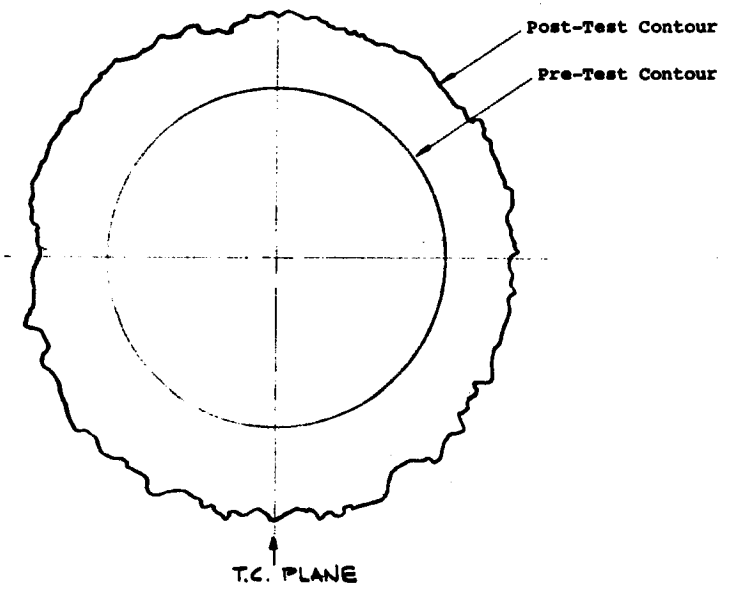
#1	0.115
#2	0.240
#3	0.282

Char and T. C. depths relative to initial surface.
All dimensions in inches.

N) Test 1135, Nozzle NL-26, O/F = 2.0

Figure 26, continued.

A-2641



Pre-Test Diameter 0.299
Post-Test Average Diameter 0.447
Average Surface Recession 0.0755
Surface Recession at Thermocouple Plane 0.084
Char Depth at Thermocouple Plane 0.266

THERMOCOUPLE DEPTHS

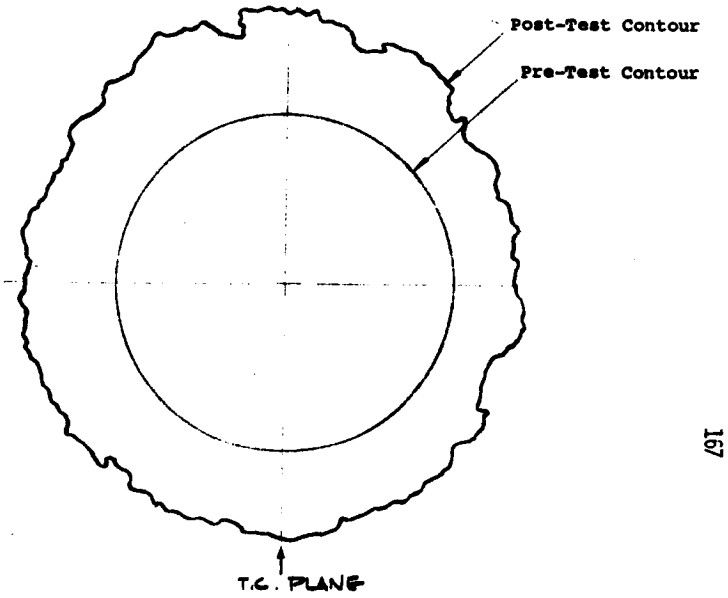
#1 0.135
#2 0.187
#3 0.279

Char and T.C. depths relative to initial surface.
All dimensions in inches.

O)Test 1134, Nozzle NL-25, O/F = 2.0

Figure 26, continued.

A-2642



Pre-Test Diameter 0.298
Post-Test Average Diameter 0.449
Average Surface Recession 0.0755
Surface Recession at Thermocouple Plane 0.084
Char Depth at Thermocouple Plane 0.245

THERMOCOUPLE DEPTHS

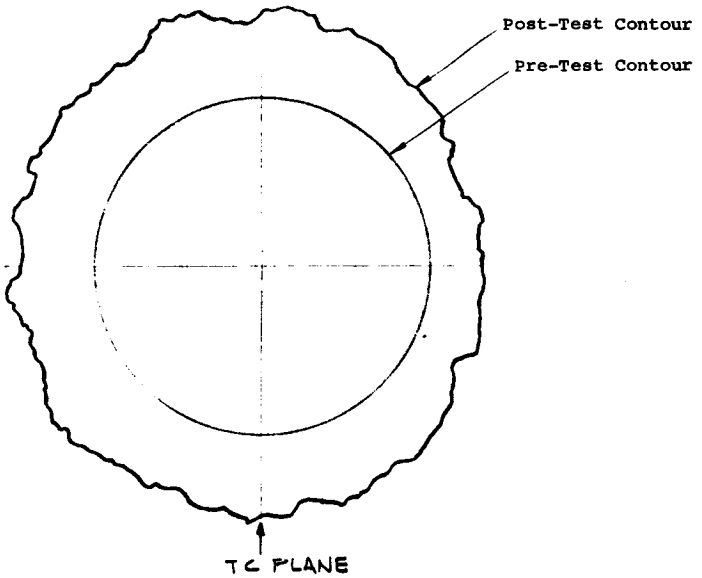
#1 0.127
#2 0.200
#3 0.280

Char and T.C. depths relative to initial surface.
All dimensions in inches.

P) Test 1124, Nozzle NL-21, O/F = 2.0

Figure 26, continued.

A-2643



Pre-Test Diameter 0.300
Post-Test Average Diameter 0.441
Average Surface Recession 0.0705
Surface Recession at Thermocouple Plane 0.082
Char Depth at Thermocouple Plane 0.260

THERMOCOUPLE DEPTHS

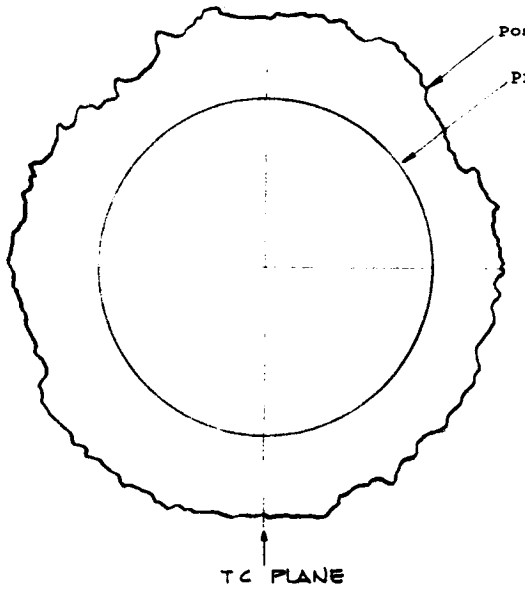
#1 0.147
#2 0.198
#3 0.282

Char and T.C. depths relative to initial surface.
All dimensions in inches.

Q) Test 1125, Nozzle NL-22, O/F = 2.0

Figure 26, continued.

A-1644



Pre-Test Diameter 0.300
Post-Test Average Diameter 0.445
Average Surface Recession 0.0725
Surface Recession at Thermocouple Plane 0.077
Char Depth at Thermocouple Plane 0.257

THERMOCOUPLE DEPTHS

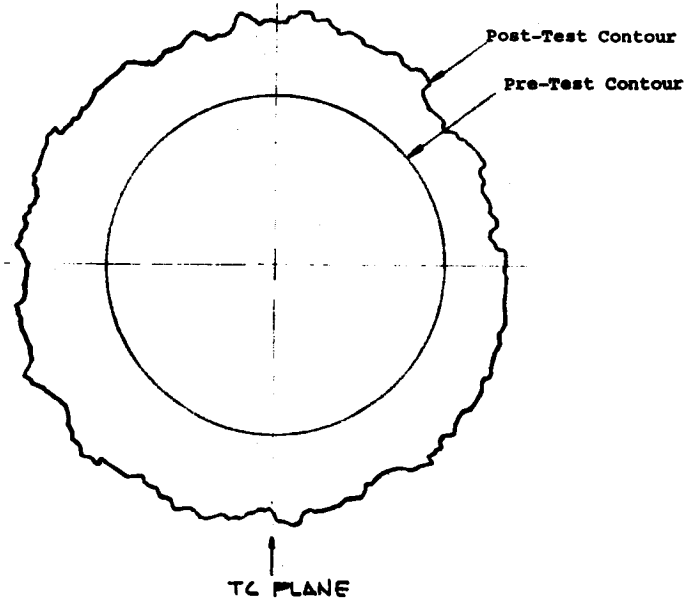
#1 0.126
#2 0.193
#3 0.274

Char and T.C. depths relative to initial surface.
All dimensions in inches.

R) Test 1128, Nozzle NL-23, O/F = 2.0

Figure 26, continued.

A-2645



Pre-Test Diameter 0.299
Post-Test Average Diameter 0.442
Average Surface Recession 0.071
Surface Recession at Thermocouple Plane 0.072
Char Depth at Thermocouple Plane 0.301

THERMOCOUPLE DEPTHS

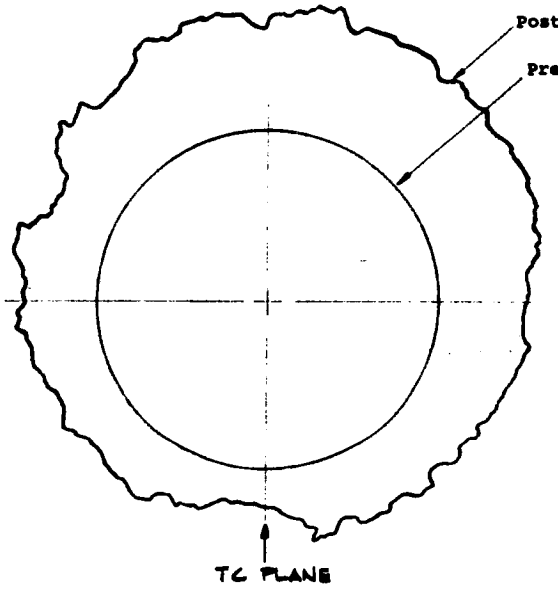
#1 0.118
#2 0.177
#3 0.284

Char and T.C. depths relative to initial surface
All dimensions in inches.

S) Test 1129, Nozzle NL-24, O/F = 2.0

Figure 26, continued.

A-2646



Pre-Test Diameter 0.302
Post-Test Average Diameter 0.452
Average Surface Recession 0.075
Surface Recession at Thermocouple Plane 0.033
Char Depth at Thermocouple Plane 0.359

THERMOCOUPLE DEPTHS

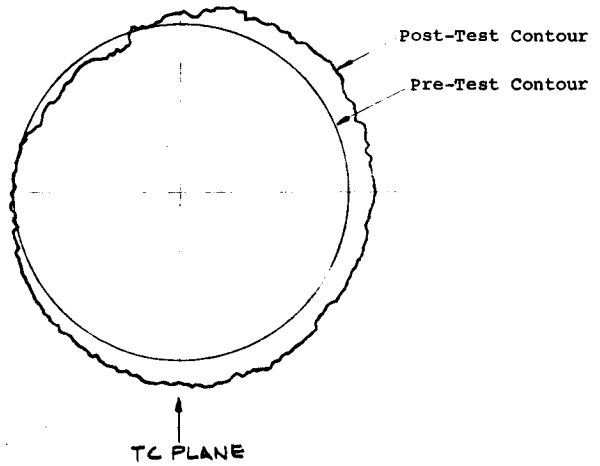
#1 0.131
#2 0.206
#3 0.274

Char and T.C. depths relative to initial surface.
All dimensions in inches.

T) Test 1120, Nozzle NL-19, O/F = 2.0

Figure 26, continued.

A-2647



Pre-Test Diameter 0.299
Post-Test Average Diameter 0.329
Average Surface Recession 0.015
Surface Recession at Thermocouple Plane 0.035
Char Depth at Thermocouple Plane 0.401

THERMOCOUPLE DEPTHS

#1 0.117

#2 0.191

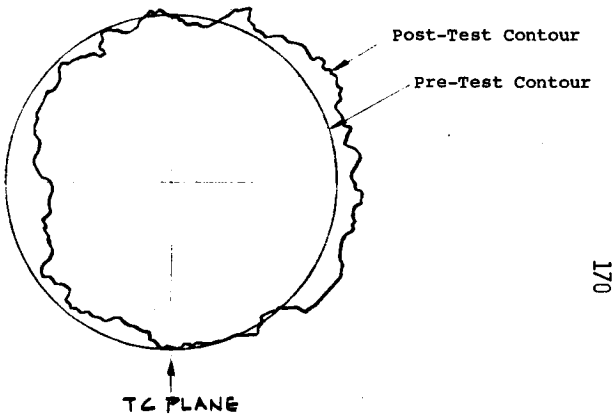
#3 0.278

Char and T.C. depths relative to initial surface.
All dimensions in inches.

U) Test 1117, Nozzle NL-18, O/F = 2.0

Figure 26 continued.

A-2648



Pre-Test Diameter 0.297
Post-Test Average Diameter 0.300
Average Surface Recession 0.0015
Surface Recession at Thermocouple Plane 0.003
Char Depth at Thermocouple Plane 0.357

THERMOCOUPLE DEPTHS

#1 0.129

#2 0.198

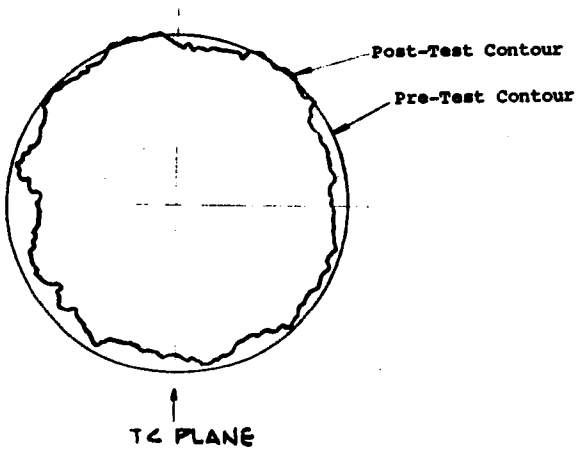
#3 0.278

Char and T.C. depths relative to initial surface.
All dimensions in inches.

V) Test 1121, Nozzle NL-20, O/F = 2.0

Figure 26, continued.

A-2649



Pre-Test Diameter 0.300
Post-Test Average Diameter 0.284
Average Surface Recession --
Surface Recession at Thermocouple Plane --
Char Depth at Thermocouple Plane 0.327

THERMOCOUPLE DEPTHS

#1 0.118

#2 0.204

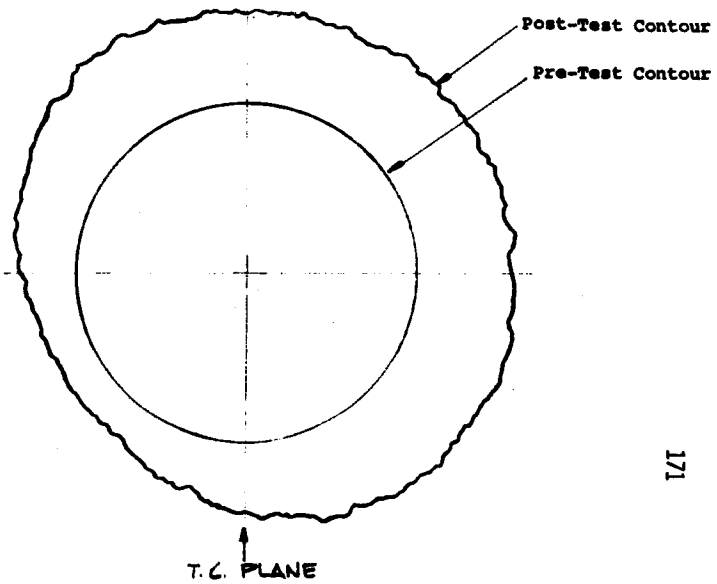
#3 0.267

Char and T.C. depths relative to initial surface.
All dimensions in inches.

W) Test 1116, Nozzle NL-17, O/F =

Figure 26, continued.

A-1650



Pre-Test Diameter 0.301"
Post-Test Average Diameter 0.451"
Average Surface Recession 0.755"
Surface Recession at Thermocouple Plane 0.072"
Char Depth at Thermocouple Plane 0.426"

THERMOCOUPLE DEPTHS

#1 0.134

#2 0.187

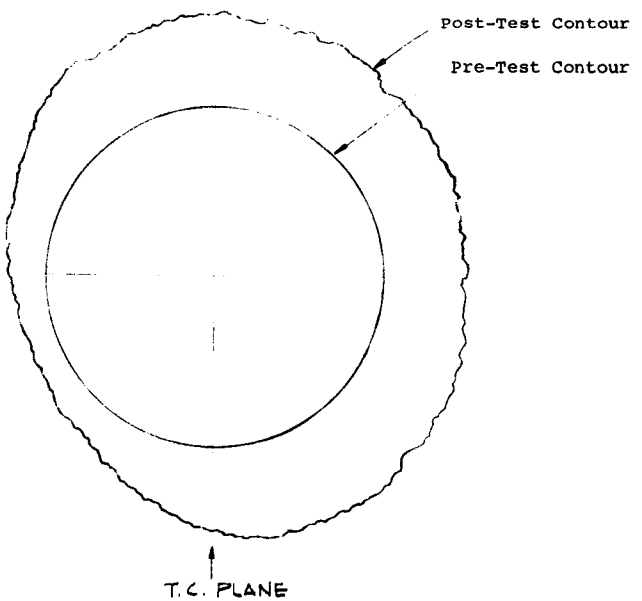
#3 0.273

Char and T.C. depths relative to initial surface.
All dimensions in inches.

X) Test 1098, Nozzle NL-16, O/F = 1.0

Figure 26, continued.

A-1651



Pre-Test Diameter 0.302
Post-Test Average Diameter 0.432
Average Surface Recession 0.065
Surface Recession at Thermocouple Plane 0.082
Char Depth at Thermocouple Plane 0.432

THERMOCOUPLE DEPTHS

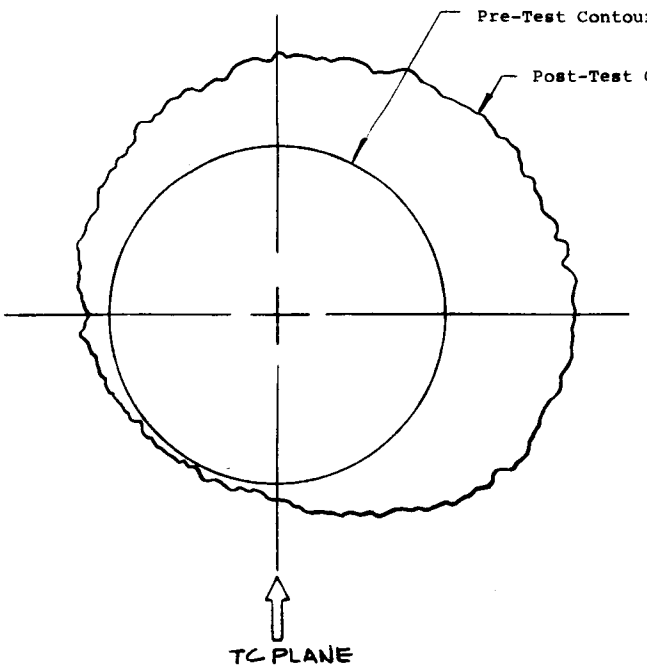
#1 0.138
#2 0.190
#3 0.280

Char and T.C. depths relative to initial surface.
All dimensions in inches.

Y) Test 1099, Nozzle NL-15

Figure 26, continued.

A-2652



Pre-Test Diameter 0.301
Post-Test Average Diameter 0.435
Average Surface Recession 0.067
Surface Recession at Thermocouple Plane 0.018
Average Char Depth 0.419

THERMOCOUPLE DEPTHS

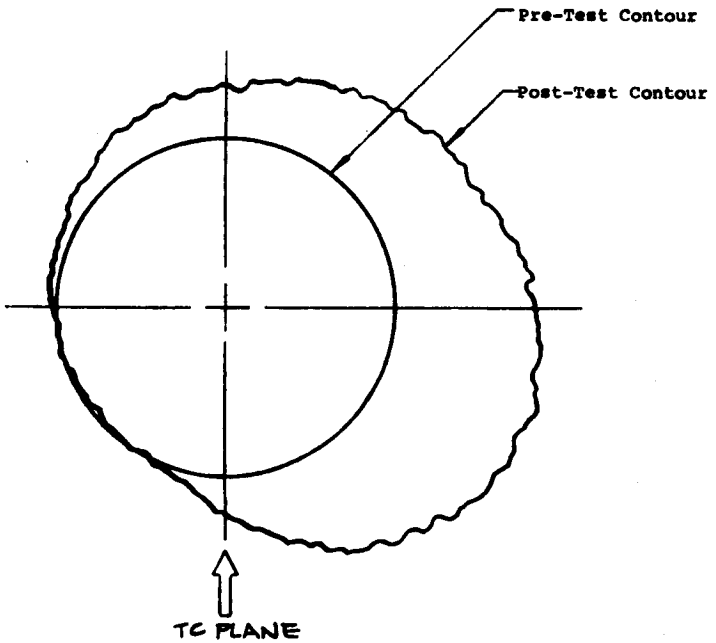
#1 0.135
#2 0.203
#3 0.261

Char and T.C. depths relative to initial surface.
All dimensions in inches.

Z) Test 1338, Nozzle NL-34, O/F = 1.0

Figure 26, continued.

A-2653



Pre-Test Diameter 0.303
Post-Test Average Diameter 0.410
Average Surface Recession 0.054
Surface Recession at Thermocouple Plane 0.032
Average Char Depth 0.464

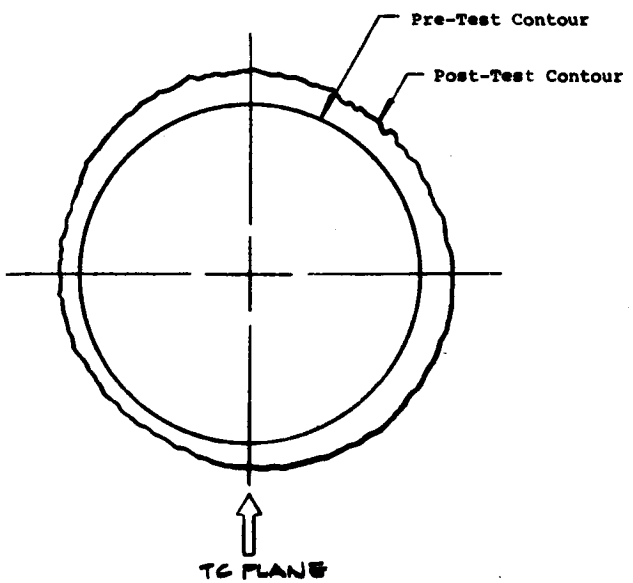
THERMOCOUPLE DEPTHS

#1	0.124
#2	0.211
#3	0.276

Char and T.C. depths relative to initial surface.
All dimensions in inches.

AA) Test 1336, Nozzle NL-32, O/F = 1.0
Figure 26, continued.

A-2654



Pre-Test Diameter 0.310
Post-Test Average Diameter 0.348
Average Surface Recession 0.019
Surface Recession at Thermocouple Plane 0.015
Average Char Depth 0.525

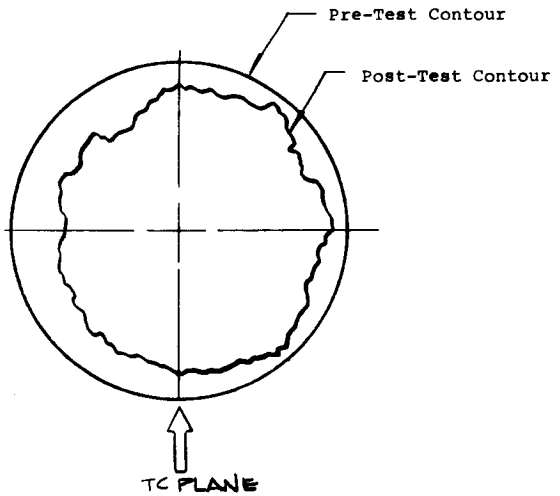
THERMOCOUPLE DEPTHS

#1	0.126
#2	0.023
#3	0.278

Char and T.C. depths relative to initial surface.
All dimensions in inches.

BB) Test 1339, Nozzle NL-35, O/F = 1.0
Figure 26, continued.

A-2655



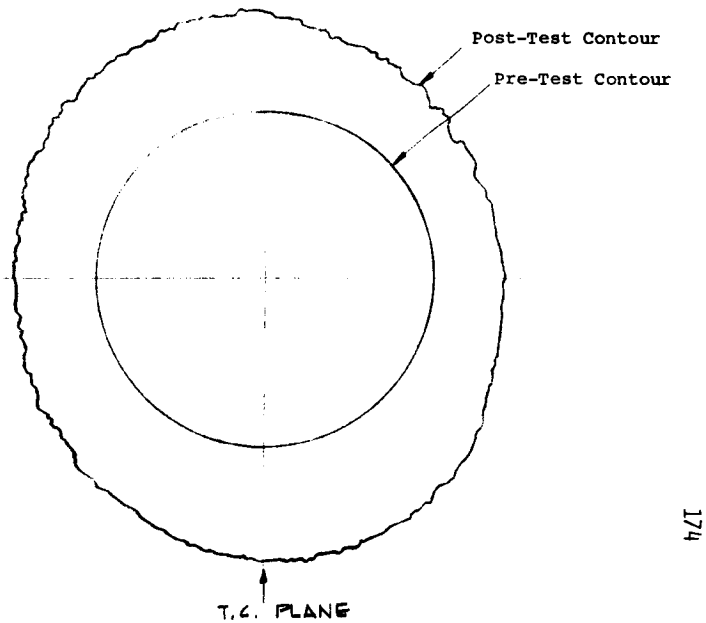
Pre-Test Diameter 0.301
Post-Test Average Diameter 0.246
Average Surface Recession -0.028
Surface Recession at Thermocouple Plane -0.023
Average Char Depth 0.324

THERMOCOUPLE DEPTHS

#1	0.146
#2	0.199
#3	0.284

Char and T.C. depths relative to initial surface.
All dimensions in inches.

CC) Test 1337, Nozzle NL-33, O/F = 1.0
Figure 26, continued. A-2656



Pre-Test Diameter 0.300
Post-Test Average Diameter 0.464
Average Surface Recession 0.082
Surface Recession at Thermocouple Plane 0.102
Char Depth at Thermocouple Plane 0.260

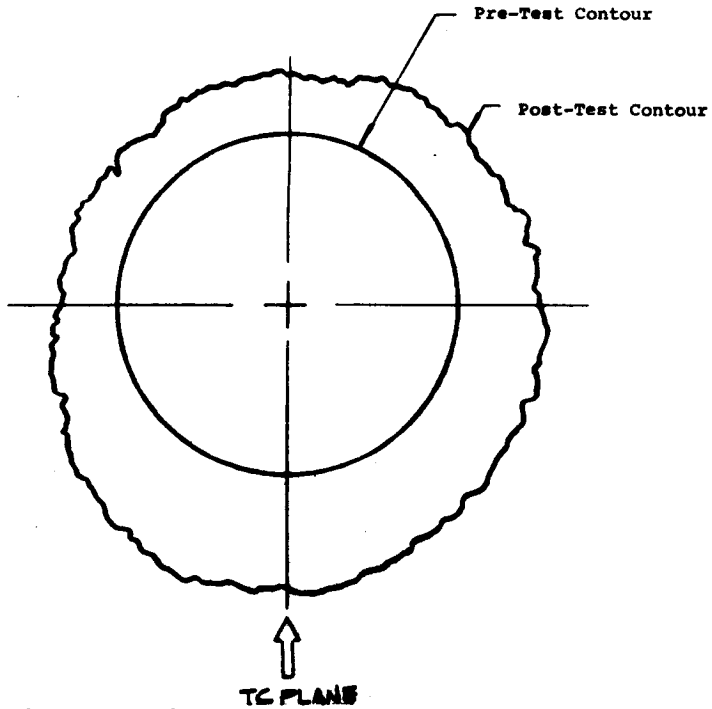
THERMOCOUPLE DEPTHS

#1	0.125
#2	0.190
#3	0.287

Char and T.C. depths relative to initial surface.
All dimensions in inches.

DD) Test 1145, Nozzle NL-10, O/F = 0.383
Figure 26, continued.

A-2657



Pre-Test Diameter 0.302
Post-Test Average Diameter 0.464
Average Surface Recession 0.081
Surface Recession at Thermocouple Plane 0.110
Average Char Depth 0.284

THERMOCOUPLE DEPTHS

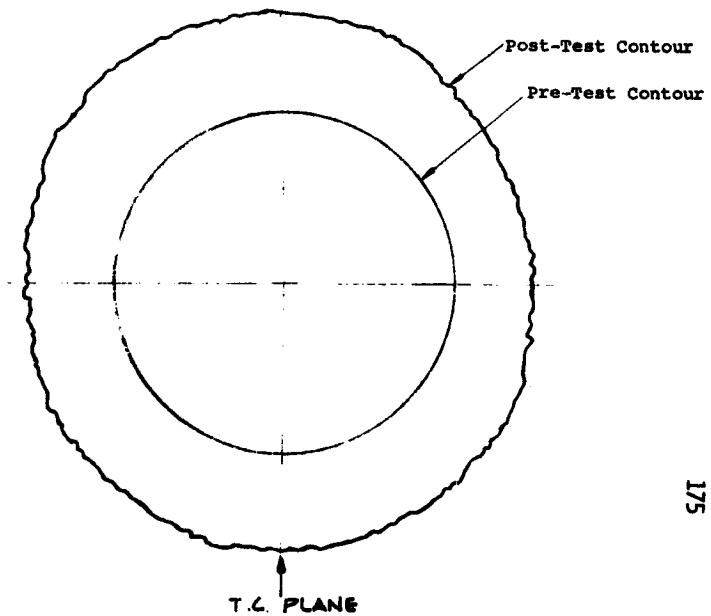
#1 0.136
#2 0.204
#3 0.272

Char and T.C. depths relative to initial surface.
All dimensions in inches.

EE) Test 1348, Nozzle NL-37, O/F = 0.38

Figure 26, continued.

A-2648



Pre-Test Diameter 0.301
Post-Test Average Diameter 0.469
Average Surface Recession 0.084
Surface Recession at Thermocouple Plane 0.093
Char Depth at Thermocouple Plane 0.253

THERMOCOUPLE DEPTHS

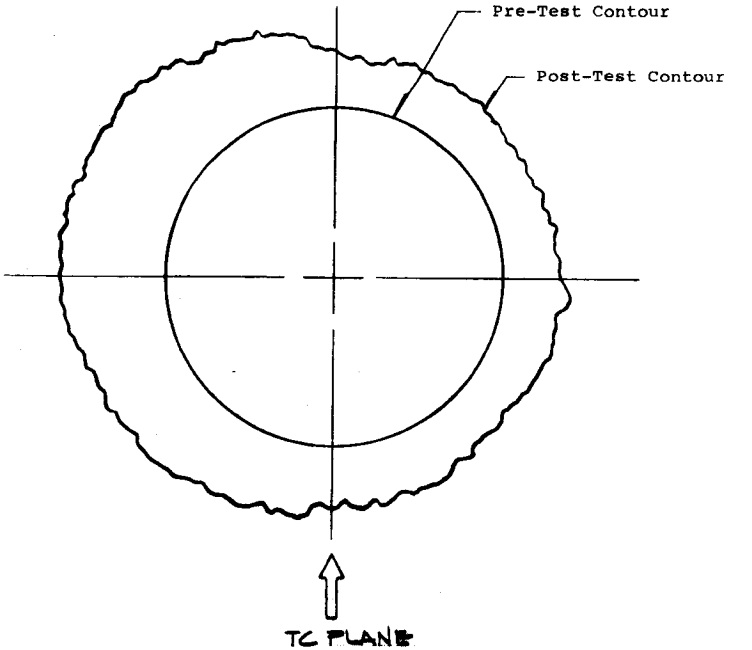
#1 0.116
#2 0.192
#3 0.261

Char and T.C. depths relative to initial surface.
All dimensions in inches.

FF) Test 1146, Nozzle NL-27, O/F = 0.383

Figure 26, continued.

A-2649



Pre-Test Diameter 0.301
Post-Test Average Diameter 0.452
Average Surface Recession 0.076
Surface Recession at Thermocouple Plane 0.076
Average Char Depth 0.300

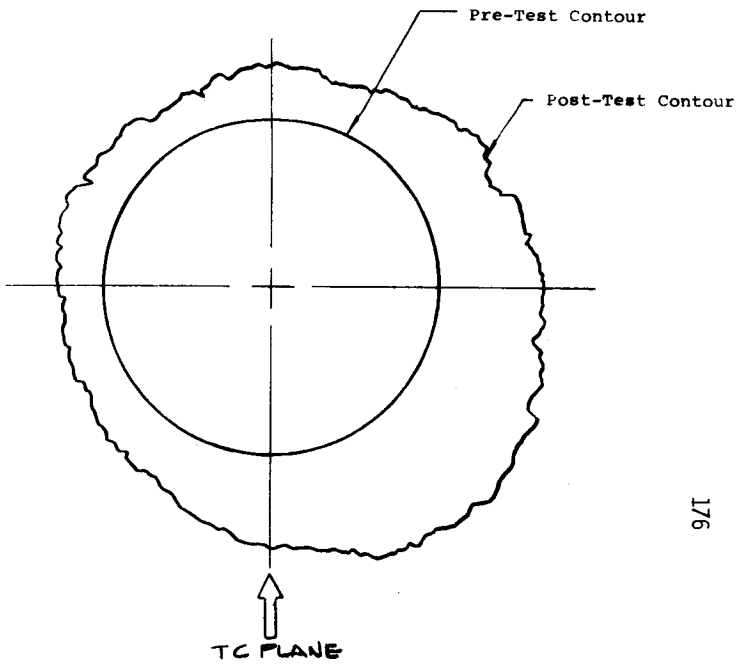
THERMOCOUPLE DEPTHS

#1	0.136
#2	0.214
#3	0.268

Char and T.C. depths relative to initial surface.
All dimensions in inches.

GG) Test 1350, Nozzle NL-39, O/F = 0.38

Figure 26, continued. A-2660



Pre-Test Diameter 0.300
Post-Test Average Diameter 0.451
Average Surface Recession 0.076
Surface Recession at Thermocouple Plane 0.090
Average Char Depth 0.371

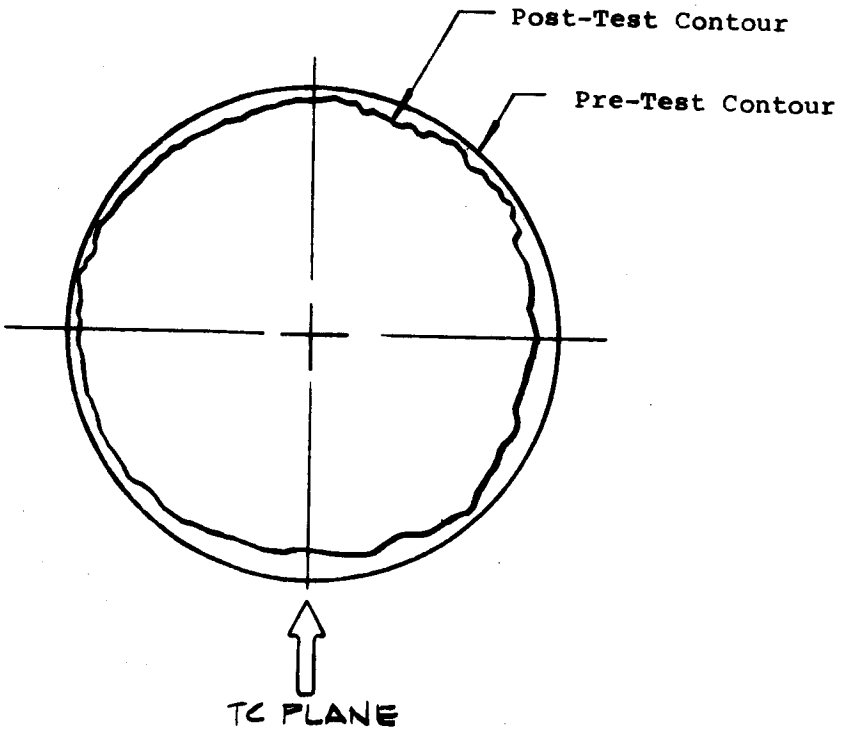
THERMOCOUPLE DEPTHS

#1	0.126
#2	0.211
#3	0.268

Char and T.C. depths relative to initial surface.
All dimensions in inches.

HH) Test 1347, Nozzle NL-36, O/F = 0.38

Figure 26, continued. A-2661



Pre-Test Diameter 0.301

Post-Test Average Diameter 0.289

Average Surface Recession -0.006

Surface Recession at Thermocouple Plane -0.016

Average Char Depth 0.444

THERMOCOUPLE DEPTHS

#1	0.133
#2	0.204
#3	0.271

Char and T.C. depths relative to initial surface.
All dimensions in inches.

II) Test 1349, Nozzle NL-38, O/F = 0.38

Figure 26, concluded.

A-2662

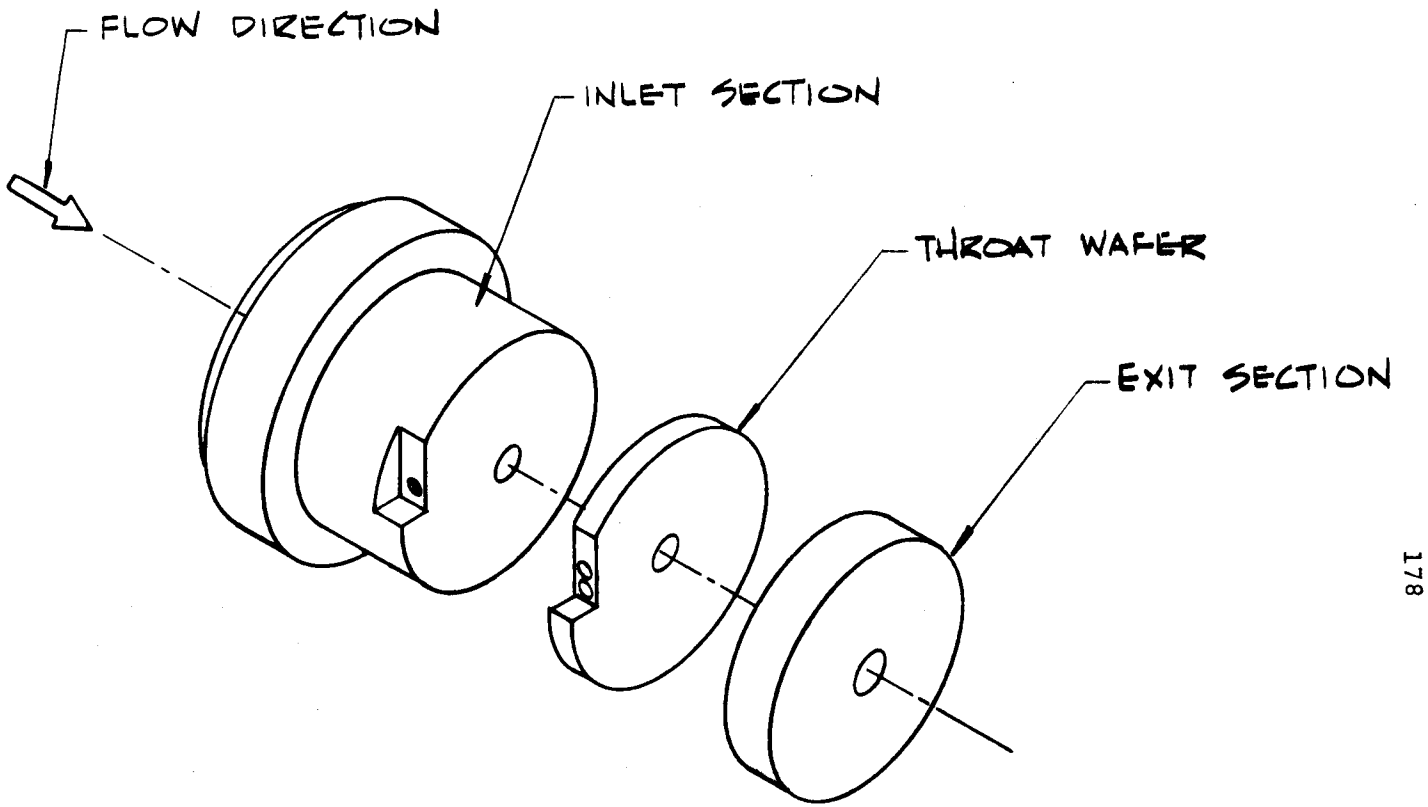
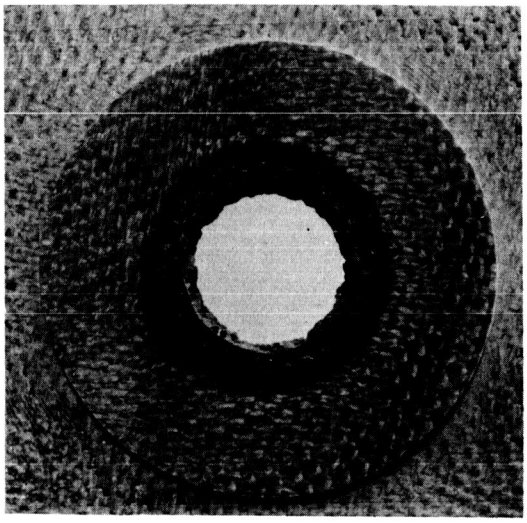
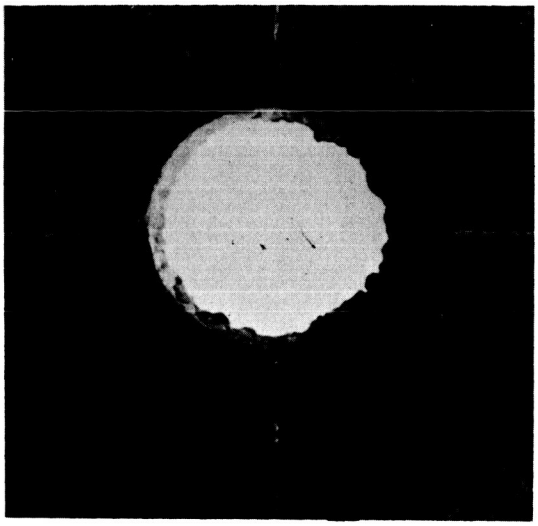


FIGURE 27 SECTIONING OF TESTED ABLATIVE NOZZLES

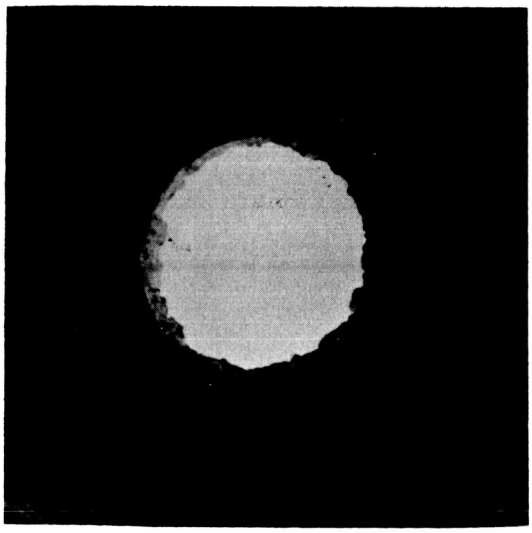
A-2663



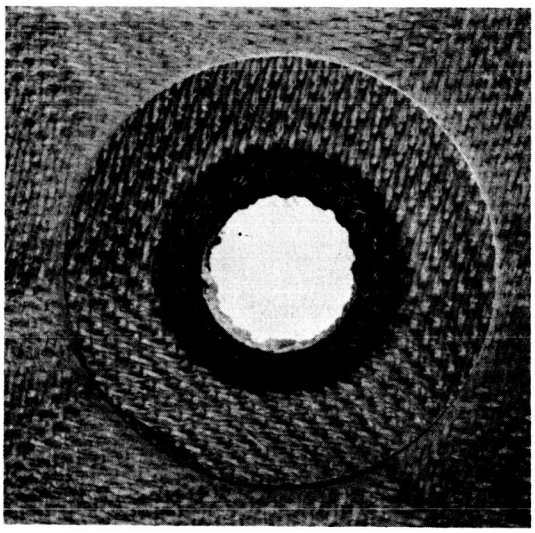
A) Test 1083, O/F=∞, NL-11



B) Test 1358, O/F=∞, NL-42

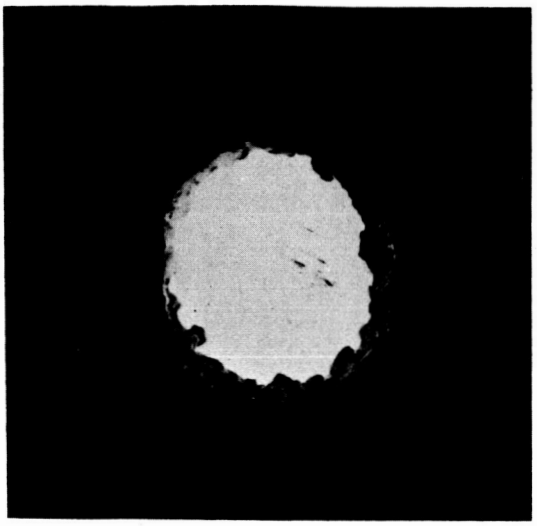


C) Test 1359, O/F=∞, NL-43

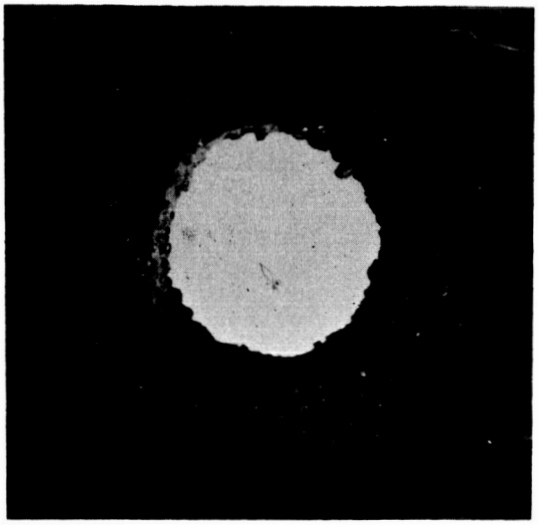


D) Test 1024, O/F=∞, NL-12

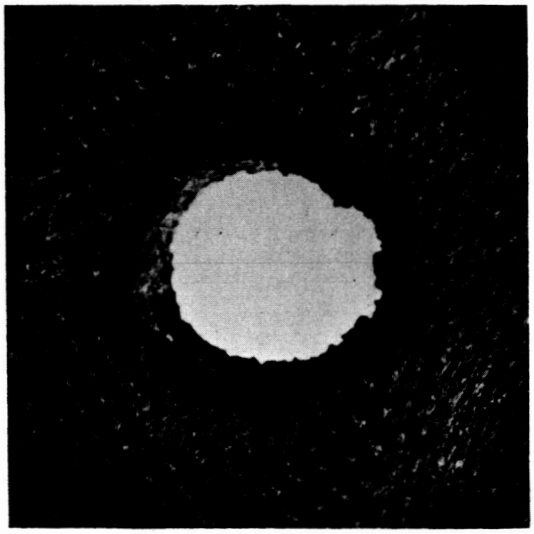
FIGURE 28 PHOTOGRAPHS OF ABLATIVE NOZZLE WAFERS



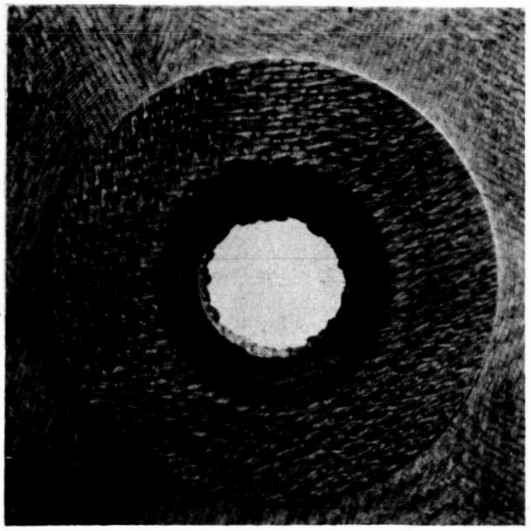
E) Test 1361, O/F=∞, NL-40



F) Test 1362, O/F=∞, NL-41

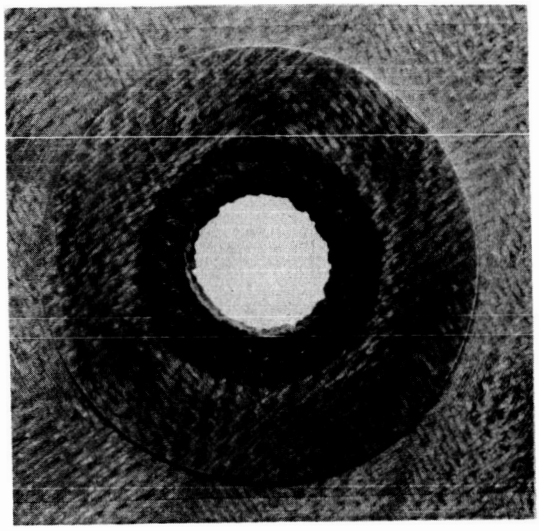


G) Test 1360, O/F=∞, NL-44

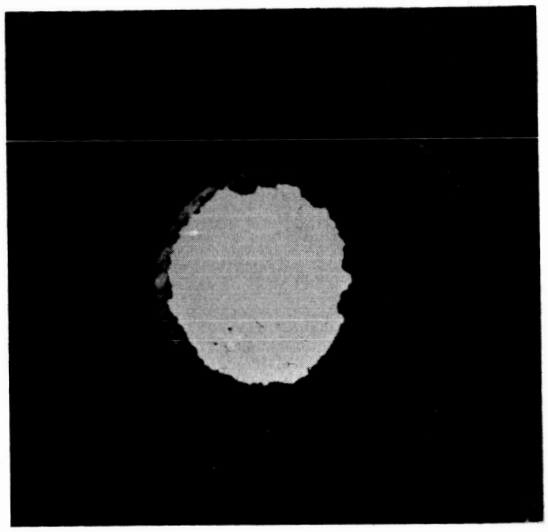


H) Test 1091, O/F=4.0,NL-13

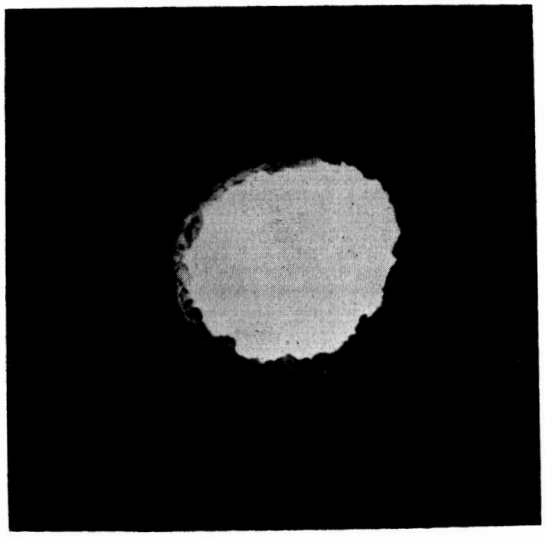
FIGURE 28, CONTINUED



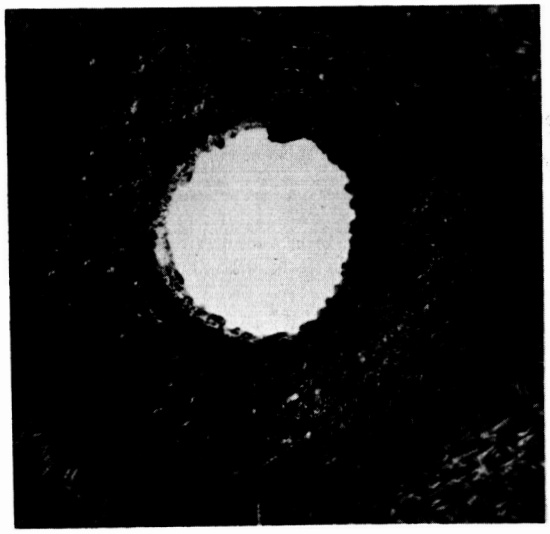
I) Test 1092, O/F=4.0,NL-14



J) Test 1329, O/F=4.0,NL-28

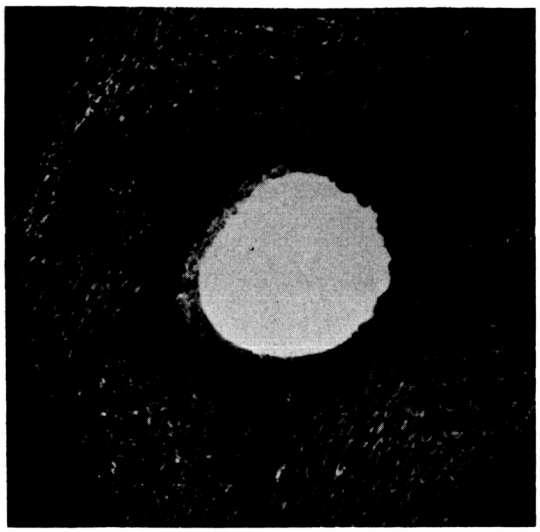


K) Test 1332, O/F=4.0,NL-31

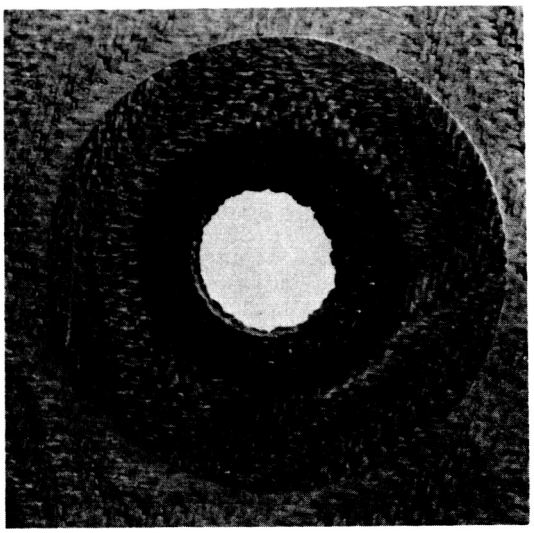


L) Test 1330, O/F=4.0,NL-29

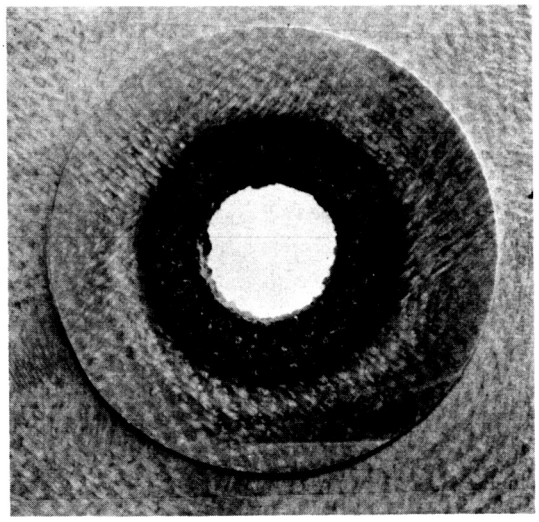
FIGURE 28, CONTINUED



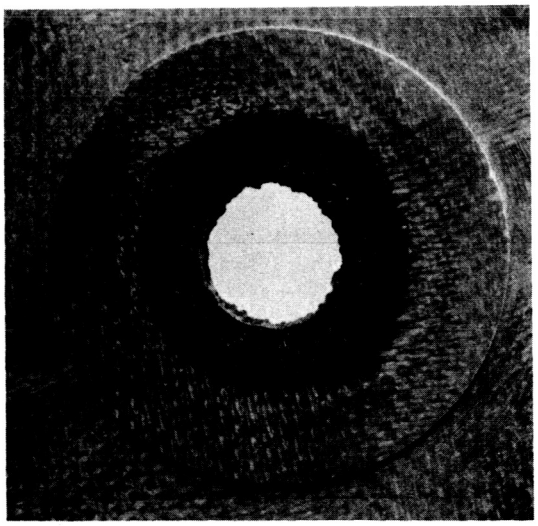
M) Test 1331, O/F=4.0,NL-30



N) Test 1135, O/F=2.0,NL-26

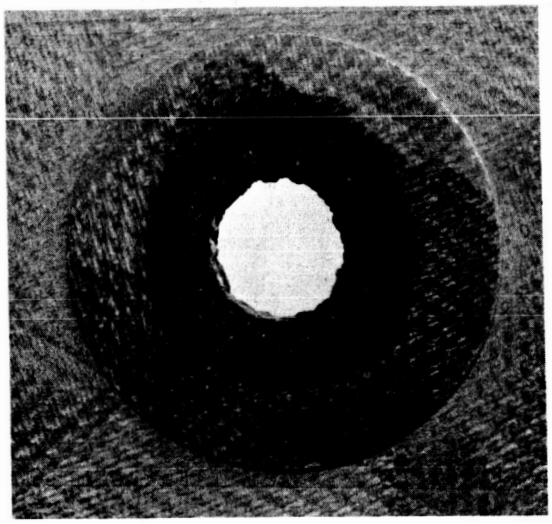


O) Test 1134, O/F=2.0,NL-25

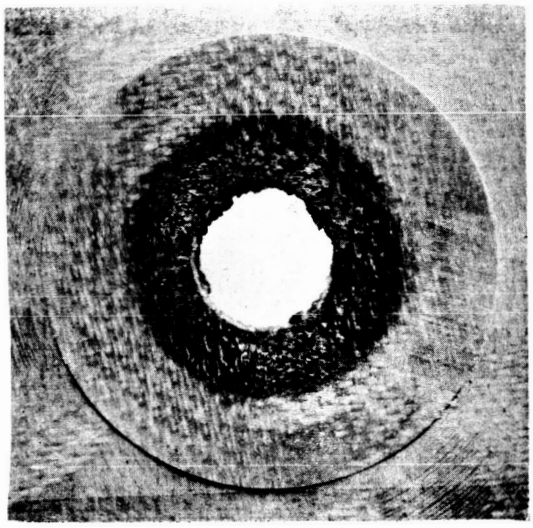


P) Test 1124, O/F=2.0,NL-21

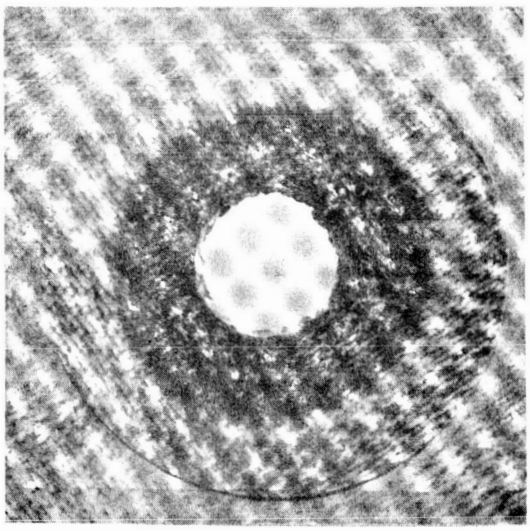
FIGURE 28, CONTINUED



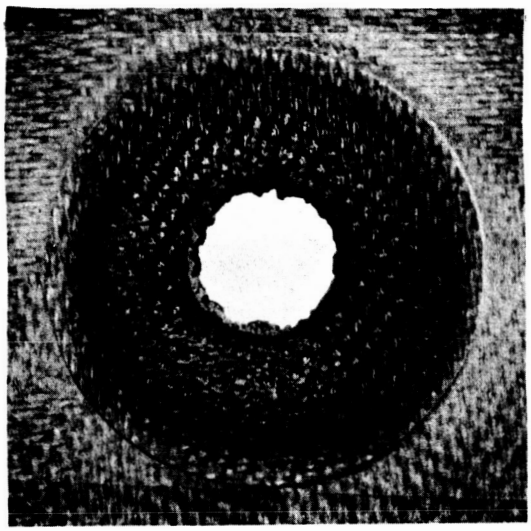
Q) Test 1125, O/F=2.0,NL-22



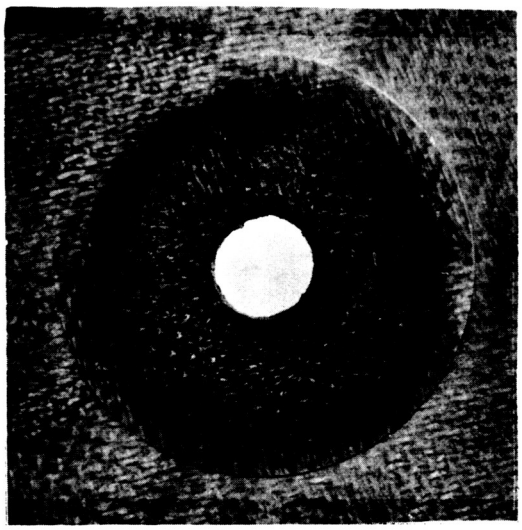
R) Test 1128, O/F=2.0,NL-23



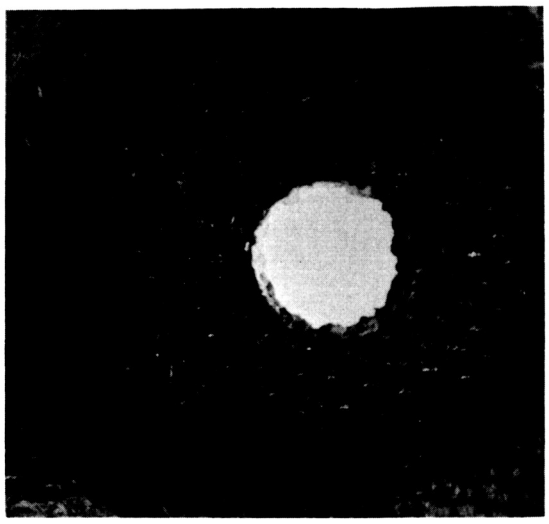
S) Test 1129, O/F=2.0,NL-24



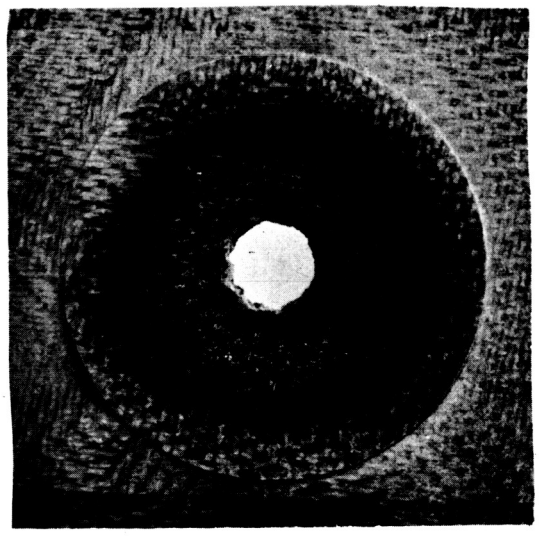
T) Test 1120, O/F=2.0,NL-19



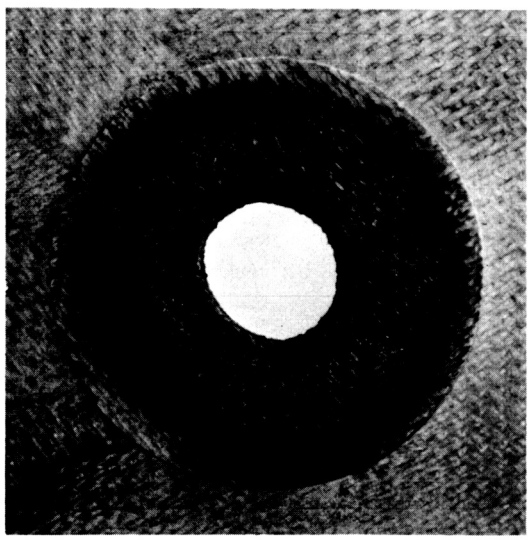
U) Test 1117, O/F=2.0,NL-18



V) Test 1121, O/F=2.0, NL-20

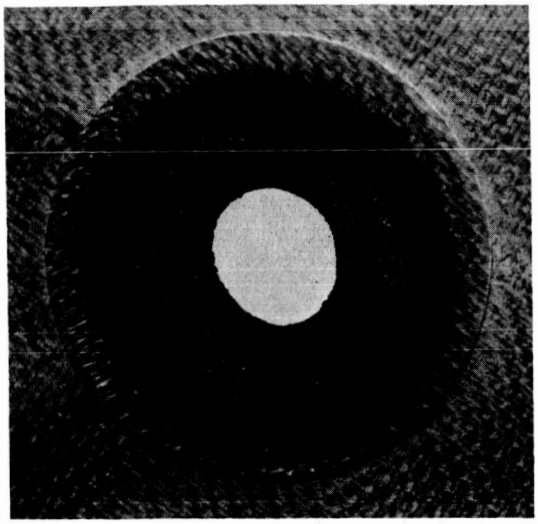


W) Test 1116, O/F=2.0,NL-17

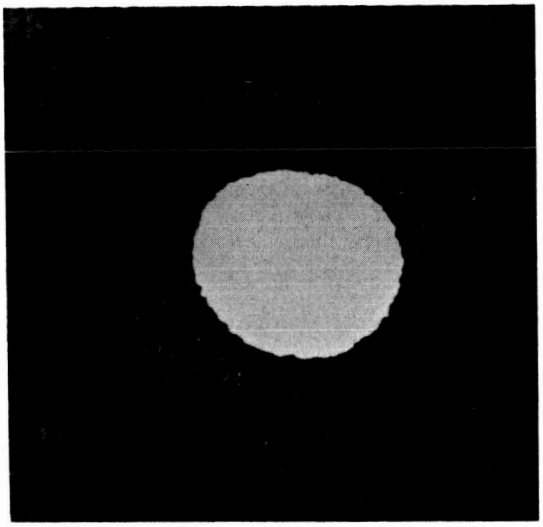


X) Test 1098, O/F=1.0,NL-16

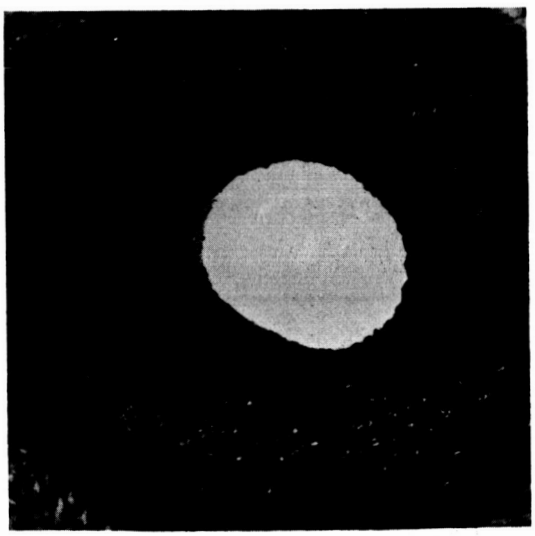
FIGURE 28, CONTINUED



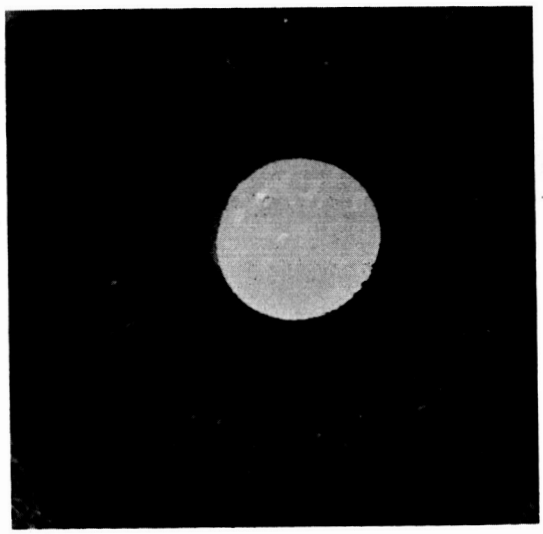
Y) Test 1099, O/F=1.0,NL-15



Z) Test 1338, O/F=1.0,NL-34

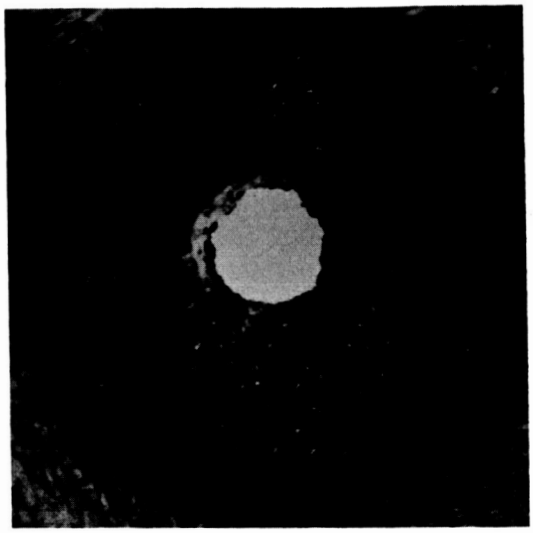


AA) Test 1336, O/F=1.0,NL-32

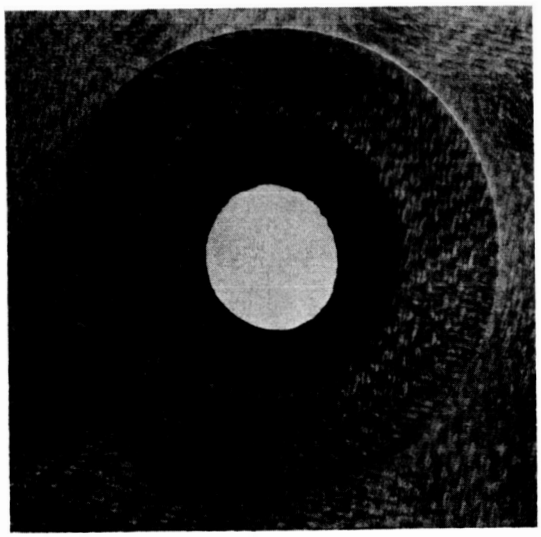


BB) Test 1339, O/F=1.0,NL-35

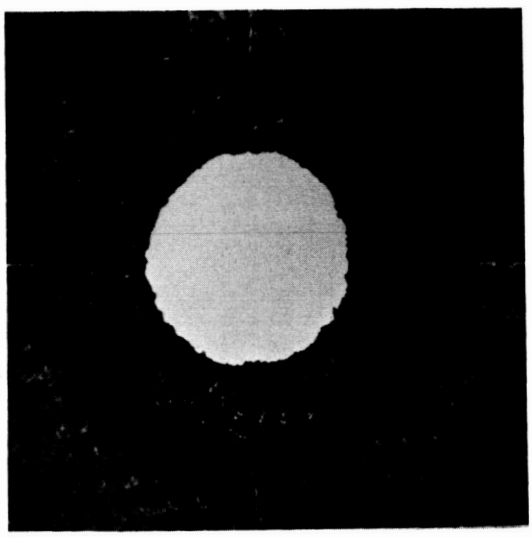
FIGURE 28, CONTINUED



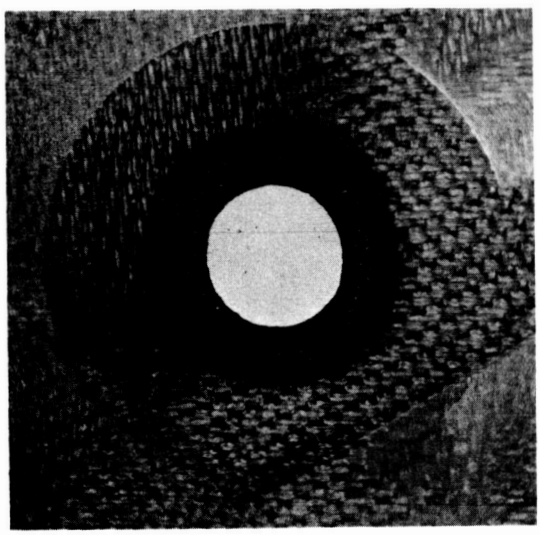
CC) Test 1337, O/F=1.0,NL-33



DD) Test 1145, O/F=0.38,NL-10

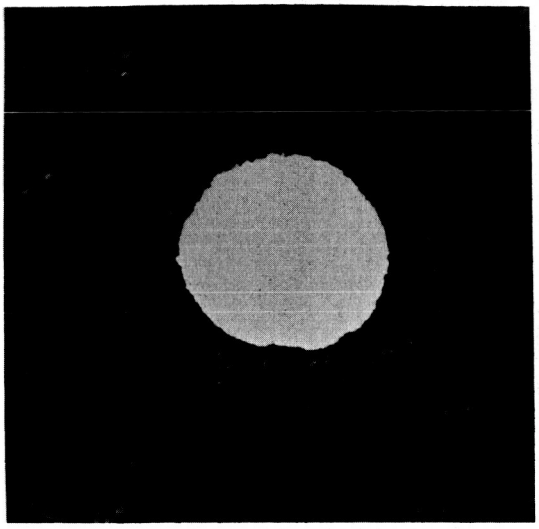


EE) Test 1348, O/F=0.38,NL-3

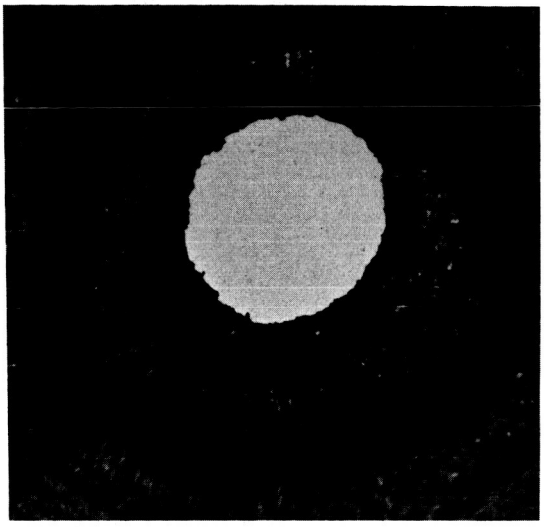


FF) Test 1146, O/F=0.38,NL-27

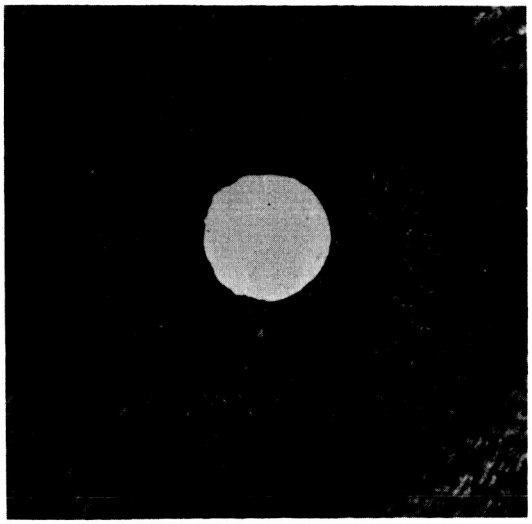
FIGURE 28, CONTINUED



GG) Test 1350, O/F=0.38,NL-39



HH) Test 1347, O/F=0.38,NL-36



II) Test 1349, O/F=0.38,NL-38

FIGURE 28, CONCLUDED

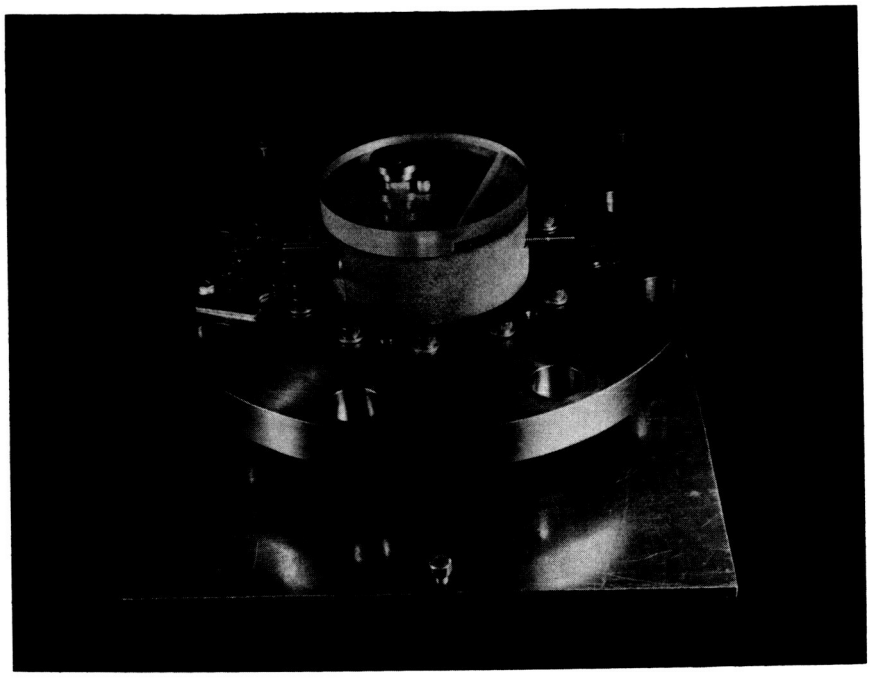


FIGURE 29. ABLATIVE NOZZLE SETUP FOR X-RAY PHOTOGRAPHY

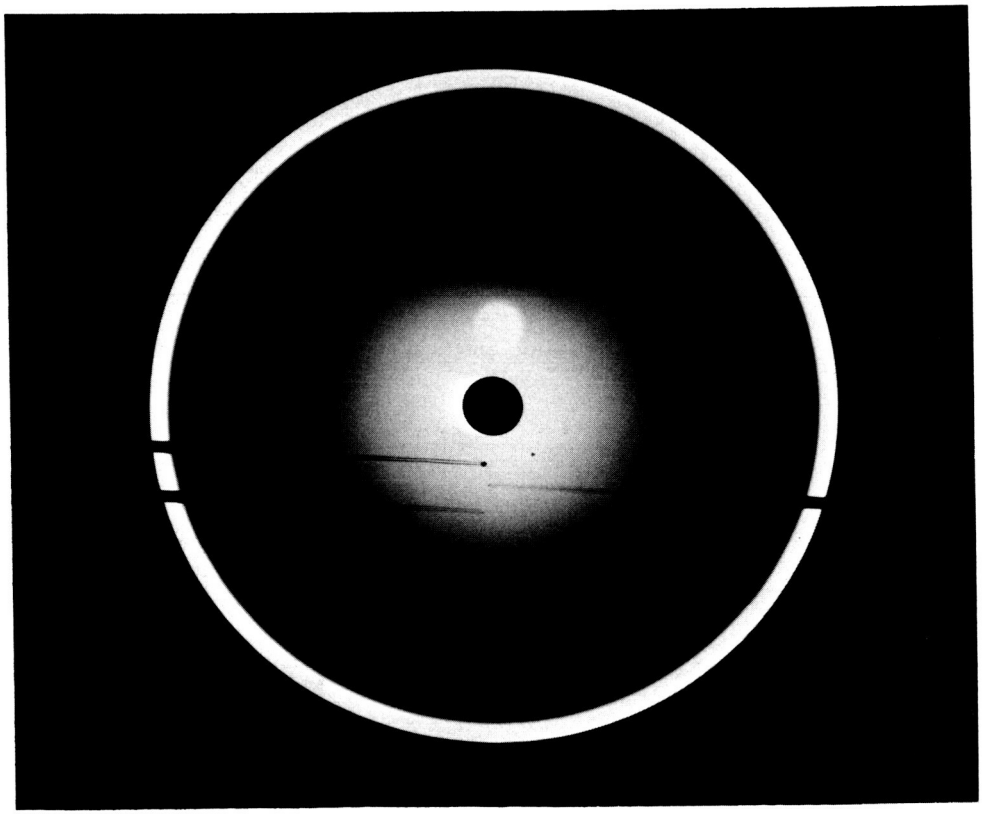


FIGURE 30. TYPICAL X-RAY PHOTOGRAPH OF AN ABLATION NOZZLE SHOWING IN-DEPTH THERMOCOUPLE

LEGEND FOR FIGURE 31

⊡ FINAL RECESSION IN TC PLANE

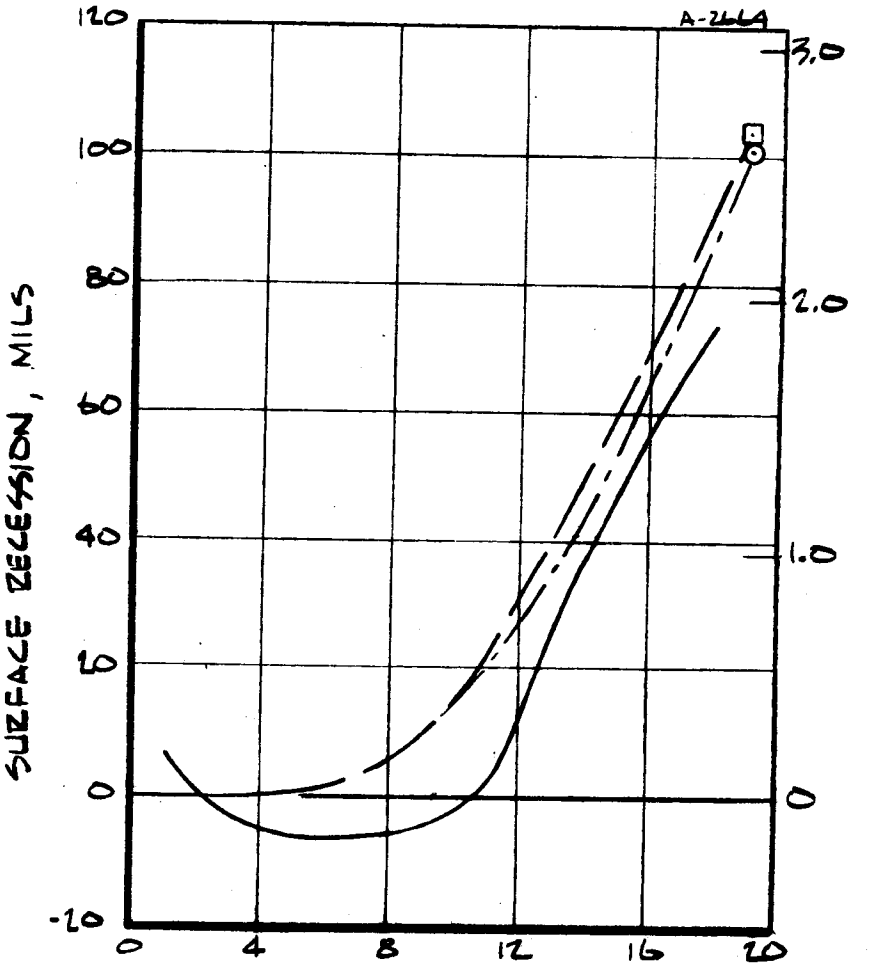
⊙ FINAL AVERAGE RECESSION

——— RECESSION BASED ON CALIBRATION PRESSURE DECAY

— — INFERRED RECESSION IN TC PLANE

—·— INFERRED AVERAGE RECESSION

—··— RECESSION BASED ON MAXIMUM PRESSURE DECAY



A) TEST 1083, O/F = ∞, NL-11

FIGURE 31, ABLATIVE NOZZLE RECESSION HISTORIES

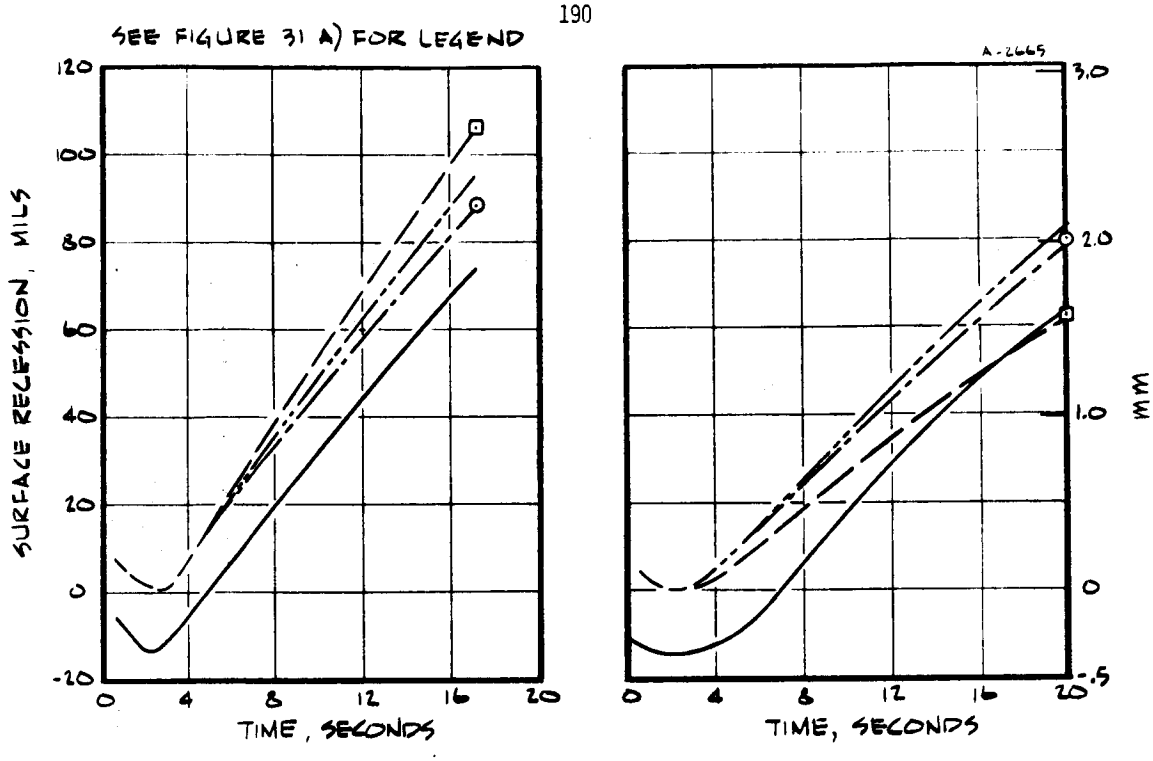


FIGURE 31, CONTINUED

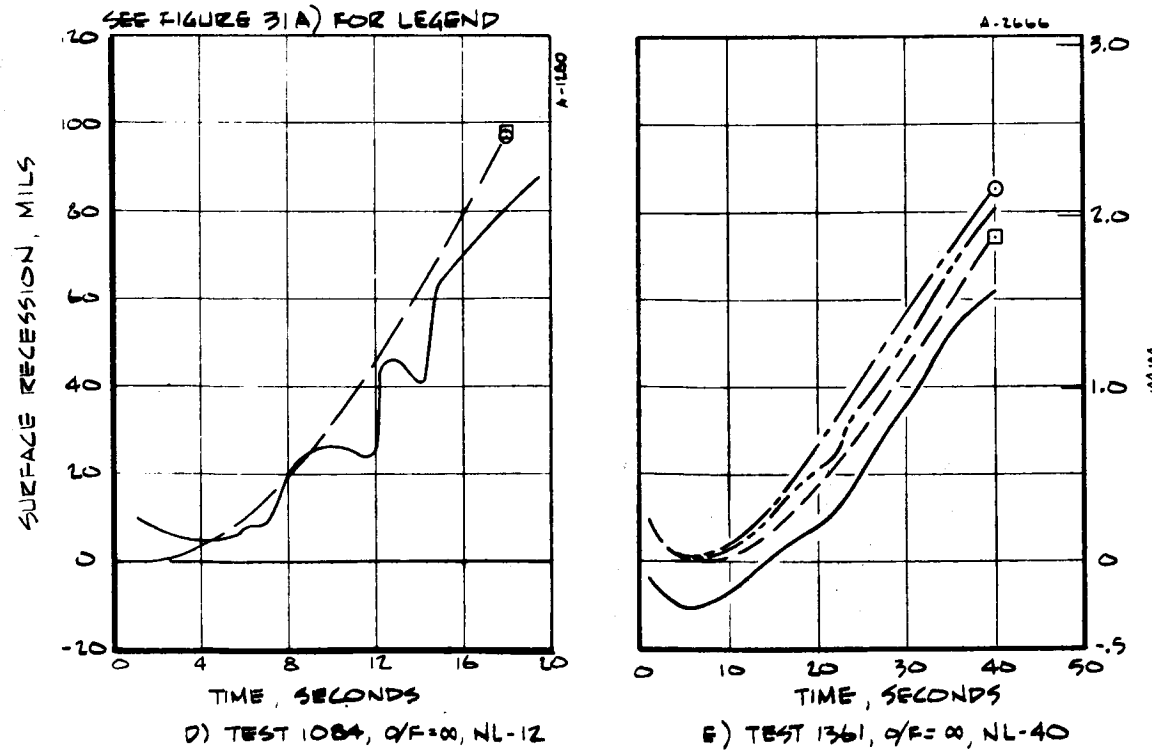
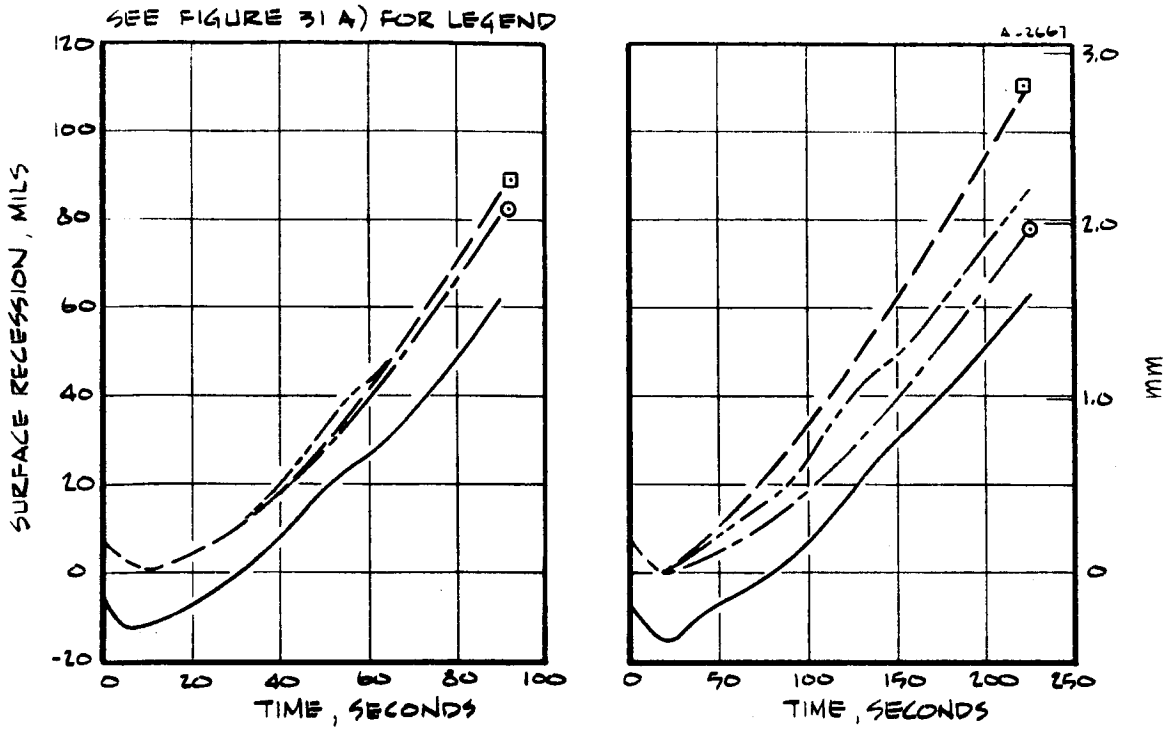
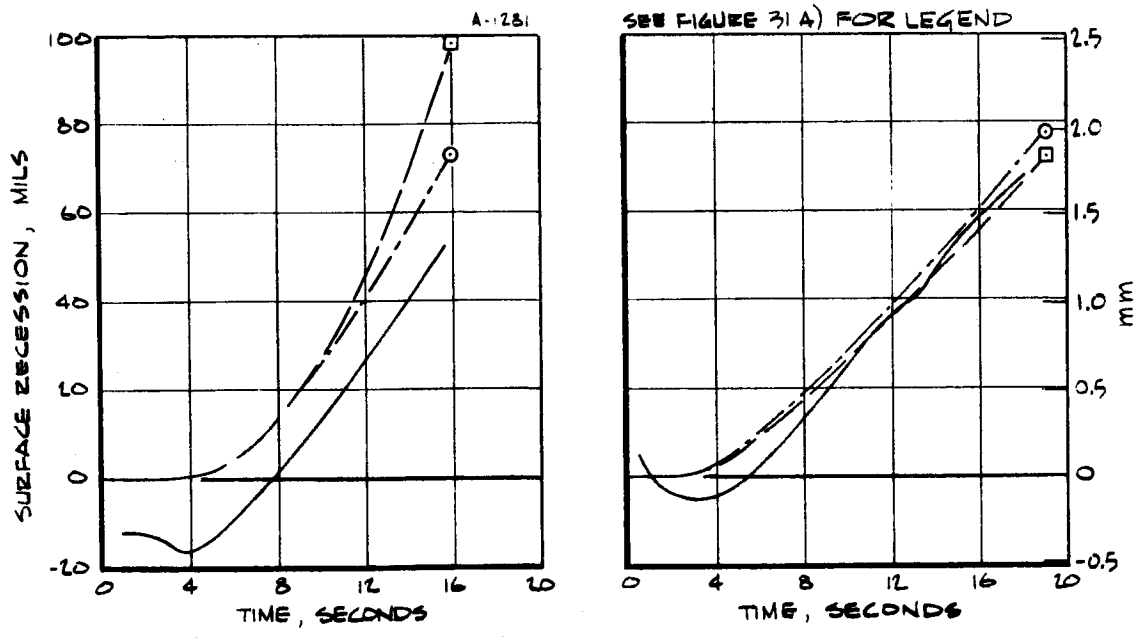


FIGURE 31, CONTINUED



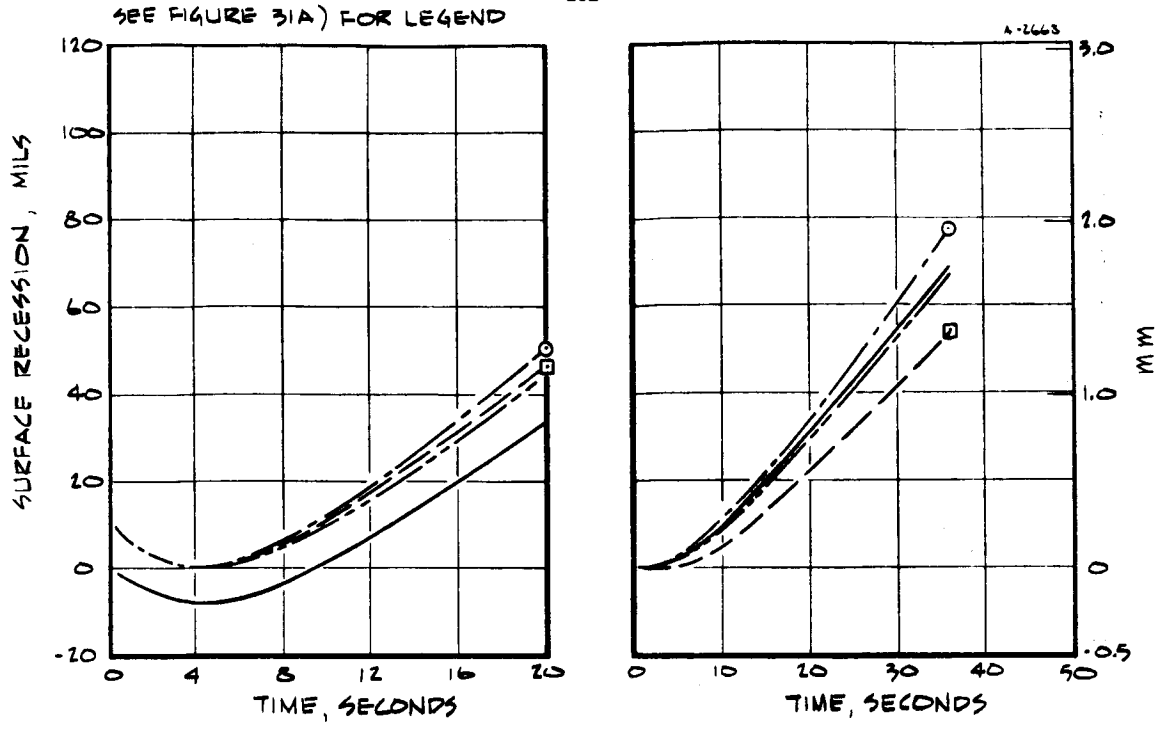
F) TEST 1362, O/F ∞, NL-41 G) TEST 1360, O/F ∞, NL-44

FIGURE 31, CONTINUED



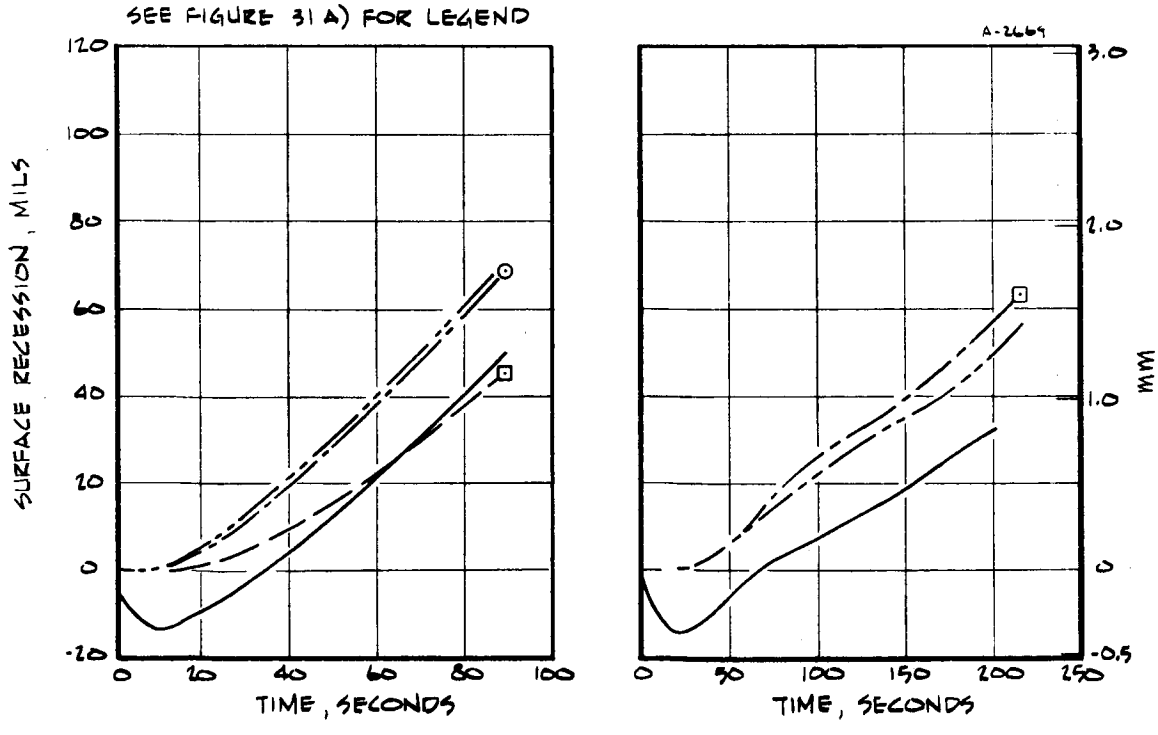
H) TEST 1091, O/F=4.0, NL-13 I) TEST 1092, O/F=4.0, NL-14

FIGURE 31, CONTINUED



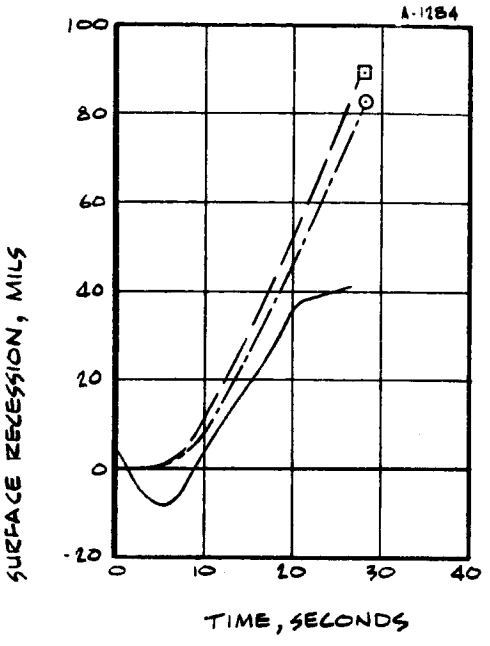
J) TEST 1329, O/F=4.0, NL-28 K) TEST 1332, O/F=4.0, NL-31

FIGURE 31, CONTINUED



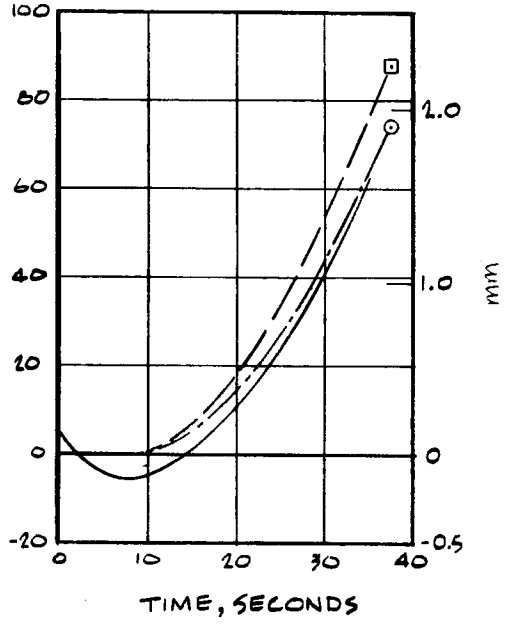
L) TEST 1330, O/F=4.0, NL-29 M) TEST 1331, O/F=4.0, NL-30

FIGURE 31, CONTINUED



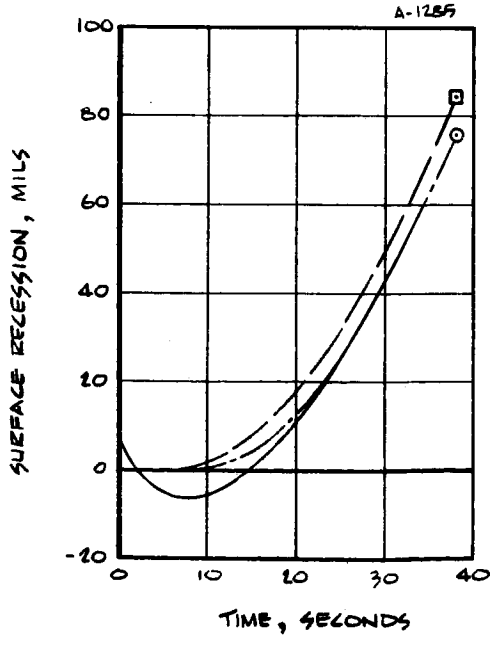
N) TEST 1135, O/F = 2.0, NL-26

SEE FIGURE 31 A) FOR LEGEND



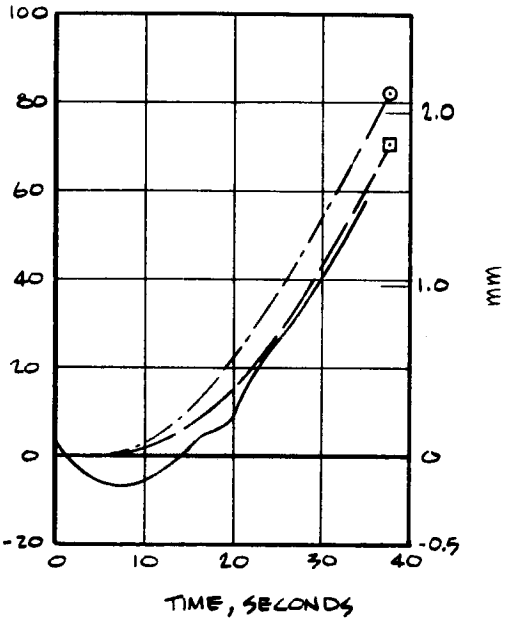
O) TEST 1134, O/F = 2.0 NL-25

FIGURE 31, CONTINUED



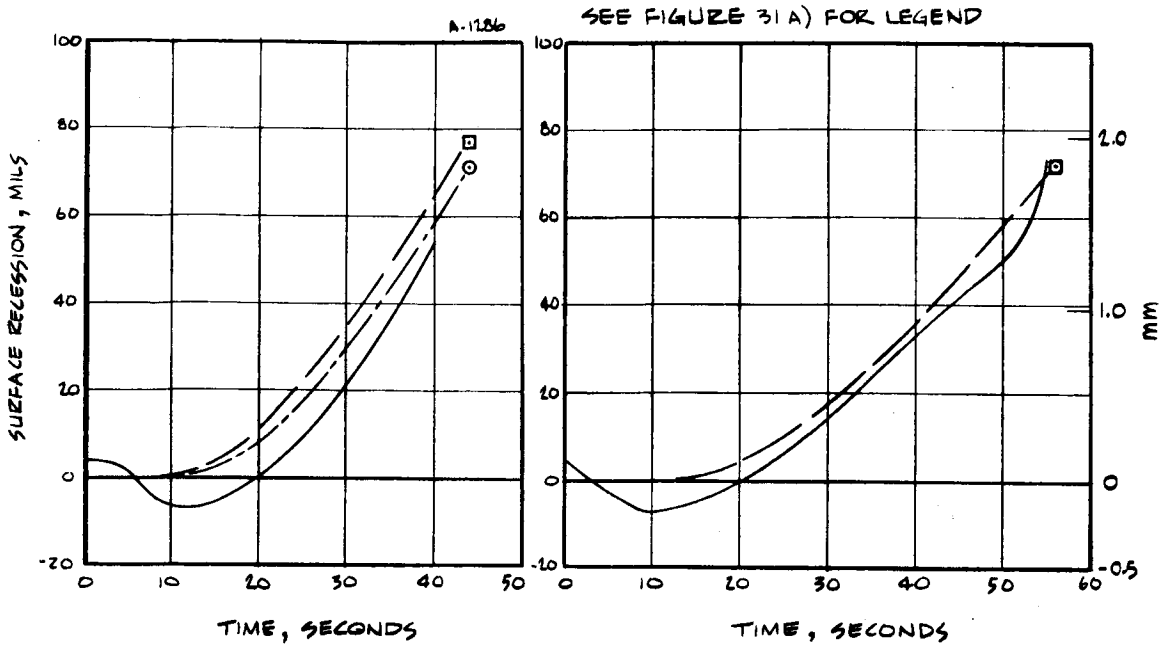
P) TEST 1124, O/F = 2.0, NL-21

SEE FIGURE 31 A) FOR LEGEND



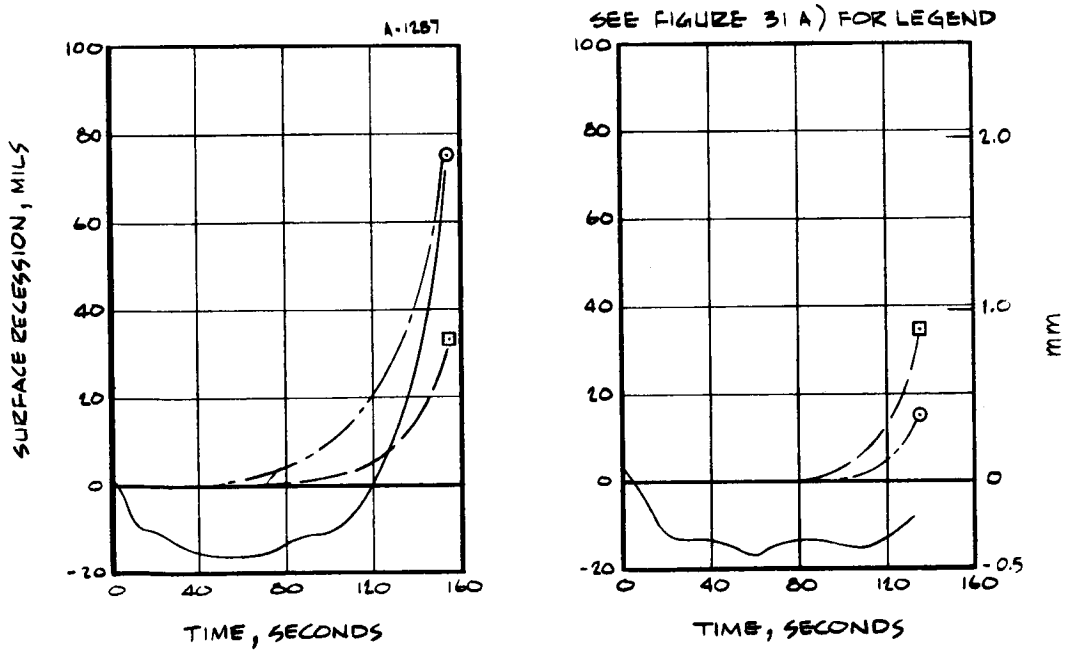
Q) TEST 1125, O/F = 2.0, NL-22

FIGURE 31, CONTINUED



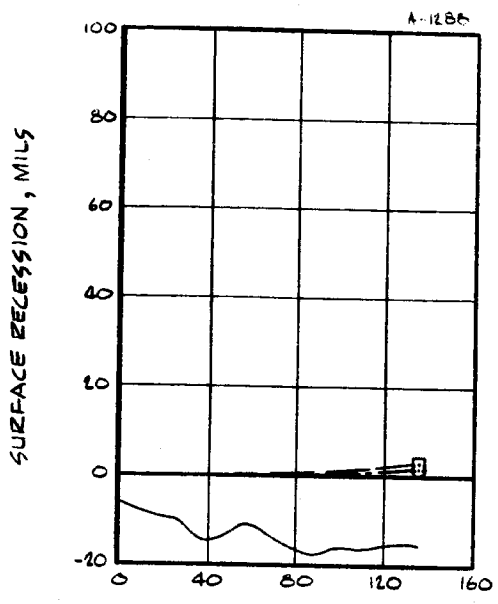
R) TEST 1128, O/F = 2.0, NL-23 S) TEST 1128, O/F = 2.0, NL-24

FIGURE 31, CONTINUED

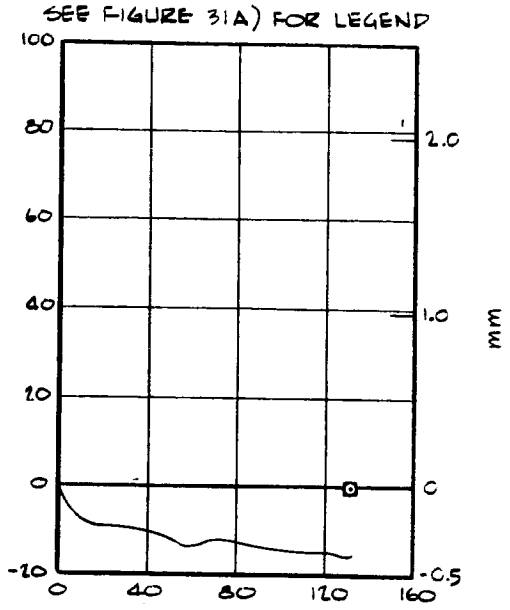


T) TEST 1120, O/F = 2.0, NL-19 U) TEST 1117, O/F = 2.0 NL-18

FIGURE 31 CONTINUED

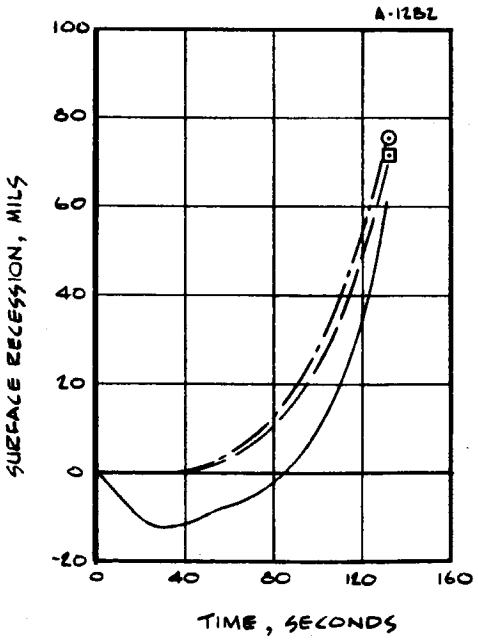


V) TEST 1121, O/F=2.0 NL-20

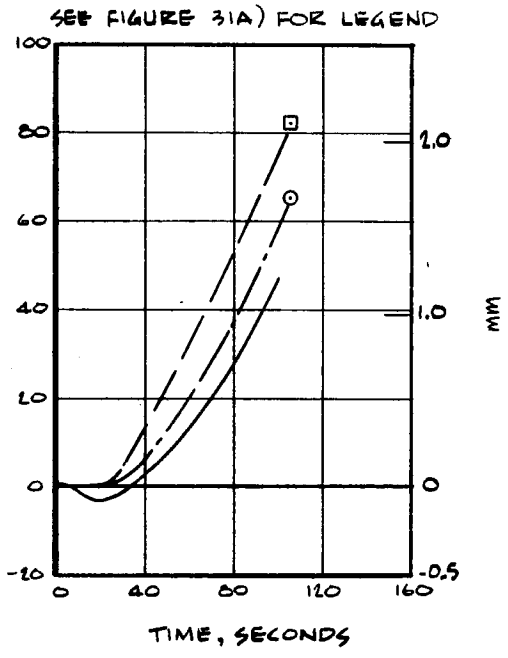


W) TEST 1116 O/F=2.0 NL-17

FIGURE 31, CONCLUDED

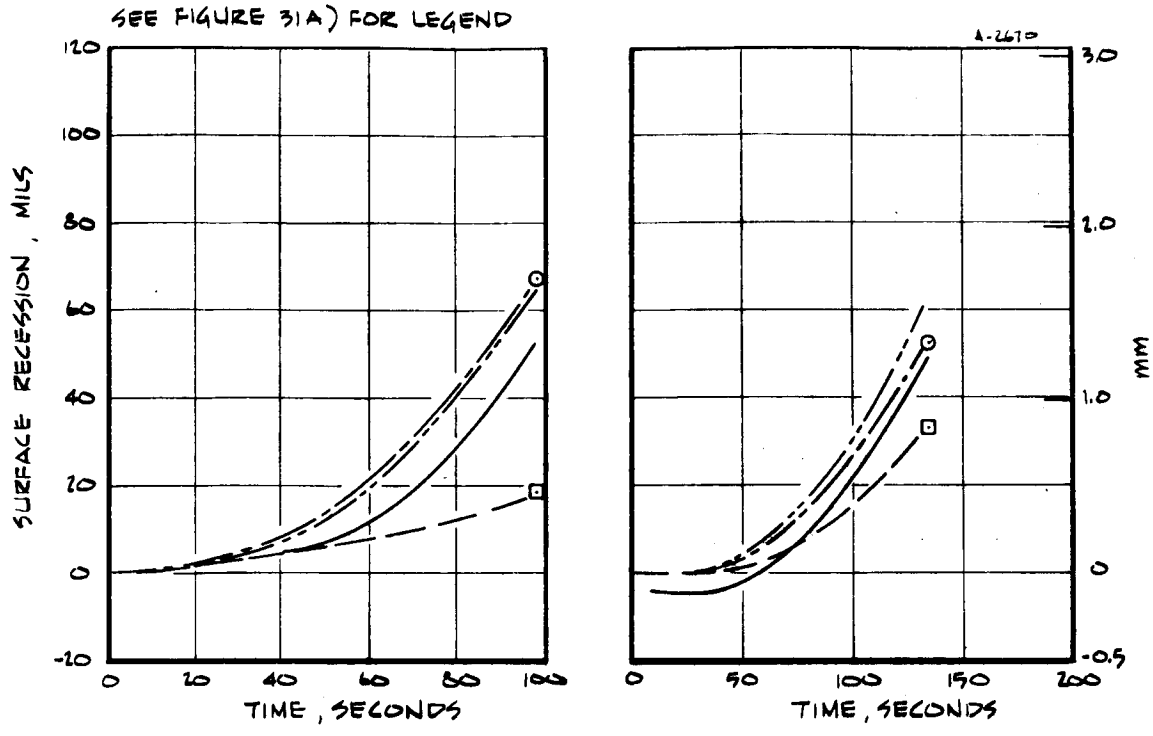


X) TEST 1098, O/F=1.0, NL-16



Y) TEST 1099, O/F=1.0, NL-15

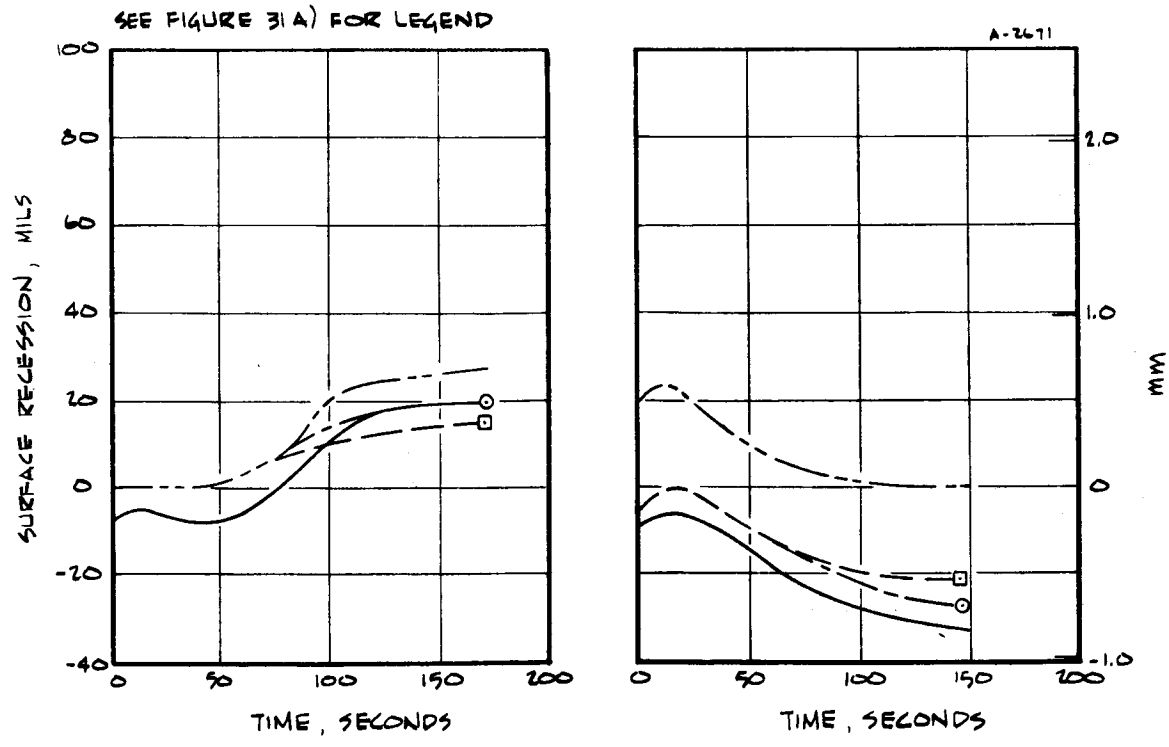
FIGURE 31, CONTINUED



Z) TEST 1338, O/F=1.0, NL-34

AA) TEST 1336, O/F=1.0, NL-32

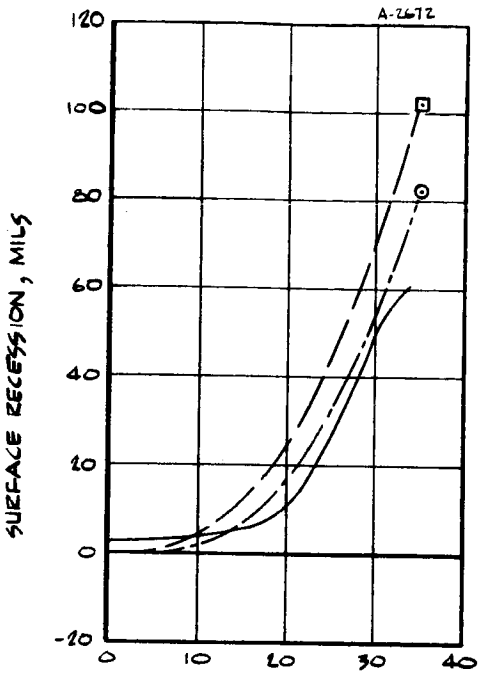
FIGURE 31, CONTINUED



BB) TEST 1339, O/F=1.0, NL-35

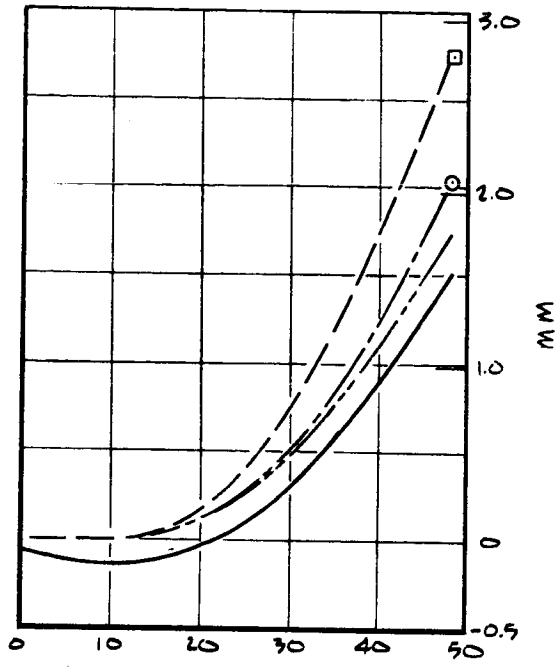
CC) TEST 1337, O/F=1.0, NL-33

FIGURE 31, CONTINUED



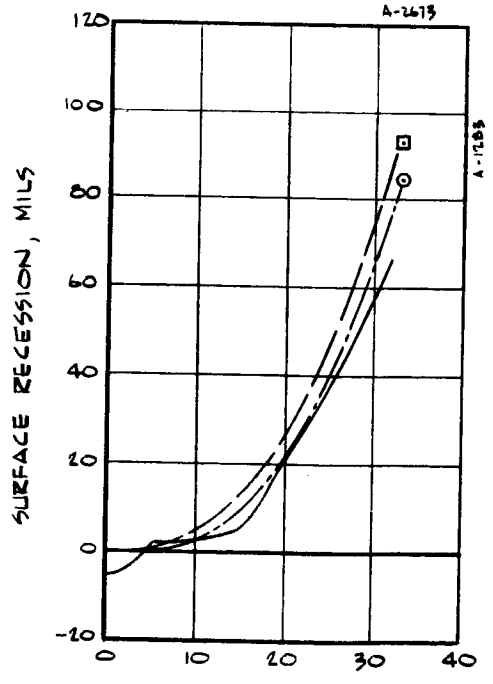
DD) TEST 1145, O/F = 0.38, NL-10

SEE FIGURE 31 A) FOR LEGEND



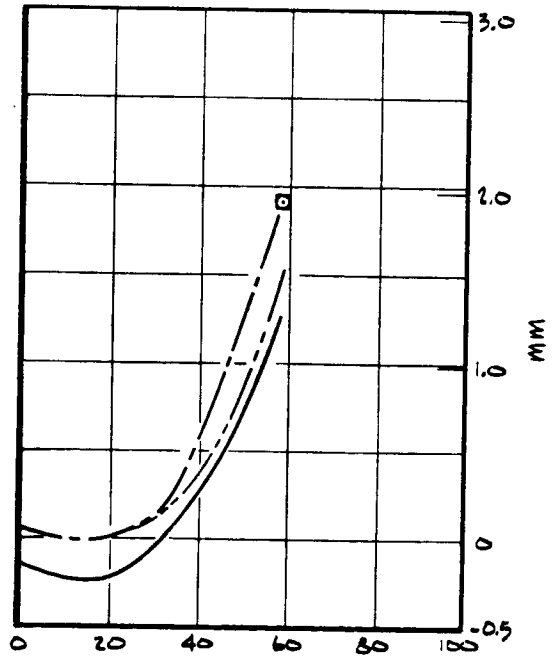
EE) TEST 1348, O/F = 0.38, NL-37

FIGURE 31, CONTINUED



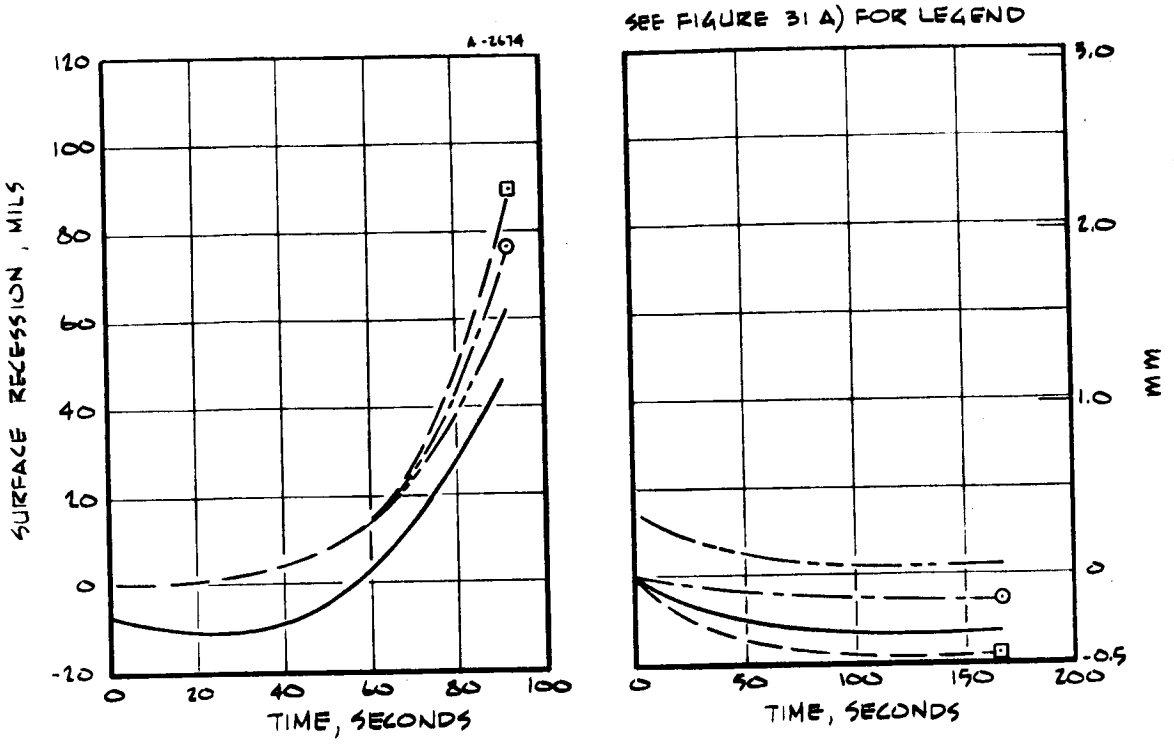
FF) TEST 1146, O/F = 0.38, NL-27

SEE FIGURE 31 A) FOR LEGEND



GG) TEST 1350, O/F = 0.38, NL-39

FIGURE 31, CONTINUED



HH) TEST 1347, O/F=0.38, NL-36

II) TEST 1340, O/F=0.38, NL-38

FIGURE 31, CONCLUDED

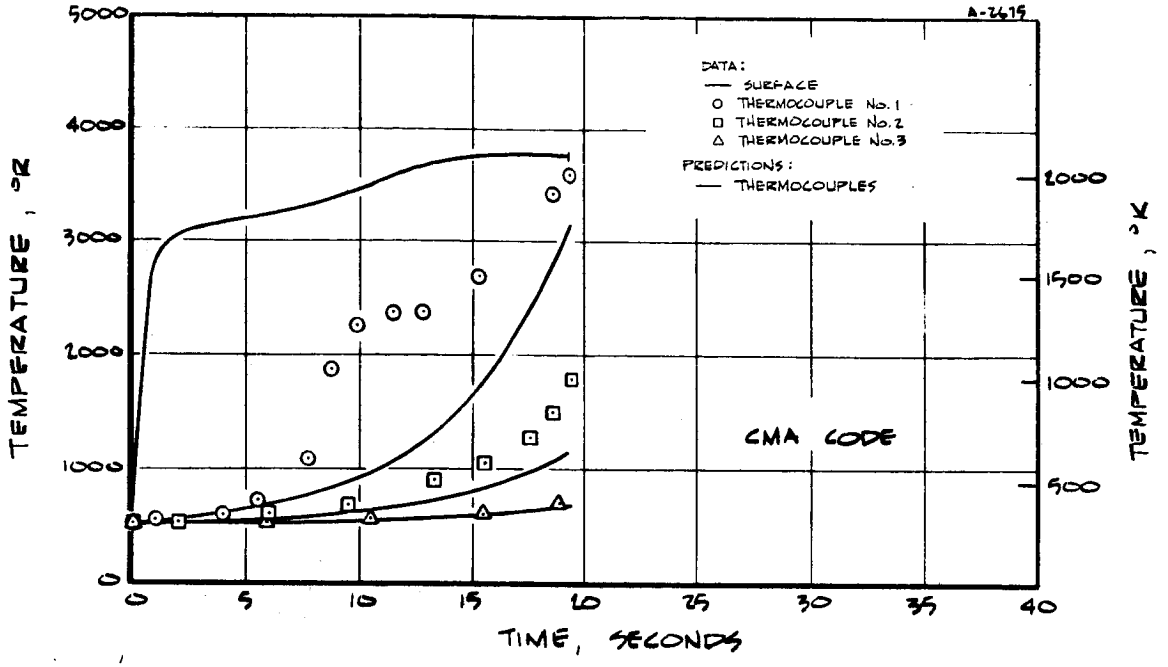


FIGURE 32, MEASURED AND PREDICTED ABLATIVE NOZZLE THERMAL RESPONSE HISTORIES

A) O/F = ∞, TEST 1083, NL-11

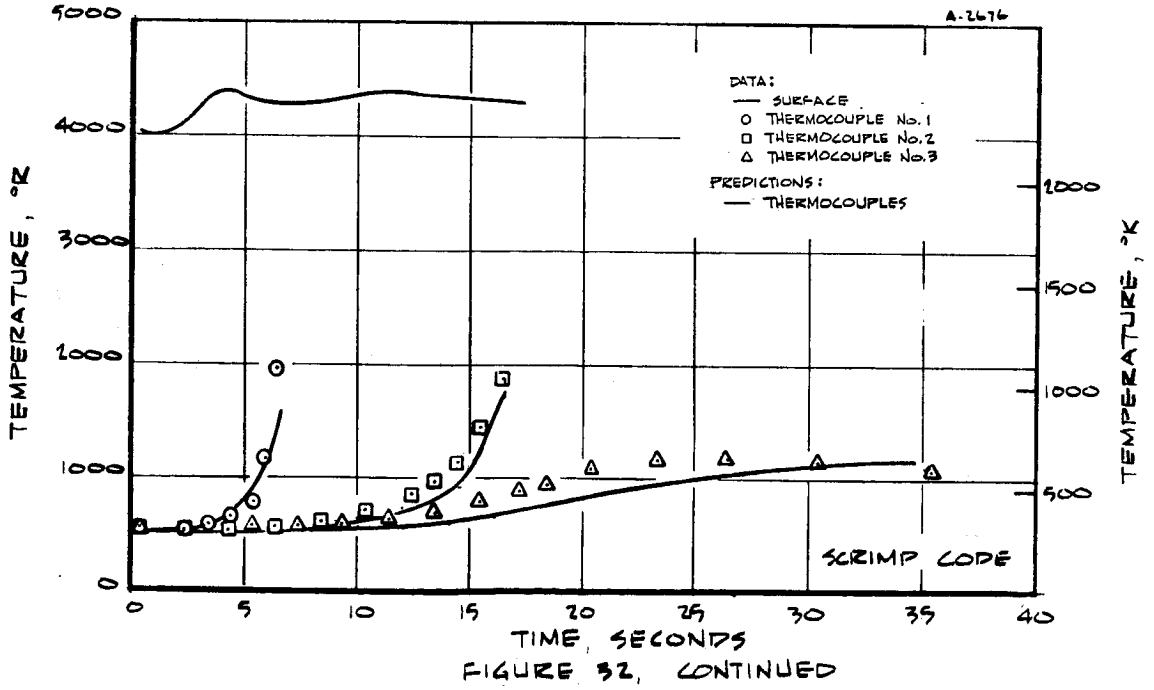


FIGURE 32, CONTINUED

B) O/F = ∞, TEST 1358, NL-42

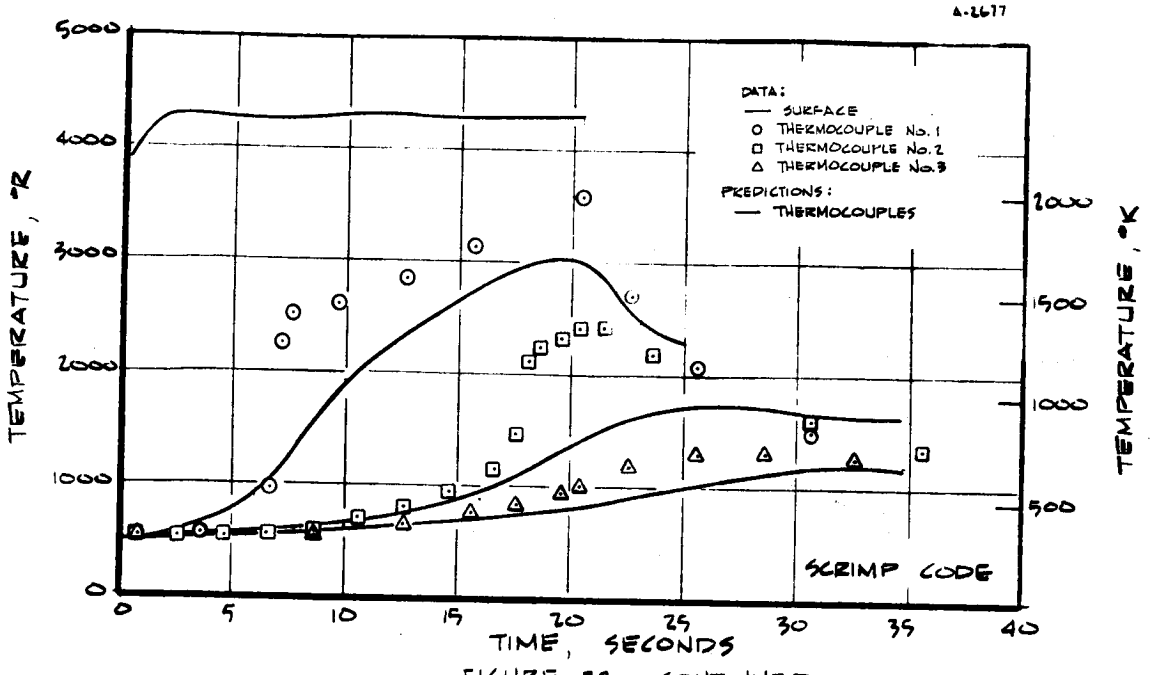


FIGURE 32, CONTINUED

C) O/F = ∞, TEST 1359, NL-29

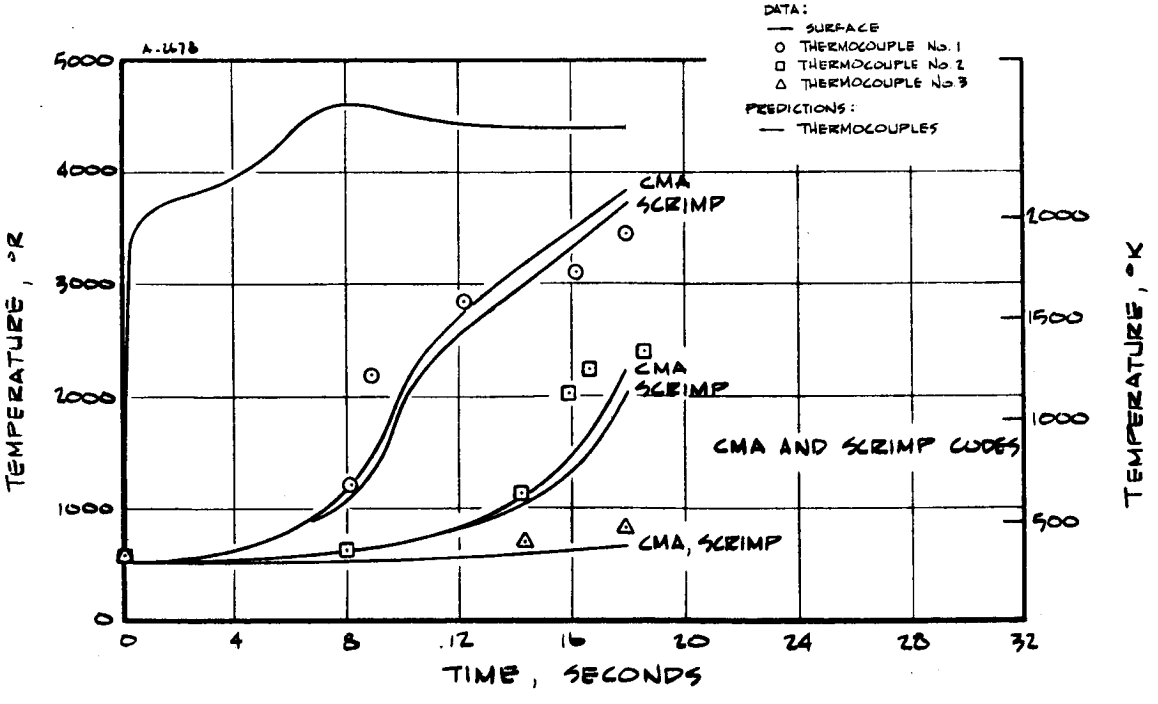


FIGURE 32, CONTINUED

D) O/F = ∞, TEST 1084, NL-12

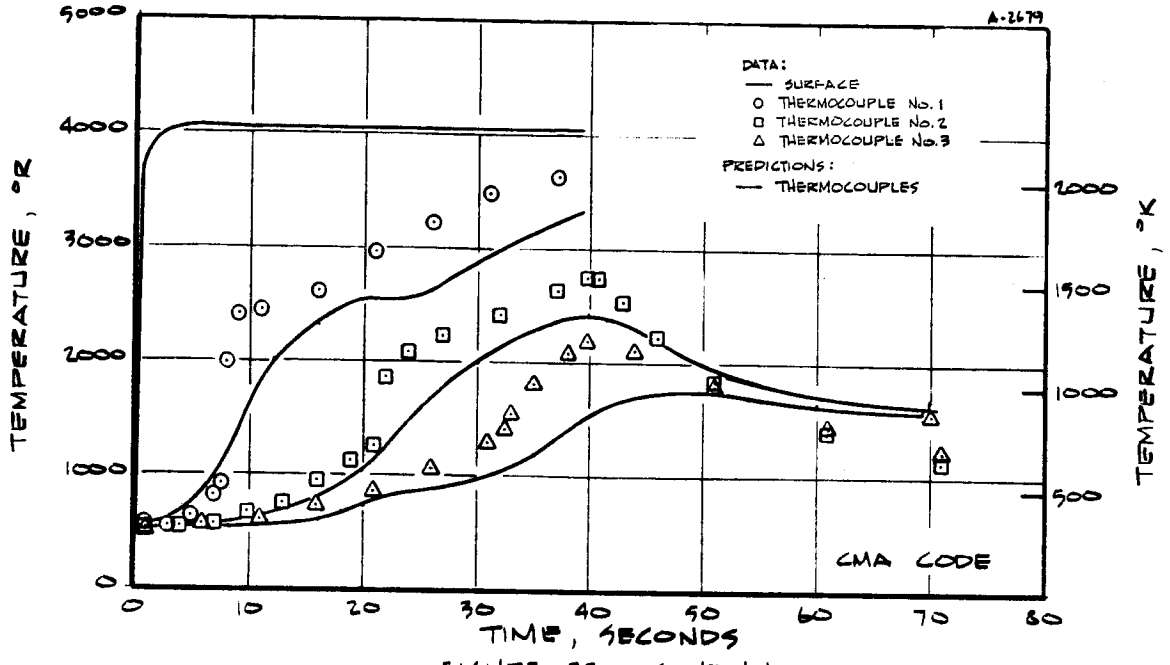


FIGURE 32, CONTINUED

E) O/F = ∞, TEST 1361, NL-40

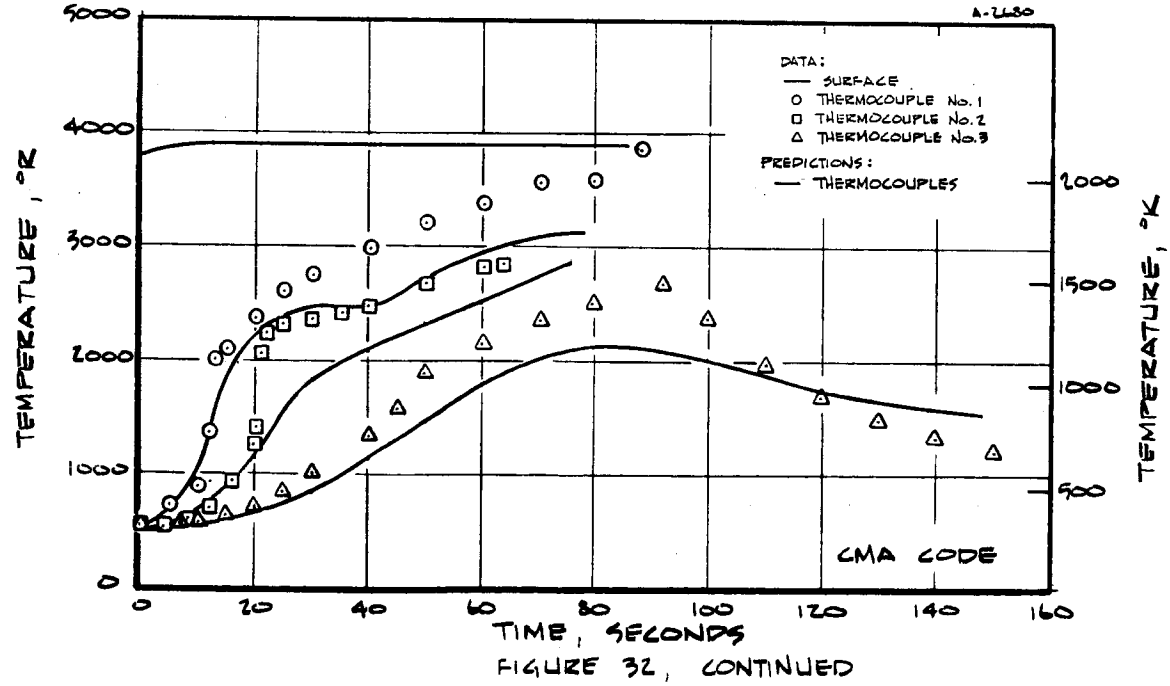


FIGURE 32, CONTINUED

F) O/F = ∞, TEST 1362, NL-41

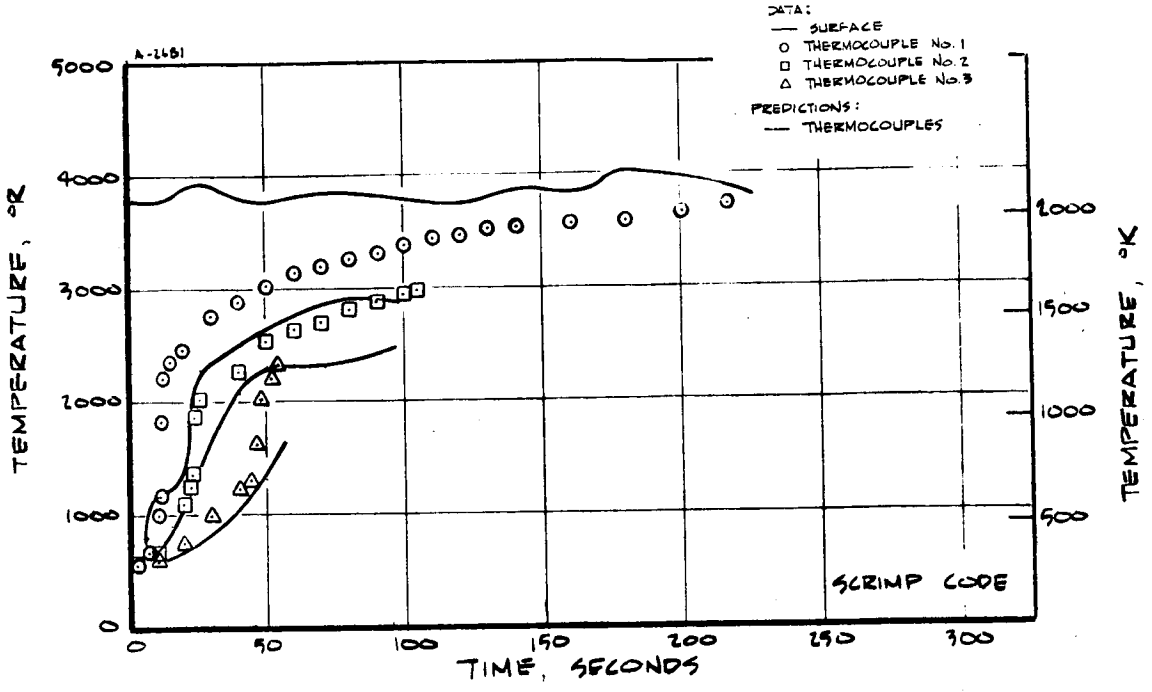


FIGURE 32, CONTINUED

G) O/F = ∞, TEST 1360, NL-44

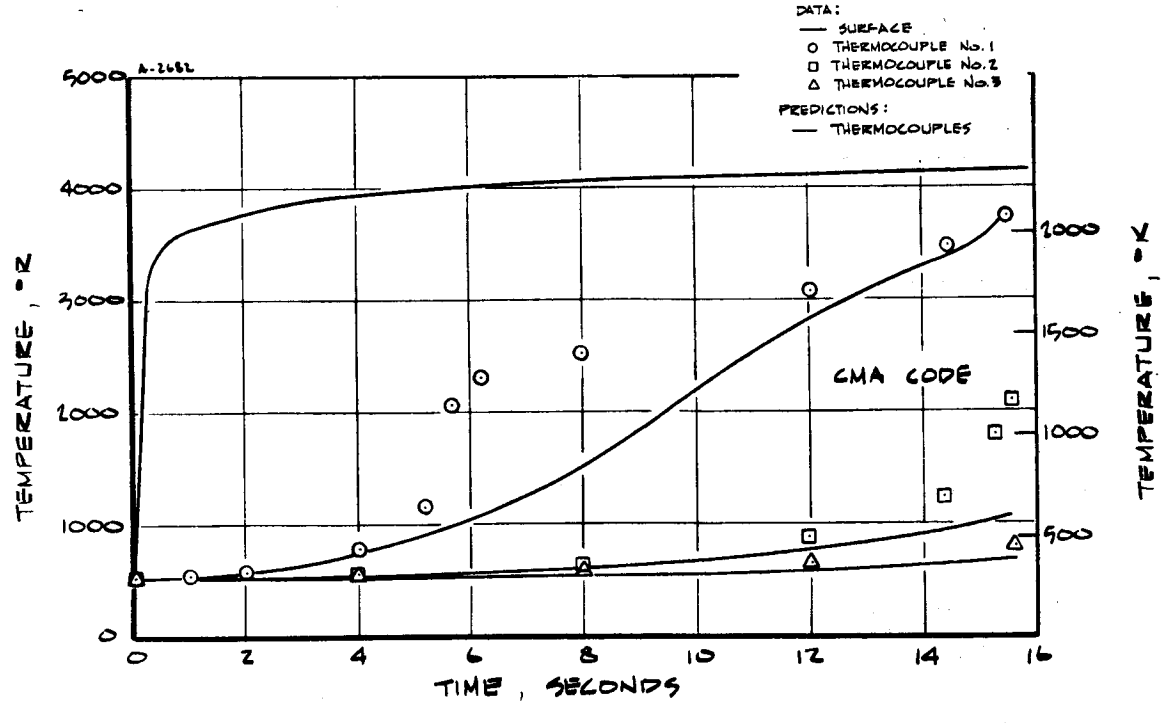


FIGURE 32, CONTINUED

H) O/F = 4.0, TEST 1091, NL-13

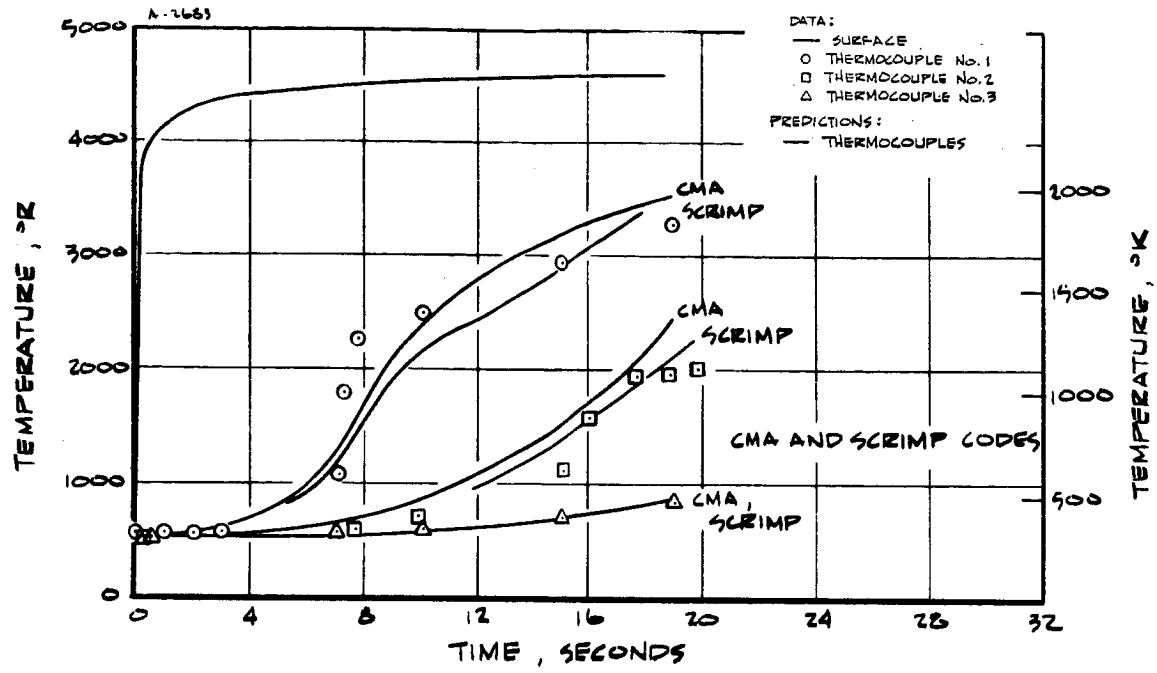


FIGURE 32, CONTINUED

I) O/F = 4.0, TEST 1092, NL-14

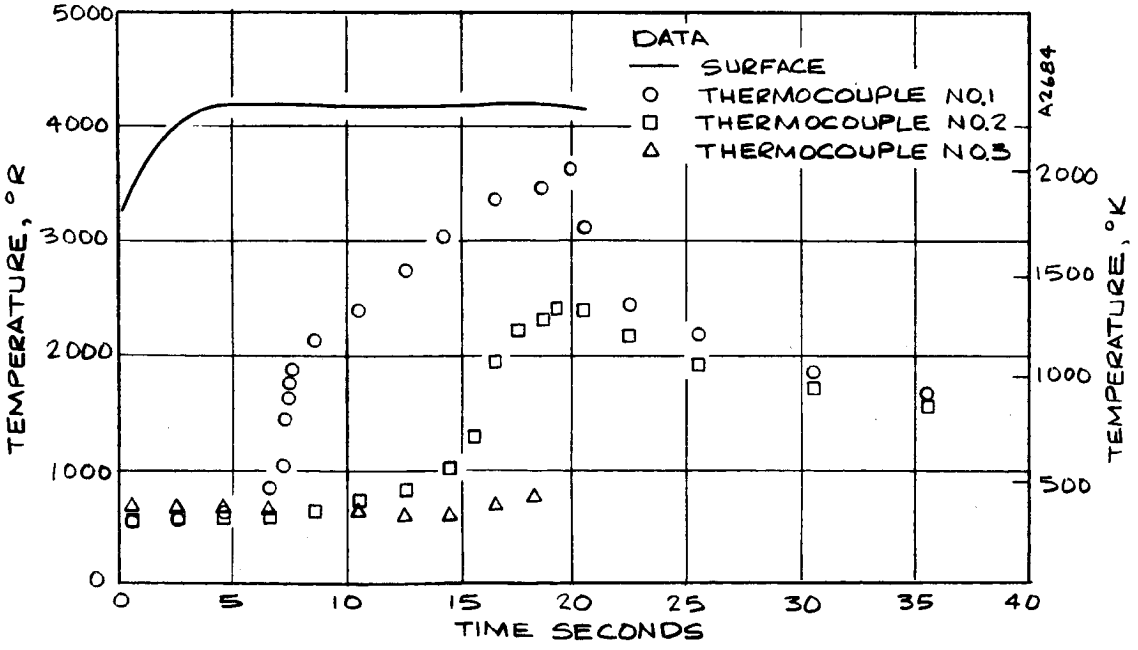


FIGURE 32, CONTINUED

J) O/F = 4.0, TEST 1329, NL-28

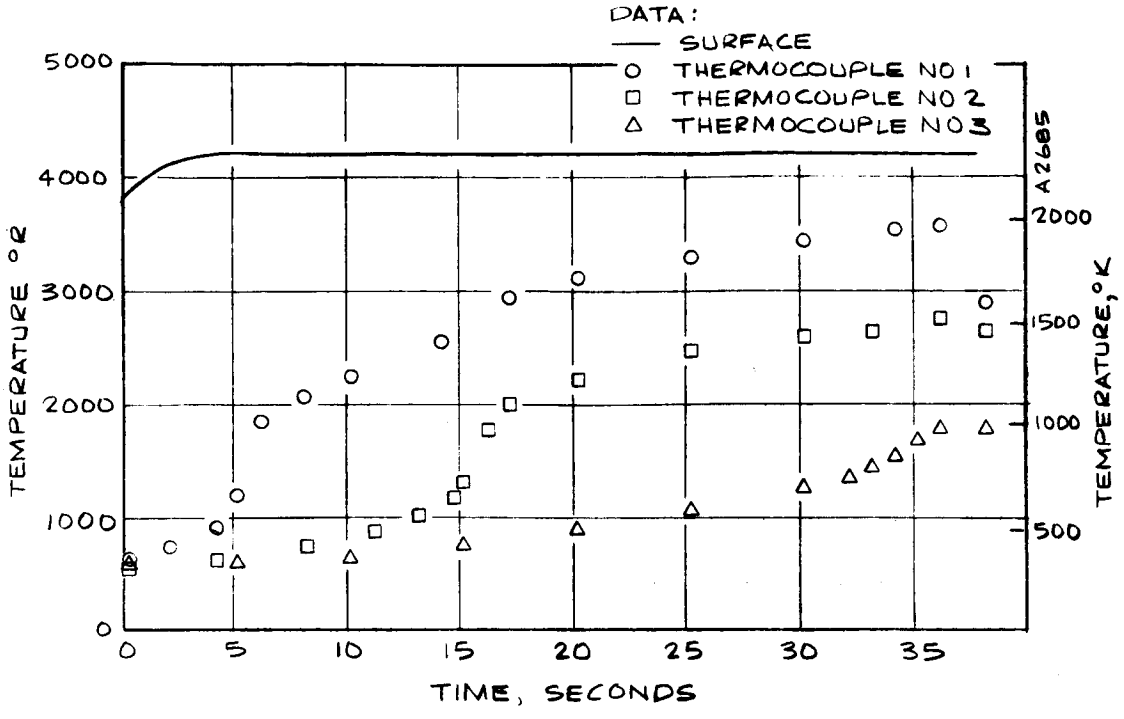


FIGURE 32, CONTINUED

K) O/F = 4.0, TEST 1332, NL-31

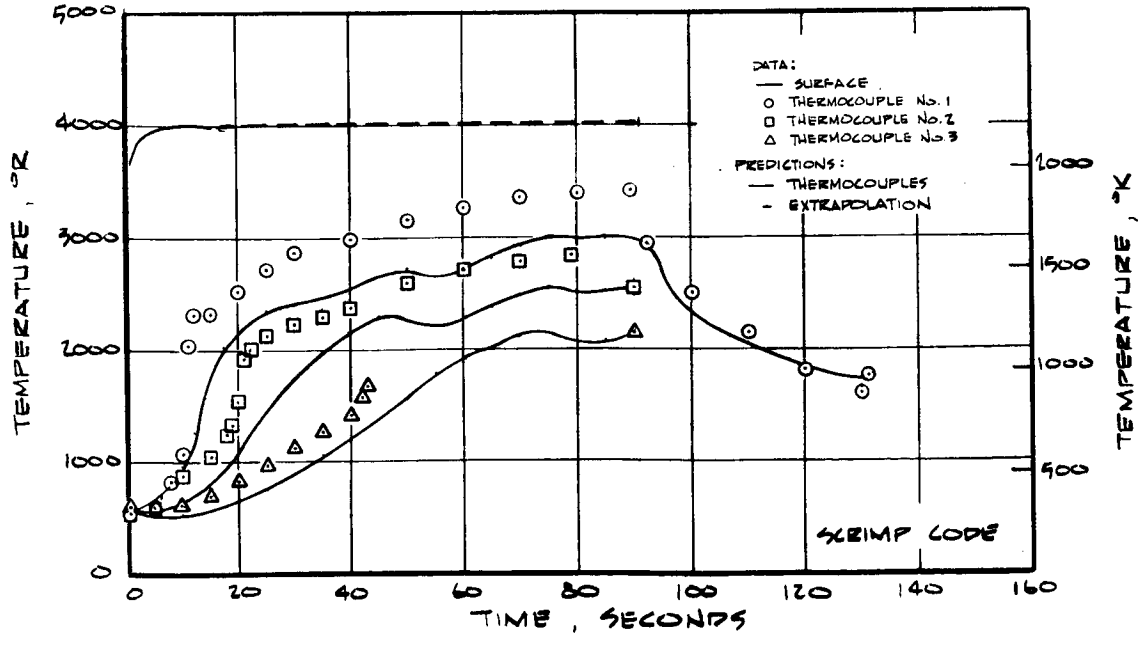


FIGURE 32, CONTINUED

L) O/F = 4.0, TEST 1330, NL-29

A-2686

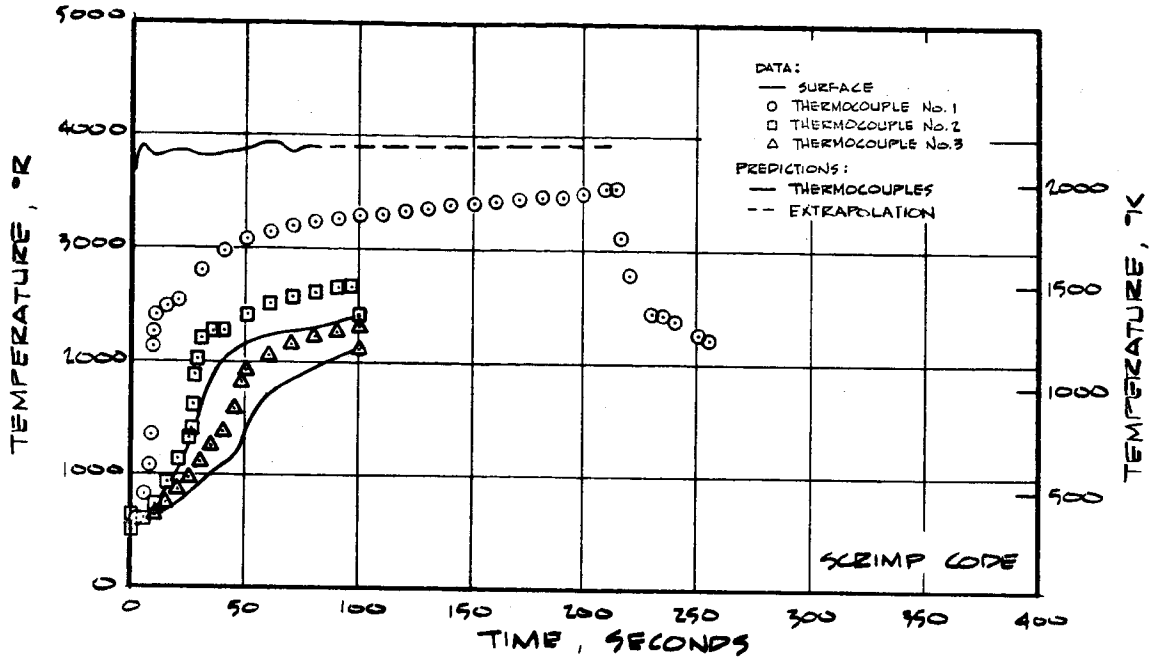


FIGURE 32, CONTINUED

M) O/F = 4.0, TEST 1331, NL-30

A-2687

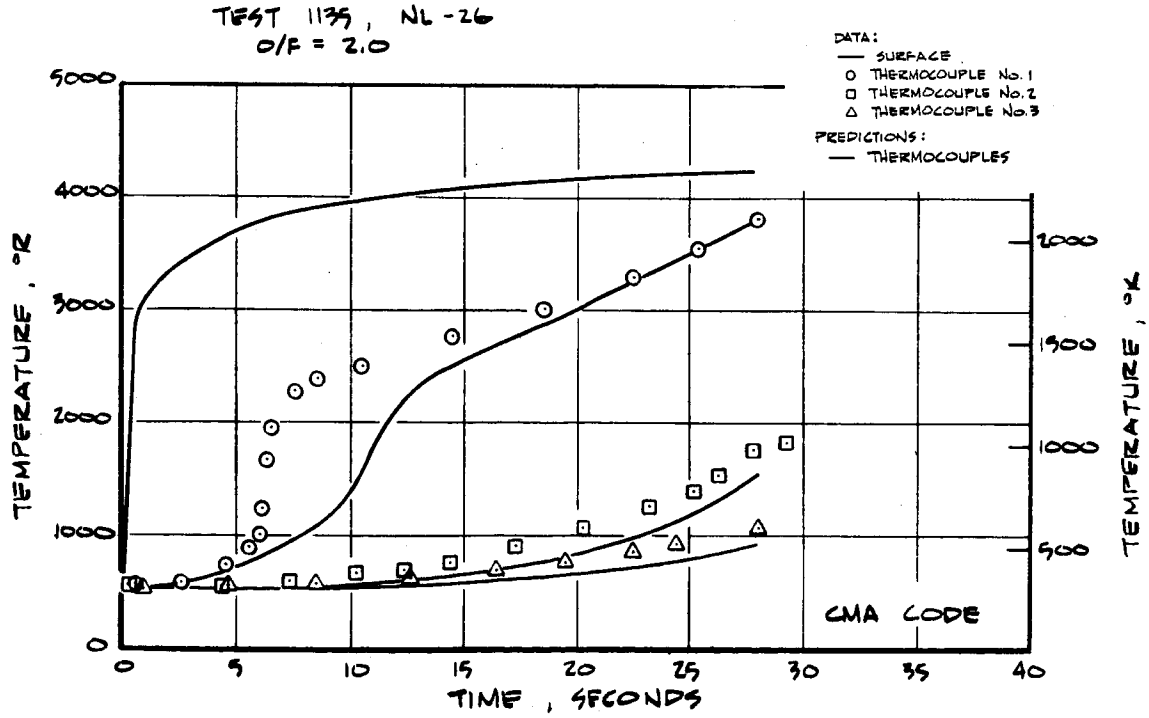


FIGURE 32, CONTINUED

N) O/F = 2.0, TEST 1135, NL-26

A-2688

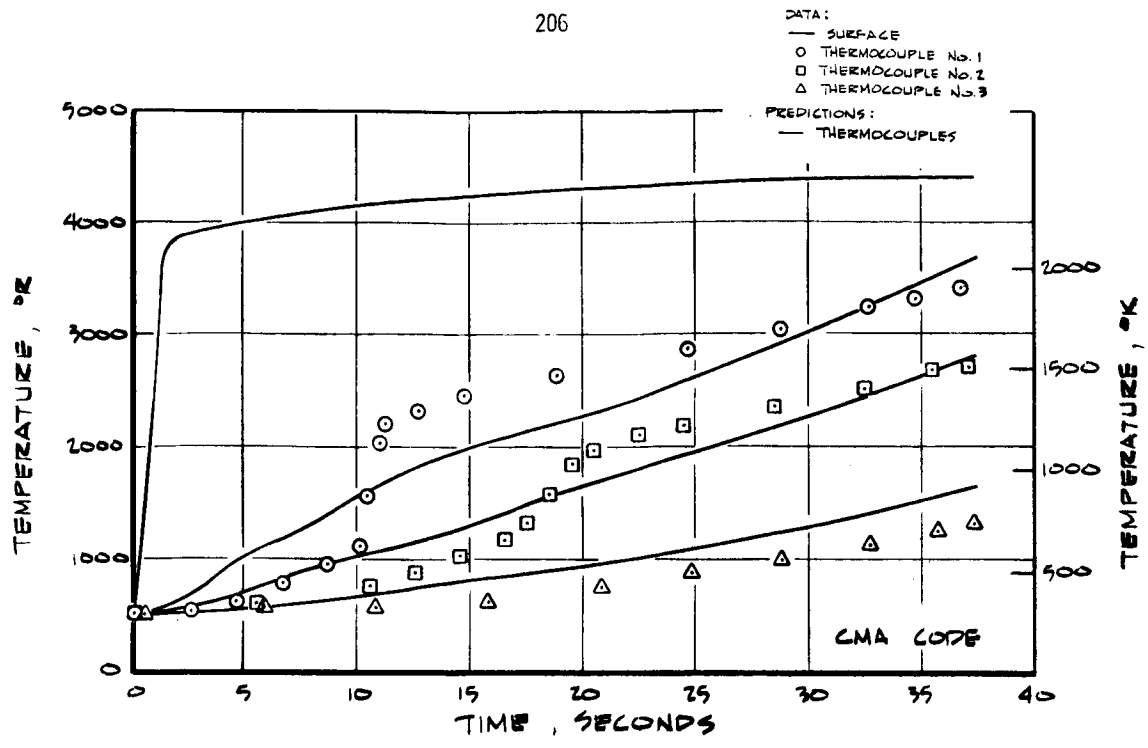


FIGURE 32, CONTINUED

o) O/F = 2.0, TEST 1134, NL-25

A-2689

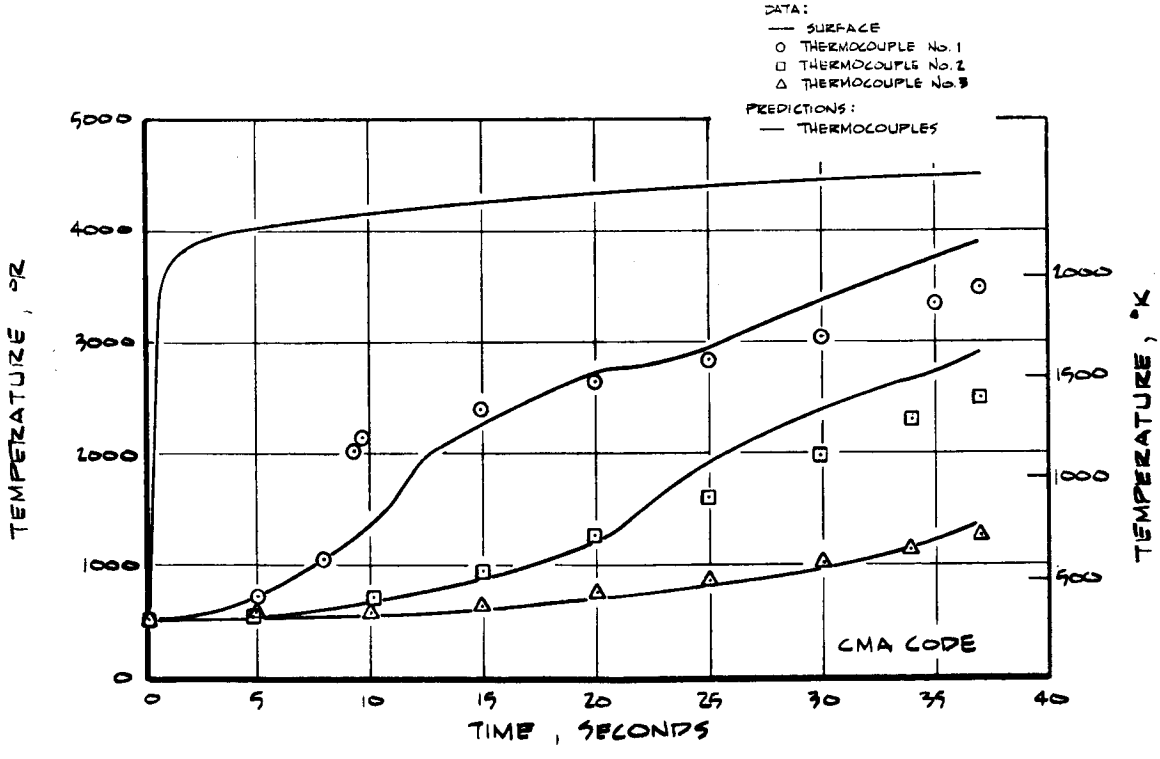


FIGURE 32, CONTINUED

P) O/F = 2.0, TEST 1124, NL-21

A-2690

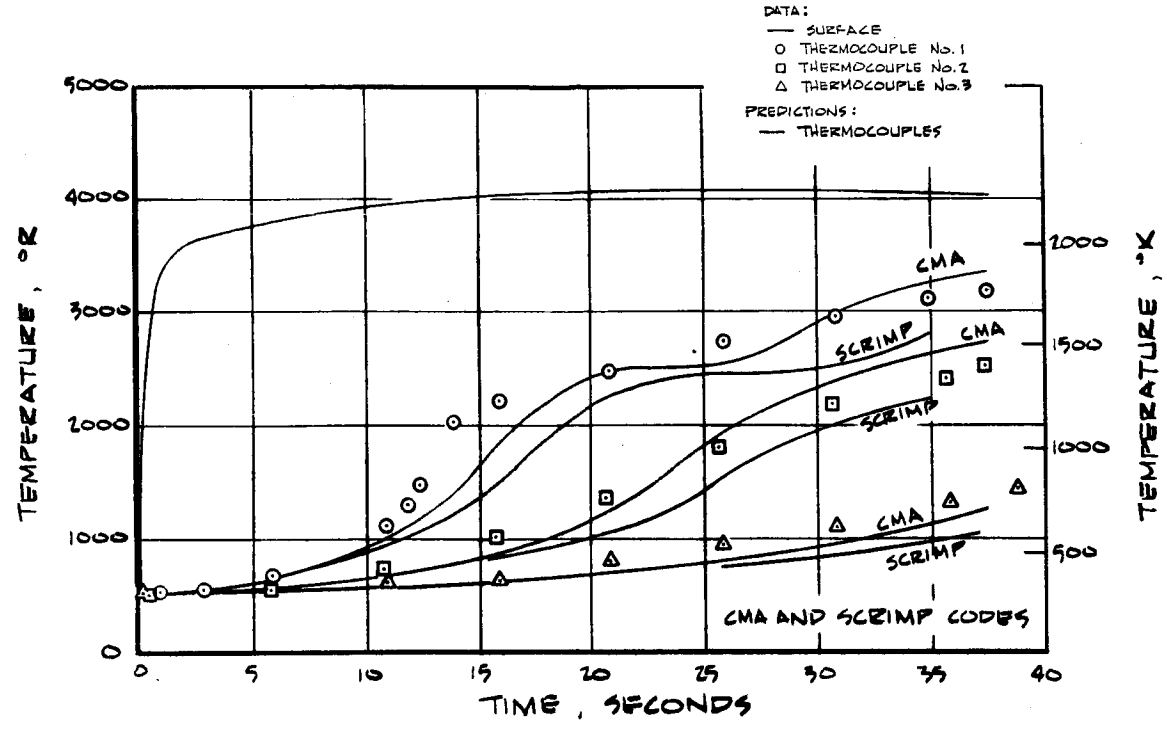


FIGURE 32, CONTINUED

Q) O/F = 2.0, TEST 1125, NL-22

A-2691

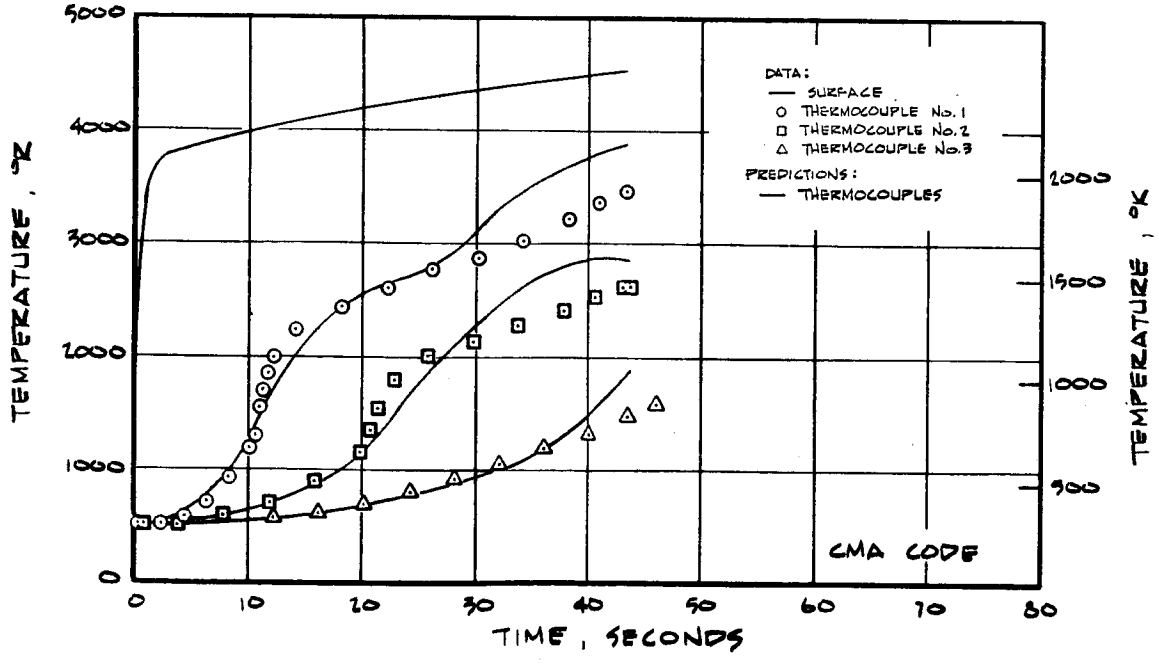


FIGURE 32, CONTINUED

R) O/F = 2.0, TEST 1128, NL-23

A-2692

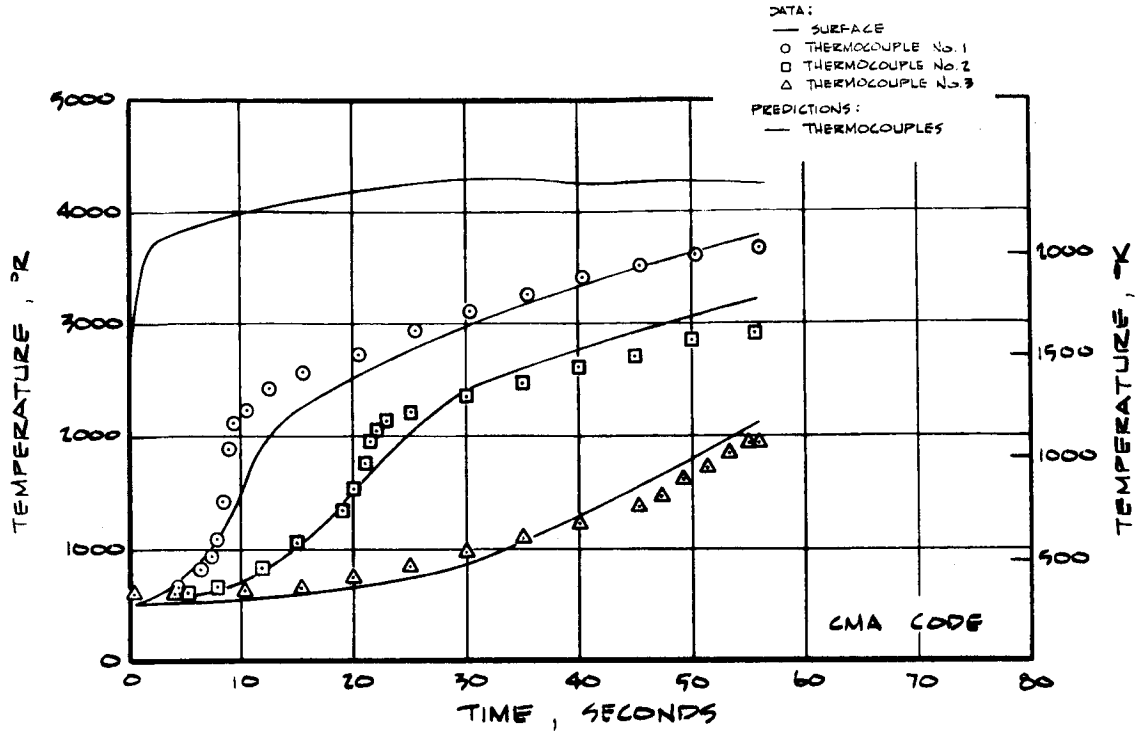


FIGURE 32, CONTINUED

S) O/F = 2.0, TEST 1129, NL-24

A-2491

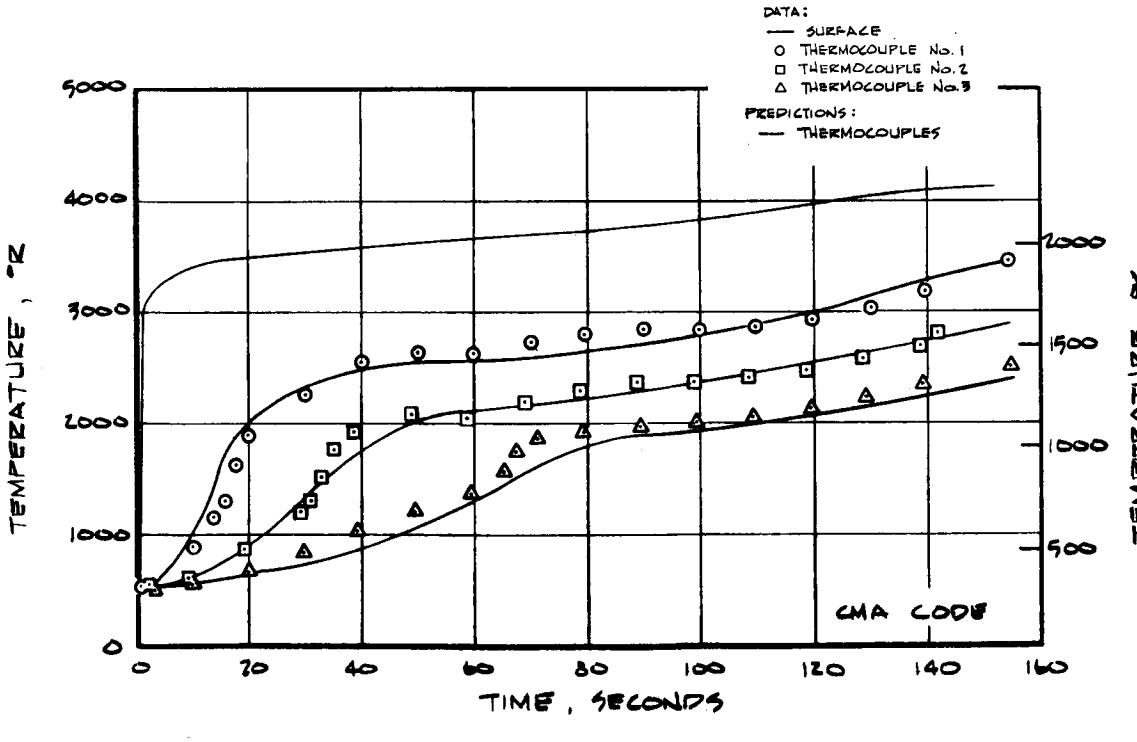


FIGURE 32, CONTINUED

T) O/F = 2.0, TEST 1120, NL-19

A-2494

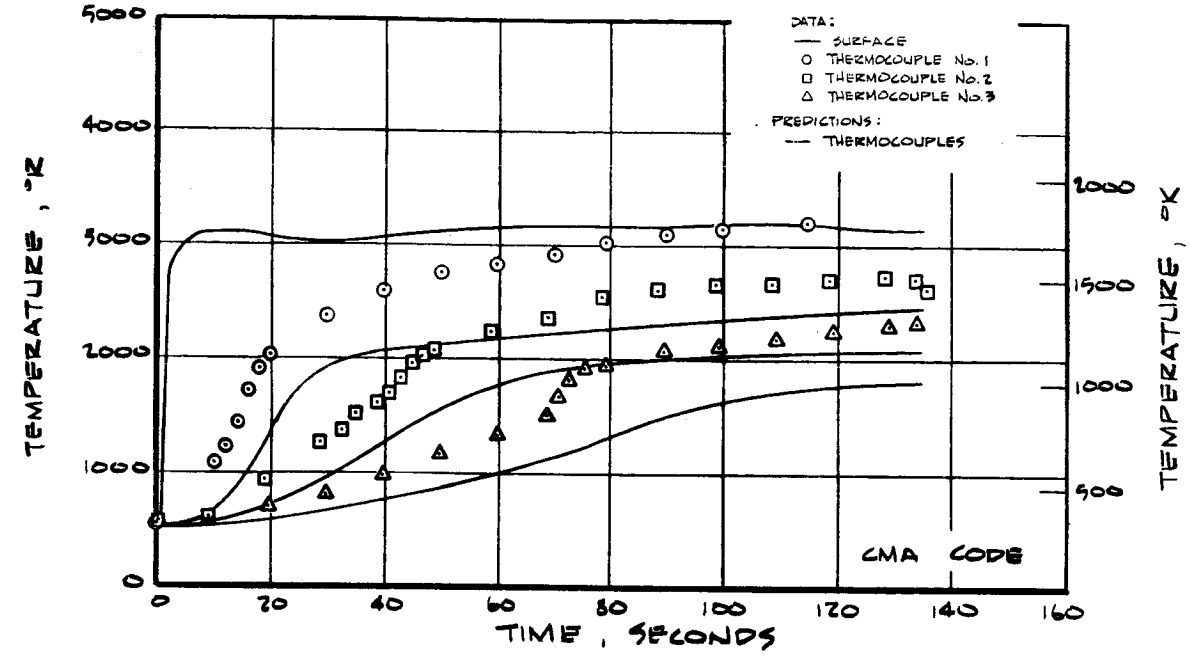


FIGURE 32, CONTINUED

U) O/F = 2.0, TEST 1117, NL-18

A-2695

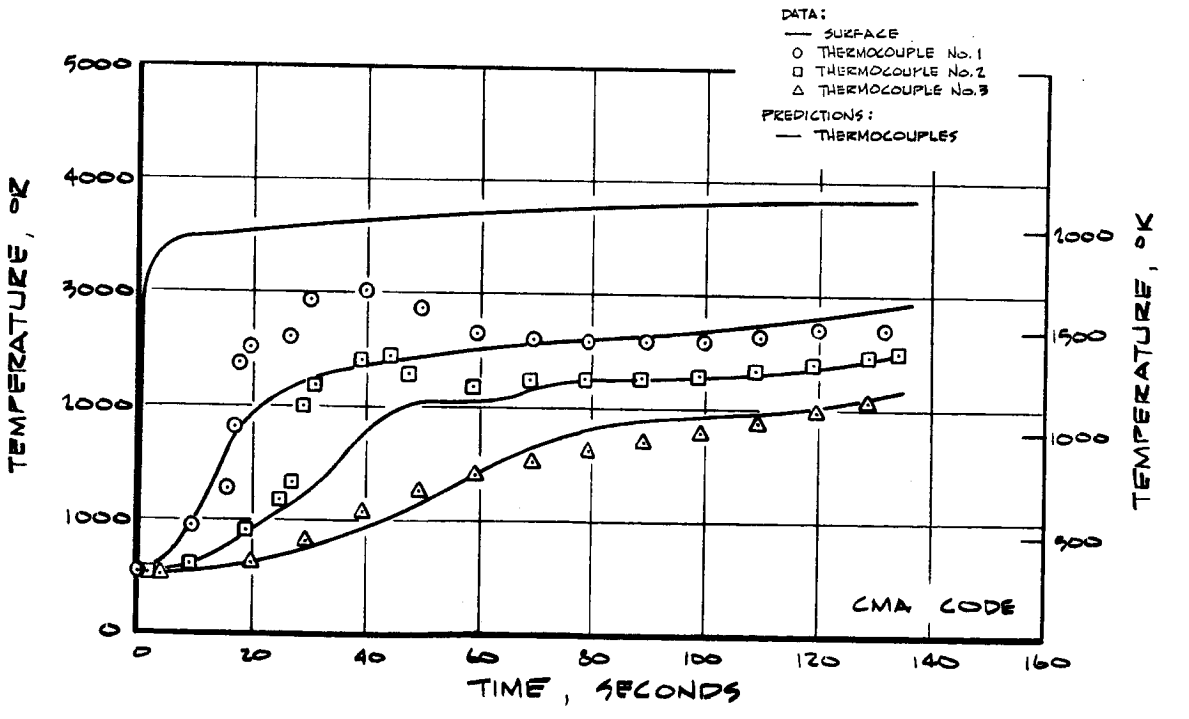


FIGURE 32, CONTINUED

V) O/F = 2.0, TEST 1121, NL-20

A-2696

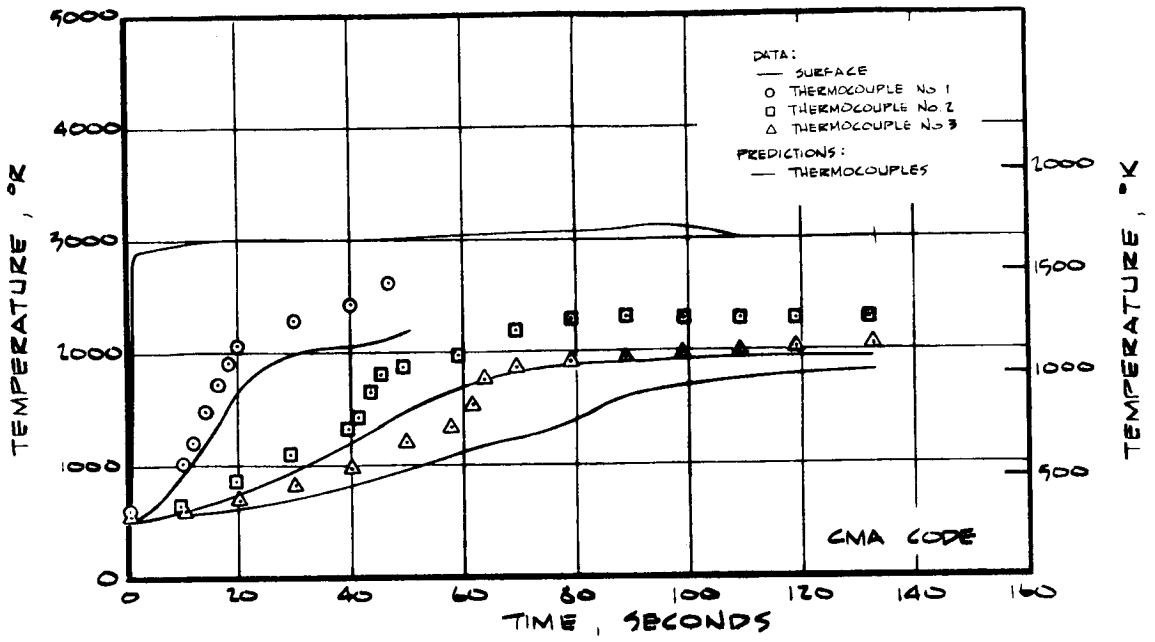


FIGURE 32, CONTINUED

W) O/F = 2.0, TEST 1116, NL-17

A-2697

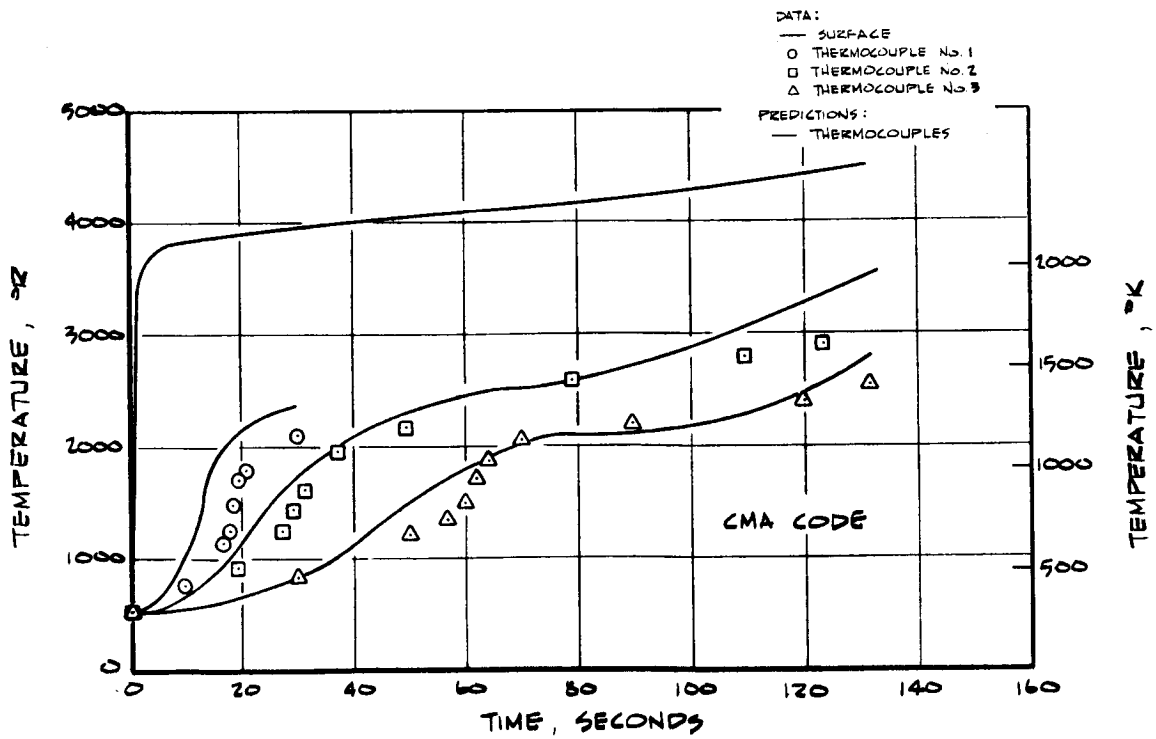


FIGURE 32, CONTINUED

X) O/F = 1.0, TEST 1098, NL-16

A-2698

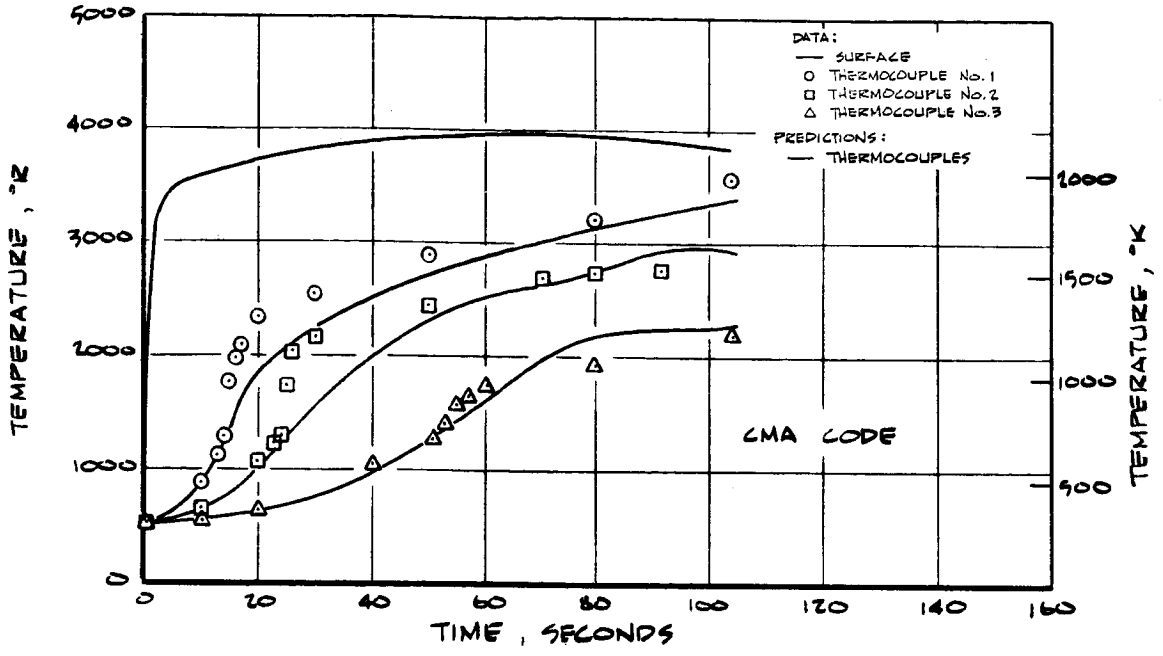


FIGURE 32, CONTINUED

Y) O/F = 1.0, TEST 1099, NL-15

A-2699

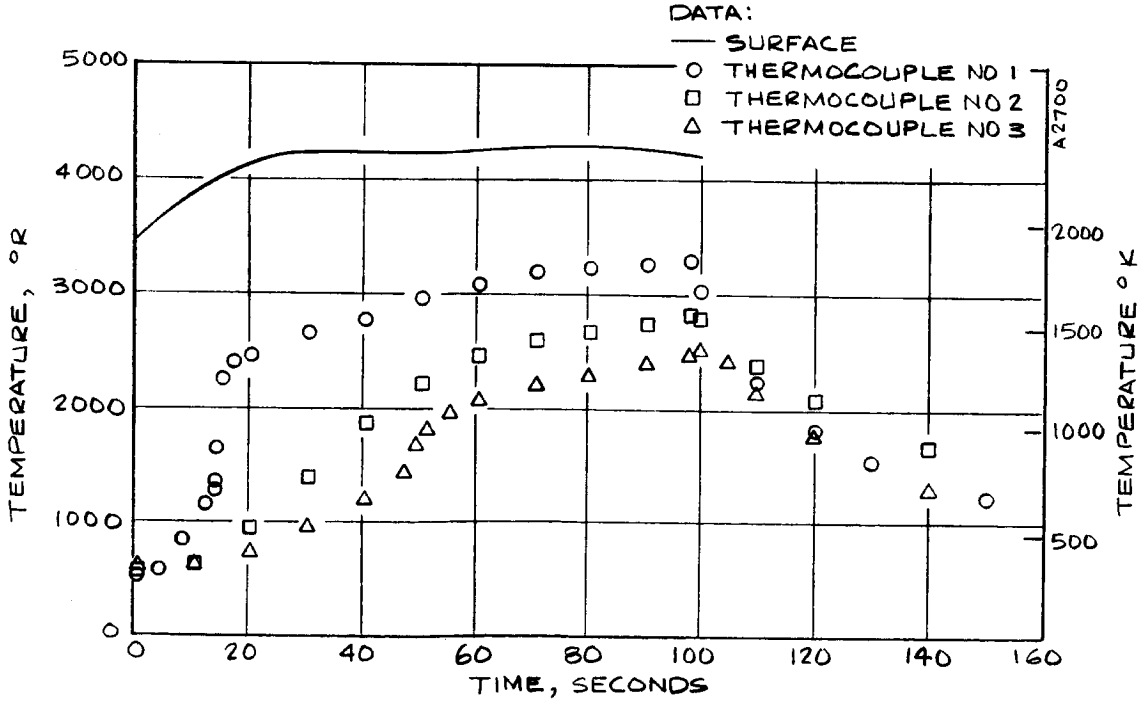


FIGURE 32, CONTINUED

Z) O/F = .38, TEST 1338, NL-34

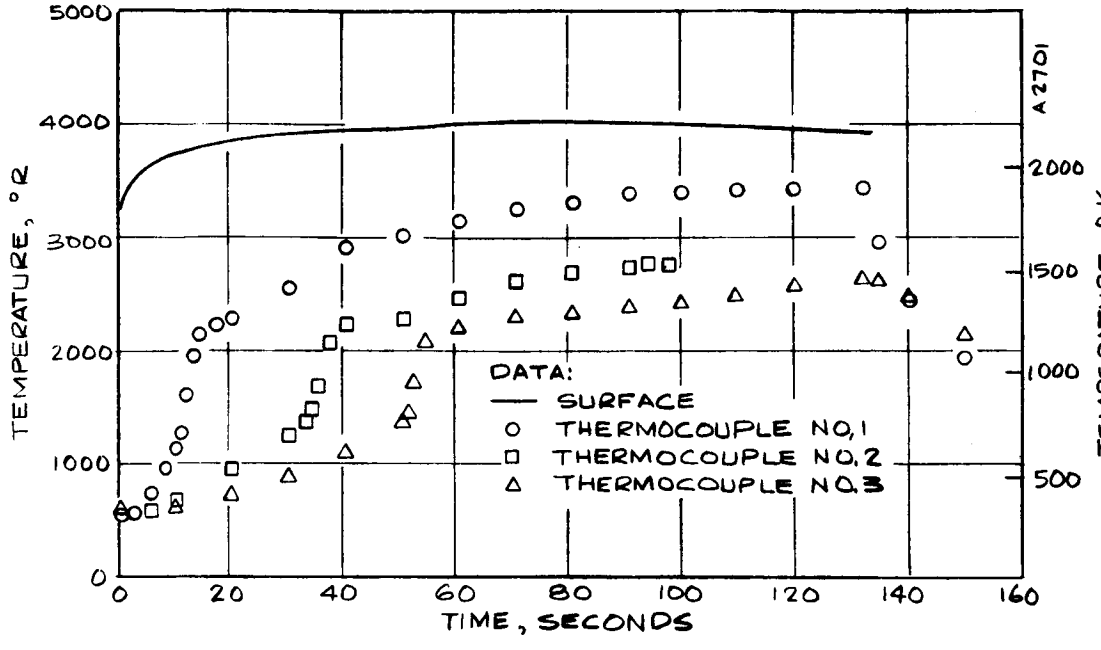


FIGURE 32, CONTINUED

AA) O/F=1.0, TEST 1336, NL-32

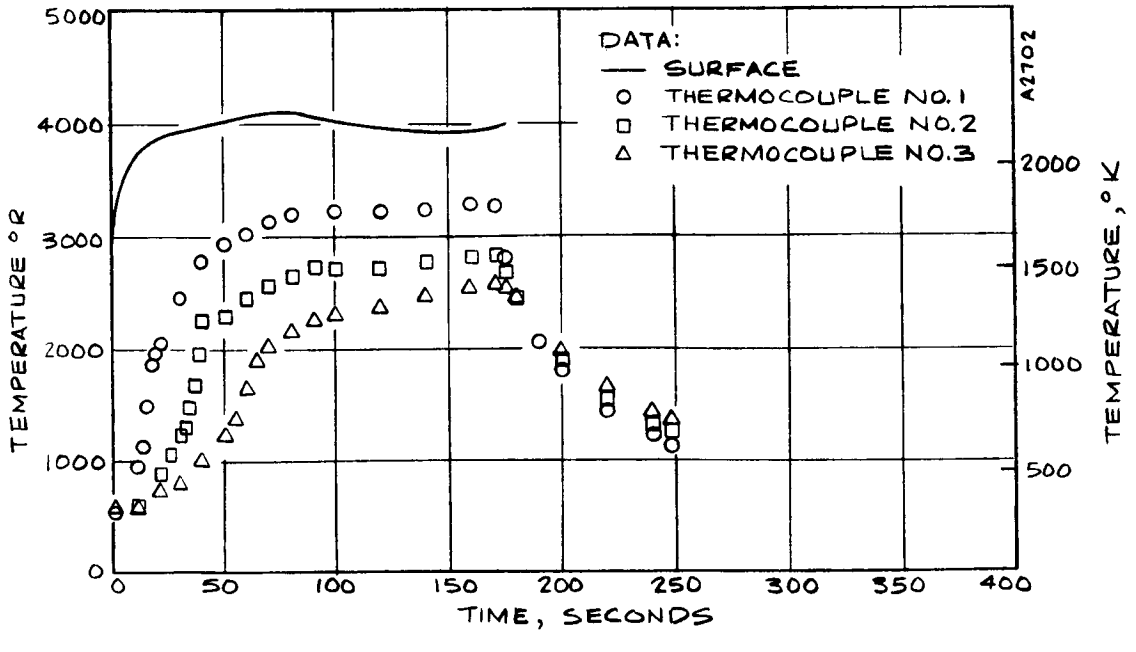


FIGURE 32, CONTINUED

BB) O/F=1.0, TEST 1339, NL-35

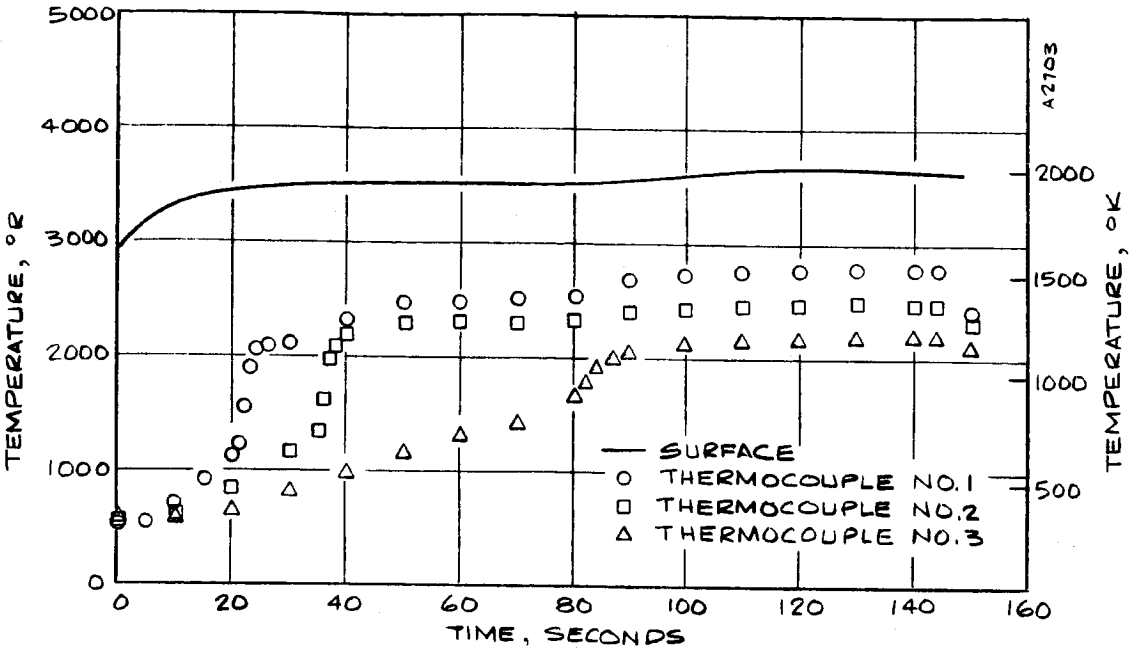


FIGURE 32, CONTINUED

CC) O/F=1.0, TEST 1337, NL-35

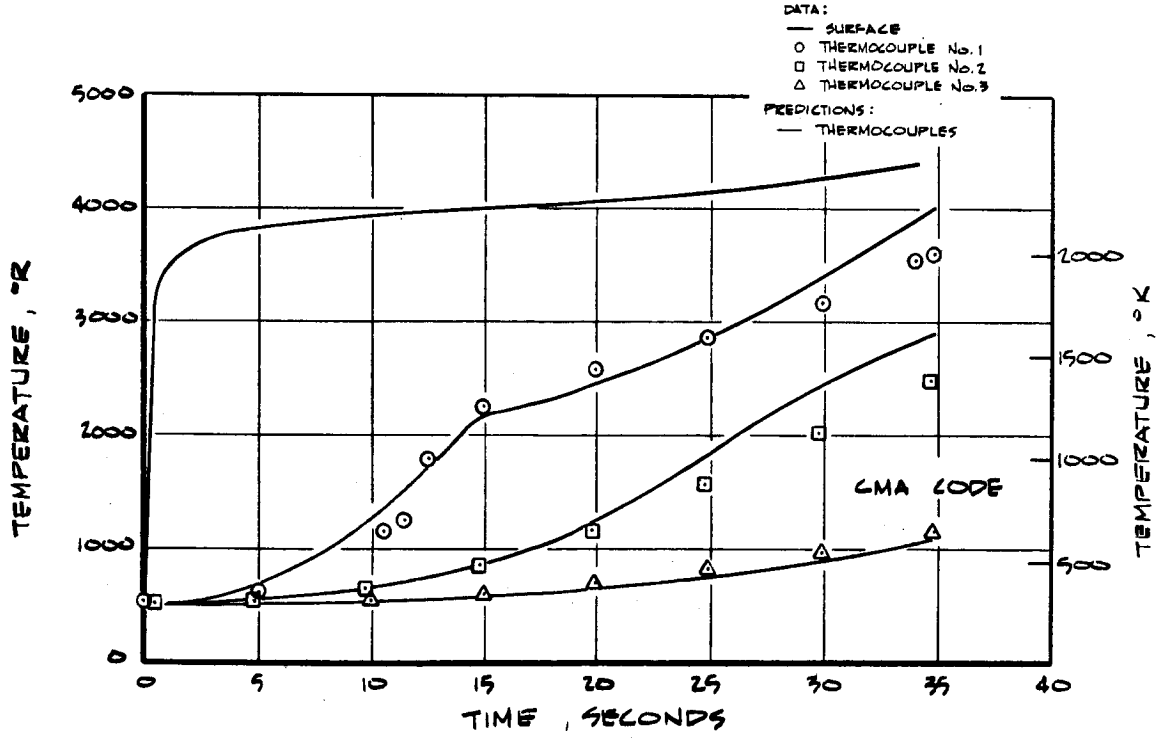


FIGURE 32, CONTINUED

DD) O/F = .38, TEST 1145, NL-10

A-2704

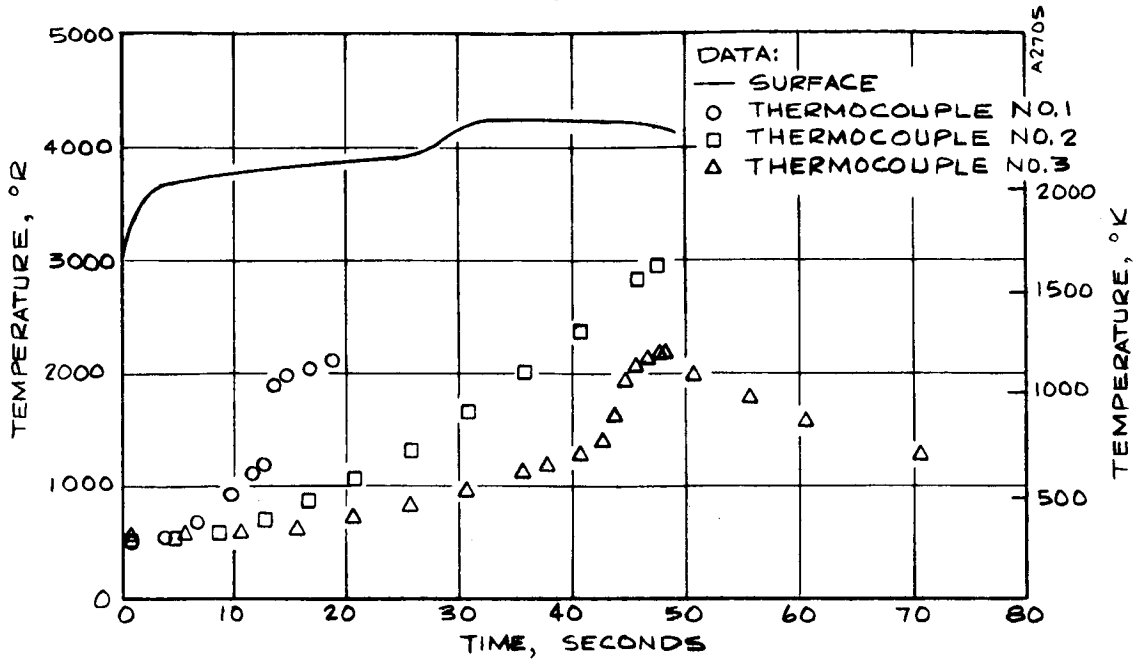


FIGURE 32, CONTINUED

EE) O/F = .38, TEST 1348, NL-37

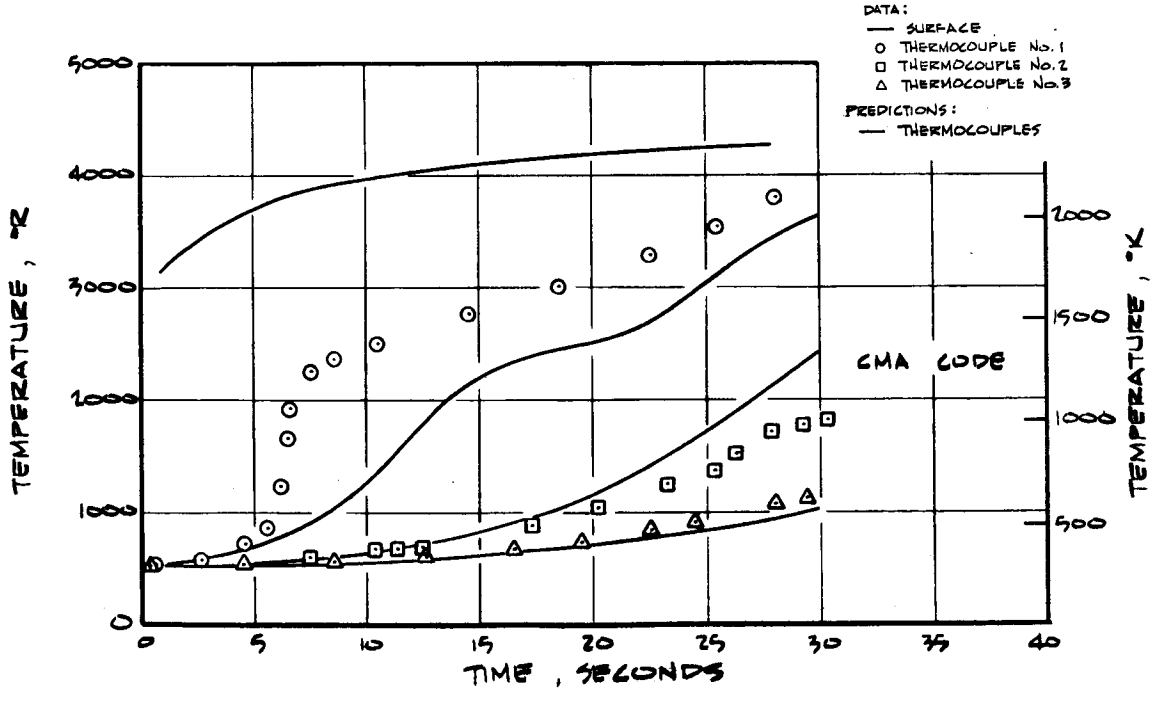


FIGURE 32, CONTINUED

FF) O/F = 0.38, TEST 1146, NL-27

A-2706

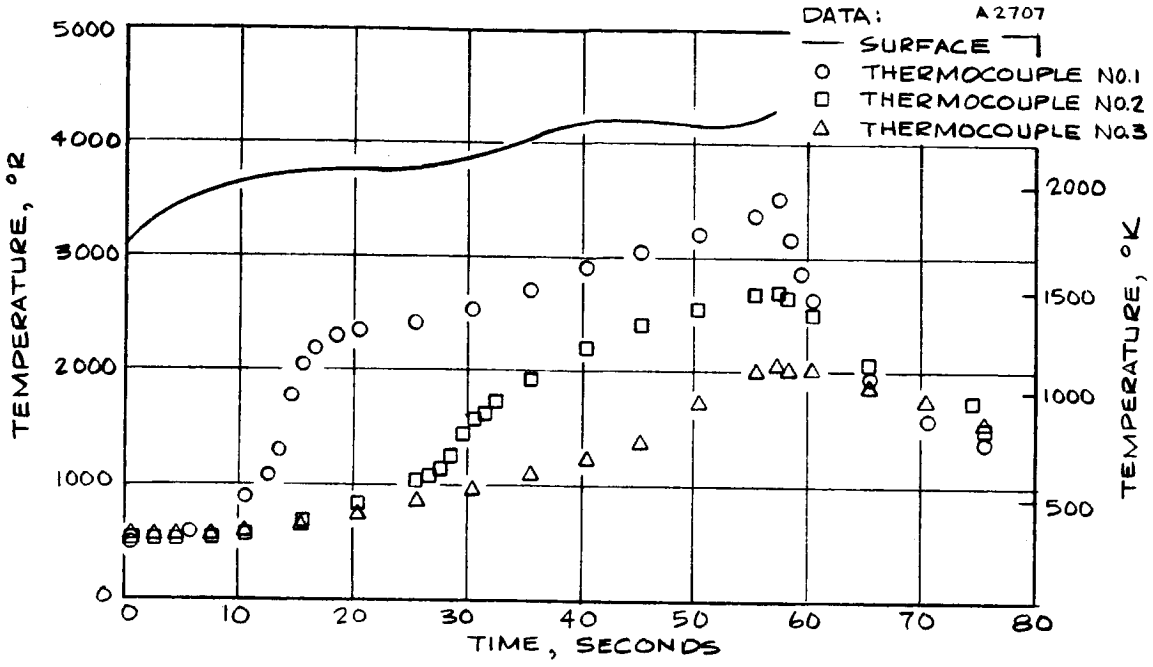


FIGURE 32, CONTINUED

GG) O/F = .38, TEST 1350, NL-39

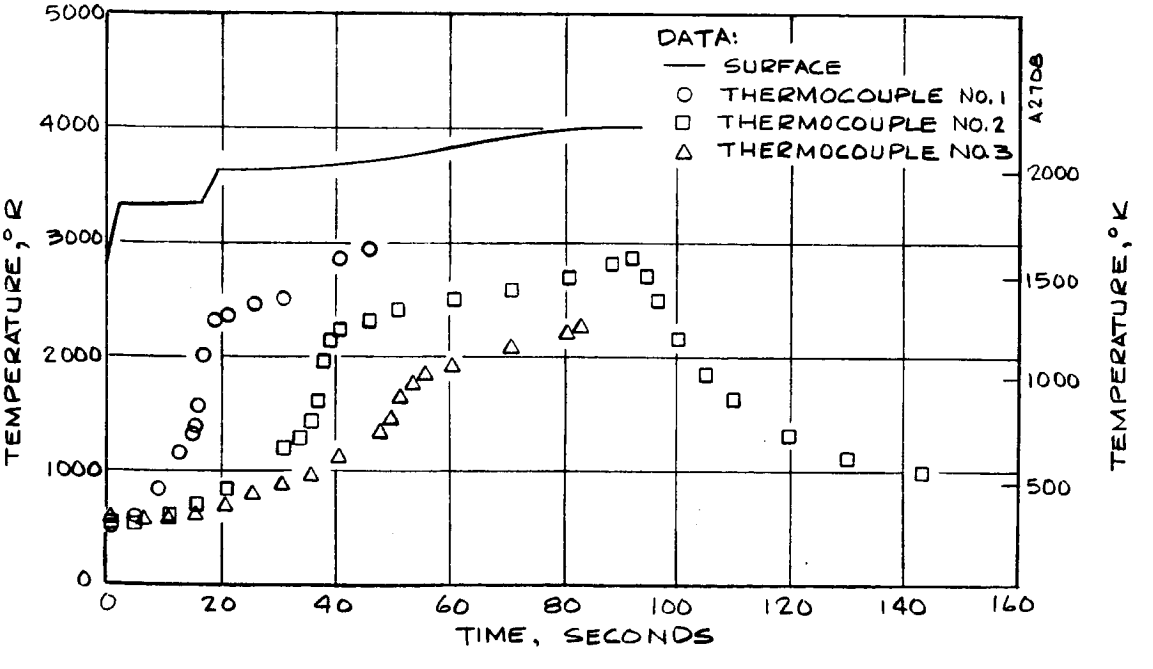


FIGURE 32, CONTINUED

HH) O/F = .38, TEST 1347, NL-36

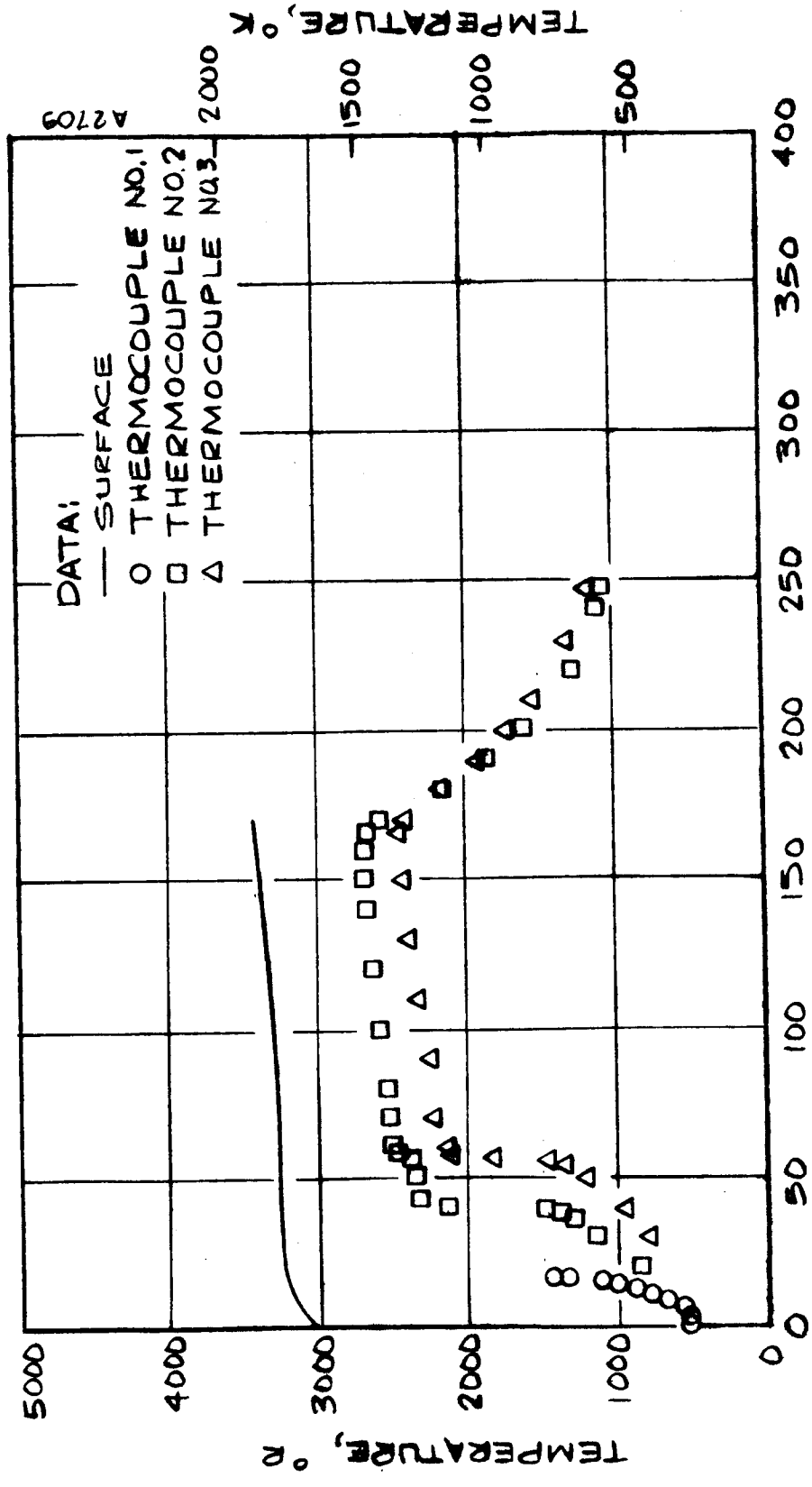


FIGURE 32, CONCLUDED
II) O/F = .38, TEST 1349, NL-38

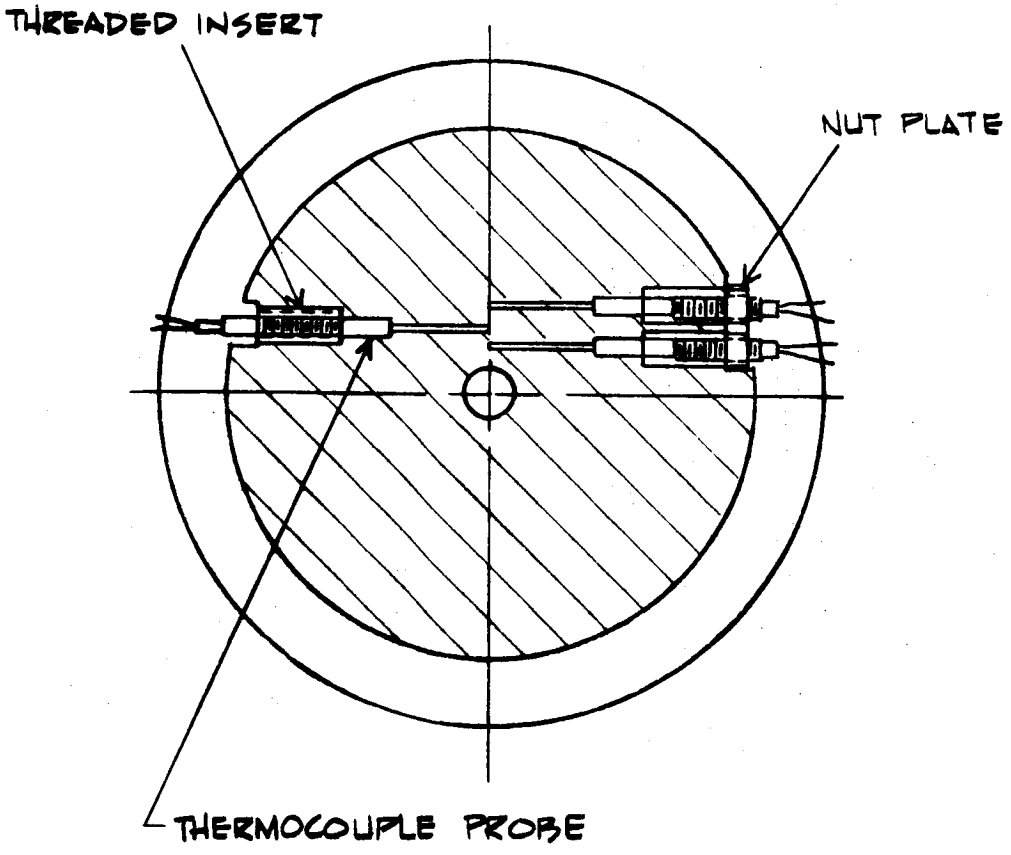
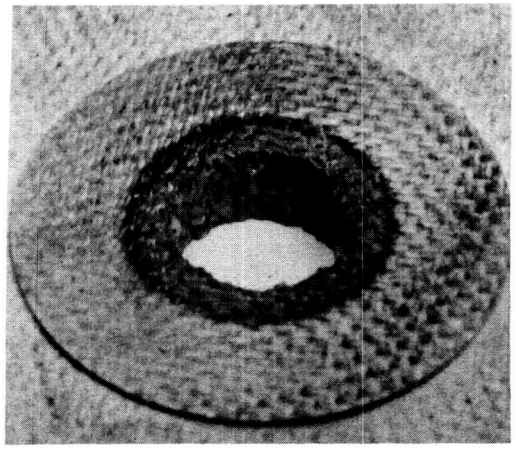
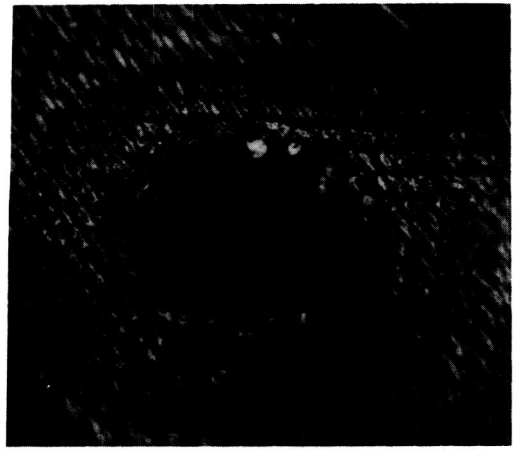


FIGURE 33 THERMOCOUPLE INSTALLATION IN ABLATIVE NOZZLE SECTION

A-2710

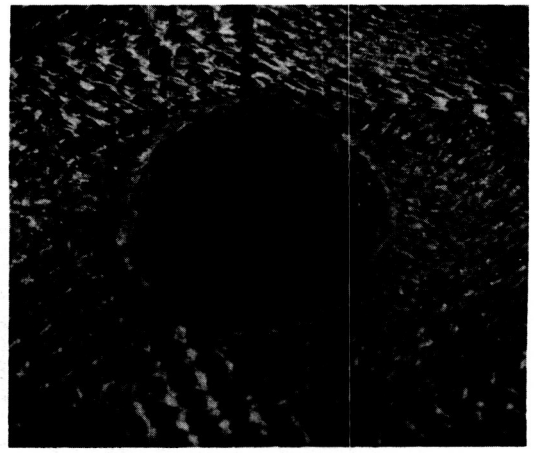


TEST 1083, NL-11, HIGH C*

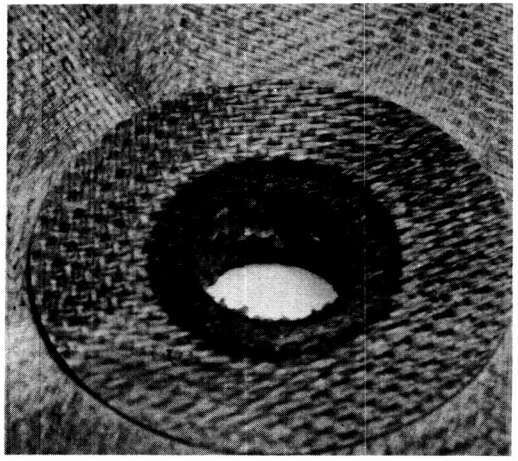


TEST 1361, NL-40, MID C*

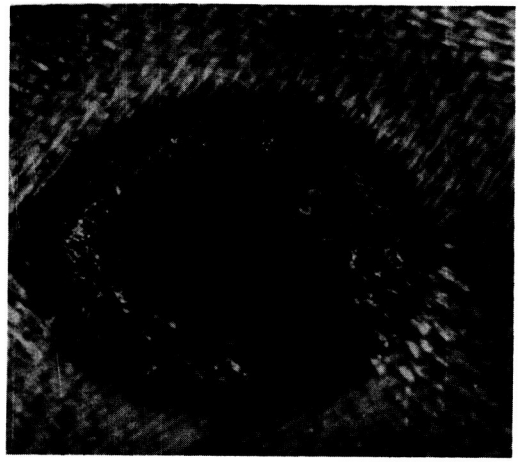
A) O/F ≈ ∞



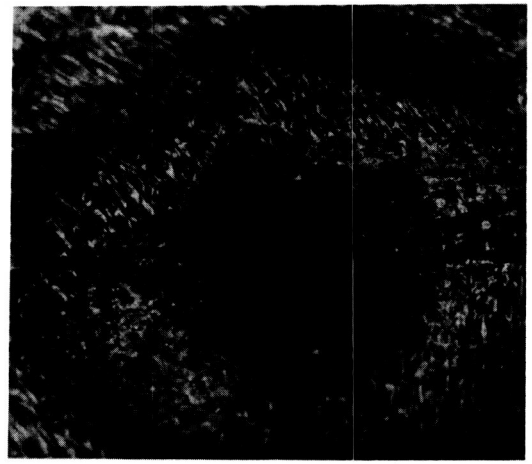
TEST 1360, NL-44, LOW C*



TEST 1091, NL-13, HIGH C*



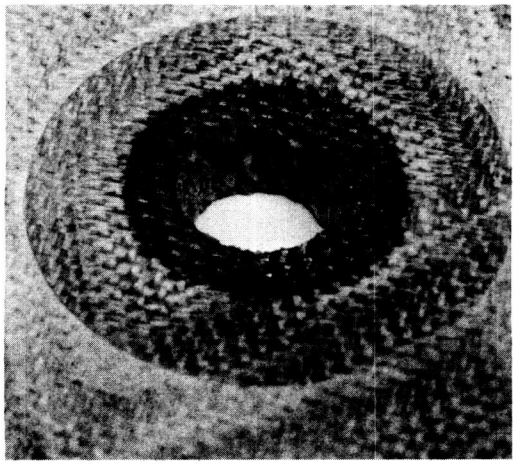
TEST 1329, NL-28, MID C*



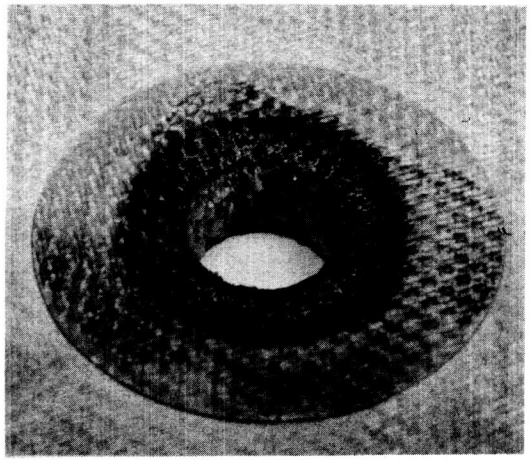
TEST 1339, NL-29, LOW C*

B) O/F =4.0

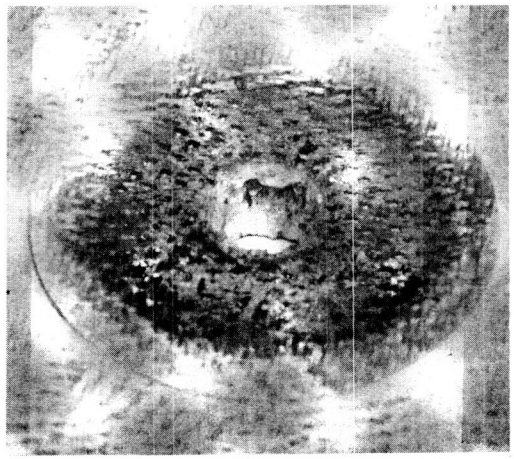
FIGURE 34, PHOTOGRAPHS OF ABLATIVE NOZZLE THROAT SURFACES



TEST 1135, NL-26, HIGH C*

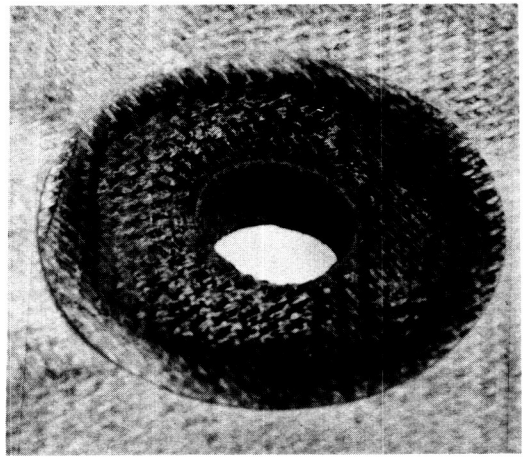


TEST 1125, NL-22, MID C*

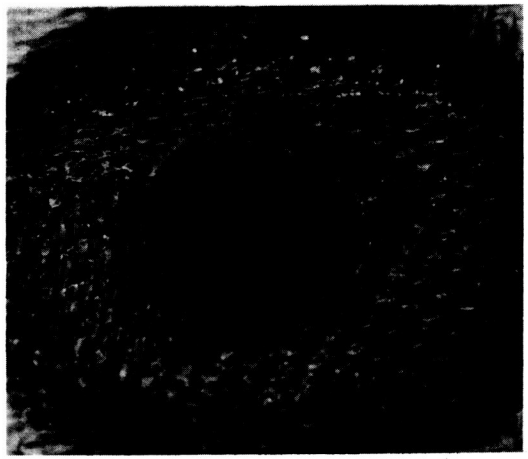


TEST 1116, NL-17, LOW C*

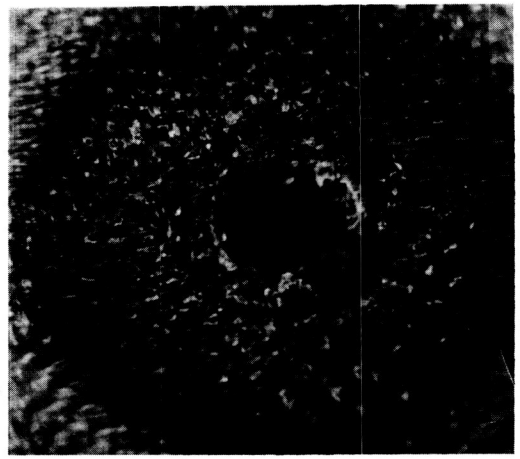
C) O/F =2.0



TEST 1098, NL-16, HIGH C*



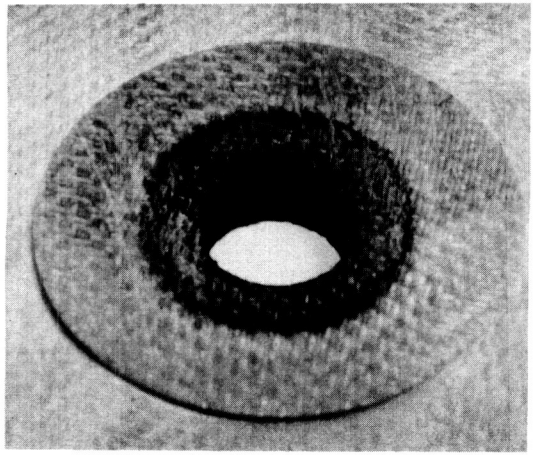
TEST 1336, NL-32, MID C*



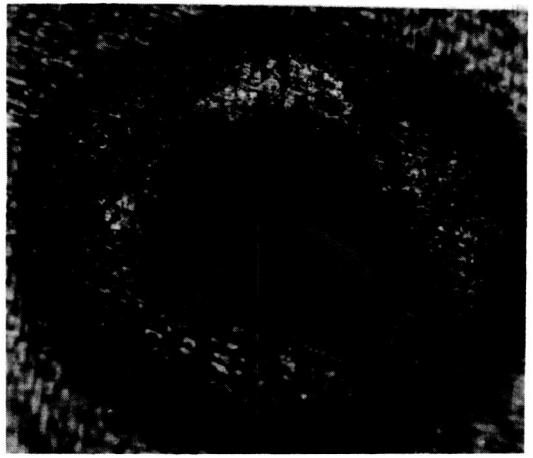
TEST 1337, NL-33, LOW C*

D) O/F =1.0

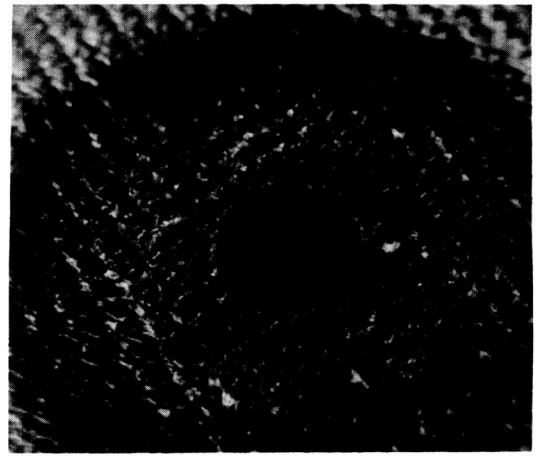
FIGURE 34, CONTINUED



TEST 1145, NL-10, HIGH C*



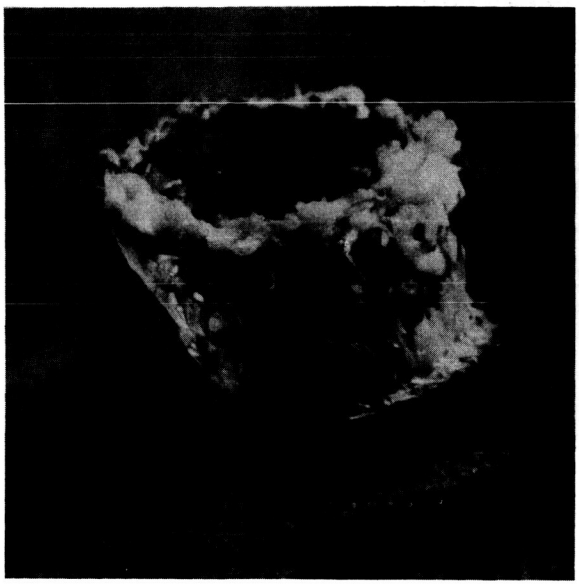
TEST 1347, NL-36, MID C*



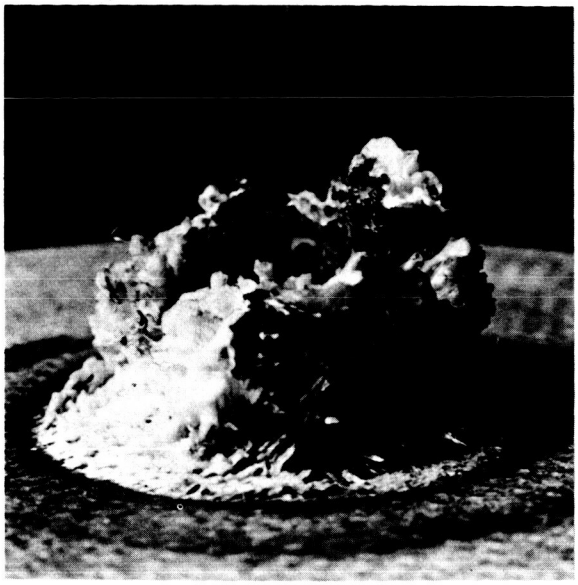
TEST 1349, NL-38, LOW C*

E) O/F =0.38

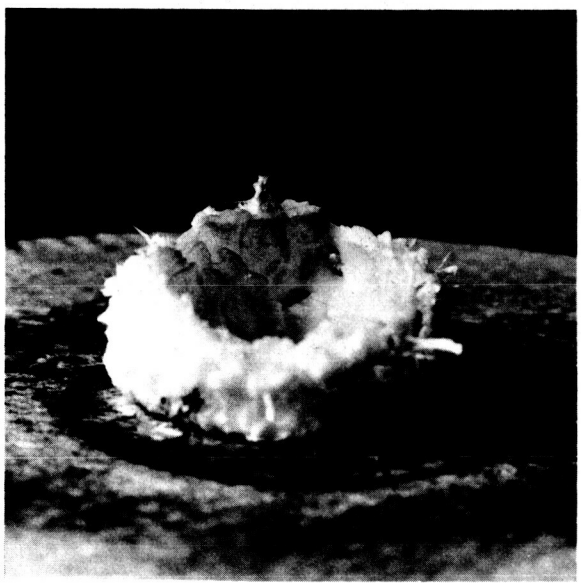
FIGURE 34, CONCLUDED



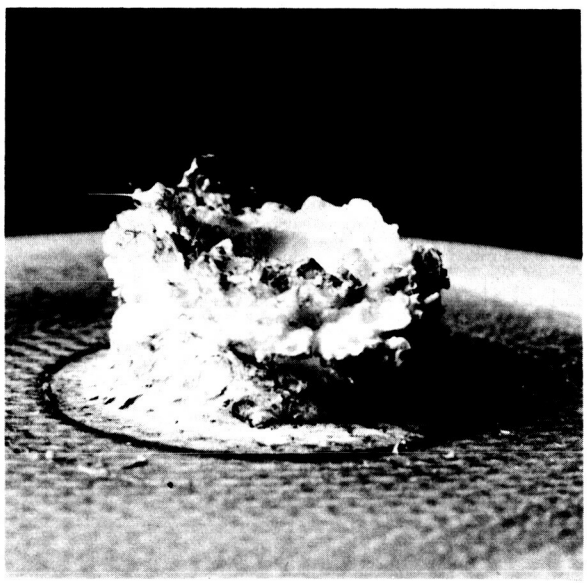
A) O/F=∞, TEST 1358, NL-42
HIGH C*



B) O/F=∞, TEST 1360, NL-44
LOW C*

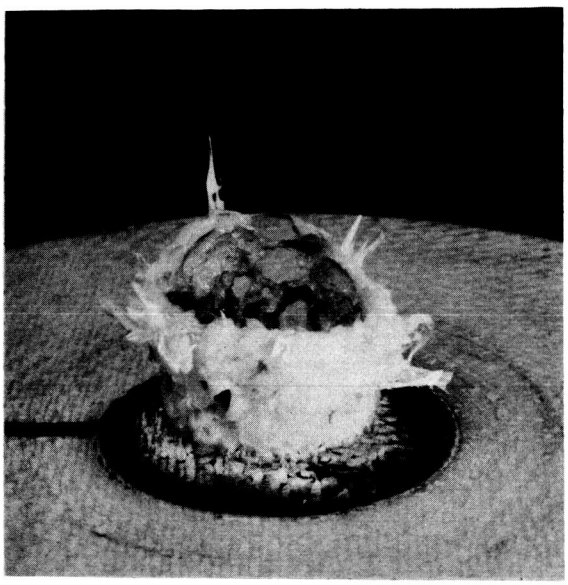


C) O/F=4, TEST 1332,NL-31
HIGH C*

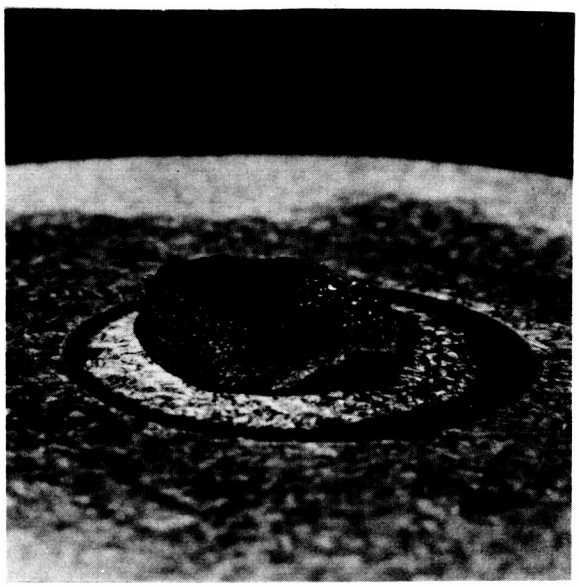


D) O/F=4, TEST 1331, NL-30
LOW C*

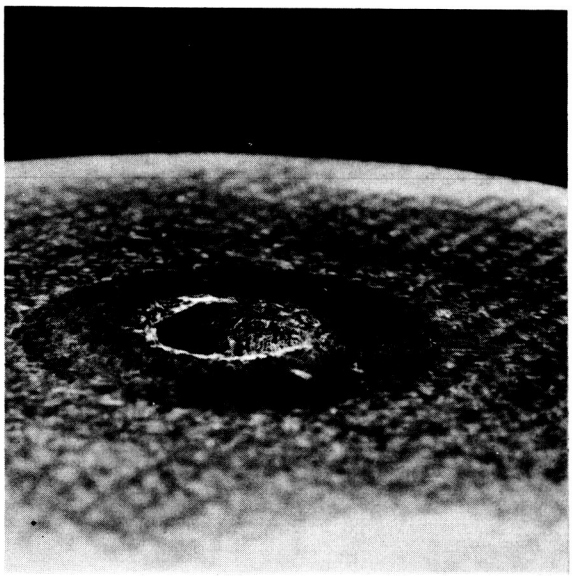
FIGURE 35 PHOTOGRAPHS OF ABLATIVE NOZZLE
EXIT CHARACTERISTICS



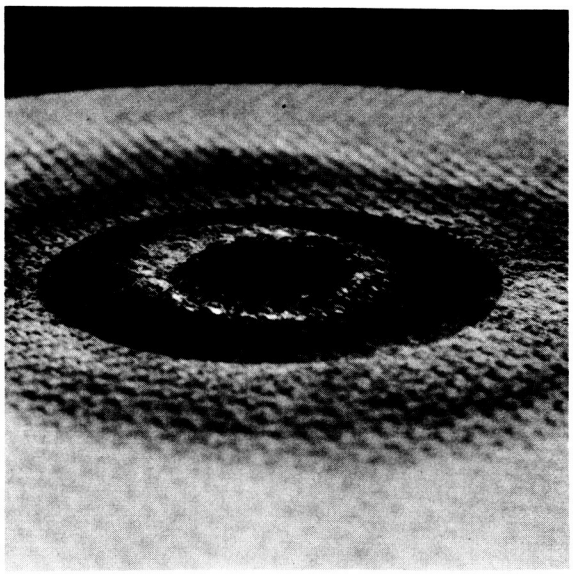
E) O/F=2.0, TEST 1128, NL-22
TYPICAL OF ALL C*



F) O/F=1.0, TEST 1338 , NL 34
HIGH C*

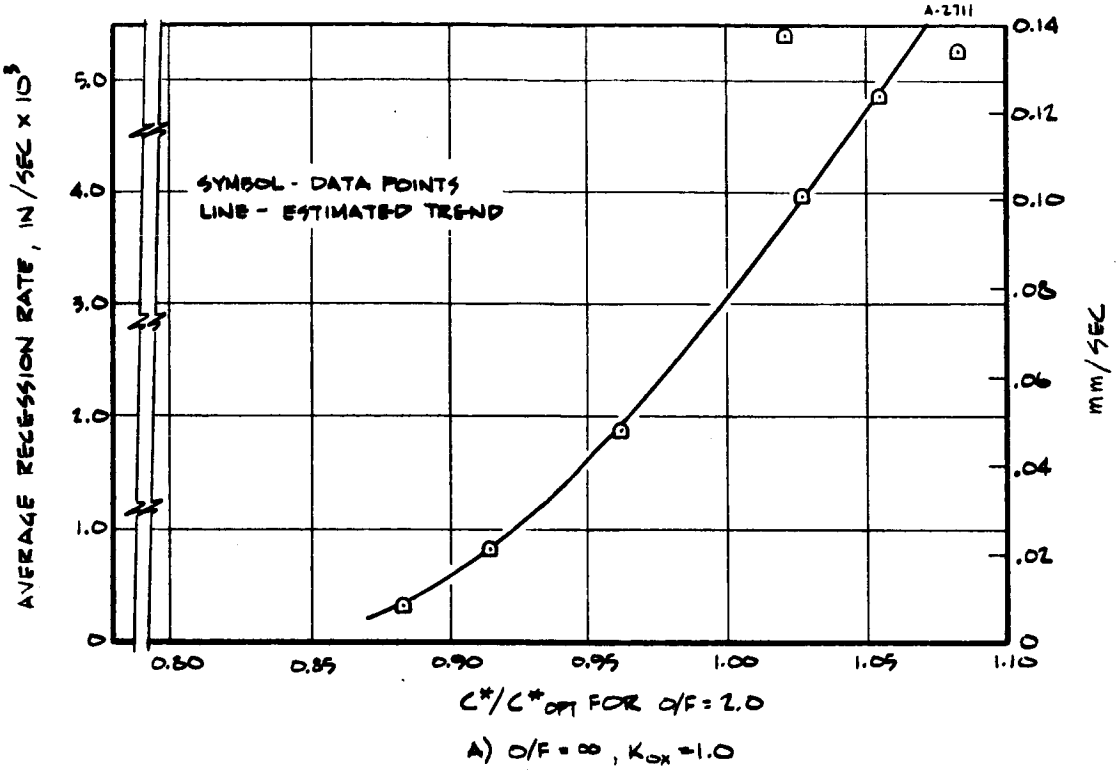


G) O/F=1.0 TEST 1337, NL-33,
LOW C*



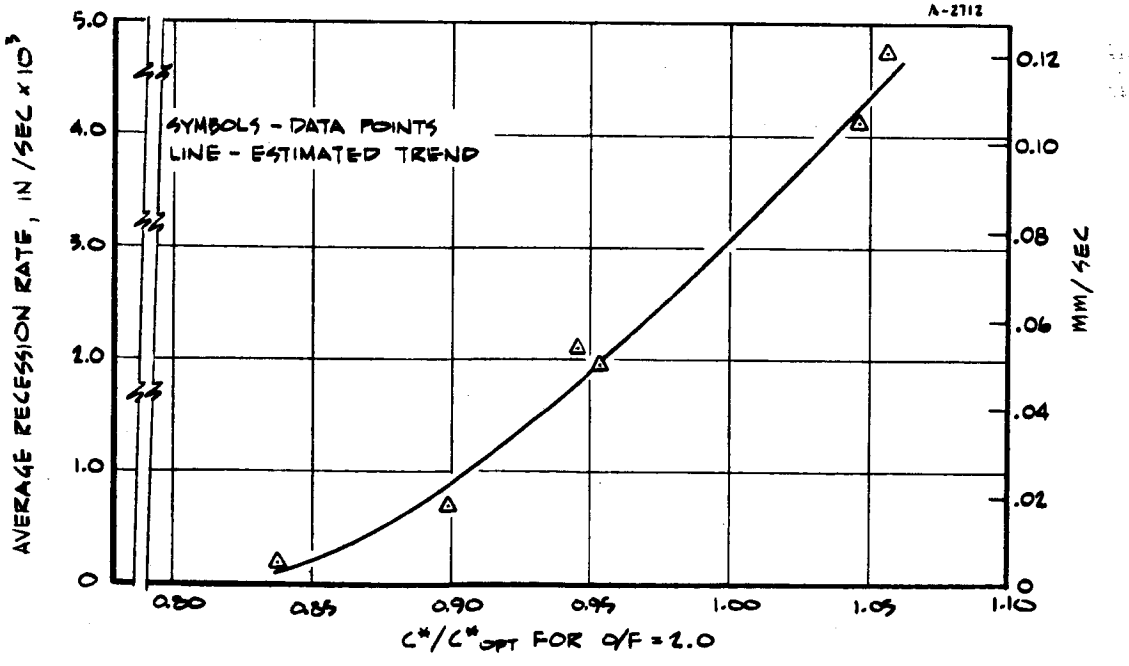
H) O/F=0.38, TEST 1349, NL-38
TYPICAL OF ALL C*

FIGURE 35 CONCLUDED



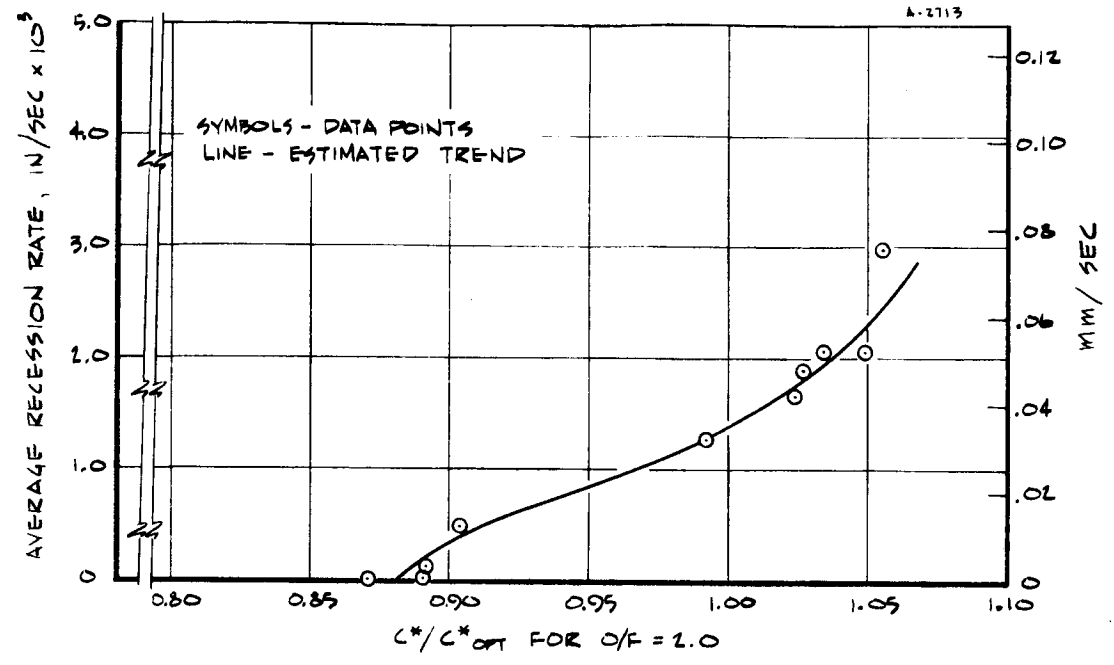
A) O/F = ∞, K_{ox} = 1.0

FIGURE 36 AVERAGE SURFACE RECESSION RATE AS A FUNCTION OF CHARACTERISTIC VELOCITY RATIO (PROPELLANT: N_2O_4-N_2H_4/UDMH, 50-50 ABLATIVE MATERIAL: MXS-89 SILICA PHENOLIC)



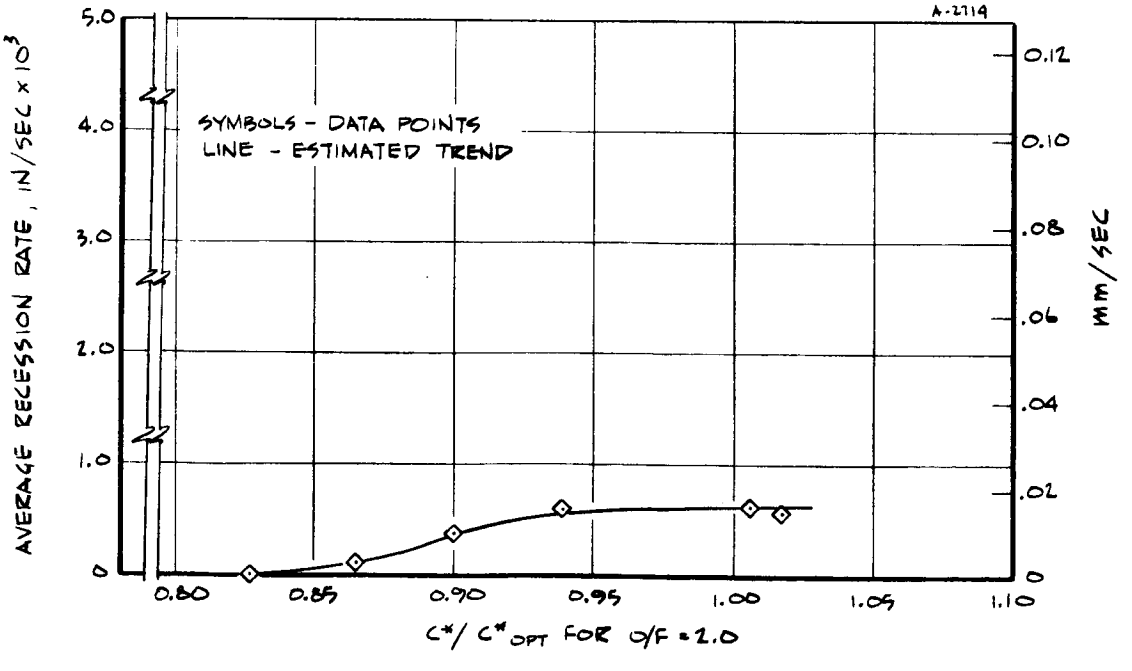
B) O/F = 4.0, K_{ox} = 0.8

FIGURE 36, CONTINUED



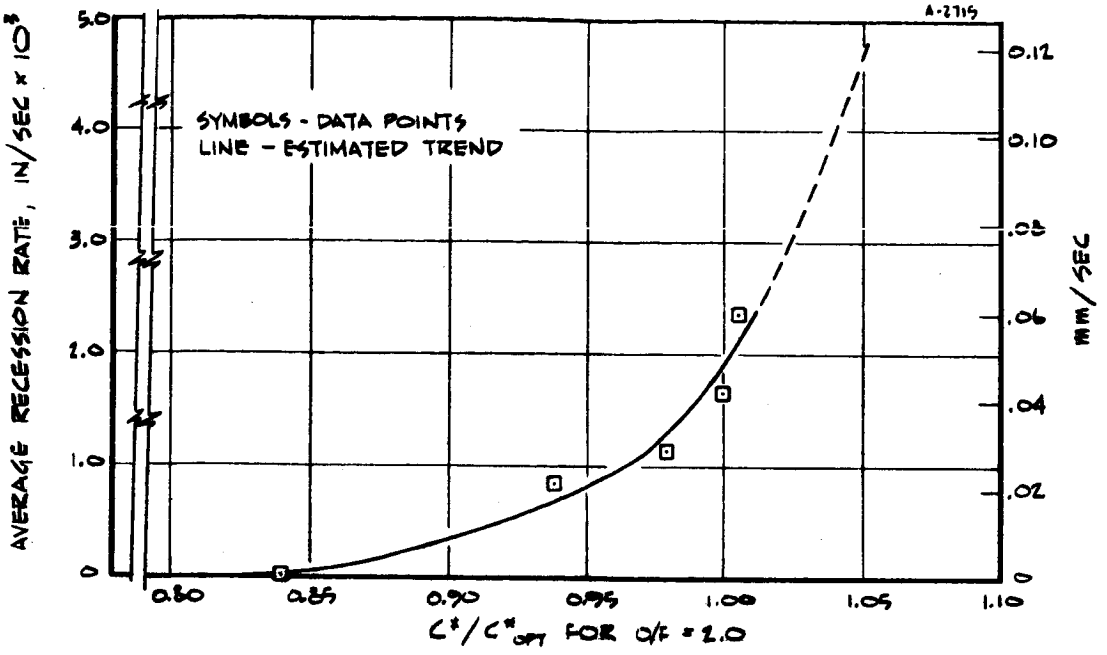
c) O/F = 2.0, K_{ox} = 0.677

FIGURE 36, CONTINUED



D) O/F = 1.0, K_{ox} = 0.500

FIGURE 36, CONTINUED



E) O/F = 0.35, K_{ox} = 0.277

FIGURE 36, CONCLUDED

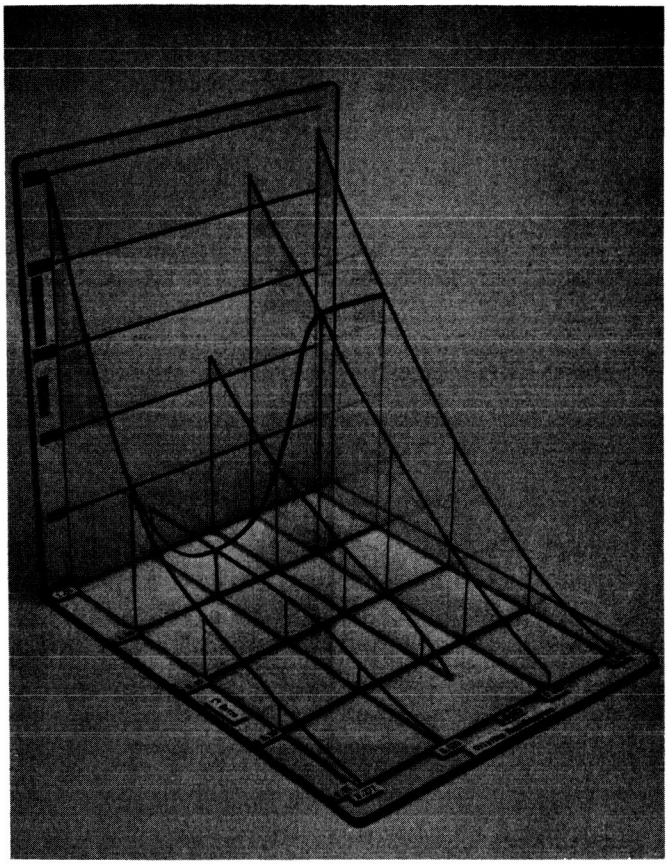


FIGURE 37 PHOTOGRAPH OF ABLATIVE NOZZLE RESPONSE THREE DIMENSIONAL MODEL

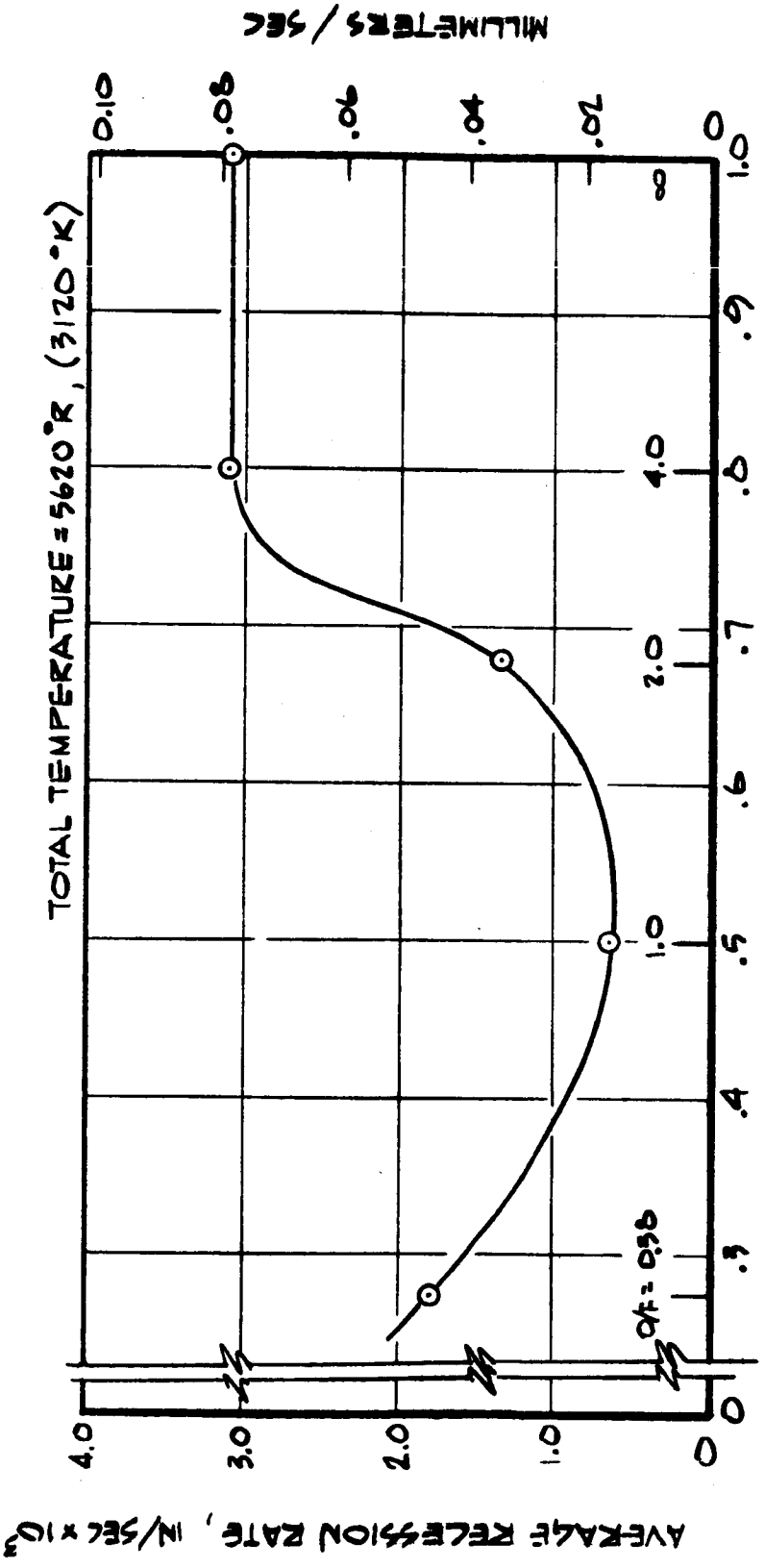


FIGURE 38 EFFECT OF TEST GAS CHEMICAL COMPOSITION ON MX5-89 SILICA PHENOLIC RECESSION RATE AT C^*/C^*_{OPT} | O/F=2 OF 1.0

A-2116

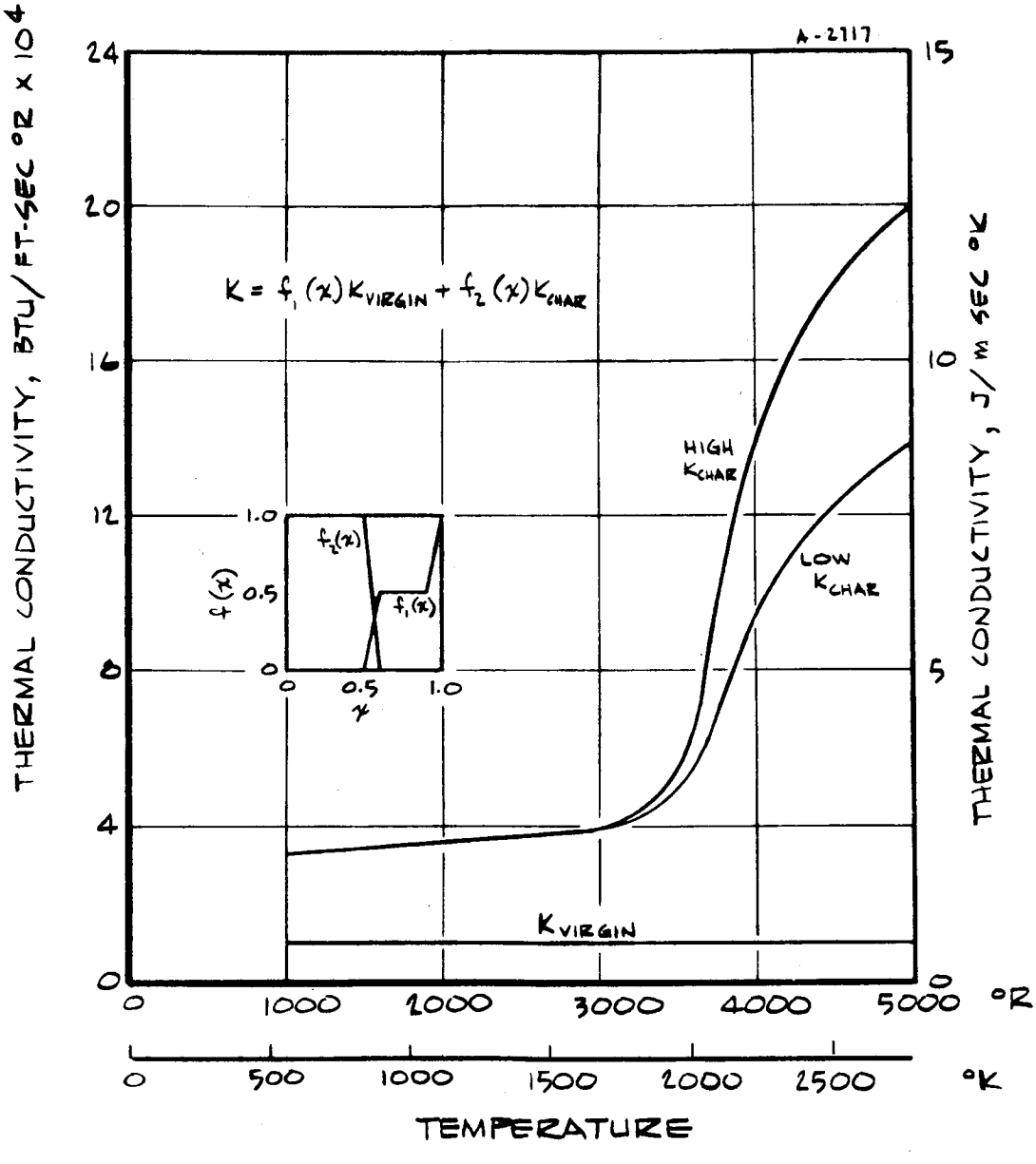


FIGURE 39 MXS-89 SILICA-PHENOLIC THERMAL CONDUCTIVITY MODELS

PARAMETRIC CALCULATIONS
SURFACE TEMPERATURE RESULTS
ACTIVE MODEL

A-2718

PRED NO	KINETICS	P(MIN)	S(MAX)	COND
123	0.1	7	2	L
126	0.1	3	10	L
134	.01	3	10	L
136	.01	3	10	H
171	0.1	3	20	H
174	0.1	3	20	L

TEST No. 1125
MODEL No. NL-22
O/F 2.0
C^*/C^*_{OPT}, O/F=2.0 1.0
⊙ MEASURED DATA

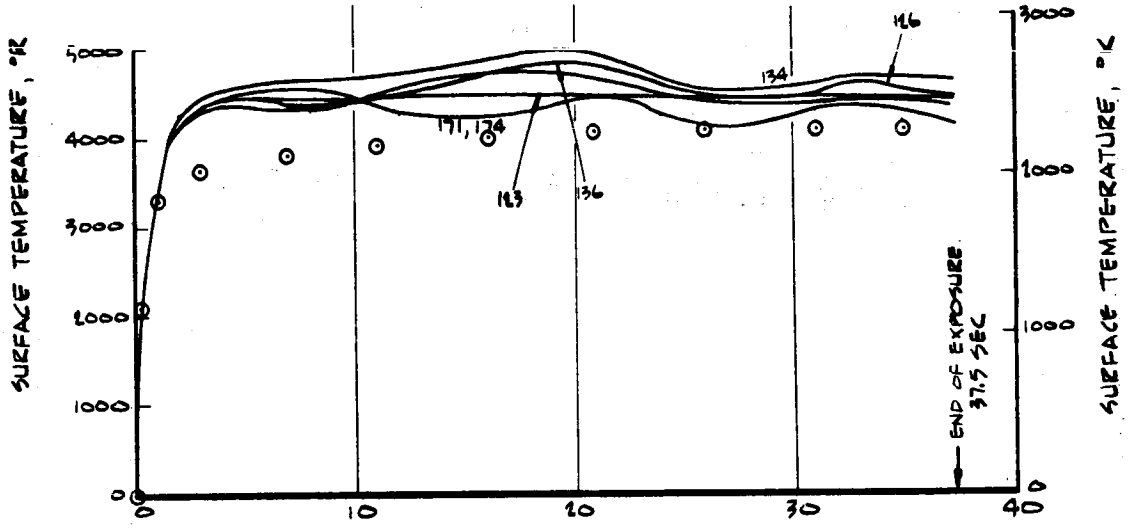


FIGURE 40 A

PARAMETRIC CALCULATIONS
SURFACE RECESSION AND
LIQUID LAYER THICKNESS RESULTS
ACTIVE MODEL

A-2719

PREDICTION	KINETICS	P(MIN)	S(MAX)	COND
123	0.1	7	2	L
126	0.1	3	10	L
133	.01	3	10	L
136	.01	3	10	H
171	.01	3	20	H
174	.01	3	20	H

TEST No. 1125
MODEL No. NL-22
O/F 2.0
C^*/C^*_{OPT}, O/F=2.0 1.0
O MEASURED DATA

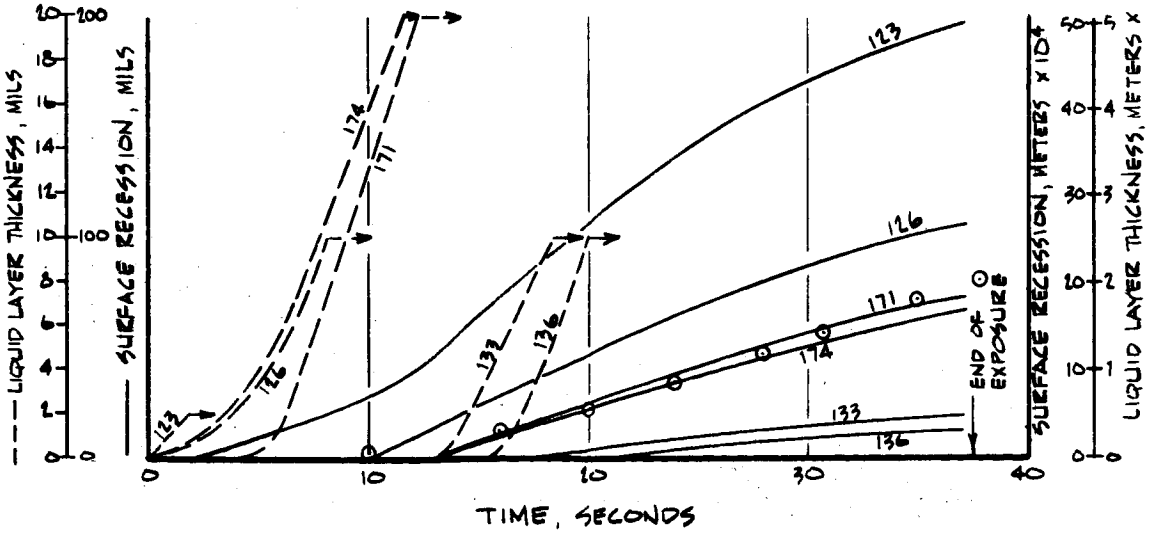


FIGURE 40 B

PARAMETRIC CALCULATIONS
SURFACE TEMPERATURE RESULTS
INERT MODEL

A-2720

PRED NO	KINETICS	P(MIN)	S (MAX)	COND
130	0.1	3	10	I
139	0.1	3	10	II
142	0.1	3	5	II
145	0.1	7	10	II
148	0.1	5	10	II
151	0.1	3	2	II
154	0.1	7	2	II
158	1.0	7	2	II
161	1.0	3	10	II
165	1.0	3	2	II
168	1.0	7	10	II

TEST NO. 1125
MODEL NO NL-22
O/F 2.0
C^*/C^*_{OPT} (O/F 2.0) 1.0
O MEASURED DATA

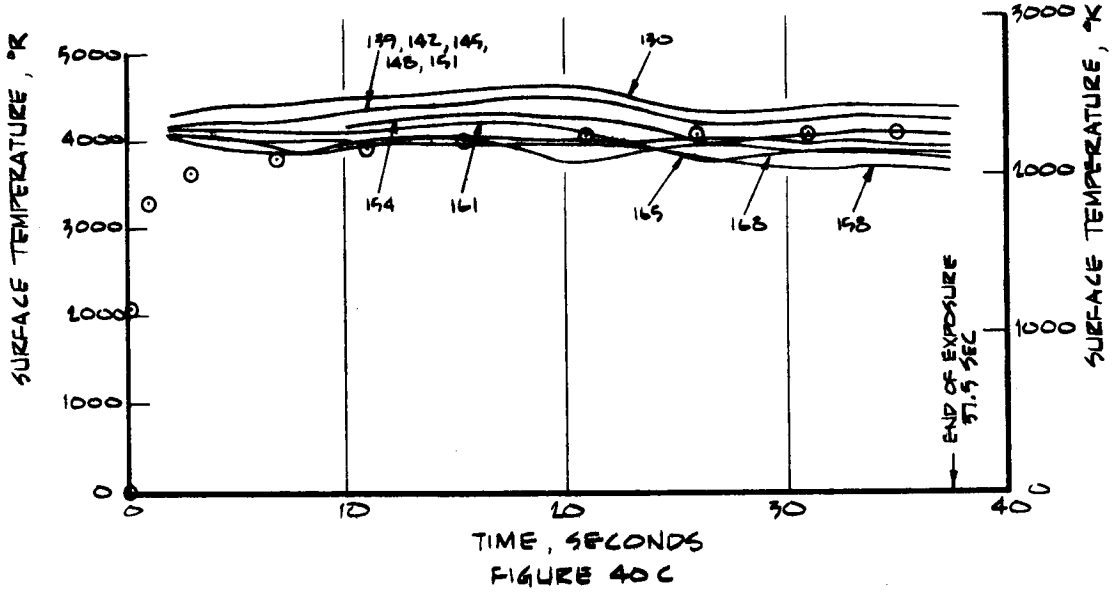


FIGURE 40C

PARAMETRIC CALCULATIONS
SURFACE RECESSION AND
LIQUID LAYER THICKNESS
RESULTS, INERT MODEL

A-2721

PREDICTION	KINETICS	P(MIN)	S(MAX)	COND
130	0.1	3	10	I
139	0.1	3	10	II
142	0.1	3	5	II
145	0.1	7	10	II
148	0.1	5	10	II
151	0.1	3	2	II
154	0.1	7	2	II
158	1.0	7	2	II
161	1.0	3	10	II
165	1.0	3	2	II
168	1.0	7	10	II

TEST No. 1125
MODEL No. NL-22
O MEASURED DATA

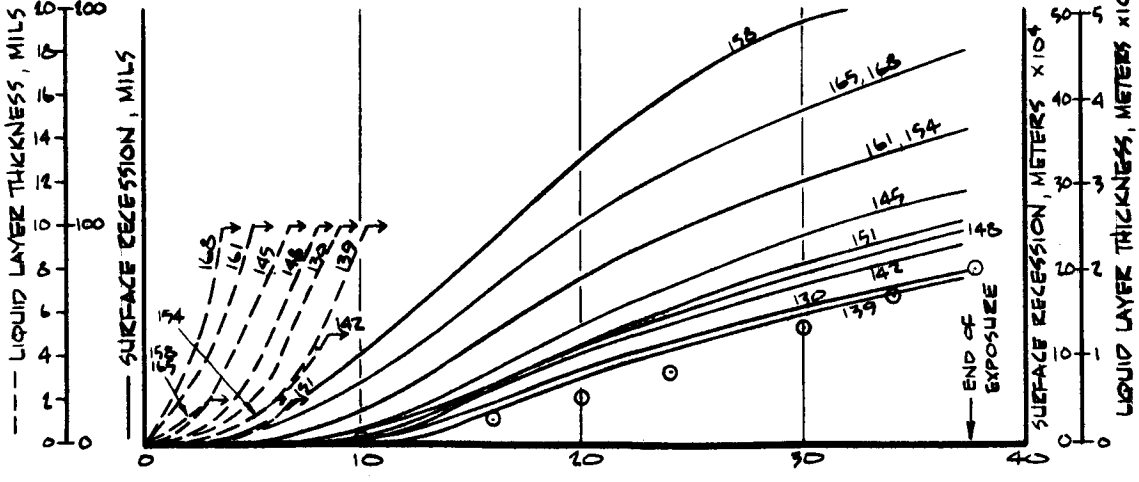


FIGURE 40D

PARAMETRIC CALCULATIONS
SURFACE TEMPERATURE RESULTS
ACTIVE MODEL

A-2122

PRED No.	KINETICS	P(MIN)	$ (MAX)	COND
124	0.1	1	2	L
127	0.1	3	10	L
134	.01	3	10	L
137	.01	3	10	H
172	0.1	3	20	H
175	0.1	3	20	L

O MEASURED DATA

TEST No. 1092
MODEL No. NL-14
O/F 4.0
C^*/C^*_{OPT}, (O/F=2.0) 1.0

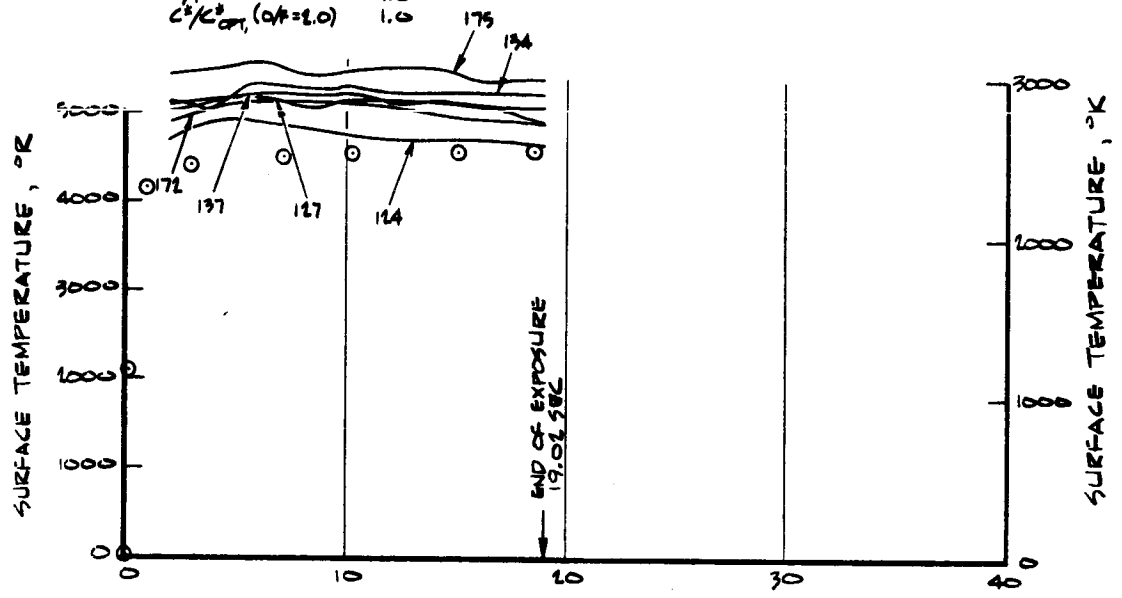


FIGURE 40E

PARAMETRIC CALCULATIONS
SURFACE RECESSION AND
LIQUID LAYER THICKNESS
RESULTS, ACTIVE MODEL

A-2123

PREDICTION	KINETICS	P(MIN)	$ (MAX)	COND
124	0.1	1	2	L
127	0.1	3	10	L
134	.01	3	10	L
137	.01	3	10	H
172	.01	3	20	H
175	.01	3	20	H

TEST No. 1092
MODEL No NL-14
O/F 4.0
C^*/C^*_{OPT}, O/F=2.0 1.0
O MEASURED DATA

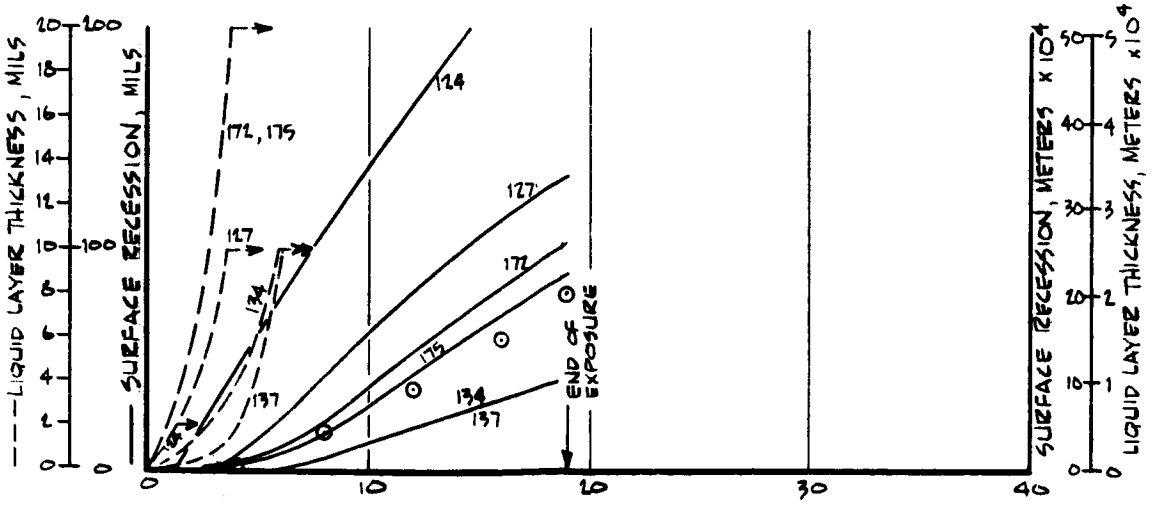


FIGURE 40F

PARAMETRIC CALCULATIONS
SURFACE TEMPERATURE
RESULTS, INERT MODEL

A-2124

PRED No	KINETICS	P(MIN)	S(MAX)	COND
132	0.1	3	10	L
140	0.1	3	10	H
143	0.1	3	5	H
146	0.1	7	10	H
149	0.1	5	10	H
152	0.1	3	2	H
155	0.1	7	2	H
159	1.0	7	2	H
162	1.0	3	10	H
166	1.0	3	2	H
169	1.0	7	10	H

TEST No. 1092
MODEL No NL-14
O/F 4.0
$C^*/C^*_{OPT,}$ (O/F=2.0) 1.0

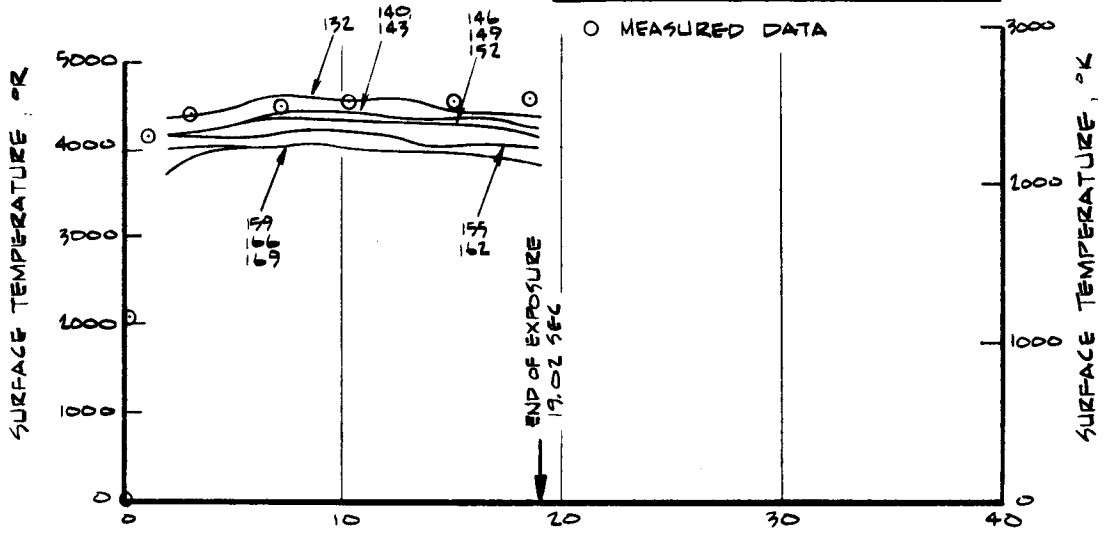


FIGURE 40G

PARAMETRIC CALCULATIONS
SURFACE RECESSION AND
LIQUID LAYER THICKNESS
RESULTS, INERT MODEL

A-2725

PREDICTION	KINETICS	P(MIN)	S(MAX)	COND
132	0.1	3	10	L
140	0.1	3	10	H
143	0.1	3	5	H
146	0.1	7	10	H
149	0.1	5	10	H
152	0.1	3	2	H
155	0.1	7	2	H
159	1.0	7	2	H
162	1.0	3	10	H
166	1.0	3	2	H
169	1.0	7	10	H

TEST No. 1092
MODEL No. NL-14
O MEASURED DATA

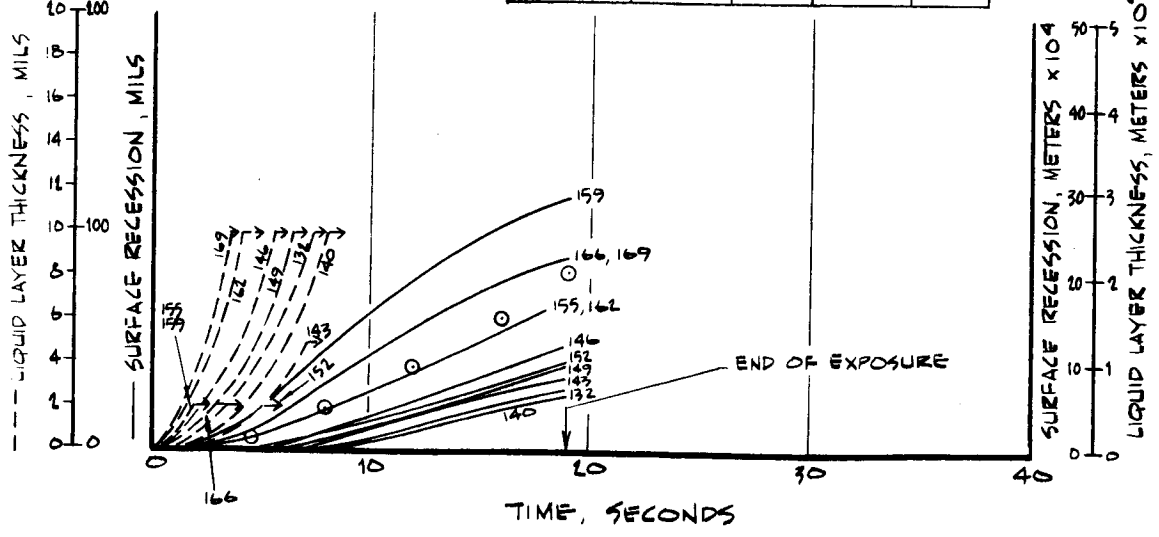


FIGURE 40H

A-2726

PARAMETRIC CALCULATIONS
SURFACE TEMPERATURE RESULTS
ACTIVE MODEL

PRED No.	KINETICS	P(MIN)	S (MAX)	COND
125	0.1	1	2	L
128	0.1	3	10	L
135	.01	3	10	L
138	.01	3	10	H

TEST No. 1084
MODEL No. NL-12
O/F ∞
$C^*/C^*_{OPT,(O/F=2.0)}$ 1.0
O MEASURED DATA

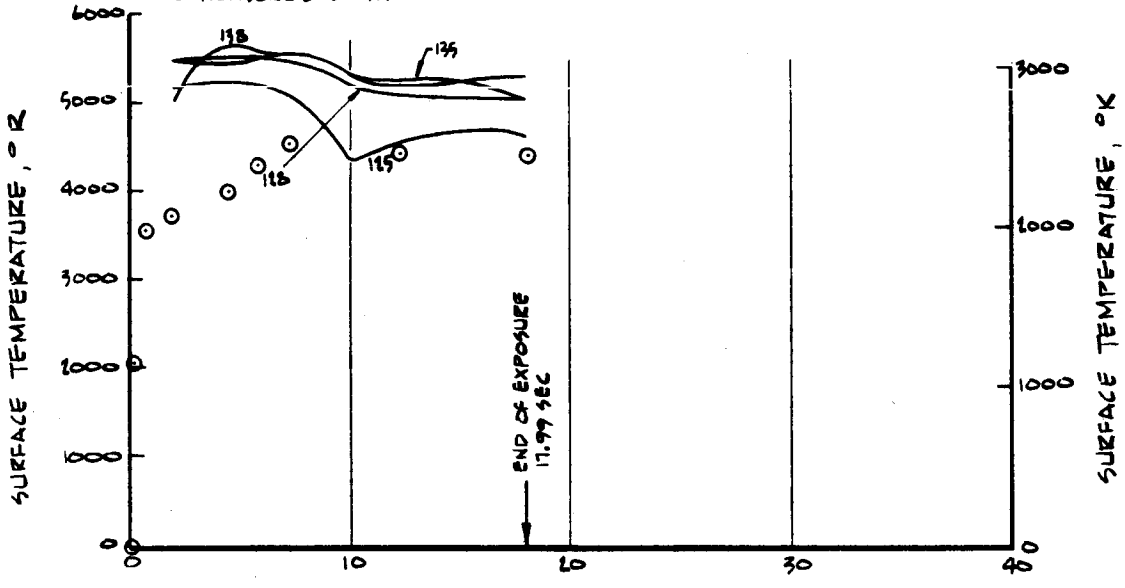


FIGURE 40 I

A-2727

PARAMETRIC CALCULATIONS
SURFACE RECESSION AND
LIQUID LAYER THICKNESS
RESULTS, ACTIVE MODEL

PREDICTION	KINETICS	P(MIN)	S (MAX)	COND
125	0.1	1	2	L
128	0.1	3	10	L
135	.01	3	10	L
138	.01	3	10	H

TEST No. 1084
MODEL No NL-12
O MEASURED DATA

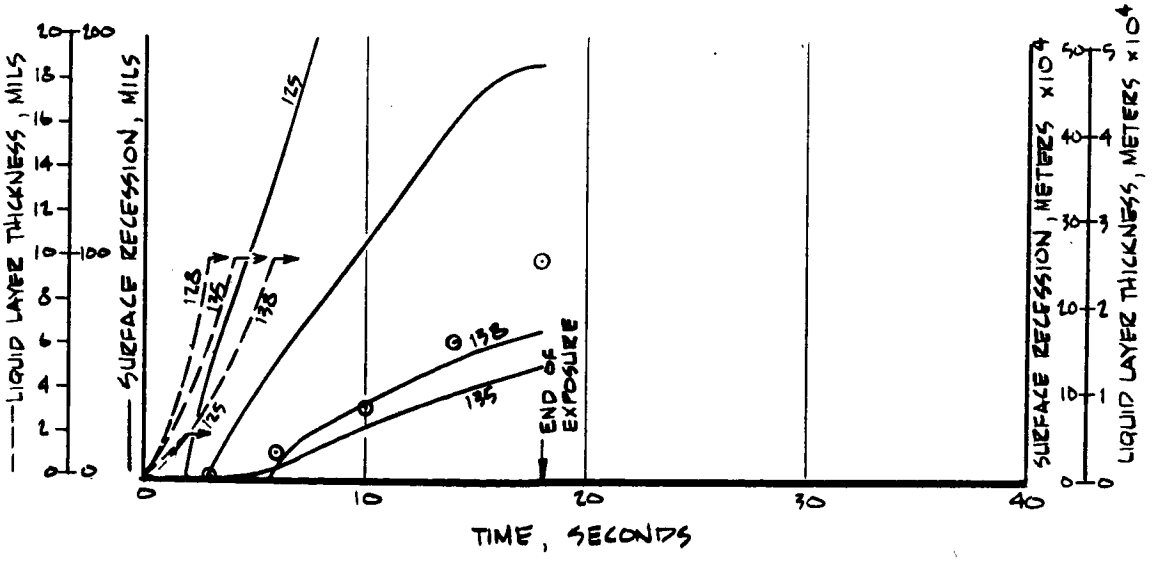


FIGURE 40 J

PARAMETIC CALCULATIONS
SURFACE TEMPERATURE
RESULTS, INERT MODEL

A-2728

PRED No.	KINETICS	P (MIN)	δ (MAX)	COND
131	0.1	3	10	L
141	0.1	3	10	H
144	0.1	3	5	H
147	0.1	7	10	H
150	0.1	5	10	H
153	0.1	3	2	H
156	0.1	7	2	H

TEST No. 1084
MODEL No. NL-12
O/F ∞
C^*/C^*_{OPT}, (O/F = 2.0) 1.0
O MEASURED DATA

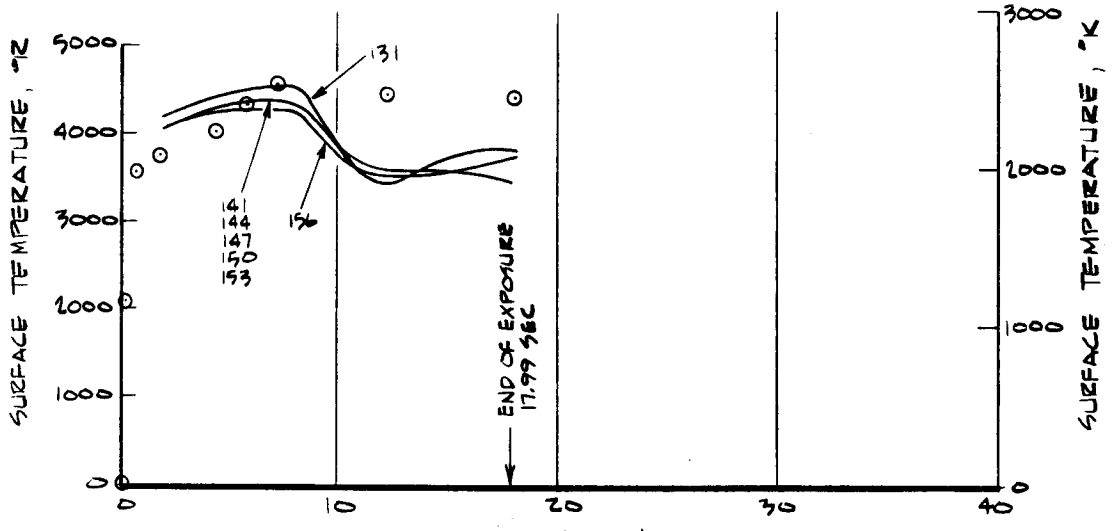


FIGURE 40K

PARAMETRIC CALCULATIONS
SURFACE RECESSION AND
LIQUID LAYER THICKNESS
RESULTS, INERT MODEL

TEST NO. 1084
MODEL NO. NL-12
O MEASURED DATA

A-2729

PREDICTION	KINETICS	P (MIN)	δ (MAX)	COND
131	0.1	3	10	L
141	0.1	3	10	H
144	0.1	3	5	H
147	0.1	7	10	H
150	0.1	5	10	H
153	0.1	3	2	H
156	0.1	7	2	H

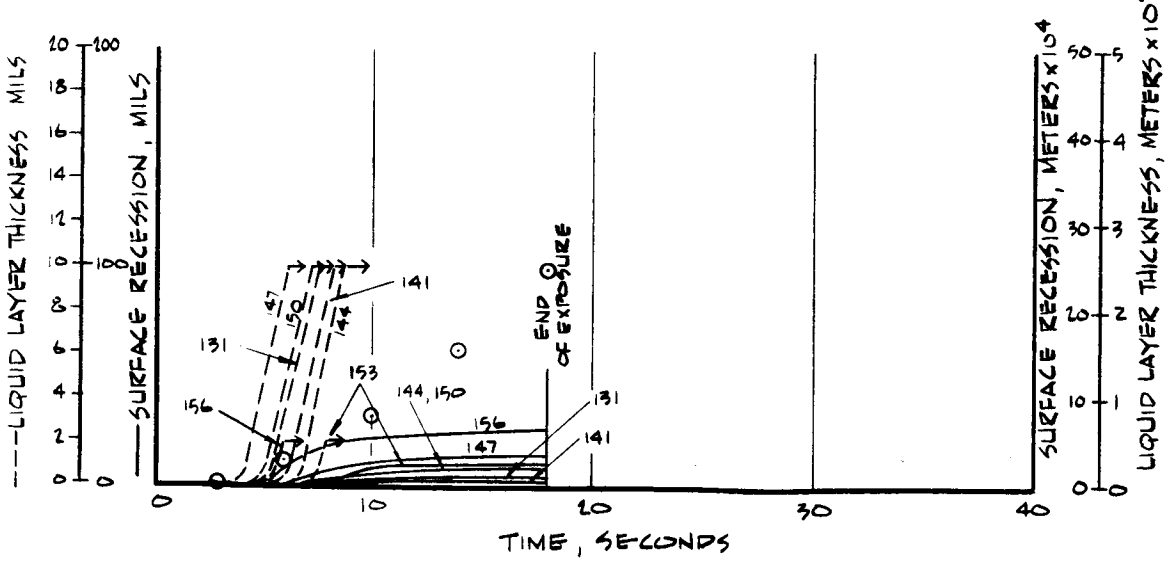


FIGURE 40L

PARAMETRIC CALCULATIONS
SURFACE TEMPERATUE RESULTS
ACTIVE MODEL

A-2750

PRED No.	KINETICS	P(MIN)	S(MAX)	COND
173	0.1	5	20	H
176	0.1	5	20	L

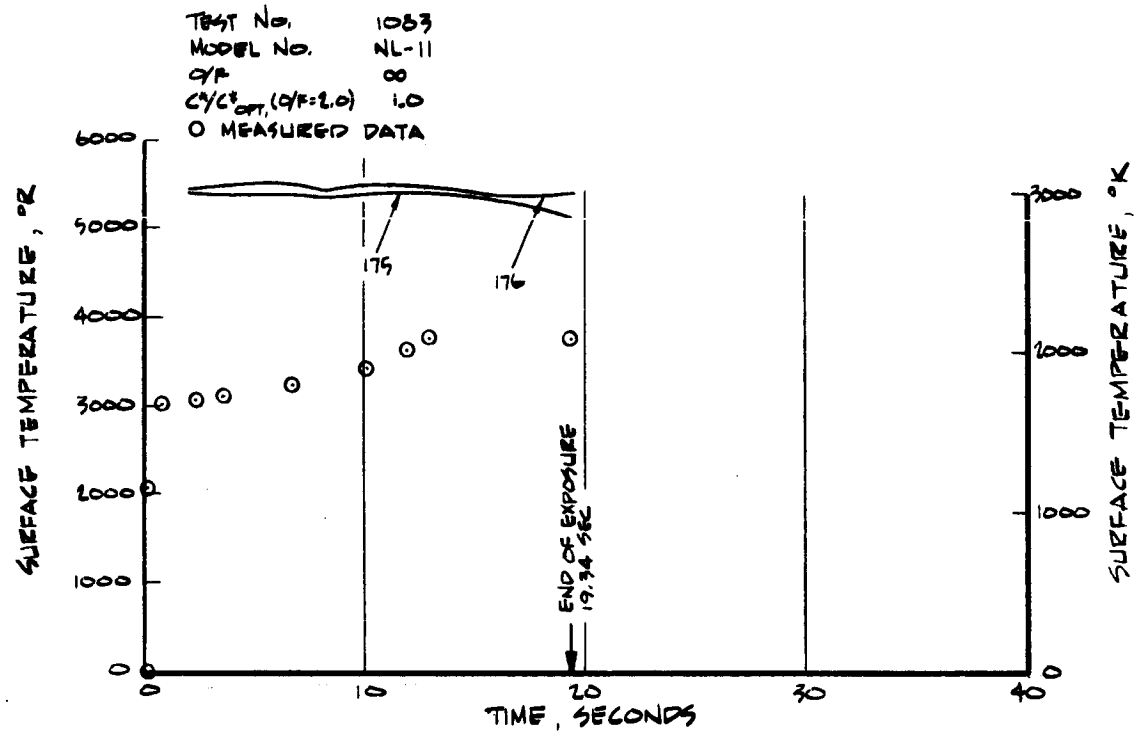


FIGURE 40M

PARAMETRIC CALCULATIONS
SURFACE RECESSION AND
LIQUID LAYER THICKNESS
RESULTS, ACTIVE MODEL

A-2751

PREDICTION	KINETICS	P(MIN)	S(MAX)	COND
173	0.1	5	20	H
176	0.1	5	20	L

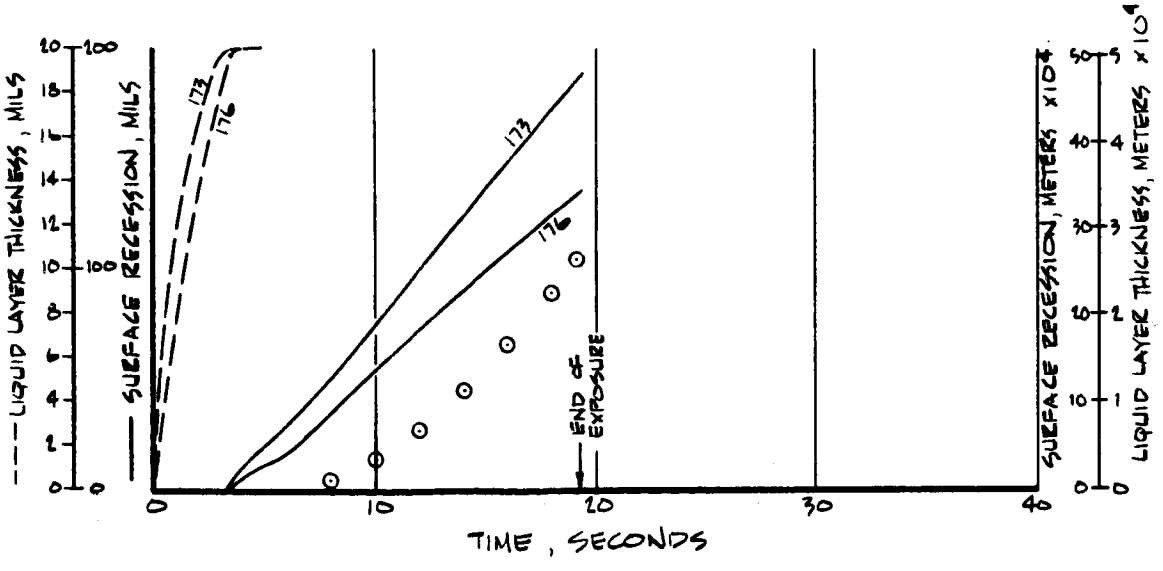


FIGURE 40N

A-2132

PARAMETRIC CALCULATIONS
SURFACE TEMPERATURE
RESULTS, INERT MODEL

PRED No.	KINETICS	P(MIN)	S(MAX)	COND
157	.1	7	2	H
163	1.0	3	10	H
164	1.0	7	2	H
167	1.0	3	2	H
170	1.0	7	10	H

TEST NO. 1083
MODEL No. NL-11
O/F ∞
C^*/C^*_{OPT} (O/F=2.0) 1.0
O MEASURED DATA

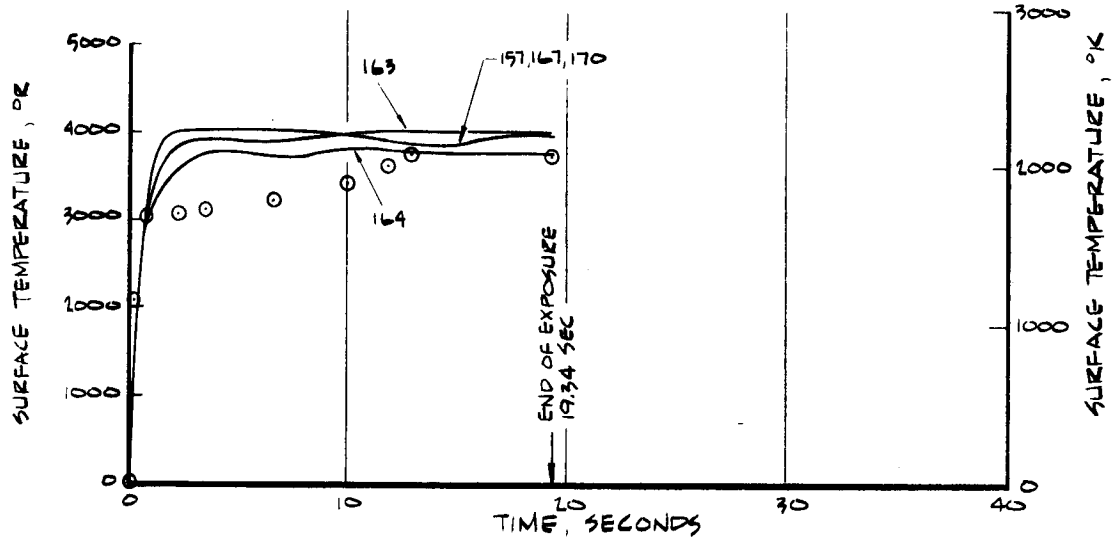


FIGURE 40 O

A-2133

PARAMETRIC CALCULATIONS
SURFACE RECESSION AND
LIQUID LAYER THICKNESS
RESULTS, INERT MODEL

PREDICTION	KINETICS	P (MIN)	S (MAX)	COND
157	0.1	7	2	H
163	1.0	3	10	H
164	1.0	7	2	H
167	1.0	3	2	H
170	1.0	7	10	H

TEST No 1083
MODEL No. NL-11
O MEASURED DATA

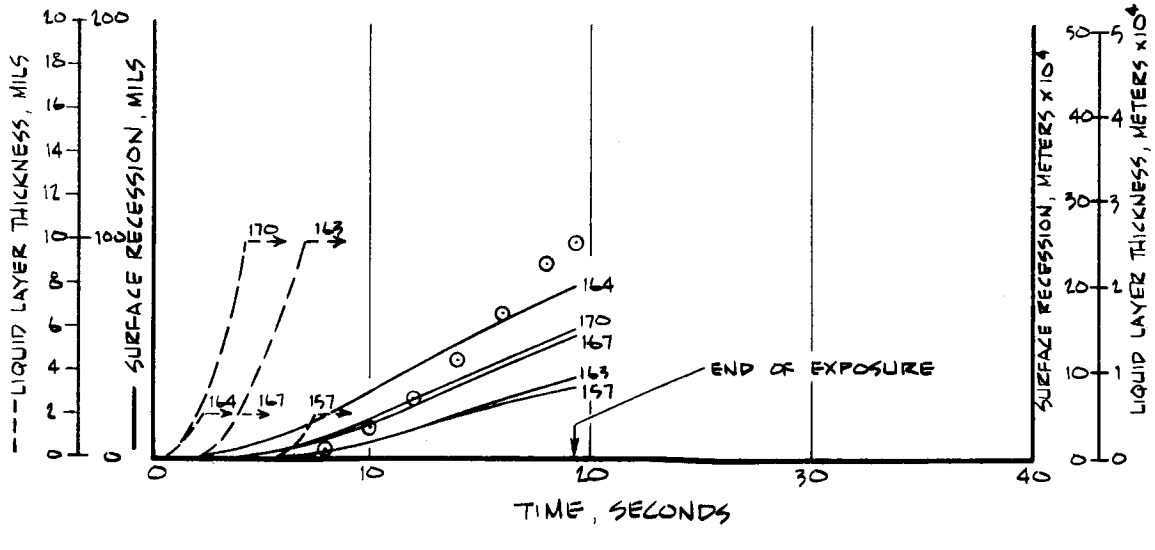
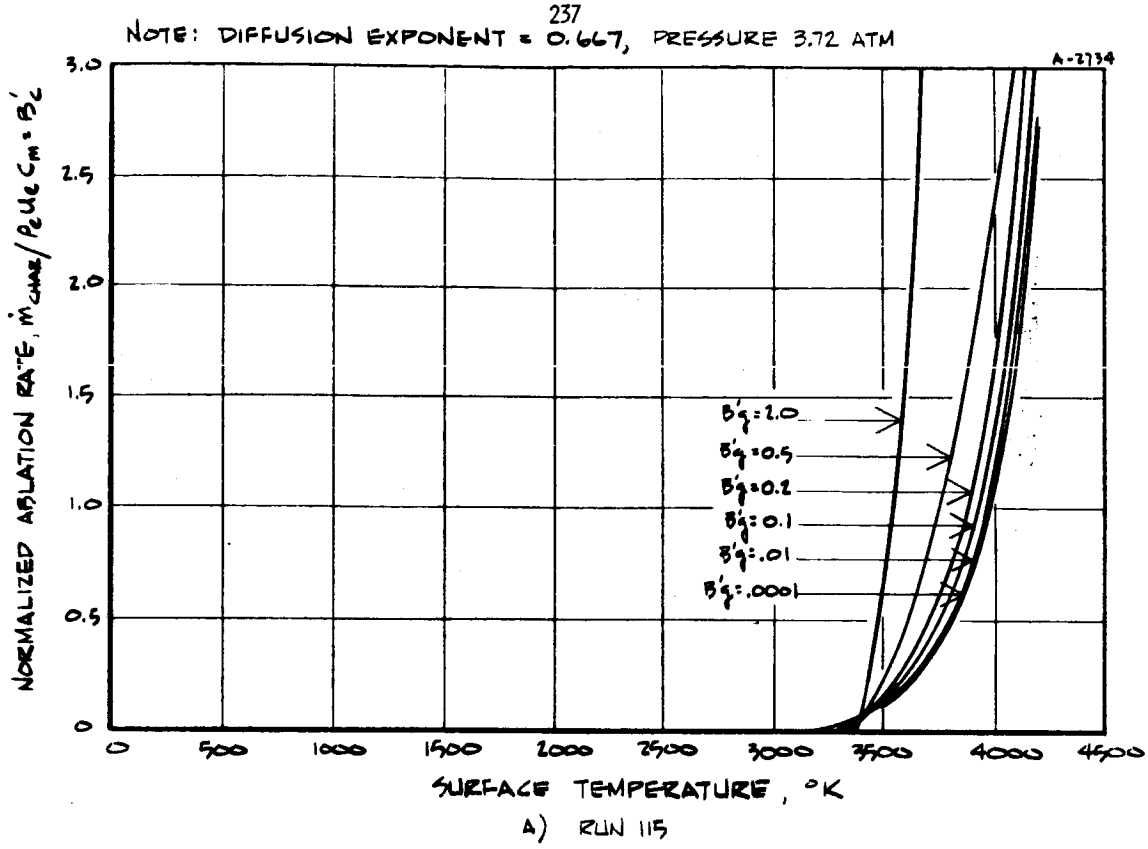
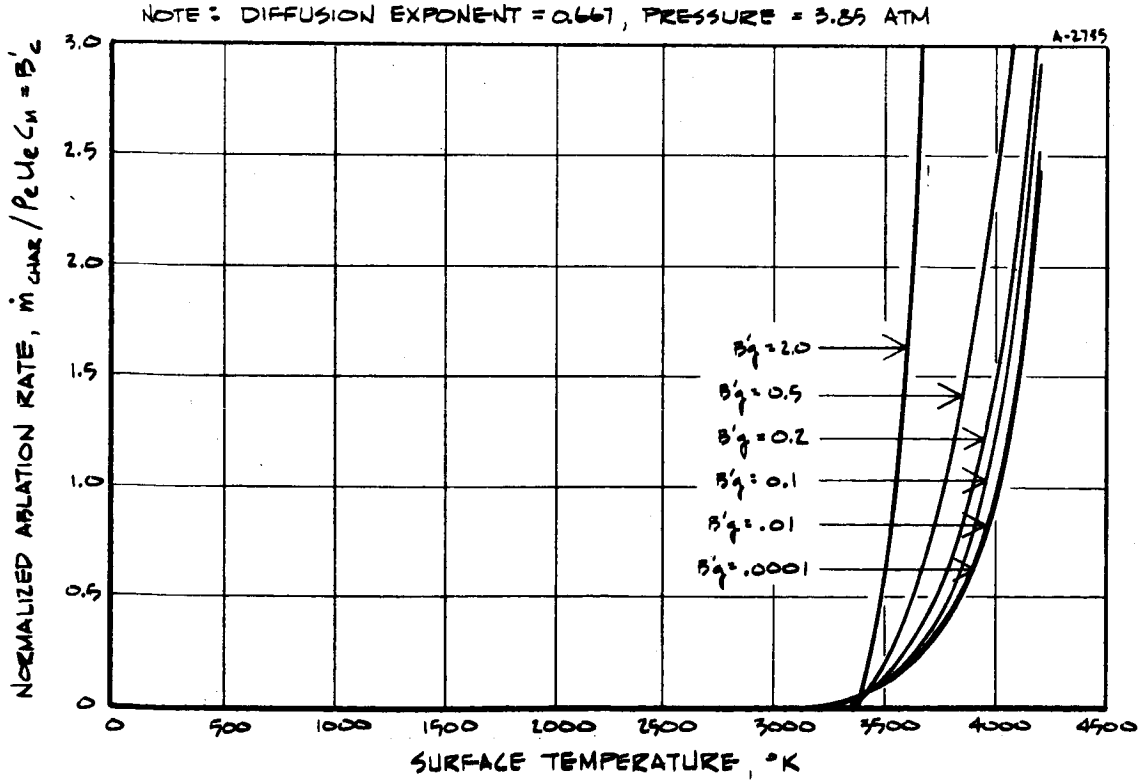


FIGURE 40 P



A) RUN 115

FIGURE 41 SURFACE THERMOCHEMICAL RESPONSE OF FM5064, GRAPHITE PHENYL-ALDEHYDE TO FLOX-PROPANE PROPELLANT



B) RUN 150

FIGURE 41, CONCLUDED

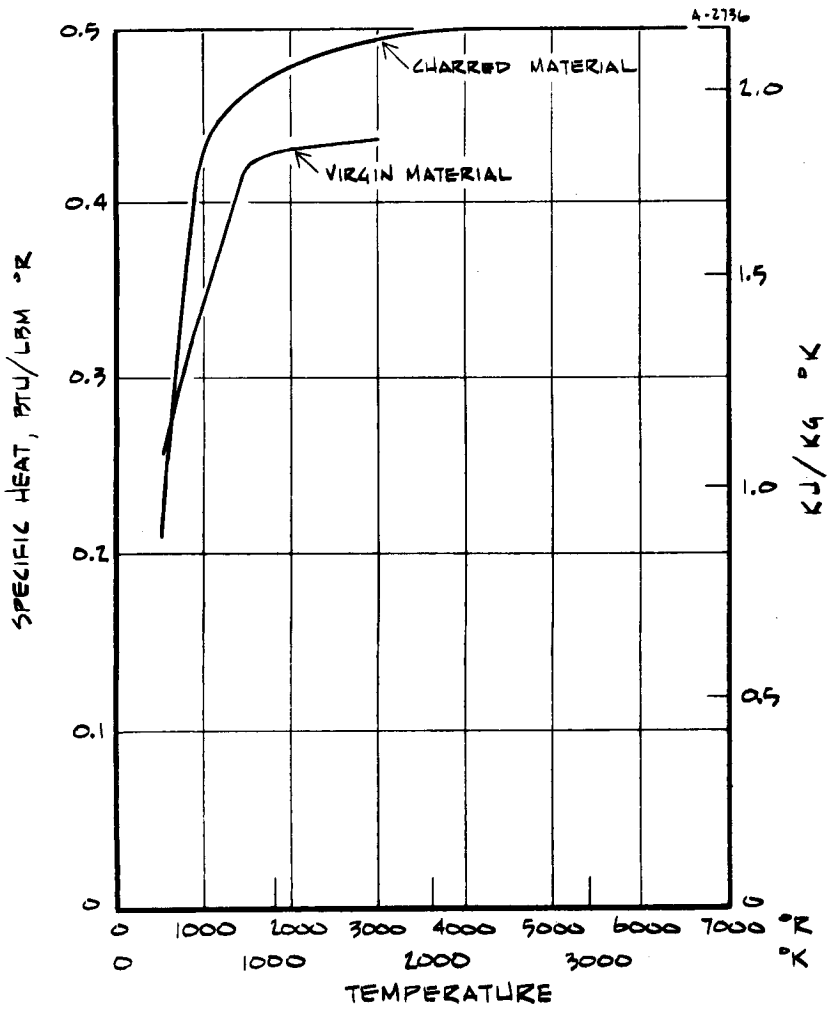


FIGURE 42 SPECIFIC HEAT OF FM 5064, GRAPHITE PHENOLIC

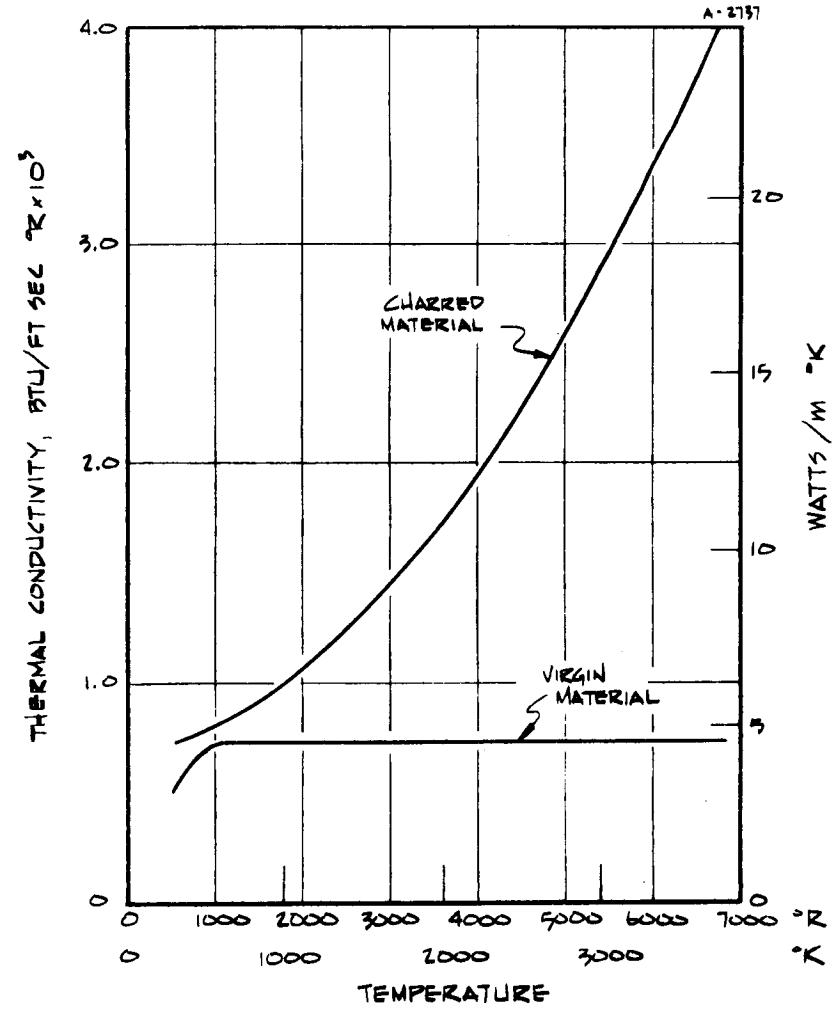


FIGURE 43 THERMAL CONDUCTIVITY OF 60° LAYUP FM 5064, GRAPHITE PHENOLIC

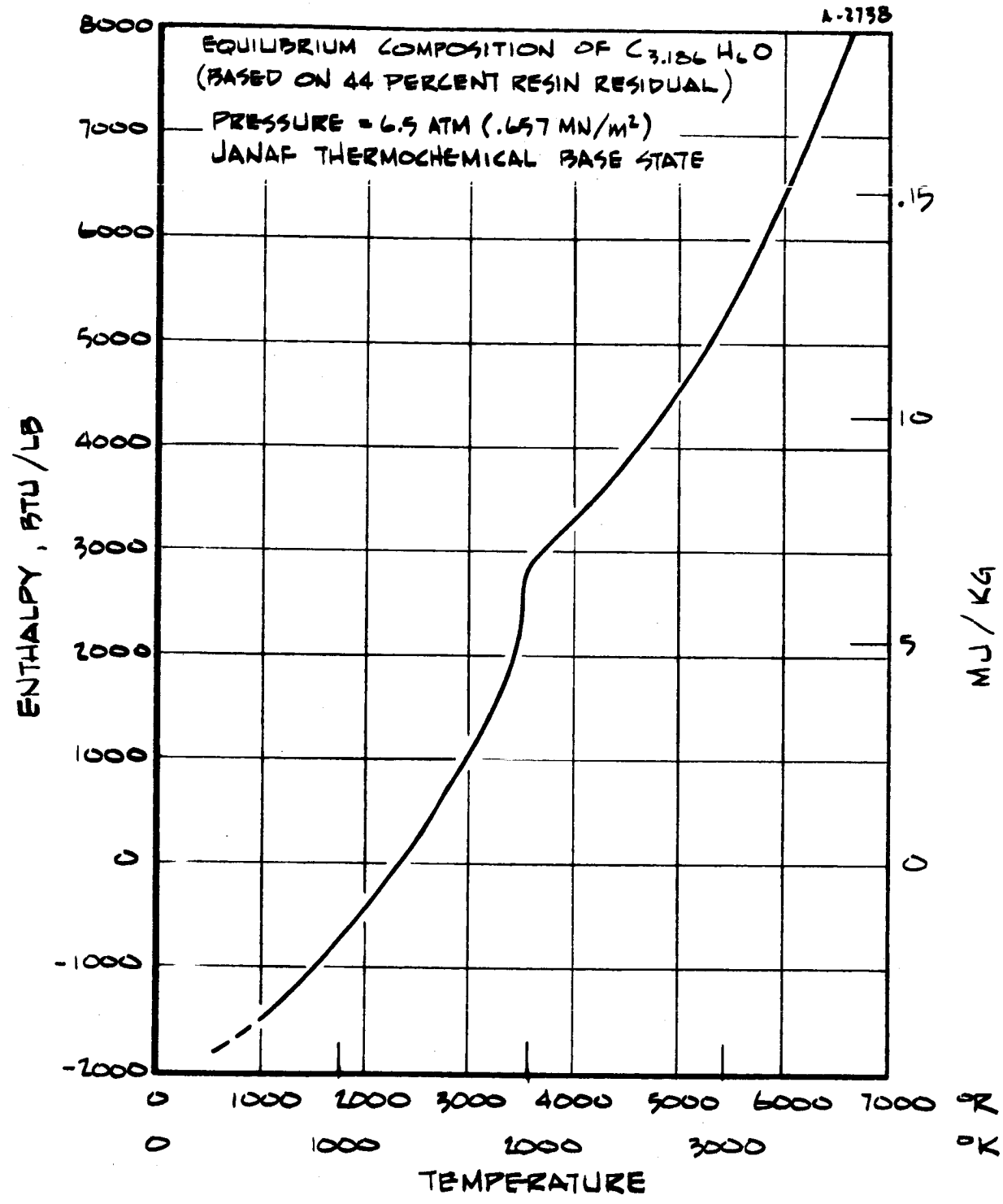
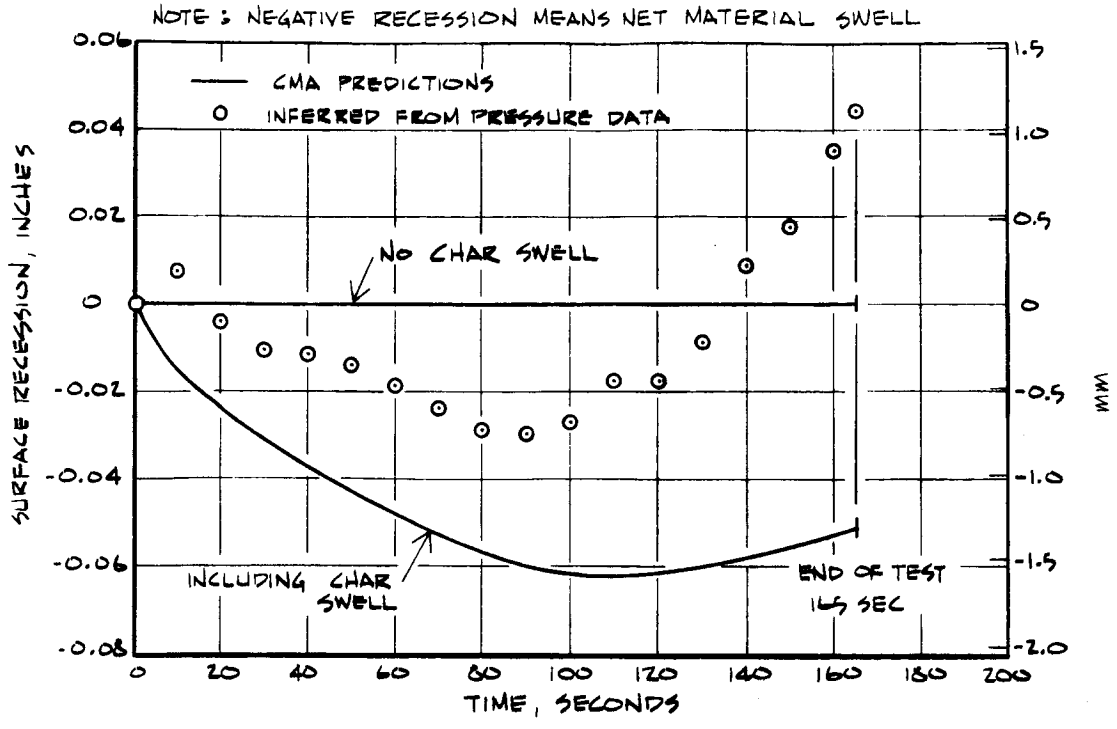


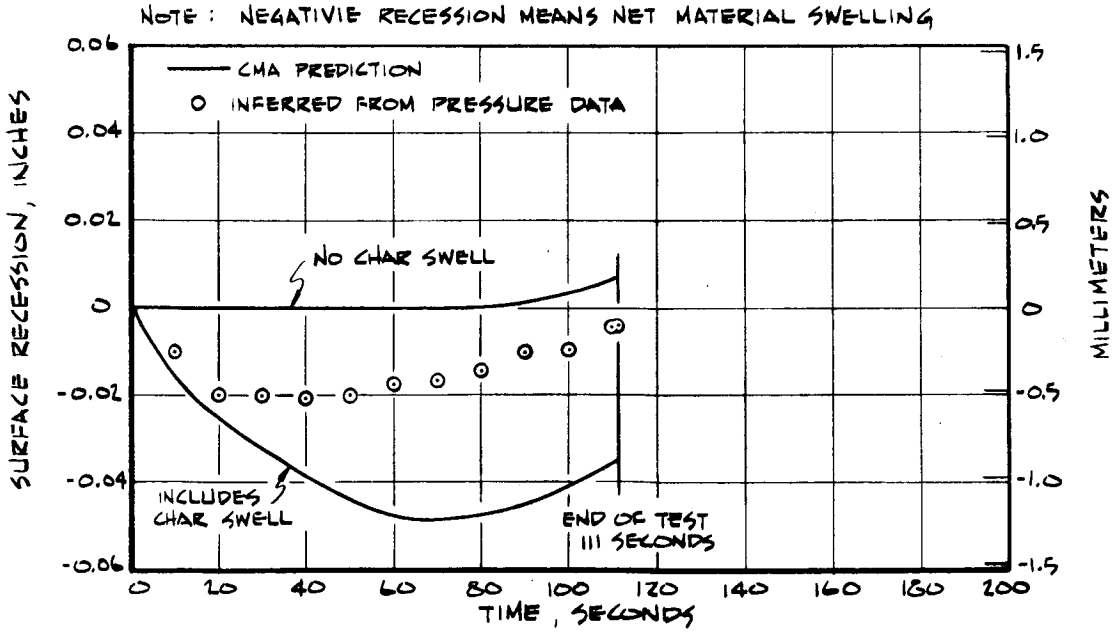
FIGURE 44 ENTHALPY OF FM5064, GRAPHITE PHENYL-ALDEHYDE PYROLYSIS GASES



A) RUN 115

FIGURE 45 COMPARISON OF MEASURED AND PREDICTED FM5064 GRAPHITE PHENYL-ALDEHYDE RESPONSE (FLOX-PROPANE PROPELLANT)

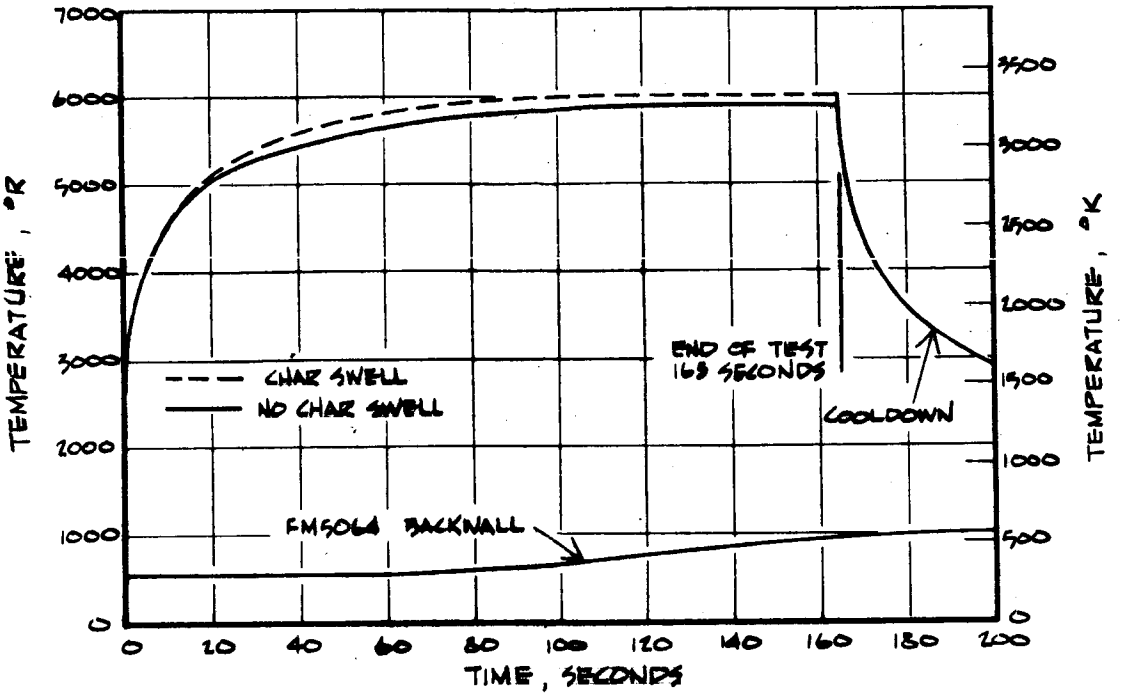
A-2119



B) RUN 150

FIGURE 45, CONCLUDED

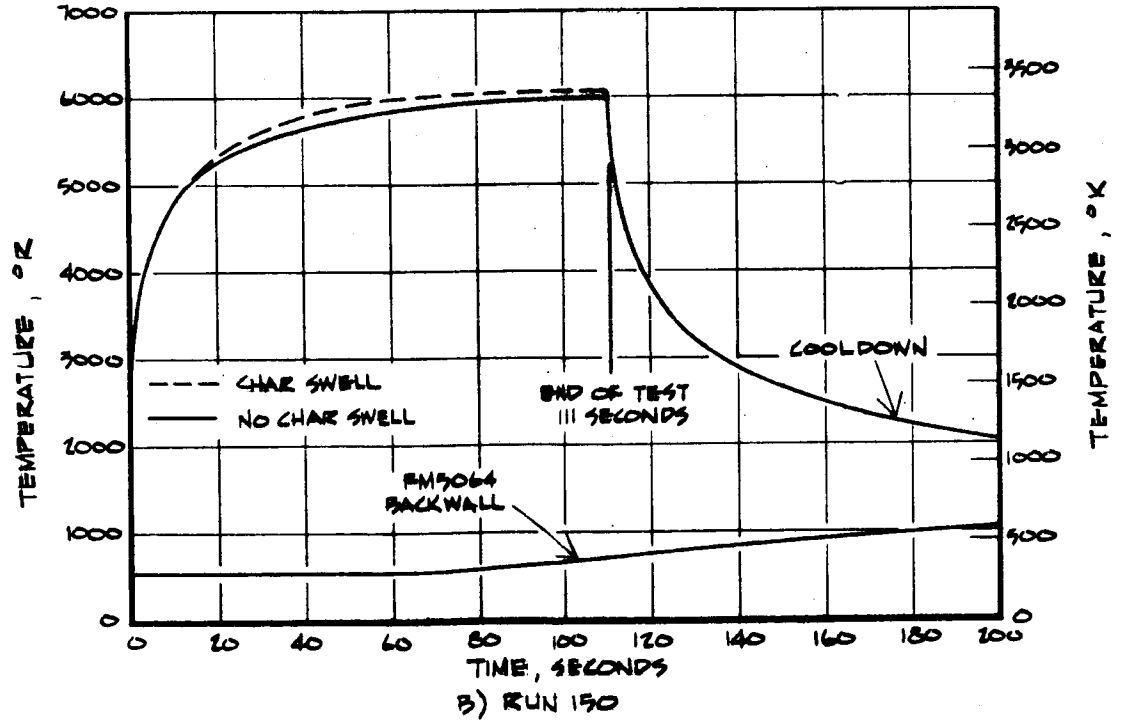
A-2140



A) RUN 115

FIGURE 46 PREDICTED TEMPERATURE RESPONSES FOR FM5064 GRAPHITE PHENYL-ALDEHYDE. (FLOX-PROPANE PROPELLANT)

A-2141



B) RUN 150

FIGURE 46, CONCLUDED

A-2142

APPENDIX A

AEROTHERM CHARRING MATERIAL ABLATIVE PROGRAM (CMA)

APPENDIX A
AEROTHERM CHARRING MATERIAL ABLATIVE PROGRAM (CMA)

General Description

The CMA program is a coded procedure for calculating the in depth thermal response of a charring, ablating material. The basic physics included correspond to simple charring. Initial versions of the program were described in Reference A-1, and subsequently a more complete description of the physics and mathematical treatment is given in Reference A-2. Reference A-3 is a program user's manual which describes input-output details.

The program is an implicit, finite-difference computational procedure for computing the one-dimensional transient transport of thermal energy in a three-dimensional isotropic material which can ablate from a front surface and which can decompose in depth. Decomposition (pyrolysis) reactions are based on a three-component model. The program permits up to eight different backup materials of arbitrary thickness. The back wall of the composite material may transfer energy by convection and radiation.

The ablating surface boundary condition may take one of three forms:

Option 1 - Film coefficient model convection-radiation heating with coupled mass transfer, including the effects of unequal heat and mass transfer coefficients (non-unity Lewis number) and unequal mass diffusion coefficients. Surface thermochemistry computations need not presume chemical equilibrium at the surface.

Option 2 - Specified surface temperature and surface recession rate.

Option 3 - Specified radiation view factor and incident radiation flux, as functions of time, for a stationary surface.

Any combination of the first three options may be used for a single computation. Option 3 is appropriate to cooldown after termination of convective heat input and is often useful in conjunction with Options 1 and 2.

The program permits the specification of a number of geometries, including plane, cylindrical or annular, and spherical. In the most general case, area may vary arbitrarily with depth.

The rear surface of the last node may be specified as insulated, or may experience convective and radiative heat transfer to a "reservoir" at a specified reservoir temperature if a rear surface convection coefficient and an emissivity are input.

Material properties such as thermal conductivity, specific heat, and emissivity are input as functions of temperature for virgin plastic and char.

For partially decomposed material, the program performs an appropriate averaging on density to determine effective material properties.

The basic solution procedure is by a finite difference approach. For each time step, the decomposition relations are solved and then the in-depth energy fluxes constructed in general terms. These are then harmonized with a surface energy balance (if a surface energy balance option is being used) and the in-depth temperatures determined. New material property values are set up and the solution is ready for the next time increment.

The CMA program outputs instantaneous mass ablation rates and blowing parameters for char and pyrolysis gas, total integrated mass ablation of char and pyrolysis gas, total recession and recession rates of surface, of the char line, and of the pyrolysis line. It also outputs the surface energy flux terms, namely, the energy convected in, energy radiated in, energy reradiated out, chemical generation, and conduction away (q_{cond}). Further, it describes how the input energy of q_{cond} is "accommodated" or "partitioned" in the solid material. Part of the energy is consumed in decomposing the plastic, part is consumed in sensible enthalpy changes of the solid, and part is "picked up" by the pyrolysis gases as they pass through the char. Thermocouple and isotherm output can also be called for.

Some Surface Energy Balance Details

In calculations under Option 1, the in-depth solution is coupled to a general film-coefficient boundary condition. This coupling could be accomplished through a direct calculation of the surface mass transfer, energy transfer, and chemical reaction events, but due to the non-linear aspect of the complicated surface events some complex iteration scheme would be required to accomplish this direct coupling. Instead of direct coupling, it has proved more expedient to prepare in advance a series of tables which include all the surface mass transfer and chemical relations. The in-depth solution may then be coupled to the surface events through a surface energy balance. For example when chemical equilibrium is achieved at the ablating surface and when no mechanical removal is occuring, the development presented in Reference A-4 describes the means for obtaining the thermodynamic state of the gas at the ablating surface in terms of the pressure, and char and pyrolysis off-gas rates.

$$\text{Thermodynamic state} = f(B'_g, B'_c, P)$$

where

$$B'_g = \frac{\dot{m}_g}{\rho_e u_e C_M} \qquad \text{(normalized pyrolysis off-gas rate)}$$

$$B'_c = \frac{\dot{m}_c}{\rho_e u_e C_M}$$ (normalized char recession rates)

P = boundary layer edge pressure

The thermodynamic state includes definition of surface temperature and gas molecular composition. This, in turn, enables evaluation of the various quantities appearing in the boundary layer driving potential for heat and mass transfer (Ref. A-4). Tables representing solutions to the functional relationship (A-1) are generated for a complete map covering the range of B'_g B'_c and P, of interest. These tables have, in the past, been generated with the Aerotherm EST program, Version 2 (Ref. A-5).

As an example of this procedure, suppose a table is prepared, which, for a parametric array of dimensionless char erosion rates (B'_c), dimensionless pyrolysis off-gas rates (B'_g), and pressure, presents the relevant ablating surface temperature and requisite boundary layer composition and enthalpy quantities. During each time step in the course of the in-depth solution the program generates a pyrolysis gas rate B'_g and computes the rate at which energy is conducted into the material from the surface. With B'_g and the pressure known, the input parametric tables then serve to define that B'_c which yields temperature and enthalpy quantities which provide a balanced, harmonized set of energy fluxes at the surface.

References to Appendix A

A-1 Rindal, R.A., Flood, D.T., and Kendall, R.M: Analytical and Experimental Study of Ablation Material for Rocket-Engine Application. Contract NAS 7-218, Vidya Report No. 201, NASA CR-54757, May 15, 1966.

A-2 Moyer, C.B. and Rindal, R. A.: Finite Difference Solution for the In-Depth Response of Charring Materials Considering Surface Chemical and Energy Balances. Aerotherm Corporation Final Report 66-7, Part II, March 14, 1967.

A-3 User's Manual, Charring Material Ablation Program (CMA) Version 2. Aerotherm Corporation, Palo Alto, California, June 1966.

A-4 Kendall, R.M., Rindal, R.A., and Bartlett, E.P.: A Multicomponent Boundary Layer Chemically Coupled to an Ablating Surface, AIAA Journal, Volume 5, No. 6, June 1967, pp. 1063-1071

A-5 User's Manual, Aerotherm Equilibrium Surface Thermochemistry Program (EST) Version 2, Aerotherm Corporation, Palo Alto, California, June 1966.

APPENDIX B

AEROTHERM CHARRING MATERIAL ABLATION PROGRAM AS MODIFIED FOR SILICA-CARBON REACTIONS INCLUDING MELTING PHENOMENA (SCRIMP)

APPENDIX B

AEROTHERM CHARRING MATERIAL ABLATION PROGRAM AS MODIFIED FOR SILICA-CARBON REACTIONS INCLUDING MELTING PHENOMENA (SCRIMP)

The SCRIMP code is a modified version of the CMA program (see Appendix A) developed specifically for silica reinforced charring materials. Two physical features important in the ablation of silica reinforced materials are not accounted for in CMA: subsurface chemical reactions between silica and carbon residue, and the removal of silica in liquid layer form.

The in-depth silica-carbon reaction is assumed to be;

$$SiO_2^* + C^* \rightarrow SiO + CO \qquad \text{(B-1)}$$

The rate of this reaction is computed for each node in the fully pyrolyed char according to the rate expression

$$\partial m_C/\partial\theta = m_C A\, e^{-E/RT} \qquad \text{(B-2)}$$

The rate parameters A and E are discussed in Reference 2. Nominal values, subject to much uncertainty, are $A = 9 \times 10^7$ sec^{-1}, E = 80000 cal/gr mole (.334 MJ/gr mole).

The computation of equation (B-2) involves two assumptions:

1. The pyrolysis gas passing through the char does not contribute carbon for this reaction. All the carbon supply is provided by the original carbon residue of pyrolysis.
2. The SiO + CO gas generated by this reaction differs sufficiently in its thermal and chemical properties from the pyrolysis gas originating from the decomposition of the resinous constituents of the virgin material that it is necessary to account for the amounts of each gas in calculating the in-depth response (and hence it is necessary in the construction of the surface thermochemistry tables to have two gas-rate parameters, rather than one, in the CMA program, as noted below).

The surface recession rate computed by SCRIMP is taken as the sum of any thermochemical erosion (usually zero, as will be discussed below) and a liquid layer removal term.

The accurate specification of the liquid layer removal rate would appear to be a highly complex matter involving pressure and shear stress

gradients, surface tension and stability phenomena, viscosity, and the role of the carbon residue matrix in supporting and retaining the silica layer. For the exploratory purposes of SCRIMP, the following simple assumptions were employed to obtain a reliable, rudimentary computation scheme which still appeared to model observed physical events with reasonable fidelity. (These assumptions are in addition to the assumptions regarding silica-carbon reactions described above; the numbering is continued):

3. A "liquid layer thickness" can be defined as the distance between the heated surface and the area where the density of carbon has been reduced, through the carbon silica reaction, to some specific value.
4. Liquid layer run off occurs so as to maintain a constant liquid layer thickness.
5. Any carbon particles in the liquid layer do not float off with any liquid layer flow.
6. The temperature drop across the liquid layer is small enough such that the removed liquid layer may be presumed isothermal and at the surface temperature.

This crude liquid layer treatment introduces two important input parameters: the carbon density ρ_c defining the location of the lower edge of the liquid layer, and the allowed liquid layer thickness δ_ℓ. It is hoped that calculations with a number of values of the two parameters can provide valuable insight useful in the construction of a more complete physical model.

The only computational aspect of this liquid layer model of particular interest concerns the calculation of the surface recession rate due to run-off. If the liquid-layer thickness is less than the maximum, the run-off recession rate is zero. If the thickness is momentarily greater than that allowed, the run-off recession rate is set equal to some value sufficient to reduce the liquid-layer thickness to the maximum allowed within the next few time steps in the computation.

The in depth reaction and liquid layer modification made to CMA to produce the SCRIMP code made necessary some changes in the surface thermochemistry treatment. Experience shows that economy of computation time and core storage limits the number of parameters in the surface thermochemistry tables to three. One must obviously be the usual thermochemical erosion rate B'_c. Another is, as usual, the pyrolysis gas injection rate B'_g. The third must be the injection rate of SiO + CO gas resulting from carbon-silica reactions in depth. The chemical composition of the "char" must be unique in order to avoid a fourth parameter, and in the absence of any

definitive information to the contrary, the composition of the chemically eroded char is assumed to be pure silica.

Thus the surface thermochemistry tables for SCRIMP have three parameters: The injection rate of pyrolysis gas; the injection rate of reaction gas, and the injection rate of char, B'_c . This contrasts with the CMA code treatment of the surface tables, which has the three parameters: pressure, pyrolysis gas rate, and char rate B'_c .

The SCRIMP program is discussed in detail in Reference 2 and 19.

APPENDIX C

AEROTHERM THERMOCHEMICAL STATE CODE (ACE)

APPENDIX C

AEROTHERM THERMOCHEMICAL STATE CODE (ACE)

General Capabilities

The ACE program solves for the equilibrium or kinetically controlled chemical composition for a variety of open or closed systems of arbitrary chemical composition. The equations which are solved, the solution procedure which is utilized, and the program characteristics are described in detail in Reference 21 and are summarized in Reference 7.

The ACE program has the following major options:

A. Closed System Chemistry
   1. Evaluation of equilibrium (or kinetically controlled time dependent) chemical state for assigned pressure, elemental composition of up to three component mixtures, and either enthalpy, entropy, or temperature. Provision is made for readily carrying out isentropic expansion and compressions.
   2. Solution of normal and oblique shock relations to provide the state of the gases downstream of the shock and the isentropic stagnation state.

B. Open System Chemistry
   1. Calculation of surface mass balances to determine a relationship between normalized char recession rate, normalized pyrolysis gas rate, surface temperature, and pressure while considering either equilibrium between the char and gases adjacent to it or while considering selected rate-controlled surface reactions.

All of these options are formulated for completely general chemical systems. Consideration of any molecular, atomic, ionic, or condensed species requires only the inclusion of the basic thermodynamic data appropriate for that species. These data are obtained, for example, from the JANAF Thermochemical Data Tables and include curve fit constants for entropy, specific heat, and heat of formation.

All options generate a complete state of the system, including molecular composition and thermodynamic and transport properties. The surface state option provides additional information as discussed below.

The surface state option of the ACE program contains a number of features which make it very powerful in the analysis of ablation data and

thus enables the determination of the governing surface physicochemical phenomena. In the first place, one does not have to choose a priori the surface species. For example, in the case of a silica reinforced material, even if minor constituents are neglected, the char surface could be SiO_2*, C*, SiC*, Si* or Si_3N_4*. The thermochemically controlling species will be discovered by ACE as part of the solution process. Secondly, it is possible to isolate species or component gas mixtures from the system or to consider rate-controlled surface reactions or surface-catalyzed homogeneous reactions. Thirdly, each condensed species can be assigned a fail temperature above which it cannot serve as the surface. This latter capability can be used to represent mechanical removal of a species or removal of a species above its melt temperature. A fourth major capability of the ACE program is that it permits consideration of unequal diffusion coefficients as well as unequal heat and mass-transfer coefficients through an application of an approximation for binary diffusion coefficients. A principal limitation of the ACE program is that the surface is considered to be homogeneous. To illustrate, the surface of a silica reinforced material would be predicted to be <u>one</u> of the species listed above, but not a mixture of two or more of these species.

The surface state options of the ACE program provide a char recession rate normalized by a mass-transfer coefficient, and other information needed to perform an energy balance on the surface of a charring ablation material, as a function of pyrolysis gas rate normalized by the same mass-transfer coefficient, surface temperature, and pressure. It thus does not by itself constitute an ablation prediction tool. In the first place, it is necessary to specify the mass-transfer coefficient and this cannot be done precisely without solving the boundary-layer equations. Secondly, the determination of surface temperature requires the solution of a surface energy balance. One procedure which is used for ablation predictions is to generate surface state solutions with the ACE program in the form of punched card output. This is then used as input to the CMA and SCRIMP programs (Option 1) which perform the surface energy balance; the operation of this coupled ablation prediction is discussed in Appendices A and B.

APPENDIX D

SYMBOLS

LIST OF SYMBOLS

A	Area or pre-exponential in Arrhenius equation.
A*	Throat area.
B'	Mass flux normalized by mass transfer coefficient.
C	Specific heat.
C*	Characteristic velocity (see equation 1)
C^*/C^*_{OPT}	Ratio of characteristic velocity to optimum characteristic velocity.
$C^*/C^*_{OPT})$ O/F=2	Specially defined C* ratio for relating arc plasma generator operating conditions to characteristic velocity.
dt	dummy temperature increment (see equation 8).
$d\tau_w/ds$, d^2p/ds^2	derivatives of shear and pressure gradient with axial coordinate.
D	diameter
E/R	activation energy of Arrhenius equation
f( )	function of
H	enthalpy, various subscripts defined locally.
K_i	mass fraction of i.
K_{KE}	mass fraction of element K in the free stream.
$\dot{m}$	mass flow rates
O/F	propellant mass oxidizer to fuel ratio
P	pressure, various subscripts
Pr	Prandtl Number
q	heat rate per unit area
R_{e_Θ}	momentum thickness Reynolds number.
S	axial nozzle flow dimension, or surface recession
$\dot{S}$	surface recession rate.
T	temperature, various subscripts defined locally
U	velocity
UDMH	unsymmetrical dimethyl hydrazine ($C_2N_2H_8$)

GREEK

Δ	finite change
ΔH_{fi}^{Td}	heat of formation of the i^{th} species at the temperature datum (T_d).
ρ	density, various subscripts.

$\rho_e U_e C_H$	heat transfer coefficient (Stanton No. times mass flux), kg/m^2 sec.
μ	viscosity (see equation 14)
Θ	time.

SUBSCRIPTS

A or arc	arc plasma generator test.
d	datum
e	edge condition.
i	summation index.
i, inj	per injection species.
o	total (chamber) condition, or non-blowing.
ox	oxidizer (i.e. nitrogen tetroxide, N_2O_4).
r	recovery.
R	rocket
w	wall (or surface)
*	throat.

REFERENCES

1. Rindal, R. A., Flood, D. T., and Kendall, R. M.: Analytical and Experimental Study of Ablation Material for Rocket-Engine Application. Vidya, Inc., Palo Alto, California, Vidya Report No. 201, NASA CR-54757, May 15, 1966.

2. Rindal, R. A., Clark, K. J., Moyer, C. B., and Flood, D. T.: Experimental and Theoretical Analysis of Ablative Material Response in A Liquid-Propellant Rocket Engine, Aerotherm Corporation, Mountain View, California, Aerotherm Report No. 67-15, NASA CR-72301 September 1967.

3. JANAF Thermochemical Tables. The Dow Co., Midland, Michigan.

4. Bartz, D. R.: A Simple Equation for Rapid Estimation of Rocket Nozzle Convective Heat-Transfer Coefficients. Jet Prop., January 1957, p. 49.

5. Blackwell, B. F. and Kaestner, P. C.: Sandia One-Dimensional Direct and Inverse Transient (SODDIT) Program. Sandia Laboratories, Albuquerque, New Mexico (to be published).

6. Touloukian, Y. S., ed.: Thermophysical Properties of High Temperature Solid Materials, Vol 1, Elements, Thermophysical Properties Research Center, Purdue University, Lafayette, Indiana, 1966.

7. Powers, C. A. and Kendall, R. M.: User's Manual, Aerotherm Chemical Equilibrium (ACE) Computer Program, Aerotherm Corporation, Mountain View, California, May 1969.

8. Schaefer, J. W., and Dahm, T. J.: Studies of Nozzle Ablative Material Performance for Large Solid Boosters. Aerotherm Corporation, Mountain View, California, Aerotherm Report 66-2, NASA CR-72080, December 1966.

9. Bartlett, E. P., and Kendall, R. M.: An Analysis of the Coupled Chemically Reacting Boundary Layer and Charring Ablator. Part III; Nonsimilar Solution of the Multicomponent Laminar Boundary Layer by an Integral Matrix Method. Aerotherm Corporation, Mountain View, California, Aerotherm Report 66-7, Part III, NASA CR-1062, June 1968.

10. Anderson, L. W., and Kendall, R. M.: A Nonsimilar Solution for Multicomponent Reacting Laminar and Turbulent Boundary Layer Flows Including Transverse Curvature. Aerotherm Corporation, Mountain View, California, Aerotherm Report 69-54, AFWL-TR-69-106, October, 1969.

11. Kays, W. M.: Convective Heat and Mass Transfer. McGraw-Hill, New York, 1966, p. 92.

12. McCuen, P. A., Schaefer, J. W., Lundberg, R. E. and Kendall, R. M.: A Study of Solid-Propellant Rocket Motor Exposed Materials Behavior. Vidya Inc., Palo Alto, California, Vidya Report No. 149, AFRPL-TR-65-33, February 1965 (AD-462331).

13. Schaefer, J. W., Baker, D. B. and Wool, M. R.: Development of a Total Heat Flux Measurement System, Phase I Report: Study and Design. Aerotherm Corporation, Mountain View, California, Contract No. F04611-68-C-0086, Aerotherm Report 68-40, September 1968.

14. Dow, M. B.: Comparisons of Measurements of Internal Temperatures In Ablation Materials by Various Thermocouple Configurations. NASA TN-D-2165, November 1964.

15. Moyer, C. B. and Rindal, R. A.: An Analysis of the Coupled Chemically Reacting Boundary Layer and Charring Ablator. Part II; Finite Difference Solution for the In Depth Response of Charring Materials Considering Surface Chemical and Energy Balances. Aerotherm Corporation, Mountain View, California, Aerotherm Report 66-7, Part II, NASA CR-1061, June 1968.

16. User's Manual, Charring Material Ablation Program (CMA), Version 2. Aerotherm Corporation, Mountain View, California, Second Edition, January 1969.

17. Fortran Variable Names, Supplement to User's Manual, Aerotherm Charring Material Ablation Program (CMA), Aerotherm Corporation, Mountain View, California, February 1966.

18. Flow Charts, Supplement to User's Manual, Aerotherm Charring Material Ablation Program (CMA), Aerotherm Corporation, Mountain View, California, April 1966.

19. User's Manual, Aerotherm Charring Material Ablation Program with Silica-Carbon Kinetics and Including Melting Phenomena (SCRIMP), Aerotherm Corporation, Mountain View, California, March 1969.

20. Moyer, C. B., Anderson, L. W. and Dahm, T. J.: A Coupled Computer Code for the Transient Response and Ablation of Non-Charring Heat Shields and Nose Tips, Aerotherm Corporation, Mountain View, California, Contract No. NAS1-8501, Aerotherm Report No. 69-60, August 1969.

21. Kendall, R. M.: An Analysis of the Coupled Chemically Reacting Boundary Layer and Charring Ablation. Part V; A General Approach to the Thermochemical Solution of Mixed Equilibrium - Nonequilibrium, Homogeneous or Heterogeneous Systems. Aerotherm Corporation, Mountain View, California, Aerotherm Report No. 66-7, Part V, NASA CR-1064, June 1968.

22. Baker, D. B., Wool, M. R. and Schaefer, J. W.: A Dynamic Technique for Determining the Thermal Conductivity of Charring Materials. Presented at the Eighth Conference on Thermal Conductivity, October 7-11, 1968.

23. Schaefer, J. W., Rodriguez, D. A., Reese, J. J., Jr. and Wool, M. R.: Studies of Ablative Material Performance for Solid Rocket Nozzle Applications. Aerotherm Corporation, Mountain View, California, Aerotherm Report 68-30, NASA CR-72429, March 1968.

24. Rindal, R. A. and Moyer, C. B.: Comment on "Carbon-Silica Reaction in Silica-Phenolic Composites" AIAA Journal, Vol. 6, No. 5, pp. 991-2, May 1968.

25. Private Communication with Erwin Edelman, NASA Lewis Research Center, March 1970.

26. Wool, M. R. and Moyer, C. B.: Theoretical Predictions of the Variation of Silica Phenolic Ablation with Liquid-Propellant Mixture Ratio. Aerotherm Corporation, Mountain View, California, Aerotherm Report 68-43 (and Appendix E, Attachment 1 to NASA CR-72512, March 1969).

27. Grose, R. D.: A study of the Boundary Flow in A Rocket Combustion Chamber. Part I, Summary. Aerotherm Corporation, Mountain View, California, Aerotherm Final Report 69-51 for NASA Contract NAS7-463, Sept. 22, 1969.

"Ablative Response of a Silica Phenolic to Simulated Liquid Propellant Rocket Engine Operating Conditions"
NAS3-10291 CR-72702 Aerotherm

DISTRIBUTION LIST FOR FINAL REPORT

Instructions:

Final reports are to be sent directly to the "Recipient" and the "Designee" per the quantities specified in the respective columns, R and D. When no copies are specified in column D, a carbon copy of the letter of transmittal should be sent to the person named as the "Designee". The letter of transmittal should contain the contract number and complete title of the final report.

The distribution list, indicating all of the Recipients and Designees, should be included in the final report as an appendix.

REPORT COPIES R	D	RECIPIENT	DESIGNEE
		National Aeronautics & Space Administration Lewis Research Center 21000 Brookpark Road Cleveland, Ohio 44135	
1		Attn: Contracting Officer, MS 500-313	
3		E. A. Bourke, M. S. 500-203	
1		Technical Report Control Office, MS 5-5	
1		Technology Utilization Office, MS 3-16	
2		AFSC Liaison Office, 501-3	
2		Library	
1		Office of Reliability & Quality Assurance, MS 500-111	
1		D. L. Nored, Chief, LRTB, MS 500-209	
8		E. A. Edelman	Project Manager, MS 500-209
1		E. W. Conrad, MS 500-204	
1		R. H. Kemp, MS 49-1	
1		R. H. Knoll, MS 501-2	
1		J. W. Gregory, M.S. 500-209	
2		Chief, Liquid Experimental Engineering, RPX Office of Advanced Research & Technology NASA Headquarters Washington, D.C. 20546	
2		Chief, Liquid Propulsion Technology, RPL Office of Advanced Research & Technology NASA Headquarters Washington, D.C. 20546	
1		Director, Launch Vehicles & Propulsion, SV Office of Space Science & Applications NASA Headquarters Washington, D.C. 20546	

REPORT COPIES R D	RECIPIENT	DESIGNEE
1	Director, Advanced Manned Missions, MT Office of Manned Space Flight NASA Headquarters Washington, D.C. 20546	
6	NASA Scientific & Technical Information Facility P.O. Box 33 College Park, Maryland 20740	
1	Director, Technology Utilization Division Office of Technology Utilization NASA Headquarters Washington, D.C. 20546	
1	National Aeronautics & Space Administration Ames Research Center Moffett Field, California 94035 Attn: Library	Hans M. Mark Mission Analysis Division
1	National Aeronautics & Space Administration Flight Research Center P.O. Box 273 Edwards, California 93523 Attn: Library	
1	National Aeronautics & Space Administration Goddard Space Flight Center Greenbelt, Maryland 20771 Attn: Library	Manfred L. Morrison, Code 620
1	National Aeronautics & Space Administration John F. Kennedy Space Center Cocoa Beach, Florida 32931 Attn: Library	Dr. Kurt H. Debus
1	National Aeronautics & Space Administration Langley Research Center Langley Station Hampton, Virginia 23365 Attn: Library	E. Cortwright Director
1	National Aeronautics & Space Administration Manned Spacecraft Center Houston, Texas 77001 Attn: Library	J. G. Thibodaux, Jr. Chief, Propulsion & Power Division
1	National Aeronautics & Space Administration George C. Marshall Space Flight Center Huntsville, Alabama 35812 Attn: Library	Leon J. Hastings James Thomas
1	Jet Propulsion Laboratory 4800 Oak Grove Drive Pasadena, California 91103 Attn: Library	Henry Burlage, Jr. Duane Dipprey

REPORT COPIES R	D	RECIPIENT	DESIGNEE
1		Defense Documentation Center Cameron Station Building 5 5010 Duke Street Alexandria, Virginia 22314 Attn: TISIA	
1		Office of the Director of Defense Research & Engineering Washington, D.C. 20301 Attn: Office of Asst. Dir. (Chem. Technology)	
1		RTD (RTNP) Bolling Air Force Base Washington, D.C. 20332	
1		Arnold Engineering Development Center Air Force Systems Command Tullahoma, Tennessee 37389 Attn: Library	Dr. H. K. Doetsch
1		Advanced Research Projects Agency Washington, D.C. 20525 Attn: Library	
1		Aeronautical Systems Division Air Force Systems Command Wright-Patterson Air Force Base, Dayton, Ohio Attn: Library	D. L. Schmidt. Code ARSCNC-2
1		Air Force Missile Test Center Patrick Air Force Base, Florida Attn: Library	L. J. Ullian
1		Air Force Systems Command Andrews Air Force Base Washington, D.C. 20332 Attn: Library	Capt. S. W. Bowen SCLT
1		Air Force Rocket Propulsion Laboratory (RPR) Edwards, California 93523 Attn: Library	
1		Air Force Rocket Propulsion Laboratory(RPM) Edwards, California 93523 Attn: Library	
1		Air Force FTC (FTAT-2) Edwards Air Force Base, California 93523 Attn: Library	Donald Ross
1		Air Force Office of Scientific Research Washington, D.C. 20333 Attn: Library	SREP, Dr. J. F. Masi

REPORT COPIES R D	RECIPIENT	DESIGNEE
1	Space & Missile Systems Organization Air Force Unit Post Office Los Angeles, California 90045 Attn: Technical Data Center	
1	Office of Research Analyses (OAR) Holloman Air Force Base, New Mexico 88330 Attn: Library RROR	
1	U. S. Air Force Washington, D.C. Attn: Library	Col. C. K. Stambaugh, Code AFRST
1	Commanding Officer U. S. Army Research Office (Durham) Box CM, Duke Station Durham, North Carolina 27706 Attn: Library	
1	U. S. Army Missile Command Redstone Scientific Information Center Redstone Arsenal, Alabama 35808 Attn: Document Section	Dr. W. Wharton
1	Bureau of Naval Weapons Department of the Navy Washington, D.C. Attn: Library	J. Kay, Code RTMS-41
1	Commander U. S. Naval Missile Center Point Mugu, California 93041 Attn: Technical Library	
1	Commander U. S. Naval Weapons Center China Lake, California 93557 Attn: Library	
1	Commanding Officer Naval Research Branch Office 1030 E. Green Street Pasadena, California 91101 Attn: Library	
1	Director (Code 6180) U. S. Naval Research Laboratory Washington, D.C. 20390 Attn: Library	H. W. Carhart J. M. Krafft
1	Picatinny Arsenal Dover, New Jersey 07801 Attn: Library	I. Forsten

REPORT COPIES R	D	RECIPIENT	DESIGNEE
1		Air Force Aero Propulsion Laboratory Research & Technology Division Air Force Systems Command United States Air Force Wright-Patterson AFB, Ohio 45433 Attn: APRP (Library)	R. Quigley C. M. Donaldson
1		Space Division Aerojet-General Corporation 9200 East Flair Drive El Monte, California 91734 Attn: Library	S. Machlawski
1		Aerojet Liquid Rocket Company P. O. Box 15847 Sacramento, California 95813 Attn: Technical Library 2484-2015A	R. Stiff
1		Aeronutronic Division of Philco Ford Corp. Ford Road Newport Beach, California 92663 Attn: Technical Information Department	Dr. L. H. Linder
1		Aerospace Corporation 2400 E. El Segundo Blvd. Los Angeles, California 90045 Attn: Library-Documents	J. G. Wilder
1		Arthur D. Little, Inc. 20 Acorn Park Cambridge, Massachusetts 02140 Attn: Library	A. C. Tobey
1		Astropower Laboratory McDonnell-Douglas Aircraft Company 2121 Paularino Newport Beach, California 92163 Attn: Library	
1		ARO, Incorporated Arnold Engineering Development Center Arnold AF Station, Tennessee 37389 Attn: Library	
1		Susquehanna Corporation Atlantic Research Division Shirley Highway & Edsall Road Alexandria, Virginia 22314 Attn: Library	
1		Beech Aircraft Corporation Boulder Facility Box 631 Boulder, Colorado Attn: Library	Douglas Pope

REPORT COPIES R D	RECIPIENT	DESIGNEE
1	Bell Aerosystems, Inc. Box 1 Buffalo, New York 14240 Attn: Library	W. M. Smith
1	Bellcomm 955 L'Enfant Plaza, S. W. Washington, D.C. Attn: Library	H. S. London
1	Boeing Company Space Division P.O. Box 868 Seattle, Washington 98124 Attn: Library	J. D. Alexander C. F. Tiffany
1	Boeing Company P.O. Box 1680 Huntsville, Alabama 35801	Ted Snow
1	Chemical Propulsion Information Agency Applied Physics Laboratory 8621 Georgia Avenue Silver Spring, Maryland 20910	Tom Reedy
1	Chrysler Corporation Missile Division P.O. Box 2628 Detroit, Michigan Attn: Library	John Gates
1	Curtiss-Wright Corporation Wright Aeronautical Division Woodridge, New Jersey Attn: Library	G. Kelley
1	Republic Aviation Fairchild Hiller Corporation Farmington, Long Island New York	
1	General Dynamics/Convair P. O. Box 1128 San Diego, California 92112 Attn: Library	Frank Dore
1	Missiles and Space Systems Center General Electric Company Valley Forge Space Technology Center P. O. Box 8555 Philadelphia, Pa. 19101 Attn: Library	A. Cohen F. Schultz

REPORT COPIES R D	RECIPIENT	DESIGNEE
1	Grumman Aircraft Engineering Corporation Bethpage, Long Island, New York Attn: Library	Joseph Gavin
1	Hercules Powder Company Allegheny Ballistics Laboratory P. O. Box 210 Cumberland, Maryland 21501 Attn: Library	
1	Honeywell Inc. Aerospace Division 2600 Ridgeway Road Minneapolis, Minnesota Attn: Library	
1	IIT Research Institute Technology Center Chicago, Illinois 60616 Attn: Library	C. K. Hersh
1	Kidde Aer-Space Division Walter Kidde & Company, Inc. 567 Main Street	R. J. Hanville
1	Ling-Temco-Vought Corporation P. O. Box 5907 Dallas, Texas 75222 Attn: Library	
1	Lockheed Missiles and Space Company P. O. Box 504 Sunnyvale, California 94087 Attn: Library	
1	Lockheed Propulsion Company P. O. Box 111 Redlands, California 92374 Attn: Library, Thackwell	H. L. Thackwell
1	Marquardt Corporation 16555 Saticoy Street Box 2013 - South Annex Van Nuys, California 91409	L. R. Bell Jr.
1	Radio Corporation of America Astro-Electronics Products Princeton, New Jersey Attn: Library	
1	Rocket Research Corporation Willow Road at 116th Street Redmond, Washington 98052 Attn: Library	F. McCullough, Jr.

REPORT COPIES R	D	RECIPIENT	DESIGNEE
1		Stanford Research Institute 333 Ravenswood Avenue Menlo Park, California 94025 Attn: Library	Dr. Gerald Marksman
1		Thiokol Chemical Corporation Redstone Division Huntsville, Alabama Attn: Library	John Goodloe
1		TRW Systems Inc. 1 Space Park Redondo Beach, California 90278 Attn: Tech. Lib. Doc. Acquisitions	D. H. Lee
1		Denver Division Martin-Marietta Corporation P. O. Box 179 Denver, Colorado 80201 Attn: Library	Dr. Morganthaler F. R. Schwartzberg
		Rocketdyne Division North American Rockwell Inc. 6633 Canoga Avenue Canoga Park, California 91304 Attn: Library, Department 596-306	Dr. R. J. Thompson S . F. Iacobellis
1		Space & Information Systems Division North American Rockwell 12214 Lakewood Blvd. Downey, California Attn: Library	
1		Northrop Space Laboratories 3401 West Broadway Hawthorne, California Attn: Library	Dr. William Howard
1		Purdue University Lafayette, Indiana 47907 Attn: Library (Technical)	Dr. Bruce Reese
1		United Aircraft Corporation United Technology Center P. O. Box 358 Sunnyvale California 94038 Attn: Library	Dr. David Altman